

COMPUTATIONAL MODELS OF SKIN  
MECHANICS AND MECHANOBIOLOGY

A DISSERTATION  
SUBMITTED TO THE DEPARTMENT OF MECHANICAL ENGINEERING  
AND THE COMMITTEE ON GRADUATE STUDIES  
OF STANFORD UNIVERSITY  
IN PARTIAL FULFILLMENT OF THE REQUIREMENTS  
FOR THE DEGREE OF  
DOCTOR OF PHILOSOPHY

Adrian Buganza Tepole  
August 2015

© 2015 by Adrian Buganza Tepole. All Rights Reserved.  
Re-distributed by Stanford University under license with the author.

This dissertation is online at: <http://purl.stanford.edu/nh346ff4872>

I certify that I have read this dissertation and that, in my opinion, it is fully adequate in scope and quality as a dissertation for the degree of Doctor of Philosophy.

**Ellen Kuhl, Primary Adviser**

I certify that I have read this dissertation and that, in my opinion, it is fully adequate in scope and quality as a dissertation for the degree of Doctor of Philosophy.

**Peter Pinsky**

I certify that I have read this dissertation and that, in my opinion, it is fully adequate in scope and quality as a dissertation for the degree of Doctor of Philosophy.

**Charles Steele**

Approved for the Stanford University Committee on Graduate Studies.

**Patricia J. Gumpert, Vice Provost for Graduate Education**

*This signature page was generated electronically upon submission of this dissertation in electronic format. An original signed hard copy of the signature page is on file in University Archives.*

# Preface

Skin is our interface to the world, it protects our internal machinery, regulates our temperature, fluid exchange, and resists constant wear and tear. Skin has remarkable mechanical properties, it is a thin structure that can undergo large deformations without rupturing, letting us move around, interact with the objects in our surroundings, and express ourselves. Additionally, our integument is a living system and it can adapt to mechanical and environmental cues. In summary, mechanical integrity of skin is crucial to our survival. Understanding the mechanics and mechanobiology of skin is also important for the clinician since disruption of mechanical homeostasis appears often in disease and repair. This dissertation focuses on the problems of plastic and reconstructive surgery in which skin adapts to mechanical scenarios. These include tissue expansion, flap design and wound healing. Tissue expansion is a well-known technique to resurface large defects by growing skin *in vivo*. Skin grows in response to overstretch. Despite its numerous advantages and wide-spread, this technique does not lack complications and suboptimal outcomes. A major reason lies in the lack of quantitative tools to understand the fundamental aspects of skin growth to overstretch that can be then used to predict and guide preoperative planning. In this thesis, I show how applying the classical theories of mechanics and incorporating the description of finite growth by the multiplicative split of the deformation gradient into growth and elastic contributions, it is possible to get biological insight into the dynamics of skin growth in response to mechanical deformations. Furthermore, this approach is suitable for an efficient computational implementation using finite elements. I show how simulations can predict the effect of different expander geometries and sizes which are variables of clinical significance. The same set of tools can be used in patient specific scenarios. I demonstrate the use of computational simulations on geometries obtained from computer tomography scans of pediatric patients. In order to validate and calibrate the model, I designed and conducted animal experiments in collaboration with surgeons at Northwestern

University. We established a novel experimental protocol that uses multi-view stereo and B-spline isogeometric analysis to capture the kinematics of expanded porcine integument. We show experimentally how overstretch triggers the growth of new skin. We compared different expander shapes and inflation protocols. We also quantified for the first time the development of residual stresses over a sizable patch of tissue. Tissue expansion is at the core of this dissertation, however, once new skin is grown there are two other processes of mechanical interest that become relevant: flap design and wound healing. These phenomena are also relevant for a vast majority of plastic and reconstructive surgery procedures and not only tissue expansion. I present the comparison of different flap designs on grown skin patches and show that the double back cut flap produces an overall lower stress distribution for the same size of defect as compared to the advancement flap. I also show how the orientation of the underlying collagen network plays an important role in the preoperative planning. Finally, another major concern regarding the restoration of mechanical homeostasis of skin is the process of wound healing and scarring. I present a generic framework for the coupled mechano-chemo-biological problem of wound healing. Starting from the mechanics perspective, I use state-of-the-art constitutive laws of skin to model it as an anisotropic hyperelastic material in terms of structurally motivated parameters. The load bearing properties of skin are attributed to the collagen content. When skin is wounded, the collagen architecture is abruptly disrupted. During healing, different cell populations act in coordination through various cell-signaling pathways in order to lay down and remodel the collagen microstructure. In the proposed framework, micro-structural parameters such as the collagen content become part of the evolving fields that have to be characterized as they change over time and space. I incorporate the mechanobiology coupling by making these parameters a function of cellular response. In turn, I introduce a new set of reaction-diffusion partial differential equations to model the dynamics of cell density fields and the chemical signals that regulate the cell behavior. The generic framework I propose is implemented in a monolithic finite element formulation. Simulations of a model problem of cutaneous wound healing shows good agreement with experiments from the literature, offering promise to more detailed simulations and experimental validation and calibration. In conclusion, the body of work presented in this dissertation is a significant step towards the better understanding of skin mechanics not only as a structure, but as a living tissue that can grow and heal. The computational tools developed are ultimately aimed at applications in clinically relevant problems of plastic and reconstructive surgery.

# Acknowledgments

The past five years that have led to this work have only been possible thanks to the support, love and collaboration of a number of people. I would like to thank my coauthors Kai, Chad, Mike, Jordan. Their work and dedication to these projects have been a great source of inspiration for me. I owe special thanks to Arun Gosain who believed in this project from the start, and has been the corner stone in bridging the theory of skin mechanics into the clinical setting. I am also indebted to Hardik Kabaria, a great friend, roommate and collaborator. His passion for work and his loyalty have made an impact on my own way of approaching life. I am of course not only grateful, but honored to have been advised by Ellen Kuhl. She has been an outstanding mentor and friend. In these few lines it is impossible to list all her qualities and express my admiration and gratitude, therefore I shall state that she is simply The best. I am grateful as well for the other members of my dissertation defense committee: Peter Pinsky, Charles Steele, Christian Linder and Adrian Lew. They have been a source of great feedback, especially towards the end of my Ph.D., helping me to figure out next steps in my career. Finally, I also owe my happiness and sanity during my time at Stanford to friends and family, especially DARE, Stanford Cycling, Mikel and Idoia, Mom and Dad.

# Contents

<b>Preface</b>	<b>iv</b>
<b>Acknowledgments</b>	<b>vi</b>
<b>1 Introduction</b>	<b>1</b>
1.1 Introduction . . . . .	1
1.2 Skin Mechanobiology . . . . .	5
1.2.1 Overview of Skin Anatomy . . . . .	5
1.2.2 Modeling Skin Kinematics from the Biological Point of View . . . . .	7
1.2.3 Mechanotransduction in Healthy Skin . . . . .	10
1.2.4 Wound Healing . . . . .	14
1.3 Skin Mechanics . . . . .	15
1.3.1 Measuring Deformations and Forces on Skin . . . . .	16
1.3.2 Material Constitutive Equations . . . . .	16
1.3.3 Mechanics of Growth and Remodeling . . . . .	18
1.3.4 Coupling Mechanics and Biology . . . . .	19
1.4 Structure of the Thesis . . . . .	20
<b>2 A Computational Model for Skin Expansion</b>	<b>23</b>
2.1 Motivation . . . . .	24
2.2 Continuum Modeling of Area Growth . . . . .	28
2.2.1 Kinematics of Area Growth . . . . .	29
2.2.2 Balance Equations of Area Growth . . . . .	30
2.2.3 Constitutive Equations of Area Growth . . . . .	31
2.3 Computational Modeling of Area Growth . . . . .	33

2.3.1	Local Newton Iteration - Growth Multiplier . . . . .	33
2.3.2	Global Newton iteration - Growing Skin . . . . .	34
2.4	Example of Skin Expansion and Growth . . . . .	37
2.4.1	Model Problem of Tissue Expander Inflation and Deflation . . . . .	37
2.4.2	Tissue Expander Inflation - Skin Growth . . . . .	38
2.4.3	Tissue Expander Deflation - Residual Stress . . . . .	40
2.4.4	Limitations . . . . .	41
2.5	Conclusion . . . . .	43
<b>3</b>	<b>Stretching Skin Beyond the Physiological Limit</b>	<b>48</b>
3.1	Motivation . . . . .	49
3.2	Continuum Modeling of Skin Growth . . . . .	53
3.2.1	Kinematics - Finite Growth . . . . .	53
3.2.2	Balance Equations - Open Systems . . . . .	56
3.2.3	Constitutive Equations - Irreversible Growth . . . . .	56
3.2.4	Constitutive Equations - Reversible Elasticity . . . . .	58
3.3	Computational Modeling of Skin Growth . . . . .	62
3.3.1	Local Newton Iteration - Growth Multiplier . . . . .	63
3.3.2	Global Newton Iteration - Growing Skin . . . . .	64
3.4	Examples - Stretching Skin Beyond its Physiological Limit . . . . .	66
3.4.1	Model Problem - Displacement vs. Force Driven Skin Growth . . . . .	67
3.4.2	Tissue Expansion and Skin Growth . . . . .	69
3.5	Discussion . . . . .	73
<b>4</b>	<b>Tissue Expansion in Pediatric Surgery</b>	<b>78</b>
4.1	Motivation . . . . .	79
4.2	Methods . . . . .	82
4.2.1	Continuum Modeling of Skin Growth . . . . .	82
4.2.2	Computational Modeling of Skin Growth . . . . .	87
4.2.3	Geometric Modeling of Skin Growth . . . . .	89
4.3	Results . . . . .	91
4.3.1	Tissue Expansion in the Scalp . . . . .	92
4.3.2	Tissue Expansion in the Forehead . . . . .	93
4.3.3	Tissue Expansion in the Cheek . . . . .	94

4.4	Discussion . . . . .	95
<b>5</b>	<b>Biomechanics and Mechanobiology of Growing Skin</b>	<b>101</b>
5.1	Motivation . . . . .	102
5.2	Methods . . . . .	105
5.2.1	Continuum Model of Growing Skin . . . . .	105
5.2.2	Computational Model of Growing Skin . . . . .	108
5.3	Results . . . . .	110
5.3.1	Model Problem - Skin Growth in Equi-biaxial Extension . . . . .	110
5.3.2	Clinical Problem - Skin Growth in Pediatric Forehead Reconstruction	111
5.4	Discussion . . . . .	118
5.4.1	Discussion of Acute Elastic Response . . . . .	119
5.4.2	Discussion of Chronic Growth Response . . . . .	119
5.4.3	Discussion of Elastic Retraction . . . . .	120
5.4.4	Discussion of Growth Heterogeneity . . . . .	121
5.4.5	Limitations . . . . .	121
5.5	Conclusion . . . . .	123
<b>6</b>	<b>IGA Kirchhoff-Love Shell for Biological Tissues</b>	<b>124</b>
6.1	Motivation . . . . .	125
6.2	NURBS Surfaces . . . . .	126
6.2.1	B-spline Curves . . . . .	126
6.2.2	B-spline Surfaces . . . . .	127
6.2.3	NURBS . . . . .	127
6.3	Element Formulation . . . . .	127
6.3.1	Kinematics . . . . .	127
6.3.2	Principle of Virtual Work . . . . .	132
6.3.3	Consistent Linearization . . . . .	134
6.4	Constitutive Equations . . . . .	134
6.4.1	St. Venant Kirchhoff Model . . . . .	135
6.4.2	Mooney-Rivlin Model . . . . .	137
6.4.3	May-Newman-Yin Model . . . . .	138
6.4.4	Gasser-Ogden-Holzapfel Model . . . . .	139
6.5	Examples . . . . .	141

6.5.1	In-Plane Biaxial Tests . . . . .	141
6.5.2	Rectangular Strip Subjected to End Shearing Force . . . . .	142
6.5.3	Inflation of a Rectangular Membrane . . . . .	143
6.6	Discussion . . . . .	144
<b>7</b>	<b>Mechanical Characterization of Living Skin</b>	<b>153</b>
7.1	Motivation . . . . .	154
7.2	Methods . . . . .	156
7.2.1	Animal Model . . . . .	156
7.2.2	Multi View Stereo . . . . .	159
7.2.3	Isogeometric Surface Representation . . . . .	159
7.2.4	Isogeometric Analysis . . . . .	160
7.2.5	Prestrain, Expansion-Induced Deformation, and Growth . . . . .	162
7.3	Results . . . . .	163
7.3.1	Characterization of Prestrain . . . . .	163
7.3.2	Characterization of Expansion-Induced Deformation . . . . .	165
7.3.3	Characterization of Growth . . . . .	167
7.4	Discussion . . . . .	170
7.4.1	Skin Prestrain . . . . .	171
7.4.2	Skin Deformation . . . . .	172
7.4.3	Skin Growth . . . . .	172
7.4.4	Limitations . . . . .	173
7.5	Concluding Remarks . . . . .	174
<b>8</b>	<b>Anisotropy of Living Skin</b>	<b>175</b>
8.1	Introduction . . . . .	176
8.2	Methods . . . . .	179
8.2.1	Animal Model . . . . .	179
8.2.2	Multi-View Stereo . . . . .	181
8.2.3	B-Spline Based Isogeometric Analysis . . . . .	182
8.2.4	Kinematic Analysis of Skin Expansion . . . . .	186
8.3	Results . . . . .	188
8.3.1	Prestrain . . . . .	189
8.3.2	Deformation . . . . .	190

8.3.3	Growth . . . . .	191
8.4	Discussion . . . . .	195
<b>9</b>	<b>The Incompatibility of Living Skin</b>	<b>199</b>
9.1	Introduction . . . . .	200
9.2	Methods . . . . .	204
9.2.1	Animal Model . . . . .	204
9.2.2	Kinematics Data Acquisition . . . . .	205
9.2.3	Kinematic Analysis of Skin Expansion . . . . .	208
9.3	Results . . . . .	211
9.3.1	Control Patches: Prestrain and Natural Growth . . . . .	211
9.3.2	Expanded Patches: Expansion-Induced Deformation and Elastic Deformation . . . . .	213
9.3.3	Control Patches vs. Expanded Patches: Expansion-Induced Skin Growth . . . . .	216
9.4	Discussion . . . . .	217
<b>10</b>	<b>Computational Modeling of Flap Design</b>	<b>225</b>
10.1	Motivation . . . . .	225
10.2	Governing Equations . . . . .	228
10.3	Finite Element Model . . . . .	232
10.3.1	Direct Advancement Flap . . . . .	233
10.3.2	Double Back-Cut Flap . . . . .	234
10.4	Results . . . . .	234
10.4.1	Direct Advancement Flap . . . . .	235
10.4.2	Double Back-Cut Flap . . . . .	235
10.5	Conclusion . . . . .	236
<b>11</b>	<b>Optimization of Flap Design in Tissue Expansion</b>	<b>241</b>
11.1	Motivation . . . . .	242
11.2	Materials and Methods . . . . .	244
11.2.1	Flap Design . . . . .	244
11.2.2	Creation of Three-dimensional Model . . . . .	244

11.2.3	Simulation of Flap Design . . . . .	245
11.3	Results . . . . .	247
11.3.1	Direct Advancement Flap . . . . .	247
11.3.2	Double Back-Cut Flap . . . . .	249
11.4	Discussion . . . . .	250
<b>12</b>	<b>Systems-Based Approaches For Wound Healing</b>	<b>253</b>
12.1	Introduction . . . . .	254
12.2	Temporal Spectrum of Wound Healing . . . . .	255
12.3	Spatial Spectrum of Wound Healing . . . . .	258
12.4	Overview of Computational Modeling for Systems Biology . . . . .	261
12.5	Guidelines . . . . .	263
12.6	Systems-Based Mathematical Models of Wound Healing . . . . .	264
12.7	Perspective . . . . .	270
<b>13</b>	<b>Computational Modeling of Wound Healing</b>	<b>274</b>
13.1	Motivation . . . . .	275
13.1.1	Wound Healing Across the Spatial Scales . . . . .	275
13.1.2	Wound Healing Across the Temporal Scales . . . . .	277
13.1.3	Modeling Wound Healing . . . . .	278
13.2	Chemo-Bio-Mechanical Problem . . . . .	280
13.2.1	Chemical Problem: Chemical Concentrations . . . . .	280
13.2.2	Biological Problem: Biological Cell Densities . . . . .	281
13.2.3	Mechanical Problem: Mechanical Deformation . . . . .	282
13.3	Model Problem of Wound Healing . . . . .	283
13.3.1	Chemical Problem: Inflammatory Signal . . . . .	283
13.3.2	Biological Problem: Fibroblasts . . . . .	284
13.3.3	Mechanical Problem: Deformation . . . . .	285
13.4	Computational Modeling of Wound Healing . . . . .	287
13.4.1	Continuous Residuals . . . . .	287
13.4.2	Discretization in Time . . . . .	288
13.4.3	Discretization in Space . . . . .	288
13.4.4	Discrete Algorithmic Residuals . . . . .	288

13.4.5 Linearization . . . . .	289
13.4.6 Algorithmic Constitutive Equations . . . . .	290
13.5 Examples . . . . .	292
13.5.1 Wound Healing Across the Temporal Scales . . . . .	292
13.5.2 Wound Healing Across the Spatio-Temporal Scales . . . . .	296
13.6 Discussion . . . . .	303
<b>Bibliography</b>	<b>307</b>

# List of Tables

2.1	Area, growth, volume, pressure, and residual stress for different expander geometries . . . . .	40
4.1	Algorithmic flowchart for strain-driven transversely isotropic area growth. . . . .	90
6.1	Material parameters for the different constitutive laws. . . . .	141
6.2	Ellipticity of inflated membranes. . . . .	144
7.1	Characterization of prestrain . . . . .	167
7.2	Characterization of expansion-induced deformation . . . . .	168
7.3	Characterization of growth . . . . .	170
8.1	Summary of prestrain for patch S. . . . .	189
8.2	Summary of deformation for patch R. . . . .	192
8.3	Summary of natural growth for patch S. . . . .	192
8.4	Summary of purely elastic deformation for patch R. . . . .	193
8.5	Summary of growth from combined analysis of patches R and S . . . . .	195
9.1	Summary of the expansion protocol with spherical expander on patch P, crescent expander on patch R, and control patch S . . . . .	209
9.2	Summary of growth . . . . .	212
9.3	Summary of prestrain . . . . .	213
9.4	Chronic deformation history $\mathbf{F}$ . . . . .	215
9.5	Acute deformation history $\mathbf{F}^a$ . . . . .	215
9.6	Summary of elastic deformation $\mathbf{F}^e$ and $\mathbf{F}^{es}$ . . . . .	216
9.7	Summary of expansion-induced growth $\mathbf{F}^{ge}$ from combining the analysis of the excised patches P and R . . . . .	217

12.1 Systematic classification of mathematical models for wound healing based on model complexity and focus area . . . . .	265
13.1 Values for the parameters used in the computations. . . . .	293

# List of Figures

1.1	Computational mechanics in reconstructive surgery . . . . .	3
1.2	Skin anatomy . . . . .	6
2.1	Tissue expansion for pediatric forehead reconstruction . . . . .	24
2.2	Schematic sequence of tissue expander inflation and deflation . . . . .	25
2.3	Commercial expanders to grow skin flaps in reconstructive surgery . . . . .	26
2.4	Discretization of expander geometries with finite elements . . . . .	38
2.5	Temporal evolution of fractional area gain and increasing expander volume	39
2.6	Spatio-temporal evolution of growth area stretch during tissue expander inflation . . . . .	45
2.7	Spatio-temporal evolution of elastic area stretch during tissue expander deflation . . . . .	46
2.8	Spatio-temporal evolution of maximum principal stress during tissue expander deflation . . . . .	47
3.1	Tissue expansion for pediatric forehead reconstruction . . . . .	49
3.2	Schematic sequence of tissue expander inflation . . . . .	51
3.3	Tissue expanders to grow skin flaps for defect correction in reconstructive surgery. . . . .	52
3.4	Kinematics of finite growth . . . . .	54
3.5	Transversely isotropic eight chain model . . . . .	58
3.6	Fit of wormlike chain model to uniaxial tension test of rabbit skin . . . . .	61
3.7	Relaxation test. Temporal evolution of total area stretch. . . . .	68
3.8	Creep test. Temporal evolution of total area stretch. . . . .	69
3.9	Finite element discretization of a skin patch for tissue expansion . . . . .	70
3.10	Temporal evolution of fractional area gain . . . . .	71

3.11	Temporal evolution of expander volume . . . . .	72
3.12	Spatio-temporal evolution of growth area stretch . . . . .	77
4.1	Tissue expansion for pediatric forehead reconstruction . . . . .	80
4.2	Schematic sequence of tissue expander inflation. . . . .	81
4.3	Tissue expanders to grow skin for defect correction in reconstructive surgery.	82
4.4	Temporal evolution of total, elastic, and growth area stretch in equi-biaxial stretch test . . . . .	86
4.5	Three-dimensional computer tomography scans from the skull of a one-year old child . . . . .	91
4.6	Mesh generation from clinical images . . . . .	92
4.7	Tissue expansion in the scalp. Temporal evolution of area stretches. . . . .	93
4.8	Tissue expansion in the scalp. Spatio-temporal evolution of area growth. . .	94
4.9	Tissue expansion in the scalp. Remaining deformation upon expander removal	95
4.10	Tissue expansion in the forehead. Temporal evolution of area stretches . . .	96
4.11	Tissue expansion in the forehead. Spatio-temporal evolution of area growth	97
4.12	Tissue expansion in the forehead. Remaining deformation upon expander removal . . . . .	98
4.13	Tissue expansion in the cheek. Temporal evolution of area stretches. . . . .	99
4.14	Tissue expansion in the cheek. Spatio-temporal evolution of area growth. .	100
4.15	Tissue expansion in the cheek. Remaining deformation upon expander removal	100
5.1	Mechanotransduction of growing skin . . . . .	103
5.2	Biomechanics of growing skin . . . . .	104
5.3	Temporal evolution of total, reversible and irreversible area stretches . . . .	111
5.4	Temporal evolution of skin thickness $t$ for displacement driven skin expansion	112
5.5	Skin expansion in pediatric forehead reconstruction . . . . .	113
5.6	Skin expansion in pediatric forehead reconstruction. Case study I. . . . .	114
5.7	Spatio-temporal evolution of area growth during skin expansion in pediatric forehead reconstruction. Case study I. . . . .	115
5.8	Skin expansion in pediatric forehead reconstruction. Case study II. . . . .	116
5.9	Spatio-temporal evolution of area growth during skin expansion in pediatric forehead reconstruction. Case study II . . . . .	117

6.1	Shell kinematics . . . . .	128
6.2	Strip biaxial test for VK, MR, MY and GOH materials . . . . .	147
6.3	Anisotropy behavior obtained through varying the preferred direction . . . . .	148
6.4	Schematic of the tip deflection benchmark example . . . . .	149
6.5	Deflections of the tip for the pulled strip subjected to end shearing force . .	149
6.6	Deflections of the tip for the pulled strip using the anisotropic material models	150
6.7	Displacement at the tip of a 30 × 10mm strip subjected to end shearing force	151
6.8	Convergence of a rectangular membrane subjected to out-of-plane pressure	151
6.9	Inflation of a rectangular membrane by applying a normal out-of-plane pressure	152
7.1	Porcine model for skin expansion . . . . .	157
7.2	Multi View Stereo extracts three-dimensional representations of scenes from a collection of multiple two-dimensional images . . . . .	158
7.3	Isogeometric surfaces . . . . .	161
7.4	Four configurations of the skin patch: ex vivo pre-expansion, in vivo pre- expansion, ex vivo post-expansion, and in vivo post-expansion . . . . .	163
7.5	Four configurations of the skin patch: prestrain, expander inflation, elastic deformation, and permanent growth . . . . .	164
7.6	Characterization of prestrain . . . . .	165
7.7	Characterization of expansion-induced deformation . . . . .	166
7.8	Characterization of growth . . . . .	169
8.1	Tissue expansion in clinical practice . . . . .	176
8.2	Nomenclature for the tattooed grids on the porcine model . . . . .	179
8.3	Skin expansion in a chronic porcine model . . . . .	180
8.4	Multi-view stereo (MVS) reconstruction . . . . .	181
8.5	Kinematics . . . . .	184
8.6	Schematic of distinct configurations of the skin patch . . . . .	187
8.7	Averaged results for the distinct configurations of the skin patch . . . . .	188
8.8	Prestrain . . . . .	190
8.9	Deformation . . . . .	191
8.10	Growth . . . . .	194
8.11	Representative tissue sections of non-expanded and expanded skin . . . . .	196

9.1	Finite growth is modeled mathematically using continuum mechanics . . . . .	202
9.2	Different tissue expander geometries are used in clinical practice . . . . .	203
9.3	Porcine expansion model with four tattooed grids of $11 \times 11$ points . . . . .	205
9.4	Configurations of skin expansion . . . . .	208
9.5	History of natural growth. . . . .	212
9.6	Prestrain upon excision and further subdivision of the control patch S . . .	214
9.7	Chronic deformation induced by tissue expansion . . . . .	222
9.8	Acute deformation induced by tissue expansion . . . . .	223
9.9	Elastic deformation released upon excision and further subdivision of the expanded patches P and R . . . . .	224
9.10	Growth induced by the expansion process . . . . .	224
10.1	Distal flap necrosis induced by excessive tissue tension . . . . .	229
10.2	Direct advancement flap schematic . . . . .	234
10.3	Double back-cut flap schematic . . . . .	235
10.4	Direct advancement flap simulation when fibers are parallel to the advancement direction . . . . .	236
10.5	Direct advancement flap simulation when fibers are perpendicular to the advancement direction . . . . .	237
10.6	Double back-cut flap simulation when fibers are parallel to the advancement direction . . . . .	238
10.7	Double back-cut flap simulation when fibers are parallel to the advancement direction . . . . .	239
11.1	Demonstration of complications of tissue expansion due to excessive tension	243
11.2	Two commonly used flap designs after tissue expansion . . . . .	245
11.3	Direct-advancement flap oriented parallel to relaxed skin tension lines . .	247
11.4	Direct-advancement flap oriented perpendicular to relaxed skin tension lines	248
11.5	Collagen fiber orientations for direct-advancement flap oriented a) parallel and b) perpendicular to relaxed skin tension lines . . . . .	248
11.6	Double back-cut flap oriented parallel to relaxed skin tension lines . . . .	249
11.7	Double back-cut flap oriented perpendicular to relaxed skin tension lines .	250
11.8	Collagen fiber orientations for double back-cut flap oriented a) parallel and b) perpendicular to relaxed skin tension lines . . . . .	251

12.1	Spatio-temporal spectrum of wound healing . . . . .	256
12.2	Angiogenesis can be manipulated by altering hyperbaric oxygen levels . . . . .	272
12.3	Collagen deposition can be manipulated by altering TGF- $\beta$ kinetics . . . . .	273
12.4	Collagen deposition and mitosis can be manipulated by altering stretch levels	273
13.1	Wound healing across the spatial scales . . . . .	276
13.2	Wound healing across the temporal scales . . . . .	278
13.3	Temporal evolution of the the inflammatory signal $c$ , the fibroblast density $\rho$ , and the collagen content $w$ . . . . .	294
13.4	Sensitivity of collagen content $w$ with respect to collagen deposition rate $\gamma$ .	295
13.5	Sensitivity of collagen content $w$ with respect to inflammation-induced collagen synthesis rate $\alpha$ . . . . .	296
13.6	Sensitivity of collagen content $w$ with respect to inflammation-induced mitotic rate $k_2$ . . . . .	297
13.7	Comparison of simulations with respect to existing models and experimental data reported in the literature . . . . .	298
13.8	Wound healing across the spatio-temporal scales for a circular wound . . . . .	299
13.9	Wound healing across the spatio-temporal scales for varying wound sizes . .	301
13.10	Wound healing across the spatio-temporal scales for varying wound ellipticities	302

# Chapter 1

## Introduction: Computational Mechanics for Plastic and Reconstructive Surgery

### 1.1 Introduction

Computational modeling and simulation of biological systems have been steadily gaining presence in the clinical scene [401]. Perhaps the most preeminent example is genomics, which is paving the way for personalized medicine [271, 296]. Yet, it has also been emphasized that characterizing the genome alone is not enough. The response of living systems to different stimuli is the result of a complex network of interactions that span several spatial and temporal scales; mechanical form and function emerge from the dynamics of such networks [401]. If we are to build predictive computational tools to aid healthcare, we cannot rely only on statistical relationships between the components of a given biological system, rather, we need to propose and validate mathematical descriptions of how the parts connect to each other. In particular, mechanical forces and deformations play a central role in several clinical scenarios. Computational mechanics in medicine aims at building the modeling and simulation tools to understand the mechanical form and function of soft tissues in health and disease [26].

The field of computational biomechanics has evolved tremendously over the past few decades. While the original efforts were centered around the characterization of mechanical properties

of tissues, recent trends are oriented at capturing the unique capability of living systems to grow, adapt, and remodel [209,361]. Initial investigations in mechanics and mechanobiology were prompted by more fundamental questions regarding the tissue structure and cellular response to mechanical cues. However, as we gradually elucidate how some of the basic mechanisms work, it has become necessary to develop novel computational frameworks to incorporate much of the basic scientific insights into cellular, tissue, organ level and multi-scale models, and to drive their introduction into the clinical pipeline. Cardiovascular biomechanics is an example. Computational simulation of blood flow in patient specific geometries has been used, for instance, to compute the Fractional Flow Reserve (FFR) non-invasively, which is the gold standard measure for coronary stenoses [370]. The momentous interest in cardiovascular mechanics has opened many other avenues for clinical research and medical applications [367]. Although a good example, cardiovascular mechanics is only one piece of the puzzle; the future of computational mechanics in medicine is closely related to the development of the Virtual Physiological Human and Physiome projects [172,198]. In this thesis, the attention is brought to the field of reconstructive surgery by looking at the mechanics and mechanobiology of living skin.

Skin is our interface with the world. It is our largest organ, accounting for approximately 15% of our body weight and covering a surface of  $2m^2$  in an average adult [413]. It is our largest sensor and the first one to develop [2]. Skin regulates our temperature and fluid exchange with the environment [409]. It even regulates our mood and decision making through mechanic and thermal sensation [2]. Despite of being a thin membrane, skin shows a remarkably complex micro-structural organization [247]. Notably as well, despite its small thickness, skin is our first line of defense against external agents; it has to isolate our entire internal machinery and protect it from chemical, mechanical, and other environmental threats. And yet, skin is highly flexible and lets us move around, walk, run, jump, express ourselves and communicate with each other. In addition to long-standing medical applications in which skin mechanical homeostasis is disrupted, with the new advent of wearable electronics and the popularity of transdermal drug delivery medical devices, the understanding of skin mechanical function and adaptation is becoming ever so more important [180,192].

Developing tools for computational mechanics in medicine to predict the effect of different treatments, optimize devices, and address fundamental scientific questions, requires a framework of intersecting disciplines. Three main areas of knowledge are the basis of

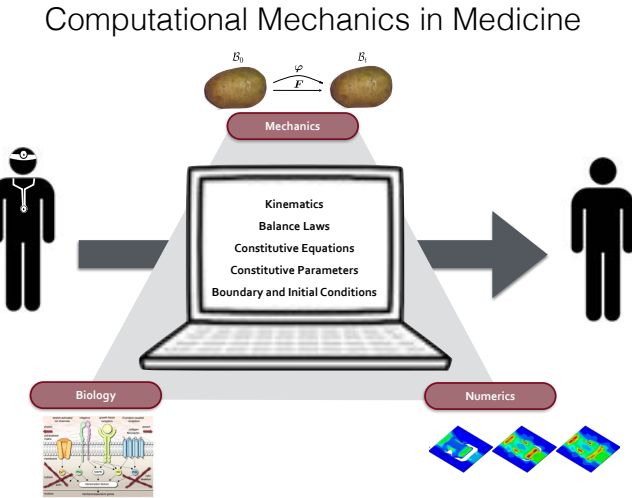


Figure 1.1: Schematic of the approach in this thesis. The development of computational tools for skin reconstructive surgery needs three knowledge areas: biology, mechanics, and numerics. Biology refers to the cellular sensing and response mechanisms to mechanical stimuli and its effect on the tissue microstructure. Mechanics describes states of deformation and loading. Numerics parts from a mathematical description and turns it into computer code in order to do simulations. Computational simulations need five ingredients: kinematics, balance laws, constitutive equations, material parameters, and initial and boundary conditions.

this approach: classical mechanics, biology, and numerics. Furthermore, thinking from the perspective of a mathematical modeler interested in predictive simulations, we adopt five ingredients that are usually considered in a classical course of continuum theories. Namely, we work with the premise that it is possible to see a given clinical scenario as an initial boundary value problem that requires a mathematical description of kinematics, balance laws, constitutive equations, constitutive parameters, and boundary and initial conditions. This approach is schematized in Fig. 1.1. We remark that despite of motivating our framework on continuum theories, the mathematical models can also be discrete or hybrid continuum-discrete. For example, a discrete model based on the explicit mathematical representation of every cell still requires a notion of kinematics, balance laws, constitutive equations, constitutive parameters, and boundary and initial conditions. A continuum model has the particularity of being described by means of partial differential equations for which there is

a plethora of well-established numerical approaches.

The three corners of the triangle in Fig. 1.1 are connected and overlap one another. At the biological corner we are interested in describing the anatomy and structure of the tissue as well as the temporal and spatial distribution of the cell types and cell signaling networks. Such description relates to the kinematics of the problem. The geometric arrangement and composition of the microstructure of the tissue are also a central part of the mechanics. The balance laws and constitutive equations that explain the biological behavior of different cell types to a given stimulus is still an evolving topic of research that belongs to the young field of computational systems biology [193]. In particular, we are interested in the biological systems in which mechanics play a central role or, in other words, we aim at characterizing the systems mechanobiology of the tissue. From the mechanics corner, the kinematics and balance laws are those from the classical theories. Kinematics from the corner of the mechanician starts from the same point as the biology. The first task is to describe the microstructure. However, kinematics from the mechanics perspective adds on the description of states of deformation, damage and failure of tissues. The balance laws for mechanics are the well-known physical principles such as conservation of energy, mass, and momentum. Yet, despite the underlying physics remaining the same, from a mechanics perspective, biological tissues do require unique theoretical considerations. One of the most interesting capabilities of soft tissues is their ability to adapt over time to their environment by growth and remodeling [361]. The mechanics of growth and remodeling has received considerable attention from theoretical and applied mechanicians in the past decade [8]. The numerics corner entails translating the mathematical description of the biology and the mechanics into computer code in order to run simulations. The constitutive parameters and boundary and initial conditions appear now. While the kinematics, balance laws, and constitutive equations are true for a given tissue in a general setting, the patient specificity and the particular medical application or experiment dictates the constitutive parameters and the boundary and initial conditions, respectively.

Focusing back our attention to skin, we will briefly review the literature guided by the schematic of the three fields depicted in Fig. 1.1. We will cover important aspects of skin biology and mechanics. We will not deal with the numerics because, in contrast to the biology and the mechanics, the numerical methods are more general rather than skin-specific. We then present three examples of prominent research areas in skin mechanics: tissue expansion, flap design, and wound healing. Finally, we close the introduction with a discussion

on the structure of the dissertation emanating from the approach and examples specified in this first chapter. The purpose of this introductory review is to be broad and to appeal to plastic and reconstructive surgeons, engineers and basic scientists. Our objective is firstly to organize the current body of knowledge related to skin mechanics and mechanobiology within the framework we just described. Secondly, we expect that structuring the literature in this way we can motivate the development of the computational approaches that are presented later in this text.

## 1.2 Skin Mechanobiology

Parting from our interest on computational mechanics in plastic and reconstructive surgery we will skew our review of the biology of skin in the direction of the mechanobiology. Nonetheless, we need to have first the description of the structure of the tissue: the anatomy.

### 1.2.1 Overview of Skin Anatomy

Human skin is a thin membrane with a well-defined and complex microstructure. Its thickness ranges between 1 to 3 mm depending on the anatomical region. It consists of two layers, the epidermis on top and the dermis beneath it. There is an additional layer of tissue which is sometimes included as part of the skin, but often considered separately and is referred to as subcutaneous tissue or hypodermis. The function of the hypodermis is to provide a transition between the dermis and the underlying muscle, thermal insulation and energy storage. Its role in the mechanical homeostasis of skin is limited [247].

The properties and characteristics of skin vary not only amongst individuals but also from one region of the body to another. The first distinction is between Glabrous (non-hairy) and hairy skin. Glabrous skin is found in the palms and sole. It has ridges and sulci known as dermatoglyphics. There are specialized tactile receptors in Glabrous skin which allow us to sense stretch, movement direction, hand and finger position, handle objects and perceive vibrations. The hairy skin, present in the rest of the body, is obviously defined by the presence of hair follicles. In addition to important functions related to thermal and fluid exchange regulation, hair follicles are the home of stem cells crucial for wound healing, and they also host specialized tactile receptors to detect hair movement including pleasant touch during caress [322].

The epidermis has little intercellular grounds substance, it is composed primarily of cells,

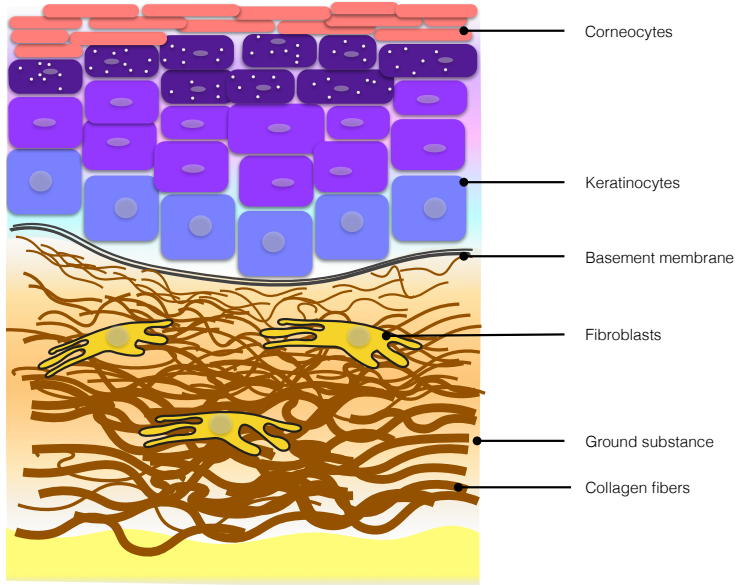


Figure 1.2: Anatomy of the skin. Skin consists of two layers, the top is the epidermis composed almost entirely of keratinocytes which originate at the basal layer and then migrate to the surface where they become corneocytes. Below the epidermis there is the dermis. The dermal-epidermal junction is called basement membrane and is composed of laminin and collagen IV. The geometry of the basement membrane is characterized by undulations named rete ridges. The dermis is mostly acellular. Fibroblasts are the most prevalent cell type. The dermis ground substance is composed of a proteoglycan gel in which a fiber network is embedded. 80% of the fibers in the dermis are made out of collagen I.

95% of which are keratinocytes. Other cell types in the epidermis are melanocytes, Merkel cells and Langerhans' cells [210]. The epidermis is our first line of defense against hazard, it must guard us from bacteria and harmful microorganisms, it must be impermeable, and it must withstand constant wear and tear. To do so, the epidermal layer is in a permanent state of self-renewal [116]. Highly proliferative keratinocytes live at the bottom of the epidermis and from there they begin a journey towards the surface giving rise to four sublayers (from bottom to top): basal, spinous, granular and stratum corneum. The graded structure of the epidermis thus reveals its functional role. As keratinocytes migrate upwards they undergo a metamorphosis from a highly metabolic columnar shape into a flat geometry that lacks organelles and is filled with keratin and lipids. This last stage in the differentiation

of the keratinocyte is called corneocyte [407]. An important feature that regulates the epidermal homeostasis is the structure and function of four different cell-cell junctions: gap junctions, desmosomes (unique to skin), adherent junctions and tight junctions. The role of the different cell-cell connections is to maintain the polarity of the differentiation process, to make the skin impermeable, and to provide mechanical stability [344].

The dermis lies immediately below the epidermis and yet its structure is remarkably different. This is a consequence of the embryologic development. While the epidermis forms from the ectoderm, the dermis is developed from the mesoderm of the embryo [247]. The interface between the epidermis and the dermis is called basement membrane. Adjacent to the keratinocytes of the basal layer there is a thin membrane made out of the protein laminin. On the side facing the dermis there is abundant collagen IV [116]. The dermal-epidermal junction is characterized by a sinuous pattern; the protrusions of the epidermis into the dermis are called rete ridges [247]. In contrast to the epidermis, the dermis is relatively acellular. The predominant cell type is the fibroblast. Another important distinction is the presence of vasculature in the dermis which is absent in the epidermis. The capillary network of the dermis allows for nourishment and waste removal for both the dermis and the epidermis. It also plays an important role in thermal regulation [413]. The dermis can be divided into two regions, the papillary dermis on top and the reticular dermis beneath it. The distinction between the two is based on the gradual change in the microstructure. The dermis' ground substance is made out of a gel of proteoglycans. However, the main structural component of the dermis is the fiber network embedded in the ground substance. Collagen I makes up about 80% of the fibers, Collagen III accounts for approximately 15%, and the rest is made out of other types of collagen, elastin, and reticulin [413]. The papillary dermis has thinner collagen fiber bundles aligned predominantly on the plane parallel to the surface of the skin. As we move from the papillary to the reticular dermis the collagen fibers become slightly more disperse and increase in thickness. The network of collagen fibers in the reticular dermis offers a basket-weave or rhomboid pattern aligned in a preferred direction [49].

### 1.2.2 Modeling Skin Kinematics from the Biological Point of View

To develop predictive computational tools, the starting point is to quantify the anatomy. The mathematical description needed will vary depending on the application. As a first

guideline to decide on the appropriate mathematical model we consider the spatial scale. Biological systems have a well defined hierarchy of structural organization, ranging from processes occurring at the molecular level, to the cell, the tissue and the organ levels. The trends in multi-scale modeling of systems biology follows this organization [352]. We make a distinction between quantification of purely structural parameters and those related to the cellular populations and the signaling networks amongst those cells. The rationale behind this consideration is that the kinematics of the structural components of skin overlaps with the description needed from the point of view of the mechanics. On the other hand, the kinematics that describe the spatial arrangement of cells and their signaling networks can be considered independently [365].

For the tissue geometry, at the coarsest level we can represent the skin anatomy using scalar values: the epidermal and dermal thicknesses [350]; average collagen fiber diameter [49]; and preferred collagen alignment [214,321]. Despite the simplicity of this approach, in some cases it is enough to look at the anatomy in such global measures. For instance, in tissue expansion, a widely-used technique, it is of interest to quantify changes in dermal and epidermal thicknesses in response to different protocols [181]. The characterization of skin lesions such as striae, scars and keloids has also been done based on overall structural changes [38,97]. The next level of spatial detail would be to consider the skin as a series of discrete compartments along the thickness direction. This description can be useful for example to study transdermal drug delivery [143]. A finer level of detail is achieved by replacing the compartments with a one-dimensional continuum or a series of one-dimensional continuums. This approach has also been used in models of transdermal drug delivery [180]. Even smaller scales have been considered, we could choose to represent the molecular arrangement of the lipid bilayer of corneocytes and their interaction with different molecules [276]. As stated before, the choice of description is governed by the application. For skin mechanobiology we advocate for descriptions from the cellular level to the tissue level. When considering the geometry of interest we also want to pay attention to the number of spatial dimensions that are required to capture the phenomenon under study. The one dimensional models which are concerned with varying properties along the thickness direction are useful to model transport phenomena in drug delivery for example. However, if we are interested in the morphology of the rete ridges we need at least a two dimensional geometric representation [76]. Surgical techniques in complex patient specific geometries often need the description of the full three-dimensional geometry [418].

The mathematical description of the kinematics goes hand in hand with experimental quantification. The ultimate goal of the computational model is to be able to predict the outcome of a given treatment or procedure; for that it needs a thorough validation against experimental data. To measure thickness, ultrasound and histological slices with hematoxylin and eosin stain (H&E stain) can be used [350, 383]. Determining the microstructural parameters, such as collagen fiber diameters and orientations, has been given continuous attention for several decades. Around half a century ago scanning electron microscopy allowed for quantification of dermal collagen arrangement [49, 131]. More recently, polarized light and confocal laser scanning microscopy with picrosirius red staining were used to determine collagen orientation in the dermis [183, 275]. These techniques have been used on explanted samples, yet, the physiological states of deformation call for microscopy methods that can be used *in vivo*. Such emphasis has brought forth the use of Raman spectroscopy and near infra-red confocal laser scanning microscopy to study skin microstructure *in vivo* [64, 313]. For the biological constituents, kinematics involves describing the spatial and temporal distribution of cell densities and chemical signals. Modeling cell populations with discrete approaches is an appealing option [253]. Cells can be allowed to take any position in the domain [119], or they can be represented by a lattice [359]. As an example, epidermal morphogenesis has been described with a cell-centered lattice-free approach [75]. For larger spatial scales, continuum descriptions become appealing. Depending on the problem of interest, different cell types would come into picture. For instance, in wound healing the main cell types present in skin are keratinocytes, fibroblasts, endothelial cells, and monocytes, which can be described as continuous fields [58]. Describing the different cell signaling pathways is a far more intricate territory for the modeler. There are many regulatory systems of cell behavior and not all may be of interest for a particular phenomenon. For instance, in tissue expansion, only a few biological markers of cell signaling are of special interest. To characterize the rate of cellular proliferation due to expansion we could explicitly consider the protein Ki-67 as one of the variables. Another crucial variable would be a protein indicative of mechanotransduction in fibroblast such as phosphorylated ERK1/2 [308]. We would like to emphasize once more that the choice of the key cell signaling pathways variables is strongly dependent on the phenomenon under study.

To validate the models, we need to be able to quantify the cell density and cell signaling landscapes over the spatial domain. One experimental tool is to perform immunohistochemical analysis (IHC) with the corresponding antibodies for the variables of interest.

Alternatively, gene expression profiling can also be related to cell behavior. For example, temporal profile of gene expression in wound healing of mice accompanied by in situ hybridization has allowed quantification of cluster of genes related to three stages of inflammation [80]. In recent years, experimental methods in systems biology have produced high throughput technologies and an overwhelming amount of data. Genomics is concerned with the sequence, structure, and content of the genome. For computational systems biology it is particularly important to determine the transcription of genes. Experimental techniques such as DNA microarrays are used to quantify the different RNA species. Proteomics tackles the quantification of a vast quantity of proteins expressed at a given state [305]. The data from high-throughput technology also enters the biological kinematics, however, its use in predictive models is not so straightforward due to the high dimensionality. There must be an intermediate step in order to translate the massive amount of data into groups or clusters, or to identify a few key players in a given condition. Dimensionality reduction of the data is needed in order to build tractable mathematical models that depend on a few variables of clinical interest, allowing the translation of the mathematical equations to the clinical pipeline.

### 1.2.3 Mechanotransduction in Healthy Skin

The mathematical modeling of skin mechanobiology accounts for specifying a set of rules or equations that can be thought of as *balance* and *constitutive* laws. While the distinction between balance and constitute equations is very clear for mechanics, the same is not true in computational systems biology. Yet, we could think of balance laws as the general principles that are true across many biological systems. For example, the inflammation response in wound healing is shared across different species and different tissues [392]. The constitutive equations in this context are the particularization of the common mechanobiological mechanisms to skin tissues. With sufficient detail, cell populations can be viewed as interacting thermodynamic systems. However, the complexity of the transport and reaction events inside and between different cells prevents a classical approach built upon fundamental physics [101]. Instead, some times heuristically developed models can give powerful insights of the underlying biology [107].

Mechanotransduction is the mechanism by which cells translate mechanical forces or deformations into chemical signals [153]. Connective tissues such as skin have evident mechanical

roles which are crucial for survival and optimal physiological function. Our interaction with the world requires a variety of forces and deformations transmitted through our skin. Therefore, to guarantee homeostasis and proper mechanical function, cutaneous cell populations have to be able to sense mechanical cues and respond accordingly [342]. The mechanical behavior of human integument is primarily determined by the mechanical properties of the dermis [182]. Fibroblasts tenanting the dermis are the cell type responsible for maintenance of the extra-cellular matrix (ECM). Mechanisms of mechanotransduction are shared amongst many cell types of the various connective tissues in the human body [395]. In general, for mechanically sensitive cells, and in particular for fibroblasts, there are three types of mechanical sensors at the cell membrane: integrins, G protein-coupled receptors, and stretch-activated ion channels. Additionally, the cytoskeleton, which provides the overall cell structural support, can undergo conformational changes when the cell as a whole is deformed, yielding an additional sensing mechanism [405]. The direct activation of the mechanical sensors leads to intracellular signaling pathways that often activate secondary messengers such as growth factors. Growth factor receptors at the cell membrane are thus another important sensing mechanism [417]. Amongst the different cytokines that are expressed in connective tissues in response to mechanical stimuli, some very important ones are transforming growth factors of the  $\beta$  family (TGF- $\beta$ ), interleukins, fibroblast growth factors (FGF), vascular endothelial growth factors (VEGF), platelet derived growth factors (PDGF), and tumor necrosis growth factors (TNF- $\alpha$ ) [395].

Dermal fibroblasts maintain their ECM by a constant deposition of collagen and proteoglycans as well as degradation of the collagen network through the release of matrix metalloproteinases (MMP). Out of all the possible mechanical cues that fibroblast are subjected to, tension is the most physiologically relevant. Thus, *in vitro* experiments have focused on the response of fibroblasts to uniaxial and biaxial strain loading conditions on flexible two-dimensional constructs [396]. To mimic the *in vivo* condition more closely, mechanical strain has also been applied to fibroblasts seeded in three dimensional collagen gels [94]. The most widely studied mechanism of force transduction in fibroblast is the integrin-ECM interaction. Applying tensile strain to the ECM produces conformational changes in the cytoplasmatic tails of the integrins, activating kinases such as focal adhesion kinase (FAK). In turn, activation of FAK is linked to mitogen-activated protein kinase (MAPK) pathways inside the cell [343]. The end effects of FAK activation are pro-inflammatory signaling,

collagen production, and reduced apoptosis [406]. In addition to direct mechanical sensing, secondary signaling pathways are crucial regulators of ECM remodeling by fibroblasts, TGF- $\beta$  in particular [264]. Fibroblasts exposed to TGF- $\beta$  show up-regulation of collagen 1 and 3 genes as well as down-regulation of Bax apoptotic gene [94]. In addition to imposed tension or strain, other mechanical stimuli dictate fibroblast behavior, such as the ECM microstructure and composition itself. For example, fibroblasts migrate preferentially along fiber directions [149, 329].

Even though the dermis is considered the load-bearing layer of skin, keratinocytes in the epidermis also exhibit mechanosensing. Deformations of the dermis are transmitted to the epidermis via the hemidesmosomes junctions at the basement membrane. Adherens junctions between neighboring keratinocytes then transmit forces to the cytoskeleton inside the keratinocytes. In turn, deformations of the overall cell shape produces intracellular signaling affecting keratinocyte mitosis [196]. Another important type of mechanoreceptors in the epidermis are stretch-activated ion channels [127]. Growth factor receptors in keratinocytes are also relevant when secondary messengers are activated downstream of a mechanical stimulus. For keratinocytes, epidermal growth factor (EGF) is involved in the control of cellular proliferation [342]. Experiments on cultured keratinocytes showed increased mitosis upon strain [364]. More recently, *in vitro* studies have looked at engineered skin, where there is a coupled mechanobiological response of the dermal and epidermal layers upon strain. Peak proliferation rate of keratinocytes and fibroblasts occurred at 20 percent strain compared to 0 and 40 percent strain [301].

Mechanotransduction *in vivo* has been studied primarily in the context of tissue expansion, a technique to grow skin by implanting a subcutaneous balloon which is inflated chronically over a period of several weeks [92, 270]. Inflation of the expanders stretches the skin beyond its physiological limit resulting in net tissue growth [54]. Analysis of expanded tissues has revealed increased cellular proliferation of keratinocytes, activation of MAPK pathway, and increased collagen deposition [31, 299, 308]. Remarkably, the growth process generates tissue with the same properties as the native, unexpanded skin.

From the modeler perspective, biological knowledge has to be translated into mathematical equations. The form of the balance and constitutive equations is tightly related to the choice of kinematic variables. Just as we remarked previously, the mathematical description is strongly influenced by the spatial scale of interest and by the nature of the system which can be discrete or continuum. For larger spatial scales, at the tissue level,

continuum approaches are prevalent, for example in wound healing modeling [381]. Since mechanotransduction deals with cellular signaling networks, cell-centered approaches are often deemed more relevant for smaller scales, and also call for modeling of discrete entities [253]. Since our focus is on mechanobiology, we must take into account the description of the mechanics, yet, that is a subsequent topic in this review. Thus, we temporarily center ourselves on the description of the cell populations themselves and the signaling networks generated due to the mechanical stimuli, but the coupling between mechanics and biology is left for later on.

At the larger spatial scales, the tissue level, it is prohibitive to represent every cell individually and the choice of continuum theories is common. Evolution in time and space of the cell populations takes the form of partial differential equations (PDE). The balance principle is that of conservation of mass. This representation has been very common to capture the dynamics of invading cell populations [339]. This approach seems more appropriate for low densities, where cell-cell contact is less influential. When adhesion between cells becomes important, the basic continuum model based on mass balance fails to capture the biological response. Non-local continuum models are one possibility [14, 130]. Alternatively, cell-centered approaches assume the existence of a potential energy function associated to each cell. The potential describes the interaction of cells with the environment and neighboring cells [101]. The limitation of cell-centered approaches, alluded to before, is the size of the domain that can be represented. For reconstructive surgery applications, the simulation of the tissue scale is ultimately desired.

The constitutive laws for the cell population dynamics depend in turn on the other class of kinematic variables associated to mechanobiology: the signaling network. Once more, looking at the larger scale balance laws take the form of reaction-diffusion PDEs. In contrast to the cell population kinetics, cytokines obey more classical models of chemical reactions [340]. However, the complexity arises when we zoom in to smaller spatial scales. Cells are the basic unit of life and their individual actions synchronize to regulate mechanical homeostasis of tissues. To understand how cells build and remodel the ECM we have to capture the intracellular signaling pathways. A widely used approach is to use ordinary differential equations (ODE) to represent so-called *network motifs* [173]. Network motifs are simple regulatory circuits that appear in the signaling cascades inside of cells. The four basic motifs are positive/negative feedback and feedforward loops [150].

### 1.2.4 Wound Healing

Wounds are an evidently common concern in plastic and reconstructive surgery [29]. From a fundamental point of view, the healing of wounds reveals a unique capacity of living materials to self-assemble and regenerate [145]. We have focused on the cellular response to perturbations in their mechanical environment, a wound is a complete disruption of the physiological condition. Remarkably, skin is capable of regenerating itself starting from a blood clot, albeit with suboptimal tissue quality [240]. Moreover, some general events taking place during wound healing are not unique to skin, but are shared amongst many tissues such as muscle, heart or liver tissue, to name just a few [392]. Being easily accessible, skin is a good model system to understand some of the fundamental mechanisms guiding tissue regeneration. It is no wonder that cutaneous wound healing has captured significant attention. Yet, we still have not uncovered all the mysteries that would allow us to heal wounds perfectly, or engineer skin with the same mechanical characteristic as the native tissue [104, 381].

Wound healing is a process spanning several spatial and temporal scales. The process starts with the formation of a clot that prevents blood loss. This initial stage is called hemostasis. The platelets trapped in the clot degrade, releasing a cocktail of growth factors that trigger the healing events. The first cell type to infiltrate the damaged zone in response to the initial signal are the leucocytes, primarily neutrophils. These cells escape the circulating blood and migrate into the wound minutes after injury. Their main role is to clean the clot from pathogens. The infiltration of neutrophils in the wound site marks the start of the inflammatory phase. A second wave of inflammatory cells is constituted by macrophages which continue the cleaning tasks. Macrophages, additionally, degrade the fibrin clot, phagocytize neutrophils, and release other growth factors and chemical signals such as TGF- $\beta$  [240]. The actual tissue regeneration occurs in the third, proliferative phase. In healthy skin there are two protagonist cell types: keratinocytes and fibroblasts. These cell populations are also main actors during the proliferative phase. The epidermis is rebuilt by the keratinocytes, which divide and migrate inward from the wound edge [330]. Fibroblasts migrate into the fibrin clot from the surrounding dermis and lay down a new collagen matrix [145]. Two other cell populations become important in the healing process. To guarantee the nutrient and oxygen supply, endothelial cells coordinate the process of new blood vessel formation called angiogenesis [333]. Importantly as well, the mechanical homeostatic state of skin requires an *in vivo* pretension. Upon wounding, all mechanical tension is released. Hence, to recover

the physiological condition the newly laid down ECM has to be contracted. Even though fibroblasts have some ability to contract collagen gels, during wound healing they differentiate into a more specialized phenotype denominated myofibroblast [372]. Myofibroblasts express  $\alpha$ -SM actin, which is the actin isoform characteristic of vascular smooth muscle cells. However, despite having similar contractile machinery, the mechanisms of force generation between smooth muscle cells and myofibroblasts is distinct [372]. Myofibroblasts generate contractile forces that can be sustained over long periods of time. Smooth muscle cell contraction is regulated primarily by intracellular  $\text{Ca}^{2+}$  levels, leading to a fast but short-lived actuation. Contraction of myofibroblasts is regulated by the Rho kinase pathway, which can control sustained contractions. It has been hypothesized that such long contractions allow for the freshly deposited collagen to lock the tissue while it is under tension, thus effectively cementing the pre-strained condition of the ECM. The last stage of wound healing is the remodeling phase. Finishing the proliferative phase, the dermis becomes relatively cellular, the new blood vessels retreat, the myofibroblasts and many fibroblasts undergo apoptosis [386]. Yet, at this stage the collagen network that has just been laid down does not resemble the uninjured tissue. The remodeling stage is slower, taking several months, and its goal is to gradually remodel the collagen matrix to approximate the healthy state [100].

### 1.3 Skin Mechanics

We focus now on the second corner of the diagram. From the point of view of the mechanician we want to be able to characterize the states of deformation, stress and failure of skin in response to reconstructive treatment and in wound healing. Of course once more our starting point has to be influenced by the spatial scale we are interested in. To capture small scales, at the sub cellular level, we would need coarse grained models. However, the mechanical response in clinical settings requires models from the cell to the tissue level where continuum mechanics are an appropriate and common option. Overall, the mechanics of skin are almost identical to the continuum theories used in engineering materials. But there is one key difference: Biological materials can grow and remodel to adapt to their mechanical environment, requiring additional considerations.

### 1.3.1 Measuring Deformations and Forces on Skin

We have already made some headway in the kinematic description by describing the anatomy and the microstructure of the different layers of skin. For mechanics, however, we want to quantify the relative deformations at the different scales in order to draw stress-strain relationships. Skin is a thin membrane, thus for some applications it is sufficient to consider the surface description and ignore or homogenize the thickness heterogeneity. Moreover, skin is conveniently exposed to the outside world, making it an ideal tissue in which to perform mechanical testing *in vivo*. For instance, motion capture technologies have been successfully used in computer graphics to estimate overall deformations of skin in everyday tasks [291, 328], and facial deformations [40]. More recently, the biomechanics community has adapted these approaches focusing on smaller surfaces for higher accuracy of the local deformation [236]. When the dynamic deformation is not of interest, other algorithms borrowed from computer vision can be used to estimate strain fields. For example, in tissue expansion, we are interested in the chronic deformation of expanded tissue. In this setting, multi-view stereo (MVS) allows for a very flexible experimental setup [60]. MVS yields a three-dimensional point cloud out of a set of uncalibrated photographs of a static scene [157]. Simultaneously to the extraction of strain fields, mechanical characterization of tissues requires measuring forces or estimating stress fields. *In vitro*, uniaxial and bi-axial tests are well-established techniques to obtain force and strain data [11]. Another option are full-field bulge tests [374]. Yet, as occurs to most living structures, their *in vivo* condition is not stress-free [229]. Due to the ease of access, there is a comprehensive literature related to *in vivo* mechanical testing of skin, including the use of extensometers [227], suction devices [93], micro-robots [111], to name a few.

### 1.3.2 Material Constitutive Equations

The stress-strain relationship of skin is highly nonlinear. The *J*-shape of the stress-strain curve is typical of collagenous soft tissues [373]. Various constitutive models have been used to characterize skin and there still does not seem to be a consensus [184]. Even nowadays, skin is described with Neo-Hookean and Ogden strain energy functions which are isotropic [113]. While for some applications this assumption has little effect, in reality skin

shows marked anisotropic material properties. In the nineteen century, Langer cut circular cuts on the skin of human cadavers and measured how the circles turned into ellipses, demonstrating the directions of higher stiffness [214]. Experiments both *in vivo* and *ex vivo* have quantified the anisotropic properties and motivated the choice of appropriate constitutive laws. Earlier on, strain energy functions based on the components of the strain tensor in a local reference frame were proposed, and they continue to be used [111]. However, the macroscopic mechanical properties of skin are linked to its well-defined fibrous microstructure. At lower strains, the collagen fibers in the dermis are undulated and barely carrying any load. As the strain increases, the fibers are straightened and aligned, showing an exponential increase in the stress [89]. Bringing together these and other evidences, the trend points out towards structurally-motivated constitutive laws to capture faithfully the mechanical response. The first structural constitutive model for skin can be attributed to Lanir [218]. He modeled each fiber as an elastic spring and proposed a statistical distribution of the degree of undulation of the fibers. To capture anisotropy, he also assumed a probabilistic distribution of the fiber orientation. The excessive computational cost of performing numerical integrals over the statistical distributions is perhaps one of the reasons why this model is not widely used in the biomechanics community [312]. The constitutive model proposed by Gasser, Ogden and Holzapfel, originally used to model arteries, introduced an exponential contribution of the fiber stretch to the strain energy, and it has become a popular constitutive law for other collagenous tissues, including skin [57].

Even though the dermis is the main load-carrying structure of skin, some phenomena require the explicit consideration of the different layers of skin. For instance, understanding and simulating wrinkling requires modeling the interaction and different material properties of the epidermis, dermis, and hypodermis [110]. Simulating shear properties of skin under large deformations is important for haptic applications; these properties are also affected by the multi-layer nature of the tissue [213]. To measure through-thickness deformations *in vitro*, image correlation techniques similar to those already listed for surface motion capture can be used on explanted skin samples [129]. *In vivo*, combining ultrasound with image processing algorithms has been successfully employed [99]. A comprehensive review of the constitutive models for skin and its experimental characterization can be found in [184]. Nonetheless, the main idea we want to convey is the importance of constitutive models developed from the bottom up, based on the tissue microstructure. The reason for this comes from the cell-centered approach for the mechanobiology that we have supported thus

far. Mathematical models of cellular mechanotransduction are intimately related to the microstructure of the tissue [121].

### 1.3.3 Mechanics of Growth and Remodeling

Unique to living systems is their ability to adapt to their environment in order to maintain mechanical function and homeostasis. As we have discussed, the study of the mechanobiology of skin deals with the transduction of forces and deformations into chemical signaling networks that ultimately regulate how cells locally remodel the surrounding tissue. Classical problems in continuum mechanics often involve inert materials with constant material properties and mass. The constitutive laws that we have briefly enunciated describe the mechanical response of skin at a given point in time; yet, the tissue is undergoing constant changes. In clinical practice, it is often necessary to predict the long term adaptation of skin. Such is the case in tissue expansion or wound healing. Growth is defined as the addition mass. Remodeling is the change in material properties over time [361]. Modeling the growth and remodeling of biological tissues has gained increasing attention in the past two decades. Several comprehensive reviews exist [20, 251]. There are two main approaches to model growth, one is based on the theory of mixtures, the other one is known as volumetric growth [8]. The latter introduces growth kinematically by splitting the central kinematic object of continuum mechanics, the deformation gradient, into growth and elastic components [320]. This approach resembles the theory of plasticity, however, there are important conceptual differences.

The deformation gradient  $\mathbf{F}$  is a tensor field which encapsulates the information related local deformations, namely, the strains at every point of the body of interest. The split  $\mathbf{F} = \mathbf{F}^e \cdot \mathbf{F}^g$ , assumes the existence of a microscopic structure associated to the cellular level in which local kinematic assumptions can be made [68]. The growth tensor  $\mathbf{F}^g$  captures the effect of the mechanobiological response. The elastic part  $\mathbf{F}^e$  contributes to the generation of internal stresses and enters the equation for balance of linear momentum. Thus, this split conveniently decouples the constitutive equations related to the mechanobiology from those that express the mechanical properties of the tissue [158]. Another relevant consequence of this split is the explicit instantiation of a stress-free incompatible configuration [59]. The fact that tissues *in vivo* are under some amount of prestrain has been known for decades [229]. Conceptually, the intermediate configuration introduced by the decomposition of  $\mathbf{F}$  is equivalent to cutting a given sample of the material into smaller and

smaller pieces. In the limit, the subdivision of the material reaches the microscopic cell environment and at that point all residual stress have been released.

### 1.3.4 Coupling Mechanics and Biology

The multiplicative decomposition of the deformation gradient into growth and elastic components,  $\mathbf{F} = \mathbf{F}^e \cdot \mathbf{F}^g$ , segregates the use of constitutive equations related to mechanobiology from those needed to capture the mechanical response of the tissue. At the same time, in the real world, the only tensor field that makes physical sense is the full deformation gradient  $\mathbf{F}$ . The coupling of mechanics and biology thus comes from requiring the solution of the balance equations in the physical domain, where there is a combined effect of the growth and elastic components.

Our aim is to capture the mechanics and mechanobiology of skin in plastic and reconstructive surgery. Bringing all the background together at this point, we propose the following approach. The end application is at the tissue level in which continuum models are well-established. For the mechanician, the classical theory of continuum mechanics is the starting point. For the computational biologist, reaction-diffusion systems and mass-balance equations can be used to describe the chemical signals and cell populations respectively. To introduce the mechanobiology we support the multiplicative split of the deformation gradient into growth and elastic contributions. This introduces an intermediate, stress-free, incompatible configuration. The map between the reference and the intermediate configuration is dictated by the balance laws of the mechanobiology of skin. Namely, at this point we can make use of local, cell-centered models for mechanotransduction such as the development of focal adhesions by fibroblasts in response to local ECM properties and morphology [43], the evolution equation of an area growth variable in response to elastic stretch [51], or the gradual reorientation of the collagen fibers in the direction of the principal stresses [250], to name a few examples. The map between the intermediate and the current configuration requires the constitutive law for the mechanical response of skin. It is evident at this point that since the mechanobiology links the cellular behavior to the local microstructure, strain energy functions based on this microstructure are the most appropriate, for example those proposed by Lanir or Gasser, Ogden and Holzapfel, which have already been fitted to skin experimental data showing good agreement [374].

We have already showcased our proposed strategy to simulate events that are relevant to

plastic and reconstructive surgery practice. We have simulated growth of skin in response to tissue expansion, a widely-used technique that grows local tissue flaps for reconstruction of large defects [51]. Emphasizing the effect of the collagen fiber arrangement and the need for full three-dimensional geometric representations, we have simulated the choice of different flap designs and shown the difference in stress fields which agree with zones of tissue necrosis [55]. Finally, we have also focused on the coupling of chemical and biological species to the tissue mechanical properties during cutaneous wound healing [58]. There is still the need for further model refinements and new developments, as well as extensive experimental validation. Yet, we are confident that our approach has enabled the conjunction of biological and mechanical knowledge, and put it within reach of plastic and reconstructive surgeons in order to understand disease and improve healthcare by means of computational simulations.

## 1.4 Structure of the Thesis

The thesis is divided in three parts which focus on three different applications of skin mechanics and mechanobiology in plastic and reconstructive surgery. The first part, which is the core of the thesis, deals with the technique of tissue expansion. The second part studies the mechanical consequences of different flap designs. The third part presents a coupled chemo-bio-mechanical framework for cutaneous wound healing.

The core topic of the thesis, tissue expansion, is covered in Chapters 2 through 9. Chapter 2 was published in the *Journal of the Mechanics and Physics of Solids* [51]. It introduces the continuum model of skin growth in response to overstretch. Chapter 3 was published in the *International Journal of Nonlinear Mechanics* and extends the original model to capture the anisotropic characteristics of skin [52]. Chapter 4 was published in *Biomechanics and Modeling in Mechanobiology* and showcases the application of the model in a clinically relevant scenario by simulation expansion on patient specific geometries [418]. Chapter 5 was published in the *Journal of Theoretical Biology* and discusses in detail the mechanobiological knowledge that links overstretch to growth [417]. Chapter 6 was published in *Computer Methods in Applied Mechanics and Engineering* and presents a novel thin shell formulation tailored for biological membranes and based on isogeometric analysis [57]. The need for this isogeometric thin shell description was motivated by an experimental protocol designed for the characterization of skin expansion which is the topic of the following three chapters in

the thesis. Chapter 7 was published in *Act Biomaterialia* [54]. It describes the methodology of our porcine animal model of tissue expansion based on multi-view stereo and isogeometric analysis. Chapter 8 was published in *Biomechanics and Modeling in Mechanobiology*, and extends the numerical analysis of the original experimental protocol by emphasizing the anisotropic response of skin [60]. Chapter 9 was submitted to the *Annals of Biomedical Engineering* and presents results of a second round of experiments. In particular, it refines the experimental protocol and allows the quantification of incompatibility attributed to the development of residual stresses during growth [59].

The second topic of the thesis is the study of flap design and is covered on Chapters 10 and 11. Chapter 10 was published in *Computers and Structures* [55]. It shows the simulation of different flap designs which is a challenging problem involving finite deformations, three dimensional geometries of thin membranes, and nonlinear material properties. Chapter 11 demonstrates the usefulness of computational simulations of flap design for medical applications. This chapter was published in *Plastic and Reconstructive Surgery*, the official journal of the American Society of Plastic Surgeons [56].

The third topic of the thesis is wound healing modeling and spans Chapters 12 and 13. Chapter 12 is a review paper published in *Pediatric Research* which synthesizes the advances and gaps in current models of wound healing [53]. One of the gaps identified in this review was the lack of state-of-the art mechanical descriptions coupled to the mechanobiological description. Chapter 13, published in *Computer Models in Biomechanics and Biomedical Engineering*, addresses precisely this gap and presents a general framework for chemo-bio-mechanical coupling of wound healing [58].

For all the manuscripts referred to above, I am responsible for conceptualizing the study and establishing the theoretical basis for the mathematical models. For the first topic of the thesis I am responsible for identifying the clinical procedure of tissue expansion as an important medical application that could benefit from computational mechanics tools. I was the one who proposed the use of the theory of finite growth to model the response of skin to overstretch. For Chapter 2, I was the leader of a team of four students; we were enrolled in Prof. Kuhl's class and the modeling of skin expansion was our final project. For Chapter 3 I was also responsible for the computational simulations. For Chapters 4 and 5 I led the study and was assisted by Alexander Zollner, a new group member at Kuhl's lab at the time, who did most of the numerical simulations and is therefore listed as the first author in those publications. I became interested in isogeometric analysis and realized its potential to model

thin biological membranes. Since only linear materials had been developed for isogeometric analysis, I proposed and implemented the theory for nonlinear materials. Hardik Kabaria helped with the geometry expertise; and I was co-advised by Kai Bletzinger who provided insightful comments and important discussions related to shell theory. For Chapters 7, 8 and 9, I designed the experiment and carried out the numerical analysis, however the experiments were carried out by our clinical collaborators in the Ann & Robert H. Lurie Children's Hospital in Chicago. I identified the need to perform simulations of different flap designs following skin expansion. Despite mechanical stresses and directions of tissue anisotropy being considered by surgeons as critical factors affecting the success of surgical procedures, there was a lack of numerical investigations in three-dimensional geometries. This motivated the design and execution of the work presented in Chapter 10. I suggested moving this work towards the clinical setting. I was assisted by Jordan Steinberg who was pivotal in translating the engineering concepts towards a medically relevant discussion. For Chapters 2, 3, 4, 5, 7, 8, 9, 10 and 11, I was advised by Dr. Arun Gosain who provided the clinical expertise. For the entirety of the work I was advised by Prof. Ellen Kuhl.

## Chapter 2

# Growing Skin: A Computational Model for Skin Expansion in Reconstructive Surgery

**Abstract.** The goal of this manuscript is to establish a novel computational model for stretch-induced skin growth during tissue expansion. Tissue expansion is a common surgical procedure to grow extra skin for reconstructing birth defects, burn injuries, or cancerous breasts. To model skin growth within the framework of nonlinear continuum mechanics, we adopt the multiplicative decomposition of the deformation gradient into an elastic and a growth part. Within this concept, we characterize growth as an irreversible, stretch-driven, transversely isotropic process parameterized in terms of a single scalar-valued growth multiplier, the in-plane area growth. To discretize its evolution in time, we apply an unconditionally stable, implicit Euler backward scheme. To discretize it in space, we utilize the finite element method. For maximum algorithmic efficiency and optimal convergence, we suggest an inner Newton iteration to locally update the growth multiplier at each integration point. This iteration is embedded within an outer Newton iteration to globally update the deformation at each finite element node. To demonstrate the characteristic features of skin growth, we simulate the process of gradual tissue expander inflation. To visualize growth-induced residual stresses, we simulate a subsequent tissue expander deflation. In

particular, we compare the spatio-temporal evolution of area growth, elastic strains, and residual stresses for four commonly available tissue expander geometries. We believe that predictive computational modeling can open new avenues in reconstructive surgery to rationalize and standardize clinical process parameters such as expander geometry, expander size, expander placement, and inflation timing.

## 2.1 Motivation

Tissue expansion has revolutionized reconstructive surgery in the last three decades. It was first proposed more than half a century ago to reconstruct a traumatic ear defect using a temporarily implanted rubber balloon [270]. However, the technique was rarely used in clinical practice until it was rediscovered over 20 years later as an option for skin expansion in post-mastectomy breast reconstruction [311]. Since then, application of tissue expansion



Figure 2.1: Tissue expansion for pediatric forehead reconstruction. The patient, a one-year old girl, presented with a giant congenital nevus involving almost 50 percent of the forehead, affecting the hairline and the left eyebrow. Three forehead and scalp expanders were implanted simultaneously for *in situ* forehead flap growth. For complete resurfacing of the region, serial tissue expansion was performed to successively stretch the previously expanded tissues until the entire nevus could be excised and resurfaced. This technique allows to resurface large anatomical areas with skin of similar color, quality, and texture. The follow-up photograph shows the patient at age three; the initial defect was excised and resurfaced with expanded forehead and scalp flaps.

for breast reconstruction has gained widespread use. The technique has since advanced as one of the key surgical procedures to create skin flaps for the resurfacing of large congenital defects of the skin including giant nevi and vascular anomalies [16, 17, 139]. It is also

widely used for the correction of skin deformity following burn injuries and other forms of traumatic skin loss [13, 91]. Skin expansion is an ideal way to grow skin that matches the color, texture, and hair bearing of the surrounding healthy skin, while minimizing scars and risk of rejection [319]. Figure 2.1 illustrates an example of tissue expansion in pediatric forehead reconstruction [141]. The patient, a one-year old girl, presented with a giant congenital nevus involving almost 50 percent of the forehead, affecting the hairline and the left eyebrow. Three forehead and scalp expanders were used simultaneously for *in situ* forehead flap growth. For complete resurfacing of the region, serial tissue expansion was then performed, successively stretching the previously expanded tissues until the entire nevus could be excised and resurfaced. In skin resurfacing, tissue expanders are typically placed in subcutaneous pockets adjacent to the skin defect, while their ports to regulate expander filling are either buried in a remote location away from the defect, or left outside the skin for ease of injection. The amount of filling is controlled by visual inspection of skin color, capillary refill, and simple palpation of the skin over the expander [319]. Multiple subsequent serial inflations stretch the skin and stimulate tissue growth. Once new skin is produced, the device is removed, and the new skin is used to repair the adjacent defect zone. The follow-up photograph in Figure 2.1, right, shows the patient at age three after the initial defect was excised and resurfaced with expanded forehead and scalp flaps. Similar expansion techniques have successfully been used to grow skin in the trunk [15], and in the upper and lower extremities [139].

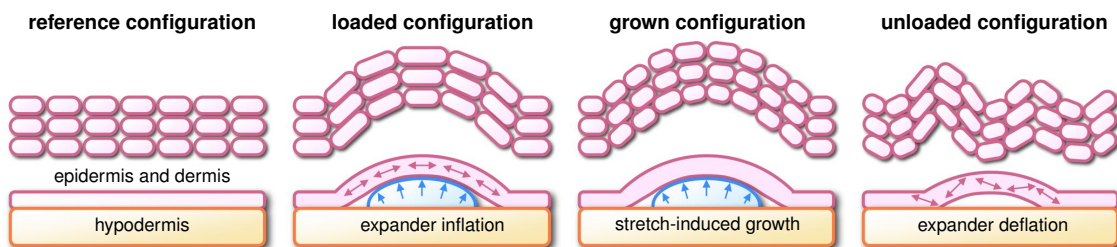


Figure 2.2: Schematic sequence of tissue expander inflation and deflation. At biological equilibrium, the skin is in a physiological state of resting tension, left. A tissue expander is implanted subcutaneously between the skin, consisting of the epidermis and dermis, and the hypodermis. When the expander is inflated, the skin is loaded in tension, middle left. Mechanical stretch induces cell proliferation causing the skin to grow. Growth restores the state of resting tension, middle right. Expander deflation reveals the irreversible nature of skin growth associated with growth-induced residual stresses in the skin layer, right.

Figure 2.2 shows a schematic sequence of the mechanical processes that occur during tissue expansion. Initially, at biological equilibrium, the skin is in a natural state of resting tension [342]. Skin is a composite material consisting of two layers: the epidermis, a 0.06 to 1.0 mm thick waterproof, protective outer layer and the dermis, a 1.0 to 4.0mm thick load bearing inner layer [342]. When used for skin resurfacing, tissue expanders are implanted in the subcutaneous tissue beneath these two skin layers. When the expander is inflated, the epidermis and the dermis are loaded in tension. Dermal stretches beyond a critical level trigger a series of stretch-induced signaling pathways [364]. Mechanotransduction affects a network of integrated cascades including cellular architecture and function such as cytoskeletal structure, extracellular matrix, enzyme activity, second messenger systems, and ion channel activity [92]. As a consequence, the skin grows and restores the state of resting tension. This cycle of expander inflation and growth is repeated multiple times, typically on a weekly basis. Remarkably, as demonstrated by immunocytochemical analyses, the expanded tissue undergoes normal cell differentiation and maintains its characteristic phenotype [402]. When the expander is removed, the skin retracts and reveals the irreversible nature of skin growth. This is associated with growth-induced residual stresses in the skin layer [137]. Although the tissue initially displays epidermal thickening and dermal thinning upon expansion, both thickness changes are reversible under expander removal [382].



Figure 2.3: Tissue expanders to grow skin flaps for defect correction in reconstructive surgery. Typical applications are birth defect correction, scar revision in burn injuries, and breast reconstruction after tumor removal. Devices are available in different shapes and sizes, circular, square, rectangular, and crescent-shaped. They consist of a silicone elastomer inflatable expander with a reinforced base for directional expansion, and a remote silicone elastomer injection dome. Reprinted with permission, Mentor Worldwide LLC.

Several studies have focused on understanding this adaptation process from a biomechanical point of view. In this endeavor, two parameters have received special attention: the rate

of expansion and the expander geometry. A series of *in vivo* experiments has demonstrated that the rate of expansion, every day over a period of two weeks versus weekly over a period of six weeks, had no significant impact on area gain and biomechanical tissue properties [414]. The expander geometry, however, seems to play a more crucial role [48]. Figure 2.3 displays four commonly used tissue expander geometries, circular, square, rectangular, and crescent-shaped. For regular circular and rectangular expanders, simple mathematical models have been proposed to kinematically correlate expander volume and surface area [103, 341]. However, it was soon recognized that purely kinematic models severely overestimate the net gain in surface area [385]. The observed difference of up to a factor four seems obvious, since these models assume that the entire deformation can be attributed to irreversible growth, completely neglecting the reversible elastic deformation that manifests itself in skin retraction upon expander removal [231], see Figure 2.2, right. To correct for this error, empirical correction factors of 6.0, 3.75, and 4.5 have been proposed for the circular, rectangular, and crescent-shaped expanders [385]. Despite these efforts, the choice of the appropriate expander geometry and size is still almost exclusively based on the surgeon's personal preference, and the discrepancy between recommended shapes, sizes, and volumes remains enormous [231]. This demonstrates the ongoing need to rationalize criteria for a standardized device selection.

In this manuscript, we propose a rigorous, mechanistic approach to systematically compare different tissue expander geometries in terms of stress, strain, and area gain. To model skin growth in response to tissue expansion, we adopt the framework of finite growth. Finite growth theories have experienced a breakthrough in continuum thermodynamics with the introduction of an incompatible growth configuration, along with the corresponding multiplicative decomposition of the deformation gradient into an elastic and a growth part [320]. This idea is not new. Its basic concept was originally developed in the context of finite strain plasticity [222], and was then adopted for biological growth [361]. Today, there seems to be a general agreement that the incompatible growth configuration is a suitable and effective approach towards finite growth, and a tremendous amount of research has been devoted to establish continuum theories of finite growth within the last decade [102, 106, 138, 233]. These theories have been applied successfully to characterize growing tumors [6, 96], tendons [122], mucous membranes [226, 266], vascular tissues [170, 207, 363], and cardiac tissues [133, 200, 314]. While earlier studies were primarily of theoretical and analytical nature [32, 120, 124], we can now observe a clear trend towards the computational modeling of

volumetric growth, typically by introducing the growth tensor as an internal variable within a finite element framework [134, 158, 332]. A recent monograph summarizes the essential findings, trends, and open questions in this progressively evolving new field [8].

Despite ongoing research in growing biological systems, the growth of thin biological membranes remains severely understudied. Only recently, first attempts have been presented to mathematically characterize growth-induced instabilities and residual stresses in thin elastic membranes [95, 137, 248]. However, despite a few exceptions [226], most of these attempts remain restricted to an axisymmetric response. Unfortunately, the same is true for the only computational model for skin growth proposed to date [351], which is unsuitable to model arbitrary tissue expander geometries. It is of axisymmetric nature and can therefore only be applied to model skin growth using a circular tissue expander. The promising first results of this study have motivated our attempts to create a fully three-dimensional computational model for tissue expansion that allows us to precisely quantify stress, strain, and area gain in response to different, arbitrarily shaped tissue expander geometries.

To document our efforts, this manuscript is organized as follows. In Section 5.2.1, we give a brief overview of the continuum equations for finite growth including the kinematic equations, the balance equations, and the constitutive equations. In particular, we introduce the growth tensor for transversely isotropic growth and the strain-driven evolution equation for its key kinematic variable, the area growth. In Section 5.2.2, we illustrate the temporal and spatial discretizations of the biological and mechanical equilibrium equations, along with their consistent algorithmic linearization. We then demonstrate the features of our model in Section 3.4, focussing on the two load cases of tissue expander inflation and deflation. After pointing out the limitations of our model, we close with some concluding remarks in Section 10.5.

## 2.2 Continuum Modeling of Area Growth

In this section, we introduce the governing equations of area growth within the framework of open system thermodynamics. We briefly summarize the kinematic equations, the balance equations, and the constitutive equations.

### 2.2.1 Kinematics of Area Growth

We adopt the kinematics of finite deformations and introduce the deformation map  $\varphi$ , which, at any given time  $t$ , maps the material placement  $\mathbf{X}$  of a physical particle in the material configuration to its spatial placement  $\mathbf{x}$  in the spatial configuration.

$$\mathbf{x} = \varphi(\mathbf{X}, t) \quad (2.1)$$

In what follows, we apply a formulation which is entirely related to the material frame of reference. Accordingly,  $\nabla\{\circ\} = \partial_{\mathbf{X}}\{\circ\}|_t$  and  $\text{Div}\{\circ\} = \partial_{\mathbf{X}}\{\circ\}|_t : \mathbf{I}$  denote the gradient and the divergence of any field  $\{\circ\}(\mathbf{X}, t)$  with respect to the material placement  $\mathbf{X}$  at fixed time  $t$ . Herein  $\mathbf{I}$  is the material identity tensor. To characterize finite growth, we adopt the multiplicative decomposition of deformation gradient

$$\mathbf{F} = \mathbf{F}^e \cdot \mathbf{F}^g \quad \text{with} \quad \mathbf{F} = \nabla_{\mathbf{X}}\varphi \quad (2.2)$$

into an elastic part  $\mathbf{F}^e$  and a growth part  $\mathbf{F}^g$  [320]. This implies that the total Jacobian

$$J = J^e J^g \quad \text{with} \quad J = \det(\mathbf{F}) > 0 \quad (2.3)$$

obeys a similar multiplicative decomposition into an elastic part  $J^e = \det(\mathbf{F}^e)$  and a growth part  $J^g = \det(\mathbf{F}^g)$ . We idealize skin as a thin layer characterized through the unit normal  $\mathbf{n}_0$  in the undeformed reference configuration. The length of the deformed skin normal  $\mathbf{n} = \text{cof}(\mathbf{F}) \cdot \mathbf{n}_0 = J \mathbf{F}^{-t} \cdot \mathbf{n}_0$  introduces the area stretch

$$\vartheta = \vartheta^e \vartheta^g \quad \text{with} \quad \vartheta = \|\text{cof}(\mathbf{F}) \cdot \mathbf{n}_0\| = J [\mathbf{n}_0 \cdot \mathbf{C}^{-1} \cdot \mathbf{n}_0]^{1/2} \quad (2.4)$$

which we can again decompose into an elastic area stretch  $\vartheta^e = \|\text{cof}(\mathbf{F}^e) \cdot \mathbf{n}_0\|$  and a growth area stretch  $\vartheta^g = \|\text{cof}(\mathbf{F}^g) \cdot \mathbf{n}_0\|$ . Here,  $\text{cof}(\circ) = \det(\circ) (\circ)^{-t}$  denotes the cofactor of the second order tensor  $(\circ)$ . As characteristic deformation measures, we introduce the right Cauchy Green tensor  $\mathbf{C}$  in the undeformed reference configuration and its elastic counterpart  $\mathbf{C}^e$  in the intermediate configuration,

$$\mathbf{C} = \mathbf{F}^t \cdot \mathbf{F} \quad \text{and} \quad \mathbf{C}^e = \mathbf{F}^{et} \cdot \mathbf{F}^e \quad (2.5)$$

where both are related through the following identity,  $\mathbf{C}^e = \mathbf{F}^{g-t} \cdot \mathbf{C} \cdot \mathbf{F}^{g-1}$ . Finally, we introduce the pull back of the spatial velocity gradient  $\mathbf{l}$  to the intermediate configuration,

$$\mathbf{F}^{e-1} \cdot \mathbf{l} \cdot \mathbf{F}^e = \mathbf{L}^e + \mathbf{L}^g \quad \text{with} \quad \mathbf{l} = \dot{\mathbf{F}} \cdot \mathbf{F}^{-1} \quad (2.6)$$

which obeys the additive split into the elastic velocity gradient  $\mathbf{L}^e = \mathbf{F}^{e-1} \cdot \dot{\mathbf{F}}^e$  and the growth velocity gradient  $\mathbf{L}^g = \dot{\mathbf{F}}^g \cdot \mathbf{F}^{g-1}$ . Here, we have applied the notation  $\{\circ\} = \partial_t \{\circ\}|_{\mathbf{X}}$  to denote the material time derivative of any field  $\{\circ\}(\mathbf{X}, t)$  at fixed material placement  $\mathbf{X}$ .

### 2.2.2 Balance Equations of Area Growth

We characterize growing tissue using the framework of open system thermodynamics in which the material density  $\rho_0$  is allowed to change as a consequence of growth [201, 202]. The balance of mass for open systems balances its rate of change  $\dot{\rho}_0$  with a possible in- or outflux of mass  $\mathbf{R}$  and mass source  $\mathcal{R}_0$  [290, 368].

$$\dot{\rho}_0 = \text{Div}(\mathbf{R}) + \mathcal{R}_0 \quad (2.7)$$

Similarly, the balance of linear momentum balances the density-weighted rate of change of the momentum  $\dot{\mathbf{v}}$ , where  $\mathbf{v} = \dot{\varphi}$  is nothing but the spatial velocity, with the momentum flux  $\mathbf{P} = \mathbf{F} \cdot \mathbf{S}$  and the momentum source  $\rho_0 \mathbf{b}$ .

$$\rho_0 \dot{\mathbf{v}} = \text{Div}(\mathbf{P} \cdot \mathbf{S}) + \rho_0 \mathbf{b} \quad (2.8)$$

Herein,  $\mathbf{P}$  and  $\mathbf{S}$  are the first and second Piola-Kirchhoff stress tensors, respectively. Last, we would like to point out that the dissipation inequality of open systems

$$\rho_0 \mathcal{D} = \mathbf{S} : \frac{1}{2} \dot{\mathbf{C}} - \rho_0 \dot{\psi} - \rho_0 \mathcal{S} \geq 0 \quad (2.9)$$

typically contains an extra entropy source  $\rho_0 \mathcal{S}$  to account for the growing nature of living biological systems [201, 249]. Equations (4.7) and (4.8) represent the mass-specific versions of the balance of momentum and of the dissipation inequality which are particularly useful in the context of growth since they contain no explicit dependencies on the changes in mass [202].

### 2.2.3 Constitutive Equations of Area Growth

To close the set of equations, we introduce the constitutive equations for the mass flux  $\mathbf{R}$ , for the mass source  $\mathcal{R}_0$ , for the momentum flux  $\mathbf{S}$ , for the momentum source  $\mathbf{b}$ , and for the growth tensor  $\mathbf{F}^g$ . For the mass flux  $\mathbf{R}$ , we adopt a definition in analogy to Fick's law,

$$\mathbf{R} = \mathbf{D} \cdot \nabla \rho_0 \quad (2.10)$$

and relate it directly to the density gradient  $\nabla \rho_0$  through the conductivity tensor  $\mathbf{D}$  [203]. In the case of transversely isotropic in-plane mass conduction, the conductivity tensor  $\mathbf{D} = d_0 [\mathbf{I} - \mathbf{n}_0 \otimes \mathbf{n}_0]$  reduces to the second order tensor for transverse isotropy  $[\mathbf{I} - \mathbf{n}_0 \otimes \mathbf{n}_0]$  scaled by the mass conduction coefficient  $d_0$ , which has the unit of length squared divided by the time. Immunocytochemistry has shown that expanded tissue undergoes normal epidermal cell differentiation [402]. Accordingly, we assume that the newly grown skin has the same density as the initial tissue. This implies that the mass source

$$\mathcal{R}_0 = \rho_0 \operatorname{tr}(\mathbf{L}^g) \quad (2.11)$$

can be expressed as the density-weighted trace of the growth velocity gradient  $\operatorname{tr}(\mathbf{L}^g) = \dot{\mathbf{F}}^g : \mathbf{F}^{g-t}$  [158]. For the sake of transparency, we model skin as an elastic material that can be characterized exclusively in terms of the Helmholtz free energy  $\psi = \hat{\psi}(\mathbf{C}, \mathbf{F}^g)$ , which we can use to evaluate the dissipation inequality (4.8).

$$\rho_0 \mathcal{D} = \left[ \mathbf{S} - \rho_0 \frac{\partial \psi}{\partial \mathbf{C}} \right] : \frac{1}{2} \dot{\mathbf{C}} + \mathbf{M}^e : \mathbf{L}^g - \rho_0 \frac{\partial \psi}{\partial \rho_0} \mathcal{R}_0 - \rho_0 \mathcal{S}_0 \geq 0 \quad (2.12)$$

Similar to finite strain plasticity [222], we observe that the Mandel stress of the intermediate configuration  $\mathbf{M}^e = \mathbf{C}^e \cdot \mathbf{S}^e$  is energetically conjugate to the growth velocity gradient  $\mathbf{L}^g = \dot{\mathbf{F}}^g \cdot \mathbf{F}^{g-1}$ . From the dissipation inequality (4.10), we obtain the definition of the second Piola Kirchhoff stress  $\mathbf{S}$  as thermodynamically conjugate quantity to the right Cauchy Green deformation tensor  $\mathbf{C}$ .

$$\mathbf{S} = 2 \rho_0 \frac{\partial \psi}{\partial \mathbf{C}} = 2 \frac{\partial \psi}{\partial \mathbf{C}^e} : \frac{\partial \mathbf{C}^e}{\partial \mathbf{C}} = \mathbf{F}^{g-1} \cdot \mathbf{S}^e \cdot \mathbf{F}^{g-t} \quad \text{with} \quad \mathbf{S}^e := 2 \rho_0 \frac{\partial \psi}{\partial \mathbf{C}^e} \quad (2.13)$$

As a side remark, the elastic constitutive moduli  $\mathbf{L}^e$  can be obtained by taking the second derivative of the Helmholtz free energy  $\psi$  with respect to the elastic part of the deformation

gradient  $\mathbf{F}^e$ .

$$\mathbf{L}^e = 2 \frac{\partial \mathbf{S}^e}{\partial \mathbf{C}^e} = 4 \rho_0 \frac{\partial^2 \psi}{\partial \mathbf{C}^e \otimes \partial \mathbf{C}^e} \quad (2.14)$$

Motivated by clinical observations [319], we represent growth as a strain-driven, transversely isotropic, irreversible process. It is characterized through one single growth multiplier  $\vartheta^g$  that reflects the irreversible area increase perpendicular to the skin normal  $\mathbf{n}_0$ .

$$\mathbf{F}^g = \sqrt{\vartheta^g} \mathbf{I} + [1 - \sqrt{\vartheta^g}] \mathbf{n}_0 \otimes \mathbf{n}_0 \quad (2.15)$$

For this particular transversely isotropic definition of the growth tensor, for which the material is not allowed to grow in the thickness direction [382], the area growth is identical to the volume growth, i.e.,  $\vartheta^g = \det(\mathbf{F}^g) = J^g$ . Because of the simple rank-one update structure, we can apply the Sherman-Morrison formula to invert the growth tensor in explicit form.

$$\mathbf{F}^{g-1} = \frac{1}{\sqrt{\vartheta^g}} \mathbf{I} + \left[ 1 - \frac{1}{\sqrt{\vartheta^g}} \right] \mathbf{n}_0 \otimes \mathbf{n}_0 \quad (2.16)$$

It introduces the following simple expression for the growth velocity gradient,

$$\mathbf{L}^g = \frac{\sqrt{\dot{\vartheta}^g}}{\sqrt{\vartheta^g}} \mathbf{I} + \left[ 1 - \frac{\sqrt{\dot{\vartheta}^g}}{\sqrt{\vartheta^g}} \right] \mathbf{n}_0 \otimes \mathbf{n}_0 \quad (2.17)$$

which proves convenient to explicitly evaluate the mass source as  $\mathcal{R}_0 = \rho_0 [1 + 2\sqrt{\dot{\vartheta}^g}/\sqrt{\vartheta^g}]$ . Motivated by physiological observations of stretch-induced skin expansion [141], we adopt the following evolution equation for the growth multiplier,

$$\dot{\vartheta}^g = k^g(\vartheta^g) \phi^g(\vartheta^e) \quad (2.18)$$

which follows a well-established functional form [233], but is now rephrased in a strain-driven format [133, 134]. To control unbounded growth, we introduce the weighting function

$$k^g = \frac{1}{\tau} \left[ \frac{\vartheta^{\max} - \vartheta^g}{\vartheta^{\max} - 1} \right]^\gamma \quad \text{with} \quad \frac{\partial k^g}{\partial \vartheta^g} = -\frac{\gamma}{\vartheta^{\max} - \vartheta^g} k^g \quad (2.19)$$

where  $\tau$  denotes the adaptation speed,  $\gamma$  calibrates the shape of the adaptation curve, and  $\vartheta^{\max} > 1$  denotes the maximum area growth [158, 233]. The growth criterion

$$\phi^g = \vartheta^e - \vartheta^{\text{crit}} = \frac{\vartheta}{\vartheta^g} - \vartheta^{\text{crit}} \quad \text{with} \quad \frac{\partial \phi^g}{\partial \vartheta^g} = -\frac{1}{\vartheta^g} \vartheta \quad (2.20)$$

is driven by the elastic area stretch  $\vartheta^e = \vartheta/\vartheta^g$ , such that growth is activated only if the elastic area stretch exceeds a critical physiological threshold value  $\vartheta^{\text{crit}}$  [133]. For displacement-driven skin expansion, the model displays a characteristic relaxation-type response, while for force-driven skin expansion, it shows a creep-type behavior [51].

## 2.3 Computational Modeling of Area Growth

The governing equations for finite growth introduced in the previous section are complex and highly nonlinear. In this section, we illustrate their computational solution within an incremental iterative nonlinear finite element framework. To characterize the growth process at each instant in time, we introduce the growth multiplier  $\vartheta^g$  as an internal variable, and solve its evolution equation (5.10) locally at each integration point using the finite difference method. To explore the interplay between growth and mechanics, we discretize the governing equations for finite growth (5.1), (4.7), and (4.11) in space using the finite element method. In this section, we first derive the discrete local residual and the corresponding tangent moduli for the local Newton iteration to iteratively determine the growth multiplier  $\vartheta^g$ . Then, we derive the stresses  $\mathbf{S}$  for the discrete global residual and the constitutive moduli  $\mathbf{L}$  for the tangent moduli for the global Newton iteration to iteratively determine the deformation  $\boldsymbol{\varphi}$ .

### 2.3.1 Local Newton Iteration - Growth Multiplier

To discretize the biological equilibrium equation (5.10) in time, we partition the time interval of interest  $\mathcal{T}$  into  $n_{\text{stp}}$  subintervals,

$$\mathcal{T} = \bigcup_{n=1}^{n_{\text{stp}}} [t_n, t_{n+1}] \quad (2.21)$$

and focus on the interval  $[t_n, t_{n+1}]$  for which  $\Delta t = t_{n+1} - t_n > 0$  denotes the current time increment. Our goal is to determine the current growth multiplier  $\vartheta^g$  for a given deformation state  $\mathbf{F}$  at time  $t$ , and a given growth multiplier  $\vartheta_n^g$  at the end of the previous time step

$t_n$ . For the sake of compactness, here and from now on, we omit the index  $(\circ)_{n+1}$  for all quantities at the end of the current time step  $t_{n+1}$ . To evaluate the material time derivative of the growth multiplier  $\dot{\vartheta}$ , we introduce the following approximation.

$$\dot{\vartheta}^g = \frac{1}{\Delta t} [\vartheta^g - \vartheta_n^g] \quad (2.22)$$

In the spirit of implicit time stepping schemes, we now reformulate the evolution equation (5.10) with the help of equation (5.13), introducing the discrete residual  $R^\vartheta$  in terms of the unknown growth multiplier  $\vartheta^\vartheta$ .

$$R^\vartheta = \vartheta^g - \vartheta_n^g - k^g \phi^g \Delta t \doteq 0 \quad (2.23)$$

We suggest to solve this nonlinear residual equation for the unknown growth multiplier using a local Newton iteration. Within each iteration step, we calculate the linearization of the residual  $R^\vartheta$  with respect to the growth multiplier  $\vartheta^g$ ,

$$K^\vartheta = \frac{\partial R^\vartheta}{\partial \vartheta^g} = 1 - \left[ \frac{\partial k^g}{\partial \vartheta^g} \phi^g + k^g \frac{\partial \phi^g}{\partial \vartheta^g} \right] \Delta t \quad (2.24)$$

with the weighting function  $k^g$  and the growth criterion  $\phi^g$  introduced in equations (5.11) and (5.12). Within each iteration step, we calculate the iterative update of the unknown growth multiplier  $\vartheta^g \leftarrow \vartheta^g - R^\vartheta / K^\vartheta$  until convergence is achieved, i.e., until the local growth update  $\Delta \vartheta^g = -R^\vartheta / K^\vartheta$  is below a user-defined threshold value. In what follows, we will assume that mass diffusion is significantly smaller than the mass source, and therefore negligible, i.e.,  $\mathbf{R} = \mathbf{0}$ . This implies that, if necessary, the remaining balance of mass,  $\dot{\rho}_0 = \rho_0 [1 + 2 \sqrt{\dot{\vartheta}} / \sqrt{\vartheta^g}]$ , can simply be evaluated locally in a post-processing step once local convergence is achieved.

### 2.3.2 Global Newton iteration - Growing Skin

With the simplifying assumptions of a vanishing momentum source,  $\mathbf{b} = \mathbf{0}$ , and negligible inertia effects,  $\dot{\mathbf{v}} = \mathbf{0}$ , the mechanical equilibrium equation (4.7) reduces to the internal force balance,  $\text{Div}(\mathbf{F} \cdot \mathbf{S}) \doteq \mathbf{0}$ . We cast it into its weak form,  $\int_{\mathcal{B}_0} \nabla \delta \varphi : [\mathbf{F} \cdot \mathbf{S}] \, dV \doteq 0$ , through the multiplication with the test function  $\delta \varphi$  and the integration over the domain of interest  $\mathcal{B}_0$ , to solve it globally on the node point level. To discretize it in space, we

partition the domain of interest  $\mathcal{B}_0$  into  $n_{el}$  finite elements  $\mathcal{B}_0^e$ .

$$\mathcal{B}_0 = \bigcup_{e=1}^{n_{el}} \mathcal{B}_0^e \quad (2.25)$$

Our goal is to determine the deformation state  $\varphi$  for a given loading at time  $t$ . To approximate the test function  $\delta\varphi$ , the unknown deformation  $\varphi$ , and their gradients  $\nabla\delta\varphi$  and  $\nabla\varphi$ , we apply an isoparametric Bubnov-Galerkin based finite element interpolation,

$$\begin{aligned} \delta\varphi &= \sum_{i=1}^{n_{en}} N^i \delta\varphi_i & \nabla\delta\varphi &= \sum_{i=1}^{n_{en}} \delta\varphi_i \otimes \nabla N^i \\ \varphi &= \sum_{j=1}^{n_{en}} N^j \varphi_j & \nabla\varphi &= \sum_{j=1}^{n_{en}} \varphi_j \otimes \nabla N^j \end{aligned} \quad (2.26)$$

where  $N^i$ ,  $N^j$  are the element shape functions and  $i, j = 1, \dots, n_{en}$  are the element nodes. We now reformulate the weak form of the balance of linear momentum (4.7) with the help of these finite element approximations, introducing the discrete residual  $\mathbf{R}_I^\varphi$  in terms of the unknown nodal deformation  $\varphi_J$ .

$$\mathbf{R}_I^\varphi = \mathbf{A} \int_{\mathcal{B}_e} \nabla N_\varphi^i \cdot [\mathbf{F} \cdot \mathbf{S}] \, dV_e \doteq \mathbf{0} \quad (2.27)$$

Herein, the operator  $\mathbf{A}$  symbolizes the assembly of all element residuals at the  $j = 1, \dots, n_{en}$  element nodes to the global residual at the global node points  $J = 1, \dots, n_{el}$ . We can evaluate the global discrete residual (4.20), once we have iteratively determined the growth multiplier  $\vartheta^g$  for the given deformation state  $\mathbf{F}$  and the given history  $\vartheta_n^g$  as described in Section 3.3.1. Then we can successively determine the growth tensor  $\mathbf{F}^g$  from equation (5.4), the elastic tensor  $\mathbf{F}^e = \mathbf{F} \cdot \mathbf{F}^g - 1$  from equation (5.1), the elastic stress  $\mathbf{S}^e$  from equation (4.11), and lastly, the second Piola Kirchhoff stress  $\mathbf{S}$ .

$$\mathbf{S} = 2 \frac{\partial \psi}{\partial \mathbf{C}} = 2 \frac{\partial \psi}{\partial \mathbf{C}^e} : \frac{\partial \mathbf{C}^e}{\partial \mathbf{C}} = \mathbf{F}^{g-1} \cdot \mathbf{S}^e \cdot \mathbf{F}^{g-t} \quad (2.28)$$

Again, we suggest an incremental iterative Newton algorithm to solve the nonlinear residual equation for the unknown deformation (4.20). The consistent linearization of the residual  $\mathbf{R}_I^\varphi$  with respect to the nodal vector of unknowns  $\varphi_J$  introduces the global stiffness matrix.

$$\mathbf{K}_{IJ}^\varphi = \frac{\partial \mathbf{R}_I^\varphi}{\partial \varphi_J} = \mathbf{A} \int_{\mathcal{B}_e} [\nabla N_\varphi^i \cdot \mathbf{F}]^{\text{sym}} \cdot \mathbf{L} \cdot [\mathbf{F}^t \cdot \nabla N_\varphi^j]^{\text{sym}} \, dV_e + \int_{\mathcal{B}_e} \nabla N_\varphi^i \cdot \mathbf{S} \cdot \nabla N_\varphi^j \, \mathbf{I} \, dV_e \quad (2.29)$$

The fourth order tensor  $\mathbf{L}$  denotes the Lagrangian constitutive moduli which we can determine directly from the linearization of the Piola Kirchhoff stress  $\mathbf{S}$  with respect to the total right Cauchy Green tensor  $\mathbf{C}$ .

$$\mathbf{L} = 2 \frac{d\mathbf{S}}{d\mathbf{C}} = 2 \left. \frac{\partial \mathbf{S}}{\partial \mathbf{C}} \right|_{\mathbf{F}^g} + 2 \left[ \left. \frac{\partial \mathbf{S}}{\partial \mathbf{F}^g} : \frac{\partial \mathbf{F}^g}{\partial \vartheta^g} \right] \otimes \left. \frac{\partial \vartheta^g}{\partial \mathbf{C}} \right|_{\mathbf{F}} \quad (2.30)$$

The first term

$$2 \frac{\partial \mathbf{S}}{\partial \mathbf{C}} = 2 \frac{\partial [\mathbf{F}^{g-1} \cdot \mathbf{S}^e \cdot \mathbf{F}^{g-t}]}{\partial \mathbf{C}} = [\mathbf{F}^{g-1} \overline{\otimes} \mathbf{F}^{g-1}] : \mathbf{L}^e : [\mathbf{F}^{g-t} \overline{\otimes} \mathbf{F}^{g-t}] \quad (2.31)$$

represents the pull back of the elastic moduli  $\mathbf{L}^e$  onto the reference configuration, where  $\mathbf{L}^e = 2 \partial \mathbf{S}^e / \partial \mathbf{C}^e$  are the constitutive moduli of the elastic material model as introduced in equation (5.18). The second term

$$\begin{aligned} \frac{\partial \mathbf{S}}{\partial \mathbf{F}^g} &= \frac{\partial [\mathbf{F}^{g-1} \cdot \mathbf{S}^e \cdot \mathbf{F}^{g-t}]}{\partial \mathbf{F}^g} \\ &= -[\mathbf{F}^{g-1} \overline{\otimes} \mathbf{S} + \mathbf{S} \underline{\otimes} \mathbf{F}^{g-1}] - [\mathbf{F}^{g-1} \overline{\otimes} \mathbf{F}^{g-1}] : \frac{1}{2} \mathbf{L}^e : [\mathbf{F}^{g-t} \underline{\otimes} \mathbf{C}^e + \mathbf{C}^e \overline{\otimes} \mathbf{F}^{g-t}] \end{aligned} \quad (2.32)$$

consists of two contributions that resemble a geometric and a material stiffness contribution known from nonlinear continuum mechanics. The third term

$$\frac{\partial \mathbf{F}^g}{\partial \vartheta^g} = \frac{1}{2 \sqrt{\vartheta^g}} [\mathbf{I} - \mathbf{n}_0 \otimes \mathbf{n}_0] \quad (2.33)$$

and the fourth term

$$\frac{\partial \vartheta^g}{\partial \mathbf{C}} = \left[ \frac{1}{\tau} \frac{1}{\vartheta^g} \left[ \frac{\vartheta^{\max} - \vartheta^g}{\vartheta^{\max} - 1} \right]^\gamma \frac{1}{K^g} \Delta t \right] \left[ \frac{1}{2} \vartheta \mathbf{C}^{-1} - \frac{1}{2} \frac{J^2}{\vartheta} [\mathbf{C}^{-1} \cdot \mathbf{n}_0] \otimes [\mathbf{C}^{-1} \cdot \mathbf{n}_0] \right] \quad (2.34)$$

depend on the particular choice for the growth tensor  $\mathbf{F}^g$  in equation (5.4) and on the evolution equation for the growth multiplier  $\vartheta^g$  in equation (5.10), respectively. For each global Newton iteration step, we iteratively update the current deformation state  $\boldsymbol{\varphi} \leftarrow \boldsymbol{\varphi} - \mathbf{K}_{IJ}^{\varphi-1} \cdot \mathbf{R}_I^{\varphi}$  until we achieve algorithmic convergence. Upon convergence, we store the corresponding growth multipliers  $\vartheta^g$  at the integration point level. To solve these nonlinear finite element equations, we implement the growth model in a custom-designed version of the multipurpose nonlinear finite element program FEAP [366].

## 2.4 Example of Skin Expansion and Growth

In this section, we specify the constitutive equations, the material parameters, the geometry, and the finite element discretization to model skin growth induced through tissue expansion. We focus on two different load cases, tissue expander inflation to simulate skin growth, and tissue expander deflation to simulate residual stresses.

### 2.4.1 Model Problem of Tissue Expander Inflation and Deflation

To focus on the impact of growth, we assume a generic isotropic Neo-Hookean baseline elasticity and specify the free energy in the following form.

$$\rho_0 \psi = \frac{1}{2} \lambda \ln^2(J^e) + \frac{1}{2} \mu [\mathbf{C}^e : \mathbf{I} - 3 - 2 \ln(J^e)]$$

According to equations (4.11) and (5.18), we can then express the elastic second Piola-Kirchhoff stress  $\mathbf{S}^e = 2 \partial \psi / \partial \mathbf{C}^e$  as

$$\mathbf{S}^e = [\lambda \ln(J^e) - \mu] \mathbf{C}^{e-1} + \mu \mathbf{I},$$

and the elastic constitutive moduli  $\mathbf{L}^e = 2 \partial \mathbf{S}^e / \partial \mathbf{C}^e$  as

$$\mathbf{L}^e = \lambda \mathbf{C}^{e-1} \otimes \mathbf{C}^{e-1} + [\mu - \lambda \ln(J^e)] [\mathbf{C}^e \overline{\otimes} \mathbf{C}^e + \mathbf{C}^e \underline{\otimes} \mathbf{C}^e].$$

Here we have used the common abbreviations,  $\{\bullet \overline{\otimes} \circ\}_{ijkl} = \{\bullet\}_{ik} \{\circ\}_{jl}$  and  $\{\bullet \underline{\otimes} \circ\}_{ijkl} = \{\bullet\}_{il} \{\circ\}_{jk}$ , for the non-standard fourth order products. For the elastic model, we assume Lamé constants of  $\lambda = 0.577$  and  $\mu = 0.0385$  and an initial density of  $\rho_0^{\text{init}} = 1.0$  [158]. For the growth model, we assume that growth takes place above the critical threshold of  $\vartheta^{\text{crit}} = 1.01$ , we restrict the maximum area growth to  $\vartheta^{\text{max}} = 2.4$ , we assume an adaptation speed of  $\tau = 1.0$ , and a growth exponent of  $\gamma = 2.0$ . Sensitivity analyses demonstrate that the material parameters  $\tau$  and  $\gamma$  influence the adaptation time and the shape of the adaptation curve [158], but not the final state of biological equilibrium [314,332]. We model the skin area under consideration as a 0.2cm thin  $12 \times 12 \text{ cm}^2$  square sheet, discretized with  $3 \times 24 \times 24 = 1728$  trilinear brick elements, with  $4 \times 25 \times 25 = 2500$  nodes and 7500 degrees of freedom. To explore the impact of different tissue expander geometries, we model a circular, a square, a rectangular, and a crescent shaped expander. For the sake of comparison, the

base surface area of all four expanders is scaled to a size of  $A_0 = 37 \text{ cm}^2$ . As illustrated in Figure 2.4, we can then model tissue expansion by pressuring the corresponding 148 light red elements from underneath while fixing the bottom nodes of all remaining white elements.

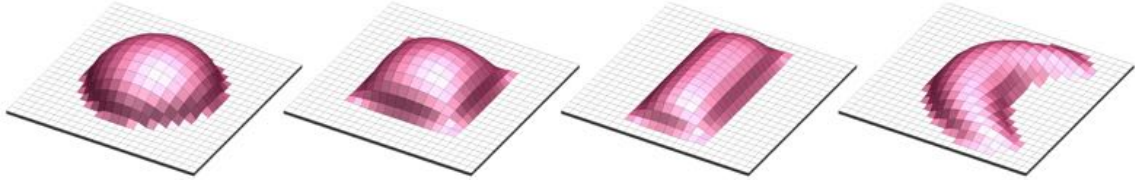


Figure 2.4: Tissue expander inflation and deflation. Skin is modeled as a  $0.2 \text{ cm}$  thin  $12 \times 12 \text{ cm}^2$  square sheet, discretized with  $3 \times 24 \times 24 = 1728$  trilinear brick elements, with  $4 \times 25 \times 25 = 2500$  nodes and 7500 degrees of freedom. We explore the impact of different tissue expander geometries, circular, square, rectangular, and crescent-shaped. The base surface area of all expanders is scaled to 148 elements corresponding to  $37 \text{ cm}^2$ . This area, here shown in light red, is gradually pressurized from underneath while the bottom nodes of all remaining elements, shown in white, are fixed.

The pressure is increased linearly in 40 steps of  $\Delta t = 0.1$  to a maximum pressure of  $p = 0.002$  at  $t = 4$ . We then keep the pressure constant and watch the skin grow. In Section 5.3.2, we explore skin growth upon tissue expander inflation. To allow the skin to gradually grow towards its biological equilibrium state, we keep the pressure constant for another 460 steps until  $t = 50$ . In Section 2.4.3, we explore the growth-induced residual stresses upon tissue expander deflation. We keep the pressure constant for another 80 steps until  $t = 12$ , and then gradually decrease the pressure back to zero throughout another 30 time steps until  $t = 15$ .

#### 2.4.2 Tissue Expander Inflation - Skin Growth

Figure 2.5 displays the fractional area gain and the increasing expander volume in response to tissue expander inflation. We model expander inflation through gradually increasing the pressure from time  $t = 0$  to  $t = 4$ , and then hold it constant from time  $t = 4$  to  $t = 50$ . Under the same pressure, we observe that the circular expander triggers the largest fractional area gain, followed by the square, the rectangular, and the crescent-shaped expanders, Figure 2.5 left. Since the base surface area is the same for all four expanders, this implies that the expander volume is largest for the circular expander, followed by the square, the

rectangular, and the crescent-shaped expanders, Figure 2.5 right. Both graphs demonstrate the characteristic creep-type growth under constant pressure with a gradual convergence towards the biological equilibrium state.

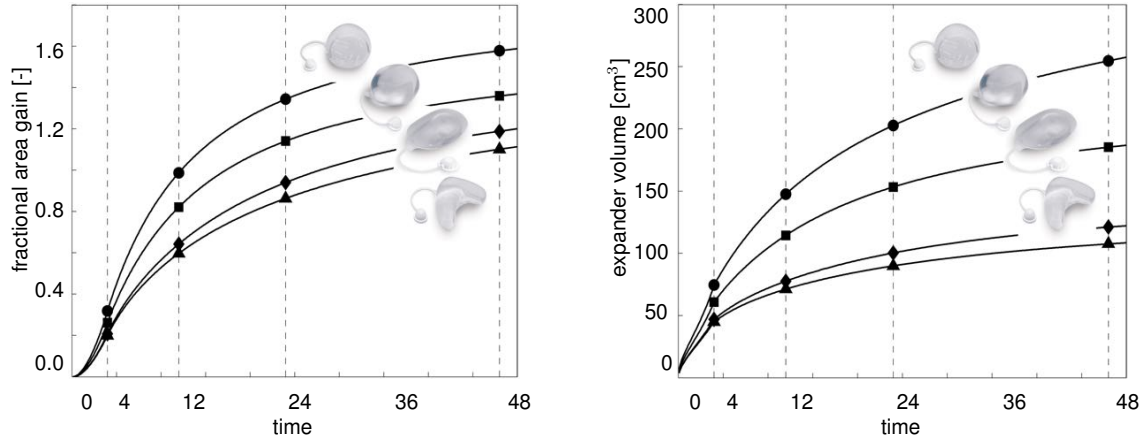


Figure 2.5: Tissue expander inflation. Temporal evolution of fractional area gain and increasing expander volume. Expanders are inflated gradually between  $t = 0$  and  $t = 4$  by linearly increasing the pressure. The pressure is then held constant from  $t = 4$  to  $t = 50$  to allow the skin to grow. Under the same pressure applied to the same base surface area, the circular expander displays the largest fractional area gain, followed by the square, the rectangular, and the crescent-shaped expanders, left. Growth causes the tissue to relax and the expander volume to increase. The expander volume is largest for the circular expander, followed by the square, the rectangular, and the crescent-shaped expanders, right. Both graphs demonstrate the characteristic creep-type growth under constant pressure with a gradual convergence towards the biological equilibrium state.

Table 2.1 displays a quantitative comparison of the four different tissue expander geometries. Following a linearly increasing and then constant pressure, at  $t = 50$ , the maximum growth multiplier is largest for the circular expander, with  $\vartheta^g = 2.364$ , followed by  $\vartheta^g = 2.349$  for the square expander,  $\vartheta^g = 2.257$  for the rectangular expander, and  $\vartheta^g = 2.247$  for the crescent-shaped expander. While the maximum area growth  $\vartheta^g$  is nothing but a local measure of growth, the global absolute area gain  $\Delta A$  characterizes the total amount of skin growth. Skin growth is again largest for the circular expander with  $\Delta A = 58.738 \text{ cm}^2$ , followed by the square expander with  $50.627 \text{ cm}^2$ , the rectangular expander with  $44.398 \text{ cm}^2$ , and the crescent-shaped expander with  $41.186 \text{ cm}^2$ , meaning that the total area of  $A_0 = 37 \text{ cm}^2$  has more than doubled in all four cases. This implies that the fractional area gain ranges from 1.588 for the circular expander to 1.368, 1.200, and 1.113 for the square,

Table 2.1: Tissue expander inflation and deflation. Maximum growth multiplier, absolute area gain, fractional area gain, and expander volume under constant pressure loading at time  $t = 50$  are largest for the circular expander, followed by the square, the rectangular, and the crescent shape expanders. Maximum principal residual stresses upon unloading after a constant pressure growth until  $t = 12$  are largest for the circular expander, followed by the square, the rectangular, and the crescent shape expanders.

	maximum growth $\vartheta^g$ [-]	initial area $A_0$ [cm <sup>2</sup> ]	absolute area gain $\Delta A$ [cm <sup>2</sup> ]	fractional area gain $\Delta A/A_0$ [-]	expander volume $V$ [cm <sup>3</sup> ]	expander pressure $p/E$ [-]	maximum residual stress $\sigma^{\max}/E$ [-]
circular	2.364	37.000	58.738	1.588	257.451	0.002	0.419
square	2.349	37.000	50.627	1.368	186.771	0.002	0.410
rectangular	2.257	37.000	44.398	1.200	122.063	0.002	0.335
crescent	2.247	37.000	41.186	1.113	108.416	0.002	0.328

the rectangular, and the crescent-shaped expanders, Figure 2.5, left. To obtain these area gains, the required expander volumes are 257.451 cm<sup>3</sup> for the circular expander, 186.771 cm<sup>3</sup> for the square expander, 122.063 cm<sup>3</sup> for the rectangular expander, and 108.416 cm<sup>3</sup> for the crescent-shaped expander. These values agree nicely with the rectangular expander volumes of 100-200 cm<sup>3</sup> typically used in the forehead and are slightly lower than the expander volumes of 140-600 cm<sup>3</sup> used in the scalp during pediatric forehead reconstruction [141].

Figure 2.6 summarizes the spatio-temporal evolution of area growth for all four expander types. Snapshots correspond to  $t = 4$ ,  $t = 12$ ,  $t = 24$ , and  $t = 48$ , from left to right, corresponding to the labels and dashed vertical lines in Figure 2.5. The color code illustrates the evolution of the growth multiplier  $\vartheta^g$  ranging from  $\vartheta^g = 1.0$  for the initially ungrown skin, shown in blue, to  $\vartheta^g = \vartheta^{\max} = 2.4$  for the fully grown state, shown in red. Figure 2.6 confirms that the circular expander induces the largest amount of growth followed by the square, the rectangular, and the crescent-shaped expanders. Remarkably, despite the large deformations of the thin skin layer, the algorithm always converges quadratically and displays no instabilities, maintaining robustness throughout the entire simulation.

#### 2.4.3 Tissue Expander Deflation - Residual Stress

Figure 2.7 documents the spatio-temporal evolution of the elastic area stretch in response to tissue expander deflation. We model expander deflation after gradual inflation from time  $t = 0$  to  $t = 4$  and a constant expander pressure from time  $t = 4$  to  $t = 12$  through a gradual decrease of the expander pressure back to zero at time  $t = 15$ . Snapshots correspond to

$t = 12$ ,  $t = 13$ ,  $t = 14$ , and  $t = 15$ , from left to right. Figure 2.7 confirms the irreversible nature of skin growth. As the expander pressure is gradually removed, from left to right, the grown skin layer collapses. Deviations from a flat surface after total unloading, right, confirm the irreversibility of the growth process. The color code illustrates the evolution of the elastic area stretch  $\vartheta^e$ , ranging from  $\vartheta^e = 0.9$  corresponding to 10% of area compression, shown in blue, to  $\vartheta^e = 1.1$  corresponding to 10% of area tension, shown in red. Growth induces compressive strains at the edges of the original base surface area, and tensile strains in the center region.

Figure 2.8 documents the spatio-temporal evolution of the maximum principal stress in response to tissue expander deflation. The four sets of snapshots at  $t = 12$ ,  $t = 13$ ,  $t = 14$ , and  $t = 15$  correspond to the same time points shown in the elastic area strain plot of Figure 2.7. The color code corresponds to the maximum principal stress  $\sigma^{\max}$ , ranging from  $\sigma^{\max} = 0.0$ , shown in blue, to  $\sigma^{\max} = 0.40$ , shown in red. The remaining stresses in the unloaded state, shown in red on the right, correspond to growth-induced residual stresses. While the existence of residual stresses in growing biological tissues has been intensely discussed in the literature [320, 363, 384], this is one of the first attempts to visually illustrate their existence upon complete unloading. Although the algorithm is capable of robustly simulating total pressure removal after time step  $t = 12$ , we would like to point out that the algorithm struggled to fully unload the biological equilibrium state after  $t = 50$  discussed in Section 5.3.2. However, the observed loss of algorithmic convergence upon unloading a severely grown skin sheet is mainly a problem of skin collapse and self contact rather than of the conceptual nature of our model.

Finally, to quantify the residual stresses in the unloaded sheet, the last column in Table 2.1 compares of the maximum principal residual stresses for all four expander geometries. In agreement with the other results of this study, residual stresses are largest when using a circular expander with  $\sigma^{\max} = 0.419$ , followed by the square expander with  $\sigma^{\max} = 0.410$ , the rectangular expander with  $\sigma^{\max} = 0.335$ , and the crescent-shaped expander with  $\sigma^{\max} = 0.328$ .

#### 2.4.4 Limitations

Although our results hold promise to reliably predict skin growth in response to tissue expansion, we would like to point out that this is only a preliminary study with several limitations. First, we model skin using an isotropic Neo-Hookean baseline elasticity

model as specified in Section 5.3.1. However, adopting a more physiological anisotropic skin model that accounts for pronounced collagen fiber orientations parallel and perpendicular to Langer’s lines [41, 205, 206] is conceptually straightforward and part of our current research efforts [51]. Along the same lines, it would be slightly more cumbersome, but possible, to introduce a progressive reorientation of the collagen network in response to expansion-induced stretch [159, 208, 250]. Second, the growth process itself may in fact be anisotropic. Given the modularity of our model, the incorporation of different growth multipliers to characterize growth parallel and perpendicular to Langer’s lines would require only minor adjustments [134]. In particular, it would affect the definition of the growth tensor (5.4), its inverse (5.5), and its derivative (4.25). Third, here, we model the epidermis and the dermis as a single homogenous material, neglecting possible internal stresses caused by the different material properties of these two layers. It would be desirable, in the future, to model both layers individually, to explore the mechanobiology of the epidermal-dermal interface and its functional role in internal-external load transfer [342]. Especially when discretizing the individual skin layers, it might become essential to model skin using membrane or shell elements to increase computational efficiency, to ensure well-conditioning of the overall system matrix, and to avoid the typical locking effects associated with thin geometries subjected to bending [351]. Fourth, the calibration of the material parameters for both the elastic model and the growth model remains a question to be addressed in the future [243]. Here, for conceptual comparison, we have only used generic material parameter values. As a first step, we have recently refined the constitutive model for skin [51], and calibrated its parameters using experiments reported in the literature [211, 217]. Fifth, for the sake of simplicity, we model the tissue expander only indirectly through controlling the applied pressure. In real tissue expansion, the control parameter following selection and implantation of the tissue expander is the volume of the expander. This implies that our virtual tissue expansion resembles a creep test under constant loading, while clinical tissue expansion resembles a relaxation test under constant deformation. Last, a more realistic model should incorporate the real expander to account for effects like interface sliding or shear [351], and, ideally, also an idealized face [245]. In addition, the expander base which we have here modeled as fixed and undeformable, should ideally be modeled as soft bedding. In reality, the expander base presses into the surrounding tissue. Despite tissue expander designs using a semi-rigid base, stretching of the base still occurs and has clinical consequence. When placed on the craniofacial skeleton, temporary but reversible bone

deformations have been observed in pediatric patients [231]. To address these limitations, we are in the process of refining the elastic model, the growth model, and the boundary conditions, to render our future simulations more realistic.

## 2.5 Conclusion

In this study, we present a fully three-dimensional computational model for tissue expansion and skin growth in reconstructive surgery. Tissue expansion is a common surgical procedure that enables the body to grow extra skin for the resurfacing of large congenital defects of the skin including giant nevi and vascular anomalies and the correction of skin deformity following burn injuries and other forms of traumatic skin loss. Tissue expansion is also widely used for breast reconstruction following the removal of breast cancer. In tissue expansion, a subcutaneous inflatable silicone expander is implanted and gradually filled with saline solution causing the skin to stretch. Increased tissue tension triggers new cells to form and the skin to grow. Skin growth is permanent but will retract to some degree when the expander is removed. Despite intense research in clinical and experimental skin growth, our understanding of the mechano-biological phenomena during tissue expansion remains poor and largely qualitative.

In this manuscript, we propose to model tissue expansion within the concept of finite growth based on the multiplicative decomposition of the deformation gradient into an elastic and a growth part. We assume that growth is an irreversible, transversely isotropic process which takes place exclusively in the skin layer, while the skin thickness is assumed to remain virtually unaffected. Accordingly, we introduce a single scalar variable, the growth multiplier, to characterize the amount of area growth. To quantify its evolution in time, we suggest a stretch driven growth law which activates growth once the strains exceed a critical physiological threshold level. This model is a significant advancement over existing purely kinematic models in that expander-induced strains are not exclusively attributed to growth alone, but are a result of both growth and elastic deformation. Accordingly, this model potentially avoids the inherent overestimation of net area surface gain observed in existing purely kinematic models.

Since skin growth is a highly nonlinear, heterogeneous process, we propose to solve the governing equations using a nonlinear finite element approach. For the first time, we model

area growth in the form of a scalar-valued growth multiplier which we introduce as an internal variable on the integration point level. We evaluate its temporal evolution locally using a finite difference approach. To guarantee maximum efficiency, stability, and optimal convergence of the algorithm, we suggest a local Newton iteration to update the growth multiplier at each integration point, embedded within a global Newton iteration to update the deformation at each finite element node. This approach requires a consistent linearization of the biological equilibrium equation on the integration point level combined with a consistent linearization of the mechanical equilibrium equation on the node point level. In contrast to existing axisymmetric models, this novel fully-three-dimensional approach allows us to model and compare arbitrarily shaped tissue expander geometries.

To explore the features of our model, we simulate skin growth in response to four commonly available tissue expander geometries, circular, square, rectangular, and crescent-shaped. For each geometry, we gradually increase the expander pressure and then hold it constant to allow the skin to grow over time. We explore two scenarios, tissue expander inflation to study skin growth, and tissue expander deflation to study residual stresses. In first case, we allow progressive skin growth until we reach the biological equilibrium state. For this state, we compare the maximum growth multiplier as a local metric for growth with the fractional area gain as a global metric for growth, and quantify the corresponding expander volumes. We observe that for the same pressure applied to the same base surface area, the circular expander induces the largest amount of growth followed by the square, the rectangular, and the crescent-shaped expanders. In the second case, we gradually remove the expander pressure. For the fully unloaded state, we compare the collapsed tissue shapes in terms of tensile and compressive regions and in terms of residual stresses. This aspect of the work is novel in the sense that the existence of residual stresses has been discussed in the literature, but rarely have they been computationally visualized.

To our knowledge, this is the first study in which skin growth in response to tissue expansion has been addressed from a mechanistic point of view. A comprehensive understanding of the gradually evolving stress and strain fields in growing skin may help the surgeon to optimize clinical process parameters such as expander geometry, expander size, expander placement, and inflation timing. Ultimately, computational tools like ours have the potential to rationalize these parameters to obtain skin flaps of desired size and shape. Overall, we believe that predictive computational modeling might open new avenues in reconstructive surgery.

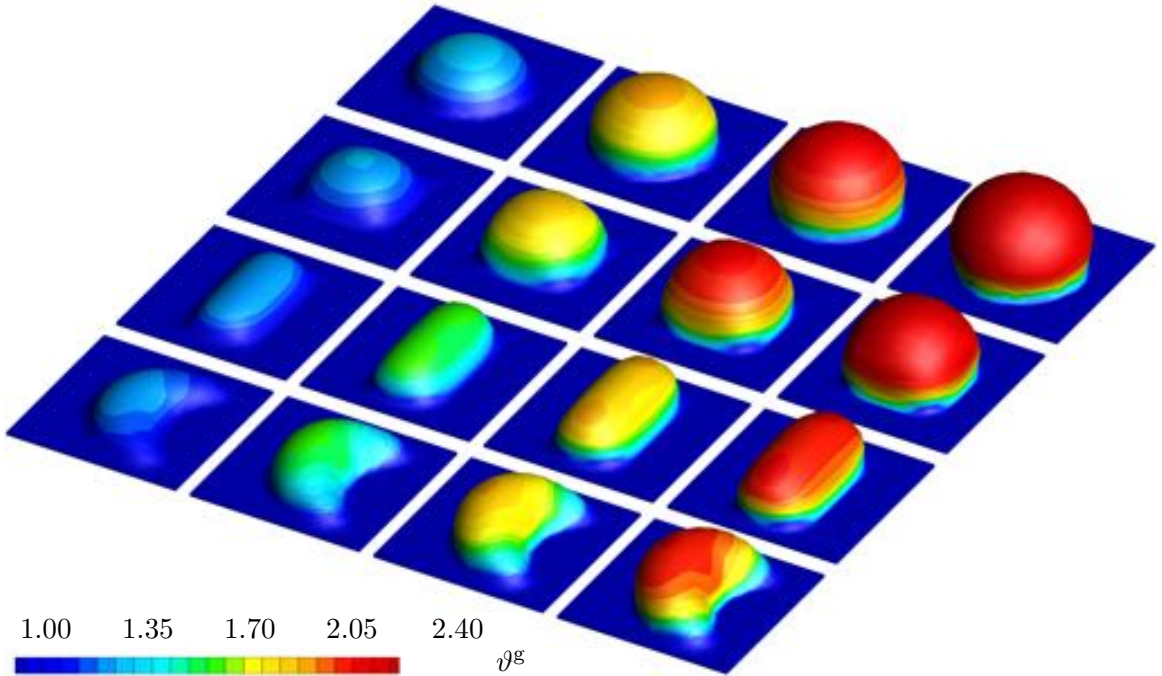


Figure 2.6: Tissue expander inflation. Spatio-temporal evolution of growth area stretch  $\vartheta^g$  for circular, square, rectangular, and crescent-shaped expanders. Under the same pressure applied to the same base surface area, the circular expander induces the largest amount of growth followed by the square, the rectangular, and the crescent-shaped expanders. The color code illustrates the evolution of the growth multiplier  $\vartheta^g$ , ranging from  $\vartheta^g = 1.0$  for the initially ungrown skin, shown in blue, to  $\vartheta^g = \vartheta^{\max} = 2.4$  for the fully grown state, shown in red. Snapshots correspond to  $t = 4, t = 12, t = 24$ , and  $t = 48$ , from left to right, corresponding to the labels in Figure 2.5.

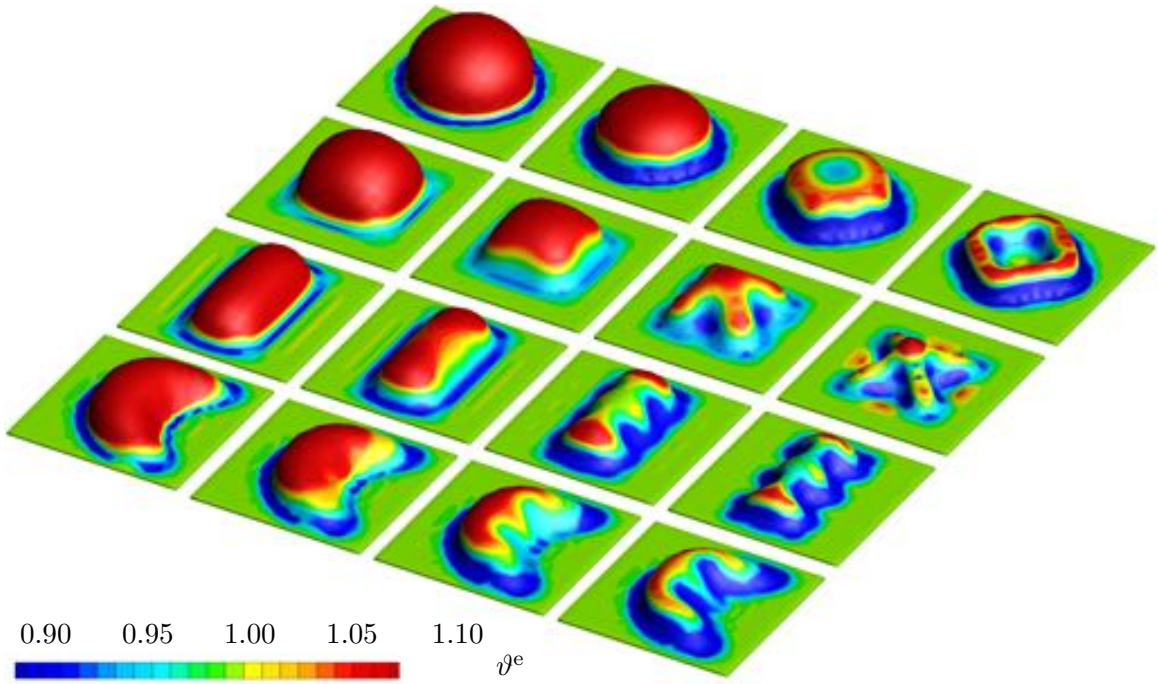


Figure 2.7: Tissue expander deflation. Spatio-temporal evolution of elastic area stretch  $\vartheta^e$  for circular, square, rectangular, and crescent-shaped expanders. As the expander pressure is gradually removed, from left to right, the grown skin layer collapses. Deviations from a flat surface after total unloading, right, demonstrate the irreversibility of the growth process. Growth induces compression at the edges of the original base surface area, and tension in the center region. The color code illustrates the evolution of the elastic area stretch  $\vartheta^e$ , ranging from  $\vartheta^e = 0.9$  corresponding to 10% of area compression, shown in blue, to  $\vartheta^e = 1.1$  corresponding to 10% of area tension, shown in red. Snapshots correspond to  $t = 12$ ,  $t = 13$ ,  $t = 14$ , and  $t = 15$ , from left to right.

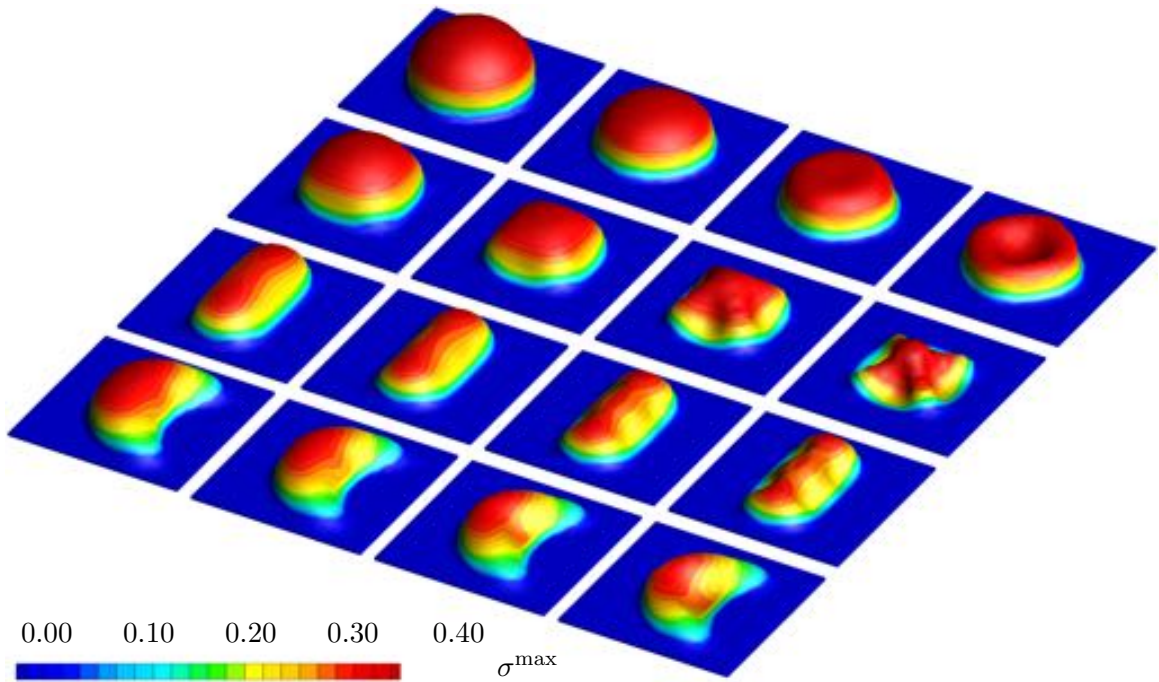


Figure 2.8: Tissue expander deflation. Spatio-temporal evolution of maximum principal stress  $\sigma^{\max}$  for circular, square, rectangular, and crescent-shaped expanders. As the expander pressure is gradually removed, from left to right, the grown skin layer collapses. Deviations from a flat surface after total unloading, right, demonstrate the irreversibility of the growth process. Remaining stresses at in the unloaded state, right, are growth-induced residual stresses. The color code illustrates the evolution of the maximum principal stress  $\sigma^{\max}$ , ranging from  $\sigma^{\max} = 0.0$ , shown in blue, to  $\sigma^{\max} = 0.40$ , shown in red. Snapshots correspond to  $t = 12$ ,  $t = 13$ ,  $t = 14$ , and  $t = 15$ , from left to right.

## Chapter 3

# Stretching Skin: The Physiological Limit and Beyond

**Abstract.** The goal of this manuscript is to establish a novel computational model for skin to characterize its constitutive behavior when stretched within and beyond its physiological limits. Within the physiological regime, skin displays a reversible, highly nonlinear, stretch locking, and anisotropic behavior. We model these characteristics using a transversely isotropic chain network model composed of eight wormlike chains. Beyond the physiological limit, skin undergoes an irreversible area growth triggered through mechanical stretch. We model skin growth as a transversely isotropic process characterized through a single internal variable, the scalar-valued growth multiplier. To discretize the evolution of growth in time, we apply an unconditionally stable, implicit Euler backward scheme. To discretize it in space, we utilize the finite element method. For maximum algorithmic efficiency and optimal convergence, we suggest an inner Newton iteration to locally update the growth multiplier at each integration point. This iteration is embedded within an outer Newton iteration to globally update the deformation at each finite element node. To illustrate the characteristic features of skin growth, we first compare the two simple model problems of displacement- and force-driven growth. Then, we model the process of stretch-induced skin growth during tissue expansion. In particular, we compare the spatio-temporal evolution of stress, strain, and area gain for four commonly available tissue expander geometries. We

believe that the proposed model has the potential to open new avenues in reconstructive surgery and rationalize critical process parameters in tissue expansion, such as expander geometry, expander size, expander placement, and inflation timing.

### 3.1 Motivation



Figure 3.1: Tissue expansion for pediatric forehead reconstruction. The patient, a one-year old boy presented with a giant congenital nevus concerning approximately 25 percent of the forehead, affecting the hairline and the cheek. Simultaneous forehead, cheek, and scalp expanders were implanted for *in situ* skin growth. This technique allows to resurface large anatomical areas with skin of similar color, quality, and texture. The follow-up photograph shows the patient at age three after forehead reconstruction.

Within its physiological limits, skin almost behaves like rubber: Its mechanical response is highly nonlinear [279], initially weak, but much stiffer at higher stretch levels, limited through a characteristic locking stretch [280]. In contrast to rubber though, skin is highly anisotropic [211], with a larger stiffness along pronounced collagen fiber orientations which manifests itself macroscopically in the form of Langer's lines [214]. When chronically stretched beyond its physiological limit, skin displays a fascinating behavior: It increases its surface area to reduce the mechanical load [92].

The controlled surface area growth through mechanical stretch was first proposed more than half a century ago to reconstruct a traumatic ear [270]. Tissue expansion has since then revolutionized reconstructive skin surgery and is now widely used to repair birth defects [17,139],

correct burn injuries [13, 91], and reconstruct breasts after tumor removal [311]. Tissue expansion is the perfect strategy to grow skin that matches the color, texture, and hair bearing of the surrounding healthy skin, while minimizing scars and risk of rejection [319]. Figure 3.1 illustrates an example of tissue expansion in pediatric forehead reconstruction [141]. The patient, a one-year old boy, presented with a giant congenital nevus concerning 25 percent of the forehead, affecting the hairline and the left cheek. Approximately one in 20,000 infants is born with giant congenital nevi, typically creating significant aesthetic distortion to the involved anatomical site, associated with severe psychological distress to the patients and their families [16]. In the patient shown in Figure 3.1, simultaneous forehead, cheek, and scalp expanders were used for *in situ* tissue growth. Tissue expander placement is typically performed via dissection of a subcutaneous pockets adjacent to the skin defect, while the expander ports to regulate expander filling are either buried in a remote location, or left outside for ease of injection. The amount of filling is controlled by visual inspection of skin color, capillary refill, and simple palpation of the stretched skin [319]. Multiple subsequent serial inflations stretch the skin and stimulate tissue growth. Once new skin is produced, the device is removed, and the new skin is used to repair the adjacent defect zone. The follow-up photograph in Figure 3.1, right, shows the patient at age three after forehead reconstruction. Similar expansion techniques have successfully been used to grow skin in the trunk [15], and in the upper and lower extremities [139].

Figure 3.2 shows a schematic sequence of the mechanical processes that occur during tissue expansion. Initially, at biological equilibrium, the skin is in a natural state of resting tension [342], left. Tissue expanders are implanted subcutaneously and gradually inflated, stretching the skin beyond the physiological limit, top. This triggers a series of stretch-induced signaling pathways [364]. Mechanotransduction affects a network of integrated cascades including cellular architecture and function such as cytoskeletal structure, extracellular matrix, enzyme activity, second messenger systems, and ion channel activity [92]. As a consequence, the skin grows and restores the state of resting tension, right.

This cycle of expander inflation, overstretch, growth, and relaxation is repeated multiple times, typically on a weekly basis, throughout a period of 6-8 weeks [78, 231]. Remarkably, as demonstrated by immunocytochemical analyses, the expanded tissue undergoes normal cell differentiation and maintains its characteristic phenotype [402]. Although the tissue initially displays epidermal thickening and dermal thinning upon expansion, both thickness changes are usually reversible under expander removal [382].

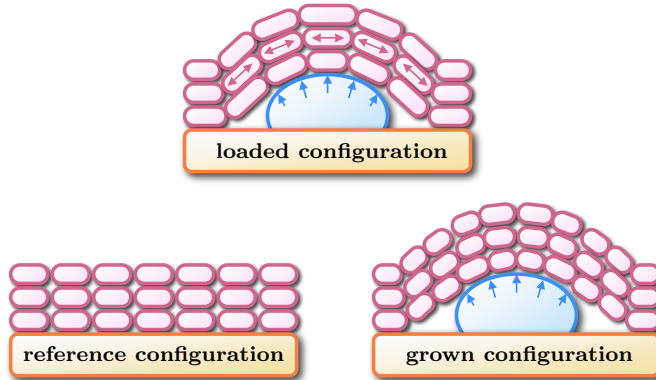


Figure 3.2: Schematic sequence of tissue expander inflation. At biological equilibrium, the skin is in a physiological state of resting tension, left. A tissue expander is implanted subcutaneously between the skin, consisting of the epidermis and dermis, and the hypodermis. When the expander is inflated, the skin is loaded in tension, top. Mechanical stretch induces cell proliferation causing the skin to grow. Growth restores the state of resting tension, right.

Several studies have focused on understanding the adaptation of skin from a biomechanical point of view. A process parameter that has received major attention is the geometry of the tissue expander [48]. Figure 3.3 displays four commonly used tissue expander geometries, circular, square, rectangular, and crescent-shaped. For regular circular and rectangular expanders, simple mathematical models have been proposed to kinematically correlate the expander volume to its surface area [103, 341]. From an engineering point, it is intuitive though that purely kinematic models severely overestimate the net gain in surface area [385]. With a discrepancy of up to a factor four, these models assume that the entire deformation can be attributed to irreversible growth, completely neglecting the elastic deformation which is reversible upon expander removal [231]. In an attempt to account for this error, empirical correction factors of 6.00, 3.75, and 4.50 have been proposed for circular, rectangular, and crescent-shaped expanders [385]. Despite these efforts, the choice of the appropriate expander geometry and size is still almost exclusively based on the surgeon's personal preference, and the discrepancy between recommended shapes, sizes, and volumes remains enormous [231]. This demonstrates the ongoing need to rationalize criteria for a standardized device selection.

In this manuscript, we propose a rigorous, mechanistic approach to systematically compare different tissue expander geometries in terms of stress, strain, and area gain. To model skin



Figure 3.3: Tissue expanders to grow skin flaps for defect correction in reconstructive surgery. Typical applications are birth defect correction, scar revision in burn injuries, and breast reconstruction after tumor removal. Devices are available in different shapes and sizes, circular, square, rectangular, and crescent-shaped. They consist of a silicone elastomer inflatable expander with a reinforced base for directional expansion, and a remote silicone elastomer injection dome. Reprinted with permission, Mentor Worldwide LLC.

growth in response to tissue expansion, we adopt the framework of finite growth based on the multiplicative decomposition of the deformation gradient into an elastic and a growth part [320]. A tremendous amount of research has been devoted to establish continuum theories for finite growth within the last decade [106, 233]. These theories have been applied successfully to characterize growing tumors [6], tendons [122], vascular tissue [207, 363], cardiac tissue [133, 314]. While earlier studies were primarily of theoretical and analytical nature [32, 361], we can now observe a clear trend towards the computational modeling of volumetric growth, typically by introducing the growth tensor as an internal variable within a finite element framework [158, 332]. We would like to point out, however, that these theories, although successful in characterizing growth on a macroscopic tissue level, remain phenomenological in nature. We would have to consult more sophisticated mixture theories [5, 170], if we wanted to understand the microstructural origin of growth. A recent monograph that compares different approaches to growth summarizes the essential findings, trends, and open questions in this progressively evolving new field [8].

Despite ongoing research in growing biological systems, the growth of thin biological membranes remains severely understudied [137]. Motivated by a first study on axisymmetric

skin growth [351], we have recently proposed a prototype model for growing isotropic membranes to model skin expansion in a general three-dimensional setting [52]. The goal of this manuscript is to significantly refine this initial isotropic model and incorporate the basic features of skin including its extreme nonlinearity, its locking behavior, and its anisotropic nature [205, 206], to precisely quantify stress, strain, and area gain in response to different, arbitrarily shaped tissue expander geometries.

This manuscript is organized as follows. In Section 5.2.1, we give a brief overview of the continuum equations for finite growth including the kinematic equations, the balance equations, and the constitutive equations. In Section 5.2.2, we illustrate the temporal and spatial discretizations of the biological and mechanical equilibrium equations, along with their consistent algorithmic linearizations. We then demonstrate the features of our model in Section 3.4 by comparing the simple model problems of displacement- and force-driven growth, and illustrate skin growth in response to tissue expander inflation. We close with a brief discussion, some limitations, and concluding remarks in Section 10.5.

## 3.2 Continuum Modeling of Skin Growth

In this Section, we illustrate the governing equations for skin growth which consist of three basic sets of equations; in Section 3.2.1 the kinematic equations based on the concept of an incompatible growth configuration and the multiplicative decomposition of the deformation gradient; in Section 3.2.2 the balance equations of open systems phrased in their mass specific format; and in Sections 3.2.3 and 3.2.4 the constitutive equations, both for overstretch-induced growth and for the baseline elastic response.

### 3.2.1 Kinematics - Finite Growth

We adopt the kinematics of finite deformations and introduce the deformation map  $\varphi$ , which, at any given time  $t \in \mathcal{T}$ , maps the material placement  $\mathbf{X}$  of a physical particle in the material configuration  $\mathcal{B}_0$  to its spatial placement  $\mathbf{x}$  in the spatial configuration  $\mathcal{B}_t$ .

$$\mathbf{x} = \varphi(\mathbf{X}, t) \quad \mathcal{B}_0 \times \mathcal{T} \rightarrow \mathcal{B}_t \quad (3.1)$$

In what follows, we apply a formulation which is entirely related to the material frame of reference. Accordingly,  $\nabla\{\circ\} = \partial_{\mathbf{X}}\{\circ\}|_t$  and  $\text{Div}\{\circ\} = \partial_{\mathbf{X}}\{\circ\}|_t : \mathbf{G}^{-1}$  denote the gradient

and the divergence of any field  $\{\circ\}(\mathbf{X}, t)$  with respect to the material placement  $\mathbf{X}$  at fixed

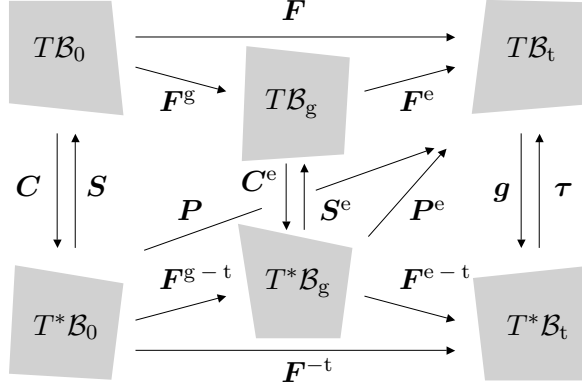


Figure 3.4: Kinematics of finite growth. Illustration of covariant spatial metric  $\mathbf{g}$ , deformation tensors  $\mathbf{C}$  and  $\mathbf{C}^e$ , stress tensors  $\mathbf{S}$ ,  $\mathbf{P}$ ,  $\mathbf{P}^e$  and  $\boldsymbol{\tau}$ , and mappings  $\mathbf{F} = \mathbf{F}^e \cdot \mathbf{F}^g$  and  $\mathbf{F}^{-t} = \mathbf{F}^{e-t} \cdot \mathbf{F}^{g-t}$  between tangent spaces  $T\mathcal{B}$  and cotangent spaces  $T^*\mathcal{B}$  in the material configuration, the intermediate configuration, and the spatial configuration [158, 260].

time  $t$ . Herein,  $\mathbf{G}^{-1}$  is the contravariant material metric. To characterize finite growth, we introduce an incompatible growth configuration [222, 345], and adopt the multiplicative decomposition of the linear tangent map [320],

$$\mathbf{F} = \nabla_{\mathbf{X}} \varphi = \mathbf{F}^e \cdot \mathbf{F}^g \quad T\mathcal{B}_0 \rightarrow T\mathcal{B}_t \quad (3.2)$$

into a reversible elastic part  $\mathbf{F}^e : T\mathcal{B}_g \rightarrow T\mathcal{B}_t$  and an irreversible growth part  $\mathbf{F}^g : T\mathcal{B}_0 \rightarrow T\mathcal{B}_g$ , see Figure 3.4. This implies that the total Jacobian

$$J = \det(\mathbf{F}) = J^e J^g \quad (3.3)$$

obeys a similar multiplicative decomposition into an elastic part  $J^e = \det(\mathbf{F}^e)$  and a growth part  $J^g = \det(\mathbf{F}^g)$ . We idealize skin as a thin layer characterized through the unit normal  $\mathbf{n}_0$  in the undeformed reference configuration. The length of the deformed skin normal  $\mathbf{n} = \text{cof}(\mathbf{F}) \cdot \mathbf{n}_0 = J \mathbf{F}^{-t} \cdot \mathbf{n}_0$  introduces the area stretch,

$$\vartheta = \|\text{cof}(\mathbf{F}) \cdot \mathbf{n}_0\| = \vartheta^e \vartheta^g \quad (3.4)$$

which we can again decompose into an elastic area stretch  $\vartheta^e = \|\text{cof}(\mathbf{F}^e) \cdot \mathbf{n}_g / \|\mathbf{n}_g\|\|$  and a growth area stretch  $\vartheta^g = \|\text{cof}(\mathbf{F}^g) \cdot \mathbf{n}_0\|$ , where  $\mathbf{n}_g = \text{cof}(\mathbf{F}^g) \cdot \mathbf{n}_0 = J^g \mathbf{F}^{g-t} \cdot \mathbf{n}_0$  denotes

the grown skin normal. Here,  $\text{cof}(\circ) = \det(\circ) (\circ)^{-t}$  denotes the cofactor of the second order tensor  $(\circ)$ , such that  $\vartheta = J [\mathbf{n}_0 \cdot \mathbf{C}^{-1} \cdot \mathbf{n}_0]^{1/2}$ . As characteristic deformation measures, we introduce the right Cauchy Green tensor  $\mathbf{C}$  and its elastic counterpart  $\mathbf{C}^e$  as the pull backs of the spatial metric  $\mathbf{g}$  to the undeformed reference configuration and to the intermediate configuration,

$$\mathbf{C} = \mathbf{F}^t \cdot \mathbf{g} \cdot \mathbf{F} \quad \text{and} \quad \mathbf{C}^e = \mathbf{F}^{et} \cdot \mathbf{g} \cdot \mathbf{F}^e \quad (3.5)$$

where both are related through the following identity,  $\mathbf{C}^e = \mathbf{F}^{g-t} \cdot \mathbf{C} \cdot \mathbf{F}^{g-1}$ . In the context of finite growth, we typically parameterize the constitutive equations in terms of the reversible elastic deformation tensor  $\mathbf{C}^e$ . Its relevant invariants

$$I_1^e = \mathbf{G}^{-1} : \mathbf{C}^e \quad I_3^e = \det(\mathbf{C}^e) \quad I_4^e = \boldsymbol{\nu}_0 \cdot \mathbf{C}^e \cdot \boldsymbol{\nu}_0 \quad (3.6)$$

and their derivatives

$$\frac{dI_1}{d\mathbf{C}^e} = \mathbf{G}^{-1} \quad \frac{dI_3}{d\mathbf{C}^e} = I_3 \mathbf{C}^{e-t} \quad \frac{dI_4}{d\mathbf{C}^e} = \boldsymbol{\nu}_0 \otimes \boldsymbol{\nu}_0 \quad (3.7)$$

then take the above representations, where we have introduced the direction of transverse isotropy  $\boldsymbol{\nu}_0$  characterizing the collagen orientation in the skin layer, or, macroscopically speaking, through the direction of Langer's lines [214]. Finally, we introduce the pull back of the spatial velocity gradient  $\mathbf{l}$  to the intermediate configuration,

$$\mathbf{F}^{e-1} \cdot \mathbf{l} \cdot \mathbf{F}^e = \mathbf{F}^{e-1} \cdot [\dot{\mathbf{F}} \cdot \mathbf{F}^{-1}] \cdot \mathbf{F}^e = \mathbf{L}^e + \mathbf{L}^g \quad (3.8)$$

which obeys the additive split into the elastic velocity gradient  $\mathbf{L}^e = \mathbf{F}^{e-1} \cdot \dot{\mathbf{F}}^e$  and the growth velocity gradient  $\mathbf{L}^g = \dot{\mathbf{F}}^g \cdot \mathbf{F}^{g-1}$ . Here, we have applied the notation  $\{\circ\} = \partial_t \{\circ\}|_{\mathbf{X}}$  to denote the material time derivative of any field  $\{\circ\}(\mathbf{X}, t)$  at fixed material placement  $\mathbf{X}$ . Figure 3.4 illustrates the kinematics of finite growth in terms of the covariant spatial metric  $\mathbf{g}$ , the deformation tensors  $\mathbf{C}$  and  $\mathbf{C}^e$ , and the mappings  $\mathbf{F} = \mathbf{F}^e \cdot \mathbf{F}^g$  and  $\mathbf{F}^{-t} = \mathbf{F}^{e-t} \cdot \mathbf{F}^{g-t}$  between tangent and cotangent spaces  $T\mathcal{B}$  and  $T^*\mathcal{B}$  in the material configuration, the intermediate configuration, and the spatial configuration.

### 3.2.2 Balance Equations - Open Systems

We characterize the growing skin layer using the framework of open system thermodynamics in which the material density  $\rho_0$  is allowed to change as a consequence of growth [201, 203]. The balance of mass for open systems balances its rate of change  $\dot{\rho}_0$  with a possible in- or outflux of mass  $\mathbf{R}$  and mass source  $\mathcal{R}_0$  [290, 368].

$$\dot{\rho}_0 = \text{Div}(\mathbf{R}) + \mathcal{R}_0 \quad (3.9)$$

Similarly, the balance of linear momentum balances the density-weighted rate of change of the momentum  $\dot{\mathbf{v}}$ , where  $\mathbf{v} = \dot{\varphi}$  is nothing but the spatial velocity, with the momentum flux  $\mathbf{P} = \mathbf{F} \cdot \mathbf{S}$  and the momentum source  $\rho_0 \mathbf{b}$ ,

$$\rho_0 \dot{\mathbf{v}} = \text{Div}(\mathbf{F} \cdot \mathbf{S}) + \rho_0 \mathbf{b} \quad (3.10)$$

here stated in its mass-specific form [202, 203].  $\mathbf{P}$  and  $\mathbf{S}$  are the first and second Piola-Kirchhoff stress tensors, respectively. Last, we would like to point out that the dissipation inequality for open systems

$$\rho_0 \mathcal{D} = \mathbf{S} : \frac{1}{2} \dot{\mathbf{C}} - \rho_0 \dot{\psi} - \rho_0 \mathcal{S} \geq 0 \quad (3.11)$$

typically contains an extra entropy source  $\rho_0 \mathcal{S}$  to account for the growing nature of living biological systems [201, 249]. Equations (4.7) and (4.8) represent the mass-specific versions of the balance of momentum and of the dissipation inequality [202].

### 3.2.3 Constitutive Equations - Irreversible Growth

To characterize the growing tissue, we introduce the constitutive equations for the mass flux  $\mathbf{R}$ , for the mass source  $\mathcal{R}_0$ , and for the growth tensor  $\mathbf{F}^g$ . In what follows, we assume that mass changes induced by diffusion are significantly smaller than local changes in mass. Accordingly, we assume that the mass flux  $\mathbf{R}$  is negligible,

$$\mathbf{R} = \mathbf{0} \quad (3.12)$$

and that all changes in mass can be attributed exclusively to the mass source  $\mathcal{R}_0$ . Immuno-cytochemistry has shown that expanded tissue undergoes normal cell differentiation [402].

Accordingly, we assume that the newly grown skin has the same density and microstructure as the initial tissue. This implies that the mass source

$$\mathcal{R}_0 = \rho_0 \operatorname{tr}(\mathbf{L}^g) \quad (3.13)$$

can be expressed as the density-weighted trace of the growth velocity gradient  $\operatorname{tr}(\mathbf{L}^g) = \dot{\mathbf{F}}^g : \mathbf{F}^{g-t}$  [158]. Motivated by clinical observations [319], we represent growth as a strain-driven, transversely isotropic, irreversible process, characterized through a single growth multiplier  $\vartheta^g$  that reflects the irreversible area increase perpendicular to the skin normal  $\mathbf{n}_0$ .

$$\mathbf{F}^g = \sqrt{\vartheta^g} \mathbf{I} + [1 - \sqrt{\vartheta^g}] \mathbf{n}_0 \otimes \mathbf{n}_0 \quad (3.14)$$

For this particular transversely isotropic definition of the growth tensor, for which the material is not allowed to grow in the thickness direction [382], the area growth is identical to the volume growth, i.e.,  $\vartheta^g = \det(\mathbf{F}^g) = J^g$ . Because of the simple rank-one update structure, we can apply the Sherman-Morrison formula to invert the growth tensor in explicit form.

$$\mathbf{F}^{g-1} = \frac{1}{\sqrt{\vartheta^g}} \mathbf{I} + \left[ 1 - \frac{1}{\sqrt{\vartheta^g}} \right] \mathbf{n}_0 \otimes \mathbf{n}_0 \quad (3.15)$$

It introduces the following simple expression for the growth velocity gradient,  $\mathbf{L}^g = \sqrt{\dot{\vartheta}^g}/\sqrt{\vartheta^g} \mathbf{I} + [1 - \sqrt{\dot{\vartheta}^g}/\sqrt{\vartheta^g}] \mathbf{n}_0 \otimes \mathbf{n}_0$  which proves convenient to explicitly evaluate the mass source as  $\mathcal{R}_0 = \rho_0 [1 + 2\sqrt{\dot{\vartheta}^g}/\sqrt{\vartheta^g}]$ . Motivated by physiological observations of stretch induced skin expansion, we introduce a strain-driven evolution law for the growth multiplier.

$$\dot{\vartheta}^g = k^g(\vartheta^g) \phi^g(\vartheta^e) \quad (3.16)$$

To control unbounded growth, we introduce the weighting function

$$k^g = \frac{1}{\tau} \left[ \frac{\vartheta^{\max} - \vartheta^g}{\vartheta^{\max} - 1} \right]^\gamma \quad (3.17)$$

where  $\tau$  denotes the adaptation speed,  $\gamma$  calibrates the shape of the adaptation curve, and  $\vartheta^{\max}$  denotes the maximum area growth [158, 233]. The growth criterion

$$\phi^g = \langle \vartheta^e - \vartheta^{\text{crit}} \rangle = \langle \vartheta / \vartheta^g - \vartheta^{\text{crit}} \rangle \quad (3.18)$$

is driven by the elastic area stretch  $\vartheta^e = \vartheta/\vartheta^g$ , such that growth is activated only if the elastic area stretch exceeds a critical physiological stretch limit  $\vartheta^{crit}$ , where  $\langle \circ \rangle$  denote the Macaulay brackets.

### 3.2.4 Constitutive Equations - Reversible Elasticity

Once we have evaluated the irreversible part of the model, i.e., the growth multiplier  $\vartheta^g$ , the growth tensor  $\mathbf{F}^g$ , the growth velocity gradient  $\mathbf{L}^g$ , and the mass source  $\mathcal{R}_0$ , we can turn to evaluate the reversible elastic part of the model, i.e., the momentum flux  $\mathbf{S}$  and the momentum source  $\mathbf{b}$ . For the sake of simplicity, we assume the latter to vanish identically,  $\mathbf{b} = \mathbf{0}$ . We model skin as a transversely isotropic elastic material that can be characterized

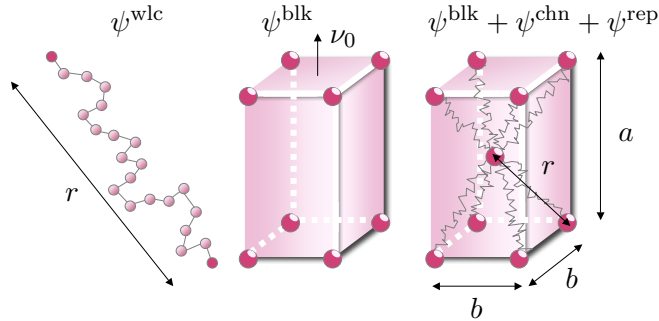


Figure 3.5: Transversely isotropic eight chain model. Individual chains are modeled as wormlike chains with an energy  $\psi^{wlc}$  parameterized in terms of the end-to-end length  $r$ . Eight chains are assembled in a transversely isotropic unit cell with dimensions  $a$  and  $b$ , and a characteristic orientation  $\nu_0$ . The energy of each unit cell consists of the bulk energy  $\psi^{blk}$ , the energy of the eight individual chains  $\psi^{chn}$ , and their repulsive contributions  $\psi^{rep}$ .

through the Helmholtz free energy  $\psi = \hat{\psi}(\mathbf{C}, \mathbf{F}^g, \boldsymbol{\nu}_0 \otimes \boldsymbol{\nu}_0)$ , parameterized in terms of the right Cauchy Green tensor  $\mathbf{C}$ , the growth tensor  $\mathbf{F}^g$ , and the preferred material orientation  $\boldsymbol{\nu}_0$  characterizing the direction of Langer's lines. We adopt a transversely isotropic eight chain model for which the free energy of a representative eight chain unit cell consists of three contributions [206] as illustrated in Figure 3.5.

$$\psi = \psi^{blk}(I_3^e) + \psi^{chn}(I_1^e, I_4^e) + \psi^{rep}(I_1^e, I_4^e) \quad (3.19)$$

The first term  $\psi^{blk}$  is purely isotropic and captures the effect of bulk incompressibility in terms of the third invariant  $I_3^e$  [122]. The second term  $\psi^{chn}$  reflects the effective assembly of the eight individual chain energies and introduces a constitutive coupling between the

first and fourth invariants  $I_1^e$  and  $I_4^e$  [205]. The third term  $\psi^{\text{rep}}$  is the repulsive term that accounts for an initial stress-free reference configuration [42]. For the individual chains, we adopt a wormlike chain model based on the single chain energy,

$$\psi^{\text{wlc}} = \psi_0^{\text{wlc}} + \frac{\gamma^{\text{chn}} k \theta L}{4 A} \left[ 2 \frac{r^2}{L^2} + \frac{1}{[1 - r/L]} - \frac{r}{L} \right] \quad (3.20)$$

where  $A$  is the persistence length,  $L$  is the contour length,  $r$  is the end-to-end length of the chain,  $\theta$  is the absolute temperature, and  $k$  is the Boltzmann constant [44]. In a transversely isotropic unit cell with dimensions  $a$  and  $b$ , the undeformed end-to-end length is  $r_0 = \sqrt{a^2 + 2b^2}/2$ , and the deformed end-to-end length  $r$  is a function of the first and fourth invariant  $I_1$  and  $I_4$  as introduced in equation (3.6).

$$r = \sqrt{I_4 a^2 + [I_1 - I_4] b^2} / 2 \quad (3.21)$$

Based on these considerations, we can introduce the individual energy terms,

$$\begin{aligned} \psi^{\text{blk}} &= \gamma^{\text{blk}} \left[ I_1 - 3 + \frac{1}{\beta} [I_3^{-\beta} - 1] \right] \\ \psi^{\text{chn}} &= \frac{\gamma^{\text{chn}} k \theta L}{4 A} \left[ 2 \frac{r^2}{L^2} + \frac{1}{[1 - r/L]} - \frac{r}{L} \right] \\ \psi^{\text{rep}} &= - \frac{\gamma^{\text{chn}} k \theta}{4 A} \left[ \frac{1}{L} + \frac{1}{4r_0[1 - r_0/L]^2} - \frac{1}{4r_0} \right] \bar{\psi}^{\text{rep}} \end{aligned} \quad (3.22)$$

where we have used the following abbreviation for the repulsive weighting factor  $\bar{\psi}^{\text{rep}}$ .

$$\bar{\psi}^{\text{rep}} = \ln(I_4^{[a^2 - b^2]/2}) + \frac{3}{2} \ln(I_1^{b^2}) \quad (3.23)$$

Here,  $\gamma^{\text{blk}}$  and  $\gamma^{\text{chn}}$  are the chain and bulk densities, and  $\beta$  is a macroscopic bulk parameter. Using the free energy (5.8), we can now evaluate the dissipation inequality (4.8).

$$\rho_0 \mathcal{D} = \left[ \mathbf{S} - \rho_0 \frac{\partial \psi}{\partial \mathbf{C}} \right] : \frac{1}{2} \dot{\mathbf{C}} + \mathbf{M}^e : \mathbf{L}^g - \rho_0 \frac{\partial \psi}{\partial \rho_0} \mathcal{R}_0 - \rho_0 \mathcal{S}_0 \geq 0 \quad (3.24)$$

Similar to finite strain plasticity, we observe that the Mandel stress of the intermediate configuration  $\mathbf{M}^e = \mathbf{C}^e \cdot \mathbf{S}^e$  is energetically conjugate to the growth velocity gradient  $\mathbf{L}^g = \dot{\mathbf{F}}^g \cdot \mathbf{F}^g^{-1}$ . Moreover, from the dissipation inequality (4.10), we obtain the definition of the second Piola Kirchhoff stress  $\mathbf{S}$  as thermodynamically conjugate quantity to the right

Cauchy Green deformation tensor  $\mathbf{C}$ .

$$\mathbf{S} = 2\rho_0 \frac{\partial\psi}{\partial\mathbf{C}} = 2\frac{\partial\psi}{\partial\mathbf{C}^e} : \frac{\partial\mathbf{C}^e}{\partial\mathbf{C}} = \mathbf{F}^{g-1} \cdot \mathbf{S}^e \cdot \mathbf{F}^{g-t} \quad (3.25)$$

Here, we have introduced the second Piola Kirchhoff stress of the intermediate configuration

$$\mathbf{S}^e = 2\rho_0 \frac{\partial\psi}{\partial\mathbf{C}^e} = \mathbf{S}^{\text{blk}} + \mathbf{S}^{\text{chn}} + \mathbf{S}^{\text{rep}} \quad (3.26)$$

in terms of the individual stress contributions corresponding to the three energy terms introduced in equations (3.22).

$$\begin{aligned} \mathbf{S}^{\text{blk}} &= \gamma^{\text{blk}} \left[ 2\mathbf{G}^{-1} - 2I_3^{-\beta} \mathbf{C}^{e-1} \right] \\ \mathbf{S}^{\text{chn}} &= \frac{\gamma^{\text{chn}} k\theta}{4A} \left[ \frac{1}{L} + \frac{1}{4r [1-r/L]^2} - \frac{1}{4r} \right] \bar{\mathbf{S}}^{\text{chn}} \\ \mathbf{S}^{\text{rep}} &= -\frac{\gamma^{\text{chn}} k\theta}{4A} \left[ \frac{1}{L} + \frac{1}{4r_0 [1-r_0/L]^2} - \frac{1}{4r_0} \right] \bar{\mathbf{S}}^{\text{rep}} \end{aligned} \quad (3.27)$$

Here, we have introduced the following abbreviations for the second order bases of the chain stress and of the repulsive stress.

$$\begin{aligned} \bar{\mathbf{S}}^{\text{chn}} &= [a^2 - b^2] \boldsymbol{\nu}_0 \otimes \boldsymbol{\nu}_0 + b^2 \mathbf{G}^{-1} \\ \bar{\mathbf{S}}^{\text{rep}} &= \frac{1}{I_4} [a^2 - b^2] \boldsymbol{\nu}_0 \otimes \boldsymbol{\nu}_0 + \frac{3}{I_1} b^2 \mathbf{G}^{-1}. \end{aligned} \quad (3.28)$$

The basis of the chain stress is a result of the derivative of the end-to-end length  $r$  with respect to the elastic right Cauchy Green tensor,  $\bar{\mathbf{S}}^{\text{chn}} = 8r dr/d\mathbf{C}^e$ . The basis of the repulsive stress  $\bar{\mathbf{S}}^{\text{rep}} = 2d\bar{\psi}^{\text{rep}}/d\mathbf{C}^e$  is used to construct the repulsive energy  $\bar{\psi}^{\text{rep}}$  in equation (3.23) such that the initial state  $r = r_0$  is stress free,  $\mathbf{S}^{\text{rep}}(r_0) \doteq -\mathbf{S}^{\text{chn}}(r_0)$  and thus  $\bar{\mathbf{S}}^{\text{rep}}(r_0) \doteq \bar{\mathbf{S}}^{\text{chn}}(r_0)$ . Figure 3.6 displays the transversely isotropic nature of our eight chain model. The dots represent experimental measurements from uniaxial tests on rabbit skin tested parallel and perpendicular to Langer's lines [42, 217]. The lines represent the corresponding computational simulation. The model nicely captures the characteristic features of skin, including the strong non-linearity, the anisotropy, and the locking stretches. Last, we can evaluate the elastic constitutive moduli  $\mathbf{L}^e$  by taking the second derivative of the

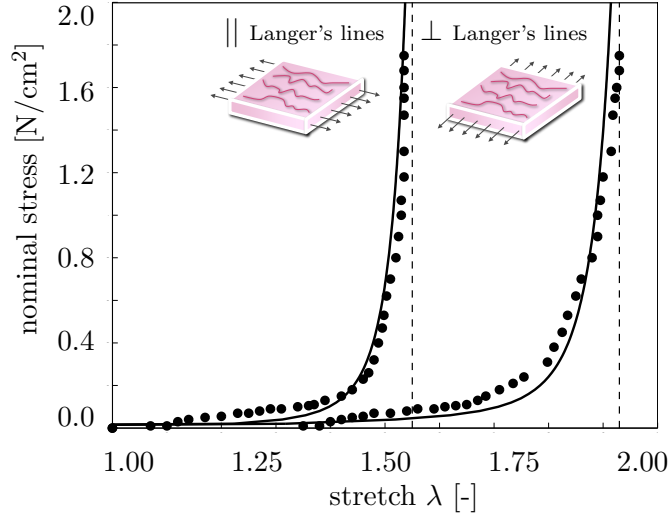


Figure 3.6: Uniaxial tension test. Transversely isotropic wormlike-chain based eight chain model. Dots represent experimental measurements on rabbit skin tested parallel and perpendicular to Langer's lines [217]. Lines represent the corresponding computational simulation. Dotted lines represent the parallel and perpendicular locking stretches. The model nicely captures the characteristic features of skin, including the strong non-linearity, the anisotropy, and the locking stretches.

Helmholtz free energy  $\psi$  with respect to the elastic right Cauchy Green tensor  $\mathbf{C}^e$ .

$$\mathbf{L}^e = 2 \frac{\partial S^e}{\partial C^e} = 4 \rho_0 \frac{\partial^2 \psi}{\partial C^e \otimes \partial C^e} = \mathbf{L}^{\text{blk}} + \mathbf{L}^{\text{chn}} + \mathbf{L}^{\text{rep}} \quad (3.29)$$

Its three individual contributions take the following forms.

$$\begin{aligned} \mathbf{L}^{\text{blk}} &= 4 \gamma^{\text{blk}} \left[ I_3^{-\beta} \mathbf{I} + \beta I_3^{-\beta} \mathbf{C}^e - 1 \otimes \mathbf{C}^e - 1 \right] \\ \mathbf{L}^{\text{chn}} &= \frac{\gamma^{\text{chn}} k \theta}{64 A r^3} \left[ 1 - \frac{1}{[1 - r/L]^2} + \frac{2 r}{L [1 - r/L]^3} \right] \bar{\mathbf{L}}^{\text{chn}} \\ \mathbf{L}^{\text{rep}} &= -\frac{\gamma^{\text{chn}} k \theta}{4 A} \left[ \frac{1}{L} + \frac{1}{4 r_0 [1 - r_0/L]^2} - \frac{1}{4 r_0} \right] \bar{\mathbf{L}}^{\text{rep}} \end{aligned} \quad (3.30)$$

The fourth order bases of the chain term  $\bar{\mathbf{L}}^{\text{chn}} = \bar{\mathbf{S}}^{\text{chn}} \otimes \bar{\mathbf{S}}^{\text{chn}}$  and of the repulsive term  $\bar{\mathbf{L}}^{\text{rep}} = 2 d \bar{\mathbf{S}}^{\text{rep}} / d \mathbf{C}^e$  can be expressed as follows.

$$\begin{aligned} \bar{\mathbf{L}}^{\text{chn}} &= [[a^2 - b^2] \boldsymbol{\nu}_0 \otimes \boldsymbol{\nu}_0 + b^2 \mathbf{G}^{-1}] \otimes [[a^2 - b^2] \boldsymbol{\nu}_0 \otimes \boldsymbol{\nu}_0 + b^2 \mathbf{G}^{-1}] \\ \bar{\mathbf{L}}^{\text{rep}} &= -\frac{2}{I_4^2} [a^2 - b^2] \boldsymbol{\nu}_0 \otimes \boldsymbol{\nu}_0 \otimes \boldsymbol{\nu}_0 \otimes \boldsymbol{\nu}_0 - \frac{6}{I_1^2} b^2 \mathbf{G}^{-1} \otimes \mathbf{G}^{-1} \end{aligned} \quad (3.31)$$

In equation (3.30),  $\mathcal{I}$  denotes the fourth order material identity defined as  $\mathcal{I} = [\mathbf{G}^{-1} \overline{\otimes} \mathbf{G}^{-1} + \mathbf{G}^{-1} \underline{\otimes} \mathbf{G}^{-1}] / 2$ . Here, we have applied the abbreviations  $\overline{\otimes}$  and  $\underline{\otimes}$  for the non-standard dyadic products according to the following component-wise definitions  $\{\bullet\overline{\otimes}\circ\}_{ijkl} = \{\bullet\}_{ik} \otimes \{\circ\}_{jl}$  and  $\{\bullet\underline{\otimes}\circ\}_{ijkl} = \{\bullet\}_{il} \otimes \{\circ\}_{jk}$ . Last, we would like to reiterate that the choice of the particular free energy (5.8) only indirectly affects the growth process itself. The growth model is inherently modular and can easily be combined with more or less complex baseline elasticity models [52].

**Remark 1 (Special case of isotropy)** *The classical eight chain model [19] naturally follows as a special case of our general chain network model by assuming that the cell dimensions  $a$  and  $b$  take equal values.*

$$a = b \quad r = \frac{1}{2} \sqrt{I_1^e} a \quad \psi^{\text{chn}}(I_1^e) \quad \psi^{\text{rep}}(I_1^e)$$

*This implies that the chain energy  $\psi^{\text{chn}}$  and the repulsive energy  $\psi^{\text{rep}}$  become functions of the first invariant  $I_1^e$  alone. The overall free energy  $\psi$  no longer depends on the fiber direction  $\boldsymbol{\nu}_0$ , rather, it characterizes an isotropic chain network response [206, 261].*

**Remark 2 (Special case of transverse isotropy)** *The special case transverse isotropy follows by assuming a degenerated unit cell for which  $b$  tends to zero.*

$$b = 0 \quad r = \frac{1}{2} \sqrt{I_4^e} a \quad \psi^{\text{chn}}(I_4^e) \quad \psi^{\text{rep}}(I_4^e)$$

*For this model, all chains are oriented in a single direction  $\boldsymbol{\nu}_0$ . The resulting fiber terms  $\psi^{\text{chn}}$  and  $\psi^{\text{rep}}$  are thus no longer functions of the first invariant  $I_1^e$ . They depend exclusively on the stretch of the chains represented through the fourth invariant  $I_4^e$ . However, this type of model, which has been termed decoupled reinforcement model [254, 255], completely neglects network effects which are a characteristic feature of skin.*

### 3.3 Computational Modeling of Skin Growth

The governing equations for finite growth introduced in the previous section are complex and highly nonlinear. In this section, we illustrate their computational solution within an

incremental iterative nonlinear finite element framework. To characterize the growth process at each instant in time, we introduce the growth multiplier  $\vartheta^g$  as an internal variable, and solve its evolution equation (5.10) locally at each integration point using the finite difference method. To explore the interplay between growth and mechanics, we discretize the governing equations for finite growth (5.1), (4.7), and (4.11) in space using the finite element method. In this section, we first derive the discrete local residual and the corresponding tangent moduli for the local Newton iteration to iteratively determine the growth multiplier  $\vartheta^g$ . Then, we derive the stresses  $\mathbf{S}$  for the discrete global residual and the constitutive moduli  $\mathbf{L}$  for the iteration matrix of the global Newton iteration to iteratively determine the deformation  $\boldsymbol{\varphi}$ .

### 3.3.1 Local Newton Iteration - Growth Multiplier

To discretize the biological equilibrium equation (5.10) in time, we partition the time interval of interest  $\mathcal{T}$  into  $n_{stp}$  subintervals,

$$\mathcal{T} = \bigcup_{n=1}^{n_{stp}} [t_n, t_{n+1}] \quad (3.32)$$

and focus on the interval  $[t_n, t_{n+1}]$  for which  $\Delta t = t_{n+1} - t_n > 0$  denotes the current time increment. Our goal is to determine the current growth multiplier  $\vartheta^g$  for a given deformation state  $\mathbf{F}$  at time  $t$ , and a given growth multiplier  $\vartheta_n^g$  at the end of the previous time step  $t_n$ . For the sake of compactness, here and from now on, we omit the index  $(\circ)_{n+1}$  for all quantities at the end of the current time step  $t_{n+1}$ . To approximate the material time derivative of the growth multiplier  $\dot{\vartheta}$ , we introduce the following finite difference approximation.

$$\dot{\vartheta}^g = \frac{1}{\Delta t} [\vartheta^g - \vartheta_n^g] \quad (3.33)$$

In the spirit of implicit time stepping schemes, we now reformulate the evolution equation (5.10) with the help of this finite difference approximation, introducing the discrete residual  $R^\vartheta$  in terms of the unknown growth multiplier  $\vartheta^g$ .

$$R^\vartheta = \vartheta^g - \vartheta_n^g - k^g \phi^g \Delta t \doteq 0 \quad (3.34)$$

We suggest to solve this nonlinear residual equation for the unknown growth multiplier using a local Newton iteration. Within each iteration step, we calculate the linearization of

the residual  $R^\vartheta$  with respect to the growth multiplier  $\vartheta^g$ .

$$K^\vartheta = \frac{\partial R^\vartheta}{\partial \vartheta^g} = 1 - \left[ \frac{\partial k^g}{\partial \vartheta^g} \phi^g + k^g \frac{\partial \phi^g}{\partial \vartheta^g} \right] \Delta t \quad (3.35)$$

From equations (5.11) and (5.12), we can extract the linearizations of the weighting function  $\partial k^g / \partial \vartheta^g = -\gamma k^g / [\vartheta^{\max} - \vartheta^g]$  and of the growth criterion  $\partial \phi^g / \partial \vartheta^g = -\vartheta / \vartheta^g$ . Within each iteration step, we calculate the iterative update of the unknown growth multiplier  $\vartheta^g \leftarrow \vartheta^g - R^\vartheta / K^\vartheta$  until convergence is achieved, i.e., until the local growth update  $\Delta \vartheta^g = -R^\vartheta / K^\vartheta$  is below a user-defined threshold value. In what follows, we will assume negligible mass diffusion,  $\mathbf{R} = \mathbf{0}$ . This implies that, if necessary, the remaining balance of mass,  $\dot{\rho}_0 = \rho_0 [1 + 2 \sqrt{\dot{\vartheta}^g} / \sqrt{\vartheta^g}]$ , can simply be evaluated locally in a post-processing step once local convergence is achieved.

### 3.3.2 Global Newton Iteration - Growing Skin

With the simplifying assumptions of a vanishing momentum source,  $\mathbf{b} = \mathbf{0}$ , and negligible inertia effects,  $\dot{\mathbf{v}} = \mathbf{0}$ , the mechanical equilibrium equation (4.7) reduces to the internal force balance,  $\text{Div}(\mathbf{F} \cdot \mathbf{S}) \doteq \mathbf{0}$ . We cast it into its weak form,  $\int_{\mathcal{B}_0} \nabla \delta \boldsymbol{\varphi} : [\mathbf{F} \cdot \mathbf{S}] \, dV \doteq 0$ , through the multiplication with the test function  $\delta \boldsymbol{\varphi}$  and the integration over the domain of interest  $\mathcal{B}_0$ , to solve it globally on the node point level. To discretize it in space, we partition the domain of interest  $\mathcal{B}_0$  into  $n_{\text{el}}$  finite elements  $\mathcal{B}_0^e$ .

$$\mathcal{B}_0 = \bigcup_{e=1}^{n_{\text{el}}} \mathcal{B}_0^e \quad (3.36)$$

Our goal is to determine the deformation state  $\boldsymbol{\varphi}$  for a given loading at time  $t$ . To approximate the test function  $\delta \boldsymbol{\varphi}$ , the unknown deformation  $\boldsymbol{\varphi}$ , and their gradients  $\nabla \delta \boldsymbol{\varphi}$  and  $\nabla \boldsymbol{\varphi}$ , we apply an isoparametric Bubnov-Galerkin based finite element interpolation,

$$\begin{aligned} \delta \boldsymbol{\varphi} &= \sum_{i=1}^{n_{\text{en}}} N^i \delta \boldsymbol{\varphi}_i & \nabla \delta \boldsymbol{\varphi} &= \sum_{i=1}^{n_{\text{en}}} \delta \boldsymbol{\varphi}_i \otimes \nabla N^i \\ \boldsymbol{\varphi} &= \sum_{j=1}^{n_{\text{en}}} N^j \boldsymbol{\varphi}_j & \nabla \boldsymbol{\varphi} &= \sum_{j=1}^{n_{\text{en}}} \boldsymbol{\varphi}_j \otimes \nabla N^j \end{aligned} \quad (3.37)$$

where  $N^i, N^j$  are the element shape functions and  $i, j = 1, \dots, n_{\text{en}}$  are the element nodes. We now reformulate the weak form of the balance of linear momentum (4.7) with the help of these finite element approximations, introducing the discrete residual  $\mathbf{R}_I^\varphi$  in terms of the

unknown nodal deformation  $\varphi_J$ .

$$\mathbf{R}_I^\varphi = \sum_{e=1}^{n_{\text{el}}} \int_{B_e} \nabla N_\varphi^i \cdot [\mathbf{F} \cdot \mathbf{S}] \, dV_e \doteq \mathbf{0} \quad (3.38)$$

Herein, the operator  $\mathbf{A}$  symbolizes the assembly of all element residuals at the  $j = 1, \dots, n_{\text{en}}$  element nodes to the global residual at the global node points  $J = 1, \dots, n_{\text{el}}$ . We can evaluate the global discrete residual (4.20), once we have iteratively determined the growth multiplier  $\vartheta^g$  for the given deformation state  $\mathbf{F}$  and the given history  $\vartheta_n^g$  as described in Section 3.3.1. Then we can successively determine the growth tensor  $\mathbf{F}^g$  from equation (5.4), the elastic tensor  $\mathbf{F}^e = \mathbf{F} \cdot \mathbf{F}^{g-1}$  from equation (5.1), the elastic stress  $\mathbf{S}^e$  from equation (4.11), and lastly, the second Piola Kirchhoff stress  $\mathbf{S}$  in terms of the stress  $\mathbf{S}^e$  in the intermediate configuration (3.26).

$$\mathbf{S} = 2 \frac{\partial \psi}{\partial \mathbf{C}} = 2 \frac{\partial \psi}{\partial \mathbf{C}^e} : \frac{\partial \mathbf{C}^e}{\partial \mathbf{C}} = \mathbf{F}^{g-1} \cdot \mathbf{S}^e \cdot \mathbf{F}^{g-t} \quad (3.39)$$

Again, we suggest an incremental iterative Newton algorithm to solve the nonlinear residual equation for the unknown deformation (4.20). The consistent linearization of the residual  $\mathbf{R}_I^\varphi$  with respect to the nodal vector of unknowns  $\varphi_J$  introduces the global stiffness matrix.

$$\begin{aligned} \mathbf{K}_{IJ}^\varphi &= \frac{\partial \mathbf{R}_I^\varphi}{\partial \varphi_J} = \sum_{e=1}^{n_{\text{el}}} \int_{B_e} [\nabla N_\varphi^i \cdot \mathbf{F}]^{\text{sym}} \cdot \mathbf{L} \cdot [\mathbf{F}^t \cdot \nabla N_\varphi^j]^{\text{sym}} \, dV_e \\ &\quad + \int_{B_e} \nabla N_\varphi^i \cdot \mathbf{S} \cdot \nabla N_\varphi^j \, dV_e \end{aligned} \quad (3.40)$$

The fourth order tensor  $\mathbf{L}$  denotes the Lagrangian constitutive moduli which we can determine directly from the linearization of the Piola Kirchhoff stress  $\mathbf{S}$  with respect to the total right Cauchy Green tensor  $\mathbf{C}$ .

$$\mathbf{L} = 2 \frac{d\mathbf{S}}{d\mathbf{C}} = 2 \frac{\partial \mathbf{S}}{\partial \mathbf{C}} \Big|_{\mathbf{F}^g} + 2 \left[ \frac{\partial \mathbf{S}}{\partial \mathbf{F}^g} : \frac{\partial \mathbf{F}^g}{\partial \vartheta^g} \right] \otimes \frac{\partial \vartheta^g}{\partial \mathbf{C}} \Big|_{\mathbf{F}} \quad (3.41)$$

The first term

$$2 \frac{\partial \mathbf{S}}{\partial \mathbf{C}} = [\mathbf{F}^{g-1} \overline{\otimes} \mathbf{F}^{g-1}] : \mathbf{L}^e : [\mathbf{F}^{g-t} \overline{\otimes} \mathbf{F}^{g-t}] \quad (3.42)$$

represents nothing but the pull back of the elastic moduli  $\mathbf{L}^e$  onto the reference configuration, where  $\mathbf{L}^e = 2 \partial \mathbf{S}^e / \partial \mathbf{C}^e$  are the constitutive moduli of the elastic material model as

introduced in equation (5.18). The second term

$$\begin{aligned}\frac{\partial \mathbf{S}}{\partial \mathbf{F}^g} &= \frac{\partial [\mathbf{F}^{g-1} \cdot \mathbf{S}^e \cdot \mathbf{F}^{g-t}]}{\partial \mathbf{F}^g} \\ &= -[\mathbf{F}^{g-1} \overline{\otimes} \mathbf{S} + \mathbf{S} \underline{\otimes} \mathbf{F}^{g-1}] \\ &\quad - [\mathbf{F}^{g-1} \overline{\otimes} \mathbf{F}^{g-1}] : \frac{1}{2} \mathbf{L}^e : [\mathbf{F}^{g-t} \underline{\otimes} \mathbf{C}^e + \mathbf{C}^e \overline{\otimes} \mathbf{F}^{g-t}]\end{aligned}\tag{3.43}$$

consists of two contributions that resemble a geometric and a material stiffness contribution known from nonlinear continuum mechanics. The third term

$$\frac{\partial \mathbf{F}^g}{\partial \vartheta^g} = \frac{1}{2\sqrt{\vartheta^g}} [\mathbf{I} - \mathbf{n}_0 \otimes \mathbf{n}_0]\tag{3.44}$$

and the fourth term

$$\begin{aligned}\frac{\partial \vartheta^g}{\partial \mathbf{C}} &= \frac{\partial \vartheta^g}{\partial \vartheta} \frac{\partial \vartheta}{\partial \mathbf{C}} \\ \frac{\partial \vartheta^g}{\partial \vartheta} &= \frac{1}{\tau} \frac{1}{\vartheta^g} \left[ \frac{\vartheta^{\max} - \vartheta^g}{\vartheta^{\max} - 1} \right]^\gamma \frac{1}{K^g} \Delta t \\ \frac{\partial \vartheta}{\partial \mathbf{C}} &= \frac{1}{2} \vartheta \mathbf{C}^{-1} - \frac{1}{2} \frac{J^2}{\vartheta} [\mathbf{C}^{-1} \cdot \mathbf{n}_0] \otimes [\mathbf{C}^{-1} \cdot \mathbf{n}_0]\end{aligned}\tag{3.45}$$

depend on the particular choice for the growth tensor  $\mathbf{F}^g$  in equation (5.4) and on the evolution equation for the growth multiplier  $\vartheta^g$  in equation (5.10), respectively. For each global Newton iteration step, we iteratively update the current deformation state  $\boldsymbol{\varphi} \leftarrow \boldsymbol{\varphi} - \mathbf{K}_{IJ}^{\boldsymbol{\varphi}-1} \cdot \mathbf{R}_I^{\boldsymbol{\varphi}}$  until we achieve algorithmic convergence. Upon convergence, we store the corresponding growth multipliers  $\vartheta^g$  at the integration point level. To solve these nonlinear finite element equations, we implement the growth model in a custom-designed version of the multipurpose nonlinear finite element program FEAP [366].

### 3.4 Examples - Stretching Skin Beyond its Physiological Limit

In contrast to the uniaxial tension test in Figure 3.6 which is only showing the acute, purely reversible elastic response of stretched skin tissue, we now explore how skin would respond chronically if we stretched it beyond its physiological limits. First, we illustrate the conceptual features of stretch-induced growth by studying two simple model problems, displacement- and force-driven skin expansion of a simple prototype sheet. Then, we focus

on the physiological problem of tissue expansion by exploring different expander geometries and their different placements with respect to Langer's lines [214]. If not stated otherwise, we choose the elastic material parameters for skin, calibrated by means of the uniaxial tension experiments shown in Figure 3.6 [42, 217]. Accordingly, our contour length is  $A = 1.85$ , our persistence length is  $L = 2.125$ , our eight chain unit cell dimensions are  $a = 2.43$  and  $b = 1.95$  [205], our chain and bulk densities are  $\gamma^{\text{chn}} = 1.75 \cdot 10^{21}$  and  $\gamma^{\text{blk}} = 100$ , and our macroscopic bulk parameter is  $\beta = 4.5$  [122]. The Boltzmann constant is  $k = 1.30 \cdot 10^{-23} \text{ J/K}$ , and the absolute temperature is  $\theta = 310 \text{ K}$ . To characterize the growth process, we choose the maximum area growth to  $\vartheta^{\max} = 2.4$  [52], the elastic stretch limit to  $\vartheta^{\text{crit}} = 1.80$  for the model problem in Section 5.3.1 and to  $\vartheta^{\text{crit}} = 1.12$  for the tissue expansion problem in Section 5.3.2, the adaptation speed to  $\tau = 1.0$ , and the shape parameter for the adaptation curve to  $\gamma = 2.0$  [52]. For the sake of illustration, in the following examples, we normalize the expansion time to  $t = 1.0$ , noting that the growth process scales linearly in time with the adaptation speed  $\tau$ . Common tissue expansion procedures involve repeated cycles of expander inflation, overstretch, growth, and relaxation, typically repeated on a weekly basis, throughout a period of multiple weeks [78, 231]. To clearly illustrate the influence of anisotropy in the following examples, we slightly decrease the cell dimension to  $b = 2/3 a$  in comparison to the calibrated response of Figure 3.6 where  $b = 4/5 a$ .

### 3.4.1 Model Problem - Displacement vs. Force Driven Skin Growth

Let us first illustrate the conceptual features of our stretch-induced growth model by exploring the two simple model problems of displacement- and force-driven skin expansion of a square skin sheet of size  $1.0 \times 1.0$  and thickness 0.2.

For the displacement-driven case, we linearly increase the prescribed displacements from 0.0 at time  $t = 0.0$  to 1.0 at time  $t = 0.4$ . This implies that the skin sheet is stretched biaxially to a final size of  $2.0 \times 2.0$ , i.e., total area stretch is  $\vartheta = 4.0$ . The displacements are then held constant from  $t = 0.4$  to  $t = 1.0$  to allow the tissue to grow. Figure 3.7 illustrates the resulting temporal evolution of the total area stretch  $\vartheta$ , the reversible elastic area stretch  $\vartheta^e$ , and the irreversible area growth  $\vartheta^g$ . The horizontal dashed lines represent the elastic stretch limit beyond which skin growth is activated  $\vartheta^{\text{crit}}$ , and the maximum area growth  $\vartheta^{\max}$ . Displacements are increased linearly up to the vertical dashed line at  $t = 0.4$ . At this time, the total area stretch is  $\vartheta = 4.000$ , the elastic area stretch  $\vartheta^e = 2.157$ , and the area growth  $\vartheta^g = 1.855$ . Then, displacements are held constant to allow the skin to grow until

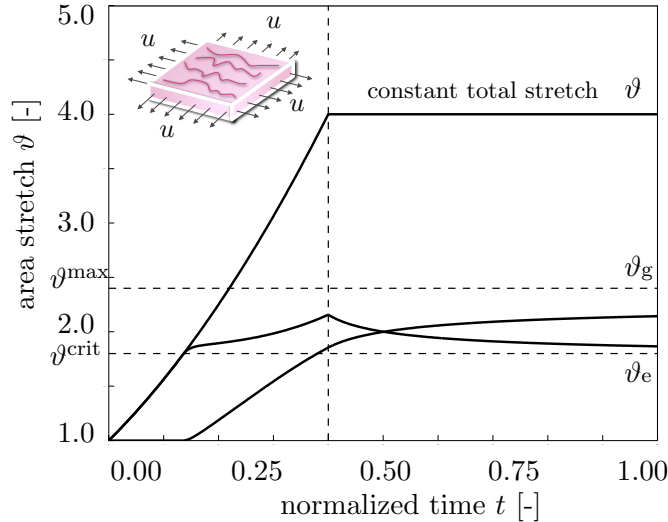


Figure 3.7: Relaxation test. Temporal evolution of total area stretch  $\vartheta$ , reversible elastic area stretch  $\vartheta^e$ , and irreversible growth area stretch  $\vartheta^g$  for displacement driven skin expansion. Horizontal dashed lines represent the elastic stretch limit beyond which skin growth is activated  $\vartheta^{crit}$ , and the maximum area growth  $\vartheta^{max}$ . Displacements are increased linearly up to the vertical dashed line and then held constant. Displacement control induces relaxation indicated through the gradual decrease in elastic stretch and stress, while the growth stretch increases at a constant total stretch.

$t = 1.0$ . At this time, growth has almost completely converged to the biological equilibrium state with a total area stretch of  $\vartheta = 4.000$ , an elastic area stretch of  $\vartheta^e = 1.866$ , and an area growth of  $\vartheta^g = 2.143$ . The curves confirm, that, at all times, the multiplicative decomposition of the deformation gradient  $\mathbf{F} = \mathbf{F}^e \cdot \mathbf{F}^g$  introduced in equation (5.1) carries over to the multiplicative decomposition of the total area stretch  $\vartheta = \vartheta^e \vartheta^g$  of equation (5.3). Obviously, upon displacement control, we observe material *relaxation* indicated through a gradual increase of growth at a constant total stretch, while the elastic stretch, and, accordingly the stresses, decrease.

For the force-driven case, we linearly increase the prescribed forces from 0.0 at time  $t = 0.0$  to 128.0 at time  $t = 0.4$ . The forces are then held constant from  $t = 0.4$  to  $t = 1.0$  to allow the tissue to grow. Figure 3.8 illustrates the corresponding temporal evolution of the total area stretch  $\vartheta$ , the reversible elastic area stretch  $\vartheta^e$ , and the irreversible growth area stretch  $\vartheta^g$ . Again, the horizontal dashed lines represent the elastic stretch limit  $\vartheta^{crit}$  beyond which skin growth is activated, and the maximum area growth  $\vartheta^{max}$ . Forces are increased linearly up to the vertical dashed line at  $t = 0.4$ . At this time, the total area stretch is

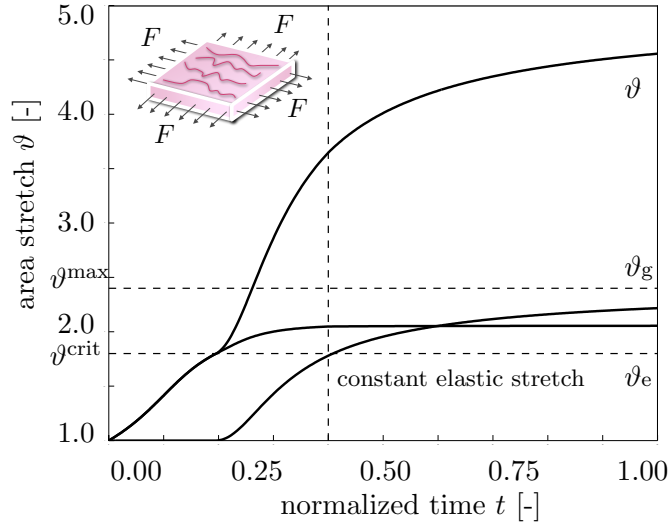


Figure 3.8: Creep test. Temporal evolution of total area stretch  $\vartheta$ , reversible elastic area stretch  $\vartheta^e$ , and irreversible growth area stretch  $\vartheta^g$  for force driven skin expansion. Horizontal dashed lines represent the elastic stretch limit beyond which skin growth is activated  $\vartheta^{\text{crit}}$ , and the maximum area growth  $\vartheta^{\text{max}}$ . Forces are increased linearly up to the vertical dashed line and then held constant. Force control induces creep indicated through the gradual increase in growth stretch and total stretch at constant elastic stretch and stress.

$\vartheta = 3.646$ , the elastic area stretch is  $\vartheta^e = 2.048$ , and the area growth is  $\vartheta^g = 1.780$ . Then, the forces are held constant to allow the skin to grow until  $t = 1.0$ . At this time, growth has almost completely converged to the biological equilibrium state with a total area stretch of  $\vartheta = 4.557$ , an elastic area stretch of  $\vartheta^e = 2.055$ , and an area growth of  $\vartheta^g = 2.217$ . Obviously, upon force control, we observe material *creep* indicated through a gradual increase of growth and of the total stretch, while the elastic stretch and the stresses remain constant.

### 3.4.2 Tissue Expansion and Skin Growth

Finally, we focus on the physiological problem of tissue expansion and compare different expander geometries and their different placements with respect to Langer's lines. As illustrated in Figure 3.9, we model skin as a 0.2 cm thin  $12 \times 12 \text{ cm}^2$  square sheet, discretized with  $3 \times 24 \times 24 = 1728$  trilinear brick elements, with  $4 \times 25 \times 25 = 2500$  nodes and 7500 degrees of freedom. To explore the impact of different tissue expander geometries, we model a circular, a square, a rectangular, and a crescent shaped expander, and place them in alignment with and orthogonal to Langer's lines. For the sake of comparison, the base surface

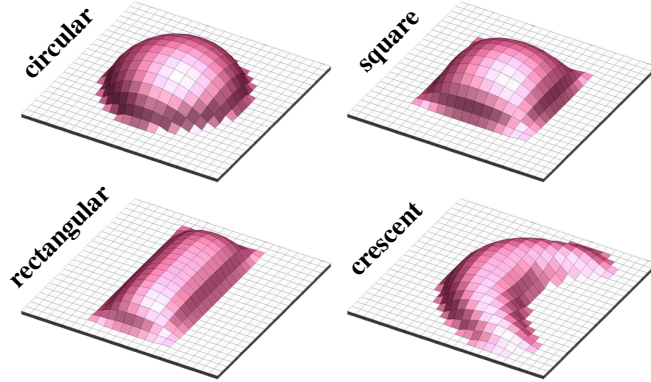


Figure 3.9: Tissue expansion and skin growth. Skin is modeled as a 0.2 cm thin  $12 \times 12 \text{ cm}^2$  square sheet, discretized with  $3 \times 24 \times 24 = 1728$  trilinear brick elements, with  $4 \times 25 \times 25 = 2500$  nodes and 7500 degrees of freedom. We explore different tissue expanders, circular, square, rectangular, and crescent shaped, when placed in alignment with and orthogonal to Langer's lines. The base surface area of all expanders is scaled to 148 elements corresponding to  $37 \text{ cm}^2$ . Expanders are placed in a subcutaneous pocket between the skin and the hypodermis, here shown in light red, while the intact, non-dissected tissue is displayed in white. The light red area is gradually pressurized from underneath, while the bottom nodes of all intact white skin elements are fixed.

area of all four expanders is scaled to a size of  $A_0 = 37 \text{ cm}^2$ . In tissue expansion, expander placement is performed via dissection of a subcutaneous pocket between the approximately 0.2 cm thick skin layer consisting of the epidermis and the dermis [342], and the thick fatty hypodermis. In Figure 3.9, the subcutaneous pocket is displayed in light red, while the intact, non-dissected tissue is displayed in white. As illustrated in Figure 3.9, we model the expansion procedure by pressuring the 148 light red elements of the subcutaneous pocket in which the expander is placed, while fixing the bottom nodes of all remaining white elements. We increase the pressure linearly up to a maximum pressure of  $p = 160$  at  $t = 0.08$ . We then keep the pressure constant and watch the skin grow until we achieve convergence towards the biological equilibrium state at  $t = 1.00$ .

Figure 3.10 displays the temporal evolution of the fractional area gain for all four expander geometries. The circular expander displays the largest fractional area gain, followed by the rectangular expander aligned with Langer's lines, the square expander, the crescent shaped expander aligned with Langer's lines, and, lastly, the crescent shaped and rectangular expanders placed orthogonal to Langer's lines. The curves demonstrate the characteristic creep-type growth under constant pressure, a response which is conceptually similar to the

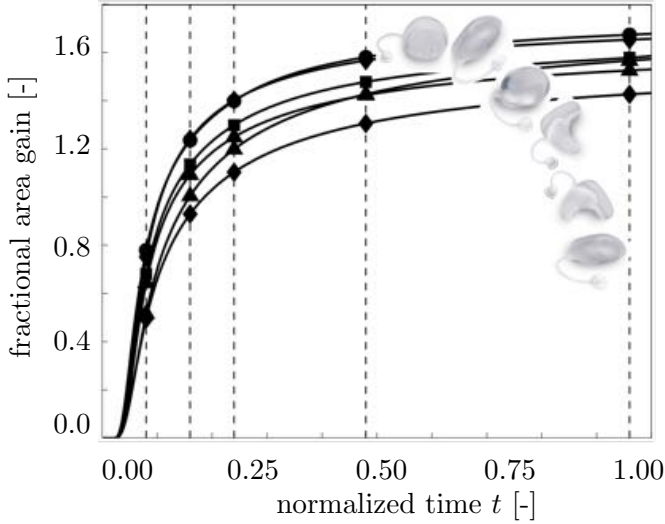


Figure 3.10: Tissue expansion and skin growth. Temporal evolution of fractional area gain. The expander pressure is increased gradually up to the first vertical dashed line and then held constant to allow the skin to grow. The rectangular and crescent shaped expanders display a larger fractional area gain when aligned with Langer's lines than when placed orthogonal to Langer's lines. The curves demonstrate the characteristic creep-type growth under constant pressure with a gradual convergence towards the biological equilibrium state.

one discussed in Figure 3.8. The fractional area gain converges towards a biological equilibrium state after a characteristic time period, here characterized through the normalized time  $t = 1.0$ , in reality a period of several days. Tissue expansion is a gradual procedure that is performed through repeated cycles of expander inflation, overstretch, growth, and relaxation. Tissue growth stagnates after several days, and expander re-inflation becomes necessary. This is why tissue expansion patients need to see their physician on a weekly basis for tissue expander re-inflation. The overall procedure takes place throughout a period of multiple weeks [231].

Figure 3.11 illustrates the temporal evolution of the corresponding expander volume. A constant pressure causes the tissue to creep and the expander volume to increase. Again, the curves clearly mimic the anisotropic response of skin. Under the same pressure, applied to the same area, the final expander volumes are larger for the rectangular and crescent-shaped expanders when aligned with Langer's lines than when placed orthogonal to Langer's lines.

Figure 3.12 demonstrates the spatio-temporal evolution of the area growth  $\vartheta^g$  for the circular, square, rectangular, and crescent-shaped expanders. Each expander is placed in two

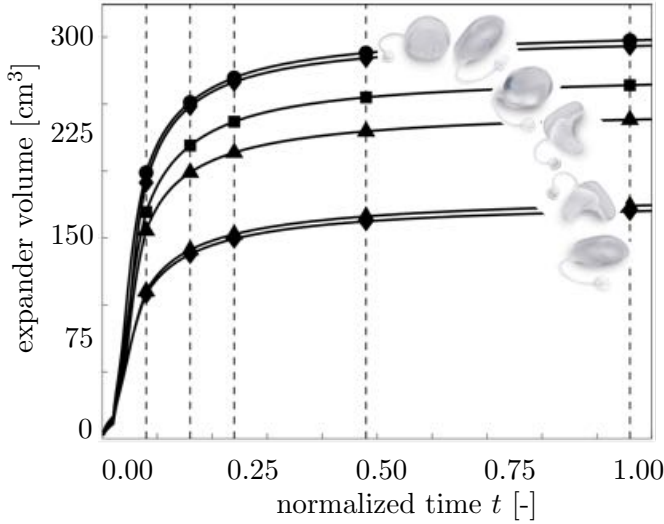


Figure 3.11: Tissue expansion and skin growth. Temporal evolution of expander volume. The expander pressure is increased gradually up to the first vertical dashed line and then held constant to allow the skin to grow. The rectangular and crescent shaped expanders display a larger expander volumes when aligned with Langer's lines than when placed orthogonal to Langer's lines. The curves demonstrate the characteristic creep-type growth under constant pressure with a gradual convergence towards the biological equilibrium state.

different positions, in alignment with and orthogonal to Langer's lines, as indicated through the vectors  $\nu_0$ . The corresponding growth contours are shown in the upper and lower row of each set. The color code ranges from  $\vartheta^g = 1.0$  for the initially ungrown state, shown in blue, to  $\vartheta^g = \vartheta^{\max} = 2.4$  for the fully grown state, shown in red. Snapshots correspond to  $t = 0.08$ ,  $t = 0.16$ ,  $t = 0.24$ ,  $t = 0.48$ , and  $t = 0.96$ , from left to right, corresponding to the vertical dashed lines in Figures 3.10 and 3.11.

Ideally, in a perfect membrane state, stresses and strains would be distributed homogeneously across the thickness, and so would the growth multiplier  $\vartheta^g$ . For this ideal state, we could have modeled skin as a perfect membrane. While the center of the expanded area is close to this ideal membrane state, the boundary experiences shear, and thus inhomogeneities across the thickness. Numerical investigations confirm that this boundary layer is restricted to approximately three rows of elements. We believe this is realistic and in good agreement with the boundary layer around the subcutaneous pocket, for example illustrated around the cheek expander in Figure 1.

Figure 3.12 shows that under the same pressure applied to the same base surface area, the

circular expander in rows 1 and 2 induces the largest amount of growth, while the rectangular and crescent-shaped expanders placed orthogonal to Langer's lines in rows 6 and 8 induce the smallest amount of growth. The contour plots confirm that it is important how the expander is positioned with respect to Langer's lines. In summary, although the growth model itself is isotropic in the skin plane, the overall skin gain is larger when the expanders are placed with their long axis along the material's strong direction, i.e., in the direction of Langer's lines.

### 3.5 Discussion

In this manuscript, we present a novel computational model for skin that allows to predict its acute and chronic behavior in response to mechanical stretch within and beyond its physiological limit. The irreversible nature of the model allows to predict the long-term outcome of tissue expansion. Tissue expansion is a common procedure in reconstructive surgery that enables the body to grow extra skin to resurface large congenital defects, to reconstruct cancerous breasts, and to correct burn injuries. In tissue expansion, an inflatable silicone expander is implanted underneath the skin and gradually filled with saline solution. When skin is stretched beyond its physiological limits, new cells form and the skin grows. Despite intense research in skin growth, our understanding of the mechanobiological phenomena during tissue expansion remains poor and largely qualitative.

In this manuscript, we propose to model tissue expansion using the concept of finite growth based on the multiplicative decomposition of the deformation gradient into an elastic and a growth part. We assume that growth is an irreversible, transversely isotropic process which takes place exclusively in the skin layer, while the skin thickness is assumed to remain virtually unchanged. To model the chronic increase of skin area, we introduce a single scalar variable, the growth multiplier. Following clinical observations, we suggest that changes in this variable are governed by a stretch driven growth law. However, growth is activated only when skin is stretched beyond its physiological limit. Within the physiological range, we characterize the reversible behavior of skin through a transversely isotropic chain network model in which eight representative chains are modeled as a wormlike chains. The resulting elastic response captures the characteristic features of skin including its extreme nonlinearity, its locking behavior, and its anisotropic nature manifesting itself macroscopically through Langer's lines.

Since skin growth is a highly nonlinear, heterogeneous process, we propose to solve the governing equations using a nonlinear finite element approach. To model the chronic increase in skin area, we introduce a scalar-valued growth multiplier which we treat as an internal variable on the integration point level. We evaluate its temporal evolution locally using a finite difference approach. To guarantee maximum efficiency, stability, and optimal convergence of the algorithm, we suggest a local Newton iteration to update the growth multiplier at each integration point. Once we know the current amount of area growth, we evaluate the remaining elastic response using the wormlike chain network model. To update the deformation at each finite element node, we propose a global Newton iteration. This approach requires a consistent linearization of the biological equilibrium equation on the integration point level embedded within a consistent linearization of the mechanical equilibrium equation on the node point level.

To explore the conceptual features of our growth model, we study two simple model problems, displacement- and force-driven skin expansion. Upon displacement control, we observe material relaxation indicated through a gradual increase of area growth at a constant total stretch, while the elastic stretch and the resulting stresses decrease. Upon force control, we observe material creep indicated through a gradual increase of growth and of the total stretch, while the elastic stretch and the stresses remain constant. Lastly, we explore different expander geometries and study the effect of anisotropy by comparing different expander placements with respect to Langers lines. Despite the postulated isotropic in-plane area growth, we observe a significant sensitivity with respect to the expander orientation. Skin gain is found to be substantially larger when the expanders are placed along the direction of Langers lines.

Beyond the fractional area gain and the expander volume, which are used as characteristic metrics in this manuscript, Figures 3.10 and 3.11, our model is also capable to provides information about the heterogeneity of the tissue expansion process, Figure 3.12. While this might be less relevant in the context of pediatric forehead reconstruction, it is a critical issue in breast reconstruction, where the grown tissue needs to adapt a certain form and shape [78]. Our clinical collaborators have expressed interest in our computational model to optimize the expansion procedure in the context of heterogeneous growth to create different skin forms and shapes [398]. However, of course, next to the plain mechanical factors, there are always biochemical factors that might influence the choice of expander type, filling volume, and timing.

Although the proposed model for skin growth represents a tremendous advancement over the generic isotropic model we have recently proposed [52], we would like to point out that some limitations remain. First, motivated by experimental observations, which report normal cell differentiation upon tissue expansion [402], we have assumed that the material microstructure remains unaffected by the growth process, i.e.,  $\mathbf{F}^g = \sqrt{\vartheta^g} \mathbf{I} + [1 - \sqrt{\vartheta^g}] \mathbf{n}_0 \otimes \mathbf{n}_0$ . It would be relatively straightforward to model the growth process itself as anisotropic [134]. This could imply growth  $\vartheta^{\parallel}$  exclusively along Langer's lines,  $\mathbf{F}^g = \mathbf{I} + [\vartheta^{\parallel} - 1] \boldsymbol{\nu}_0^{\parallel} \otimes \boldsymbol{\nu}_0^{\parallel}$ , or major in-plane growth  $\vartheta^{\parallel}$  along Langer's lines combined with minor in-plane growth  $\vartheta^{\perp}$  orthogonal to Langer's lines,  $\mathbf{F}^g = \vartheta^{\parallel} \boldsymbol{\nu}_0^{\parallel} \otimes \boldsymbol{\nu}_0^{\parallel} + \vartheta^{\perp} \boldsymbol{\nu}_0^{\perp} \otimes \boldsymbol{\nu}_0^{\perp} + \mathbf{n}_0 \otimes \mathbf{n}_0$ . Similarly, we could even introduce a progressive reorientation of the collagen network to allow the material to align with the maximum principal strains [159, 208, 250]. To truly account for the microstructural origin of growth, which is beyond the scope of this manuscript, we could elaborate the use of mixture theories, which would allow us to model the turnover of the individual constituents such as collagen and elastin throughout the growth process [5, 170]. Second, for the sake of simplicity, we have modeled the tissue expander only implicitly through controlling the applied pressure. In real tissue expansion, the external control parameter is the expander volume [231]. In line with our discussion in Section 5.3.1, this implies that our virtual tissue expansion displays creep under constant loading, while clinical tissue expansion might rather display relaxation under constant deformation.

Third, here, we have assumed that the expander is connected tightly to the expanded tissue, neglecting effects of interface sliding and shear [351]. However, this seems to be a reasonable first assumption, since most current expanders have well-designed textures to promote mild tissue in-growth, primarily to prevent expander migration [27]. To address these potential limitations, we are currently refining the elastic model, the growth model, and the boundary conditions, to render our future simulations more realistic, and place it on an idealized face [245].

Last, while our computational model seems well suited to provide qualitative guidelines and trends, at its present state, it is not recommended for quantitative statements. We believe that using the equations on nonlinear continuum mechanics represents a significant advancement over the current gold standard to predict tissue growth exclusively in terms of kinematic quantities [341, 385]. However, acute and chronic in vitro and in vivo experiments will need to be performed to truly calibrate the underlying material parameters, to potentially refine, and eventually fully validate the model.

In summary, we have presented a novel computational model to simulate the acute and chronic response of skin when stretched within its physiological limits and beyond. This model captures the basic features of skin including its extreme nonlinearity, its locking behavior, its anisotropic nature, and its ability to grow when exposed to chronically elevated stretch levels. A comprehensive understanding of the gradually evolving stress and strain fields in growing skin may help the surgeon to optimize clinical process parameters such as expander geometry, expander size, expander placement, and inflation timing. Ultimately, through inverse modeling, computational tools like ours have the potential to rationalize these parameters to obtain skin flaps of desired size and shape. Overall, we believe that predictive computational modeling might open new avenues in reconstructive surgery and enhance treatment for patients with birth defects, burn injuries, or breast tumor removal.

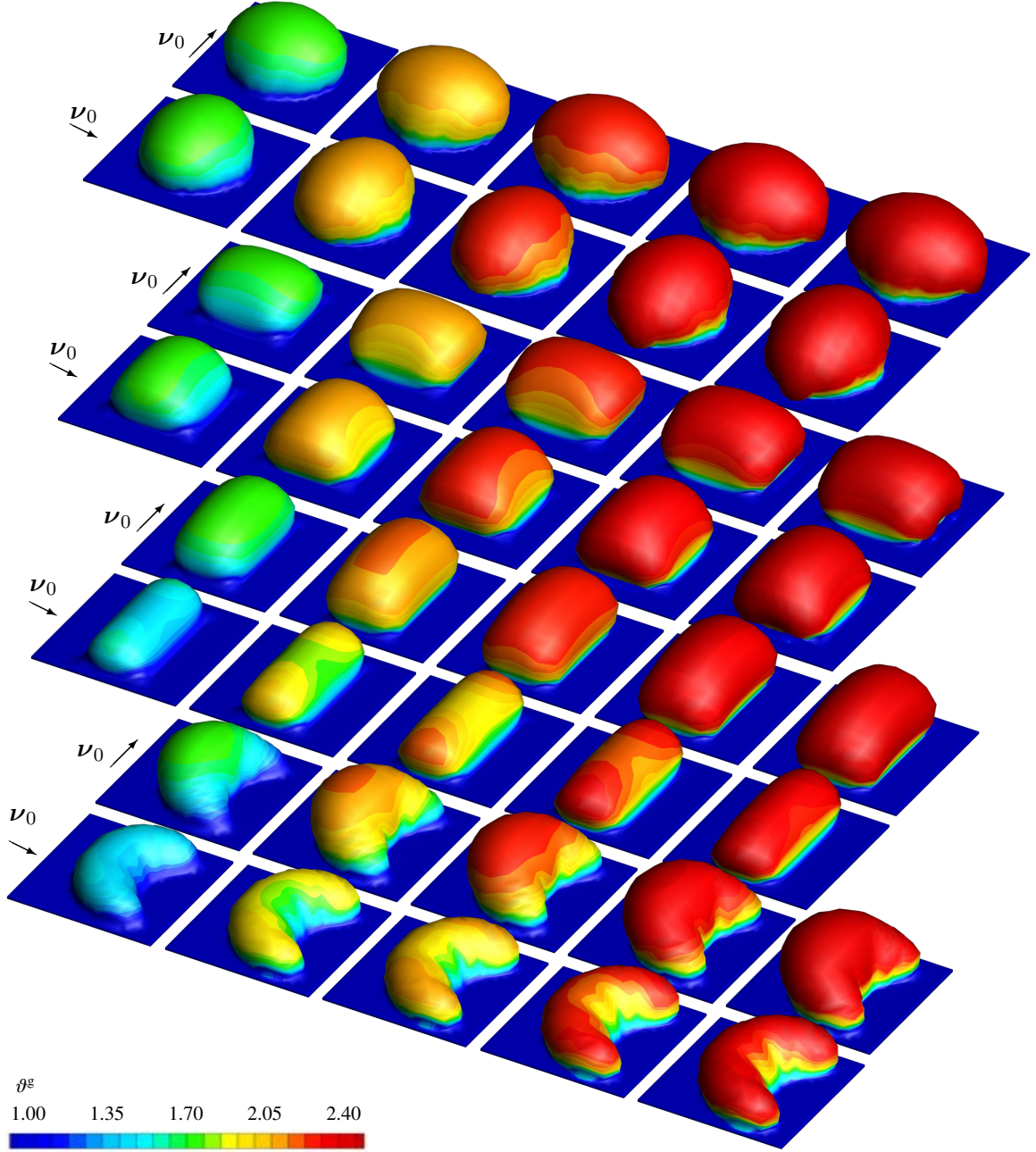


Figure 3.12: Tissue expansion and skin growth. Spatio-temporal evolution of growth area stretch  $\vartheta^g$  for circular, square, rectangular, and crescent-shaped expanders with two different orientations with respect to Langer's lines  $\nu_0$  for each set. Growth is larger when the expanders are positioned along material's strong direction, aligned with Langer's lines. Under the same pressure applied to the same base surface area, the circular expander in rows 1 and 2 induces the largest amount of growth; the rectangular and crescent-shaped expanders placed orthogonal to Langer's lines in rows 6 and 8 induce the smallest amount of growth. The color code illustrates the evolution of the growth multiplier  $\vartheta^g$ , ranging from  $\vartheta^g = 1.0$  for the initially ungrown skin, shown in blue, to  $\vartheta^g = \vartheta^{\max} = 2.4$  for the fully grown state, shown in red. Snapshots correspond to  $t = 0.08$ ,  $t = 0.16$ ,  $t = 0.24$ ,  $t = 0.48$ , and  $t = 0.96$ , from left to right, corresponding to the labels in Figures 3.10 and 3.11.

## Chapter 4

# Growing Skin: Tissue Expansion in Pediatric Forehead Reconstruction

**Abstract.** Tissue expansion is a common surgical procedure to grow extra skin through controlled mechanical over-stretch. It creates skin that matches the color, texture, and thickness of the surrounding tissue, while minimizing scars and risk of rejection. Despite intense research in tissue expansion and skin growth, there is a clear knowledge gap between heuristic observation and mechanistic understanding of the key phenomena that drive the growth process. Here, we show that a continuum mechanics approach, embedded in a custom-designed finite element model, informed by medical imaging, provides valuable insight into the biomechanics of skin growth. In particular, we model skin growth using the concept of an incompatible growth configuration. We characterize its evolution in time using a second-order growth tensor parameterized in terms of a scalar-valued internal variable, the in-plane area growth. When stretched beyond the physiological level, new skin is created, and the in-plane area growth increases. For the first time, we simulate tissue expansion on a patient-specific geometric model, and predict stress, strain, and area gain at three expanded locations in a pediatric skull: in the scalp, in the forehead, and in the cheek. Our results may help the surgeon to prevent tissue over-stretch and make informed decisions about expander geometry, size, placement, and inflation. We anticipate our study to open new avenues in reconstructive surgery, and enhance treatment for patients with birth defects, burn injuries, or breast tumor removal.

## 4.1 Motivation

One percent of neonates is born with congenital melanocytic nevi, dark-colored surface lesions present at birth [65]. Congenital nevi may vary in size, shape, texture, color, hairiness, and location, but they have one thing in common: their high malignant potential [186]. Birthmarks larger than 10 cm in diameter are classified as giant congenital nevi and have a prevalence of one in 20,000 infants [309]. Because giant congenital nevi place the child at an increased risk to develop skin cancer, surgical excision remains the standard treatment option [139]. Cosmetic deformity, significant aesthetic disfigurement, and severe psychological distress are additional compelling reasons for nevus removal, especially in the craniofacial region [186].

To reconstruct the defect, preserve function, and maintain aesthetic appearance, tissue expansion has become a major treatment modality in the management of giant congenital nevi [231]. Tissue expansion was first proposed more than half a century ago to reconstruct a traumatic ear and has since then revolutionized reconstructive surgery [270]. Today it is widely used to repair birth defects [16], correct burn injuries [13], and reconstruct breasts after tumor removal [311]. Tissue expansion is the ideal strategy to grow skin that matches the color, texture, hair bearing, and thickness of the surrounding healthy skin, while minimizing scars and risk of rejection [319].

Figure 4.1, left, shows a one-year old boy who presented with a giant congenital nevus concerning 25 percent of his forehead, extending to the right temporal scalp and cheek [141]. To resurface the nevus region and stimulate *in situ* skin growth, three simultaneous forehead, cheek, and scalp expanders are used. They are implanted in subcutaneous pockets adjacent to the defect, where they are gradually filled with saline solution. The amount of filling is controlled by visual inspection of skin color and capillary refill [319]. Multiple serial inflations stretch the skin and stimulate tissue growth over a period of several weeks [414]. Once enough skin is created, the expanders are removed, the nevus is excised, and the newly grown skin flaps are advanced to close the defect zone. Figure 4.1, right, shows the boy at age three, after completed forehead, scalp, and cheek reconstruction.

Figure 4.2 shows a schematic sequence of the mechanical processes during tissue expansion. Initially, at biological equilibrium, the skin is in a natural state of resting tension [342]. When the expander is implanted and inflated, skin is loaded in tension. Stretch beyond a critical level triggers a series of signaling pathways eventually leading to the creation of



Figure 4.1: Tissue expansion for pediatric forehead reconstruction. The patient, a one-year old boy presented with a giant congenital nevus involving 25 percent of his forehead, extending to the right temporal scalp and cheek. Simultaneous forehead, cheek, and scalp expanders were implanted for *in situ* skin growth. This technique allows to resurface large anatomical areas with skin of similar color, quality, and texture. The follow-up photograph shows the boy at age three, after completed forehead, scalp, and cheek reconstruction.

new skin [364]. On the cellular level, mechanotransduction affects a network of several integrated cascades including growth factors, cytoskeletal rearrangement, and protein kinases [92]. On the tissue level, skin growth induces stress relaxation and restores the state of resting tension [342]. The cycle of expander inflation, stretch, growth, and relaxation is repeated multiple times, typically on a weekly basis [414]. As demonstrated by immunocytochemistry, the expanded tissue undergoes normal cell differentiation and maintains its characteristic phenotype [402]. Skin initially displays thickness changes upon expansion, however, these changes are fully reversible upon expander removal [382]. When the expander is removed, the skin retracts and reveals the irreversible nature of skin growth, associated with growth-induced residual stresses [137, 249]. Figure 4.3 shows a commonly used tissue expander to grow skin in reconstructive surgery.

To predict stress, strain, and area gain during tissue expansion in pediatric forehead reconstruction, we adopt a novel mechanistic approach [51, 52], based on the continuum framework of finite growth [320]. Originally developed for isotropic volumetric growth [106, 233], finite growth theories are based on the multiplicative decomposition of the deformation gradient into an elastic and a growth part [124, 234], a concept adopted from finite plasticity [222].

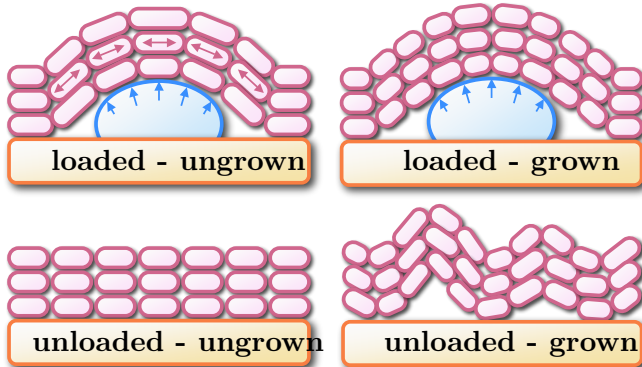


Figure 4.2: Schematic sequence of tissue expander inflation. At biological equilibrium, the skin is in a physiological state of resting tension, unloaded and ungrown. When an expander is implanted and inflated, the skin is stretched, loaded and ungrown. Mechanical stretch beyond a critical level triggers a series of signaling pathways eventually leading to the creation of new skin to restore the state of resting tension, loaded and grown. Upon expander removal, elastic deformations retract and inelastic deformations remain, unloaded and grown.

Depending on the format of their growth tensor, continuum growth theories have been refined to characterize isotropic [138, 207], transversely isotropic [314, 361], orthotropic [134], or generally anisotropic growth [248, 250], either compressible [248] or incompressible [332]. Recent trends focus on the computational modeling of finite growth [158], typically by introducing the growth tensor as an internal variable within a finite element framework [133, 200], a strategy that we also adopt here. A recent monograph that compares different approaches to growth and summarizes the essential findings, trends, and open questions in this progressively evolving new field [8]. Despite ongoing research in growing biological systems, the growth of thin biological membranes remains severely understudied. Only few attempts address the growth of thin biological plates [95] and membranes [248]. Motivated by a first study on axisymmetric skin growth [351], we have recently established a prototype model for growing membranes to predict skin expansion in a general three-dimensional setting [51]. This study capitalizes on recent developments in reconstructive surgery, continuum mechanics of growing tissues, and computational modeling, supplemented by medical image analysis. It documents our first attempts to model and simulate skin expansion in pediatric forehead reconstruction using a real patient-specific geometry.



Figure 4.3: Tissue expander to grow skin for defect correction in reconstructive surgery. Typical applications are birth defects, burn injuries, and breast reconstruction. Devices consist of a silicone elastomer inflatable expander with a reinforced base for directional expansion, and a remote silicone elastomer injection dome. Courtesy of Mentor Worldwide LLC.

## 4.2 Methods

### 4.2.1 Continuum Modeling of Skin Growth

We adopt the kinematics of finite deformations and introduce the deformation map  $\varphi$ , which, at any given time  $t$  maps the material placement  $\mathbf{X}$  of a physical particle in the material configuration to its spatial placement  $\mathbf{x}$  in the spatial configuration,  $\mathbf{x} = \varphi(\mathbf{X}, t)$ . We choose a formulation which is entirely related to the material frame of reference, and use  $\nabla\{\circ\} = \partial_{\mathbf{X}}\{\circ\}|_t$  and  $\text{Div}\{\circ\} = \partial_{\mathbf{X}}\{\circ\}|_t : \mathbf{I}$  to denote the gradient and the divergence of any field  $\{\circ\}(\mathbf{X}, t)$  with respect to the material placement  $\mathbf{X}$  at fixed time  $t$ . Here,  $\mathbf{I}$  is the material identity tensor. To characterize finite growth, we introduce an incompatible growth configuration, and adopt the multiplicative decomposition of the deformation gradient

$$\mathbf{F} = \nabla_{\mathbf{X}}\varphi = \mathbf{F}^e \cdot \mathbf{F}^g \quad (4.1)$$

into a reversible elastic part  $\mathbf{F}^e$  and an irreversible growth part  $\mathbf{F}^g$ . This multiplicative decomposition, reminiscent of the decomposition of the elastoplastic deformation gradient [222], was first used to describe growth of biological tissues in [320]. Similarly, we can then decompose the total Jacobian

$$J = \det(\mathbf{F}) = J^e J^g \quad (4.2)$$

into an elastic part  $J^e = \det(\mathbf{F}^e)$  and a growth part  $J^g = \det(\mathbf{F}^g)$ . We idealize skin as a thin layer characterized through the unit normal  $\mathbf{n}_0$  in the undeformed reference configuration. The length of the deformed skin normal  $\mathbf{n} = \text{cof}(\mathbf{F}) \cdot \mathbf{n}_0 = J \mathbf{F}^{-t} \cdot \mathbf{n}_0$  introduces the

area stretch

$$\vartheta = \|\operatorname{cof}(\mathbf{F}) \cdot \mathbf{n}_0\| = \vartheta^e \vartheta^g \quad (4.3)$$

which we can again decompose into an elastic area stretch  $\vartheta^e = \|\operatorname{cof}(\mathbf{F}^e) \cdot \mathbf{n}_g / \|\mathbf{n}_g\|\|$  and a growth area stretch  $\vartheta^g = \|\operatorname{cof}(\mathbf{F}^g) \cdot \mathbf{n}_0\|$  [51]. Here,  $\mathbf{n}_g = \operatorname{cof}(\mathbf{F}^g) \cdot \mathbf{n}_0 = J^g \mathbf{F}^{g-t} \cdot \mathbf{n}_0$  denotes the grown skin normal, and  $\operatorname{cof}(\circ) = \det(\circ) (\circ)^{-t}$  denotes the cofactor of the second order tensor  $(\circ)$ . As characteristic deformation measures, we introduce the right Cauchy Green tensor  $\mathbf{C}$  in the undeformed reference configuration

$$\mathbf{C} = \mathbf{F}^t \cdot \mathbf{F} = \mathbf{F}^{gt} \cdot \mathbf{F}^{et} \cdot \mathbf{F}^e \cdot \mathbf{F}^g \quad (4.4)$$

and its elastic counterpart  $\mathbf{C}^e = \mathbf{F}^{et} \cdot \mathbf{F}^e = \mathbf{F}^{g-t} \cdot \mathbf{C} \cdot \mathbf{F}^{g-1}$  in the intermediate configuration. This allows us to rephrase the total area stretch as  $\vartheta = J [\mathbf{n}_0 \cdot \mathbf{C}^{-1} \cdot \mathbf{n}_0]^{1/2}$ . Finally, we introduce the pull back of the spatial velocity gradient  $\mathbf{l} = \dot{\mathbf{F}} \cdot \mathbf{F}^{-1}$  to the intermediate configuration,

$$\mathbf{F}^{e-1} \cdot \mathbf{l} \cdot \mathbf{F}^e = \mathbf{L}^e + \mathbf{L}^g \quad (4.5)$$

which obeys the additive decomposition into the elastic velocity gradient  $\mathbf{L}^e = \mathbf{F}^{e-1} \cdot \dot{\mathbf{F}}^e$  and the growth velocity gradient  $\mathbf{L}^g = \dot{\mathbf{F}}^g \cdot \mathbf{F}^{g-1}$ . Here,  $\{\dot{\circ}\} = \partial_t \{\circ\}|_{\mathbf{X}}$  denotes the material time derivative of any field  $\{\circ\}(\mathbf{X}, t)$  at fixed material placement  $\mathbf{X}$ .

We characterize growing tissue using the framework of open system thermodynamics in which the material density  $\rho_0$  is allowed to change as a consequence of growth [201, 203]. The balance of mass for open systems balances its rate of change  $\dot{\rho}_0$  with a possible in- or outflux of mass  $\mathbf{R}$  and mass source  $\mathcal{R}_0$  [204, 290].

$$\dot{\rho}_0 = \operatorname{Div}(\mathbf{R}) + \mathcal{R}_0 \quad (4.6)$$

Similarly, the balance of linear momentum balances the density-weighted rate of change of the velocity  $\rho_0 \mathbf{v} = \rho_0 \dot{\varphi}$ , with the momentum flux  $\mathbf{P} = \mathbf{F} \cdot \mathbf{S}$ , and the momentum source  $\rho_0 \mathbf{b}$ ,

$$\rho_0 \dot{\mathbf{v}} = \operatorname{Div}(\mathbf{F} \cdot \mathbf{S}) + \rho_0 \mathbf{b} \quad (4.7)$$

here stated in its mass-specific form [202].  $\mathbf{P}$  and  $\mathbf{S}$  are the first and second Piola-Kirchhoff stress tensors. Last, we would like to point out that the dissipation inequality for open

systems

$$\rho_0 \mathcal{D} = \mathbf{S} : \frac{1}{2} \dot{\mathbf{C}} - \rho_0 \dot{\psi} - \rho_0 \mathcal{S} \geq 0 \quad (4.8)$$

typically contains an extra entropy source  $\rho_0 \mathcal{S}$  to account for the growing nature of living biological systems [201, 249]. Equations (4.7) and (4.8) represent the mass-specific versions of the balance of momentum and of the dissipation inequality which are particularly useful in the context of growth since they contain no explicit dependencies on the changes in mass [202].

To close the set of equations, we introduce the constitutive equations for the mass source  $\mathcal{R}_0$ , for the momentum flux  $\mathbf{S}$ , and for the growth tensor  $\mathbf{F}^g$ , assuming that the mass flux  $\mathbf{R} = \mathbf{0}$ , the momentum source  $\mathbf{b} = \mathbf{0}$ , and the acceleration  $\dot{\mathbf{v}} = \mathbf{0}$  are negligibly small. On the cellular level, immunocytochemistry has shown that expanded tissue undergoes normal epidermal cell differentiation [402]. On the organ level, mechanical testing has confirmed that the newly grown skin has the same material properties as the initial tissue [414]. Accordingly, we assume that the newly grown skin has the same density as the initial tissue. This implies that the mass source

$$\mathcal{R}_0 = \rho_0 \operatorname{tr} (\mathbf{L}^g) \quad (4.9)$$

can be expressed as the density-weighted trace of the growth velocity gradient  $\operatorname{tr} (\mathbf{L}^g) = \dot{\mathbf{F}}^g : \mathbf{F}^{g-t}$  [158]. We model skin as a hyperelastic material characterized through the Helmholtz free energy  $\psi = \hat{\psi}(\mathbf{C}, \mathbf{F}^g)$ , which we use to evaluate the dissipation inequality (4.8).

$$\rho_0 \mathcal{D} = \left[ \mathbf{S} - \rho_0 \frac{\partial \psi}{\partial \mathbf{C}} \right] : \frac{1}{2} \dot{\mathbf{C}} + \mathbf{M}^e : \mathbf{L}^g - \rho_0 \frac{\partial \psi}{\partial \rho_0} \mathcal{R}_0 - \rho_0 \mathcal{S}_0 \geq 0 \quad (4.10)$$

We observe that the Mandel stress of the intermediate configuration  $\mathbf{M}^e = \mathbf{C}^e \cdot \mathbf{S}^e$  is energetically conjugate to the growth velocity gradient  $\mathbf{L}^g = \dot{\mathbf{F}}^g \cdot \mathbf{F}^{g-1}$ . From the dissipation inequality (4.10), we obtain the definition of the second Piola Kirchhoff stress  $\mathbf{S}$  as thermodynamically conjugate quantity to the right Cauchy Green deformation tensor  $\mathbf{C}$ .

$$\mathbf{S} = 2 \rho_0 \frac{\partial \psi}{\partial \mathbf{C}} = 2 \frac{\partial \psi}{\partial \mathbf{C}^e} : \frac{\partial \mathbf{C}^e}{\partial \mathbf{C}} = \mathbf{F}^{g-1} \cdot \mathbf{S}^e \cdot \mathbf{F}^{g-t} \quad (4.11)$$

According to this definition, the first derivative of the Helmholtz free energy  $\psi$  with respect to the elastic right Cauchy Green tensor  $\mathbf{C}^e$  introduces the elastic second Piola Kirchhoff

stress  $\mathbf{S}^e$ , while the second derivative defines the elastic constitutive moduli  $\mathbf{L}^e$ .

$$\mathbf{S}^e = 2\rho_0 \frac{\partial\psi}{\partial\mathbf{C}^e} \quad \text{and} \quad \mathbf{L}^e = 2 \frac{\partial\mathbf{S}^e}{\partial\mathbf{C}^e} = 4\rho_0 \frac{\partial^2\psi}{\partial\mathbf{C}^e \otimes \partial\mathbf{C}^e} \quad (4.12)$$

To focus on the impact of growth, rather than adopting a sophisticated anisotropic material model for skin [52, 205], we assume a classical Neo-Hookean free energy  $\rho_0\psi = \frac{1}{2}\lambda\ln^2(J^e) + \frac{1}{2}\mu[\mathbf{C}^e : \mathbf{I} - 3 - 2\ln(J^e)]$ , introducing the elastic second Piola Kirchhoff stress  $\mathbf{S}^e = [\lambda\ln(J^e) - \mu]\mathbf{C}^{e-1} + \mu\mathbf{I}$ , and the elastic constitutive moduli  $\mathbf{L}^e = \lambda\mathbf{C}^{e-1} \otimes \mathbf{C}^{e-1} + [\mu - \lambda\ln(J^e)][\mathbf{C}^e \bar{\otimes} \mathbf{C}^e + \mathbf{C}^e \underline{\otimes} \mathbf{C}^e]$ . Motivated by clinical observations [319], we classify skin growth as a strain-driven, transversely isotropic, irreversible process. It is characterized through one single growth multiplier  $\vartheta^g$  that reflects the irreversible area increase perpendicular to the skin normal  $\mathbf{n}_0$ .

$$\mathbf{F}^g = \sqrt{\vartheta^g}\mathbf{I} + [1 - \sqrt{\vartheta^g}] \mathbf{n}_0 \otimes \mathbf{n}_0 \quad (4.13)$$

For this particular type of transversely isotropic growth, for which all thickness changes are reversibly elastic [382], area growth is identical to volume growth, i.e.,  $\vartheta^g = \det(\mathbf{F}^g) = J^g$ . Because of the simple rank-one update structure in (5.4), we can invert the growth tensor explicitly,  $\mathbf{F}^{g-1} = 1/\sqrt{\vartheta^g}\mathbf{I} + [1 - 1/\sqrt{\vartheta^g}]\mathbf{n}_0 \otimes \mathbf{n}_0$ , using the Sherman-Morrison formula. This explicit representation introduces the following simple expression for the growth velocity gradient,

$$\mathbf{L}^g = \sqrt{\dot{\vartheta}^g}/\sqrt{\vartheta^g}\mathbf{I} + [1 - \sqrt{\dot{\vartheta}^g}/\sqrt{\vartheta^g}] \mathbf{n}_0 \otimes \mathbf{n}_0 \quad (4.14)$$

which proves convenient to explicitly evaluate the mass source in equation (4.9) as  $\mathcal{R}_0 = \rho_0[1 + 2\sqrt{\dot{\vartheta}^g}/\sqrt{\vartheta^g}]$ . Motivated by physiological observations of stretch-induced skin expansion [141], we adopt the following evolution equation for the growth multiplier,

$$\dot{\vartheta}^g = k^g(\vartheta^g)\phi^g(\vartheta^e) \quad (4.15)$$

which follows a well-established functional form [233], but is now rephrased in a strain-driven format [134]. To control unbounded growth, we introduce the weighting function

$$k^g = \frac{1}{\tau} \left[ \frac{\vartheta^{\max} - \vartheta^g}{\vartheta^{\max} - 1} \right]^\gamma \quad (4.16)$$

where  $1/\tau$  controls the adaptation speed, the exponent  $\gamma$  calibrates the shape of the growth curve, and  $\vartheta^{\max} > 1$  is the maximum area growth [158, 233]. The growth criterion

$$\phi^g = \langle \vartheta^e - \vartheta^{\text{crit}} \rangle = \langle \vartheta / \vartheta^g - \vartheta^{\text{crit}} \rangle \quad (4.17)$$

is driven by the elastic area stretch  $\vartheta^e = \vartheta / \vartheta^g$ , such that growth is activated only if the elastic area stretch exceeds a critical physiological stretch limit  $\vartheta^{\text{crit}}$ . Here,  $\langle \circ \rangle$  denote the Macaulay brackets.

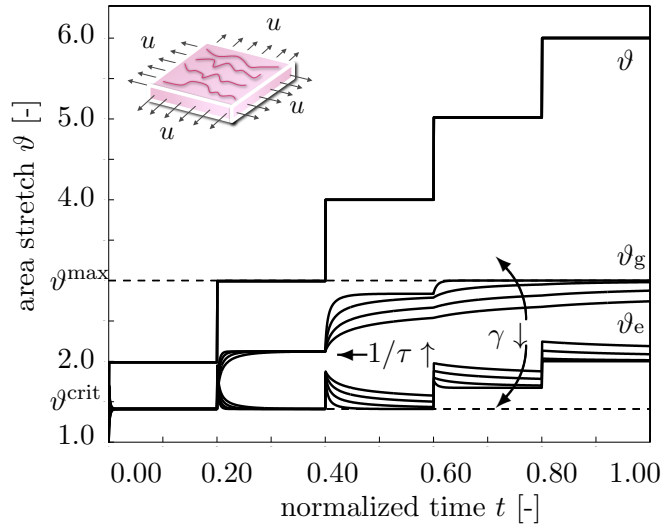


Figure 4.4: Tissue expansion in equi-biaxial stretch. Temporal evolution of total, elastic, and growth area stretch  $\vartheta$ ,  $\vartheta^e$ , and  $\vartheta^g$  for displacement driven skin expansion at varying growth exponents  $\gamma$ . At a piecewise constant total stretch  $\vartheta$ , the growth stretch increases gradually while the elastic stretch  $\vartheta^e$  decreases. This induces stress relaxation. Horizontal dashed lines represent the elastic stretch limit beyond which skin growth is activated  $\vartheta^{\text{crit}}$ , and the maximum area growth  $\vartheta^{\max}$ .

Figure 4.4 displays the constitutive response of the four-parameter growth model in equi-biaxial stretch. At a prescribed piecewise constant total stretch  $\vartheta$ , the growth stretch  $\vartheta^g$  increases gradually while the elastic stretch  $\vartheta^e$  decreases. This induces stress relaxation. Horizontal dashed lines represent the elastic stretch limit beyond which skin growth is activated  $\vartheta^{\text{crit}}$  and the maximum area growth  $\vartheta^{\max}$ . Increased adaptation speeds  $1/\tau \uparrow$  and decreased growth exponents  $\gamma \downarrow$  both accelerate convergence towards the biological equilibrium [158], but do not affect the final equilibrium state [314, 332]. At all times, the multiplicative decomposition of the deformation gradient  $\mathbf{F} = \mathbf{F}^e \cdot \mathbf{F}^g$  introduced in

equation (5.1) carries over to the multiplicative decomposition of the total area stretch  $\vartheta = \vartheta^e \vartheta^g$  of equation (5.3).

#### 4.2.2 Computational Modeling of Skin Growth

We solve the coupled biological and mechanical equilibrium for skin growth within an incremental iterative finite element setting [369]. To characterize the growth process at each instant in time, we introduce the growth multiplier  $\vartheta^g$  as an internal variable, and solve the biological equilibrium (5.10) locally at the integration point level. For the temporal discretization, we partition the time interval of interest  $\mathcal{T}$  into  $n_{\text{stp}}$  subintervals,  $\mathcal{T} = \mathbf{U}_{n=1}^{n_{\text{stp}}} [t_n, t_{n+1}]$  and focus on the interval  $[t_n, t_{n+1}]$  for which  $\Delta t = t_{n+1} - t_n > 0$  denotes the current time increment. Our goal is to determine the current growth multiplier  $\vartheta^g$  for a given deformation state  $\mathbf{F}$  at time  $t$ , and a given growth multiplier  $\vartheta_n^g$  at the end of the previous time step  $t_n$ . For the sake of compactness, we omit the index  $(\circ)_{n+1}$  for all quantities at the end of the current time step  $t_{n+1}$ . We evaluate the material time derivative of the growth multiplier  $\dot{\vartheta}^g = [\vartheta^g - \vartheta_n^g] / \Delta t$  using a finite difference approximation. In the spirit of implicit time integration schemes, we now reformulate the evolution equation (5.10), introducing the discrete residual  $R^\vartheta$  in terms of the unknown growth multiplier  $\vartheta^g$ .

$$R^\vartheta = \vartheta^g - \vartheta_n^g - k^g \phi^g \Delta t \doteq 0 \quad (4.18)$$

We solve this nonlinear residual equation using a local Newton iteration. Within each iteration step, we calculate the linearization of the residual  $R^\vartheta$  with respect to the growth multiplier  $\vartheta^g$ ,

$$K^\vartheta = \frac{\partial R^\vartheta}{\partial \vartheta^g} = 1 - \left[ \frac{\partial k^g}{\partial \vartheta^g} \phi^g + k^g \frac{\partial \phi^g}{\partial \vartheta^g} \right] \Delta t \quad (4.19)$$

with the derivatives of the weighting function  $\partial k^g / \partial \vartheta^g = -\gamma k / [\vartheta^{\max} - \vartheta^g]$  and the growth criterion  $\partial \phi^g / \partial \vartheta^g = -\vartheta / \vartheta^g$  introduced in equations (5.11) and (5.12). Within each iteration step, we iteratively update the unknown growth multiplier  $\vartheta^g \leftarrow \vartheta^g - R^\vartheta / K^\vartheta$  until convergence is achieved, i.e., until the local growth update  $\Delta \vartheta^g = -R^\vartheta / K^\vartheta$  reaches a user-defined tolerance.

To explore the interplay between growth and mechanics, we discretize the deformation map  $\varphi$  as nodal degree of freedom, and solve the mechanical equilibrium (4.7) globally at the node point level. To solve the quasi-static mechanical equilibrium,  $\text{Div}(\mathbf{F} \cdot \mathbf{S}) = \mathbf{0}$ , we

cast it into its weak form,  $\int_{\mathcal{B}_0} \nabla \delta \varphi : [\mathbf{F} \cdot \mathbf{S}] \, dV = 0$ , through multiplication with the test function  $\delta \varphi$  and integration over the domain of interest  $\mathcal{B}_0$ . For the spatial discretization, we partition the domain of interest  $\mathcal{B}_0 = \bigcup_{e=1}^{n_{el}} \mathcal{B}_e^e$  into  $n_{el}$  finite elements  $\mathcal{B}_e^e$ . Our goal is to determine the deformation state  $\varphi$  for a given load at time  $t$ . To approximate the test function  $\delta \varphi = \sum_{i=1}^{n_{en}} N^i \delta \varphi_i$ , the unknown deformation  $\varphi = \sum_{j=1}^{n_{en}} N^j \delta \varphi_j$ , and their gradients  $\nabla \delta \varphi = \sum_{i=1}^{n_{en}} \delta \varphi_i \otimes \nabla N^i \varphi$  and  $\nabla \varphi \sum_{j=1}^{n_{en}} \varphi_j \otimes \nabla N^j$ , we apply an isoparametric Bubnov-Galerkin based finite element interpolation, where  $N^i$  and  $N^j$  are the element shape functions and  $i, j = 1, \dots, n_{en}$  are the element nodes. We now reformulate the weak form of the balance of linear momentum (4.7) with the help of these finite element approximations, introducing the discrete residual  $\mathbf{R}_I^\varphi$  in terms of the unknown nodal deformation  $\varphi_J$ .

$$\mathbf{R}_I^\varphi = \sum_{e=1}^{n_{el}} \int_{\mathcal{B}_e} \nabla N_\varphi^i \cdot [\mathbf{F} \cdot \mathbf{S}] \, dV_e \doteq \mathbf{0} \quad (4.20)$$

Here, the operator  $\mathbf{A}$  symbolizes the assembly of all element residuals at the  $j = 1, \dots, n_{en}$  element nodes to the global residual at the global node points  $J = 1, \dots, n_{el}$ . We evaluate the global discrete residual (4.20), once we have iteratively determined the growth multiplier  $\vartheta^g$  for the given deformation state  $\mathbf{F}$  and the given history  $\vartheta_n^g$  as described in the previous section. Then we successively determine the growth tensor  $\mathbf{F}^g$  from equation (5.4), the elastic tensor  $\mathbf{F}^e = \mathbf{F} \cdot \mathbf{F}^{g-1}$  from equation (5.1), the elastic stress  $\mathbf{S}^e$  from equation (5.18), and lastly, the second Piola Kirchhoff stress  $\mathbf{S}$  from equation (4.11). Again, we suggest an incremental iterative Newton algorithm to solve the nonlinear residual equation for the unknown deformation (4.20). The consistent linearization of the residual  $\mathbf{R}_I^\varphi$  with respect to the nodal vector of unknowns  $\varphi_J$  introduces the global stiffness matrix.

$$\begin{aligned} \mathbf{K}_{IJ}^\varphi &= \frac{\partial \mathbf{R}_I^\varphi}{\partial \varphi_J} = \sum_{e=1}^{n_{el}} \int_{\mathcal{B}_e} \nabla N_\varphi^i \cdot \mathbf{S} \cdot \nabla N_\varphi^j \, \mathbf{I} \\ &\quad + [\nabla N_\varphi^i \cdot \mathbf{F}]^{\text{sym}} \cdot \mathbf{L} \cdot [\mathbf{F}^t \cdot \nabla N_\varphi^j]^{\text{sym}} \, dV_e \end{aligned} \quad (4.21)$$

The fourth order tensor  $\mathbf{L}$  denotes the Lagrangian constitutive moduli which, we can determine directly from the linearization of the Piola Kirchhoff stress  $\mathbf{S}$  with respect to the total right Cauchy Green tensor  $\mathbf{C}$  [133].

$$\mathbf{L} = 2 \frac{d\mathbf{S}}{d\mathbf{C}} = 2 \left. \frac{\partial \mathbf{S}}{\partial \mathbf{C}} \right|_{\mathbf{F}^g} + 2 \left[ \left. \frac{\partial \mathbf{S}}{\partial \mathbf{F}^g} : \frac{\partial \mathbf{F}^g}{\partial \vartheta^g} \right] \otimes \left. \frac{\partial \vartheta^g}{\partial \mathbf{C}} \right|_{\mathbf{F}} \quad (4.22)$$

The first term

$$2 \frac{\partial S}{\partial C} = [\mathbf{F}^{g-1} \overline{\otimes} \mathbf{F}^{g-1}] : \mathbf{L}^e : [\mathbf{F}^{g-t} \overline{\otimes} \mathbf{F}^{g-t}] \quad (4.23)$$

represents the pull back of the elastic moduli  $\mathbf{L}^e$  introduced in equation (5.18) onto the reference configuration. Here we have used the abbreviations  $\{\bullet \overline{\otimes} \circ\}_{ijkl} = \{\bullet\}_{ik} \{\circ\}_{jl}$  and  $\{\bullet \underline{\otimes} \circ\}_{ijkl} = \{\bullet\}_{il} \{\circ\}_{jk}$  for the non-standard fourth order products. The second term

$$\begin{aligned} \frac{\partial S}{\partial F^g} = & -[\mathbf{F}^{g-1} \overline{\otimes} \mathbf{S} + \mathbf{S} \underline{\otimes} \mathbf{F}^{g-1}] \\ & - [\mathbf{F}^{g-1} \overline{\otimes} \mathbf{F}^{g-1}] : \frac{1}{2} \mathbf{L}^e : [\mathbf{F}^{g-t} \underline{\otimes} \mathbf{C}^e + \mathbf{C}^e \overline{\otimes} \mathbf{F}^{g-t}] \end{aligned} \quad (4.24)$$

consists of two terms that resemble a geometric and a material stiffness in nonlinear continuum mechanics. The third term

$$\frac{\partial \mathbf{F}^g}{\partial \vartheta^g} = \frac{1}{2\sqrt{\vartheta^g}} [\mathbf{I} - \mathbf{n}_0 \otimes \mathbf{n}_0] \quad (4.25)$$

and the fourth term

$$\begin{aligned} \frac{\partial \vartheta^g}{\partial \mathbf{C}} = & \frac{1}{\tau} \frac{1}{\vartheta^g} \left[ \frac{\vartheta^{\max} - \vartheta^g}{\vartheta^{\max} - 1} \right]^\gamma \frac{1}{K^g} \Delta t \\ & \frac{1}{2} \vartheta \mathbf{C}^{-1} - \frac{1}{2} \frac{J^2}{\vartheta} [\mathbf{C}^{-1} \cdot \mathbf{n}_0] \otimes [\mathbf{C}^{-1} \cdot \mathbf{n}_0] \end{aligned} \quad (4.26)$$

depend on the particular choice for the growth tensor  $\mathbf{F}^g$  in equation (5.4) and on the evolution equation for the growth multiplier  $\vartheta^g$  in equation (5.10), respectively. For each global Newton iteration step, we iteratively update the current deformation state  $\boldsymbol{\varphi} \leftarrow \boldsymbol{\varphi} - \mathbf{K}_{IJ}^{\boldsymbol{\varphi}-1} \cdot \mathbf{R}_I^{\boldsymbol{\varphi}}$  until we achieve algorithmic convergence. Upon convergence, we store the corresponding growth multipliers  $\vartheta^g$  at the integration point level. Table 4.1 summarizes the algorithmic treatment of skin growth at the integration point level.

### 4.2.3 Geometric Modeling of Skin Growth

To simulate skin growth on an anatomically exact geometry, we create a finite element mesh on the basis of three-dimensional computer tomography images shown in Figure 4.5. Figure 4.6 summarizes the sequence of steps to generate our patient-specific geometric model. First, we identify the skin region by a distinct grey scale value in the computer tomography scans and extract point cloud data of its boundary. Figure 4.6, left, mimics the discrete nature

Table 4.1: Algorithmic flowchart for strain-driven transversely isotropic area growth.

given  $\mathbf{F}$  and  $\vartheta_n^g$   
 initialize  $\vartheta^g \leftarrow \vartheta_n^g$

---

local Newton iteration

check growth criterion  $\phi^g = \vartheta^e - \vartheta^{\text{crit}} \geq 0$  ?  
 (5.12)

calculate residual  $R = \vartheta^g - \vartheta_n^g - k^g \phi^g \Delta t$   
 (5.14)

calculate tangent  $K = \partial R / \partial \vartheta^g$       (5.15)

update growth stretch  $\vartheta^g \leftarrow \vartheta^g - R / K$

check convergence  $R \leq \text{tol}$  ?

---

calculate growth tensor  $\mathbf{F}^g$       (5.4)

calculate elastic tensor  $\mathbf{F}^e = \mathbf{F} \cdot \mathbf{F}^{g-1}$       (5.1)

calculate elastic right Cauchy Green tensor  $\mathbf{C}^e$   
 (4.4)

calculate elastic second Piola Kirchhoff stress  $\mathbf{S}^e$   
 (5.18)

---

calculate second Piola Kirchhoff stress  $\mathbf{S}$       (4.11)

calculate Lagrangian moduli  $\mathbf{L}$       (5.17)

of the extracted point cloud, with high point densities in the scanning plane and low point densities between the distinct planes. To smoothen the data and decreases the overall number of points, we homogenize the point cloud using a median filter. Next, we create a triangular surface mesh from the smoothed point cloud by applying a ball-pivoting algorithm [37]. Ball-pivoting algorithms are particularly suited for surface reconstruction of large data sets. After placing an initial seed element, the ball-pivoting algorithm rotates a sphere over the edges of this element and sequentially creates new elements whenever the sphere touches three data points. However, since our data are based on plane-wise computer tomography scans, ball-pivoting algorithms typically fail to automatically create smooth surfaces. Unfortunately, other fully automated meshing strategies such as convex hull or shrink wrap algorithms are not suitable for non-convex geometries like the face, which possesses several non-convexities in the eye, nose, mouth, and ear regions [197]. Accordingly, we smoothen the triangular surface mesh semi-manually, as illustrated in Figure 4.6, middle.

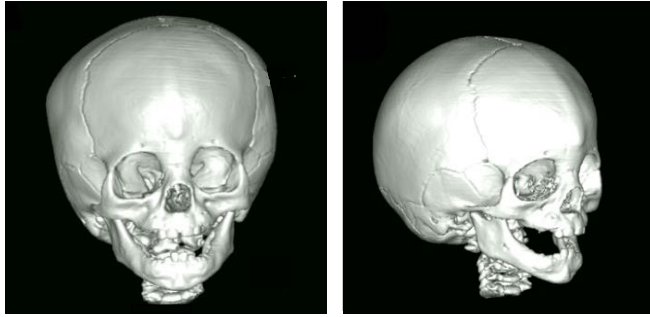


Figure 4.5: Three-dimensional computer tomography scans from the skull of a one-year old child. We create a patient-specific geometric model using discrete boundary points extracted from sliced image sections across the skull.

From the smoothed surface mesh, we finally create a one-element thick volume mesh of the pediatric skull, discretized with 61,228 nodes, 183,684 degrees of freedom, and 30,889 tri-linear brick elements. As a first approximation, we assume that all eight integration points within each element possess the same skin plane normal  $\mathbf{n}_0$ , corresponding to the normal from the initial surface mesh. We virtually implant three tissue expanders as shown in Figure 4.6, right, motivated by the tissue expansion case illustrated in Figure 4.1. First, we implant an expander in the scalp, discretized with 4,356 nodes, 13,068 degrees of freedom, and 2,088 tri-linear brick elements, covering an initial area of  $50.4\text{ cm}^2$ , shown in red. Second, we implant an expander in the cheek, discretized with 2,542 nodes, 7,626 degrees of freedom, and 1,200 tri-linear brick elements, covering an initial area of  $29.3\text{ cm}^2$ , shown in yellow. Third, we implant an expander in the forehead, discretized with 3,782 nodes, 11,346 degrees of freedom, and 1,800 tri-linear brick elements, covering an initial area of  $48.5\text{ cm}^2$ , shown in blue. To simulate tissue expansion, we fix all nodes and release only the expander degrees of freedom, which we then pressurize from underneath.

### 4.3 Results

We illustrate the impact of tissue expansion at three characteristic locations of the skull, in the scalp, the forehead, and the cheek. For the elastic model, we assume Lamé constants of  $\lambda = 0.7141 \text{ MPa}$  and  $\mu = 0.1785 \text{ MPa}$ , which would correspond to a Poisson's ratio of  $\nu = 0.4$  and a Young's modulus of  $E = 0.5 \text{ MPa}$  in the linear regime [3, 337]. For the growth model, we assume a critical threshold of  $\vartheta^{\text{crit}} = 1.1$ , a maximum area growth of

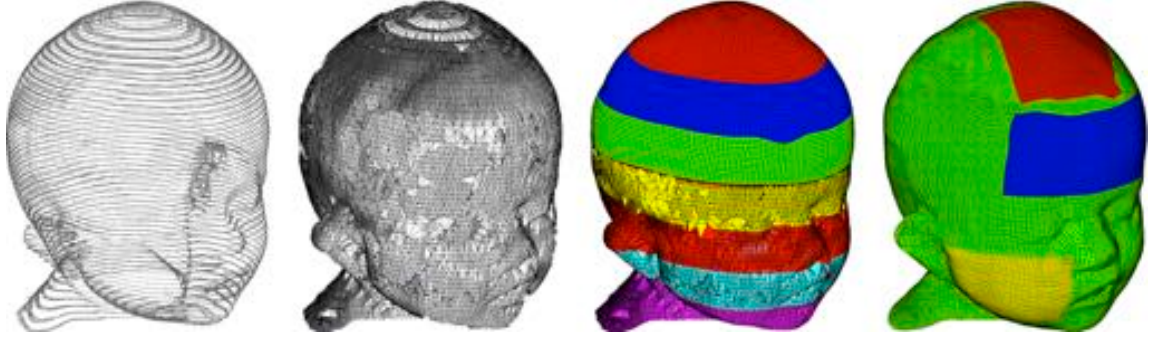


Figure 4.6: Mesh generation from clinical images. From the computer tomography scans, we extract discrete point cloud data (left), which we filter and mesh using a ball-pivoting algorithm. This generates a triangular surface mesh, which is further smoothed (middle) and turned into a final volume mesh (right). The final discretization of the skull consists of 61,228 nodes, 183,684 degrees of freedom, and 30,889 tri-linear brick elements. We virtually implant three tissue expanders, one in the scalp, discretized with 4,356 nodes, 13,068 degrees of freedom, and 2,088 brick elements (red), one in the cheek, discretized with 2,542 nodes, 7,626 degrees of freedom, and 1,200 brick elements (yellow), and one in the forehead, discretized with 3,782 nodes, 11,346 degrees of freedom, and 1,800 brick elements (blue).

$\vartheta^{\max} = 4.0$ , a growth exponent of  $\gamma = 3.0$ , and an adaptation speed of  $1/\tau = 12$ . We gradually pressurize the tissue expanders,  $0.0 < t \leq 0.125$ , then hold the pressure constant to allow the tissue to grow,  $0.125 < t \leq 0.75$ , and finally remove the pressure to visualize the grown area,  $0.75 < t \leq 1.0$ .

### 4.3.1 Tissue Expansion in the Scalp

Figures 4.7, 4.8, and 4.9 illustrate the tissue expansion process in the scalp. Figure 4.7 displays the temporal evolution of the normalized total area, elastic area, and growth area upon subsequent expander inflation, constant pressure, and expander removal. Once the elastic area stretch reaches the critical threshold of  $\vartheta^{\text{crit}} = 1.1$ , slightly before the total pressure is applied, at  $t = 0.125$ , the tissue starts to grow. As the expander pressure is held constant, growth increases gradually causing the total area to increase as well. Then, at  $t = 0.75$ , the pressure is decreased to remove the expander. The elastic area retracts gradually, while the grown area remains constant. The vertical dashed lines correspond

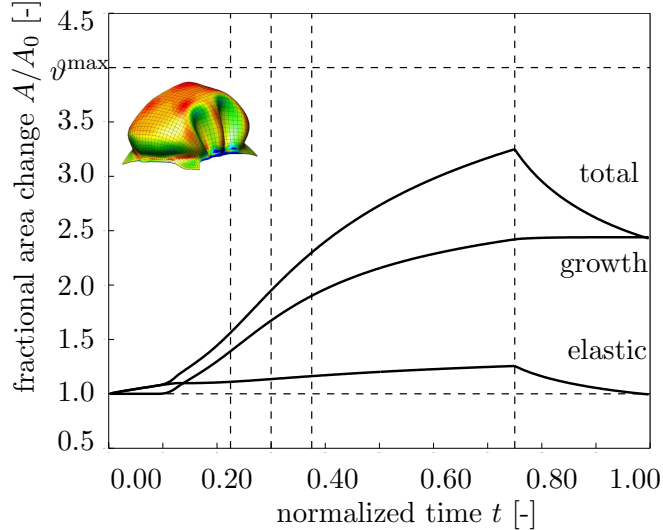


Figure 4.7: Tissue expansion in the scalp. Temporal evolution of normalized total area, elastic area, and growth area upon gradual expander inflation,  $0.0 < t \leq 0.125$ , constant pressure  $0.125 < t \leq 0.75$ , and deflation  $0.75 < t \leq 1.0$ . The final fractional area gain is 2.44, corresponding to  $122.8 \text{ cm}^2$ . Vertical dashed lines correspond to the time points displayed in Figure 4.8.

to the discrete time points,  $t = 0.225$ ,  $t = 0.300$ ,  $t = 0.375$  and  $t = 0.750$ , displayed in Figure 4.8. Figure 4.8 illustrates the spatio-temporal evolution of area growth  $\vartheta^g$ . Growth is first initiated at the center of the expander, where the elastic stretch is largest. As growth spreads throughout the entire expanded area, the initial area of  $50.4 \text{ cm}^2$  increases gradually as the grown skin area increases from  $70.07 \text{ cm}^2$ , to  $84.25 \text{ cm}^2$ , to  $95.73 \text{ cm}^2$ , and finally to  $121.87 \text{ cm}^2$ , from left to right. Figure 4.9 summarizes the final outcome of the expansion in the scalp in terms of the remaining deformation upon expander removal. The elastic area strain of  $0.95 \leq \vartheta^e \leq 1.05$  indicates an area change of  $\pm 5\%$  giving rise to residual stresses, left. The area growth of  $1.0 \leq \vartheta^g \leq 3.5$  shows that skin has more than doubled its initial area, right. This is in agreement with the final fractional area gain of 2.44, corresponding to an area growth in the scalp of  $122.8 \text{ cm}^2$ .

### 4.3.2 Tissue Expansion in the Forehead

Figures 4.10, 4.11, and 4.12 summarize the tissue expansion process in the forehead. Figure 4.10 displays the temporal evolution of the normalized total area, elastic area, and growth

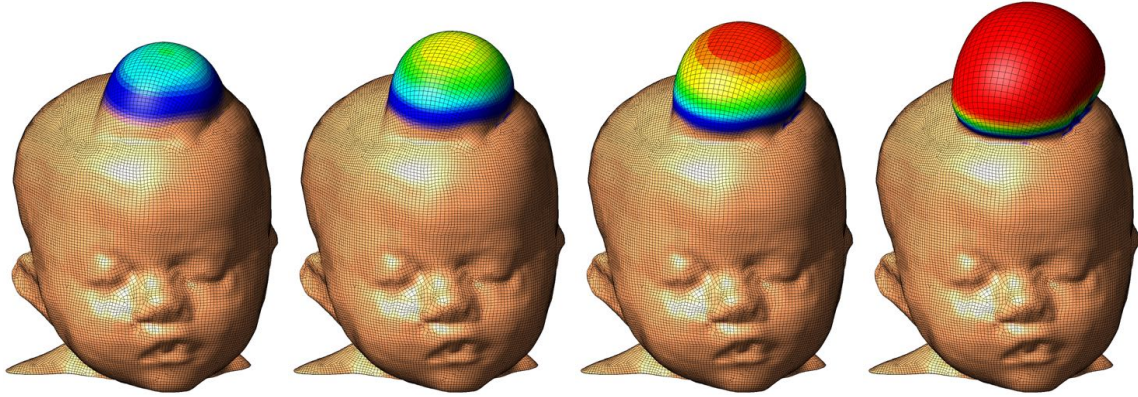


Figure 4.8: Tissue expansion in the scalp. Spatio-temporal evolution of area growth displayed at  $t = 0.225$ ,  $t = 0.300$ ,  $t = 0.375$  and  $t = 0.750$ . The initial area of  $50.4 \text{ cm}^2$  increases gradually as the grown skin area increases from  $70.07 \text{ cm}^2$ , to  $84.25 \text{ cm}^2$ , to  $95.73 \text{ cm}^2$ , and finally to  $121.87 \text{ cm}^2$ , from left to right.

area upon gradual expander inflation, constant pressure, and gradual expander removal. Similar to the expansion in the scalp, growth begins at stretches beyond the critical threshold level, then increases gradually upon constant pressure, and remains constant upon expander removal. Figure 4.11 illustrates the spatio-temporal evolution of area growth  $\vartheta^g$  at four characteristic time points indicated through the vertical dashed lines in figure 4.10. The growth process starts in the center of the forehead and spreads out throughout the entire forehead area. As it does, the initial area of  $48.5 \text{ cm}^2$  increases gradually as the grown skin area increases from  $66.56 \text{ cm}^2$ , to  $76.54 \text{ cm}^2$ , to  $85.96 \text{ cm}^2$ , and finally to  $116.55 \text{ cm}^2$ , from left to right. Figure 4.12 displays the remaining deformation upon expander removal. The final fractional area gain during forehead expansion is 2.44, corresponding to an area growth of  $118.1 \text{ cm}^2$ .

### 4.3.3 Tissue Expansion in the Cheek

Figures 4.13, 4.14, and 4.15 document the tissue expansion process in the cheek. Figure 4.13 summarizes the temporal evolution of the normalized total area, elastic area, and growth area upon gradual expander inflation, constant pressure, and gradual expander removal.

Again, the growth process is initiated once the stretches reach the critical threshold of  $\vartheta^{\text{crit}} = 1.1$ . Upon constant pressure, growth increases gradually. Upon pressure removal,

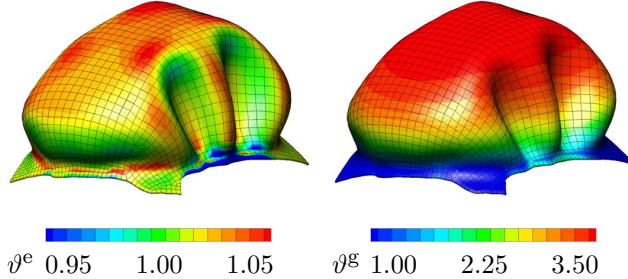


Figure 4.9: Tissue expansion in the scalp. Remaining deformation upon expander removal. The elastic area strain of  $0.95 \leq \vartheta^e \leq 1.05$  indicates an area change of  $\pm 5\%$  giving rise to residual stresses (left). The area growth of  $1.0 \leq \vartheta^g \leq 3.5$  shows that skin has more than doubled its initial area (right). The final fractional area gain is 2.44, corresponding to  $122.8 \text{ cm}^2$ .

growth remains constant displaying the irreversible nature of the growth process. Figure 4.14 illustrates the spatio-temporal evolution of area growth  $\vartheta^g$  in the cheek. Again, growth begins in center of cheek, where the elastic area stretch is largest. As the growth process spreads out throughout the entire cheek area, the initial area of  $29.3 \text{ cm}^2$  increases gradually as the grown skin area increases from  $42.74 \text{ cm}^2$ , to  $52.03 \text{ cm}^2$ , to  $59.39 \text{ cm}^2$ , and finally to  $76.86 \text{ cm}^2$ , from left to right. Figure 4.15 summarizes the outcome of the expansion in the cheek with a final fractional area gain of 2.64, corresponding to an area growth of  $77.4 \text{ cm}^2$ .

## 4.4 Discussion

Tissue expansion is one of the basic treatment modalities in modern reconstructive surgery. Inducing controlled tissue growth through well-defined overstretch, it creates skin that matches the color, texture, hair bearing, and thickness of the surrounding healthy skin, while minimizing scars and risk of rejection [141]. Despite its widespread use, the choice of the appropriate tissue expander is almost exclusively based on the surgeon's personal preference, and the discrepancy between recommended shapes, sizes, and volumes remains enormous [231]. The current gold standard for expander selection is to predict tissue growth by calculating the difference between the inflated and non-inflated expander surface [103, 341]. From an engineering point of view, it is quite intuitive, that this purely kinematic approach severely overestimates the net gain in surface area [385]. With a discrepancy of up to a factor four, these models assume that the entire deformation can be attributed to

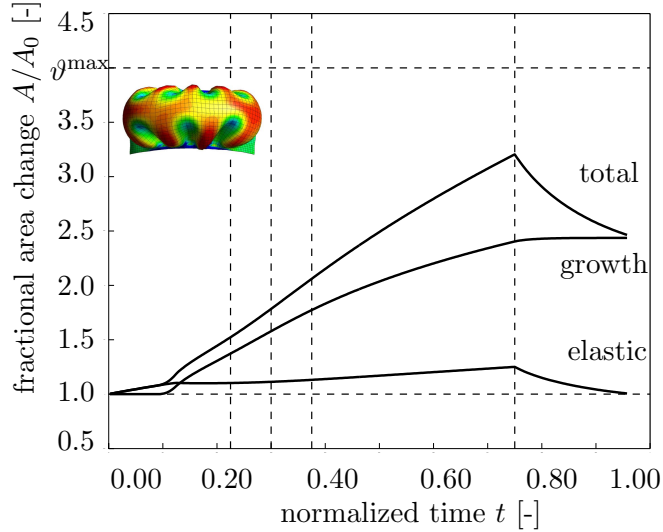


Figure 4.10: Tissue expansion in the forehead. Temporal evolution of normalized total area, elastic area, and growth area upon gradual expander inflation,  $0.0 < t \leq 0.125$ , constant pressure  $0.125 < t \leq 0.75$ , and deflation  $0.75 < t \leq 1.0$ . The final fractional area gain is 2.44, corresponding to  $118.1 \text{ cm}^2$ . Vertical dashed lines correspond to the time points displayed in Figure 4.11.

irreversible growth, completely neglecting the elastic deformation, which is reversible upon expander removal [231]. In an attempt to account for this error, empirical correction factors of 6.00, 3.75, and 4.50 have been proposed for circular, rectangular, and crescent-shaped expanders [385]. This demonstrates the vital need to rationalize criteria for a standardized device selection.

Motivated by a first study on axisymmetric skin growth [351], we have recently established a prototype model for growing membranes to simulate tissue expansion in a general three-dimensional setting [51]. We have applied our model to quantitatively compare four commonly available tissue expander geometries, round, square, rectangular, and crescent [52], however, only on initially flat geometries. Here, for the first time, we demonstrate the potential of the model during tissue expansion in pediatric forehead reconstruction using a real patient-specific model. To embed the solution into a nonlinear finite element environment, we discretize the governing equations for in-plane area growth in time and space. To solve the nonlinear set of equations, we apply an incremental iterative Newton-Raphson solution strategy based on the consistent algorithmic linearization. The resulting algorithm is remarkably efficient, stable, and robust. It is capable of predicting tissue expander inflation,

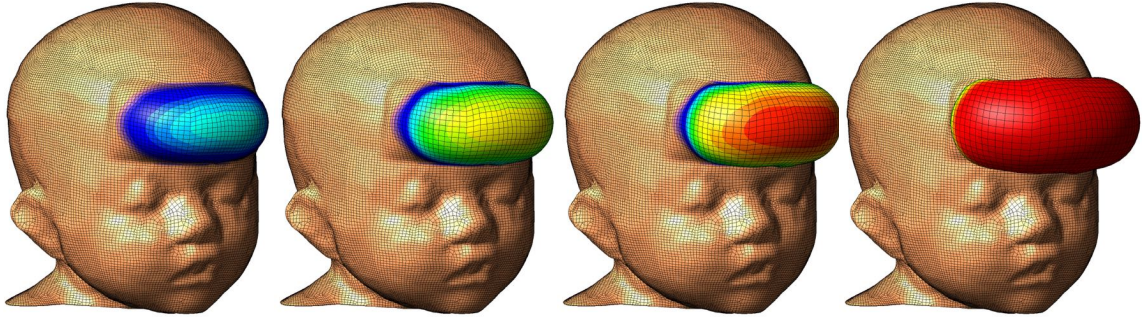


Figure 4.11: Tissue expansion in the forehead. Spatio-temporal evolution of area growth displayed at  $t = 0.225$ ,  $t = 0.300$ ,  $t = 0.375$  and  $t = 0.750$ . The initial area of  $48.5 \text{ cm}^2$  increases gradually as the grown skin area increases from  $66.56 \text{ cm}^2$ , to  $76.54 \text{ cm}^2$ , to  $85.96 \text{ cm}^2$ , and finally to  $116.55 \text{ cm}^2$ , from left to right.

tissue growth, and expander deflation at different locations of a human skull within the order of minutes on a standard laptop computer. Because of its geometric flexibility, our general algorithm could also be adapted to predict tissue expansion in the trunk [15] or in the upper and lower extremities [139].

Although the proposed model for skin growth represents a significant advancement over the axisymmetric growth model previously proposed [351], we would like to point out that some limitations remain. First, motivated by experimental observations, which report normal cell differentiation upon tissue expansion [402], we have assumed that the material microstructure remains unaffected by the growth process,  $\mathbf{F}^g = \sqrt{\vartheta^g} \mathbf{I} + [1 - \sqrt{\vartheta^g}] \mathbf{n}_0 \otimes \mathbf{n}_0$ . Here, for the sake of simplicity, we have modeled this microstructure as isotropic and elastic. We have recently shown that it is straightforward to combine our growth model with in-plane anisotropy, introduced through pronounced stiffness along Langer's lines [52, 205]. It might also be interesting to elaborate out-of-plane anisotropy and model the different skin layers individually [243]. We have demonstrated how to model the growth process itself as anisotropic as well [133]. This could imply growth  $\vartheta^{\parallel}$  exclusively along specific microstructural directions such as Langer's lines,  $\mathbf{F}^g = \mathbf{I} + [\vartheta^{\parallel} - 1] \boldsymbol{\nu}_0^{\parallel} \otimes \boldsymbol{\nu}_0^{\parallel}$ , or major in-plane growth  $\vartheta^{\parallel}$  along Langer's lines combined with minor in-plane growth  $\vartheta^{\perp}$  orthogonal to Langer's lines,  $\mathbf{F}^g = \vartheta^{\parallel} \boldsymbol{\nu}_0^{\parallel} \otimes \boldsymbol{\nu}_0^{\parallel} + \vartheta^{\perp} \boldsymbol{\nu}_0^{\perp} \otimes \boldsymbol{\nu}_0^{\perp} + \mathbf{n}_0 \otimes \mathbf{n}_0$ . Similarly, we could even introduce a progressive reorientation of the collagen network to allow for the material to

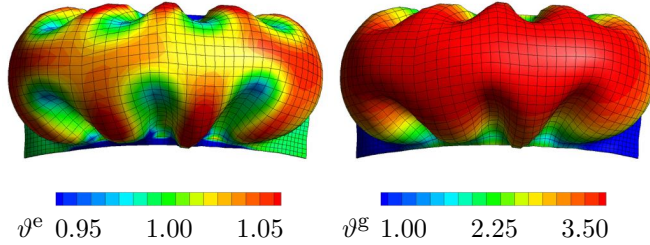


Figure 4.12: Tissue expansion in the forehead. Remaining deformation upon expander removal. The elastic area strain of  $0.95 \leq \vartheta^e \leq 1.05$  indicates an area change of  $\pm 5\%$  giving rise to residual stresses (left). The area growth of  $1.0 \leq \vartheta^g \leq 3.5$  shows that skin has more than doubled its initial area (right). The final fractional area gain is 2.44, corresponding to  $118.1 \text{ cm}^2$ .

align with the maximum principal strains [208, 250]. Ideally, the growth law would be tied to the underlying mechanobiology [92]. Comparative tissue histology of grown and ungrown tissue samples could help to identify the mechanisms that trigger skin growth to validate or, if necessary, refine our evolution equation (5.4) for the growth tensor.

Second, for the sake of simplicity, our finite element mesh consists of one single brick element with two integration points across the skin thickness. We have previously studied the sensitivity of growth with respect to thickness refinement using a higher resolution across the thickness [51, 52]. However, our results were rather insensitive to mesh refinement. This insensitivity might be explained by the fact that, upon expander inflation, the skin is almost in a pure membrane state. During deflation, however, we observe buckling associated with strain gradients across the skin thickness, which might play a critical role in the development of residual stresses. To explore these residual stresses further, we are currently refining our model utilizing a shell kinematics [315] with a higher resolution across the thickness direction. This will also allow us to simulate the individual skin layers [223, 342] and their interaction during the expansion process, which we believe to be a major source of residual stress in real tissue expansion cases [249, 407].

Third, for the sake of simplicity, we have modeled tissue expansion only implicitly through controlling the applied pressure. In real tissue expansion, the external control parameter is the expander volume [231]. This implies that our virtual tissue expansion displays creep under constant loading, while clinical tissue expansion might rather display relaxation under constant deformation [52], similar to our parameter study in Figure 4.4.

Fourth, here, we have assumed that the expander is connected tightly to the expanded

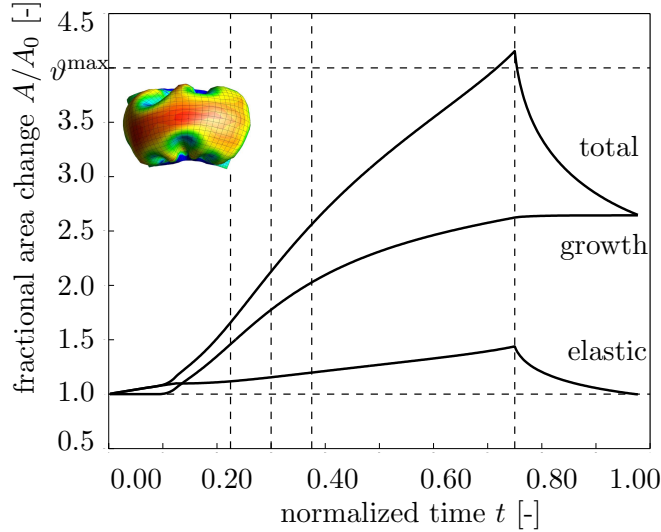


Figure 4.13: Tissue expansion in the cheek. Temporal evolution of normalized total area, elastic area, and growth area upon gradual expander inflation,  $0.0 < t \leq 0.125$ , constant pressure  $0.125 < t \leq 0.75$ , and deflation  $0.75 < t \leq 1.0$ . The final fractional area gain is 2.64, corresponding to  $77.4 \text{ cm}^2$ . Vertical dashed lines correspond to the time points displayed in Figure 4.14.

tissue, neglecting effects of interface sliding and shear [351]. This seems to be a reasonable first assumption though, since most current expanders have well-designed textures to promote mild tissue in-growth, primarily to prevent expander migration [27]. To address these potential limitations, we are currently refining the elastic model, the growth model, and the boundary conditions, to render our future simulations more realistic.

Last, while our computational model seems well suited to provide qualitative guidelines and trends, at its present state, it is not recommended for quantitative statements. We will need to perform acute and chronic in vitro and in vivo experiments to truly calibrate the underlying material parameters, to potentially refine and fully validate our model, to eventually make it applicable for clinical practice. Nevertheless, we believe that using the equations on nonlinear continuum mechanics represents a significant advancement over the current gold standard to predict tissue growth exclusively in terms of kinematic quantities [341, 385]. We have presented a novel computational model to predict the chronic adaptation of thin biological membranes when stretched beyond their physiological limit. Here, to illustrate the features of this model, we have demonstrated its performance during tissue expansion in pediatric forehead reconstruction. We have quantified reversibly elastic and irreversibly

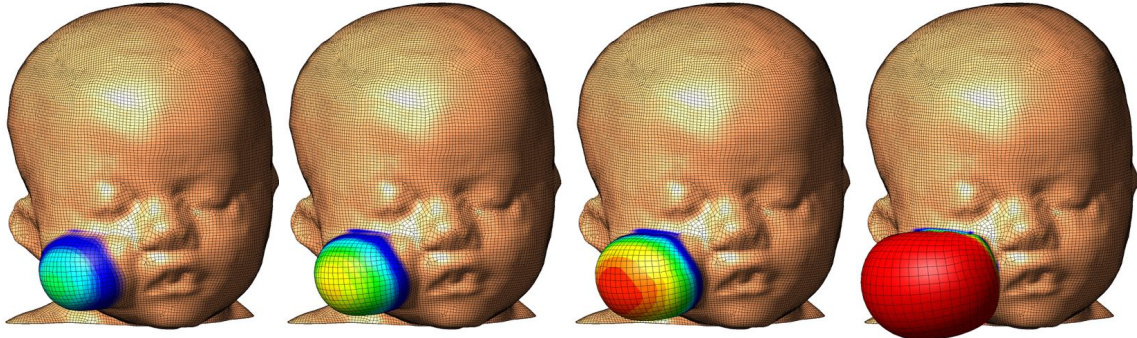


Figure 4.14: Tissue expansion in the cheek. Spatio-temporal evolution of area growth displayed at  $t = 0.225$ ,  $t = 0.300$ ,  $t = 0.375$  and  $t = 0.750$ . The initial area of  $29.3 \text{ cm}^2$  increases gradually as the grown skin area increases from  $42.74 \text{ cm}^2$ , to  $52.03 \text{ cm}^2$ , to  $59.39 \text{ cm}^2$ , and finally to  $76.86 \text{ cm}^2$ , from left to right.

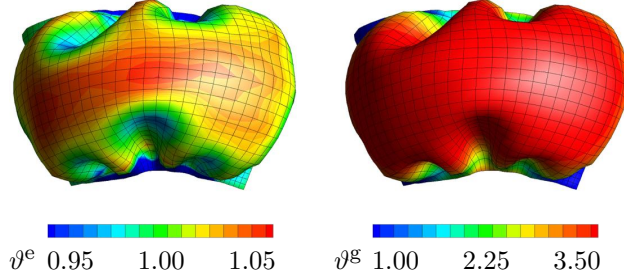


Figure 4.15: Tissue expansion in the cheek. Remaining deformation upon expander removal. The elastic area strain of  $0.95 \leq \vartheta^e \leq 1.05$  indicates an area change of  $\pm 5\%$  giving rise to residual stresses (left). The area growth of  $1.0 \leq \vartheta^g \leq 3.5$  shows that skin has more than doubled its initial area (right). The final fractional area gain is 2.64, corresponding to  $77.4 \text{ cm}^2$ .

grown area changes in response to skin expansion in the scalp, the forehead, and the cheek of a one-year-old child. In general, our generic computational model is applicable to arbitrary skin geometries, and has the potential to predict area gain in skin expansion during various common procedures in reconstructive surgery. A comprehensive understanding of the gradually evolving stress and strain fields in growing skin may help the surgeon to prevent tissue damage and optimize clinical process parameters such as expander geometry, expander size, expander placement, and inflation timing. Overall, we believe that predictive computational modeling might open new avenues in reconstructive surgery and enhance treatment for patients with birth defects, burn injuries, or breast tumor removal.

## Chapter 5

# On the Biomechanics and Mechanobiology of Growing Skin

**Abstract.** Skin displays an impressive functional plasticity, which allows it to adapt gradually to environmental changes. Tissue expansion takes advantage of this adaptation, and induces a controlled *in situ* skin growth for defect correction in plastic and reconstructive surgery. Stretches beyond the skin's physiological limit invoke several mechanotransduction pathways, which increase mitotic activity and collagen synthesis, ultimately resulting in a net gain in skin surface area. However, the interplay between mechanics and biology during tissue expansion remains unquantified. Here we present a continuum model for skin growth that summarizes the underlying mechanotransduction pathways collectively in a single phenomenological variable, the strain-driven area growth. We illustrate the governing equations for growing biological membranes, and demonstrate their computational solution within a nonlinear finite element setting. In displacement-controlled equi-biaxial extension tests, the model accurately predicts the experimentally observed histological, mechanical, and structural features of growing skin, both qualitatively and quantitatively. Acute and chronic elastic uniaxial stretches are 25% and 10%, compared to 36% and 10% reported in the literature. Acute and chronic thickness changes are -28% and -12%, compared to -22% and -7% reported in the literature. Chronic fractional weight gain is 3.3, compared to 2.7 for wet weight and 3.3 for dry weight reported in the literature. In two clinical cases of skin expansion in pediatric forehead reconstruction, the model captures the clinically observed mechanical and structural responses, both acutely and chronically. Our results demonstrate that the field theories of continuum mechanics can reliably predict the mechanical

manipulation of thin biological membranes by controlling their mechanotransduction pathways through mechanical overstretch. We anticipate that the proposed skin growth model can be generalized to arbitrary biological membranes, and that it can serve as a valuable tool to virtually manipulate living tissues, simply by means of changes in the mechanical environment.

## 5.1 Motivation

Human skin is a remarkable organ that can be stretched to manyfold its original size, while remaining phenotypically similar to its initial state, without any reported malignant transformation [31, 92]. To enable this incredible expansion, skin is a highly specialized mechanoresponsive interface, characterized through a network of interrelated cascades involving extracellular, membrane, cytosolic, cytoskeletal, and nuclear mechanisms [342]. When skin is stretched beyond its physiological limit, these mechanisms act in concert to restore the homeostatic equilibrium state. In this regulatory process, transmembrane mechanosensors in the form of stretch-activated ion channels, integrins, growth factor receptors, and G-protein-coupled receptors play a key role in translating extracellular events into intracellular signals [175, 403], see Figure 5.1.

Stretch-activated ion channels open in response to elevated membrane strains, allowing positively charged calcium ions ( $\text{Ca}^{2+}$ ) and other cations to enter the cell. Changes in the intracellular calcium concentration are known to regulate intracellular signaling and cytoskeletal remodeling [342]. Integrins are receptors that mediate attachment between a cell and the extracellular matrix [344]. They play a central role in force transmission across the cell membrane, triggering targets such as nitric oxide (NO) signaling, mitogen-associated protein kinases (MAPK), Rho GTPases, and phosphoinositol-3-kinase (PI3K). Growth factor receptors bind to growth factors outside the cell, thereby turning on several receptor mediated pathways inside the cell, such as nitric oxide (NO) signaling and mitogen-associated protein kinases (MAPK) [175]. Mitogen-associated protein kinase signaling pathways convey information to effectors, coordinate incoming information from other signaling cascades, amplify signals, and initiate a variety of response patterns.

G protein-coupled receptors are seven-transmembrane proteins, which can potentially be activated by mechanical stretch outside the cell to initiate mechanotransduction pathways inside the cell through second messengers such as nitric oxide (NO) signaling and

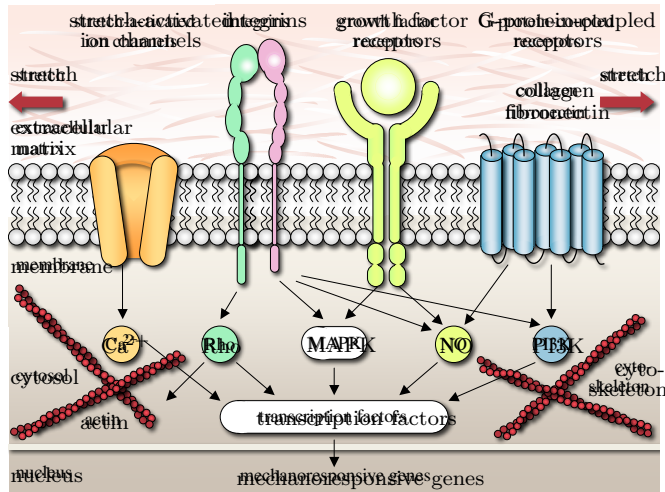


Figure 5.1: Mechanotransduction of growing skin. Transmembrane mechanosensors in the form of stretch-activated ion channels, integrins, growth factor receptors, and G-protein-coupled receptors translate extracellular signals into intracellular events, which activate a cascade of interconnected signaling pathways. Biomechanical and biochemical signals converge in the activation of transcription factors, activating gene expression. Mechanotransduction triggers increased mitotic activity and increased collagen synthesis, resulting in an increase in skin surface area to restore the homeostatic equilibrium state [175, 403].

phosphoinositol-3-kinase (PI3K). Last, intracellular strain can induce conformational changes in the cytoskeleton itself. These changes may affect the binding affinities to specific molecules and thereby activate additional signaling pathways [216].

In summary, mechanical activation initiates multiple signaling pathways, which can have a substantial overlap and crosstalk. However, since mechanically-induced signaling pathways may be shared with classical receptor-mediated pathways, they are typically difficult to study in isolation. It is clear, however, that all these signaling pathways converge to activate transcription factors, which stimulate gene expression and other nuclear events [403]. Overall, the underlying principle is that stretch invokes a cascade of events that trigger increased mitotic activity and increased collagen synthesis, which ultimately result in increased skin surface area to restore the homeostatic equilibrium state [364].

Taking advantage of mechanotransduction is a powerful approach to endogenously engineer new skin. Since it was first introduced in the mid 1950s [270], the controlled mechanical manipulation of skin has opened a whole new frontier in reconstructive surgery. Today tissue expansion is widely used to repair birth defects [16], correct burn injuries [13], and

reconstruct breasts after tumor removal [311]. It is the ideal strategy to grow skin that matches the color, texture, hair bearing, and thickness of the surrounding healthy skin, while minimizing scars and risk of rejection [319].

Tissue expansion is an iterative procedure of controlled overstretch, progressive skin growth, and gradual restoration of the homeostatic equilibrium state, repeated in several weekly intervals [139]. To grow skin in a desired location, the surgeon dissects a subcutaneous pocket between the dermis and the hypodermis [141], in which he places the expander. The expander is successively filled with saline solution by a remote injection port, see Figure 5.2. By visual inspection of skin color, capillary refill, and palpation of the expanded skin, the surgeon heuristically determines the amount of filling [319]. Once enough new skin is produced, typically after a period of multiple weeks, the device is removed, and the new skin is used to repair the adjacent defect zone. Although tissue expansion is a common surgical procedure today, there are no scientific guidelines for optimal device selection. Accordingly, the appropriate choice of expander shape, expander size, expander location, filling volume, and filling timing remains almost exclusively based on the surgeon's experience and personal preference [231].

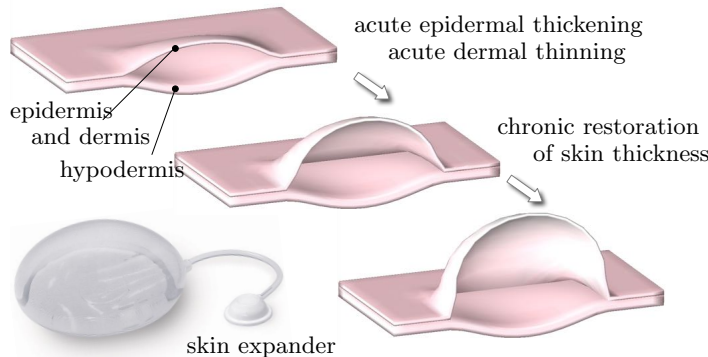


Figure 5.2: Biomechanics of growing skin. At biological equilibrium, the skin is in a homeostatic state of resting tension. To grow skin for defect repair, a tissue expander is placed in a subcutaneous pocket underneath the epidermis and the dermis, above the hypodermis. When the expander is inflated, the skin is stretched, associated with an acute dermal thinning attributed to the Poisson effect. Stretches beyond a critical level trigger a series of signaling pathways leading to the creation of new skin. Skin restores its homeostatic state, associated with the chronic restoration of the original thickness. Upon expander removal, elastic deformations retract and inelastic deformations remain.

The first quantitative model for growing skin was proposed only a few years ago, and has unfortunately not received a lot of attention to date [351]. Motivated by this first study

on axisymmetric skin growth, conceptually similar to an axisymmetric model for growing cell walls [136], we have recently established a prototype model for growing biological membranes to predict skin growth in a general three-dimensional setting [52]. The model is based on the continuum framework of finite growth [320], originally developed for the isotropic volumetric growth of biological solids [6, 106, 233]. Its key kinematic feature is the multiplicative decomposition of the deformation gradient into a reversible elastic part and an irreversible growth part [124, 234], a concept that was adopted from finite plasticity [222]. Over the past decade, continuum growth theories have been rapidly developed and intensely refined to characterize isotropic [76, 138, 207], transversely isotropic [314, 361], orthotropic [134, 362], and generally anisotropic [7, 250] growth phenomena, both compressibly [248] and incompressibly [170, 332].

Recent trends focus on the computational modeling of finite growth [8, 158], typically by introducing the growth tensor as an internal variable within a nonlinear finite element framework [133, 200], a strategy that we also adopt here. To predict the biomechanics and mechanobiology of growing skin and their impact on stress, strain, and area gain, we adopt a transversely isotropic growth model [51, 52], in which all cellular and molecular mechanisms are collectively summarized in a single phenomenological internal variable, the in-plane area growth. Here, in contrast to our previous model formulated in the material frame of reference [417], we introduce a spatial formulation, which lends itself to a computationally elegant and highly efficient algorithm. To simulate heterogeneous growth phenomena on anatomically realistic geometries, we integrate the growth model into a multi-purpose nonlinear finite element program [366]. We illustrate its features by means of the simple model problem of equi-biaxial extension and through two clinical cases of skin expansion in pediatric forehead reconstruction.

## 5.2 Methods

### 5.2.1 Continuum Model of Growing Skin

To accurately represent the finite deformations during skin expansion, we adopt the kinematics of finite growth, and introduce the deformation map  $\varphi$ , which, at any given time  $t$ , maps the material placement  $\mathbf{X}$  of a physical particle onto its spatial placement  $\mathbf{x} =$

$\varphi(\mathbf{X}, t)$ . We then introduce the multiplicative decomposition of the deformation gradient [320],

$$\mathbf{F} = \nabla_{\mathbf{X}} \varphi = \mathbf{F}^e \cdot \mathbf{F}^g \quad (5.1)$$

into a reversible elastic part  $\mathbf{F}^e$  and an irreversible growth part  $\mathbf{F}^g$ , in agreement with experimental findings [385]. Here,  $\nabla\{\circ\} = \partial_{\mathbf{X}}\{\circ\}|_t$  denotes the gradient of a field  $\{\circ\}(\mathbf{X}, t)$  with respect to the material placement  $\mathbf{X}$  at fixed time  $t$ . Its Jacobian defines the overall change in tissue volume,

$$J = \det(\mathbf{F}) = J^e J^g \quad (5.2)$$

which we can equivalently decompose into a reversibly elastic volume change  $J^e = \det(\mathbf{F}^e)$  and an irreversibly grown volume change  $J^g = \det(\mathbf{F}^g)$ . Skin is a composite material consisting of a 0.1-1.0 mm thick, waterproof, protective outer layer, the epidermis, and a 1.0-4.0 mm thick, load bearing inner layer, the dermis [342], which we idealize jointly as a single layer. We characterize its area stretch through Nanson's formula

$$\vartheta = ||\text{cof}(\mathbf{F}) \cdot \mathbf{n}_0|| = \vartheta^e \vartheta^g \quad (5.3)$$

in terms of the skin plane normal  $\mathbf{n}_0$  in the undeformed reference configuration, where  $\text{cof}(\circ) = \det(\circ)(\circ)^{-t}$  denotes the cofactor of a second order tensor  $(\circ)$ . The area stretch obeys the multiplicative decomposition into a reversibly elastic area stretch  $\vartheta^e$  and an irreversibly grown area stretch  $\vartheta^g = ||\text{cof}(\mathbf{F}^g) \cdot \mathbf{n}_0||$ . To model stretch-induced skin growth, we collectively summarize the effects of mechanotransduction in a single scalar-valued variable  $\vartheta^g$ , which characterizes the evolution of the in-plane area growth, while the response in the thickness direction  $\mathbf{n}_0$  is assumed to be purely elastic [31]. Accordingly, we can express the growth tensor  $\mathbf{F}^g$  in the following simple format.

$$\mathbf{F}^g = \sqrt{\vartheta^g} \mathbf{I} + [1 - \sqrt{\vartheta^g}] \mathbf{n}_0 \otimes \mathbf{n}_0 \quad (5.4)$$

Since the material is not assumed to grow in the thickness direction  $\mathbf{n}_0$  [319, 382], its area growth is identical to its volume growth, i.e.,  $\vartheta^g = \det(\mathbf{F}^g) = J^g$ . Using the simple rank-one update structure of  $\mathbf{F}^g$ , we can apply the Sherman-Morrison formula to invert the growth tensor explicitly,

$$\mathbf{F}^{g-1} = \frac{1}{\sqrt{\vartheta^g}} \mathbf{I} + \left[ 1 - \frac{1}{\sqrt{\vartheta^g}} \right] \mathbf{n}_0 \otimes \mathbf{n}_0 \quad (5.5)$$

and obtain an explicit representation of the elastic tensor  $\mathbf{F}^e$ ,

$$\mathbf{F}^e = \frac{1}{\sqrt{\vartheta^g}} \mathbf{F} + \left[ 1 - \frac{1}{\sqrt{\vartheta^g}} \right] \mathbf{n} \otimes \mathbf{n}_0 \quad (5.6)$$

in terms of the spatial normal  $\mathbf{n} = \mathbf{F} \cdot \mathbf{n}_0$ . From the push forward of the contravariant material and intermediate metric tensors  $\mathbf{G}^{-1}$  and  $\mathbf{G}^{g-1}$ , we obtain the left Cauchy Green tensor  $\mathbf{b} = \mathbf{F} \cdot \mathbf{G}^{-1} \cdot \mathbf{F}^t$  and its counterpart  $\mathbf{b}^e$  in the deformed, current configuration.

$$\mathbf{b}^e = \mathbf{F}^e \cdot \mathbf{G}^{g-1} \cdot \mathbf{F}^{et} = \frac{1}{\vartheta^g} \mathbf{b} + \left[ 1 - \frac{1}{\vartheta^g} \right] \mathbf{n} \otimes \mathbf{n} \quad (5.7)$$

To focus on the impact of growth, we assume skin to behave isotropically elastic within the *in vivo* loading range of interest. Accordingly, we introduce the following Helmholtz free energy

$$\psi = \frac{1}{2} \lambda \ln^2(J^e) + \frac{1}{2} \mu [\mathbf{g} : \mathbf{b}^e - 3 - 2 \ln(J^e)] \quad (5.8)$$

to evaluate the standard dissipation inequality, which defines the Kirchhoff stress  $\boldsymbol{\tau}$  as thermodynamically conjugate to covariant spatial metric  $\mathbf{g}$ .

$$\boldsymbol{\tau} = 2 \frac{\partial \psi}{\partial \mathbf{g}} = [\lambda \ln(J^e) - \mu] \mathbf{g}^{-1} + \mu \mathbf{b}^e \quad (5.9)$$

This implies that the newly created skin will have the same microstructure, density, and stiffness, as the original, native tissue [31, 52]. We model skin growth as a strain-driven process [141], and introduce the following evolution equation for the area growth,

$$\dot{\vartheta}^g = k^g(\vartheta^g) \phi^g(\vartheta^e) \quad (5.10)$$

in which  $k^g(\vartheta^g)$  is a weighting function and  $\phi^g(\vartheta^e)$  is a growth criterion similar to a yield function in the theory of plasticity. For the weighting function, we adopt a well-established functional form [233], which we rephrase here in a strain-driven format [133, 134], to control unbounded growth.

$$k^g = \frac{1}{\tau} \left[ \frac{\vartheta^{\max} - \vartheta^g}{\vartheta^{\max} - 1} \right]^\gamma \quad (5.11)$$

The adaptation speed  $\tau$  and the shape parameter for the adaptation curve  $\gamma$  control the speed of adaptation, whereas the maximum area growth  $\vartheta^{\max}$  defines the biological equilibrium state [158, 233]. For the growth criterion, we assume that growth is driven by the

elastic area stretch  $\vartheta^e$ ,

$$\phi^g = \langle \vartheta^e - \vartheta^{\text{crit}} \rangle = \langle \vartheta / \vartheta^g - \vartheta^{\text{crit}} \rangle \quad (5.12)$$

and that it is activated only if the elastic area stretch exceeds a critical physiological limit  $\vartheta^{\text{crit}}$ , where  $\langle \circ \rangle$  denote the Macaulay brackets.

### 5.2.2 Computational Model of Growing Skin

To solve the nonlinear finite element equations of stretch-induced skin growth, we implement the growth model in a custom-designed version of the multipurpose nonlinear finite element program FEAP [366]. To characterize the growth process at each instant in time, we introduce the area growth  $\vartheta^g$  as an internal variable, and solve the biological equilibrium equation (5.10) locally at the integration point level. At each discrete time step  $t$ , we determine the current area growth  $\vartheta^g$  for a given current deformation state  $\mathbf{F}$  and a given area growth  $\vartheta_n^g$  from the previous time step  $t_n$ . Accordingly, we introduce the following finite difference approximation for the material time derivative of the area growth,

$$\dot{\vartheta}^g = [\vartheta^g - \vartheta_n^g] / \Delta t \quad (5.13)$$

where  $\Delta t = t - t_n$  denotes the current time increment. In the spirit of implicit time stepping schemes, we now reformulate the evolution equation (5.10) with the help of equation (5.13), introducing the discrete residual  $R^\vartheta$  in terms of the unknown area growth  $\vartheta^g$ .

$$R^\vartheta = \vartheta^g - \vartheta_n^g - k^g \phi^g \Delta t \doteq 0 \quad (5.14)$$

We solve this nonlinear equation using a local Newton iteration. Within each iteration step, we calculate the linearization of the residual  $R^\vartheta$  with respect to the area growth  $\vartheta^g$ ,

$$K^\vartheta = \frac{\partial R^\vartheta}{\partial \vartheta^g} = 1 - \left[ \frac{\partial k^g}{\partial \vartheta^g} \phi^g + k^g \frac{\partial \phi^g}{\partial \vartheta^g} \right] \Delta t \quad (5.15)$$

in terms of the linearizations of the weighting function  $\partial k^g / \partial \vartheta^g = -\gamma k^g / [\vartheta^{\max} - \vartheta^g]$  and the growth criterion  $\partial \phi^g / \partial \vartheta^g = -\vartheta / \vartheta^{g2}$  introduced in equations (5.11) and (5.12). We update the unknown area growth iteratively,

$$\vartheta^g \leftarrow \vartheta^g - R^\vartheta / K^\vartheta \quad (5.16)$$

until we achieve convergence, i.e., until the absolute value of the local growth update  $\Delta\vartheta^g = -R^\vartheta / K^\vartheta$  is below a user-defined threshold value. Once we have iteratively determined the current area growth  $\vartheta^g$ , we can successively determine the growth tensor  $\mathbf{F}^g$  from equation (5.4), the elastic tensor  $\mathbf{F}^e = \mathbf{F} \cdot \mathbf{F}^g^{-1}$  from equation (5.6), the Kirchhoff stress  $\boldsymbol{\tau}$  from equation (5.9), and, finally, the fourth order tensor  $\mathbf{e}$  of the Eulerian constitutive moduli.

$$\mathbf{e} = 2 \frac{d\boldsymbol{\tau}}{dg} = \mathbf{e}^e + \mathbf{e}^g = 2 \left. \frac{\partial \boldsymbol{\tau}}{\partial g} \right|_{\mathbf{F}^g} + \left. \frac{\partial \boldsymbol{\tau}}{\partial \vartheta^g} \otimes 2 \frac{\partial \vartheta^g}{\partial g} \right|_{\mathbf{F}} \quad (5.17)$$

The first term, the partial derivative of the Kirchhoff stress  $\boldsymbol{\tau}$  with respect to the covariant spatial metric  $\mathbf{g}$ , defines elastic constitutive moduli  $\mathbf{e}^e = 2 \partial \boldsymbol{\tau} / \partial \mathbf{g}$ ,

$$2 \frac{\partial \boldsymbol{\tau}}{\partial g} = \lambda \mathbf{g}^{-1} \otimes \mathbf{g}^{-1} + [\mu - \lambda \ln(J^e)] [\mathbf{g}^{-1} \overline{\otimes} \mathbf{g}^{-1} + \mathbf{g}^{-1} \underline{\otimes} \mathbf{g}^{-1}] \quad (5.18)$$

where we have used the common abbreviations,  $\{\bullet \overline{\otimes} \circ\}_{ijkl} = \{\bullet\}_{ik} \{\circ\}_{jl}$  and  $\{\bullet \underline{\otimes} \circ\}_{ijkl} = \{\bullet\}_{il} \{\circ\}_{jk}$ , for the non-standard fourth order products. The second term

$$\frac{\partial \boldsymbol{\tau}}{\partial \vartheta^g} = -\frac{1}{\vartheta^{g,2}} [\lambda \vartheta^g \mathbf{g}^{-1} + \mu [\mathbf{b} - \mathbf{n} \otimes \mathbf{n}]] \quad (5.19)$$

depends directly on the constitutive formulation for the Kirchhoff stress  $\boldsymbol{\tau}$  in equation (5.9) and indirectly on the particular format of the growth tensor  $\mathbf{F}^g$  in equation (5.4). The third term

$$2 \frac{\partial \mathcal{F}}{\partial g} = \frac{1}{\tau} \frac{1}{\vartheta^g} \left[ \frac{\vartheta^{\max} - \vartheta^g}{\vartheta^{\max} - 1} \right]^\gamma \frac{1}{K^g} \Delta t \left[ \vartheta \mathbf{g}^{-1} - \frac{J^2}{\vartheta} [\mathbf{F}^{-t} \cdot \mathbf{n}_0] \otimes [\mathbf{F}^{-t} \cdot \mathbf{n}_0] \right] \quad (5.20)$$

consists of the algorithmic linearization of the time discrete evolution equation for the area growth  $\partial \vartheta^g / \partial \vartheta$  in equation (5.16) and of the linearization of the area stretch  $2 \partial \vartheta / \partial \mathbf{g}$  in equation (5.3). The local stress of equation (5.9) and the local consistent tangent of equation (5.17) enter the global righthand side vector and the global iteration matrix of the global Newton iteration. Upon its convergence, we store the corresponding area growth  $\vartheta^g$  locally at the integration point level.

## 5.3 Results

We illustrate the features of the proposed growth model for the simple model problem of displacement driven equi-biaxial extension and for the clinical case of tissue expansion in pediatric forehead reconstruction. For the elastic model, we assume Lamé constants of  $\lambda = 0.7141$  MPa and  $\mu = 0.1785$  MPa, which would correspond to a Young's modulus of  $E = 0.5$  MPa and Poisson's ratio of  $\nu = 0.4$  in the linear regime [3,337]. For the growth model, we assume that growth takes place above the critical threshold of  $\vartheta^{\text{crit}} = 1.21$ , corresponding to uniaxial stretches of 10% [31]. We restrict the maximum area growth to  $\vartheta^{\text{max}} = 4.0$ , and assume an adaptation speed of  $\tau = 1/12$  and growth exponents of  $\gamma = 2.0$  and  $\gamma = 12.0$  in examples 5.3.1 and 5.3.2. Sensitivity analyses demonstrate that the parameters  $\tau$  and  $\gamma$  influence the adaptation time and the shape of the adaptation curve, but not the final state of biological equilibrium [158,418].

### 5.3.1 Model Problem - Skin Growth in Equi-biaxial Extension

We illustrate the conceptual features of our growth model by exploring the simple model problem of displacement-driven skin expansion of a square  $1.0 \times 1.0 \times 0.2$  sheet. In an equi-biaxial setting, we increase the prescribed displacements such that the in-plane area stretch is increased from  $\vartheta = 1.0$  to 2.0, 3.0, and 4.0, indicated through the vertical dashed lines in Figure 5.3. This implies that the skin sheet is gradually stretched to a final size of  $2.0 \times 2.0$ , i.e., to four times its original size. After applying the deformation, we allow the tissue to adapt, and recover its homeostatic equilibrium state. After three load increments, we remove the applied stretch and allow the tissue to relax.

Figure 5.3 illustrates the resulting temporal evolution of the total area stretch  $\vartheta$ , the reversible elastic area stretch  $\vartheta^e$ , and the irreversible area growth  $\vartheta^g$ . The horizontal dashed lines represent the elastic stretch limit  $\vartheta^{\text{crit}}$  beyond which skin growth is activated, and the maximum area growth  $\vartheta^{\text{max}}$ . The curves confirm, that, at all times, the multiplicative decomposition of the deformation gradient  $\mathbf{F} = \mathbf{F}^e \cdot \mathbf{F}^g$  introduced in equation (5.1) carries over to the multiplicative decomposition of the total area stretch  $\vartheta = \vartheta^e \vartheta^g$  of equation (5.3). Convergence towards the homeostatic state manifests itself through a gradual increase of growth  $\vartheta^g$  at a constant total stretch  $\vartheta$ , while the elastic stretch  $\vartheta^e$ , and, accordingly the stresses, decrease. Upon removal of the applied displacements, the elastic stretch instantaneously returns to its baseline value of one,  $\vartheta^e = 1$ . Since the growth process is assumed to

be irreversible, the growth stretch remains constant,  $\vartheta^g = \text{const}$ . The total stretch instantaneously adapts the value of the growth stretch,  $\vartheta = \vartheta^g$ .

Figure 5.4 shows the temporal evolution of the skin thickness. Upon loading, the thickness decreases acutely from 1.0 to 0.72, but then returns chronically to its loaded baseline value of 0.88. This value, indicated through the lower horizontal line, is slightly smaller than the original thickness because of the Poisson effect. Upon removal of the applied displacements, the skin thickness immediately returns to its original value of  $t = 1.0$ , indicated through the upper horizontal line. Since the model assumes no growth in thickness direction,  $t^g = 1.0$ , all thickness changes are fully reversible,  $t^e = t$ .

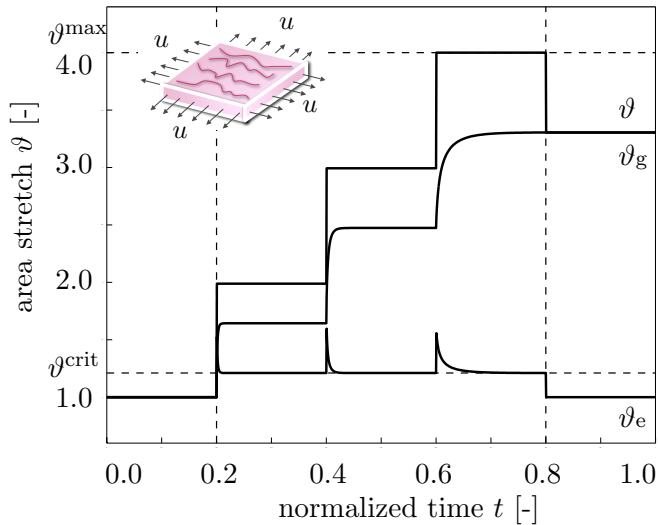


Figure 5.3: Temporal evolution of total area stretch  $\vartheta$ , reversible elastic area stretch  $\vartheta^e$ , and irreversible growth area stretch  $\vartheta^g$  for displacement driven skin expansion. Displacements are increased and then held constant in three intervals between the vertical dashed lines, and then relaxed. Displacement control induces relaxation indicated through the gradual decrease in elastic stretch  $\vartheta^e$  and stress, while the growth stretch  $\vartheta^g$  increases at a constant total stretch  $\vartheta$ . Horizontal dashed lines represent the elastic stretch limit beyond which skin growth is activated  $\vartheta^{\text{crit}}$ , and the maximum area growth  $\vartheta^{\text{max}}$ .

### 5.3.2 Clinical Problem - Skin Growth in Pediatric Forehead Reconstruction

To illustrate the full potential of our model, we simulate skin expansion in pediatric forehead reconstruction for two clinical cases, a one-year old girl in case study I [140], and a

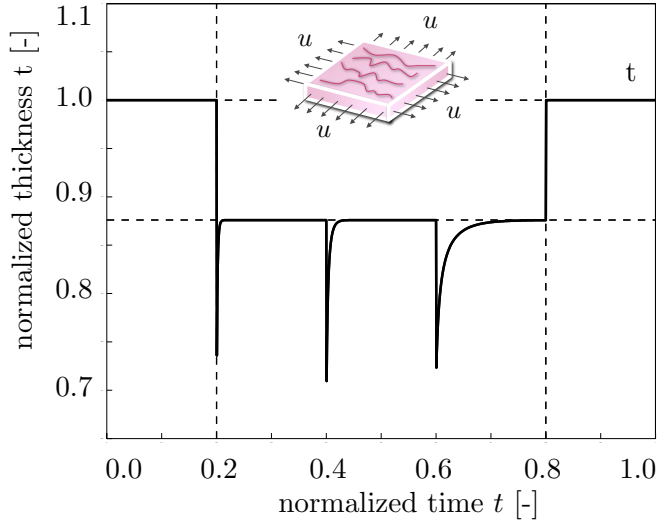


Figure 5.4: Temporal evolution of skin thickness  $t$  for displacement driven skin expansion. Displacements are increased and then held constant in three intervals between the vertical dashed lines, and then relaxed. Upon stretching, the skin thickness decreases acutely to 0.72, but then returns chronically to the homeostatic equilibrium thickness of 0.88 indicated through the lower horizontal line. This value is smaller than the original thickness because of the Poisson effect. Upon displacement relaxation, however, the skin thickness immediately returns to its original value of 1.0, indicated through the upper horizontal line.

one-year old boy in case study II [141], both born with giant congenital nevi affecting almost half of their foreheads, see Figure 5.5. Because giant congenital nevi place the child at an increased risk of skin cancer, the nevus is typically removed in the early childhood [139]. To reconstruct the defect, preserve function, and maintain aesthetic appearance, both children underwent controlled tissue expansion [231]. To simulate the process of tissue expansion in an anatomically exact geometry, we create a finite element mesh from three-dimensional computer tomography images of a child of similar age following the procedure outlined in [418]. We identify the skin region by its distinct grey scale value in the computer tomography scans to create a triangular surface mesh, which we further smoothen semi-manually. From the smoothed surface mesh, we create a volume mesh of the skin layer, discretized with 61,228 nodes, 183,684 degrees of freedom, and 30,889 tri-linear brick elements. Last, we assign each element a skin plane normal  $\mathbf{n}_0$ , corresponding to the normal of the initial surface mesh.

#### *Case study I:*

*Simultaneous forehead, anterior and posterior scalp expansion*



Figure 5.5: Skin expansion in pediatric forehead reconstruction. The patients, a one-year old girl, case study I shown in the top row [140], and a one-year old boy, case study II shown in the bottom row [141], both presented with a giant congenital nevus. Three forehead, scalp, and cheek expanders were implanted simultaneously for *in situ* skin growth. After enough skin is grown, the nevus is removed and the new skin is pulled over the wound to close it.

The first case study mimics the case of a one-year old girl, whose nevus covered her left posterior forehead [140]. To grow extra skin to cover the defect area, she underwent simultaneous tissue expansion in the forehead and in the anterior and posterior scalp as shown in Figure 5.5, top row. To model her case, we virtually implant three expanders. First, we implant an expander in the posterior scalp, discretized with 4,726 nodes, 14,178 degrees of freedom, and 2,270 tri-linear brick elements, covering an initial area of  $53.1\text{ cm}^2$ . Second, we implant two closely connected expanders in the forehead and in the scalp, discretized together with 7,954 nodes, 23,862 degrees of freedom, and 3,820 tri-linear brick elements, covering an initial area of  $96.3\text{ cm}^2$ . To simulate tissue expansion, we fix all nodes and release only the expander degrees of freedom, which we then pressurize from underneath. We assume that the adjacent dermis and hypodermis remain closely connected [351].

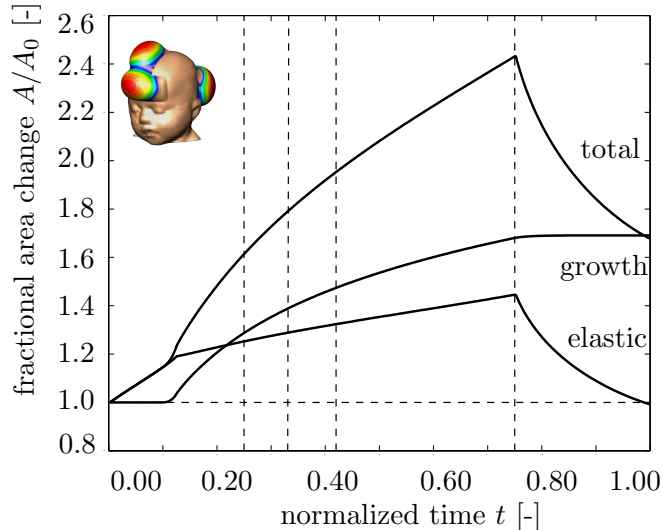


Figure 5.6: Skin expansion in pediatric forehead reconstruction. Case study I: Simultaneous forehead, anterior and posterior scalp expansion. Temporal evolution of normalized total area, elastic area, and growth area upon gradual expander inflation,  $0.0 < t \leq 0.125$ , constant pressure  $0.125 < t \leq 0.75$ , and deflation  $0.75 < t \leq 1.0$ . The expanded area increases from  $149.4\text{ cm}^2$  to  $251.2\text{ cm}^2$ , corresponding to a final fractional area gain of 1.68. Vertical dashed lines correspond to the time points displayed in Figure 5.7.

Figure 5.6 displays the temporal evolution of the normalized total area, elastic area, and growth area upon gradual expander inflation, constant pressure, and gradual expander removal. Once the elastic area stretch reaches the critical threshold of  $\vartheta^{\text{crit}} = 1.21$ , slightly before the total pressure is applied, at  $t = 0.125$ , the tissue starts to grow. As the expander

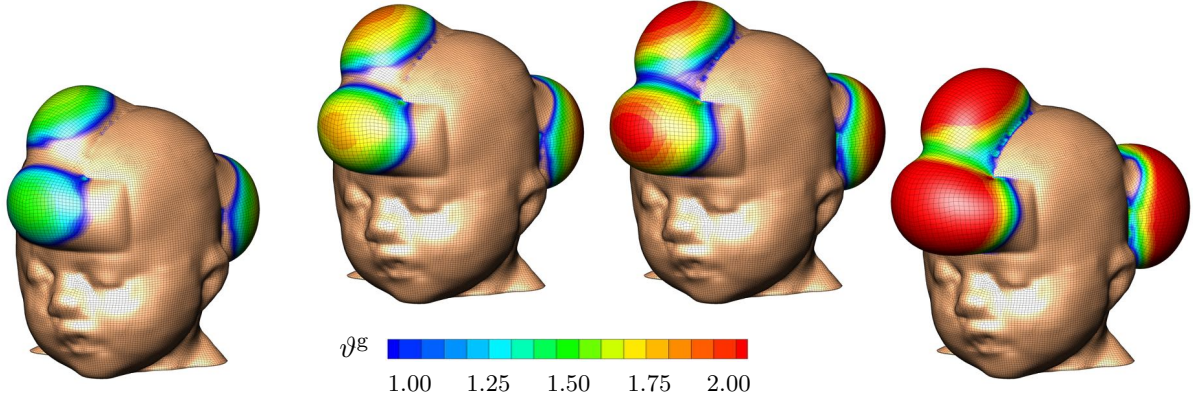


Figure 5.7: Skin expansion in pediatric forehead reconstruction. Case study I: Simultaneous forehead, anterior and posterior scalp expansion. Spatio-temporal evolution of area growth displayed at  $t = 0.24$ ,  $t = 0.33$ ,  $t = 0.42$  and  $t = 0.75$ . The initial area of  $149.4 \text{ cm}^2$  increases gradually as the grown skin area increases to  $190.2 \text{ cm}^2$ ,  $207.4 \text{ cm}^2$ ,  $220.4 \text{ cm}^2$ , and finally  $251.2 \text{ cm}^2$ , from left to right.

pressure is held constant, growth increases gradually causing the total area to increase. Then, at  $t = 0.75$ , the pressure is decreased to remove the expander. The elastic area retracts gradually, while the grown area remains constant. The vertical dashed lines correspond to the discrete time points,  $t = 0.24$ ,  $t = 0.33$ ,  $t = 0.42$  and  $t = 0.75$ , displayed in Figure 5.7.

Figure 5.7 illustrates the spatio-temporal evolution of the area growth  $\vartheta^g$ . Growth is first initiated at the center of the expanders, where the elastic stretch is largest. As growth spreads throughout the entire expanded areas, the initial area of  $149.4 \text{ cm}^2$  increases gradually as the grown skin area increases to  $190.2 \text{ cm}^2$ ,  $207.4 \text{ cm}^2$ ,  $220.4 \text{ cm}^2$ , and finally  $251.2 \text{ cm}^2$ , displayed from left to right. In detail, we observe that the final area in the posterior scalp region is  $91.5 \text{ cm}^2$ , corresponding to a fractional area gain of 1.73. In the combined forehead and anterior scalp regions, the final area is  $159.6 \text{ cm}^2$ , corresponding to a slightly lower fractional area gain of 1.66. Area growth displays regional variations within  $1.0 \leq \vartheta^g \leq 2.0$ , i.e., in some regions, the skin has doubled its initial area. Area growth is largest in the center regions and smallest in the peripheries.

#### *Case study II:*

*Simultaneous forehead, scalp, and cheek expansion*

The second example mimics the case of a one-year old boy whose nevus covered his right anterior forehead [141]. We simulate his simultaneous tissue expansion with expanders in the forehead, scalp, and cheek as shown in Figure 5.5, bottom row. First, we virtually implant an expander in the scalp, discretized with 4,356 nodes, 13,068 degrees of freedom, and 2,088 tri-linear brick elements, covering an initial area of  $50.5 \text{ cm}^2$ . Second, we implant an expander in the cheek, discretized with 2,542 nodes, 7,626 degrees of freedom, and 1,200 tri-linear brick elements, covering an initial area of  $29.3 \text{ cm}^2$ . Third, we implant an expander in the forehead, discretized with 3,782 nodes, 11,346 degrees of freedom, and 1,800 tri-linear brick elements, covering an initial area of  $48.8 \text{ cm}^2$ . Again, we fix all nodes and release only the expander degrees of freedom, which we then pressurize from underneath, assuming that the adjacent skin remains unaffected.

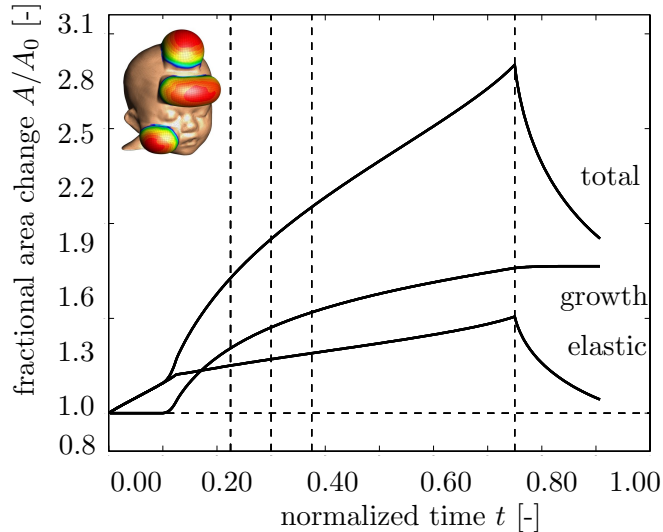


Figure 5.8: Skin expansion in pediatric forehead reconstruction. Case study II: Simultaneous forehead, scalp, and cheek expansion. Temporal evolution of normalized total area, elastic area, and growth area upon gradual expander inflation,  $0.0 < t \leq 0.125$ , constant pressure  $0.125 < t \leq 0.75$ , and deflation  $0.75 < t \leq 1.0$ . The expanded area increases from  $128.7 \text{ cm}^2$  to  $227.1 \text{ cm}^2$ , corresponding to a final fractional area gain of 1.77. Vertical dashed lines correspond to the time points displayed in Figure 5.9.

Figure 5.8 displays the temporal evolution of the normalized total area, elastic area, and growth area upon gradual expander inflation, constant pressure, and gradual expander removal. Similar to Figure 5.6, the tissue begins to grow once the elastic area stretch reaches the critical threshold of  $\vartheta^{\text{crit}} = 1.21$ . Slightly after, at  $t = 0.125$ , the total pressure is held

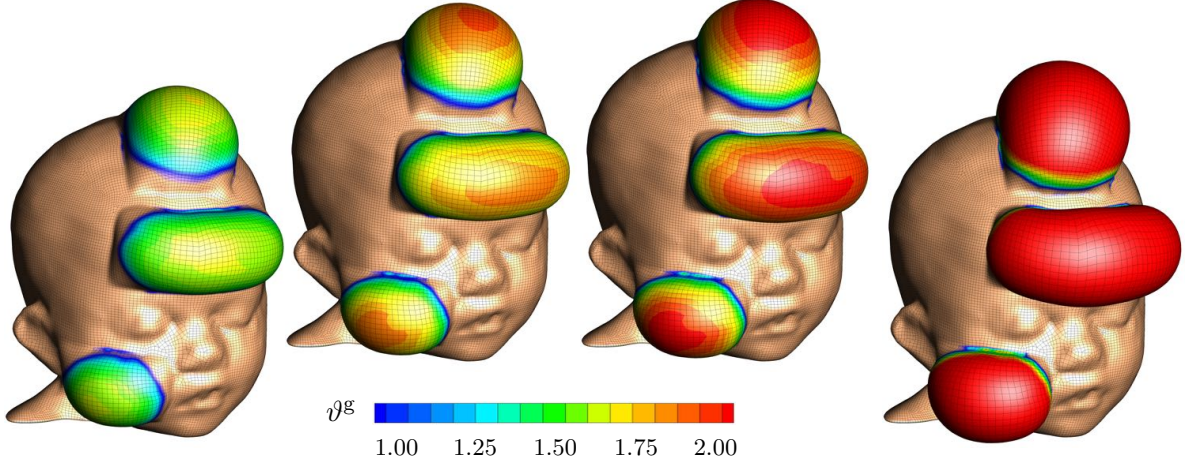


Figure 5.9: Skin expansion in pediatric forehead reconstruction. Case study II: Simultaneous forehead, scalp, and cheek expansion. Spatio-temporal evolution of area growth displayed at  $t = 0.24$ ,  $t = 0.33$ ,  $t = 0.42$  and  $t = 0.75$ . The initial area of  $128.7 \text{ cm}^2$  increases gradually as the grown skin area increases to  $176.0 \text{ cm}^2$ ,  $191.3 \text{ cm}^2$ ,  $202.1 \text{ cm}^2$ , and finally  $227.1 \text{ cm}^2$ , from left to right.

constant. Similar to the first case study, the skin grows gradually in all three expanded regions. When the pressure is gradually decreased at  $t = 0.75$ , the elastic area retracts, while the grown area remains constant. The vertical dashed lines correspond to the discrete time points,  $t = 0.24$ ,  $t = 0.33$ ,  $t = 0.42$  and  $t = 0.75$ , displayed in Figure 5.9.

Figure 5.9 illustrates the spatio-temporal evolution of the area growth  $\vartheta^g$ . Since area stretches are largest at the center of the expander, growth is first initiated in this region, spreading gradually throughout the entire expanded areas. During the growth process, the initial area of  $128.7 \text{ cm}^2$  increases to  $176.0 \text{ cm}^2$ ,  $191.3 \text{ cm}^2$ ,  $202.1 \text{ cm}^2$ , and finally  $227.1 \text{ cm}^2$ , displayed from left to right. In detail, we observe that the new area in the scalp is  $87.9 \text{ cm}^2$  with a fractional area gain of 1.74, in the cheek it is  $50.6 \text{ cm}^2$  with a fractional area gain of 1.72, and in the forehead it is  $88.6 \text{ cm}^2$  with the largest fractional area gain of 1.82. The area grows varies locally within the range of  $1.0 \leq \vartheta^g \leq 2.0$  with largest values in the center regions, where skin typically more than doubles its initial area.

## 5.4 Discussion

Motivated by the mechanotransduction pathways outlined in Section 13.1, we have introduced a continuum model for growing skin in response to chronic mechanical overstretch. From a kinematic point of view, the model is based on the multiplicative decomposition of the deformation gradient into an elastic part and a growth part [320]. From a constitutive point of view, it introduces four material parameters with a clear physiological interpretation [233, 417], the critical physiological stretch limit  $\vartheta^{\text{crit}}$ , the maximum area growth  $\vartheta^{\text{max}}$ , the adaptation speed  $\tau$ , and the shape of the adaptation curve  $\gamma$ . From a computational point of view, the model is embedded in a standard nonlinear finite element framework, in which the area growth  $\vartheta^g$  is introduced locally as an internal variable on the integration point level [158, 207]. From an algorithmic point of view, the biological equilibrium problem for this internal variable is solved using a local Newton iteration embedded in a global Newton iteration to solve the mechanical equilibrium problem [133, 314]. Overall, our growth model is unconditionally stable, robust, efficient, conceptually modular, and easily portable. In contrast to the only other skin growth model by other authors, which is based on a rotationally symmetric formulation [351], our model is conceptually generic, and can handle arbitrary skin geometries. In contrast to our own first prototype of the model, which is based on a material formulation [52, 417], the new realization based on a spatial formulation is computationally elegant and efficient, reducing simulation times by approximately factor five.

In Section 5.3.1, we have demonstrated the conceptual characteristics of our growth model by means of a simple model problem of successive equi-biaxial extension. Upon displacement control, the model predicts the following features: (i) an acute increase in the elastic area stretch  $\vartheta^e$ , (ii) an acute decrease in thickness  $t$ , (iii) a chronic increase in area growth  $\vartheta^g$ , (iv) a chronic restoration of the homeostatic elastic area stretch  $\vartheta^e \rightarrow \vartheta^{\text{crit}}$ , and (v) a chronic restoration of the homeostatic equilibrium thickness  $t$ . Upon displacement relaxation, the model predicts the following features: (vi) an acute retraction of the elastic area stretch back to its baseline value of  $\vartheta^e = 1.0$  and (vii) an acute arrest of further growth with  $\vartheta = \vartheta^g = \text{const}$ , see Figures 5.3 and 5.4.

Our *in silico* predictions are in excellent agreement with the *in vivo* findings reported in the literature. More than three decades ago, the first experimental studies confirmed a net gain in skin area upon tissue expansion [21, 22]. Unexpectedly, this area gain was found

to take place upon conservation of cellular morphology, preservation of phenotype, and maintenance of functionality, without an inflammatory response, and without evidence of malignant degeneration [31]. This suggested that the increase in tissue surface area is a result of new tissue being regenerated, instead of being recruited from neighboring regions [92]. It supports our fundamental model assumption that skin is capable to chronically increase its area, represented through equation (5.3), upon mechanical overstretch, incorporated through equation (5.12), see Figure 5.3.

In what follows, we will compare the response of our model to skin growth experiments in the literature [22, 25, 31, 382, 385, 402]. Unfortunately, almost all existing data are based on in vivo tissue expansion studies. For the lack of experimental data, we assume that the in vivo strain state of a pressurized thin membrane is close to our in silico state of equi-biaxial extension. Alternatively, we could simulate the true state of tissue expansion using finite element models [51, 52]. However, since this would introduce additional discretization and modeling errors, we will assume a homogeneous strain state here, and focus on comparing the constitutive, material point response.

#### 5.4.1 Discussion of Acute Elastic Response

Acutely, tissue expansion has been associated with slight epidermal thickening and significant dermal thinning [22], resulting in an overall thinning and a reduced tensile strength [25]. Mechanically, a study in rodents reported an acute increase in uniaxial stretch of approximately 36% [31]. This is in nice agreement with our model, which predicts an acute elastic area stretch of 1.52, 1.60, and 1.56, corresponding to an average increase in uniaxial stretch of 25%, see Figure 5.3. Structurally, the same study identified an initial acute decrease in skin thickness from  $407 \pm 3 \mu\text{m}$  to  $317 \pm 4 \mu\text{m}$  corresponding to an acute thickness reduction of 22% [31]. Again, this is in good quantitative agreement with our model, which predicts an acute average normalized thickness of 0.74, 0.71, and 0.72 corresponding to an acute average thickness decrease of 28%, see Figure 5.4. Since these acute thickness changes can be attributed primarily to the Poisson effect, they can be utilized to calibrate the elastic material parameters, in particular Poisson's ratio.

#### 5.4.2 Discussion of Chronic Growth Response

Chronically, tissue expansion is associated with the gradual restoration of baseline histology, baseline mechanics, and baseline structure [25]. Histologically, a comparison of piglet

tissue in expanded and non-expanded regions demonstrated a chronic restoration of the number of epidermal cell layers and a chronic restoration of the epidermal thickness [382]. In addition, immunocytochemistry confirmed that the expanded tissue maintains its phenotypical characteristics and native program of cellular differentiation [402]. Mechanically, in a multiple time-point study in rodents, an acutely increased uniaxial stretch of 36% was reduced chronically to approximately 10% 32 days post expansion [31]. This is in excellent agreement with our model, which predicts an acutely increased uniaxial stretch of 25% and a chronic reduction to 10%, see Figure 5.3. A uniaxial stretch of 10% would corresponds to an area stretch of  $\vartheta^{\text{crit}} = 1.21$ . In our model, the model parameter  $\vartheta^{\text{crit}}$  takes the interpretation of the physiological threshold value, to which the elastic area stretch tends to return during adaptive skin growth, see equation (5.12). Structurally, after an initial acute thickness decrease of 22%, the same study reports a chronic restoration of the homeostatic equilibrium thickness from initially  $425 \pm 4 \mu\text{m}$  to  $398 \pm 3 \mu\text{m}$ , corresponding to a chronic thickness reduction of 7% [31]. This agrees well with our model, which predicts a normalized homeostatic equilibrium thickness of 0.88, corresponding to a chronic thickness reduction 12%, see Figure 5.4. The chronic rodent study also reported that the overall weight of the tissue sample almost tripled, with a fractional weight gain of approximately 2.7 for wet weight and 3.3 for dry weight [31]. In our model, the fractional weight gain is directly proportional to the fractional area gain of  $\vartheta^g = 3.3$  which agrees nicely with these experimental findings, see Figure 5.3. Finally, the study found a conservation of the mechanical properties, for example, a constant breaking strength acutely right after expansion and chronically long term [31]. These findings support our model assumption that ultimately, the newly created skin will have the same microstructure, density, and stiffness, as the original, native tissue [51, 52].

#### 5.4.3 Discussion of Elastic Retraction

Acutely, upon expander removal, an instantaneous retraction of the elastic deformation significantly reduces the overall skin area. In controlled *in vivo* experiments in pigs, the ratio between the reversible elastic deformation to irreversible growth was almost 2:1 [385]. Since our model assumes that the overall deformation gradient can be multiplicatively decomposed into an elastic and growth part, represented through equation (5.1), it is perfectly capable of reproducing the effect of elastic retraction upon expander removal, see Figures 5.3, 5.6, and 5.8.

#### 5.4.4 Discussion of Growth Heterogeneity

Figures 5.7 and 5.9 clearly indicate the heterogeneity of the growth process with larger values in the center region and smaller values in the periphery. This is in agreement with *in vivo* studies, which report a fractional area gain of 3.14, i.e., 50% above average, in the center region, and 2.06, i.e., 25% below average, in the periphery [31]. The authors hypothesized that larger strains in the center region would trigger larger growth. This is in agreement with our model in equation (5.10), where the evolution of area growth is directly correlated to the amount of overstretch through the growth criterion defined in equation (5.12).

#### 5.4.5 Limitations

Although we have presented both qualitative and quantitative comparisons of the proposed model with acute and chronic tissue expansion experiments from the literature, several limitations remain. First and foremost, the most challenging aspect would be to tie the growth law in equation (5.4) more closely to the underlying mechanobiology described in detail in the introduction section. Comparative gene expression assays and immunohistochemistry of grown versus ungrown tissue samples could help to identify the mechanisms that trigger skin growth on the molecular and cellular level. Similar approaches have been proposed for amelogenesis [83] and tumorigenesis [18, 304] in the past and could also be adopted here. Ideally, this would help to specify our evolution equation for the growth tensor (5.4) in terms of discrete mechanotransduction cascades through selected extracellular and intracellular events. To this end, we are currently designing a test setup to stretch and grow explanted tissue samples *ex vivo*. Since most existing data sets on skin growth are based on *in vivo* measurements of inflated membranes, an *ex vivo* setting will allow us to create well-defined geometries and boundary conditions such as the equi-biaxial extension test suggested here. Second, since our goal was to focus primarily on the kinematic characterization of the growth process, the constitutive modeling of the elastic baseline properties of skin has played a minor role. However, the proposed model is inherently modular and the incorporation of more sophisticated constitutive models [387] is relatively straightforward. A typical candidate is a multiple-constituent anisotropic skin model with in-plane anisotropy introduced through a pronounced stiffness along Langer's lines [205, 206], which we have successfully combined with the proposed growth model in the past [51]. In addition, the growth process

itself could be modeled as anisotropic [134], e.g., attributed to a pronounced growth along specific microstructural directions. Similarly, through the deposition of large bundles of compacted immature collagen [25, 199], the underlying collagen network could reorient itself, e.g., to align with the maximum principal strains [159, 208]. Here, we model growth as a strain driven process. This implies that the elastic material parameters, or, accordingly, the corresponding stresses, play a less important role than in stress-driven growth, e.g., in hypertension [207, 314]. In other words, when using the same model with different Lamé constants or different constitutive models, we would require different expander pressures to obtain the same deformation pattern, but the growth process itself would still be affected by kinematical quantities only. Along the same lines, we have assumed that the effects of resting tension and residual stress are negligible. Both play a critical role when studying instabilities and buckling [137, 384]. In a previous study, we have explored these phenomena in more detail [52]. Within the context of finite deformations, resting tension and residual stress could be incorporated through another second order tensor, which would mimic the mapping to a pre-strained or residually stressed configuration [250, 363].

Third, for the sake of simplicity, we have modeled skin as homogeneous across the thickness, neglecting its individual layers and their potential interaction. We are currently refining our model utilizing shell kinematics with a higher resolution across the thickness direction. This will facilitate to model the individual skin layers [342], which we believe to be a major source of heterogeneities and residual stresses in real tissue expansion cases [249]. Alternatively, to explore the biomechanical interaction between the growing dermis and the underlying hypodermis during tissue expansion, we could even model growing skin through its own boundary energy [179].

Fourth, at this stage, the chronic response of our model is not yet calibrated in time. We have assumed that chronic growth takes place within a normalized time interval from zero to one. In reality, growth periods range from the order of days in rodents [31] to weeks in pigs [385] and humans [141]. However, with the appropriate experimental data, the duration of the adaptation process can be calibrated easily through the adaptation speed  $\tau$  [417].

Fifth, we have modeled the tissue expander only implicitly through controlling the expander pressure. In real tissue expansion, the external control parameter is the expander volume [231]. This implies that our simulation displays creep under constant loading, while clinical tissue expansion might rather display relaxation under constant deformation [51]. Moreover, we have assumed that the expander is connected tightly to the expanded tissue,

neglecting effects of interface sliding and shear [351]. However, this seems to be a reasonable first assumption, since most current expanders have well-designed textures to promote mild tissue in-growth, primarily to prevent expander migration [27].

Last, while our computational model seems well suited to provide qualitative guidelines and trends, in its present state, it is not recommended for quantitative statements. We will need to perform acute and chronic *in vitro* and *in vivo* experiments to truly identify the underling mechanisms which have, up until now, only been represented phenomenologically. Nevertheless, we believe that using the equations of nonlinear continuum mechanics to characterize skin growth represents a significant advancement over the current gold standard to predict tissue growth exclusively in terms of areas, volumes, and empiric correction factors [341, 385].

## 5.5 Conclusion

We have presented a continuum model for growing biological membranes in which the underlying mechanobiology is collectively summarized in a single pheonomenological internal variable, the in-plane area growth. The model can reliably predict the characteristic histological, mechanical, and structural features of controlled overstretch-induced skin growth, both acutely and chronically. We anticipate that the proposed skin growth model can be generalized to arbitrary biological membranes, and that it can serve as a valuable tool to virtually manipulate membrane area simply by means of changes in the mechanical environment.

## Chapter 6

# Isogeometric Kirchhoff-Love Shell Formulations for Biological Membranes

**Abstract.** Computational modeling of thin biological membranes can aid the design of better medical devices. Remarkable biological membranes include skin, alveoli, blood vessels, and heart valves. Isogeometric analysis is ideally suited for biological membranes since it inherently satisfies the  $C^1$ -requirement for Kirchhoff-Love kinematics. Yet, current isogeometric shell formulations are mainly focused on linear isotropic materials, while biological tissues are characterized by a nonlinear anisotropic stress-strain response. Here we present a thin shell formulation for thin biological membranes. We derive the equilibrium equations using curvilinear convective coordinates on NURBS tensor product surface patches. We linearize the weak form of the generic linear momentum balance without a particular choice of a constitutive law. We then incorporate the constitutive equations that have been designed specifically for collagenous tissues. We explore three common anisotropic material models: Mooney-Rivlin, May Newmann-Yin, and Gasser-Ogden-Holzapfel. Our work will allow scientists in biomechanics and mechanobiology to adopt the constitutive equations that have been developed for solid three-dimensional soft tissues within the framework of isogeometric thin shell analysis.

## 6.1 Motivation

Biological membranes appear often in nature, fulfilling crucial physiological roles for the survival of different forms of life. Perhaps one of the most evident examples is our skin, an essential barrier from the outside world with notable elastic properties [417]. Several other examples of membranes - although hidden to our eyes - are equally important because of their prominent functions: the alveoli, the pericardium, or the valve leaflets, to name just a few [315]. Characterizing the behavior of these thin structures in distinct mechanical scenarios is key to improve our understanding of the mechanical aspects of disease and to design more effective medical devices [191]. Biological membranes are lightweight structures that often experience large deformations, large rotations, and extreme membrane strains [325]. The mechanical behavior of most biological membranes is a result of the well-defined tissue microstructure: a water-based matrix, often considered incompressible, in which fibers such as collagen form a complex network responsible for tissue anisotropy and nonlinearity [52]. Thin membranes can be represented using Kirchhoff-Love kinematics. This strategy has been deemed appropriate and verified with experiments for thin biological structures including skin and heart leaflets, which show thicknesses that rarely exceed a few millimeters [109,374]. While the physiological loading situation is often associated with a plain membrane state, where no bending energy is considered [169], many applications of interest deal with diseased and non-physiological scenarios for which bending stresses may become critical [241]. This thin shell approach requires a high continuity representation of the domain, which has traditionally been an obstacle for conventional finite element implementations. Recently, however, the development of isogeometric analysis tools has made it possible to develop Kirchhoff-Love shells that easily satisfy the requirement of  $C^1$  continuity across element boundaries [188]. Yet, to date, mainly linear St. Venant-Kirchhoff materials have been used within this approach [163]. While the St. Venant-Kirchhoff model provides reasonable results in the large-deformation-small-strain regime, it might be inappropriate for biological tissues, which are typically anisotropic, nonlinear, and subjected to large strains [73]. Here we present a isogeometric shell formulation especially tailored for thin biological membranes. We employ the Kirchhoff-Love kinematic assumption and represent the geometry of a three-dimensional elastic body by parametrizing the mid surface using tensor product NURBS surface patches. We present the standard virtual work formulation of the equations of mechanical equilibrium and perform the generic consistent linearization without choosing

a particular constitutive model. We then explore the constitutive equations available for biological membranes and incorporate them into our formulation by imposing the plane stress assumption. Finally, we demonstrate the performance of the formulation by selected numerical examples.

The formulation presented here departs from currently available isogeometric shell models in that our virtual work and consistent linearization are expressed for general constitutive models in the neighborhood of the mid-surface by avoiding the explicit integration across the thickness. This flexibility allows us to explore, for the first time, the incorporation of constitutive equations developed for three dimensional biological tissues within the context of thin isogeometric shells by imposing the plane stress condition.

## 6.2 NURBS Surfaces

### 6.2.1 B-spline Curves

A B-spline curve is a piece-wise polynomial function that maps a segment of the real line to the three-dimensional Euclidean space  $\gamma : \xi \in \mathbb{R} \rightarrow \mathbb{R}^3$ . For a curve of degree  $p$  we need a knot vector  $\Xi$  and a set of control points  $\mathbf{P}_i \in \mathbb{R}^3$ . The knot vector consists of non-decreasing numbers  $\Xi = [\xi_0, \xi_1, \dots, \xi_n]$ . The number of control points is  $m = n - p - 1$ . The first and last values of the knot vector  $\xi_0$  and  $\xi_n$  are repeated  $p + 1$  times. We define basis functions recursively. The zeroth order basis functions are

$$N_{i,0} = \begin{cases} 1 & \xi_i \leq \xi < \xi_{i+1} \\ 0 & \text{otherwise.} \end{cases} \quad (6.1)$$

Higher order functions of degree  $p \geq 1$  result from the recursive definition,

$$N_{i,p} = \frac{\xi - \xi_i}{\xi_{i+p} - \xi_i} N_{i,p-1}(\xi) + \frac{\xi_{i+p+1} - \xi}{\xi_{i+p+1} - \xi_{i+1}} N_{i+1,p-1}(\xi). \quad (6.2)$$

The curve is defined as a sum over the basis functions  $N_i$  and the control points  $P_i$ ,

$$\gamma = \sum_{i=0}^m N_{i,p}(\xi) \mathbf{P}_i. \quad (6.3)$$

### 6.2.2 B-spline Surfaces

There are several alternatives to create surfaces based on B-spline basis functions. The most common is to build tensor product surfaces which arise as a tensor product of two B-spline curves. A B-spline surface is thus a map  $\mathcal{S} : \xi = [\xi, \eta] \in \mathbb{R} \times \mathbb{R} \rightarrow \mathbb{R}^3$ . Naturally, we require two knot vectors  $\Xi$  and  $\Omega$ , similarly we define two sets of basis functions  $N_{i,p}$  and  $Q_{j,q}$  coming from each of the knot vectors. The surface is defined with the control net  $\mathbf{P}_{i,j} \in \mathbb{R}^3$ ,

$$\mathcal{S} = \sum_{i=0}^m \sum_{j=0}^r N_{i,p}(\xi) Q_{j,q}(\eta) \mathbf{P}_{i,j}. \quad (6.4)$$

### 6.2.3 NURBS

The term NURBS is an abbreviation for non-uniform rational B-Splines. As the name suggests, NURBS are constructed with rational basis functions instead of polynomials. To do so, each control point has an associated weight  $w_i$  such that a point in three-dimensional space corresponds to the point  $[w_i X, w_i Y, w_i Z, w_i]$  in the projective plane. A NURBS curve is expressed in terms of the corresponding B-spline basis functions as follows

$$\hat{\gamma} = \frac{\sum_{i=0}^m N_{i,p}(\xi) \mathbf{P}_i w_i}{\sum_{i=0}^m N_{i,p}(\xi) w_i}. \quad (6.5)$$

And we can define a NURBS surfaces by the same tensor product construction employed for B-spline surfaces,

$$\hat{\mathcal{S}} = \frac{\sum_{i=0}^m \sum_{j=0}^r N_{i,p}(\xi) Q_{j,q}(\eta) \mathbf{P}_{i,j} w_{i,j}}{\sum_{i=0}^m \sum_{j=0}^r N_{i,p}(\xi) Q_{j,q}(\eta) w_{i,j}}. \quad (6.6)$$

## 6.3 Element Formulation

### 6.3.1 Kinematics

We consider two surfaces embedded in  $\mathbb{R}^3$  representing the reference and deformed configurations of the mid-surface of the membrane under study. The reference surface,  $\mathcal{S}_0$ , is mapped from the parametric plane  $\xi = [\xi, \eta]$  onto the three-dimensional Euclidian space by the map  $\Psi(\xi)$ . Similarly, the deformed surface,  $\mathcal{S}$  is defined by the map  $\psi : \xi \rightarrow \mathbb{R}^3$ . Our objective is to establish a model for the membrane to incorporate arbitrary material constitutive equations, which meet the plane stress condition. This implies that we are

interested in particles that occupy a small neighborhood of the mid-surface. The volume of the membrane then appears by considering a small thickness with respect to the midsurface. The reference configuration of the membrane defines a solid  $\mathcal{B}_0$  by mapping the mid-surface plus a small displacement along the normal,

$$\mathbf{x} = \Psi(\xi) + \zeta \mathbf{N}(\xi). \quad (6.7)$$

Here  $\mathbf{N}(\xi)$  is the surface normal and  $\zeta \in [-H/2, H/2]$  parametrizes the thickness  $H$  with respect to the normal direction. Similarly, the particles of the deformed membrane compose a body  $\mathcal{B}$  defined by

$$\mathbf{y} = \psi(\xi) + \zeta h(\xi) \mathbf{d}(\mathbf{N}, \xi), \quad (6.8)$$

where  $h(\xi)$  characterizes changes in thickness, and  $\mathbf{d}(\mathbf{N}, \xi)$  describes the motion of the reference normal. The deformation map  $\varphi$  then establishes the relationship between the reference and deformed membranes as illustrated in Figure 6.1, it describes the motion of the membrane using the coordinates  $\hat{\xi} = [\xi, \eta, \zeta]$ , such that  $\varphi(\hat{\xi}) : \mathcal{B}_0 \rightarrow \mathcal{B}$ .

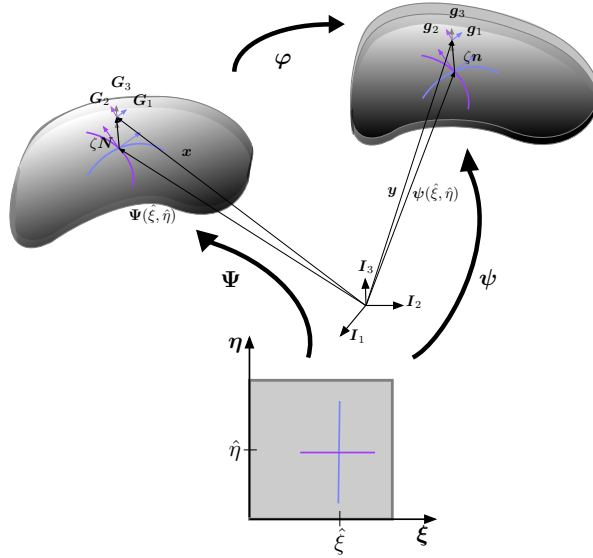


Figure 6.1: Shell kinematics. The reference mid surface is described by the embedding  $\mathbf{x} = \Psi(\xi)$  while the deformed mid-surface is described by  $\mathbf{y} = \psi(\xi)$ . In the neighborhood of the mid surface the corresponding metrics  $\mathbf{G}_i$  and  $\mathbf{g}_i$  are defined for the reference and deformed configurations and the relationship between the two is the gradient of the deformation  $\varphi$ .

When employing Kirchhoff-Love kinematics, the normal to the reference mid-surface remains normal as the membrane deforms and the thickness director is inextensible. The particles of the deformed membrane can be located using only a displacement vector  $\mathbf{u}$  from the reference mid-surface into the deformed mid-surface,

$$\mathbf{y} = \varphi(\mathbf{x}) = \Psi(\xi) + \mathbf{u}(\xi) + \zeta \mathbf{n}(\xi). \quad (6.9)$$

The surfaces are constructed using NURBS surfaces patches such that,

$$\begin{aligned} \mathbf{x} &= R_a(\xi) \mathbf{x}_s^a + \zeta \mathbf{N} \\ \mathbf{y} &= R_a(\xi) (\mathbf{x}_s^a + \mathbf{u}_s^a) + \zeta \mathbf{n}, \end{aligned} \quad (6.10)$$

where the  $R_a$  are the NURBS surface basis functions and  $\mathbf{x}_s^a$ ,  $\mathbf{x}_s^a + \mathbf{u}_s^a$  are the corresponding control points. We note that in the previous equations and further on, we use of the summation convention, where latin indices take the values  $\{1, 2, 3\}$  and greek indices take values  $\{1, 2\}$ . We use curvilinear coordinates to locally describe the geometry. The basis vectors at every point of the reference surface are

$$\begin{aligned} \mathbf{E}_1 &= R_{a,\xi} \mathbf{x}_s^a \\ \mathbf{E}_2 &= R_{a,\eta} \mathbf{x}_s^a, \end{aligned} \quad (6.11)$$

and those at the deformed mid surface are

$$\begin{aligned} \mathbf{e}_1 &= R_{a,\xi} \mathbf{x}_s^a + R_{a,\xi} \mathbf{u}_s^a \\ \mathbf{e}_2 &= R_{a,\eta} \mathbf{x}_s^a + R_{a,\eta} \mathbf{u}_s^a. \end{aligned} \quad (6.12)$$

The comma indicates the partial differentiation. The dual basis satisfies  $\mathbf{e}^\alpha \cdot \mathbf{e}_\beta = \delta_\beta^\alpha$ ,  $\mathbf{E}^\alpha \cdot \mathbf{E}_\beta = \delta_\beta^\alpha$ , such that the normal is a function of the surface basis vectors,

$$\mathbf{N} = \frac{\mathbf{E}_1 \times \mathbf{E}_2}{\|\mathbf{E}_1 \times \mathbf{E}_2\|} \quad \text{and} \quad \mathbf{n} = \frac{\mathbf{e}_1 \times \mathbf{e}_2}{\|\mathbf{e}_1 \times \mathbf{e}_2\|}. \quad (6.13)$$

To describe local deformations, we consider the reference metric, which consists of the

covariant basis vectors in the neighborhood of the mid-surface

$$\begin{aligned}\mathbf{G}_1 &= R_{a,\xi} \mathbf{x}_s^a + \zeta \frac{\partial \mathbf{N}}{\partial \xi}, \\ \mathbf{G}_2 &= R_{a,\eta} \mathbf{x}_s^a + \zeta \frac{\partial \mathbf{N}}{\partial \eta}, \\ \mathbf{G}_3 &= \mathbf{N}.\end{aligned}\tag{6.14}$$

The dual basis of the metric satisfies  $\mathbf{G}^i \cdot \mathbf{G}_j = \delta_j^i$ . The deformed metric is constructed in the same fashion with the corresponding covariant basis vectors near the deformed mid-surface,

$$\begin{aligned}\mathbf{g}_1 &= R_{a,\xi} \mathbf{x}_s^a + R_{a,\xi} \mathbf{u}_s^a + \zeta \frac{\partial \mathbf{n}}{\partial \xi}, \\ \mathbf{g}_2 &= R_{a,\eta} \mathbf{x}_s^a + R_{a,\eta} \mathbf{u}_s^a + \zeta \frac{\partial \mathbf{n}}{\partial \eta}, \\ \mathbf{g}_3 &= \mathbf{n}.\end{aligned}\tag{6.15}$$

At this point we have completely defined the kinematics of the reference and deformed surfaces as function of the coordinates  $\hat{\boldsymbol{\xi}}$  and the kinematics in the neighborhood of the corresponding mid-surfaces. Now the relationship between the reference and deformed metrics follows from using the chain rule,

$$\mathbf{g}_i = \frac{\partial \varphi(\mathbf{x})}{\partial \mathbf{x}} \cdot \frac{\partial \mathbf{x}}{\partial \hat{\xi}^i} = \mathbf{F} \cdot \mathbf{G}_i,\tag{6.16}$$

where  $\mathbf{F}$  is the total deformation gradient with

$$\mathbf{F} = \mathbf{g}_i \otimes \mathbf{G}^i.\tag{6.17}$$

The deformation gradient is the key kinematic quantity as it encodes the local deformation of the body. For the constitutive models in Section 6.4, it proofs convenient to additively decompose the total deformation gradient  $\mathbf{F}$ ,

$$\mathbf{F} = \mathbf{F}_S + \mathbf{F}_N,\tag{6.18}$$

where  $\mathbf{F}_S$  and  $\mathbf{F}_N$  denote the surface and normal contributions,

$$\mathbf{F}_S = \mathbf{g}_\alpha \otimes \mathbf{G}^\alpha \quad \text{and} \quad \mathbf{F}_N = \lambda_N \mathbf{n} \otimes \mathbf{N}.\tag{6.19}$$

We can understand the surface deformation gradient  $\mathbf{F}_S$  as the surface projection of the total deformation gradient  $\mathbf{F}$  by means of the surface unit tensor  $\mathbf{I}_S$ ,

$$\mathbf{F}_S = \mathbf{F} \cdot \mathbf{I}_S \quad \text{with} \quad \mathbf{I}_S = \mathbf{I} - \mathbf{N} \otimes \mathbf{N} = \mathbf{G}_\alpha \otimes \mathbf{G}^\alpha. \quad (6.20)$$

The surface unit tensor  $\mathbf{I}_S$  allows us to introduce the pseudo inverse of the surface deformation gradient  $\mathbf{F}_S^{-1}$  as

$$\mathbf{F}_S^{-1} \cdot \mathbf{F}_S = \mathbf{I}_S \quad \text{with} \quad \mathbf{F}_S^{-1} = \mathbf{G}_\alpha \otimes \mathbf{g}^\alpha. \quad (6.21)$$

Similarly, we decompose the right Cauchy Green deformation tensor,

$$\mathbf{C} = \mathbf{F}^T \cdot \mathbf{F} = \mathbf{C}_S + \mathbf{C}_N, \quad (6.22)$$

into surface and normal contributions,

$$\mathbf{C}_S = \mathbf{F}_S^T \cdot \mathbf{F}_S \quad \text{and} \quad \mathbf{C}_N = C_N \mathbf{N} \otimes \mathbf{N}, \quad (6.23)$$

where the normal contribution,  $C_N = \lambda_N^2$ , is equivalent to the squared stretch in thickness direction  $\lambda_N$ . The inverse of the right Cauchy Green surface deformation tensor,  $\mathbf{C}_S^{-1} = \mathbf{F}_S^{-1} \cdot \mathbf{F}_S^{-T}$ , follows in terms of the pseudo inverse of the surface deformation gradient  $\mathbf{F}_S^{-1}$  defined in eq. (6.21). We can then introduce the corresponding invariants. For the total right Cauchy Green deformation tensor, we adopt the standard definitions,

$$I_1 = \mathbf{C} : \mathbf{I} \quad I_3 = \det(\mathbf{C}) \quad I_4 = \mathbf{C} : \mathbf{A} \otimes \mathbf{A}, \quad (6.24)$$

where the vector  $\mathbf{A}$  belongs to the tangent space spanned by  $\mathbf{G}_\alpha$  and denotes the local direction of material anisotropy. For the surface right Cauchy Green deformation tensor, we use the following generalized definitions,

$$I_{S1} = \mathbf{C}_S : \mathbf{I}_S \quad I_{S3} = \widehat{\det}(\mathbf{C}_S) \quad I_{S4} = \mathbf{C}_S : \mathbf{A} \otimes \mathbf{A}, \quad (6.25)$$

such that  $I_1 = I_{S1} + C_N$  and  $I_4 = I_{S4}$ . To calculate the determinant of the surface deformation tensor associated with the tangent space of the surface,  $\widehat{\det}(\mathbf{C}_S)$ , we adopt the

following generalized relation [147],

$$\widehat{\det}(\mathbf{C}_S) = \frac{||\mathbf{g}_1 \times \mathbf{g}_2||^2}{||\mathbf{G}_1 \times \mathbf{G}_2||^2}. \quad (6.26)$$

Finally, we decompose the Green Lagrange strain tensor,

$$\mathbf{E} = \frac{1}{2} [\mathbf{F}^T \cdot \mathbf{F} - \mathbf{I}] = \mathbf{E}_S + \mathbf{E}_N \quad (6.27)$$

into surface strains  $\mathbf{E}_S$  and normal strains  $\mathbf{E}_N$  with

$$\mathbf{E}_S = (\mathbf{g}_\alpha \cdot \mathbf{g}_\beta - \mathbf{G}_\alpha \cdot \mathbf{G}_\beta) \mathbf{G}^\alpha \otimes \mathbf{G}^\beta \quad \text{and} \quad \mathbf{E}_N = E_N \mathbf{N} \otimes \mathbf{N}, \quad (6.28)$$

with the normal contribution  $E_N = \frac{1}{2}[C_N - 1] = \frac{1}{2}[\lambda_N^2 - 1]$ .

### 6.3.2 Principle of Virtual Work

The internal virtual work in the reference configuration is,

$$\delta W_{int} = \int_{\mathcal{B}_0} \mathbf{S} : \delta \mathbf{E} \, dV, \quad (6.29)$$

where  $\mathbf{S}$  is the second Piola Kirchhoff stress tensor,  $\mathbf{E}$  is the Green Lagrange strain tensor, and  $\delta \mathbf{E}$  is the variation of  $\mathbf{E}$  with respect to the virtual displacement vector  $\delta \mathbf{u}$ ,

$$\delta \mathbf{E} = D(\mathbf{E})[\delta \mathbf{u}] = \frac{d}{d\epsilon} \mathbf{E}(\mathbf{x} + \epsilon \delta \mathbf{u})|_{\epsilon=0}. \quad (6.30)$$

We begin by considering the variation of the deformed metric basis vectors. The variation of the covariant basis vectors yields

$$\begin{aligned} \delta \mathbf{g}_1^a &= D(\mathbf{g}_1)[\delta \mathbf{u}_s^a] = R_{a,\xi} \delta \mathbf{u}_s^a + \zeta D(\partial \mathbf{n}/\partial \xi)[\delta \mathbf{u}_s^a] \\ \delta \mathbf{g}_2^a &= D(\mathbf{g}_2)[\delta \mathbf{u}_s^a] = R_{a,\eta} \delta \mathbf{u}_s^a + \zeta D(\partial \mathbf{n}/\partial \eta)[\delta \mathbf{u}_s^a] \\ \delta \mathbf{g}_3^a &= D(\mathbf{g}_3)[\delta \mathbf{u}_s^a] = D(\mathbf{n})[\delta \mathbf{u}_s^a]. \end{aligned} \quad (6.31)$$

The variation of the normal and the normal derivatives benefits from a more detailed discussion. We have avoided the use of common objects of surface differential geometry, such as the second fundamental form, to keep a strain notation that is amenable to the constitutive laws for biological materials. The constitutive equations we will encounter often appear

in terms of the invariants of  $\mathbf{E}$ . Following this reasoning, the normal derivatives can be expressed in terms of the surface covariant basis vectors,

$$\frac{\partial \mathbf{n}}{\partial \xi} = \frac{\partial \mathbf{n}}{\partial \mathbf{e}_\alpha} \cdot \frac{\partial \mathbf{e}_\alpha}{\partial \xi} \quad \text{and} \quad \frac{\partial \mathbf{n}}{\partial \eta} = \frac{\partial \mathbf{n}}{\partial \mathbf{e}_\alpha} \cdot \frac{\partial \mathbf{e}_\alpha}{\partial \eta}. \quad (6.32)$$

The variation of the normal follows from using the chain rule,

$$D(\mathbf{n})[\delta \mathbf{u}_s^a] = \frac{\partial \mathbf{n}}{\partial \mathbf{e}_\alpha} \cdot D(\mathbf{e}_\alpha)[\delta \mathbf{u}_s^a]. \quad (6.33)$$

The variation of the surface base vectors takes the following simple form,

$$\begin{aligned} D(\mathbf{e}_1)[\delta \mathbf{u}_s^a] &= R_{a,\xi} \delta \mathbf{u}_s^a \\ D(\mathbf{e}_2)[\delta \mathbf{u}_s^a] &= R_{a,\eta} \delta \mathbf{u}_s^a. \end{aligned} \quad (6.34)$$

The variation of the normal derivatives can be obtained similarly through the chain rule,

$$D\left(\frac{\partial \mathbf{n}}{\partial \xi}\right)[\delta \mathbf{u}_s^a] = D\left(\frac{\partial \mathbf{n}}{\partial \mathbf{e}_\alpha}\right)[\delta \mathbf{u}_s^a] \cdot \frac{\partial \mathbf{e}_\alpha}{\partial \xi} + \frac{\partial \mathbf{n}}{\partial \mathbf{e}_\alpha} \cdot D\left(\frac{\partial \mathbf{e}_\alpha}{\partial \xi}\right)[\delta \mathbf{u}_s^a] \quad (6.35)$$

$$D\left(\frac{\partial \mathbf{n}}{\partial \eta}\right)[\delta \mathbf{u}_s^a] = D\left(\frac{\partial \mathbf{n}}{\partial \mathbf{e}_\alpha}\right)[\delta \mathbf{u}_s^a] \cdot \frac{\partial \mathbf{e}_\alpha}{\partial \eta} + \frac{\partial \mathbf{n}}{\partial \mathbf{e}_\alpha} \cdot D\left(\frac{\partial \mathbf{e}_\alpha}{\partial \eta}\right)[\delta \mathbf{u}_s^a], \quad (6.36)$$

with

$$D\left(\frac{\partial \mathbf{n}}{\partial \mathbf{e}_\alpha}\right)[\delta \mathbf{u}_s^a] = \frac{\partial^2 \mathbf{n}}{\partial \mathbf{e}_\beta \partial \mathbf{e}_\alpha} \cdot D(\mathbf{e}_\beta)[\delta \mathbf{u}_s^a] \quad (6.37)$$

and

$$\begin{aligned} D\left(\frac{\partial \mathbf{e}_1}{\partial \xi}\right)[\delta \mathbf{u}_s^a] &= R_{a,\xi\xi} \delta \mathbf{u}_s^a \\ D\left(\frac{\partial \mathbf{e}_1}{\partial \eta}\right)[\delta \mathbf{u}_s^a] &= R_{a,\xi\eta} \delta \mathbf{u}_s^a = D\left(\frac{\partial \mathbf{e}_2}{\partial \xi}\right)[\delta \mathbf{u}_s^a] \\ D\left(\frac{\partial \mathbf{e}_2}{\partial \eta}\right)[\delta \mathbf{u}_s^a] &= R_{a,\eta\eta} \delta \mathbf{u}_s^a. \end{aligned} \quad (6.38)$$

With variation of the deformation gradient,

$$\delta \mathbf{F} = \delta \mathbf{g}_i \otimes \mathbf{G}^i, \quad (6.39)$$

the desired variation of the Green Lagrange strain tensor is readily computed,

$$\delta \mathbf{E} = \frac{1}{2} (\delta \mathbf{F}^T \mathbf{F} + \mathbf{F}^T \delta \mathbf{F}). \quad (6.40)$$

### 6.3.3 Consistent Linearization

To solve the resulting nonlinear system we require the linearization of the internal virtual work,

$$D(\delta W_{int})[\Delta \mathbf{u}] = \int_{\mathcal{B}_0} D\mathbf{E} : \mathbb{C} : \delta \mathbf{E} dV + \int_{\mathcal{B}_0} \mathbf{S} : D\delta \mathbf{E} dV. \quad (6.41)$$

Here,  $\mathbb{C}$  denotes the material fourth order elasticity tensor  $\mathbb{C} = \partial \mathbf{S} / \partial \mathbf{E}$ . The linearization is done with the directional derivative  $D(\bullet)[\Delta \mathbf{u}]$  defined above (6.30). The linearization  $D\mathbf{E}$  is essentially the same as the first variation  $\delta \mathbf{E}$  but now in the direction of the increment  $\Delta \mathbf{u}$ . The linearization of the first variation,  $D\delta \mathbf{E}$ , consists of four terms,

$$D\delta \mathbf{E} = \frac{1}{2} (\delta \mathbf{F}^T D\mathbf{F} + D\mathbf{F}^T \delta \mathbf{F} + D\delta \mathbf{F}^T \mathbf{F} + \mathbf{F}^T D\delta \mathbf{F}), \quad (6.42)$$

including the second variation of the deformed metric,

$$D\delta \mathbf{F} = D\delta \mathbf{g}_i \otimes \mathbf{G}^i, \quad (6.43)$$

which requires the second directional derivatives of the deformed metric basis vectors,

$$\begin{aligned} D\delta \mathbf{g}_1^{ab} &= D^2(\partial \mathbf{n} / \partial \xi)[\delta \mathbf{u}_s^a, \Delta \mathbf{u}_s^b] \\ D\delta \mathbf{g}_2^{ab} &= D^2(\partial \mathbf{n} / \partial \eta)[\delta \mathbf{u}_s^a, \Delta \mathbf{u}_s^b] \\ D\delta \mathbf{g}_3^{ab} &= D^2(\mathbf{n})[\delta \mathbf{u}_s^a, \Delta \mathbf{u}_s^b]. \end{aligned} \quad (6.44)$$

Since the linearization of all variations in (6.38) vanishes, we only need to include the linearization of (6.37),

$$D^2 \left( \frac{\partial \mathbf{n}}{\partial e_\alpha} \right) [\delta \mathbf{u}_s^a, \Delta \mathbf{u}_s^b] = \frac{\partial^3 \mathbf{n}}{\partial e_\gamma \partial e_\beta \partial e_\alpha} : (D(\mathbf{e}_\beta)[\delta \mathbf{u}_s^a] \otimes D(\mathbf{e}_\gamma)[\Delta \mathbf{u}_s^b]). \quad (6.45)$$

## 6.4 Constitutive Equations

So far, we have kept the principle of virtual work for a three-dimensional solid in an effort to keep our derivations as general as possible before choosing a specific constitutive equation. In this setting we are unable to perform an explicit integration of the residual forces through the thickness to obtain resulting forces and moments in terms of the first and second fundamental forms of the midsurface, a common procedure when deriving thin

shell formulations [188].

When modeling biological materials, constitutive laws such as the St. Venant-Kirchhoff model may not be the best choice to accurately capture the mechanical behavior of the tissues under large deformations. When biological membranes undergo large physiological deformations they require constitutive laws that recreate a complex relationship between stresses and strains that is highly nonlinear and anisotropic [112]. Determining appropriate constitutive equations for soft biological materials is a problem on its own that has drawn significant attention [316]. Early work on the modeling of blood vessels employed isotropic strain energy potentials of the Mooney-Rivlin type. However, it is now commonly accepted that transverse isotropic descriptions are more appropriate. Most soft tissues have a well defined microstructure characterized by the presence of fibers such as collagen. The preferred orientation of these fiber bundles, which is responsible for tissue anisotropy has been incorporated in more recent constitutive models [162].

When exploring constitutive laws for membranes we can take two alternative approaches: we can either establish reduced two-dimensional constitutive equations dependent on the in-plane deformation only or adapt a fully three-dimensional strain energy function for solids and enforce plane stress conditions. Here we focus on the second approach. To show the flexibility of our formulation, we briefly discuss four constitutive models that can be easily embedded within our framework. Many other constitutive models can be adapted in a similar way. In general, for arbitrary, nonlinear constitutive models, it is always possible to iteratively determine the normal strain that satisfies the plane stress condition [194].

#### 6.4.1 St. Venant Kirchhoff Model

Although the expression for the stress of the St. Venant Kirchhoff (VK) material adjusted to thin membranes is well known, we briefly illustrate the derivation starting from the three-dimensional strain energy function to show that we indeed have an identical formulation to the one in the literature [188] before the explicit integration across the thickness. The strain energy function is

$$\psi = \frac{1}{2} \lambda (\text{tr} \mathbf{E})^2 + \mu \mathbf{E} : \mathbf{E}, \quad (6.46)$$

from which the second Piola Kirchhoff stress tensor follows,

$$\mathbf{S} = \frac{\partial \psi}{\partial \mathbf{E}} = \lambda (\text{tr} \mathbf{E}) \mathbf{I} + 2\mu \mathbf{E}. \quad (6.47)$$

To satisfy the plane stress condition, we consider the Green Lagrange strain tensor as the sum of the surface strain and the normal strain,  $\mathbf{E} = \mathbf{E}_S + \mathbf{E}_N$ . Then the stress follows a similar additive decomposition,

$$\mathbf{S} = \mathbf{S}_S + \mathbf{S}_N, \quad (6.48)$$

in terms of the surface and normal contributions,

$$\begin{aligned} \mathbf{S}_S &= \lambda (\mathbf{E}_S : \mathbf{I}_S + E_N) \mathbf{I}_S + 2\mu \mathbf{E}_S \\ \mathbf{S}_N &= \lambda (\mathbf{E}_S : \mathbf{I}_S + E_N) \mathbf{N} \otimes \mathbf{N} + 2\mu \mathbf{E}_N. \end{aligned} \quad (6.49)$$

By setting the normal stress to zero,  $S_N = \lambda (\mathbf{E}_S : \mathbf{I}_S) + (\lambda + 2\mu) E_N \doteq 0$ , we obtain an explicit expression for the normal strain  $E_N$  in terms of the surface strain  $\mathbf{E}_S$ ,

$$E_N = \frac{-\lambda}{\lambda + 2\mu} (\mathbf{E}_S : \mathbf{I}_S), \quad (6.50)$$

which we substitute back into the definition of the surface stress in eq. (6.49),

$$\mathbf{S}_S = \frac{2\mu\lambda}{\lambda + 2\mu} (\mathbf{E}_S : \mathbf{I}_S) \mathbf{I}_S + 2\mu \mathbf{E}_S. \quad (6.51)$$

In the small-strain limit, we can express the Lamé constants  $\lambda$  and  $\mu$  in terms of the Young's modulus  $E$  and Poisson's ratio  $\nu$ ,

$$\mathbf{S}_S = \frac{E\nu}{1 - \nu^2} (\mathbf{E}_S : \mathbf{I}_S) \mathbf{I}_S + \frac{E}{1 + \nu} \mathbf{E}_S, \quad (6.52)$$

which is the final expression for the stress as function of the surface deformation, equivalent to the literature [188]. The material tangent follows from using the chain rule,

$$\mathbb{C} = \frac{\partial \mathbf{S}}{\partial \mathbf{E}} = \frac{\partial \mathbf{S}}{\partial \mathbf{E}_S} : \frac{\partial \mathbf{E}_S}{\partial \mathbf{E}}. \quad (6.53)$$

The first term is straightforward to compute,

$$\mathbb{C}_S = \frac{\partial \mathbf{S}}{\partial \mathbf{E}_S} = \frac{2\mu\lambda}{\lambda + 2\mu} \mathbf{I}_S \otimes \mathbf{I}_S + 2\mu \mathbb{I}_S, \quad (6.54)$$

where  $\mathbb{I}_S$  is the fourth order identity tensor of the surface tangent space. The second term,

$$\frac{\partial \mathbf{E}_S}{\partial \mathbf{E}} = \frac{\partial (\mathbf{E} - E_N \mathbf{N} \otimes \mathbf{N})}{\partial \mathbf{E}} = \mathbb{I} + \frac{\lambda}{\lambda + 2\mu} \mathbf{N} \otimes \mathbf{N} \otimes \mathbf{I}_S, \quad (6.55)$$

accounts for the fact that the surface and normal strains are related to satisfy the plane stress condition. Here we have used the fact that the projection,  $\mathbf{I}_S : \partial\mathbf{E}_S/\partial\mathbf{E} = \mathbf{I}_S$ , is equivalent to the surface unit tensor. Contracting  $\mathbb{C}_S$  with  $\partial\mathbf{E}_S/\partial\mathbf{E}$  in eq. (6.53) has no effect, and  $\mathbb{C} \equiv \mathbb{C}_S$ .

#### 6.4.2 Mooney-Rivlin Model

Mooney Rivlin (MR) constitutive equations, often used to describe rubber materials, were amongst the first choices to model arteries and other biomembranes [168]. The three-dimensional strain energy function of Mooney Rivlin type, supplemented by a contribution in the fiber direction, is

$$\psi = \mu [(I_1 - 3) + \alpha(I_2 - 3) + \beta(I_4 - 1)^2]. \quad (6.56)$$

Here we introduce the Mooney Rivlin potential to model orthotropic membranes directly in terms of the surface strains [212]. This formulation applies to some biological structures such as cell membranes or soft tissues at low strain regimes [347]. We reformulate the strain energy function in terms of the surface invariants defined in eq. (6.25),

$$\psi_S = \mu[(I_{IS} + I_{SS}^{-1} - 3) + \alpha(I_{S3} + I_{S1}I_{SS}^{-1} - 3) + \beta(I_{S4} - 1)^2]. \quad (6.57)$$

We obtain the second Piola Kirchhoff surface stress  $\mathbf{S}_S$  as

$$\begin{aligned} \mathbf{S}_S = 2\frac{\partial\psi_S}{\partial\mathbf{C}_S} = & 2\mu[(1 + \alpha I_{SS}^{-1})\mathbf{I}_S + (\alpha(I_{S3} - I_{S1}I_{SS}^{-1}) - I_{SS}^{-1})\mathbf{C}_S^{-1} \\ & + 2\beta I_{S4}\mathbf{A} \otimes \mathbf{A}], \end{aligned} \quad (6.58)$$

and the corresponding surface tangent moduli as,

$$\begin{aligned} \mathbb{C}_S = 2\frac{\partial\mathbf{S}_S}{\partial\mathbf{C}_S} = & 4\mu \left[ (\alpha(I_{S3} - I_{S1}I_{SS}^{-1}) + I_{SS}^{-1})\mathbf{C}_S^{-1} \otimes \mathbf{C}_S^{-1} \right. \\ & + (\alpha I_{3S} - I_{SS}^{-1} - \alpha I_{S1}I_{SS}^{-1})\frac{\partial\mathbf{C}_S^{-1}}{\partial\mathbf{C}_S} \\ & - \alpha I_{SS}^{-1}(\mathbf{I}_S \otimes \mathbf{C}_S^{-1} + \mathbf{C}_S^{-1} \otimes \mathbf{I}_S) \\ & \left. + 2\beta \mathbf{A} \otimes \mathbf{A} \otimes \mathbf{A} \otimes \mathbf{A} \right]. \end{aligned} \quad (6.59)$$

### 6.4.3 May-Newman-Yin Model

Constitutive equations for cardiac tissues have received special attention. This is not surprising – heart valves, for example, are obvious examples of biological membranes with crucial mechanical roles in the human body. The seminal work by May-Newman and Yin (MY) introduced a constitutive law with an exponential contribution to the strain energy that was used successfully to model heart valves under biaxial tests [242]. More recent work by Prot and Holzapfel modified the strain energy function proposed by May-Newman and Yin and used it to explore more realistic out-of-plane deformations while, at the same time, imposing incompressibility [307]. Here we revisit the latter implementation within our formulation. Its strain energy function is

$$\psi = c_0 [\exp(c_1(I_1 - 3)^2 + c_2(I_4 - 1)^2) - 1]. \quad (6.60)$$

To impose incompressibility, we adopt a Lagrange multiplier approach,

$$\hat{\psi} = c_0 [\exp(c_1(I_1 - 3)^2 + c_2(I_4 - 1)^2) - 1] + p(J - 1). \quad (6.61)$$

The second Piola Kirchhoff stress tensor follows as

$$\mathbf{S} = 2 \frac{\partial \hat{\psi}}{\partial \mathbf{C}} = 2\psi_1 \mathbf{I} + 2\psi_4 \mathbf{A} \otimes \mathbf{A} + 2p \mathbf{C}^{-1}. \quad (6.62)$$

Here  $\psi_i = \partial\psi/\partial I_i$  denotes the derivatives of the strain energy function with respect to the first and fourth invariants of  $\mathbf{C}$ . We adopt the additive decomposition of the right Cauchy Green strain tensor into surface and normal contributions,  $\mathbf{C} = \mathbf{C}_S + \mathbf{C}_N$ . We solve for the pressure to satisfy the plane stress condition and calculate the normal strain component explicitly using the incompressibility constraint,

$$p = -2\psi_1 C_N \quad \text{with} \quad C_N = 1/I_{S3}. \quad (6.63)$$

After substituting  $I_1 = I_{S1} + C_N$  and  $I_4 = I_{S4}$  in the expressions for  $\psi_i$ , the stress in eq. (6.62) is now only a function of the surface strain invariants,

$$\mathbf{S} = \mathbf{S}_S = 2\psi_1 \mathbf{I}_S + 2\psi_4 \mathbf{A} \otimes \mathbf{A} - 2\psi_1/I_{S3} \mathbf{C}_S^{-1}. \quad (6.64)$$

The tangent moduli follow as

$$\mathbb{C} = 2 \frac{\partial \mathbf{S}}{\partial \mathbf{C}} = 2 \frac{\partial \mathbf{S}_S}{\partial \mathbf{C}_S} : \frac{\partial \mathbf{C}_S}{\partial \mathbf{C}}. \quad (6.65)$$

The first term denotes the surface tangent moduli,

$$\begin{aligned} \mathbb{C}_S &= 2 \frac{\partial \mathbf{S}_S}{\partial \mathbf{C}_S} \\ &= 2\psi_{11}\mathbf{I}_S \otimes \mathbf{I}_S + 2\psi_{14}(\mathbf{I}_S \otimes \mathbf{A} \otimes \mathbf{A} + \mathbf{A} \otimes \mathbf{A} \otimes \mathbf{I}_S) \\ &\quad + 2\psi_{44}\mathbf{A} \otimes \mathbf{A} \otimes \mathbf{A} \otimes \mathbf{A} - 2\psi_{11}I_{S3}^{-1}\mathbf{C}_S^{-1} \otimes \mathbf{I}_S \\ &\quad - 2\psi_{14}I_{S3}^{-1}\mathbf{C}_S^{-1} \otimes \mathbf{A} \otimes \mathbf{A} \\ &\quad + 2\psi_1I_{S3}^{-1}(\mathbf{C}_S^{-1} \otimes \mathbf{C}_S^{-1} - \frac{\partial \mathbf{C}_S^{-1}}{\partial \mathbf{C}}), \end{aligned} \quad (6.66)$$

where the abbreviation  $\psi_{ij}$  denotes the second derivatives of the strain energy with respect to the surface invariants,  $\psi_{ij} = \partial\psi_i/\partial I_{Sj}$ . The second term is

$$\frac{\partial \mathbf{C}_S}{\partial \mathbf{C}} = \mathbb{I} - C_N \mathbf{N} \otimes \mathbf{N} \otimes \mathbf{N} \otimes \mathbf{N}. \quad (6.67)$$

Contracting  $\mathbb{C}_S$  with  $\partial \mathbf{C}_S / \partial \mathbf{C}$  in eq. (6.65) has no effect, and  $\mathbb{C} \equiv \mathbb{C}_S$ .

#### 6.4.4 Gasser-Ogden-Holzapfel Model

Originally developed to model arteries, the strain energy function proposed by Gasser, Ogden and Holzapfel (GOH), has been readily adopted to model other thin biological tissues with a well-defined microstructure such as skin [12, 126]. This constitutive law accounts for an isotropic response due to the water-based matrix, and an exponential contribution from a distributed family of fibers. While the original model assumes a three-dimensional fiber dispersion function, in thin biological membranes, fibers lie primarily within the plane, and a two-dimensional fiber dispersion function seems appropriate [81]. The strain energy function then becomes a sum of a three-dimensional Neo-Hookean contribution, plus an exponential term from a two dimensional fiber family,

$$\psi = c(I_1 - 3) + \frac{k_1}{2k_2} \exp[k_2(\kappa I_{S1} + (1 - 2\kappa)I_{S4} - 1)]^2 - 1. \quad (6.68)$$

Again, we impose incompressibility using a Lagrange multiplier approach,

$$\hat{\psi} = c(I_1 - 3) + \frac{k_1}{2k_2} \exp[k_2(\kappa I_{S1} + (1 - 2\kappa)I_{S4} - 1)^2] - 1 + p(J - 1). \quad (6.69)$$

The second Piola Kirchhoff stress tensor is

$$\mathbf{S} = 2 \frac{\partial \hat{\psi}}{\partial \mathbf{C}} = 2c\mathbf{I} + 2\psi_1 \mathbf{I}_S : \frac{\partial \mathbf{C}_S}{\partial \mathbf{C}} + 2\psi_4 \mathbf{A} \otimes \mathbf{A} + 2p \mathbf{C}^{-1}, \quad (6.70)$$

where  $\psi_i = \partial\psi/\partial I_{Si}$  denotes the derivative of the strain energy function with respect to the first and fourth surface invariants of  $\mathbf{C}_S$ . The decomposition of the right Cauchy Green deformation tensor into surface and normal contributions allows us to explicitly define the pressure  $p$  using the incompressibility constraint,

$$p = -c C_N \quad \text{with} \quad C_N = 1/I_{S3}. \quad (6.71)$$

The derivative of the surface deformation tensor with respect to the total deformation tensor is

$$\frac{\partial \mathbf{C}_S}{\partial \mathbf{C}} = \mathbb{I} + C_N \mathbf{N} \otimes \mathbf{N} \otimes \mathbf{N} \otimes \mathbf{N}, \quad (6.72)$$

and the second Piola Kirchhoff stress that satisfies the plane stress condition reduces to the following expression,

$$\mathbf{S} = \mathbf{S}_S = 2c\mathbf{I} + 2\psi_1 \mathbf{I}_S + 2\psi_4 \mathbf{A} \otimes \mathbf{A} - 2c I_{S3}^{-1} \mathbf{C}^{-1}. \quad (6.73)$$

The tangent moduli for this constitutive law are

$$\begin{aligned} \mathbb{C}_S = & 4\psi_{11} \mathbf{I}_S \otimes \mathbf{I}_S + 4\psi_{14} (\mathbf{I}_S \otimes \mathbf{A} \otimes \mathbf{A} + \mathbf{A} \otimes \mathbf{A} \otimes \mathbf{I}_S) \\ & + 4\psi_{44} \mathbf{A} \otimes \mathbf{A} \otimes \mathbf{A} \otimes \mathbf{A} + 4c I_{S3}^{-1} (\mathbf{C}_S^{-1} \otimes \mathbf{C}_S^{-1} - \frac{\partial \mathbf{C}_S^{-1}}{\partial \mathbf{C}_S}), \end{aligned} \quad (6.74)$$

where the abbreviation  $\psi_{ij}$  denotes the second derivatives of the strain energy with respect to the surface invariants,  $\psi_{ij} = \partial\psi_i/\partial I_{Sj}$ .

## 6.5 Examples

### 6.5.1 In-Plane Biaxial Tests

To probe the correct implementation of the four material subroutines outlined before, we perform simple strip-biaxial tests. We use the material parameters indicated in Table 6.1. The parameters for the GOH model are taken from skin tissue simulations and the remaining parameters were obtained by a simple numerical fit of three biaxial testing scenarios [55]. In all cases we start with a square geometry of unit size parametrized with quadratic B-splines and knot vectors  $\Xi = \Omega = [0, 0, 0, 0.25, 0.5, 0.75, 1, 1, 1]$  and impose final principal stretches  $\lambda_x = 1.2$ ,  $\lambda_y = 1.0$ . Plots of the Cauchy stresses  $\sigma_{xx}$  and  $\sigma_{yy}$  for varying  $\lambda_x$  are depicted in Figure 6.2 for each material. For the anisotropic constitutive laws, we employ  $\mathbf{A} = \mathbf{G}_1$  which coincides with the  $x$  coordinate axis. The materials exhibit mild nonlinearity. We obtain homogeneous deformations and the curves match the theoretical results, which provides confidence in the implementation of the element, the constitutive law, and the corresponding tangent moduli.

Table 6.1: Material parameters for the different constitutive laws.

Const. Law	Parameters
VK	$\mu = 1.59 \times 10^{-2}$ MPa, $\lambda = 51.63$
MR	$\mu = 0.0245$ MPa, $\alpha = 0.0297$ , $\beta = 0.347$
MY	$c_0 = 5.95$ MPa, $c_1 = 1.48 \times 10^{-3}$ MPa, $c_2 = 6.74 \times 10^{-4}$
GOH	$c = 0.0511$ MPa, $k_1 = 0.015$ MPa, $k_2 = 0.0418$ , $\kappa = 0.05$

For the anisotropic materials, Figure 6.3 shows the variation of  $\sigma_{xx}$  and  $\sigma_{yy}$  at  $(x, y) = (0.5, 0.5)$  for  $\lambda_x = 1.20$  obtained through varying  $\theta$ . The angle  $\theta$  corresponds to the in-plane rotation with respect to the covariant base vector  $\mathbf{G}_1$ , thus,  $\theta = 0$  indicates a preferred stiffness direction  $\mathbf{A} = \mathbf{G}_1$ , here aligned with the  $x$  coordinate, and  $\theta = \pi/2$  corresponds to

$\mathbf{A} = \mathbf{G}_2$  aligned with  $y$  axis. The anisotropic stress contribution is of the form  $f_{I_4} \cdot \mathbf{A} \otimes \mathbf{A}$  where  $f_{I_4}$  denotes a function of the stretch,  $I_4$  of  $\mathbf{A}$ . The largest contribution in the  $xx$  component of the stress naturally occurs when  $\mathbf{A} = \mathbf{G}_1$  and contributions can only decrease for different  $\theta$ . For the  $yy$  component, however, the structural tensor  $\mathbf{A} \otimes \mathbf{A}$  has no contribution when  $\mathbf{A} = \mathbf{G}_1$  and  $I_4$  is maximum, and has full contribution when  $\mathbf{A} = \mathbf{G}_2$ , but then  $I_4 = 0$ . This interplay between the structural tensor and the stretch of  $\mathbf{A}$  results in a bell-shaped curve with maximum  $\sigma_{yy}$  at  $\theta = \pi/4$ .

### 6.5.2 Rectangular Strip Subjected to End Shearing Force

We analyze the performance of our formulation with respect to a popular benchmark problem, a strip pulled by a shear force at its free edge [360]. The geometry consists of a rectangular shell of dimensions  $10 \times 1$  and thickness 0.05. We first simulate the VK material with  $E = 1.2 \times 10^6$  and  $\nu = 0$ . No units are specified. The objective in this example is to compare our results to a popular benchmark problem. To impose the clamped-edge boundary condition, we adopt a method from the literature and fix the  $z$ -coordinate of the second row of control points closest to the clamped edge to fix the tangent at that edge [188]. Figure 6.4 shows the schematic of the problem and Figure 6.5 exhibits the plot of the solution and the reference values [360]. These results correspond to quadratic B-splines meshes with 25 elements along the length and 3 in across the width. The present formulation excellently matches the reference values.

To showcase the choice of other materials, we performed simulations for the anisotropic materials listed in Table 6.1. The dimension is now  $10 \times 1\text{mm}$  and the forces applied at the end are on the order of Newtons. Figure 6.6 shows the deflection curves when  $\mathbf{A} = [1, 0, 0]$  for the same mesh as before consisting of  $25 \times 3$  elements. The additional flexibility of the proposed constitutive laws to incorporate the anisotropy of non-linear materials allows to capture interesting geometric effects: For instance, we perform a similar simulation as before but in a strip of dimensions  $30 \times 10\text{mm}$  meshed with a  $25 \times 12$  elements patch and employ the GOH model with a fiber direction oriented obliquely at  $\theta = \pi/4$ , where  $\theta$  is the angle between the anisotropy direction  $\mathbf{A}$  and the covariant vector  $\mathbf{G}_1$ . We impose a force of  $P = 0.04\text{N}$ . Figure 6.7 shows the result of the  $y$  displacement at the tip of the strip. For the isotropic material and for anisotropic materials with  $\mathbf{A}$  aligned with  $\mathbf{G}_1$ , the  $y$  displacement is identically zero at the free edge. Now, the inclusion of an oblique fiber

direction breaks the symmetry. This is similar to heart valve leaflets, for example, where the presence of a non-trivial fiber distributions can create rich and complex deformation patterns, even for simple loading scenarios.

### 6.5.3 Inflation of a Rectangular Membrane

A major motivation for the present work is the application to relevant clinical problems. For instance, in plastic reconstructive surgery, tissue expansion is a widely employed procedure that allows to ultimately grow skin *in situ* by imposing stretches beyond the physiological limit. In an idealized geometry, skin expansion can be viewed as the inflation of a rectangular membrane. As reference geometry, we take a square of  $10 \times 10\text{cm}$  and apply a normal pressure of  $1\text{kPa}$  to induce out-of-plane deformation.

Figure 6.8 illustrates the convergence of the formulation for the MR material with parameters  $\mu = 1$ ,  $\alpha = 0.0245$ ,  $\beta = 0.0297$ , and  $\mathbf{A}$  forming a  $0.347$  angle with respect to  $\mathbf{G}_1$ . We are interested in tracking the solution upon  $h$ - and  $k$ -refinement [167]. We perform the simulation with meshes of  $5, 10, 20, 40$  elements per side and degrees of the B-spline basis functions  $2, 3, 4$ . Figure 6.8 shows the vertical displacement at the center of the membrane. It confirms that all meshes rapidly approach the same value of  $19.3112\text{mm}$  upon  $h$ - and  $k$ -refinement.

We are also interested in capturing the unique deformations resulting from anisotropy. A inflated rectangular membrane deforms differently in the directions parallel and perpendicular to its fiber orientation  $\mathbf{A}$  and creates a characteristic *bean* shape. This is illustrated in Figure 6.9, where we show the four final configurations of the different materials subjected to the same pressure. We used  $12 \times 12$  meshes of quadratic B-splines and imposed  $1\text{kPa}$  of normal pressure. The VK material deforms isotropically turning into a spheroid, while the other three geometries exhibit marked anisotropy. Table 6.2 summarizes the degree of anisotropy by measuring the lengths of the  $XZ$  and  $YZ$  cross sections at the center of the membrane as a measure of ellipticity. While the coarse mesh does not capture the details of the deformation at the corners, it is capable of correctly resolving the ellipticity and the overall shape. For example, inflation of the GOH material results in an identical value of  $0.68$  for both the coarse mesh and the  $30 \times 30$  mesh.

Table 6.2: Ellipticity of inflated membranes. Applying normal pressure to a flat VK material leads to isotropic deformation while materials with preferred stiffness direction (MR, MY and GOH) lead to bean-like shapes.

Const. Law	Pressure [kPa]	Length <sub>XZ</sub> [mm]	Length <sub>YZ</sub> [mm]	Ellipticity [-]
VK	1	217.2	217.2	0.00
MR	1	237.3	314.0	0.65
MY	1	201.3	210.7	0.29
GOH	1	224.2	307.3	0.68

## 6.6 Discussion

We have presented a thin shell formulation based on Kirchhoff-Love kinematics and isogeometric analysis tailored for nonlinear anisotropic materials. Isogeometric analysis has been readily used to formulate thin shell elements because of its inherent  $C^1$  continuity required for Kirchoff-Love kinematics [188]. However, with a few exceptions [73], attention has remained on linear isotropic constitutive laws. Yet, numerous research efforts have motivated constitutive equations that incorporate the highly nonlinear and markedly anisotropy behavior of biological tissues [316]. Our objective was to incorporate constitutive equations that have been specifically designed for collagenous tissues with preferred fiber orientations into the isogeometric framework of thin shells [54].

We summarized the kinematics of a thin shell using convective curvilinear coordinates. Following the Kirchhoff-Love assumptions, we imposed the constraint that the normal to the mid surface remains normal and un-stretched. We presented the weak form of the linear momentum balance for a three-dimensional solid. At this point, however, we departed from existing isogeometric thin shell models [188]. While it is common to perform explicit integration through the thickness and express the balance equations in terms of force and moment normals, here we kept the fully three-dimensional version of the equilibrium equations. This setup keeps the formulation as close as possible to the description familiar to the biomechanics community [163]. We then performed the consistent linearization with respect to the degrees of freedom. At this point our formulation remains open for the constitute model, which best suits the desired application. We remark that the integration across the thickness has to be performed numerically. Here we have followed recommendations from

nonlinear shell analysis, which suggest the use of 3-point Lobatto integration for smooth integrals [164]. However, more careful considerations can become necessary; ideally, the integration scheme is adjusted to the individual deformation pattern of underlying application.

To illustrate the flexibility of the current approach, we incorporated four widely used constitutive laws: the St. Venant Kirchhoff (VK), Mooney-Rivlin (MR), May Newmann-Yin (MY) and Gasser-Ogden-Holzapfel (GOH) models. For each model, we showed how to adapted it to satisfy the plane stress condition and derived the consistent tangent moduli. This procedure is conceptually generic and can easily be adopted for other hyperelastic material models. Within the context of biological membranes, it is worth raising the question of whether a shell formulation is necessary or whether it is sufficient to consider a membrane formulation alone. If we postulate that nature optimizes form and function, it would be reasonable to assume that biological systems *in vivo* are loaded such that bending moments are minimized [190]. Yet, any living system can be subjected to non-physiological conditions, especially in disease, where bending stresses might become important. For example, studies of bio-prosthetic heart valves have shown how leaflets undergo significant changes in curvature leading to tissue damage over many loading cycles [132, 241]. We believe it is important to consider both—membrane and bending energies—with a thin shell description. We analyzed selected benchmark examples to illustrate the performance of our formulation and its ability to capture the rich deformations that occur in response to material anisotropy. To demonstrate the correct implementation of the constitutive law and the corresponding tangent moduli, we analyzed the homogeneous deformation in simple strip biaxial tests. We also discussed a benchmark problem to illustrate the equivalence between the present work and the St. Venant Kirchhoff model [188]. We selected a rectangular strip subjected to a shear force at its free edge. Incorporating oblique fiber directions induced deformations that were not present in the isotropic case. We finally turned our attention to a more clinically inspired example, a clamped membrane inflated by a transverse pressure. This example resembles the process of skin expansion, a widely used reconstructive technique [51]. We demonstrated the convergence of the problem upon  $h$ - and  $k$ -refinement. For the four different materials, the final configuration under the same pressure displayed significant differences: The VK material deformed isotropically as expected. The MY material showed anisotropy, yet with a mild degree of ellipticity. The MR and GOH materials, on the contrary, generated highly anisotropic *bean* shape patterns. This type of deformation

agrees with experimental observations. We have conducted controlled experiments of skin expansion and found significant differences in strains parallel and orthogonal to Langer's lines, which are associated with collagen fiber orientations [60].

Here, for the sake of comparison with the literature, we have presented only simulations of simple geometries constructed from a single tensor product surface patch. To simulate complex geometries of multiples surface patches, we could adopt the bending strip method or Nitsche's method [148, 189]. For shell geometries with sharp corners, a hybrid shell formulation with combined Kirchhoff-Love kinematics for smooth regions and Reissner-Mindlin kinematics for sharp regions has been recently proposed [36]. The efforts in this direction have proven critical for the simulation of very intricate geometries in engineering applications such as wind turbines [30].

In summary, isogeometric analysis is a powerful tool to develop shell formulations with inherent high continuity. By embedding a set constitutive models for nonlinear anisotropic materials, we hope to unleash the benefits of isogeometric analysis within the biomechanics community, in which recent research efforts have generated a library of constitutive models for soft biological tissues. Our generic framework has various natural and potentially high impact applications. In particular, we will use this model to simulate heart valve leaflets and skin deformations in cardiac and reconstructive surgery.

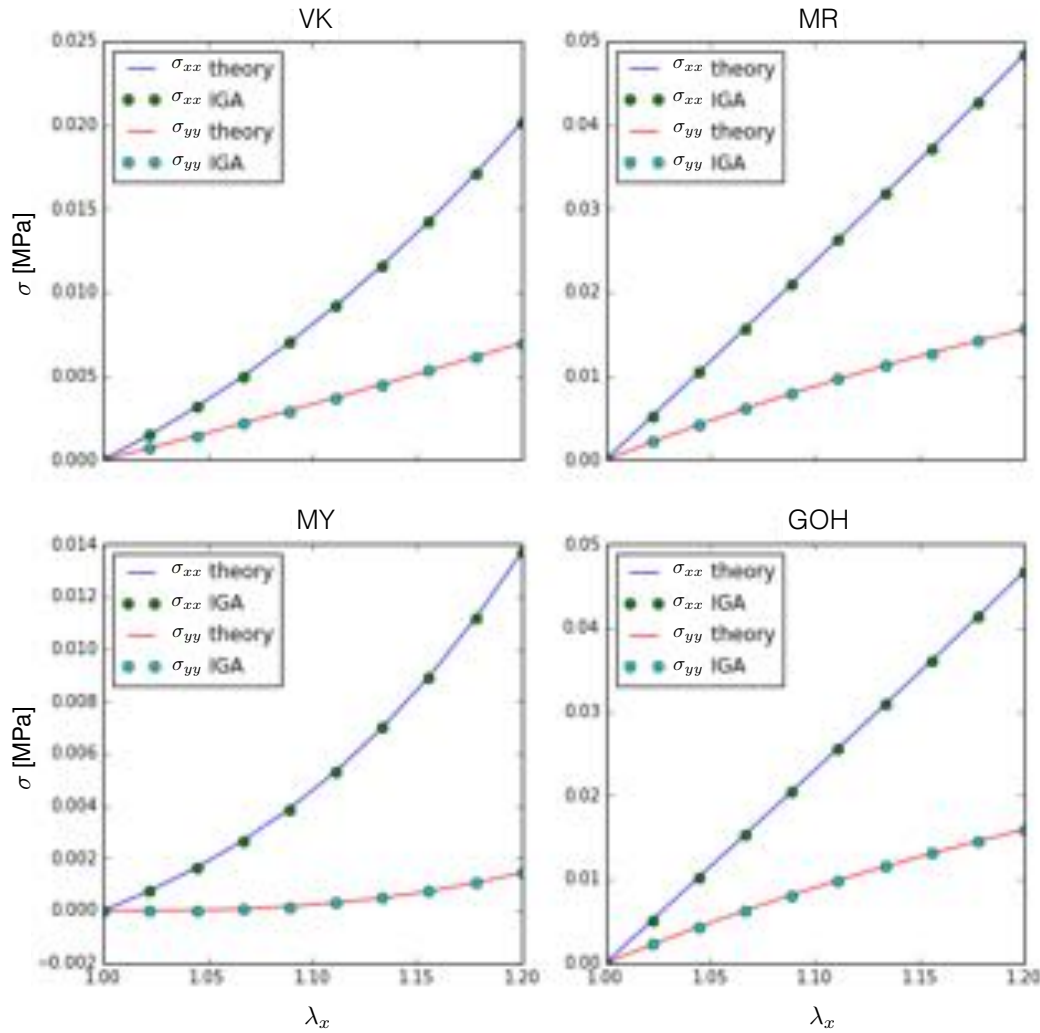


Figure 6.2: Strip biaxial test for the four different constitutive equations outlined: VK, MR, MY and GOH. The original geometry is a square discretized with  $6 \times 6$  elements mesh. While the sample is fixed in the  $y$  direction, a displacement is gradually applied in the  $x$  direction. The simulations yield a homogeneous deformation which agrees with the theoretical result. The materials exhibit mild nonlinearity, particularly for the MY model it is evident the influence of the exponential term as the strain increases.

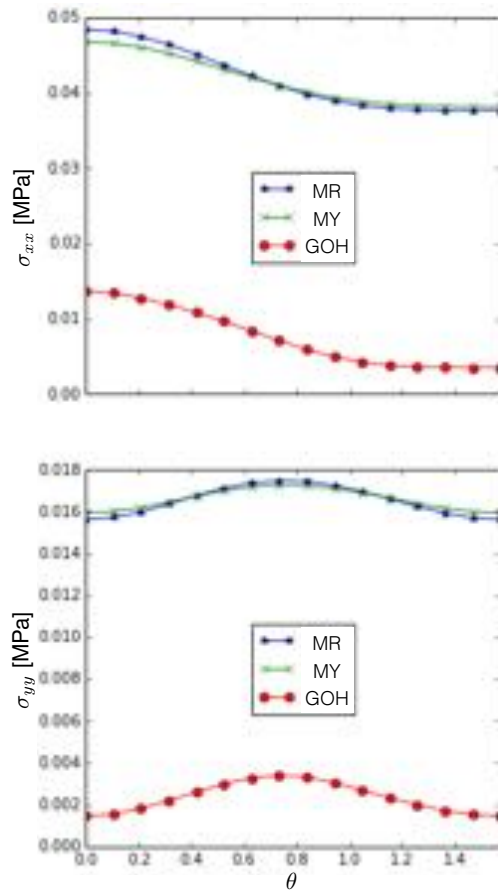


Figure 6.3: Anisotropy behavior obtained through varying the preferred direction  $\mathbf{A}$  determined by  $\theta$ , the angle with respect to  $\mathbf{G}_1$ . The  $xx$  component of the stress decreases while the  $yy$  component achieves its maximum at  $\theta = \pi/4$ .

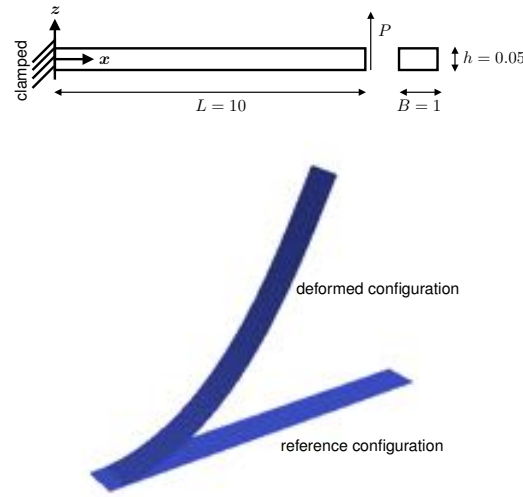


Figure 6.4: Schematic of the tip deflection example used as a popular benchmark test for thin shells. The geometry is a rectangular strip clamped at one end. A vertical shearing force is applied at the opposite end. The bottom part of the figure shows the reference geometry and the resulting deformation when the maximum load is applied.

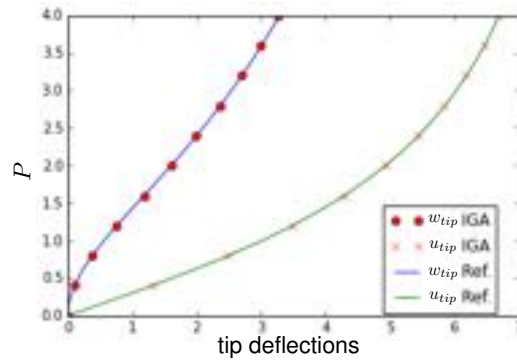


Figure 6.5: Deflections of the tip for the pulled strip subjected to end shearing force.  $w_{tip}$  corresponds to the displacement in the  $z$  coordinate while  $u_{tip}$  denotes the negative of the  $x$  displacement. The simulation results obtained with the present formulation agree well with the reference solution for a mesh of  $25 \times 3$  elements.

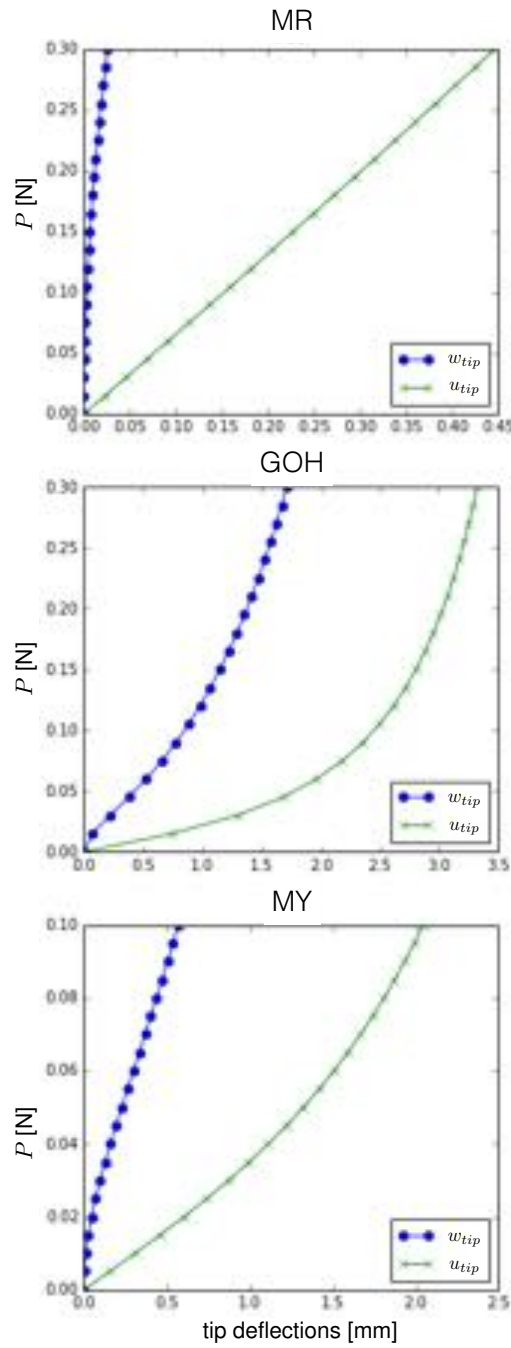


Figure 6.6: Deflections of the tip for the pulled strip using the anisotropic material models subjected to end shearing force.  $w_{tip}$  corresponds to the displacement in  $z$  while  $u_{tip}$  denotes the negative of the  $x$  displacement. Very different curves are seen for the different materials. The MY case deflects under less loading and the MR material exhibits the least deflection out of the three anisotropic models studied.

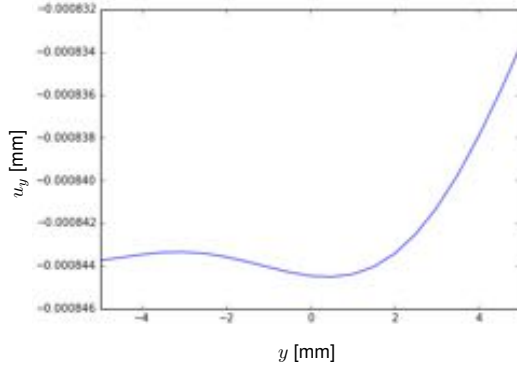


Figure 6.7:  $y$  displacement at the tip of a  $30 \times 10$ mm strip subjected to end shearing force. Unlike the isotropic case or an orthotropic membrane aligned with the loading, the presence of an oblique anisotropic direction induces more complex three-dimensional deformations. For isotropic membranes a vertical shearing force causes exactly zero  $y$  displacements, while the same loading for an anisotropic strip with oblique preferred direction results in an interesting deformation at the tip with non-zero  $y$  motion.

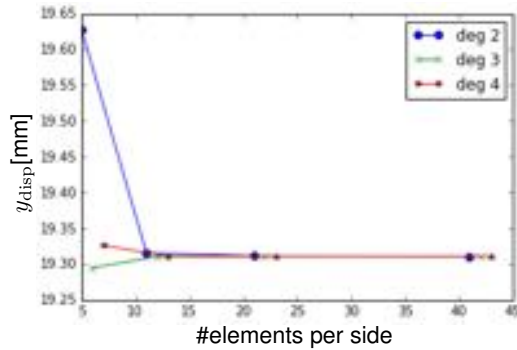


Figure 6.8: Convergence of a rectangular membrane subjected to out-of-plane pressure. The plot shows the vertical displacement of the center point of the membrane for a pressure of 1kPa for different mesh sizes and degrees of the basis functions. The resulting deformation converges rapidly upon both  $h$  and  $k$  refinement.

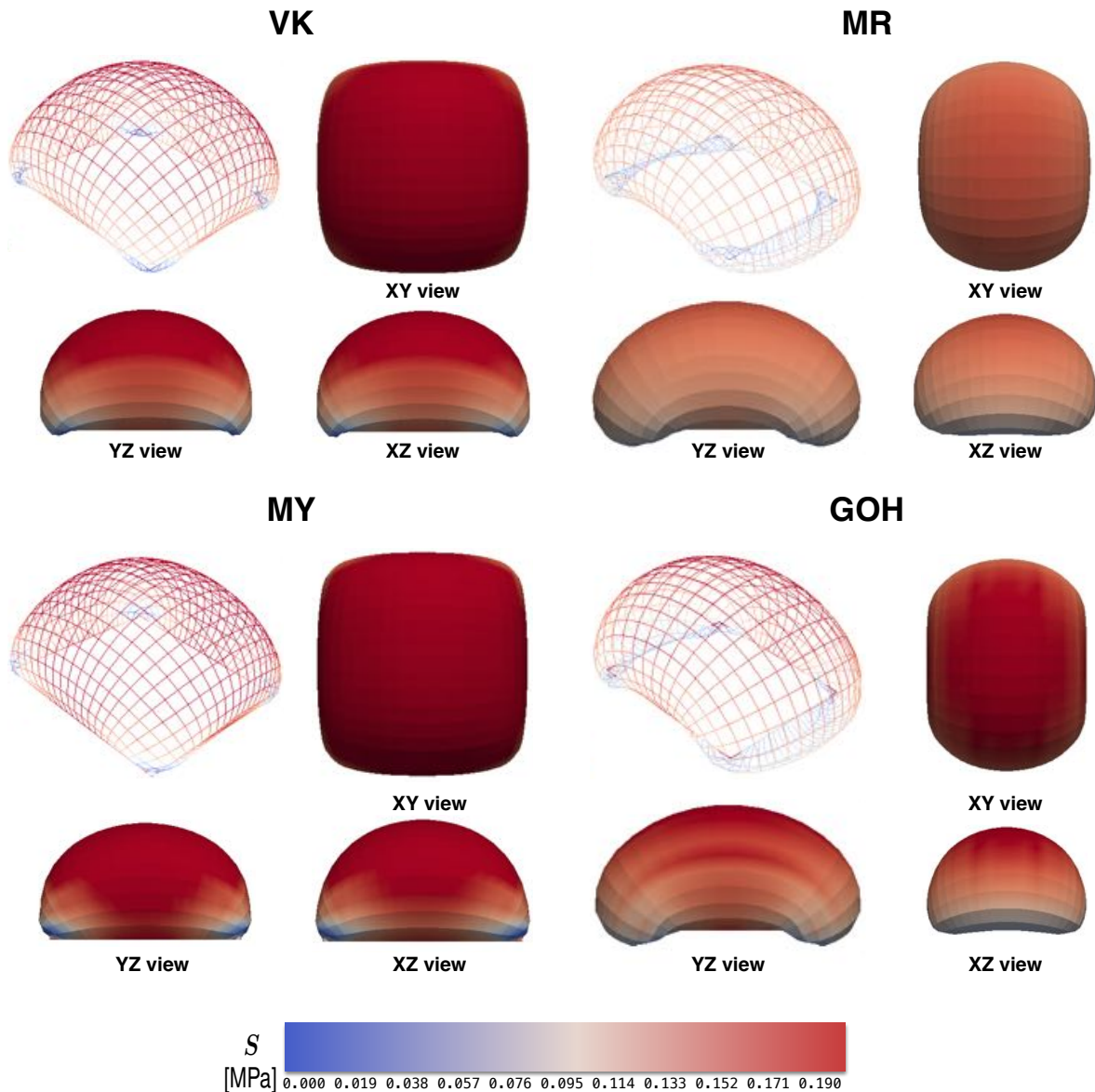


Figure 6.9: Inflation of a rectangular membrane by applying a normal out-of-plane pressure. The four final configurations shown correspond to the different constitutive laws under study. The VK material exhibits an isotropic deformation while all other three reach a final state with greater deformation opposite to the preferred direction of anisotropy. Particularly the MR and GOH materials show marked bean shapes.

## Chapter 7

# Mechanical Characterization of Living Skin Using Multi View Stereo and Isogeometric Analysis

**Abstract.** Skin is our interface with the outside world. In its natural environment, it displays unique mechanical characteristics such as prestrain and growth. While there is a general agreement on the physiological importance of these features, they remain poorly characterized, mainly because they are difficult to access with standard laboratory techniques. Here we present a new *in vivo* experiment to characterize the mechanics of living skin using multi view stereo and isogeometric analysis. To demonstrate our method, we quantify prestrain, deformation, and growth in a controlled porcine model of chronic skin expansion. Over a period of five weeks, we gradually inflate an implanted tissue expander, take weekly photographs of the experimental scene, reconstruct the geometry from a tattooed surface grid, and create parametric representations of the skin surface. After five weeks of expansion, our method reveals an average area prestretch of 1.44, an average area stretch of 1.87, and an average area growth of 2.25. Prestretch was maximal in the ventral region with 2.37, area stretch and growth were maximal above the center of the expander with 4.05 and 4.81. Our study has immediate impact on understanding living skin to optimize treatment planning and surgical decision making. Beyond these direct implications,

our experimental design has broad applications in clinical research and basic sciences: It serves as a robust, inexpensive, easy-to-use tool to reconstruct living membranes, which are difficult to characterize in a conventional laboratory setup.

## 7.1 Motivation

Characterizing deformations under controlled ex vivo and natural in vivo conditions is key to understand the mechanics of living membranes [171]. With a surface area of  $2\text{m}^2$ , skin is the largest living membrane of our body. Healthy skin is vital to our existence: It protects, senses, regulates, and controls the biochemical, thermal, and mechanical interactions with our environment [228]. Four decades ago, pioneering experiments have, for the first time, characterized the ex vivo mechanics of explanted rabbit skin using uniaxial and biaxial testing [217,373]. Other popular ex vivo test setups for biological tissues include compression [45], inflation [269], and bulge testing [374]. Recent attempts have focused on characterizing the mechanics of skin in vivo using either indentation [285] or aspiration [244]. Both are particularly valuable when combined with inverse finite element analysis [24]. Yet, with most conventional test setups, characterizing living membranes in vivo over long periods of time remains challenging. A possible way do this is to label characteristic anatomic landmarks with implanted radiopaque markers, follow them chronically over long periods of time, and reconstruct the surface geometry using biplane videofluoroscopy and continuum mechanics [315]. However, this approach is not only expensive and highly invasive, but also relies on a sophisticated, difficult-to-reproduce experimental setup.

Skin has two major advantages that distinguish it from many biological tissues: It is a thin membrane defined primarily through its surface representation [160], and it is conveniently exposed to facilitate surface imaging. Reconstructing skin surfaces from two-dimensional image capture is not a new idea; recent bulge experiments have used stereoscopic digital image correlation to identify the material parameters of explanted human skin samples [375]. Yet, these experiments require a restrictive laboratory setup and have so far only been used in ex vivo and acute conditions. Here, we propose an alternative, inexpensive, easy-to-use method for surface reconstruction of living surfaces in vivo: multi view stereo. Multi view stereo is a technique that allows us to extract three-dimensional representations of scenes from a collection of multiple two-dimensional images [335]. This challenge has emerged in computer graphics in the seventies, but it has only been within

the past decade that it has rapidly evolved into a robust and reliable tool [157, 225]. Initial stereo vision relied on sophisticated calibrations and precisely known camera positions [348]. The power of multi view stereo has rocketed with the automatization of these calibrations allowing us to use random sets of photographs with arbitrary camera angles [355]. Not surprisingly, multi view stereo is now finding its way into several commercial tools including the popular Cubify Capture and Autodesk 123D Catch. The high accuracy of model reconstruction with errors of the order of 1% suggests that multi view stereo can be used to reliably reconstruct triangulations of living surfaces in their natural *in vivo* environment [117].

To analyze the reconstructed three-dimensional scenes, it is critical to create parametric surface representations to quantify the relative deformation between points in space and time. A powerful computational approach for generating and analyzing free form surfaces is isogeometric analysis [82]. In contrast to conventional finite element analysis [166], isogeometric analysis employs B-spline basis function to represent both the geometry and the fields of interest [167]. Isogeometric analysis offers several advantages, which become particularly relevant when characterizing thin membranes [105]: B-spline basis functions enable the representation of smooth surfaces with only a few arbitrary control points [34]; their high polynomial degree inherently ensures high continuity, which is critical to characterize surface strain, surface curvature, and higher order derivatives [188]; and they allow us to use the same surface parametrization for different surfaces to easily quantify kinematic changes in both space and time.

Here, we are particularly interested in kinematic changes in time to characterize membrane growth [8]. Living membranes grow and remodel in response to mechanical cues [318]. When stretched beyond the physiological limit, skin increases its surface area to achieve mechanical homeostasis [92]. Plastic and reconstructive surgery capitalize on this phenomenon with an *in situ* procedure known as skin expansion, which creates skin with the same color, texture, hair bearing characteristics, and mechanical properties as the surrounding tissue [141]. Skin expansion is widely used to correct large birth defects, burn injuries, regions of tumor removal, and regions after mastectomy [231].

The clinical relevance of skin expansion has long drawn the attention of clinical scientists and researchers who have conducted various studies to investigate the biological, biochemical, biomechanical, and physical changes in expanded skin [21]. As a result, our understanding of the mechanobiology of the dermis has largely improved [53, 342]; yet, several important aspects are still understudied and require ongoing research efforts [48, 54].

Perhaps the most crucial limitation of skin expansion is the lack of a quantitative mechanistic understanding of the interplay between reversible elastic deformation and permanent area growth [385]. This limits the use of the procedure to senior and very experienced surgeons [341].

Chronically expanded skin grows primarily in the plane, while its thickness remains virtually unchanged [31]. Continuum models for skin growth represent this effect by decomposing the deformation gradient into an elastic part and a growth part [320]. For skin, the growth part is a transversely isotropic second order tensor parameterized in a single scalar-valued variable, the in-plane area growth [51]. We have demonstrated that area growth models can qualitatively predict skin growth for different tissue expander shapes [52] and for different patient specific geometries [418]. However, to serve as a quantitative predictive clinical tool, the model needs further experimental calibration and validation [419]. This is the main motivation for the present work.

## 7.2 Methods

### 7.2.1 Animal Model

We select young minipigs as animal model for skin expansion. The anatomy and mechanical properties of porcine skin closely resembles those of human skin [256, 263]. Porcine models of wound healing agreed to 78% with human studies, while small animal models and in vitro studies only displayed an agreement of 53% and 57% [356]. The absence of redundant skin and a panniculus carnosus layer makes pigs a preferred model system whose structure closely resembles human conditions [28].

#### Surgical Procedure

A one-month-old male Yucatan mini pig (Sinclair Biolabs, Columbus, MO) acclimated to standard housing and was fed ad libitum under a protocol approved by the Ann & Robert H. Lurie Children's Hospital of Chicago Research Center Animal Care and Use Committee.

On the day of surgery, we administer pre-procedural antibiotics and clean the dorsal skin with chlorhexidine-based surgical soap. We transfer  $10\text{ cm} \times 10\text{ cm}$  grids with 1cm line markings to the pig's skin using tattoo transfer medium in four areas, left caudal (P), right caudal (Q), left rostral (R), and right rostral (S), as illustrated in Figure 7.1. Our template

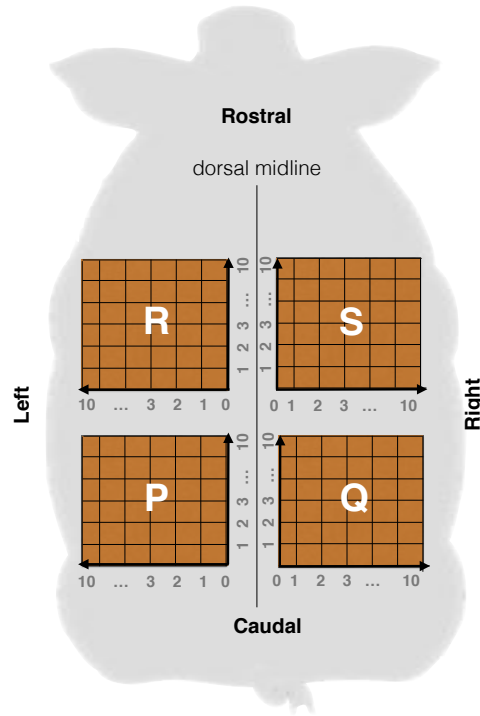


Figure 7.1: Porcine model for skin expansion. Four zones are identified by  $10\text{ cm} \times 10\text{ cm}$  grids tattooed on the pig's back in the left caudal (P), right caudal (Q), left rostral (R), and right rostral (S) regions. Rectangular tissue expanders are placed beneath the left caudal (P) and right rostral (S) regions; the right caudal (Q) and left rostral (R) regions serve as controls.

contains a midline reference to ensure symmetric placement of the grid patterns. The grids are permanently tattooed onto the pig's skin using a commercially available tattoo machine.

We record measurements and take photographs of the setup before preparing the skin and draping it in standard sterile fashion. We inject local anesthetic (1% lidocaine with 1 : 100000 epinephrine) subcutaneously at the site of each planned incision. We place two 120 cc textured, rectangular tissue expanders of dimensions 4 cm  $\times$  6 cm (PMT Corporation, Chanhassen, MN) beneath the left caudal (P) and right rostral (S) tattooed grid. Each expansion site has a mirror image grid of non-expanded tissue, (Q) and (R), as an internal control for prestrain and growth. A subcutaneous filling port near the dorsal midline, outside of the measurement grid, connects to each expander and allows for controlled inflation.

We close the incisions in standard fashion, and remove the sutures 14 days postoperatively. We monitor the animal postoperatively until it is able to maintain upright posture.

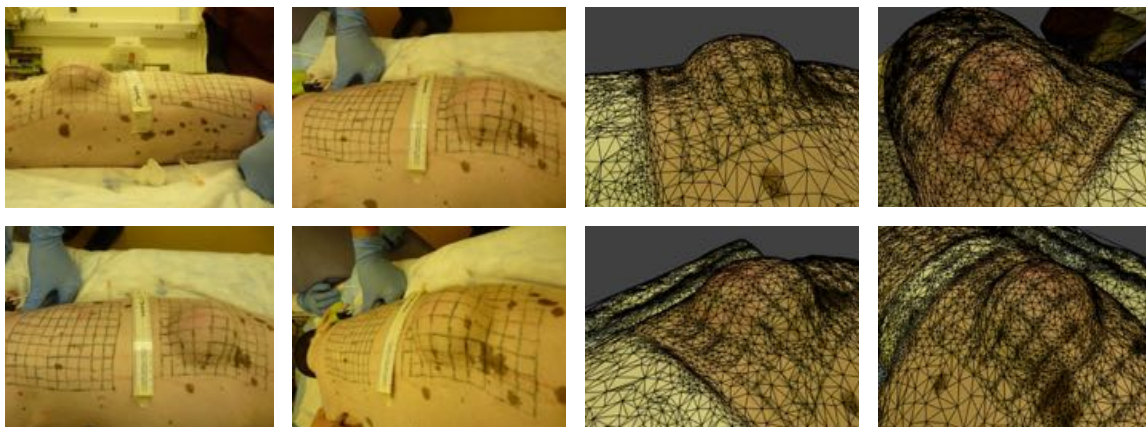


Figure 7.2: Multi view stereo is a technique to extract three-dimensional representations of scenes from a collection of multiple two-dimensional images. Selected photographs from different camera angles show the experimental setup with the tattooed grid and the inflated tissue expander in the left caudal region, left. Similar views show the reconstructed triangular surface representation of the scene created using online multi view stereo, right.

We continue antibiotic prophylaxis for 48 hours (Combi-Pen-48, Bimeda, Inc., Dublin, Ireland), and buprenorphine (0.05-0.1mg/kg) for analgesia via intramuscular injection every 12 hours for 4 doses, with additional doses available for evidence of animal distress.

### Skin Expansion

We leave the incisions to heal for three weeks before beginning expansion. Weekly, we fill the right rostral expander (S) by 25 cc and the left causal expander (P) by 50 cc, for five consecutive expansions to total volumes of 125 cc and 250 cc. Following the fifth expansion, we let the tissues settle for five days before we perform a final small expansion of 15 cc and 30 cc three days before tissue harvest.

### Tissue Harvest and Euthanasia

On the day of tissue harvest, we anesthetize the animal as described above and record final tissue measurements. We excise the four tattooed skin patches and euthanize the animal using intravenous overdose of pentobarbital (90mg/kg). We take photographs of the explanted tissues, fix them, and embed them in paraffin for subsequent analyses.

### 7.2.2 Multi View Stereo

Every week, before and after filling, we take 20 photographs of the experimental scene from different camera angles. We reconstruct the three-dimensional geometry from these multiple two-dimensional images using online multi view stereo (Autodesk 123D Catch). To calibrate the lengths and quantify the error of the geometric reconstruction we include a ruler during photo acquisition.

Figure 7.2 illustrates our geometric reconstruction process. Figure 7.2, left, shows four different views of the experimental setup. Figure 7.2, right, depicts similar views of the reconstructed triangular surface representation. To calibrate the lengths, for each set of images, we fit a cubic spline to the ruler and determine the individual lengths  $l_i$  along the spline between the  $i = 1, \dots, n$  one-cm-long ruler segments. We scale the geometry between the acquired images and the physical world using the average length  $l = \sum_{i=1}^n l_i / n$ . To quantify the average reconstruction error, we calculate the average error  $e = \sum_{i=1}^n e_i / n$  as the average of the individual reconstruction errors of each segment,  $e_i = [l_i - l] / l$ .

### 7.2.3 Isogeometric Surface Representation

To create a functional surface representation of the skin patch, we fit a B-spline surfaces through the  $11 \times 11$  tattooed nodes. B-spline surfaces are tensor products of B-spline curves. A B-spline curve  $\mathcal{C}(\xi)$  is the sum of a set of the basis functions  $N_i(\xi)$  multiplied by the coordinates of a set of control points  $\mathbf{P}_i$  summed over all  $i = 1, \dots, n_{\text{cp}}$  control points,

$$\mathcal{C}(\xi) = \sum_{i=0}^{n_{\text{cp}}} N_i(\xi) \mathbf{P}_i. \quad (7.1)$$

The B-spline basis functions  $N_i(\xi)$  of degree  $p$  are associated with a knot vector  $\Xi$ , a set of non-decreasing numbers  $\Xi = [\xi_0, \xi_1, \dots, \xi_n]$ , in which the first and last values,  $\xi_0$  and  $\xi_n$ , are repeated  $p+1$  times. The basis functions  $N_i(\xi)$  follow a recursive definition based on the zeroth order basis function for  $p = 0$ ,

$$N_i^0(\xi) = \begin{cases} 0 & \xi_i \leq \xi \leq \xi_{i+1} \\ 1 & \text{otherwise,} \end{cases} \quad (7.2)$$

combined with the recursion equation for the higher order basis functions for  $p \geq 1$ ,

$$N_i^p(\xi) = \frac{\xi - \xi_i}{\xi_{i+p} - \xi_i} N_i^{p-1}(\xi) + \frac{\xi_{i+p+1} - \xi}{\xi_{i+p+1} - \xi_{i+1}} N_{i+1}^{p-1}(\xi). \quad (7.3)$$

A B-spline surface  $\mathcal{S}(\xi, \eta)$  is the sum of a set of surface basis functions  $N_i(\xi, \eta)$  multiplied by the coordinates of a set of control points  $\mathbf{P}_i$  summed over all  $i = 1, \dots, n_{cp}$  control points,

$$\mathcal{S}(\xi, \eta) = \sum_{i=0}^{n_{cp}} N_i(\xi, \eta) \mathbf{P}_i. \quad (7.4)$$

The surface basis functions  $N_i(\xi, \eta)$  are the tensor products of the B-spline basis functions  $N_i(\xi)$  and  $N_j(\eta)$  defined in equations (9.1) and (9.2). To approximate our tattooed grid, we choose B-spline basis functions of polynomial degree  $p = 3$  based on a knot vector  $\Xi = [0, 0, 0, 0, 1, 2, \dots, 9, 10, 10, 10, 10]$ . Using a best fit algorithm, we determine the sets of optimal control points  $\mathbf{P}_i$  with

$$\sum_{n=1}^{121} \| \mathbf{X}_n - \mathcal{S}_0(\xi, \eta) \| \rightarrow \min, \quad (7.5)$$

to characterize the surface  $\mathcal{S}(\xi, \eta)$ , which best approximates the  $n = 1, \dots, 11 \times 11$  coordinates of the tattooed nodes.

#### 7.2.4 Isogeometric Analysis

Figure 7.3 illustrates two isogeometric surfaces reconstructed from our tattooed grid. To characterize the relative deformation between two points in time, we create two parametric surface representations of the skin patch, one at the reference state  $\mathcal{S}_0$  and one at the current state  $\mathcal{S}_t$ .

Using the B-spline surfaces representation (9.3), we approximate the referential and current coordinates,

$$\begin{aligned} \mathbf{X} &= \sum_{i=0}^{n_{cp}} N_i(\xi, \eta) \mathbf{P}_i \\ \mathbf{x} &= \sum_{i=0}^{n_{cp}} N_i(\xi, \eta) \mathbf{p}_i, \end{aligned} \quad (7.6)$$

where  $N_i(\xi, \eta)$  are the B-spline basis functions defined in equations (9.1) and (9.2) and  $\mathbf{P}_i$  and  $\mathbf{p}_i$  are the sets of optimal control points defined through the best fit (7.5). From the partial derivatives of the surface basis function with respect to the parametric coordinates,  $N_{i,\xi}$  and  $N_{i,\eta}$ , we calculate the sets of covariant surface base vectors in the reference and

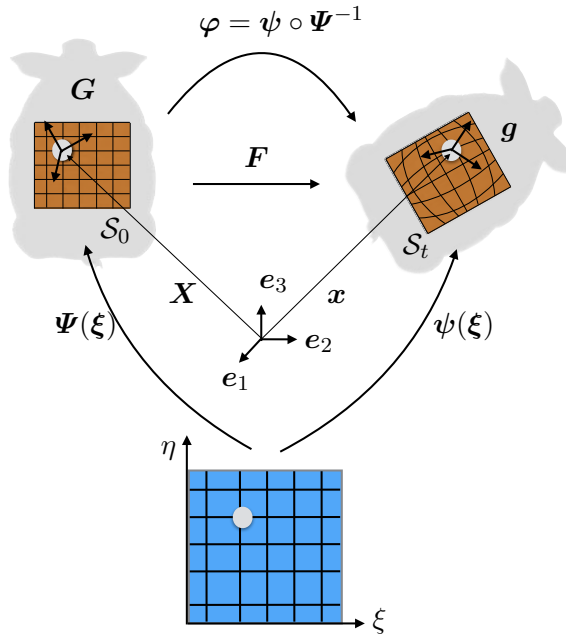


Figure 7.3: Isogeometric surfaces. The two mappings  $\Psi$  and  $\psi$  map the common parameter space  $(\xi, \eta)$  onto the reference and current surfaces  $S_0$  and  $S_t$ . The deformation  $\varphi = \psi \circ \Psi^{-1}$  maps points between both surfaces as  $\mathbf{x} = \varphi(\mathbf{X})$ . The deformation gradient  $\mathbf{F} = \mathbf{g}_\alpha \otimes \mathbf{G}^\alpha$  is the key kinematic quantity to characterize pointwise relative deformation between the two surfaces.

current configurations,

$$\begin{aligned}\mathbf{G}_1 &= \sum_{i=0}^{n_{cp}} N_{i,\xi} \mathbf{P}_i & \mathbf{G}_2 &= \sum_{i=0}^{n_{cp}} N_{i,\eta} \mathbf{P}_i \\ \mathbf{g}_1 &= \sum_{i=0}^{n_{cp}} N_{i,\xi} \mathbf{p}_i & \mathbf{g}_2 &= \sum_{i=0}^{n_{cp}} N_{i,\eta} \mathbf{p}_i.\end{aligned}\quad (7.7)$$

To determine the contravariant base vectors  $\mathbf{G}^\alpha$ , we calculate the covariant surface metric,

$$G_{\alpha\beta} = \mathbf{G}_\alpha \cdot \mathbf{G}_\beta \quad \text{with } \alpha, \beta = 1, 2 \quad (7.8)$$

invert it to calculate the contravariant surface metric  $G^{\alpha\beta}$ , and map the covariant base vectors  $\mathbf{G}_\beta$  onto their contravariant counterparts,

$$\mathbf{G}^\alpha = G^{\alpha\beta} \mathbf{G}_\beta \quad \text{with } G^{\alpha\beta} = [G_{\alpha\beta}]^{-1}. \quad (7.9)$$

Finally, we calculate the deformation gradient  $\mathbf{F}$  as the dyadic product between the covariant current base vectors  $\mathbf{g}_\alpha$  and the contravariant reference base vectors  $\mathbf{G}^\alpha$ ,

$$\mathbf{F} = \mathbf{g}_\alpha \otimes \mathbf{G}^\alpha. \quad (7.10)$$

The deformation gradient is the key kinematic quantity to characterize the expansion process between any two time points across the tattooed grid. Its determinant characterizes the area stretch  $\vartheta$ ,

$$\vartheta = \det(\mathbf{F}), \quad (7.11)$$

the change in surface area between a surface element in the reference configuration  $\mathcal{S}_0$  and in the current configuration  $\mathcal{S}_t$ .

### 7.2.5 Prestrain, Expansion-Induced Deformation, and Growth

Figure 7.4 illustrates the four distinct configurations of the skin patch to characterize prestrain, expansion-induced deformation, and growth. We define the explanted, stress free skin patch (Q) as the ex vivo pre-expansion configuration, which we map onto the in vivo pre-expansion configuration via the prestrain  $\mathbf{F}^P$ . This implies that the in vivo pre-expansion configuration is not necessarily stress-free; yet, it is convenient to choose it as a reference state since it coincides with the specific time point at the beginning of the experiment. We define the harvested, explanted skin patch (P) as the ex vivo grown patch, defined either through mapping the ex vivo pre-expansion patch with the growth tensor  $\mathbf{F}^g$  or through the released elastic deformation  $\mathbf{F}^{e-1}$  when compared with the in vivo expanded state. Figure 7.4 illustrates the relations between the total deformation gradient  $\mathbf{F}$ , the prestrain  $\mathbf{F}^P$ , the elastic tensor  $\mathbf{F}^e$ , and the growth tensor  $\mathbf{F}^g$ ,

$$\mathbf{F} \cdot \mathbf{F}^P = \mathbf{F}^e \cdot \mathbf{F}^g. \quad (7.12)$$

This implies that the corresponding determinants,

$$\vartheta \vartheta^P = \vartheta^e \vartheta^g, \quad (7.13)$$

are also multiplicatively related. In particular,  $\vartheta$  represents the expansion-induced area change,  $\vartheta^P$  is the area prestretch,  $\vartheta^e$  is the reversible elastic area change, and  $\vartheta^g$  is the

permanently grown area change.

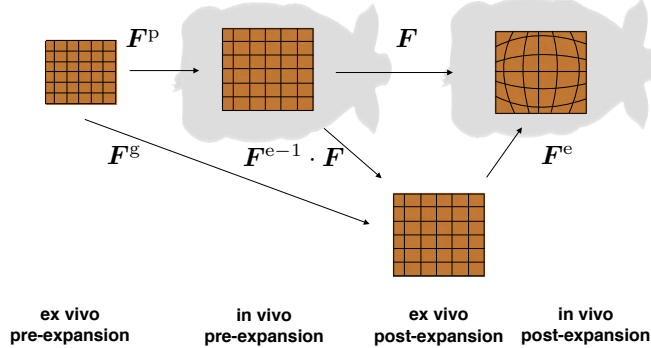


Figure 7.4: Four configurations of the skin patch: ex vivo pre-expansion, in vivo pre-expansion, ex vivo post-expansion, and in vivo post-expansion. The ex vivo pre-expansion patch can be mapped onto the in vivo post-expansion patch via prestrain  $\mathbf{F}^p$  and deformation  $\mathbf{F}$ , or, alternatively, via growth  $\mathbf{F}^g$  and elastic deformation  $\mathbf{F}^e$ .

## 7.3 Results

The right rostral expansion (S) failed due to leakage of the inflation port. The left caudal expansion (P) was successfully completed. The expansion process spanned a total of five weeks with weekly filling volumes of 50 cc and three final days with an additional filling volume of 30 cc towards a total volume of 280 cc. The unexpanded right caudal region (Q) served as control. Figure 7.4 summarizes the four configurations of interest to characterize prestrain, expansion-induced deformation, and growth.

### 7.3.1 Characterization of Prestrain

Figure 7.4, left, shows the kinematics associated with the prestrain  $\mathbf{F}^p$  as the mapping from the ex vivo to the in vivo configuration. We use the tattooed grid of the unexpanded right caudal region (Q) to quantify the regional variation of prestrain throughout the entire patch. Prestrain manifests itself as the tissue retraction upon explantation to reach a nearly stress free configuration.

Figure 7.5, left, summarizes the kinematics associated with prestrain. To re-establish the initial unit-square-sized skin patch with the tattooed grid of 10 cm  $\times$  10 cm, we would have to stretch the retracted ex vivo tissue patch by an average area prestretch of  $\vartheta^p = 1.44$ .

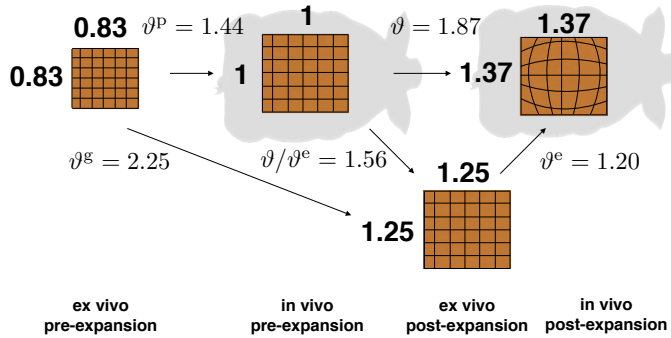


Figure 7.5: Four configurations of the skin patch. Prestain induces an average area change of  $\vartheta^p = 1.44$ . Expander inflation induces an average area change of  $\vartheta = 1.87$ , of which  $\vartheta^e = 1.20$  are reversible elastic and  $\vartheta/\vartheta^e = 1.56$  are permanently grown. When compared to the ex vivo pre-expansion skin patch, the ex vivo post-expansion patch has grown in area by  $\vartheta^g = 2.25$ .

This corresponds to an area increase of 44% from the ex vivo to the in vivo configuration, or equivalently, to an area shrinkage of 31% upon explantation, corresponding to a retracted patch of 8.3 cm × 8.3 cm.

Figure 7.6 illustrates the characterization of prestrain using multi view stereo and isogeometric analysis. The two columns show the skin patch in the ex vivo and in the restrained in vivo configuration. The top row shows representative photographs of the experimental setup for each configuration. Using multi view stereo, we create three-dimensional representations of the tattooed skin patch before the animal is sacrificed and after excising the patch. The middle row shows the geometric reconstruction of the skin patch. We choose the ex vivo pre-expansion state as reference configuration and the in vivo pre-expansion state as the current configuration. Using isogeometric analysis, we calculate the prestrain  $\mathbf{F}^p$  as the gradient of the mapping between both configurations. The associated area prestretch is  $\vartheta^p = \det(\mathbf{F}^p)$ . The bottom row portrays the contour plot in the isogeometric parameter space.

Table 7.1 summarizes the results of the prestrain analysis with an average area prestretch of  $\vartheta_{\text{avg}}^p = 1.44$ , a maximum area prestretch of  $\vartheta_{\text{max}}^p = 2.37$ , and a minimum area prestretch of  $\vartheta_{\text{min}}^p = 0.63$ . The average reconstruction error is 7.5%.

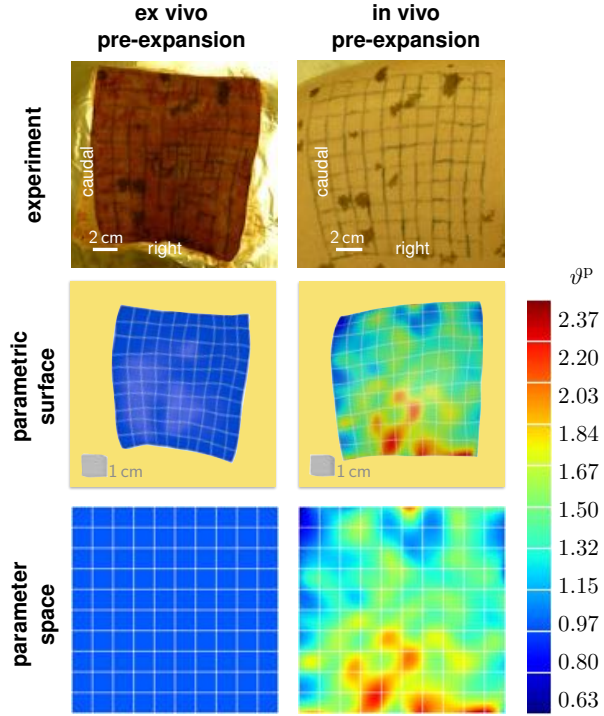


Figure 7.6: Characterization of prestrain using multi view stereo and isogeometric analysis. Representative photographs of the experimental setup (top) enable reconstruction of the skin geometry using multi view stereo (middle) to calculate the relative area change using isogeometric analysis (bottom). The area change between the ex vivo pre-expansion configuration (left) and the in vivo pre-expansion configuration (right) characterizes the amount of prestrain  $\vartheta^P$ .

### 7.3.2 Characterization of Expansion-Induced Deformation

Figure 7.4, top right, shows the kinematics associated with the expansion-induced deformation  $\varphi$  and the deformation gradient  $\mathbf{F}$  as the mapping from the in vivo pre-expansion configuration to the in vivo post-expansion configuration. We use the tattooed grid of the expanded left caudal region (P) to quantify the regional variation of the deformation throughout the entire patch.

Figure 7.5, top right, summarizes the kinematics associated with expansion-induced deformation. Within five weeks, the gradual expansion stretches the initial tattooed grid of  $10\text{ cm} \times 10\text{ cm}$  by  $\vartheta = 1.87$ . The surface area of the tattooed patch increases by 87%, which is the equivalent of a stretched patch with a side length of  $13.7\text{ cm} \times 13.7\text{ cm}$ .

Figure 7.7 illustrates the detailed time sequence of the expansion process. The top and

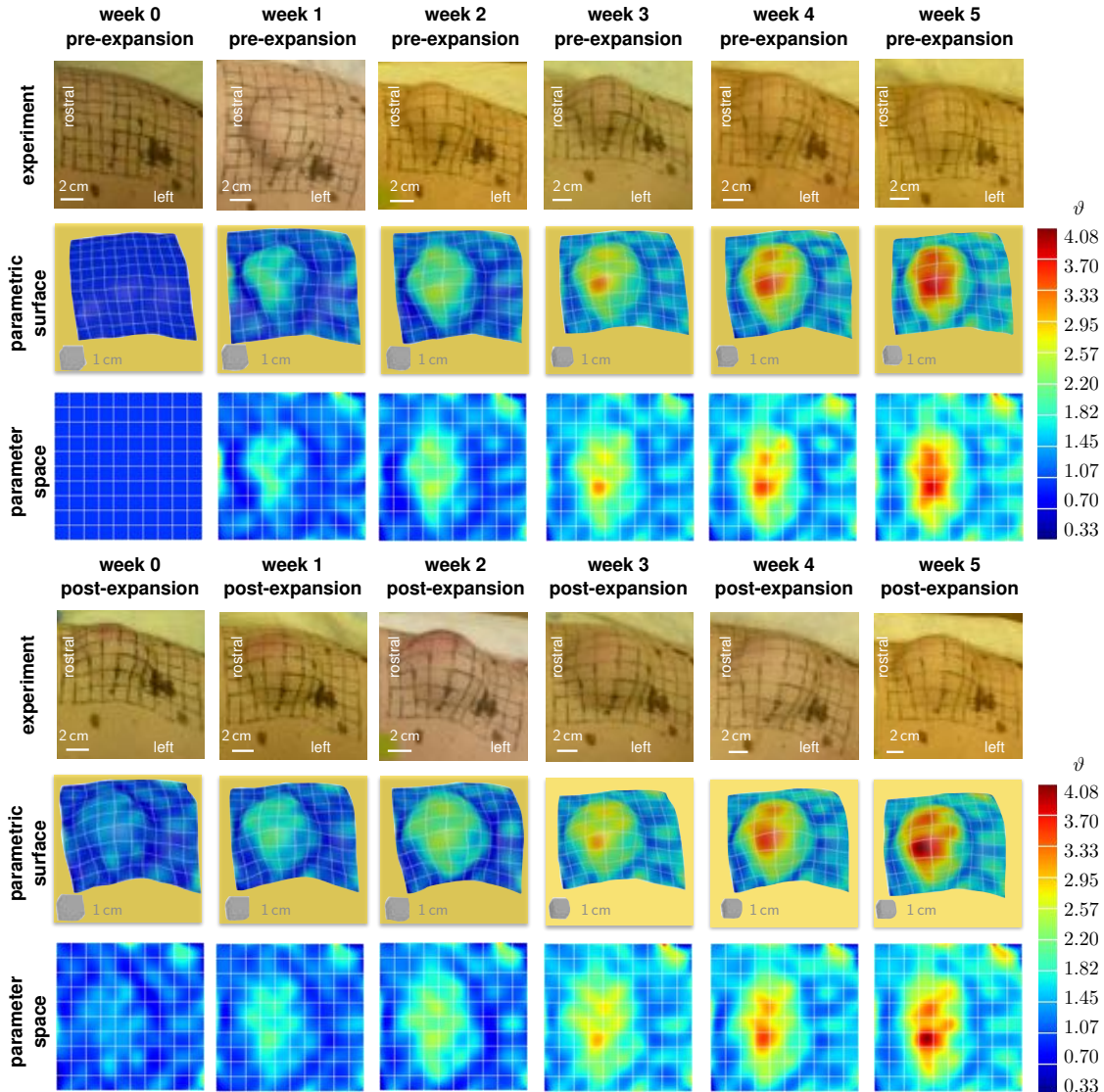


Figure 7.7: Characterization of expansion-induced deformation using multi view stereo and isogeometric analysis. The top and bottom image sets show the skin patch in the pre-expanded and post-expanded configuration. Representative photographs of the experimental setup (top) enable reconstruction of the skin geometry using multi view stereo (middle) to calculate the area change using isogeometric analysis (bottom). Differences between the pre- and post-expansion characterize the acute stretch (top to bottom); differences between the post-expansion states characterize the chronic stretch (left to right).

Table 7.1: Characterization of average, maximum, and minimum area prestretch between the ex vivo pre-expansion and in vivo pre-expansion configurations.

area prestretch	$\vartheta_{\text{avg}}^{\text{P}}$ (-)	$\vartheta_{\text{max}}^{\text{P}}$ (-)	$\vartheta_{\text{min}}^{\text{P}}$ (-)	error ( %)
ex vivo → in vivo pre	1.44	2.37	0.63	7.5

bottom image sets show weekly photographs of the skin patch in vivo before and after the inflation step. Using multi view stereo, we create a three-dimensional representation of each skin patch and compare it with the in vivo pre-expansion patch as reference configuration. Using isogeometric analysis, we calculate the deformation gradient  $\mathbf{F}$  as the gradient of the mapping between both configurations and extract the total area change  $\vartheta = \det(\mathbf{F})$ . For each configuration, Figure 7.7 shows a photograph of the experimental setup, the B-spline surface color-coded with the area stretch  $\vartheta$ , and the contour plot of  $\vartheta$  in the isoparametric parameter space. The comparison from top to bottom characterizes the acute area stretch, imposed by abruptly filling the expander by 50 cc every week; the comparison from left to right characterizes the chronic area stretch, imposed by gradually increasing the filling volume to 280 cc. The contour plots reveal lower area stretches towards the beginning of the inflation process and higher area stretches towards the end. Changes in surface area displays drastic regional variations: Stretches are larger in the center of the expanded region and smaller in the periphery.

Table 7.2 summarizes time sequence of the expansion process throughout the five-week-long experiment. Triggered by the increase in expander volume, the average area stretch  $\vartheta$  increases monotonically. At the end of week five, when the expander is filled to 280 cc, the average area stretch is  $\vartheta_{\text{avg}} = 1.87$ , the maximum area stretch in the center region is  $\vartheta_{\text{max}} = 4.05$ , and the minimum area stretch in the periphery is  $\vartheta_{\text{min}} = 0.53$ . The geometric reconstruction error is largest for the initial configuration with a value of 4.7%, but takes values on the order of 1% for the remaining period of the experiment.

### 7.3.3 Characterization of Growth

Figure 7.4, bottom, shows the kinematics associated with growth  $\mathbf{F}^g$  as the mapping from the ex vivo pre-expansion configuration to the ex vivo post-expansion configuration. Since we cannot compare the explanted ungrown and grown configurations of one and the same

Table 7.2: Characterization of average, maximum, and minimum expansion-induced area stretch between the in vivo pre-expansion and in vivo post-expansion configurations. Throughout the five-week-long experiment, the expander volume increases weekly by 50 cc until it reaches its final value of 280 cc.

time (weeks)	volume (cc)	$\vartheta_{\text{avg}}$ (-)	$\vartheta_{\text{max}}$ (-)	$\vartheta_{\text{min}}$ (-)	error (%)
0 <sup>pre</sup>	0	1.00	1.00	1.00	4.7
0 <sup>post</sup>	50	1.17	2.49	0.41	0.9
1 <sup>pre</sup>	50	1.27	3.25	0.54	1.2
1 <sup>post</sup>	100	1.31	2.79	0.50	1.0
2 <sup>pre</sup>	100	1.38	2.86	0.37	0.9
2 <sup>post</sup>	150	1.43	3.21	0.33	1.0
3 <sup>pre</sup>	150	1.65	3.21	0.48	1.2
3 <sup>post</sup>	200	1.73	4.08	0.46	1.5
4 <sup>pre</sup>	200	1.73	3.50	0.36	1.2
4 <sup>post</sup>	250	1.77	3.52	0.48	1.2
5 <sup>pre</sup>	250	1.86	3.81	0.73	1.4
5 <sup>post</sup>	280	1.87	4.05	0.53	0.6

patch, we postulate that the dorsal midline acts as symmetry plane and assume that the amount of prestrain in the left caudal region (P) is equivalent to the amount of prestrain in the right caudal region (Q).

Figure 7.5, bottom, summarizes the kinematics associated with growth. To stretch the ex vivo post-expansion skin patch of average dimensions of 8.3 cm  $\times$  8.3 cm to the size of the explanted grown tissue patch of average dimensions of 12.5 cm  $\times$  12.5 cm, skin needs to grow by  $\vartheta^g = 2.25$ . This corresponds to an area increase of 125% from the ex vivo pre-expansion to the ex vivo post-expansion skin patch. When compared to the in vivo post-expansion patch of average dimensions of 13.7 cm  $\times$  13.7 cm, the ex vivo post-expansion tissue patch shrinks by 17%, which corresponds to an elastic area stretch of  $\vartheta^e = 1.20$ .

Figure 7.8 illustrates the characterization of growth using multi view stereo and isogeometric analysis. The first column shows the in vivo pre-expansion configuration with the build-in prestretch  $\vartheta^p = \det(\mathbf{F}^p)$ . The second column showcases the in vivo post-expansion configuration, the physiological state after the expander has been filled to its full capacity, for which the area change is  $\vartheta \vartheta^p = \det(\mathbf{F} \cdot \mathbf{F}^p)$ . The third column alludes to the ex vivo post-expansion configuration of the explanted, stress free, grown patch, which characterizes

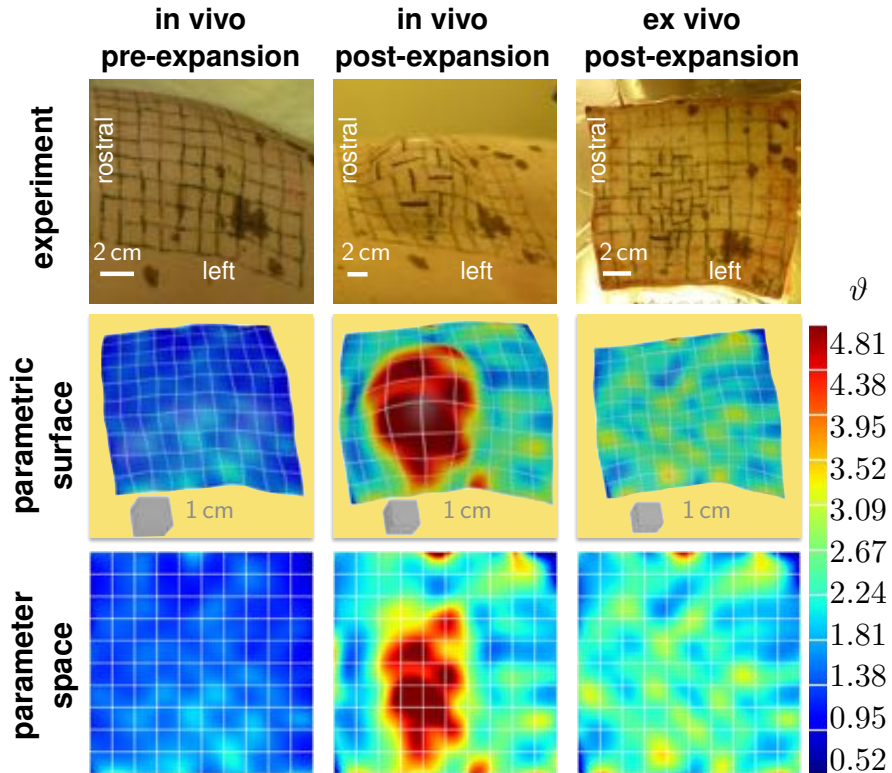


Figure 7.8: Characterization of growth using multi view stereo and isogeometric analysis. Representative photographs of the experimental setup (top) enable reconstruction of the skin geometry using multi view stereo (middle) to calculate the area change using isogeometric analysis (bottom). The area change in the in vivo pre-expansion state characterizes the amount of pre-strain  $\vartheta^P$  (left). The area change in the in vivo post-expansion configuration includes combined effects of pre-strain and expansion-induced deformation  $\vartheta \vartheta^P$  (middle). The area change in the ex vivo post-expansion configuration characterizes the amount of growth  $\vartheta^g$  (right).

area growth as  $\vartheta^g = \det(\mathbf{F}^g)$ . For each configuration in Figure 7.8 we show a representative photograph of the experimental setup, the isoparametric surface reconstruction with the contour plot of the area change, and the contour plot in the isoparametric parameter space. The contour plots reveal that deformation-induced changes in surface area vary drastically across the tattooed patch: It appears that skin grows fastest in zones with highest overall deformation induced by expander inflation.

Table 7.3: Characterization of average, maximum, and minimum area stretch between the ex vivo pre-expansion and in vivo post-expansion configurations and area growth between the ex vivo pre-expansion and ex vivo post-expansion configurations.

total area change	$(\vartheta \vartheta^P)_{\text{avg}}$ (-)	$(\vartheta \vartheta^P)_{\text{max}}$ (-)	$(\vartheta \vartheta^P)_{\text{min}}$ (-)	error ( %)
ex vivo → in vivo post	2.70	6.99	0.53	13.1
area growth	$\vartheta^g_{\text{avg}}$ (-)	$\vartheta^g_{\text{max}}$ (-)	$\vartheta^g_{\text{min}}$ (-)	error ( %)
ex vivo → ex vivo post	2.25	4.81	0.52	13.1

Table 7.3 summarizes the results of the total deformation analysis of combined prestrain and deformation and of the growth analysis. When compared to the ex vivo pre-expansion patch, the in vivo post-expansion patch has undergone a total area stretch of  $(\vartheta \vartheta^P)_{\text{avg}} = (\vartheta^e \vartheta^g)_{\text{avg}} = 2.70$ , a maximum area stretch of  $(\vartheta \vartheta^P)_{\text{max}} = (\vartheta^e \vartheta^g)_{\text{max}} = 6.99$ , and a minimum area stretch of  $(\vartheta \vartheta^P)_{\text{min}} = (\vartheta^e \vartheta^g)_{\text{min}} = 0.53$ . When compared to the ex vivo pre-expansion patch, the ex vivo post-expansion patch has undergone an average area growth of  $\vartheta^g_{\text{avg}} = 2.25$ , a maximum area growth of  $\vartheta^g_{\text{max}} = 4.81$ , and a minimum area growth of  $\vartheta^g_{\text{min}} = 0.52$ . i.e., the patch has more than doubled its initial area. The average reconstruction errors are 13.1% and 13.1%.

## 7.4 Discussion

We have designed and prototyped a novel experiment to quantitatively characterize the mechanics of living skin using multi view stereo and isogeometric analysis. Our average reconstruction error of the order of 1% suggests that this method can serve as a highly accurate, easy-to-use tool to reconstruct arbitrary three-dimensional surfaces.

Skin displays an incredible ability to adapt to mechanical cues from which we benefit in

all day life during our development, growth, and wound healing. Understanding the biomechanics and mechanobiology of skin has received great attention: It can impact the design of medical devices, improve cosmetic products, and influence the outcomes of surgical procedures. Not surprisingly, intense research has been dedicated to characterize the mechanical properties of explanted, isolated specimens of skin. Yet, the mechanical characteristics of *living* skin in its natural environment remain poorly understood.

Here we perform controlled experiments of living skin to characterize prestrain, deformation, and growth in a minipig model of skin expansion. We take advantage of two recent trends in computer graphics: multi view stereo and isogeometric analysis. Multi view stereo is a technique to reconstruct of three-dimensional shapes from several two-dimensional images of the same scene. One of its major advantages is that it naturally captures physiologically relevant surface characteristics across the entire scene. Based on easy-to-create hand-held camera images, multi view stereo is less expensive and more versatile than conventional, geometrically restrictive laboratory experiments. Isogeometric analysis allows us to use the resulting three-dimensional reconstructions to create smooth parametric surface representations. Isogeometric surfaces naturally satisfy the continuity requirements of thin membranes with relatively few arbitrary control points in space. To create a fixed set of control points, we tattooed a permanent grid onto the skin surface. This allows us to precisely quantify the relative deformation between different points in space and time and to identify regions of local extrema. Embedded into the framework of fictitious configurations, our isogeometric analysis naturally defines finite prestrain, deformation, and growth.

#### 7.4.1 Skin Prestrain

Our study shows that living skin is prestrained with an average area stretch of  $\vartheta^P=1.44$ . The existence of prestrain in skin is in agreement with previous findings [182]. The amount of natural prestrain is also consistent, at least in magnitude, with experiments of humans skin, which report an average prestretch of 1.57 in the forearm [112]. While prestrain has been widely characterized in arteries using opening angle experiments [114], disappointingly few studies address the natural tension in skin. Some studies attempt to address this without excising the tissue, but recognize that this approach has severe limitations [111]. To our knowledge, our study is the first to characterize the regional distribution of prestrain across a sizable patch of skin. Naturally, a potential limitation is that the excised patch itself may still be under internal tension, which we could further release by cutting the patch into

successively smaller pieces.

Prestain has significant implications for our understanding of thin biological membranes [317]. Conceptually, prestrain is superposed to all *in vivo* deformation processes [9]. In the finite strain setting, this superposition is multiplicative - not just additive - which makes the inclusion of prestrain even more relevant: Prestain shifts the stress-stretch curve to the left, here by a stretch of approximately -0.20. This implies that the characteristic strain stiffening associated with the untangling and stretching of collagen fibers takes place much earlier *in vivo* than predicted by *ex vivo* testing. Without including prestrain in the *ex vivo* test setup, the stiffness of skin is hugely overestimated. We have recently shown that the *in vivo* and *ex vivo* stiffnesses of biological membranes may differ by up to three orders of magnitude [316]. Our results support the hypothesis that prestrain is important to position thin biological membranes *in vivo* into their optimal operating range, right at the transition point of the exponential stiffening regime [317].

#### 7.4.2 Skin Deformation

Our study shows that living skin can be stretched locally by up to 4.05 in area without displaying signs of damage or rupture. This remarkable four-fold increase in area is made possible by gradually increasing the deformation over a period of several weeks. Specifically, our study reveals an average area stretch of 1.87 in response to a rectangular 4 cm × 6 cm tissue expander filled to 280 cc. This agrees well with reported values in the literature which range between 1.51 and 2.35 [385]. Several investigations have attempted to quantify the expansion process in the past [48]; however, most of them introduce restrictive approximations and their resolutions are coarse compared to ours. A unique feature of our method is the characterization of regional variations in area change using isogeometric analysis [52]. Our analysis verifies our common intuition that the deformation is not homogeneous across the expanded area: The area change is largest in the center of the expanded region and decays gradually towards the edges of the skin patch. This agrees excellently with our computational simulations of skin growth, which predict a four-fold local area increase in the center region and gradual decay towards the periphery [51].

#### 7.4.3 Skin Growth

Our study shows that skin responds to chronic overstretch by growing in area, in our specific case by a factor 2.25. This implies that the skin patch more than doubled its initial area

within a period of five weeks. Using a symmetric control patch from the same animal, we were able to quantify, for the first time, the amount of skin growth with respect to the stress free ex vivo configuration. We observe that the total area increase of 2.70, which is a result of combined prestretch of 1.44 and expander-induced deformation of 1.87, reflects the combined effects of a reversible elastic stretch of 1.20 and permanent growth of 2.25. Our contour plots display a regional variation of growth with local maxima of 4.81, a four-fold increase in area around the center region, and local minimal of 0.52, a decrease in area around the periphery. This is in excellent agreement with previous experimental measurements [31] and computational predictions [51]. It appears that, in general, regions with large overall deformation also exhibit large growth [417]. However, regions with extreme deformation do display large but not extreme growth. These observations provoke two speculations: First, growth seems to be triggered by chronic mechanical overstretch. Second, the amount of growth seems to be limited by the rate at which new skin can be created. Accordingly, zones with extreme overall deformation may not exhibit extreme growth. A potential limitation is obviously that we only examine the animal for five weeks and do not follow up long-term.

#### 7.4.4 Limitations

Our experimental setup has a few additional limitations: First, as a proof of concept, this study is based on only one minipig, which does not allow us to make statistic statements about the growth process. Second, even though the precision of multi view stereo has rapidly improved within the past decade and we are confident that our geometric reconstructions are sufficiently accurate, our method lacks an exact error measure. Third, the isogeometric analysis relies on following material points from one time point to the next; here, these are the  $11 \times 11$  nodes of the tattooed grid. This may be too coarse for an accurate interpolation, in particular in the analysis of prestrain for which finer grids and a successive subdivision of the explanted patch would be desirable. Fourth, as a first step, we have only considered the area change in skin, while it would be desirable to separately characterize the kinematics along and perpendicular to the directions of tissue anisotropy. Fifth, a longitudinal study with multiple time points of tissue harvest would be desirable to truly quantify the speed of growth. Finally, an obvious limitation is the related to generalizing our findings from animals to human.

## 7.5 Concluding Remarks

We have presented a novel approach towards characterizing the mechanics of thin biological membranes in their natural *in vivo* environment. Our method combines multi view stereo and isogeometric analysis to quantify the kinematics of living skin. We illustrate our approach by means of a porcine model of skin expansion to explore the key aspects of pre-strain, deformation, and growth. Globally, our method reveals an average area prestretch of 1.44, an average area stretch of 1.87 after five weeks of expansion, and an average area growth of 2.25. Beyond quantifying these average global quantities, our method is inherently designed to characterize local variations and identify regions of extreme deformation. Locally, our analysis reveals a maximum prestretch of 2.37 in the ventral region, a maximum expansion-induced area stretch of 4.05 in the center region of the expander, and a maximum area growth of 4.81 in the region of maximum stretch. The next logical step would be to identify the underlying biochemical mechanisms of prestrain, deformation, and growth and correlate them to our kinematic measurements. Our study has immediate impact on understanding living skin to optimize treatment planning and establish predictive tools to guide surgical decision making. Our experimental design has broad applications beyond skin expansion: It is a robust, inexpensive, easy-to-use tool for the surface reconstruction of living membranes, which are difficult to characterize in a conventional laboratory setup.

## Chapter 8

# Multi-view Stereo Analysis Reveals Anisotropy of Prestrain, Deformation, and Growth in Living Skin

**Abstract.** Skin expansion delivers newly grown skin that maintains histological and mechanical features of the original tissue. Although it is the gold standard for cutaneous defect correction today, the underlying mechanisms remain poorly understood. Here we present a novel technique to quantify anisotropic prestrain, deformation, and growth in a porcine skin expansion model. Building on our recently proposed method, we combine two novel technologies, multi-view stereo and isogeometric analysis, to characterize skin kinematics: Upon explantation, a unit square retracts *ex vivo* to a square of average dimensions of  $0.83 \times 0.83$ . Upon expansion, the unit square deforms *in vivo* into a rectangle of average dimensions of  $1.40 \times 1.34$ . Deformations are larger parallel than perpendicular to the dorsal midline suggesting that skin responds anisotropically with smaller deformations along the skin tension lines. Upon expansion, the patch grows *in vivo* by  $1.62 \times 1.40$  with respect to the explanted, unexpanded state. Growth is larger parallel than perpendicular to the midline, suggesting that elevated stretch activates mechanotransduction pathways to stimulate tissue growth. The proposed method provides a powerful tool to characterize the kinematics of living skin. Our results shed light on the mechanobiology of skin and help us to better understand and

optimize clinically relevant procedures in plastic and reconstructive surgery.

## 8.1 Introduction

Skin expansion is a common technique in plastic and reconstructive surgery [270]. It is based on the evidence that skin grows and remodels to achieve mechanical homeostasis [92, 342]. During the procedure, an expander is placed below the skin and inflated periodically to chronically overstretch the tissue beyond its physiological limit [288, 417]. Skin grows *in situ* producing local flaps that can be used to correct large defects such as giant congenital nevi, burn injuries, and regions of tumor removal [139, 231, 239]. Fig. 8.1 illustrates the use

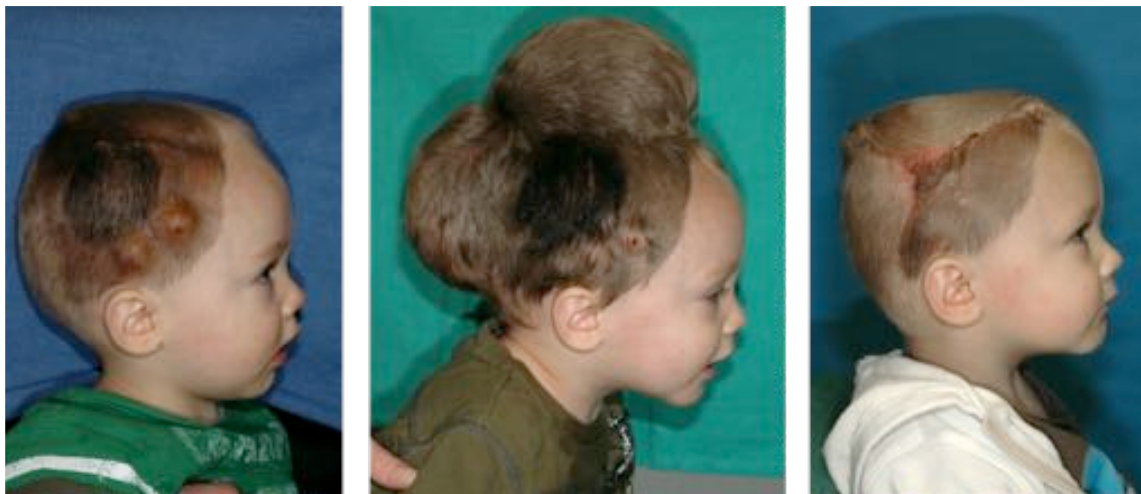


Figure 8.1: Skin expansion is routinely performed in reconstructive surgery to correct large cutaneous defects. To grow extra skin for defect repair, tissue expanders are implanted underneath the skin, left. The expanders are gradually filled with saline solution to apply mechanical overstretch and trigger controlled skin growth, middle. Several weeks post implantation, the expanders are removed, the defect is excised, and the defect area is covered by the newly grown skin, right.

of skin expansion to correct a cutaneous defect in a one year-old boy with a giant congenital nevus [419]. To grow extra skin for defect repair, two tissue expanders are implanted and gradually filled with saline solution, left. Expander inflation creates mechanical overstretch and triggers controlled skin growth, middle. After several weeks, the expanders are removed, the nevus is excised, and the defect area is covered with the newly grown skin, right [56]. One preeminent advantage of this technique is the production of skin with the same hair,

mechanical properties, color and texture of the surrounding tissue, making it ideal from an aesthetic point of view [319]. At the same time, tissue expansion remains challenging, several open questions prevail, and surgeons have to rely on their own decade-long experience to successfully plan and execute this technique [39].

In response to the indisputable importance of mechanical factors during the skin expansion process [299], we have proposed a mathematical model to capture the relationship between overstretch and skin adaptation using the theory of finite growth within a continuum mechanics framework [52]. We have successfully applied our model to different expander geometries as well as different patient specific scenarios, and we have shown good qualitative comparison with the clinical observations [51, 418]. Computational models are being steadily integrated into medical applications and hold the promise of enhancing medical device design and improving treatments efficacy in reconstructive surgery [55]. Measuring and predicting prestrain, deformation, and growth during a routine skin expansion procedure is practically impossible and the usefulness of a computational approach is unquestionable [286]. However, despite the increasing acceptance of computational tools, their integration into clinically relevant scenarios is slow due to the lack of experimental data to calibrate and validate the models.

Here we establish a chronic porcine model to quantify skin kinematics during tissue expansion. This work builds on our recently proposed methodology to characterize prestrain, deformation, and growth [54]. Our experimental setup uses two novel technologies that allow us to obtain the desired data without imposing constraints on a regular expansion procedure: We employ multi-view stereo techniques to reconstruct the three dimensional geometry out of photographs, and adopt isogeometric analysis tools to describe the kinematics of thin membranes. We decompose the total deformation of tissue expansion using the concept of incompatible configurations. The continuum interpolation of the displacement field allows us to quantify regional variations of prestrain, deformation, and growth.

Multi-view stereo (MVS) is the extraction of three-dimensional geometries out of photographs. Originally motivated by the need of creating volumetric representations from medical images, this field of computer vision has seen growing research interest in the past decade [157, 335]. In a very simplistic manner, MVS can be understood by considering first binocular stereo. Animals generate depth information from two images since the brain knows the calibration parameters of one eye with respect to the other. In MVS algorithms, such parameters are unknown, however, by having many pairs of images from a single scene,

we can determine the calibration values based on feature matching [87]. The accuracy of MVS, with errors as low as 2%, together with its low cost and ease of use, rivals once believed unbeatable reconstruction techniques such as laser scanning [117]. In the field of experimental biomechanics, common reconstruction techniques employ restrictive experimental setups and specialized equipment to track material points [236, 374]. The fact that we can readily appreciate the deformations of skin with our naked eye naturally suggests the possibility of capturing its shape by tracking a few interpolatory points with MVS techniques.

B-splines are used commonly as basis functions for smooth interpolation of curves and surfaces in the CAD (Computer Aided Design) industry [298]. Mechanical analysis relies heavily on the finite element technologies based on discretizing the spatial domain by meshing it into several small pieces [166]. Recently, an effort to bridge the gap between design and analysis has brought forth isogeometric analysis (IGA) [167]. The main idea behind IGA is to employ the same basis functions that lie beneath the CAD technology to solve partial differential equations in the exact geometric representation. IGA has received significant attention in recent years and has shown tremendous potential for thin shell analysis [188]. B-spline basis functions offer an advantageous building block for smooth parametric representation of surfaces with high continuity and good approximation over relatively coarse meshes [57].

During skin expansion, tracking a small set of points becomes practical with MVS algorithms. Then, from the coordinates of a few material points, B-spline tensor product patches with a prescribed parametrization can smoothly interpolate deformations using the IGA concept. Using simple finite element meshes to parametrize the deformation would yield strain fields with poor spatial resolution and would require additional subdivision steps [133].

Skin is a thin biological membrane that constitutes our interface with the outside world displaying noteworthy mechanical properties under large strains [112]. Like all biological systems, it actively adapts to its mechanical environment by growth, remodeling, and morphogenesis [361]. When skin is mechanically loaded, the observable changes in the geometrical configuration over time become a combination of reversible and irreversible contributions [8]. The deformation gradient extracted from the IGA membrane description is the key object that links mechanical cues to the final amount of skin growth. For soft tissues, growth can be expressed kinematically through the multiplicative decomposition

of the deformation gradient into elastic and growth components [209]. For skin as a thin membrane, we assume that growth takes place exclusively in the plane, and the growth tensor is symmetric and orthotropic [419].

## 8.2 Methods

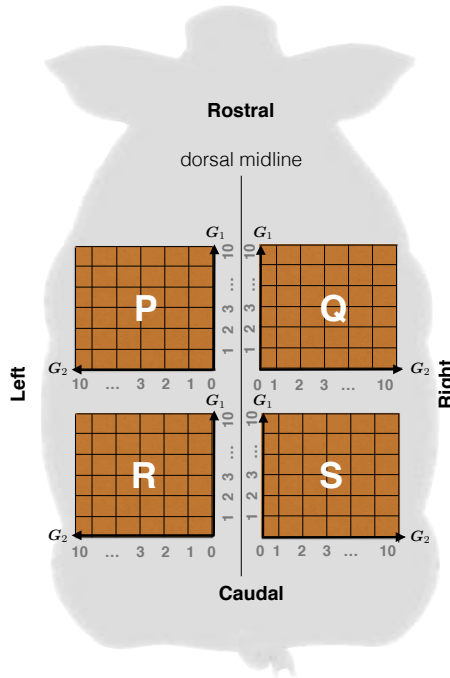


Figure 8.2: Nomenclature for the tattooed grids on the porcine model. We label the grids as **P** anterior-left, **Q** anterior-right, **R** posterior-left, and **S** posterior-right. Symmetry with respect to the midline ensures expanded and control grids. Coordinates on the grid parametrize each zone along the directions  $G_1$ , parallel to the dorsal midline, and  $G_2$ , perpendicular to the dorsal midline along the skin tension lines.

### 8.2.1 Animal Model

Porcine models are a natural choice for tissue expansion [28]. Experiments in porcine models have improved our understanding of the histological and biomechanical changes of

skin upon hyper-stretch [181]. The main reason to choose a porcine expansion model is the similarity between the anatomical and mechanical characteristics of human and young porcine integument [257, 258, 263]. From a clinical point of view, tissue expansion in the pig is similar to tissue expansion in humans, with similar criteria for expander selection, filling volume, and inflation timing [28].

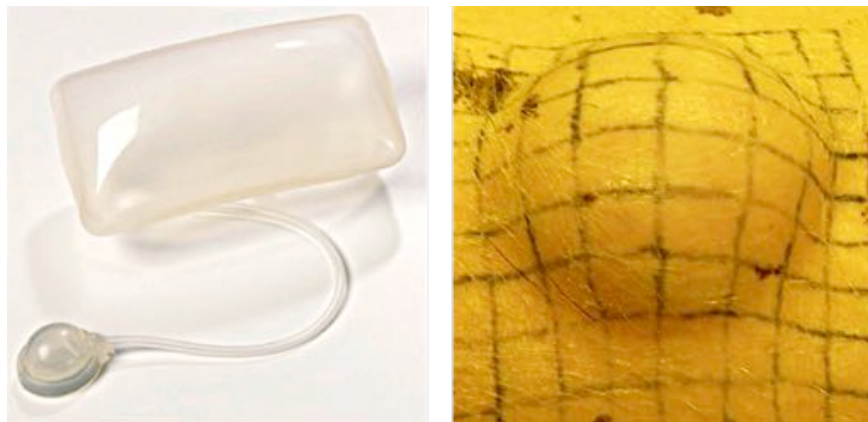


Figure 8.3: Skin expansion in a chronic porcine model. The rectangular tissue expander, left, is implanted subcutaneously underneath a tattooed  $10\text{ cm} \times 10\text{ cm}$  grid and gradually inflated over a period of five weeks. Skin expansion creates mechanical overstretch and triggers controlled skin growth, right.

### Surgical Procedure

We perform skin expansion on a month-old Yucatan pig (Sinclair Biolabs, Columbus, MO) [54]. The pig acclimated to the laboratory facilities at the Robert H. Lurie Children's Hospital of Chicago according to approved protocols. Following the arrangement in Fig. 8.2, we tattoo four  $10\text{ cm} \times 10\text{ cm}$  grids on the back of the pig, symmetrically with respect to the midline. We parameterize each grid discretely with coordinates in the interval  $[0, 10]$  along the directions  $\mathbf{G}_1$  and  $\mathbf{G}_2$ . We implant two expanders of  $4\text{ cm} \times 6\text{ cm}$  with filling volumes of 120cc as shown in Fig. 8.3 (PMT Corporation, Chanhassen, MN), one in the anterior-right grid Q, and one in the posterior-left R. Grids P and S serve as controls. After inserting the expanders, we wait 14 days to allow the wounds to heal until we remove the sutures.

### Skin Expansion

Expansion begins after the initial sutures heal. On day  $t = 0$ , we begin the expansion by injecting 25cc of saline solution into the anterior expander Q and 50cc into the posterior expander R. We repeat this protocol weekly at days  $t = 8, 15, 22$ , and 29. On day  $t = 35$ , we complete the expansion with a final injection of 15cc and 30cc into the anterior Q and posterior R expanders. Each week, we acquire the deformation by taking 15 photographs from different angles, both before and after expansion.

### Tissue Harvest and Euthanasia

On day  $t = 38$ , we anesthetize the animal and acquire the last set of *in vivo* photographs of the tattooed grids. We then euthanize the animal by using intravenous overdose of pentobarbital (90mg/kg) and excise the four grids. We photograph the excised samples *ex vivo* for further reconstruction and analysis.

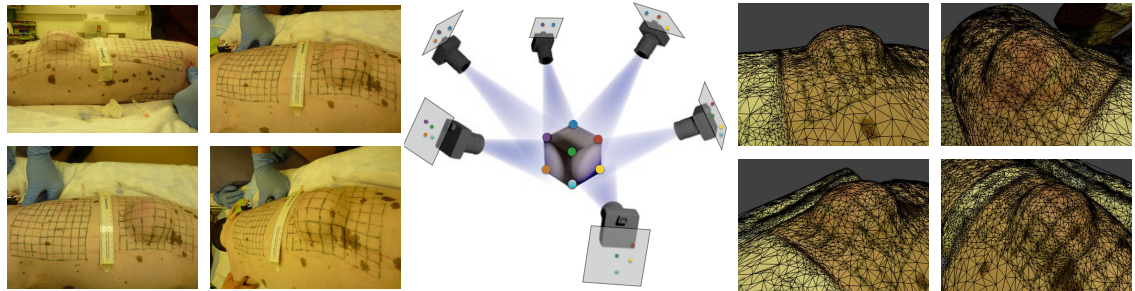


Figure 8.4: Multi-view stereo (MVS) reconstruction. The top shows four photographs of the experimental setup. As illustrated in the middle, the MVS algorithm finds common features between pairs of photographs to find the camera calibration parameters. The bottom depicts four different views of the reconstructed, triangulated surface.

#### 8.2.2 Multi-View Stereo

At the end of the experiment, we have collected seven sets of photographs, pre and post expansion, from 15 different angles for each grid [54]. Fig. 8.4, middle, illustrates this setting. MVS algorithms match common points in pairs of photographs to calculate the camera position and extract the coordinates of these points in the three-dimensional Euclidean space  $\mathbb{R}^3$ . The details of MVS algorithms escape the focus of the present publication; we refer the interested reader to the literature for further details [87]. We adopt an online service

for the geometric reconstruction of our experimental setup [23]. Fig. 8.4, top, shows four different views of a particular time point of interest, while Fig. 8.4, bottom, illustrates the resulting surface reconstruction approximated with a triangular mesh.

To quantify the accuracy of the reconstruction, we include a ruler in the photograph and we fit a cubic spline to the points to the 1cm marks of the ruler. We calculate the length  $l_i$  between every pair of points along the spline and obtain the average length  $\bar{l}$ . We defined the relative reconstruction error  $e$  as

$$e = \frac{\sum e_i}{n} \quad \text{with} \quad e_i = \frac{l_i - \bar{l}}{\bar{l}}, \quad (8.1)$$

where  $n$  is the number of spline sections and  $\bar{l}$  is the scaling factor with respect to the physical world where  $\bar{l} = 1\text{cm}$ . Fig. 8.2 illustrates each grid with 121 material points parametrized by a tensor product space of coordinates along directions  $\mathbf{G}_1$ , parallel to the dorsal midline, and  $\mathbf{G}_2$ , perpendicular to the dorsal midline along the skin tension lines. For example, the points  $\mathbf{P}_{ab}^t \in \mathbb{R}^3$  from the MVS reconstruction specify the grid  $\mathbf{P}$  at time  $t$ , with  $a, b$  the integers in the interval  $[0, 10]$ .

### 8.2.3 B-Spline Based Isogeometric Analysis

#### B-spline Curves

A B-spline curve is a piece-wise polynomial function that maps a segment of a line to the three-dimensional Euclidean space  $\gamma : \xi \in \mathbb{R} \rightarrow \mathbb{R}^3$ . The representation of B-spline curve of degree  $p$  requires a knot vector  $\Xi$  and a set of control points  $\mathbf{P}_i \in \mathbb{R}^3$ . The knot vector consists of non-decreasing numbers  $\Xi = [\xi_0, \xi_1, \dots, \xi_n]$ . The number of control points is  $m = n - p - 1$ . The first and last values of the knot vector  $\xi_0$  and  $\xi_n$  are repeated  $p + 1$  times. We define basis functions recursively. The zeroth order basis functions are

$$N_{i,0} = \begin{cases} 1 & \xi_i \leq \xi < \xi_{i+1} \\ 0 & \text{otherwise.} \end{cases} \quad (8.2)$$

Higher order functions of degree  $p \geq 1$  follow from the recursive definition,

$$N_{i,p} = \frac{\xi - \xi_i}{\xi_{i+p} - \xi_i} N_{i,p-1}(\xi) + \frac{\xi_{i+p+1} - \xi}{\xi_{i+p+1} - \xi_{i+1}} N_{i+1,p-1}(\xi). \quad (8.3)$$

The B-spline curve  $\gamma$  is the sum of the basis functions and control points,

$$\gamma = \sum_{i=0}^m N_{i,p}(\xi) \mathbf{P}_i. \quad (8.4)$$

### B-spline Surfaces

There are several alternatives to create surfaces based on B-spline basis functions. We employ tensor product surfaces, which are constructed from a tensor product of two B-spline curves. A B-spline surface is a map from the parametric two-dimensional space to the Euclidean three-dimensional space  $\mathcal{S} : \boldsymbol{\xi} = [\xi, \eta] \in \mathbb{R} \times \mathbb{R} \rightarrow \mathbb{R}^3$ . This implies that we require two knot vectors  $\Xi$  and  $\Omega$  that define two sets of basis functions  $N_{i,p}$  and  $Q_{j,q}$ . The B-spline surface is then defined with the control net  $\mathbf{P}_{i,j} \in \mathbb{R}^3$

$$\mathcal{S} = \sum_{i=0}^m \sum_{j=0}^r N_{i,p}(\xi) Q_{j,q}(\eta) \mathbf{P}_{i,j} \quad (8.5)$$

### B-Spline Isogeometric Analysis of Skin Expansion

Here we explain the analysis for region P, but it similarly applies for the other three regions Q, R, and S. We begin with the 121 points  $\mathbf{P}_{ab}^t$  for time  $t$ . We fit a bi-cubic B-spline surface patch  $\mathcal{S}^t(\xi, \eta)$  with the following parametrization: We choose the knot vectors to be  $\boldsymbol{\xi} = \boldsymbol{\eta} = [0, 0, 0, 0, 2, 3, \dots, 9, 10, 10, 10, 10]$  and we interpolate such that  $\mathbf{P}_{ab}^t = \mathcal{S}^t(\hat{\xi}_a, \hat{\eta}_b) \forall t$ , with  $\hat{\xi}_a = a$ ,  $\hat{\eta}_b = b$  constant for all interpolations. As a result the parametrization remains the same for any time point.

Any given pair of time points  $t = t_1, t_2$  defines a pair of surfaces  $\mathcal{S} = \mathcal{S}^{t_1}, \mathcal{S}^{t_2}$ . We choose  $t_1$  as the reference and  $t_2$  as the deformed configuration of the mid-surface of the membrane under study. Fig. 8.5-left shows the reference surface,  $\mathcal{S}^{t_1}$ , embedded from the parametric plane  $\boldsymbol{\xi} = [\xi, \eta] = \mathbb{R} \times \mathbb{R}$  into the three-dimensional Euclidian space. Fig. 8.5-right shows the deformed surface,  $\mathcal{S}^{t_2}$ , also embedded from  $\boldsymbol{\xi}$ . As a consequence of using the same parametric domain for both surfaces, points  $\mathbf{x}^{t_1}, \mathbf{x}^{t_2}$  follow from summation over the same basis functions  $R_{ab}$ ,

$$\begin{aligned} \mathbf{x}^{t_1} &= \mathcal{S}^{t_1}(\boldsymbol{\xi}) = \sum_{a,b=0}^{10} R_{ab}(\boldsymbol{\xi}) \mathbf{P}_{ab}^{t_1} \\ \mathbf{x}^{t_2} &= \mathcal{S}^{t_2}(\boldsymbol{\xi}) = \sum_{a,b=0}^{10} R_{ab}(\boldsymbol{\xi}) \mathbf{P}_{ab}^{t_2}. \end{aligned} \quad (8.6)$$

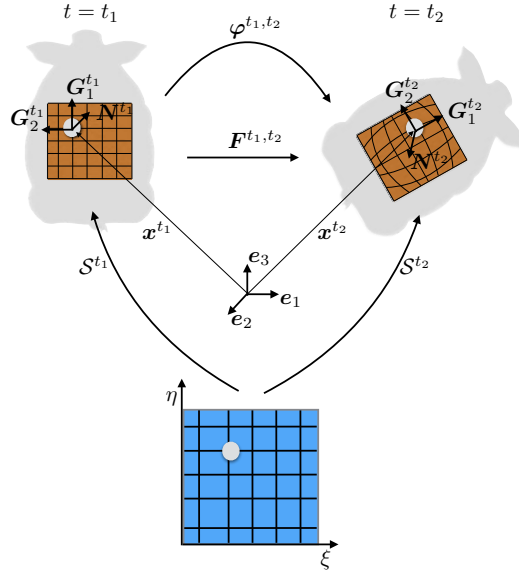


Figure 8.5: Kinematics. Any pair of time points  $t_1, t_2$  defines a pair of surface embeddings  $\mathcal{S}^{t_1}, \mathcal{S}^{t_2}$  from the same parametric domain  $\xi$  into the three dimensional space  $\mathbb{R}^3$ . At every point  $\mathbf{x}^{t_1}$ , the covariant vectors  $\mathbf{G}_1^{t_1}, \mathbf{G}_2^{t_1}$  span the tangent space of the surface, and together with the normal  $\mathbf{N} = \mathbf{G}_3^{t_1}$  they are a basis for  $\mathbb{R}^3$ . The same is true for  $\mathbf{x}^{t_2}$ . The deformation map between the two configurations is  $\varphi^{t_1, t_2}$  and its spatial gradient is  $\mathbf{F}^{t_1, t_2}$ .

Fig. 8.5 depicts the deformation map  $\varphi^{t_1, t_2}$ , which establishes the relationship between the reference and deformed membranes. The deformation map,  $\varphi^{t_1, t_2}(\xi) : \mathcal{S}^{t_1} \rightarrow \mathcal{S}^{t_2}$ , takes a material point from the reference surface,  $\mathcal{S}^{t_1}$ , to the position of that point on the deformed surface  $\mathcal{S}^{t_2}$  [54]. In Kirchhoff-Love kinematics, the normal to the reference mid-surface remains normal and there is no deformation across the thickness as the membrane deforms [57]. The material points of the deformed membrane can be located by a displacement vector  $\mathbf{u}^{t_1, t_2}$  of the mid-surface alone,

$$\mathbf{x}^{t_2} = \varphi^{t_1, t_2}(\mathbf{x}^{t_1}) = \mathcal{S}^{t_2}(\xi) + \mathbf{u}^{t_1, t_2}(\xi), \quad (8.7)$$

or, by incorporating the B-spline surface definition,

$$\mathbf{x}^{t_2} = \sum_{a,b=0}^{10} R_{ab}(\xi) (\mathbf{P}_{ab}^{t_1} + \mathbf{u}_{ab}^{t_1, t_2}). \quad (8.8)$$

Since our geometric description is based on curvilinear coordinates, the tangent space at the point  $\mathbf{x}^{t_1}$  is spanned locally by the covariant basis vectors,

$$\begin{aligned}\mathbf{G}_1^{t_1} &= \sum_{a,b=0}^{10} R_{ab,\xi} \mathbf{P}_{ab}^{t_1} \\ \mathbf{G}_2^{t_1} &= \sum_{a,b=0}^{10} R_{ab,\eta} \mathbf{P}_{ab}^{t_1},\end{aligned}\tag{8.9}$$

where a comma denotes the partial differentiation. This implies that  $\mathbf{G}_1^{t_1}$  are the tangent vectors to the coordinate lines aligned with the longitudinal axis of the pig, while  $\mathbf{G}_2^{t_1}$  are the tangent vectors to the coordinate lines in the transverse direction illustrated in Figures 8.2 and 8.5. We extend the covariant basis vectors with the normal,

$$\mathbf{G}_3^{t_1} = \mathbf{N}^{t_1} = \frac{\mathbf{G}_1^{t_1} \times \mathbf{G}_2^{t_1}}{\|\mathbf{G}_1^{t_1} \times \mathbf{G}_2^{t_1}\|}.\tag{8.10}$$

The triad  $\mathbf{G}_i^{t_1}$ ,  $i = 1, 2, 3$  spans the three-dimensional space  $\mathbb{R}^3$  locally, at every point  $\mathbf{x}^{t_1}$  as shown in Figure 8.5. The dual basis is composed of contra-variant vectors  $\mathbf{G}_{t_1}^i$  that satisfy  $\mathbf{G}_{t_1}^i \cdot \mathbf{G}_j^{t_1} = \delta_j^i$ , where  $\delta_j^i$  denotes the Kronecker delta. The deformed covariant basis vectors follow from the partial differentiation of the deformed surface with respect to the parametric coordinates,

$$\begin{aligned}\mathbf{G}_1^{t_2} &= \mathbf{G}_1^{t_1} + \sum_{a,b=0}^{10} R_{ab,\xi} \mathbf{u}_{ab}^{t_1,t_2} \\ \mathbf{G}_2^{t_2} &= \mathbf{G}_2^{t_1} + \sum_{a,b=0}^{10} R_{ab,\eta} \mathbf{u}_{ab}^{t_1,t_2},\end{aligned}\tag{8.11}$$

and we extend the set of these covariant basis with the deformed normal  $\mathbf{G}_3^{t_2} = \mathbf{N}^{t_2}$  such that  $\mathbf{G}_i^{t_2}$  spans the three-dimensional space  $\mathbb{R}^3$  at points  $\mathbf{x}^{t_2}$ . The dual basis of the deformed surface satisfies  $\mathbf{G}_{t_2}^i \cdot \mathbf{G}_j^{t_2} = \delta_j^i$ . The deformation gradient  $\mathbf{F}^{t_1,t_2} = \partial \varphi^{t_1,t_2} / \partial \mathbf{x}^{t_1}$  is the key kinematic object, it encapsulates the local deformation between the reference and deformed surfaces,  $\mathcal{S}^{t_1}$  and  $\mathcal{S}^{t_2}$ . Using the chain rule we map the covariant base vectors of the reference configuration,  $\mathbf{G}_i^{t_1}$ , onto the covariant bases vectors of the deformed configuration,  $\mathbf{G}_i^{t_2}$ , as

$$\mathbf{G}_i^{t_2} = \frac{\partial \varphi^{t_1,t_2}}{\partial \mathbf{x}^{t_1}} \frac{\partial \mathbf{x}^{t_1}}{\partial \xi^i} = \mathbf{F}^{t_1,t_2} \mathbf{G}_i^{t_1}.\tag{8.12}$$

The deformation gradient follows from the summation of the dyadic product of the covariant deformed and contravariant reference basis vectors,

$$\mathbf{F}^{t_1, t_2} = \mathbf{G}_i^{t_2} \otimes \mathbf{G}_{t_1}^i. \quad (8.13)$$

### 8.2.4 Kinematic Analysis of Skin Expansion

Fig. 8.6 displays all configurations of interest. At the beginning of expansion at day  $t = 0$ , skin in vivo is not stretch free [249]: the deformation gradient with respect to the ex vivo state, denoted as  $\mathbf{F}^p$ , characterizes the prestain state [9,111]. From the deformation gradient we calculate the Right Cauchy Green Deformation tensor  $\mathbf{C}^p$ . We are interested in three measures of stretch, the total area change,

$$\vartheta^p = \det(\mathbf{F}^p) \quad \text{with} \quad \mathbf{C}^p = \mathbf{F}^{pt} \cdot \mathbf{F}^p, \quad (8.14)$$

and the two stretches in the covariant directions,

$$\lambda_1^p = \sqrt{\mathbf{G}_1 \cdot \mathbf{C}^p \cdot \mathbf{G}_1} \quad \text{and} \quad \lambda_2^p = \sqrt{\mathbf{G}_2 \cdot \mathbf{C}^p \cdot \mathbf{G}_2}, \quad (8.15)$$

parallel to the dorsal midline and perpendicular to the dorsal midline along the skin tension lines.

Fig. 8.6 illustrates the deformation  $\mathbf{F}$  at day  $t = n$  with respect to the in vivo state. The total deformation,  $\mathbf{F} \cdot \mathbf{F}^p$ , is not fully elastic. Growth can be captured kinematically by splitting the deformation gradient into elastic and growth contributions,  $\mathbf{F}^e \cdot \mathbf{F}^g$ . Fig. 8.6 portrays the map between the ex vivo and the in vivo patch at day  $t = n$ , denoted as  $\mathbf{F}^e$ , which stores the elastic part. The growth part,  $\mathbf{F}^g$ , can be further decomposed into growth occurring naturally,  $\mathbf{F}^{gn}$ , and growth attributed exclusively to the expansion process  $\mathbf{F}^{ge}$ ,

$$\mathbf{F} \cdot \mathbf{F}^p = \mathbf{F}^e \cdot \mathbf{F}^{ge} \cdot \mathbf{F}^{gn} \quad (8.16)$$

This approach implies that only the elastic deformation,  $\mathbf{F}^e = \mathbf{F} \cdot \mathbf{F}^p \cdot \mathbf{F}^{gn-1} \cdot \mathbf{F}^{en-1}$ , generates stress [316]. We assume that skin grows exclusively in the plane while its thickness remains constant [417]. We allow the in plane area growth to be anisotropic with preferred directions  $\mathbf{G}_1$  and  $\mathbf{G}_2$  parallel and perpendicular to the midline, such that the growth tensor

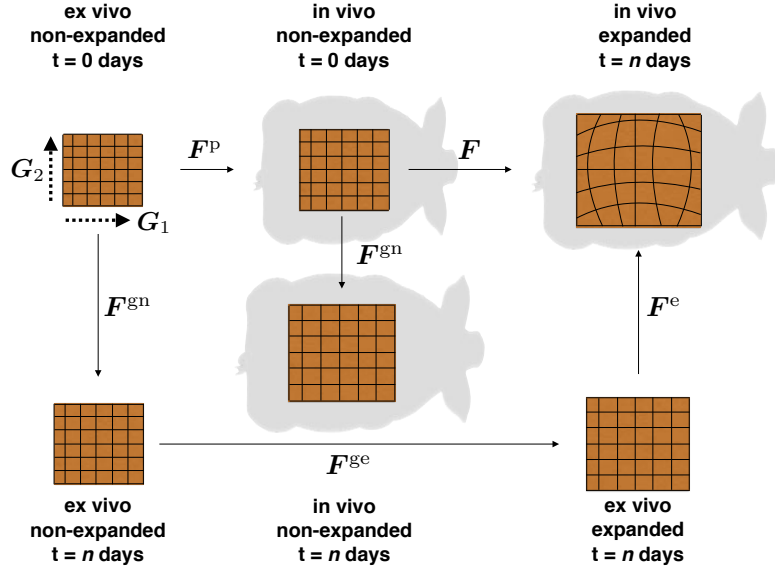


Figure 8.6: Distinct configurations of the skin patch. In vivo, skin is subjected to prestrain,  $\mathbf{F}^P$ . Expansion induces deformation,  $\mathbf{F}$ . Excising the expanded patch releases the reversible, elastic deformation,  $\mathbf{F}^e$ . Skin growth,  $\mathbf{F}^g$ , consists of natural growth,  $\mathbf{F}^{gn}$ , and expansion-induced growth,  $\mathbf{F}^{ge}$ .

takes the following format [134],

$$\mathbf{F}^g = \lambda_1^g \mathbf{G}_1 \otimes \mathbf{G}_1 + \lambda_2^g \mathbf{G}_2 \otimes \mathbf{G}_2 + \mathbf{N} \otimes \mathbf{N}. \quad (8.17)$$

This particular format allows us to multiplicatively correlate area changes associated with the total deformation  $\vartheta$ , prestrain  $\vartheta^P$ , elastic deformation  $\vartheta^e$ , expander-induced growth  $\vartheta^{ge}$ , and natural growth  $\vartheta^{gn}$ ,

$$\vartheta \vartheta^P = \vartheta^e \vartheta^{ge} \vartheta^{gn}. \quad (8.18)$$

The total area growth is simply the product of the stretches parallel and perpendicular to the midline,  $\vartheta^g = \det(\mathbf{F}^g) = \lambda_1^g \cdot \lambda_2^g$ , where the anisotropic growth stretches  $\lambda_1^g = \lambda_1^{gn} \lambda_1^{ge}$  and  $\lambda_2^g = \lambda_2^{gn} \lambda_2^{ge}$  admit the split into natural and expander-induced contributions.

### 8.3 Results

We apply our mathematical analysis to the posterior region R and S. The anterior expansion P and Q failed due to port leakage. The entire expansion process spanned a period of  $t = 37$  days. At the end of the procedure, the expander underneath the left-posterior grid R was filled to 280cc and the unexpanded right-posterior grid S served as control. Fig. 8.7 shows the different configurations of the skin patches with the summary of our analysis. We are interested in quantifying three measures of local deformation: prestrain, deformation, and growth. We have previously quantified isotropic area changes [54], which we include here to complement our current orthotropic characterization.

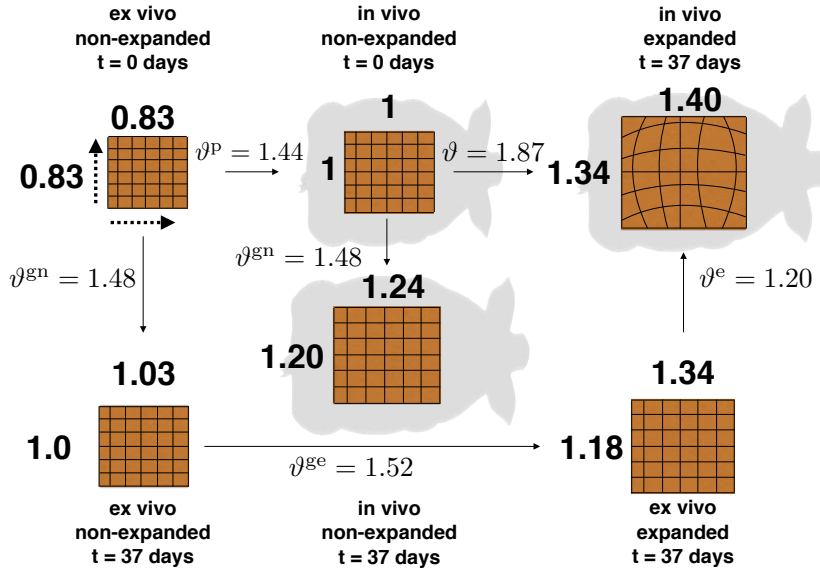


Figure 8.7: Distinct configurations of the skin patch. Upon explantation, an in vivo unit square retracts to a square of dimensions  $0.83 \times 0.83$  due to prestrain. Upon expansion, the unit square transforms into a  $1.40 \times 1.34$  rectangle, with greater stretch in the direction parallel to the midline. During expansion, the patch grows naturally by  $1.24 \times 1.20$ . The final size of the expanded patch includes natural and expander-induced growth, which turns a  $1.03 \times 1.00$  naturally grown patch into the final  $1.34 \times 1.18$  ex vivo patch.

Table 8.1: Summary of prestrain for patch S.

prestrain measure	ex vivo non-expanded $t=37$ days	in vivo non-expanded $t=37$ days
$\vartheta_{\text{avg}}^{\text{P}}$ [-]	1.00	1.44
$\vartheta_{\max}^{\text{P}}$ [-]	1.00	2.37
$\vartheta_{\min}^{\text{P}}$ [-]	1.00	0.63
$\lambda_{1,\text{avg}}^{\text{P}}$ [-]	1.00	1.21
$\lambda_{1,\text{max}}^{\text{P}}$ [-]	1.00	1.62
$\lambda_{1,\text{min}}^{\text{P}}$ [-]	1.00	0.70
$\lambda_{2,\text{avg}}^{\text{P}}$ [-]	1.00	1.21
$\lambda_{2,\text{max}}^{\text{P}}$ [-]	1.00	1.54
$\lambda_{2,\text{min}}^{\text{P}}$ [-]	1.00	0.91
error $e$ [%]	13.1	2.00

### 8.3.1 Prestrain

Tissues in vivo are not stress free [317]. Upon explantation, the flap of skin retracts revealing that skin in vivo is under some amount of deformation. Our experimental setup lets us use the unexpanded control patch to quantify the amount of prestrain. We create two three-dimensional models from the S patch at  $t = 37$  days, once before the animal is sacrificed, once of the excised tissue. The deformation map between these two configurations, indicated as  $\mathbf{F}^{\text{P}}$  in Fig. 8.6, defines the area change due to prestrain at every point across the grid. We assume the excised tissue to be stress free and label the total deformation of skin in vivo as  $\mathbf{F}^{\text{P}}$ . We calculate the local area change as  $\vartheta^{\text{P}} = \det(\mathbf{F}^{\text{P}})$ . We quantify the average area change as  $\vartheta_{\text{avg}}^{\text{P}} = 1.44$ , with maximum and minimum values of  $\vartheta_{\max}^{\text{P}} = 2.37$  and  $\vartheta_{\min}^{\text{P}} = 0.63$ . We calculate the prestretch in the directions of the covariant basis vectors  $\mathbf{G}_1$  and  $\mathbf{G}_2$ , which correspond to the sagittal and transverse directions. The prestretches average  $\lambda_1^{\text{P}} = 1.21$  and  $\lambda_2^{\text{P}} = 1.21$ . Table 8.1 summarizes the results of the prestrain analysis. Fig. 8.8 illustrates the contour plots of the total area prestrain  $\vartheta^{\text{P}}$  as well as the prestretches  $\lambda_1^{\text{P}}$  and  $\lambda_2^{\text{P}}$  parallel to the dorsal midline and perpendicular to the dorsal midline along the skin tension lines.

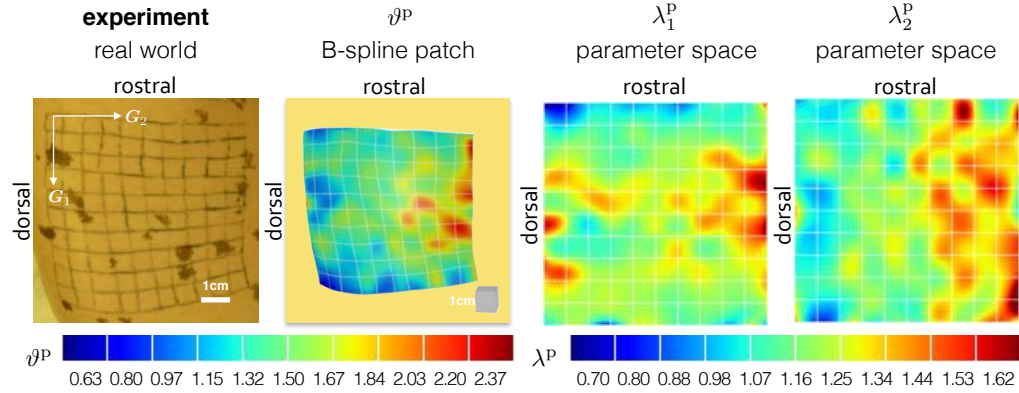


Figure 8.8: Prestrain. The first column shows the experimental setup. The second column shows the geometric representation using a B-spline patch with the overlaid contour plot of the total area change  $\vartheta^P$ , which averages 1.44. The third and fourth columns show the contour plots of the anisotropic prestretches  $\lambda_1^P$  and  $\lambda_2^P$  in the directions parallel and perpendicular to the midline, both directions exhibit average values 1.21

### 8.3.2 Deformation

Fig. 8.7 summarizes the result of the deformation analysis with the non-expanded in vivo patch R at day  $t = 0$  as reference configuration. Every week, we obtain the deformation of the patch with respect to the reference configuration and calculate the corresponding gradient  $\mathbf{F}$ . We are interested in the total area change  $\vartheta$  and two in-plane stretches  $\lambda_1$  and  $\lambda_2$  parallel and perpendicular to the midline. Table 8.2 summarizes the results of the weekly inflations.

The average area stretch increases monotonically with each inflation, reaching a final value of  $\vartheta_{\text{avg}} = 1.87$  with respect to the non-expanded reference patch at day  $t = 0$ . The stretches in the directions parallel and perpendicular to the midline display an interesting trend: The stretch perpendicular to the midline  $\lambda_2$  is always smaller than the corresponding parallel stretch  $\lambda_1$ . This implies that the tissue is stretched more parallel than perpendicular to the long axis of the animal. After the expansion process is complete, the average stretches are  $\lambda_{1,\text{avg}} = 1.40$  and  $\lambda_{2,\text{avg}} = 1.34$ . This deformation corresponds to a unit square stretched to a rectangle of dimensions  $1.40 \times 1.34$  as illustrated in Fig. 8.7.

Fig. 8.9 shows the contour plots of the total area stretch  $\vartheta$  and the stretches  $\lambda_1$  and  $\lambda_2$

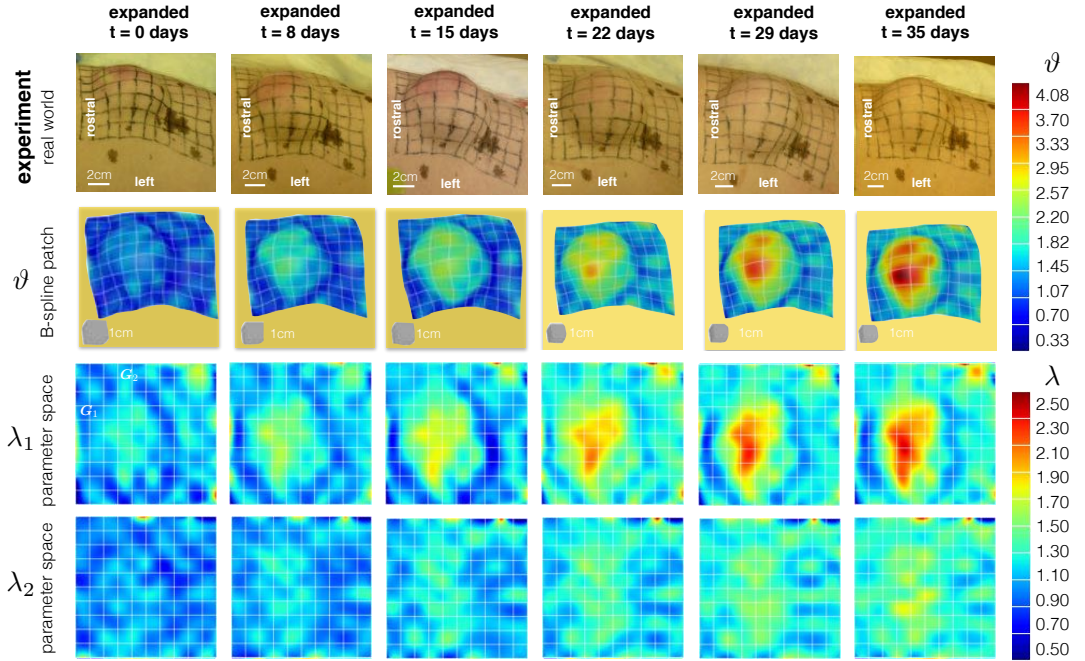


Figure 8.9: Deformation. The columns depict the chronic overstretch due to weekly inflations. The first row shows photographs of the experimental setup at different points in time. Sets of photographs at each time point allow us to reconstruct the B-spline patches in the second row. We are interested in the total area change  $\vartheta$  as well as stretches  $\lambda_1$  and  $\lambda_2$  parallel and perpendicular to the midline. The contour plots reveal larger strains at the center of the expander and smaller strains in the periphery.

parallel and perpendicular to the midline. The total deformation is greater in the center of the expander and it decreases towards the edges of the patch. The stretches  $\lambda_1$  parallel to the midline shows a similar distribution to the total area stretch. The stretches  $\lambda_2$  perpendicular to the midline show slightly higher values near the center of the expander, but their overall contour profile appears to be more homogeneous.

### 8.3.3 Growth

While the expansion process is taking place, the animal undergoes natural growth. We quantify the total physiological growth comparing the control patch  $S$  at days  $t = 0$  and

Table 8.2: Summary of deformation for patch R.

time [days]	volume [cc]	$\vartheta_{\text{avg}}$ [-]	$\vartheta_{\text{max}}$ [-]	$\vartheta_{\text{min}}$ [-]	$\lambda_{1,\text{avg}}$ [-]	$\lambda_{1,\text{max}}$ [-]	$\lambda_{1,\text{min}}$ [-]	$\lambda_{2,\text{avg}}$ [-]	$\lambda_{2,\text{max}}$ [-]	$\lambda_{2,\text{min}}$ [-]	error $e$ %
0	0	1.00	1.00	1.00	1.00	1.00	1.00	1.00	1.00	1.00	4.7
0	50	1.17	2.49	0.41	1.13	2.24	0.52	1.04	2.23	0.45	0.9
8	100	1.31	2.79	0.50	1.19	2.08	0.43	1.10	2.16	0.60	1.0
15	150	1.43	3.21	0.33	1.22	2.29	0.38	1.17	2.58	0.49	1.0
22	200	1.73	4.08	0.46	1.40	2.64	0.39	1.24	2.89	0.70	1.5
29	250	1.77	3.52	0.48	1.36	2.30	0.48	1.29	2.71	0.55	1.2
35	280	1.87	4.05	0.53	1.39	2.43	0.41	1.34	2.72	0.55	0.6

$t = 37$  before the animal is sacrificed. The gradient of the deformation between these two configurations,  $\mathbf{F}^{\text{gn}}$ , is illustrated in Fig. 8.6. The natural area growth is  $\vartheta^{\text{gn}} = \det(\mathbf{F}^{\text{gn}})$ . On average, skin grows naturally by  $\vartheta_{\text{avg}}^{\text{gn}} = 1.49$ . Remarkably, growth is anisotropic averaging  $\lambda_{1,\text{avg}}^{\text{gn}} = 1.24$  and  $\lambda_{2,\text{avg}}^{\text{gn}} = 1.20$  parallel and perpendicular to the midline. Graphically, natural growth can be visualized as a unit square turned into a rectangle of dimensions  $1.24 \times 1.20$  drawn in Fig. 8.7. Table 8.3 compiles these findings.

Table 8.3: Summary of natural growth for patch S.

growth	in vivo non-expanded $t=0$ days	in vivo non-expanded $t=37$ days
$\vartheta_{\text{avg}}^{\text{gn}} [-]$	1.00	1.48
$\vartheta_{\text{max}}^{\text{gn}} [-]$	1.00	2.36
$\vartheta_{\text{min}}^{\text{gn}} [-]$	1.00	1.07
$\lambda_{1,\text{avg}}^{\text{gn}} [-]$	1.00	1.24
$\lambda_{1,\text{max}}^{\text{gn}} [-]$	1.00	1.57
$\lambda_{1,\text{min}}^{\text{gn}} [-]$	1.00	0.78
$\lambda_{2,\text{avg}}^{\text{gn}} [-]$	1.00	1.20
$\lambda_{2,\text{max}}^{\text{gn}} [-]$	1.00	1.83
$\lambda_{2,\text{min}}^{\text{gn}} [-]$	1.00	0.95
error $e$ [%]	2.07	2.00

In response to deformations beyond the physiological limits, skin grows to re-establish a state of mechanical homeostasis. At the end of the expansion procedure, the excised,

expanded tissue patch partially retracts and exposes the reversible, purely elastic part of the deformation  $\mathbf{F}^e$ . We create kinematic representations of the patch R at day  $t = 37$ , both in vivo and ex vivo. The determinant of deformation gradient  $\mathbf{F}^e$  between these two configurations defines the elastic area change, which averages  $\vartheta_{\text{avg}}^e = 1.20$ . The elastic stretches parallel and perpendicular to the midline are  $\lambda_{1,\text{avg}}^e = 1.05$  and  $\lambda_{2,\text{avg}}^e = 1.14$ . Table 8.4 collects these results.

Table 8.4: Summary of purely elastic deformation for patch R.

elastic deformation	ex vivo expanded t=37 days	in vivo expanded t=37 days
$\vartheta_{\text{avg}}^e [-]$	1.00	1.20
$\vartheta_{\text{max}}^e [-]$	1.00	2.52
$\vartheta_{\text{min}}^e [-]$	1.00	0.63
$\lambda_{1,\text{avg}}^e [-]$	1.00	1.05
$\lambda_{1,\text{max}}^e [-]$	1.00	1.63
$\lambda_{1,\text{min}}^e [-]$	1.00	0.61
$\lambda_{2,\text{avg}}^e [-]$	1.00	1.14
$\lambda_{2,\text{max}}^e [-]$	1.00	2.02
$\lambda_{2,\text{min}}^e [-]$	1.00	0.65
error $e [\%]$	1.7	0.6

The remaining deformation of the expanded patch contains the information related to skin growth. The total area growth can itself be understood as the multiplicative decomposition into natural growth and expansion-induced growth,  $\mathbf{F}^g = \mathbf{F}^{ge} \cdot \mathbf{F}^{gn}$ . Following the diagram in Fig. 8.6, we can compute the total growth using the prestrain, natural growth, and elastic deformation tensors already available, then  $\mathbf{F}^g = \mathbf{F}^{e^{-1}} \cdot \mathbf{F} \cdot \mathbf{F}^p$ .

The average total area growth is  $\vartheta_{\text{avg}}^g = 2.25$ , of which  $\vartheta_{\text{avg}}^{ge} = 1.52$  can be attributed exclusively to expansion-induced growth. The average total growth parallel and perpendicular to the midline is  $\lambda_{1,\text{avg}}^g = 1.62$  and  $\lambda_{2,\text{avg}}^g = 1.43$ . Again, we can deduct the amount of natural growth to obtain the average expansion-induced growth  $\lambda_{1,\text{avg}}^{ge} = 1.31$  and  $\lambda_{2,\text{avg}}^{ge} = 1.19$ . Growth of a unit square is anisotropic, both natural growth and expansion-induced growth induce a larger tissue gain parallel to the midline. Table 8.5 summarizes these findings. Fig. 8.10 shows the contour plots of the three different growth quantities.

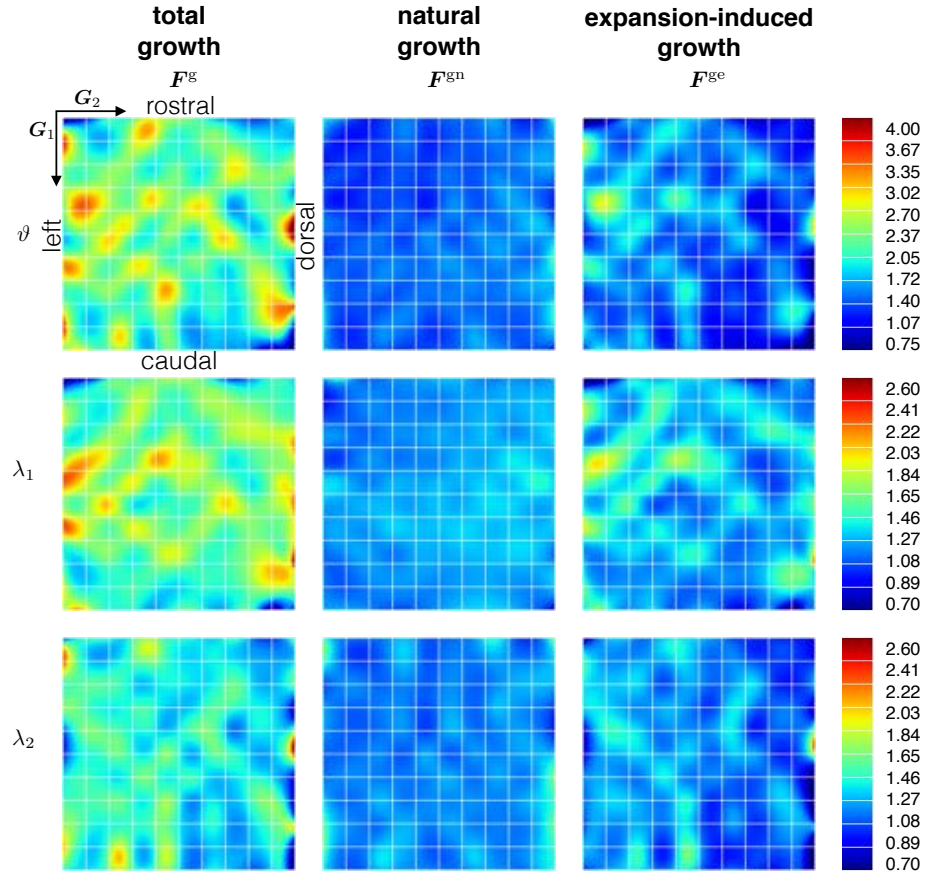


Figure 8.10: Growth. Total, natural, and expansion-induced growth are calculated from prestrain, total deformation, and elastic deformation. The columns show the decomposition of the total growth tensor  $F^g$  into natural growth  $F^{gn}$  and expansion-induced growth  $F^{ge}$ . The rows showcase the total area growth  $\vartheta^g$  and the corresponding growth stretches  $\lambda_1^g$  and  $\lambda_2^g$  parallel and perpendicular to the midline. Natural growth is more homogeneous than expansion-induced growth, which is larger in regions where the overall deformation is larger.

Table 8.5: Summary of total growth, natural growth, and expansion-induced growth, from analyzing patches R and S.

growth	avg	max	min
$\vartheta^g [-]$	2.25	4.81	0.52
$\vartheta^{gn} [-]$	1.48	2.36	1.07
$\vartheta^{ge} [-]$	1.54	3.30	0.28
$\lambda_1^g [-]$	1.62	3.24	0.61
$\lambda_1^{gn} [-]$	1.24	1.57	0.78
$\lambda_1^{ge} [-]$	1.31	2.65	0.43
$\lambda_2^g [-]$	1.43	2.98	0.57
$\lambda_2^{gn} [-]$	1.20	1.83	0.95
$\lambda_2^{ge} [-]$	1.19	2.61	0.40

## 8.4 Discussion

Skin grows in response to chronic overstretch: at the end of a tissue expansion procedure, the total deformation is a combination of reversible and irreversible contributions. Plastic and reconstructive surgeons typically guess the time point, by which they have expanded the tissue enough to create a sufficiently large patch for defect correction. In clinical practice, this lack of knowledge leads to severe and unnecessary overgrowth.

Here we extend our novel experimental setup [54] towards a new anisotropic characterization of prestrain, deformation, and growth using a porcine skin expansion model. We combine two recent technologies, multi-view stereo (MVS) and isogeometric analysis (IGA), within the continuum theory of finite growth. MVS allows us to reconstruct three-dimensional models from a set of uncalibrated photographs with unknown camera positions. Isogeometric analysis uses B-spline basis functions to smoothly interpolate surface deformation maps and strain fields over relatively coarse meshes. The theory of finite growth captures reversible and irreversible deformation by splitting the total deformation gradient into an elastic and a growth part. Here we are specifically interested in quantifying three aspects of the expansion process: prestrain, deformation, and growth.

We find that skin *in vivo* is prestretched isotropically, on average by  $\vartheta^p = 1.44$ , i.e., by  $\lambda^p = 1.21$  parallel and perpendicular to the midline. Ventral porcine integument has revealed prestretch on the same order of magnitude, with average *in vivo* stretches of 1.26 transversely and 1.65 longitudinally [182]. Experiments on human forearm skin displayed

similar values with an almost isotropic area prestrain on the order of 1.57 [111]. The quantification of isotropic prestrain is thought-provoking: While skin is clearly anisotropic, this does not necessarily imply that prestrain has to be anisotropic as well. Human skin in the forearm displayed similar prestrain values in two orthogonal directions [111], while ventral pig skin exhibited marked anisotropic prestrain [182]. Unfortunately, the purely kinematic analysis of our experimental setup fails to shed light on the morphogenetic processes that explain the observed prestrain patterns. However, throughout our expansion protocol, we have also performed biochemical assays including the immunohistochemistry in Fig. 8.11, which we are currently analyzing with the objective to correlate biochemical and mechanical phenomena and reveal directional information.

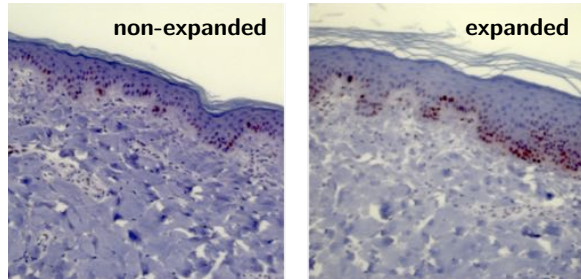


Figure 8.11: Representative tissue sections of non-expanded and expanded skin immunostained for Ki-67, a nuclear protein associated with cell proliferation. The control skin patch, left, displays a normal epidermal thickness and a normal number of dividing cells. The expanded skin patch, right, shows an increase in epidermal thickness and an increased number of dividing cells indicating skin growth. In both sections, the dermis displays a diffuse collagen orientation.

By subcutaneously implanting an expander underneath a  $10 \times 10\text{cm}$  grid and filling it gradually up to 280cc, the overlaying skin is chronically stretched beyond its physiological limit [52]. At the end of five weekly timed inflations, the initial patch is stretched on average by  $1.40 \times 1.34$  parallel and perpendicular to the midline, respectively. It is interesting to highlight the anisotropy of the resulting deformation. Just like most soft biological tissues, skin is known to exhibit anisotropic material properties [219]. In fact, Langer mapped the preferred stiffness directions of skin over the human body more than a century ago [214]. Tension lines in the pig have been characterized in great detail [321]. Uniaxial tension tests of rabbit skin and biaxial testing of porcine skin have initiated the development of microstructurally based anisotropic material constitutive laws [182,373]. It seems reasonable

that the anisotropic microstructure of skin induces anisotropic deformation upon pressure-induced expansion with smaller stretches along the skin tension lines [250]. It is noteworthy that our maximum stretch values occur perpendicular to the midline, although on average, the general trend indicates the opposite. To further explore this phenomenon, our current and future efforts aim at tracking the collagen fiber arrangement before, during, and after tissue expansion using high resolution ultrasound and immunohistochemistry. Fig. 8.11 illustrates our first attempts along these lines, which will eventually allow us to correlate skin growth to cellular and subcellular phenomena including cell proliferation.

At the culmination of the expansion process, on day  $t = 37$ , the total deformation is a combination of growth and elastic components. We excise the expanded tissue to quantify the elastic contribution and observe that the average area change is  $\vartheta^e = 1.20$ . A square region retracts  $0.95 \times 0.88$  parallel and perpendicular to the midline. This finding is intriguing. From our prestrain quantification, we conclude that if we excise the original *in vivo* patch before expansion, it shrinks to a square of dimensions  $0.83 \times 0.83$ . A possible explanation for the mismatch between elastic deformations before and after expansion is that the morphogenetic processes that result in the stable  $\vartheta^p = 1.44$  area stretch *in vivo* is different from the equilibrium resulting from tissue expansion. Another plausible hypothesis is that the grown skin has not yet fully recovered its homeostatic equilibrium state. We plan to follow up expanded skin patches for longer time periods to determine the final equilibrium state of the expanded tissue.

Accounting for prestrain and elastic retraction, we calculate the resulting tissue growth. On average, tissue grows by  $\vartheta^g = 2.25$  in area. We find, once more, that skin kinematics are different in the two directions of interest. An *ex vivo* unit square at day  $t = 0$  transforms into a  $1.62 \times 1.43$  rectangle *ex vivo* after  $t = 37$  days of expansion. Growth also shows a distinct regional variation. As we would intuitively expect, growth is largest in the center region, which experiences the largest stretch. This supports the hypothesis that overstretch drives skin growth [417]. Several factors can explain the regional variation parallel and perpendicular to the midline. First, we find that while the expansion takes place the skin patch grows naturally in an approximately homogeneous, yet anisotropic manner on average by  $1.24 \times 1.20$  times. From our contour plots we can also observe that the deformation induced by expansion is greater in the parallel direction. Nonetheless, there is still debate whether microstructural cues, such as the arrangement of the collagen architecture, guide anisotropic growth. This question also motivates further experiments.

Our study has a few limitations. We recognize that there is no one-to-one correspondence between the material properties and anatomies of porcine and human integument. Another limitation is that we have only performed this study at a single location in a single porcine model. Nonetheless, we believe that our results provide promising evidence for our experimental design and prompt us to replicate the analysis in a larger group. Towards these efforts, we are currently designing instrumented expanders to measure the expander pressure before and after expansion [287]. This will eventually allow us to characterize the stiffness of living skin stiffness using an inverse finite element approach [286]. The shape of the expander could also bias the resulting deformation contours [51]. We are therefore replicating the experiment on a larger sample set to account for different expander geometries and to demonstrate statistical significance of our results.

Taken together, we presented a highly flexible experimental setting to accurately track surface kinematics using multi-view stereo. Multi-view stereo is a robust, inexpensive, non-invasive technology that can be readily used in plastic and reconstructive surgery, where skin is conveniently exposed to the outside world. Performing numerical analysis within the isogeometric setting resolves rich regional variations, which could ultimately lead to address and propose more fundamental questions. Indeed, in this manuscript we start from a particular medical application, skin expansion, a widely used reconstructive technique. An accurate kinematical characterization of tissue expansion could improve pre-operative planning and optimize treatment options. When combined with histological and biochemical essays at smaller scales, our continuum interpolation of mechanical fields has the potential to uncover mechanotransduction pathways in living skin and inspires us to manipulate biological membranes by mechanical stretch.

## Chapter 9

# The Incompatibility of Living Systems: Experimental Characterization on Expanded Skin

**Abstract.** Skin expansion is an important technique in reconstructive surgery used to correct large cutaneous defects. In clinical practice, surgeons face the challenge of selecting an expansion protocol based only on their experience. Predictive simulation of controlled skin growth holds promise for effective preoperative planning. Here we model growing skin within the framework of continuum mechanics using the popular concept of incompatible grown configurations. Despite the broad use of this approach, the incompatibility originating from residual stresses induced by growth remains largely understudied. We present the kinematic analysis of an expansion protocol in a porcine model: We implanted and inflated two expanders, crescent and spherical, and filled them to 225cc throughout a period of 21 days. We then excised the tissue patches and subdivided them into smaller pieces to quantify the amount prestrain developed during growth. Skin growth averaged 1.17 times the original area for the spherical and 1.10 for the crescent expander. Understanding the controlled manipulation of skin through mechanical stretch will allow us to improve—and ultimately personalize—treatment planning in plastic and reconstructive surgery.

## 9.1 Introduction

Common techniques in plastic and reconstructive surgery often lack quantitative understanding of the fundamental mechanisms that explain how tissues react to mechanical stimuli [184, 406]. Even with a thorough knowledge of the mechanobiology, personalizing treatment to an individual patient, a specific treatment modality, or a set of physiological conditions introduces an additional layer of complexity; planning the optimal procedure is virtually impossible by mere intuition [108]. Predictive computational simulations are an ideal tool for clinicians, linking basic material behavior and adaptation response to a clinical application in a patient specific case. Not surprisingly, new mechanical modeling and simulation paradigms are being constantly developed towards this goal [26].

Tissue expansion is one prominent example of a popular medical procedure for which preoperative planning requires knowledge of the fundamental adaptation processes of skin under extraordinary loading conditions, as well as a profound understanding of the clinical control variables: placement of the expander, timing of the inflation, shape of the expander, and geometries of the individual patient [52]. Despite its wide-spread use, tissue expansion does not lack complications or suboptimal results [141, 231]. The execution of this technique still relies heavily on the surgeon's experience [187]. However, recent computational approaches are beginning to address this need [51, 288].

Virtual tissue expansion in a personalized scenario is now within reach [418]. Using finite elements, we are able to represent complicated geometries encountered in the clinic and predict the acute and chronic tissue response [55, 417]. However, the roadmap towards clinical acceptance crucially relies on the experimental validation of these models. Numerous studies have looked at different markers of tissue adaptation during tissue expansion using different animal models [28]. For example, it has been shown how at the end of the procedure, when the flap is harvested, skin typically retracts implying that not all the deformation is irreversible skin growth; skin expansion also induces some reversible elastic deformation [227]. Other groups have tested the mechanical properties of expanded skin at different time points and have showed that expanding skin *in vivo* leads to the deposition of new tissue which retains the same mechanical properties as the original, unexpanded skin [31, 415]. More closely aligned with clinical outcomes, the quantification of net area gain has shown differences between different expander geometries and timing of inflations [265, 385].

Significant advancements have been made regarding the mechanotransduction pathways in stretched skin. We now know that stretching beyond the physiological regime triggers enhanced cellular proliferation, collagen deposition, and revascularization [92, 299, 342]. This stretch is sensed by fibroblasts within the dermis to change their gene expression, which eventually results in the macroscopic effect of net tissue growth [396].

However, despite tremendous progress, the numerous experiments around skin expansion and growth have mainly left out one key ingredient towards predictive medicine: a mathematical field theory capable of bridging the mechanics of tissue adaptation and the clinical loading scenario. We recently prototyped a novel experimental design motivated by the continuum mechanics of finite growth in living systems [54]. We use a well-established approach and introduce an intermediate incompatible configuration by splitting the deformation gradient into elastic and grown contributions [209]. When carried over to the experimental characterization of skin expansion, this conceptual approach is capable of revealing detailed regional variations of anisotropic skin stretch and growth [60]. Here we adopt this methodology to study the kinematics of skin expansion in a chronic porcine model using three basic ingredients: multi-view stereo, isogeometric analysis, and the continuum theory of finite growth.

Multi-view stereo is a technique we adopt from computer vision that allows the reconstruction of three-dimensional geometries out of a sequence of two dimensional photographs [87]. The main advantages of multi-view stereo are its high accuracy and its versatility [335]. Unlike other experimental approaches such as binocular stereo, multi-view stereo does not require a restrictive setup with a controlled camera position; rather, its algorithm relies on a large amount of samples from a static scene and uses feature matching between pairs of photographs to calculate the calibration parameters of the camera [157]. Once the camera position and orientation are calibrated, an additional optimization routine generates a dense three-dimensional point cloud of the scene [117].

Isogeometric analysis is a computational approach to combine geometry and mechanical analysis. Once we have obtained the three-dimensional geometry from multi-view stereo, we need to represent it in such a way that is suitable for a continuum analysis. Traditionally, finite elements have been used to discretize the spatial domain and parameterize the fields of interest including the elastic strains and growth. Here we use B-splines surface patches to represent the geometry. B-spline isogeometric analysis is currently gaining increasing attention [167]. Particularly, isogeometric analysis has been found suitable for thin shell

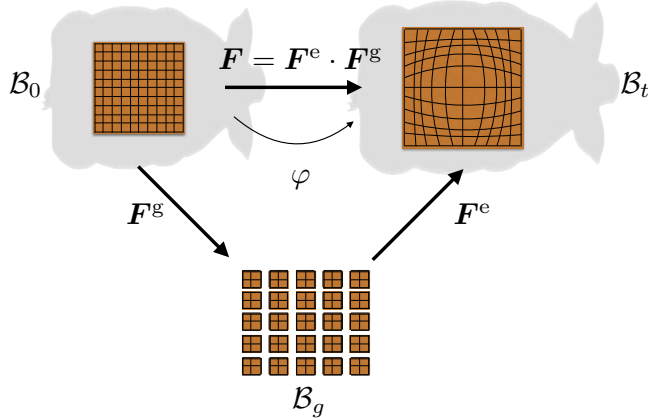


Figure 9.1: Finite growth is modeled mathematically using continuum mechanics. The reference configuration  $\mathcal{B}_0$  is mapped to the deformed configuration  $\mathcal{B}_t$  by  $\varphi$ . The gradient of this deformation,  $\mathbf{F}$ , is split into an elastic contribution  $\mathbf{F}^e$  and growth  $\mathbf{F}^g$ . This introduces an incompatible intermediate configuration  $\mathcal{B}_g$ .

descriptions of biological membranes such as skin [57]. Furthermore, a three-dimensional B-spline surface patch is defined explicitly over a two-dimensional parametric domain, inherently providing the same parameterization for every configuration of the tissue as it is expanded.

The continuum theory of finite growth serves to distinguish reversible, elastic deformations from irreversible, permanent growth. Following the classical theory, we introduce a reference configuration  $\mathcal{B}_0$  and a deformed configuration  $\mathcal{B}_t$  at time  $t$ . The map between the two is  $\varphi$  and its gradient  $\mathbf{F} = \nabla_X \varphi$  is the key kinematic object that describes local changes. Figure 9.1 illustrates the multiplicative split of the deformation gradient into elastic contributions and growth,  $\mathbf{F} = \mathbf{F}^e \cdot \mathbf{F}^g$ . This theory, originally proposed two decades ago [320], has been widely used to mathematically characterize the adaptation of different tissues to mechanical cues [134]. The split of the deformation gradient introduces an intermediate incompatible configuration depicted in Figure 9.1 [251]. We can visualize this intermediate configuration by cutting the reference configuration into several small pieces, which are allowed to grow without constraints or applied forces according to the tensor field  $\mathbf{F}^g$ . Clearly  $\mathbf{F}^g$  defined in this fashion is not necessarily the gradient of a vector field, which is reflected through the notion of incompatibility. The elastic part of the deformation is indicated by  $\mathbf{F}^e$  in Figure 9.1. This field reflects the deformation required to patch the incompatibly grown parts together and apply the load. In other words,  $\mathbf{F}^g$  captures the

biology,  $\mathbf{F}^e$  captures the loading and the residual stresses due to growth, and  $\mathbf{F}$  captures the observed tissue deformation, which is a combination of elastic components and growth. Although this theoretical framework has become increasingly popular, the experimental characterization of the intermediate incompatible configuration attributed to growth does not seem to have been thoroughly studied except for very few special cases such as the well-known open angle experiment [128, 230].



Figure 9.2: Different tissue expander geometries are used in clinical practice. We are interested in comparing spherical expanders (top), rectangular expanders (middle), and crescent expanders (bottom).

We have previously quantified, for the first time, the detailed kinematics of an expansion procedure with rectangular tissue expander [54]. In clinical practice, however, expanders come in different sizes and shapes [319]. Figure 9.2 shows several commercial tissue expanders. Choosing one geometry over another is not a trivial task. Simulations

and experiments have shown that different shapes produce different patterns of skin deformation and ultimately of skin growth [48, 51]. Here we present a quantitative comparison of three expander geometries: spherical, rectangular, and crescent. For all three, we retain a strong interest in understanding the basic mechanisms that guide tissue adaptation. Within this focus, we seek to ultimately establish a constitutive equation that links tissue stretch to growth over time. With this basic scientific motivation in mind, the data from our new experiment complement our initial investigations [60]. An important step forward is associated with the notion of incompatibility induced by growth. For the first time, we quantify the effect of regional variations in growth on the evolution of residual deformations, deformations that are stored within the tissue even in the absence of loading.

## 9.2 Methods

### 9.2.1 Animal Model

Porcine models are a natural choice to study tissue expansion [28]. Experiments in pigs have improved our understanding of the histological and biomechanical changes of skin upon hyper-stretch [181]. The primary reason to choose a porcine expansion model is the similarity between the anatomical and mechanical characteristics of human and young porcine integument [257, 258, 263]. From a clinical point of view, tissue expansion in the pig is similar to tissue expansion in humans, with similar criteria for expander selection, filling volume, and inflation timing [385].

According to the protocol approved by the Ann & Robert H. Lurie Children's Hospital of Chicago Research Center Animal Care and Use Committee, we perform the experiment on a one-month-old male Yucatan mini pig (Sinclair Biolabs, Columbus, MO). We tattoo 10 cm × 10 cm grids with 1cm line markings to the pig's skin using tattoo transfer medium in four areas: left caudal (P), right caudal (Q), left rostral (R), and right rostral (S), as illustrated in Figure 9.3. We inject local anesthetic (1% lidocaine with 1 : 100000 epinephrine) subcutaneously at the site of each planned incision. We investigate three expanders geometries (PMT Corporation, Chanhassen, MN): spherical (P), rectangular (Q), and crescent (R), as illustrated in Figure 9.2. Region S serves as an internal control for prestrain and growth. A subcutaneous filling port allows for controlled inflation. We wait 14 days postoperatively to remove the sutures. We continue antibiotic prophylaxis for 48 hours (Combi-Pen-48, Bimeda, Inc., Dublin, Ireland), and buprenorphine (0.05-0.1mg/kg)

for analgesia via intramuscular injection every 12 hours for 4 doses, with additional doses available in case of animal distress.

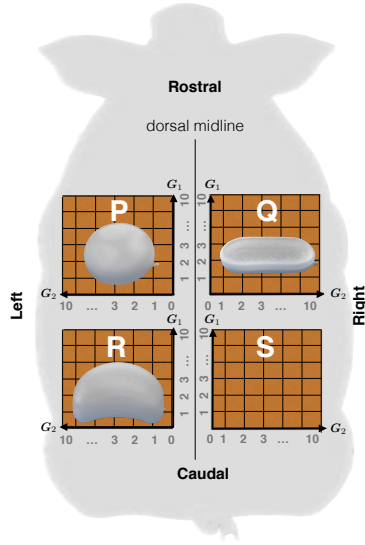


Figure 9.3: Porcine expansion model with four tattooed grids of  $11 \times 11$  points. A spherical expander is implanted underneath grid P, a rectangular expander underneath grid Q, and a crescent expander underneath grid R. Region S serves as control. Tangent vectors  $\mathbf{G}_1$  are aligned from caudal to rostral and vectors  $\mathbf{G}_2$  from midline to left and right.

We wait for the incisions to heal before beginning expansion. We perform five inflation steps at 0, 2, 7, 10, and 15 days with total filling volumes of 50, 75, 105, 165, and 225 cc. On day 21, we anesthetize the animal and record final measurements. We excise the four tattooed skin patches and euthanize the animal using intravenous overdose of pentobarbital (90mg/kg). We take photographs of the explanted tissues. Finally, we perform a subdivision step and cut the original  $11 \times 11$  grid into  $5 \times 5$  smaller square pieces to further release residual stress. We fix the tissues, and embed them in paraffin for subsequent analyses.

### 9.2.2 Kinematics Data Acquisition

At every inflation step, we acquire 20 photographs of the experimental scene from different camera angles before and after filling. On the day of tissue harvest we photograph the final *in vivo* configuration, the excised *ex vivo* patches, and the subdivided pieces. We

reconstruct the three-dimensional surface geometry from the two-dimensional images using an online multi-view stereo service [23] (Autodesk Inc., San Rafael, California).

For calibration, we include two perpendicular rulers during the photo acquisition. The lengths of the rulers in the geometric reconstruction provide the scaling factors and allow us to quantify the relative error of the multi-view stereo algorithm. To scale each geometric model, we fit a cubic spline to the reconstruction of the rulers and determine the individual lengths  $l_i$  along the spline between the  $i = 1, \dots, n$  one-cm-long ruler segments. We use the average length  $l = \sum_{i=1}^n l_i / n$  as scaling factor. The average error  $e = \sum_{i=1}^n e_i / n$ , calculated as the average of the individual reconstruction errors of each segment,  $e_i = [l_i - l] / l$ , serves as a measure of algorithmic accuracy.

We create a B-spline surface patch for each grid by fitting the control points of the spline to best interpolate the  $11 \times 11$  tattooed nodes. B-spline surfaces are tensor products of B-spline curves [298]. A B-spline curve  $\mathcal{C}(\xi)$  is the sum of a set of the basis functions  $N_i(\xi)$  multiplied by the coordinates of a set of control points  $\mathbf{P}_i$ . The B-spline basis functions  $N_i(\xi)$  of degree  $p$  are defined by a knot vector  $\Xi$  which is a set of non-decreasing numbers  $\Xi = [\xi_0, \xi_1, \dots, \xi_n]$ . The basis functions  $N_i(\xi)$  are defined recursively from the zeroth order basis function,

$$N_i^0(\xi) = \begin{cases} 0 & \xi_i \leq \xi \leq \xi_{i+1} \\ 1 & \text{otherwise,} \end{cases} \quad (9.1)$$

with higher order functions,  $p \geq 1$ , obtained as

$$N_i^p(\xi) = \frac{\xi - \xi_i}{\xi_{i+p} - \xi_i} N_i^{p-1}(\xi) + \frac{\xi_{i+p+1} - \xi}{\xi_{i+p+1} - \xi_{i+1}} N_{i+1}^{p-1}(\xi). \quad (9.2)$$

A B-spline surface  $\mathcal{S}(\xi, \eta)$  is the sum of a set of surface basis functions  $N_i(\xi, \eta)$  multiplied by the coordinates of a net of  $n_{cp}$  control points  $\mathbf{P}_i$ .

$$\mathcal{S}(\xi, \eta) = \sum_{i=0}^{n_{cp}} N_i(\xi, \eta) \mathbf{P}_i. \quad (9.3)$$

The surface basis functions  $N_i(\xi, \eta)$  are the tensor products of the B-spline basis functions  $N_i(\xi)$  and  $N_j(\eta)$ . We parameterize the regions P, Q, R, and S at every time point with B-spline basis functions of polynomial degree  $p = 3$  based on a knot vectors  $\Xi = \Theta = [0, 0, 0, 0, 1, 2, \dots, 9, 10, 10, 10, 10]$ . By fitting the same parameterization independently for all skin patches, we can easily extract the relative deformation between any two grids. For

instance, choosing one of the B-spline surfaces as the reference state  $\mathcal{S}_0$  and one as the deformed state  $\mathcal{S}_t$ , we immediately recover the referential and current coordinates over the same set of basis functions,

$$\mathbf{X} = \sum_{i=0}^{n_{\text{cp}}} N_i(\xi, \eta) \mathbf{P}_i \quad \text{and} \quad \mathbf{x} = \sum_{i=0}^{n_{\text{cp}}} N_i(\xi, \eta) \mathbf{p}_i , \quad (9.4)$$

The partial derivatives of the surface basis function with respect to the parametric coordinates define the covariant surface base vectors in the reference and deformed configurations,

$$\begin{aligned} \mathbf{G}_1 &= \sum_{i=0}^{n_{\text{cp}}} N_{i,\xi} \mathbf{P}_i & \mathbf{G}_2 &= \sum_{i=0}^{n_{\text{cp}}} N_{i,\eta} \mathbf{P}_i \\ \mathbf{g}_1 &= \sum_{i=0}^{n_{\text{cp}}} N_{i,\xi} \mathbf{p}_i & \mathbf{g}_2 &= \sum_{i=0}^{n_{\text{cp}}} N_{i,\eta} \mathbf{p}_i . \end{aligned} \quad (9.5)$$

The vectors  $\mathbf{G}_1$  and  $\mathbf{g}_1$  are aligned longitudinally, parallel to the long axis of the animal, while the vectors  $\mathbf{G}_2$  and  $\mathbf{g}_2$  are tangent to transverse coordinate lines. To determine the contravariant base vectors  $\mathbf{G}^\alpha$ , we calculate the covariant surface metric,

$$G_{\alpha\beta} = \mathbf{G}_\alpha \cdot \mathbf{G}_\beta \quad \text{with} \quad \alpha, \beta = 1, 2 \quad (9.6)$$

invert it to calculate the contravariant surface metric  $G^{\alpha\beta}$ , and map the covariant base vectors  $\mathbf{G}_\beta$  onto their contravariant counterparts,

$$\mathbf{G}^\alpha = G^{\alpha\beta} \mathbf{G}_\beta \quad \text{with} \quad G^{\alpha\beta} = [G_{\alpha\beta}]^{-1} . \quad (9.7)$$

Finally, we calculate the deformation gradient  $\mathbf{F}$  as the dyadic product between the covariant deformed base vectors  $\mathbf{g}_\alpha$  and the contravariant reference base vectors  $\mathbf{G}^\alpha$ ,

$$\mathbf{F} = \mathbf{g}_\alpha \otimes \mathbf{G}^\alpha . \quad (9.8)$$

The deformation gradient is the key kinematic object to characterize the expansion process between any two time points across the tattooed grids. From it, we derive three measures of stretch. The area stretch  $\vartheta$  captures the change in surface area between a surface element in the reference configuration  $\mathcal{S}_0$  and in the deformed configuration  $\mathcal{S}_t$ , and is the determinant of the deformation gradient,

$$\vartheta = \det(\mathbf{F}) . \quad (9.9)$$

To characterize the anisotropy of the expansion processes, we use the right Cauchy Green deformation tensor  $\mathbf{C} = \mathbf{F}^T \cdot \mathbf{F}$  and calculate the stretches,

$$\lambda_1 = \sqrt{\mathbf{G}_1 \cdot \mathbf{C} \cdot \mathbf{G}_1} \quad \text{and} \quad \lambda_2 = \sqrt{\mathbf{G}_2 \cdot \mathbf{C} \cdot \mathbf{G}_2}, \quad (9.10)$$

along the longitudinal and transverse directions.

### 9.2.3 Kinematic Analysis of Skin Expansion

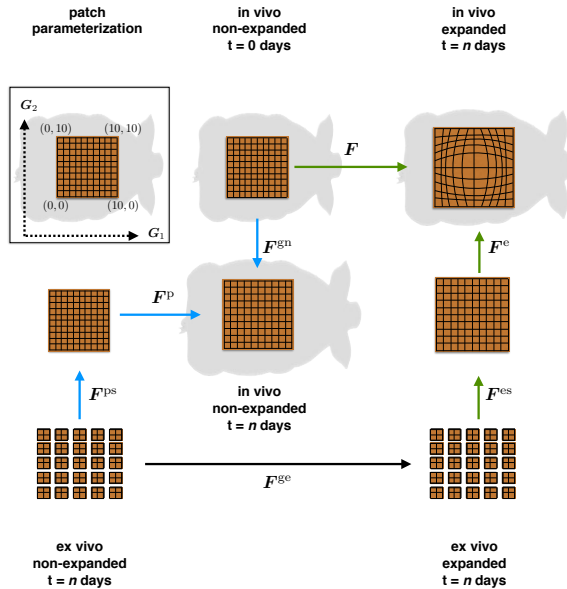


Figure 9.4: Configurations of skin expansion. In vivo, skin is subjected to prestrain,  $\mathbf{F}^p \cdot \mathbf{F}^{ps}$ . Expansion induces deformation,  $\mathbf{F}$ . Excising the expanded patch releases the reversible, elastic deformation,  $\mathbf{F}^e \cdot \mathbf{F}^{es}$ . Skin growth,  $\mathbf{F}^g$ , consists of natural growth,  $\mathbf{F}^{gn}$ , and expansion-induced growth,  $\mathbf{F}^{ge}$ .

The deformation observed in the expanded patches is a combination of elastic components and growth. We build upon the usual split of the deformation gradient into two tensor fields,  $\mathbf{F} = \mathbf{F}^e \cdot \mathbf{F}^g$ . However, we refine this approach to account for prestrain and natural growth [60]. Figure 9.4 summarizes the important configurations during tissue expansion. The complete kinematic description of tissue adaptation under supra-physiological stretch requires the analysis of both the control and expanded patches. The control patch delivers information of prestrain and natural growth. The expanded patch captures the elastic

Table 9.1: Summary of the expansion protocol with spherical expander on patch P, crescent expander on patch R, and control patch S. The rectangular expander on patch Q migrated out of the reference grid. The final filling volume at the end of the protocol at day  $t = 21$  was 225 cc. We reconstructed the geometry of every grid, at every time point, before and after expansion. On day  $t = 21$  we reconstructed the *in vivo* patch, the *ex vivo* excised patch, and the subdivided excised patch.

patch	t=0		t=2		t=7		t=10		t=15		t=21		
	pre	post	pre	post	pre	post	pre	post	pre	post	pre	ex-vivo	sub
P	V[cc]	0	50	50	75	75	105	105	165	165	225	-	-
	error [%]	1.5	1.2	1.5	2.0	1.3	1.4	1.3	1.1	1.0	1.2	1.5	1.8
R	V[cc]	0	50	50	75	75	105	105	165	165	225	-	-
	error [%]	1.5	1.2	1.5	2.0	1.3	1.4	1.3	1.1	1.0	1.2	1.5	0.8
S	V[cc]	0	0	0	0	0	0	0	0	0	0	-	-
	error [%]	1.0	1.5	1.6	1.6	1.1	2.0	0.5	1.4	1.0	1.5	0.9	1.6

deformation and growth. By combining these different measures of deformation, we can calculate the amount of growth solely attributed to the expansion process.

The blue path in Figure 9.4 refers to the kinematics of the control patch. While the expansion process takes place, from day  $t = 0$  to day  $t = 21$ , the specimen grows naturally according to  $\mathbf{F}^{\text{gn}}$ . Skin, like most biological tissues, is not stress-free in its physiological state [9]. Furthermore, the morphological processes of growth and remodeling can lead to complex patterns of defaturation and build-up of residual stresses [361]. The biological considerations that backup the multiplicative split of the deformation gradient to include volumetric growth introduce a tensor field which is not the gradient of a deformation and is thus incompatible [419]. We therefore quantify the amount of prestrain in two steps. First, we look at the continuous deformation field that describes the retraction of an entire patch when harvesting it from its *in vivo* environment. This field is described through the tensor  $\mathbf{F}^{\text{p}}$  in Figure 9.4. Then, we subdivide the entire grid into  $5 \times 5$  smaller pieces and record the corresponding deformation  $\mathbf{F}^{\text{ps}}$ .

The green path in Figure 9.4 refers to the kinematics of the expanded patches. The field  $\mathbf{F}$  describes the deformation at day  $t = n$  with respect to the *in vivo* state at day  $t = 0$ . At the end of the expansion process, not all of this deformation is irreversible skin growth, but some of it is elastic. By excising the patch and analyzing its retraction, we obtain a first approximation of the remaining elastic deformation at the end of an expansion procedure  $\mathbf{F}^{\text{e}}$ . Similarly to the control patches, the growth process described by the multiplicative split of the deformation gradient alludes to an intermediate incompatible configuration and

the existence of residual stresses. We further subdivide the *ex vivo* expanded patches into  $5 \times 5$  smaller pieces and calculate the incompatible field  $\mathbf{F}^{\text{es}}$ .

The black arrow in Figure 9.4 refers to the kinematics of the growth attributed exclusively to the expansion process. Mathematically, we can summarize Figure 9.4 through the following composition of mappings,

$$\mathbf{F} \cdot \mathbf{F}^{\text{gn}^{-1}} \cdot \mathbf{F}^{\text{p}} \cdot \mathbf{F}^{\text{ps}} = \mathbf{F}^{\text{e}} \cdot \mathbf{F}^{\text{es}} \cdot \mathbf{F}^{\text{ge}}. \quad (9.11)$$

Assuming that the prestrain of the control patches is the same throughout the expansion process we can rearrange this mapping as follows,

$$\mathbf{F} \cdot \tilde{\mathbf{F}}^{\text{p}} \cdot \tilde{\mathbf{F}}^{\text{ps}} = \mathbf{F}^{\text{e}} \cdot \mathbf{F}^{\text{es}} \cdot \mathbf{F}^{\text{ge}} \cdot \mathbf{F}^{\text{gn}}, \quad (9.12)$$

where the pairs  $\{\mathbf{F}^{\text{p}}, \tilde{\mathbf{F}}^{\text{p}}\}$  and  $\{\mathbf{F}^{\text{ps}}, \tilde{\mathbf{F}}^{\text{ps}}\}$  differ only by a rigid body motion. In this setup, only the elastic deformation,  $\mathbf{F}^{\text{e}} \cdot \mathbf{F}^{\text{es}}$ , generates stress [316].

We postulate that skin grows only in the plane such that the thickness of an unloaded tissue sample will remain constant throughout the growth process [417]. We allow the in-plane area growth to be anisotropic with different growth factors longitudinally, along  $\mathbf{G}_1$ , and transversely, along  $\mathbf{G}_2$  [134], such that

$$\mathbf{F}^{\text{g}} = \mathbf{F}^{\text{ge}} \cdot \mathbf{F}^{\text{gn}} = \lambda_1^{\text{g}} \mathbf{G}_1 \otimes \mathbf{G}_1 + \lambda_2^{\text{g}} \mathbf{G}_2 \otimes \mathbf{G}_2 + \mathbf{N} \otimes \mathbf{N}. \quad (9.13)$$

This definition introduces a multiplicative split of the stretch measures. For the areal stretch, this implies that

$$\vartheta \vartheta^{\text{p}} \vartheta^{\text{ps}} = \vartheta^{\text{e}} \vartheta^{\text{es}} \vartheta^{\text{ge}} \vartheta^{\text{gn}}. \quad (9.14)$$

The specific assumption for the growth tensor introduces the total area growth as the product of the longitudinal and transverse stretches,  $\vartheta^{\text{g}} = \det(\mathbf{F}^{\text{g}}) = \lambda_1^{\text{g}} \lambda_2^{\text{g}}$ , with the anisotropic growth variables  $\lambda_1^{\text{g}} = \lambda_1^{\text{gn}} \lambda_1^{\text{ge}}$  and  $\lambda_2^{\text{g}} = \lambda_2^{\text{gn}} \lambda_2^{\text{ge}}$  also admitting a multiplicative split of the composed mappings  $\mathbf{F}^{\text{ge}}$  and  $\mathbf{F}^{\text{gn}}$ .

The deformation gradient  $\mathbf{F}$  is calculated with respect to the *in vivo* state at dat  $t = 0$ . Hence, it captures the chronic deformation induced by the expansion process over the entire duration of the experiment. However, it is also of interest to determine the acute deformation [286, 287]. It seems reasonable to assume that the acute deformation due to a single inflation step is mainly elastic. To calculate the acute deformation at the inflation

step  $i$  we simply take the patch right before the inflation as the reference configuration and the patch immediately after the inflation as the deformed configuration. The gradient of this deformation  $\mathbf{F}_i^a$  neither affects the calculation of the chronic response nor of the final amount of skin growth.

### 9.3 Results

The expansion of the rectangular expander underneath grid Q failed due to device migration out of the reference grid. The expansion of the spherical and crescent expanders underneath grids P and R was successfully completed. Grid S was successfully explanted to serve as control. Table 9.1 summarizes the time points, volumes, and the reconstruction errors for grids P, R, and S.

Following the schematic in Figure 9.4, we first present the results from the control patch S from which we calculate the natural growth tensor field,  $\mathbf{F}^{gn}$ , and the prestrain fields,  $\mathbf{F}^p$  and  $\mathbf{F}^{ps}$ . From the analysis of the expanded patches P and R, we extract the deformation fields of the expansion-induced deformation,  $\mathbf{F}$ , and the fields of the elastic deformation revealed from the tissue harvest,  $\mathbf{F}^e$  and  $\mathbf{F}^{es}$  for the spherical and crescent expanders. The difference between expansion and control patches defines the expansion-induced growth,  $\mathbf{F}^{ge}$ , which we present last.

#### 9.3.1 Control Patches: Prestrain and Natural Growth

Patch S, which was not subjected to expansion, reveals the amount of natural growth and prestrain. These deformation fields are illustrated in Figure 9.4 by the blue path that connects the *in vivo* non-expanded state at day  $t = 0$  with the *ex vivo* subdivided patch at day  $t = 21$ .

Table 9.2 summarizes the results of the natural growth,  $\mathbf{F}^{gn}$ . Figure 9.5 shows the temporal evolution of natural growth over time in terms of the total area stretch  $\vartheta^{gn}$  and the stretches  $\lambda_1^{gn}$  and  $\lambda_2^{gn}$ . Natural growth is isotropic and almost linear with directional growth of approximately 1% per day: In 21 days of natural growth, before excision, a unit square grows on average to a rectangle of dimensions  $1.19 \times 1.17$  yielding an average *in vivo* area gain of 1.38.

Table 9.3 summarizes the minimum, maximum, and average values of the three prestrain

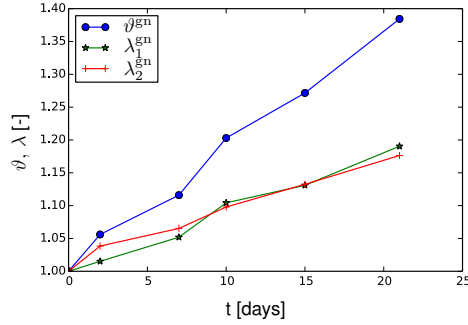


Figure 9.5: History of natural growth. Evolution of the naturally grown area  $\vartheta^{\text{gn}}$  and the naturally grown stretches  $\lambda_1^{\text{gn}}$  and  $\lambda_2^{\text{gn}}$ . Natural growth is isotropic and almost linear with directional growth of approximately 1% per day. During 21 days, a unit square grows to a rectangle of dimensions  $1.19 \times 1.17$  with an average area gain of 1.38.

measures, the area stretch  $\vartheta$ , the longitudinal stretch  $\lambda_1$ , and the transverse stretch  $\lambda_2$ , for the initial excision  $\mathbf{F}^{\text{p}}$ , for further subdivision  $\mathbf{F}^{\text{ps}}$ , and for the combination of both,  $\mathbf{F}^{\text{p}} \cdot \mathbf{F}^{\text{ps}}$ . Excising the grids reveals the first component of the prestrain,  $\mathbf{F}^{\text{p}}$ . To illustrate that remaining residual stress, we further subdivide the excised control patch into  $5 \times 5$  smaller pieces, which define the discontinuous field,  $\mathbf{F}^{\text{ps}}$  [8].

Figure 9.6 illustrates the spatial distribution of the total prestrain. The prestrain field is neither homogeneous nor continuous: The subdivision step reveals the discontinuity of the deformation map. The prestrain measures plotted in Figure 9.6 are continuous within each of the smaller patches, but discontinuous across the patch boundaries, illustrating the incompatible configuration associated with the continuum mechanics description of finite growth.

Table 9.2: Summary of growth  $\mathbf{F}^{\text{gn}}$  from analyzing patch  $S$  between the non-expanded states at days  $t = 0$  and  $t = 21$ .

deformation	max	min	avg
$\vartheta^{\text{gn}} [-]$	1.90	0.92	1.38
$\lambda_1^{\text{gn}} [-]$	1.39	0.91	1.17
$\lambda_2^{\text{gn}} [-]$	1.51	0.87	1.19

Table 9.3: Summary of prestrain  $\mathbf{F}^P$  and  $\mathbf{F}^{PS}$  from analyzing patch S upon excision and further subdivision.

deformation	max	min	avg
$\vartheta^P [-]$	2.12	0.66	1.24
$\lambda_1^P [-]$	1.60	0.70	1.12
$\lambda_2^P [-]$	1.63	0.75	1.12
$\vartheta^{PS} [-]$	2.00	0.65	1.05
$\lambda_1^{PS} [-]$	1.81	0.70	1.00
$\lambda_2^{PS} [-]$	1.49	0.75	1.04
$\vartheta^P \cdot \vartheta^{PS} [-]$	1.90	0.92	1.38
$\lambda_1^P \cdot \lambda_1^{PS} [-]$	2.33	0.77	1.14
$\lambda_2^P \cdot \lambda_2^{PS} [-]$	2.10	0.79	1.19

### 9.3.2 Expanded Patches:

#### Expansion-Induced Deformation and Elastic Deformation

Patches P and R provide information related to the expansion-induced deformation and the final elastic deformation. The maps describing these relations are shown with the arrows colored in green in Figure 9.4. By taking the pig at day  $t = 0$  as reference configuration, we quantify the deformation induced throughout the expansion process. This deformation is characterized by its gradient  $\mathbf{F}$ .

Figure 9.7 shows the contour plots of the spatial distribution of the chronic deformation for patches P and R of the spherical and crescent expanders. We use the term *chronic* deformation because at every time point we are interested in the map with respect to the reference pig at day  $t = 0$ . Table 9.4 summarizes our findings. The expansion process spans  $t = 21$  days with inflations at days  $t = 0, 2, 7, 10, 15$ . At the end of  $t = 21$  days the spherical and crescent expanders are filled to a final volume of 225 cc. The spherical expander deforms a unit square into a rectangle of dimensions  $1.33 \times 1.27$ . The crescent expander deforms a unit square into a rectangle of dimensions  $1.25 \cdot 20$ . In both cases the longitudinal direction deforms more than the transverse direction.

Figure 9.8 illustrates the deformation that occurs during each inflation step, which we refer to as *acute*. Each contour plot illustrates the measures of strain with the patch right before the inflation as reference configuration and the patch immediately after the inflation as deformed configuration. This setup defines the deformation gradient  $\mathbf{F}_i^a$  for each inflation

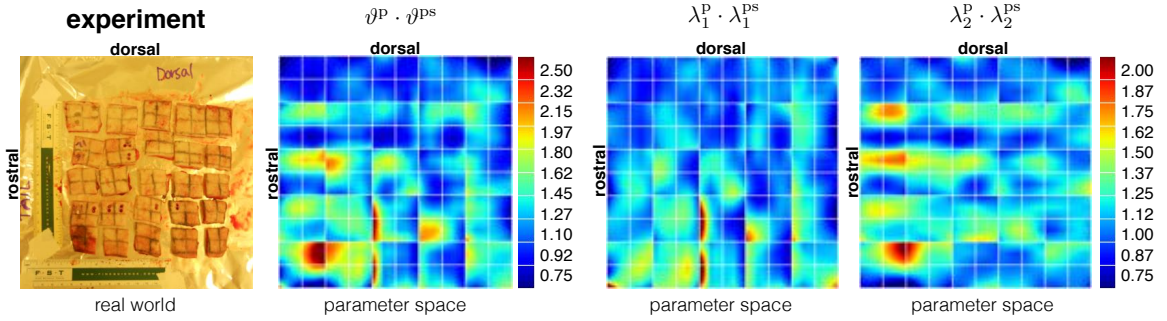


Figure 9.6: Prestrain upon excision and further subdivision of the control patch S. Skin releases the elastic stresses upon excision and subdivision, left. The prestrain field is a composition of the excision and subdivision maps  $\mathbf{F}^P$  and  $\mathbf{F}^{PS}$ . The resulting configuration is incompatible. The contour maps highlight the incompatibility of the total area prestretch and the prestretch in longitudinal and transverse directions.

i.

Table 9.5 summarizes the results of the acute deformation. The values across the different inflation steps remain fairly similar and close to one. There is, however, a marked regional variation: the total area stretch and the longitudinal stretch exhibit larger values towards the central area of the expander and compressive stretches in the periphery of the expanded regions. The transverse stretch does not follow this trend. We remark though that the acute deformation does not enter the calculation of the final growth.

Figure 9.9 summarizes the elastic deformation released upon excision and further subdivision of the expanded patches P and R. Upon excision, the expanded patches retract revealing that not all the deformation imposed by the expansion process is attributed to growth. This retraction is the elastic deformation  $\mathbf{F}^e$  of the total deformation at the end of the experimental protocol. However, the excised patch might still not be stress-free. The biological description of growth as a local deposition of new material suggests the subdivision of the patch into smaller pieces to further relieve residual stresses. Figure 9.9 left depicts photographs of the experimental setup in which the excised patches P and R are subdivided into  $5 \times 5$  pieces. The resulting tensor  $\mathbf{F}^{es}$  captures the incompatibility between the excised and subdivided patches. The composition of both tensors yields the total elastic deformation  $\mathbf{F}^e \cdot \mathbf{F}^{es}$ . The contour maps of Figure 9.9 summarize the area, longitudinal and transverse stretches, of this composed map for the spherical and crescent expanders.

Table 9.6 synthesizes the analysis of the excised expanded patches. The elastic deformation is slightly larger in the transverse direction than in the longitudinal direction. The

Table 9.4: Chronic deformation history  $\mathbf{F}$  from analyzing patches P and R during tissue expansion between days  $t = 0$  and  $t = 21$ .

t [days]	expander [-]	volume [cc]	$\vartheta$ [-]			$\lambda_1$ [-]			$\lambda_2$ [-]		
			max	min	avg	max	min	avg	max	min	avg
0	sphere	50	1.44	0.71	0.98	1.37	0.76	1.00	1.17	0.84	0.97
	crescent	50	1.46	0.76	0.98	1.24	0.79	1.00	1.17	0.84	0.98
2	sphere	75	1.74	0.68	1.08	1.51	0.73	1.08	1.19	0.75	1.00
	crescent	75	1.43	0.66	1.00	1.31	0.65	1.00	1.26	0.77	1.00
7	sphere	105	2.01	0.69	1.21	1.70	0.75	1.13	1.32	0.84	1.07
	crescent	105	1.66	0.83	1.15	1.40	0.87	1.11	1.33	0.86	1.03
10	sphere	165	2.26	0.74	1.36	1.76	0.77	1.21	1.39	0.83	1.11
	crescent	165	1.86	0.87	1.26	1.58	0.80	1.15	1.45	0.83	1.09
15	sphere	225	2.77	0.72	1.52	2.01	0.69	1.29	1.47	0.89	1.18
	crescent	225	1.87	0.83	1.32	1.46	0.84	1.17	1.44	0.92	1.14
21	sphere	225	3.09	0.93	1.70	2.13	0.90	1.33	1.62	0.98	1.27
	crescent	225	2.25	0.87	1.49	1.66	0.85	1.25	1.67	0.96	1.20

Table 9.5: Acute deformation history  $\mathbf{F}^a$  from analyzing patches P and R during tissue expansion at days  $t = 0$  to  $t = 15$ .

t [days]	expander [-]	volume [cc]	$\vartheta^a$ [-]			$\lambda_1^a$ [-]			$\lambda_2^a$ [-]		
			max	min	avg	max	min	avg	max	min	avg
0	Sphere	50	1.32	0.72	0.98	1.44	0.75	1.00	1.23	0.83	0.97
	Crescent	50	1.50	0.71	0.98	1.30	0.80	1.00	1.21	0.84	0.98
2	Sphere	75	1.36	0.69	0.98	1.26	0.66	1.00	1.20	0.80	0.98
	Crescent	75	1.31	0.61	0.98	1.24	0.80	1.01	1.34	0.68	0.97
7	Sphere	105	1.40	0.79	0.98	1.30	0.57	1.00	1.20	0.77	0.98
	Crescent	105	1.37	0.59	1.00	1.46	0.83	1.02	1.16	0.77	0.98
10	Sphere	165	1.60	0.73	1.01	1.35	0.60	1.02	1.25	0.75	0.99
	Crescent	165	1.48	0.58	1.01	1.42	0.75	1.02	1.22	0.77	1.00
15	Sphere	225	1.27	0.73	1.01	1.35	0.55	1.02	1.22	0.79	0.98
	Crescent	225	1.34	0.54	1.02	1.37	0.80	1.02	1.32	0.81	1.00

Table 9.6: Summary of elastic deformation  $\mathbf{F}^e$  and  $\mathbf{F}^{es}$  from analyzing the excised patches P and R corresponding to the spherical and crescent expanders.

deformation	sphere			crescent		
	max	min	avg	max	min	avg
$\vartheta^e [-]$	2.55	0.73	1.42	1.98	0.77	1.27
$\lambda_1^e [-]$	1.71	0.75	1.19	1.50	0.69	1.13
$\lambda_2^e [-]$	1.90	0.90	1.21	1.65	0.88	1.14
$\vartheta^{es} [-]$	1.93	0.46	0.97	1.89	0.69	1.02
$\lambda_1^{es} [-]$	1.56	0.67	0.96	1.55	0.69	0.98
$\lambda_2^{es} [-]$	1.89	0.56	1.00	1.79	0.74	1.03
$\vartheta^e \cdot \vartheta^{es} [-]$	3.40	0.60	1.39	2.29	0.74	1.32
$\lambda_1^e \cdot \lambda_1^{es} [-]$	1.85	0.63	1.15	1.83	0.66	1.12
$\lambda_2^e \cdot \lambda_2^{es} [-]$	2.38	0.83	1.22	2.11	0.87	1.18

spherical expander induces a larger elastic retraction than the crescent expander. On average, a unit square from patch P retracts to a rectangle of dimensions  $0.87 \times 0.82$  while a unit square from patch R shrinks into a  $0.88 \times 0.87$  rectangle. There is significant regional variation in both cases, the total area stretch as well as the longitudinal stretch reflect the placement of the expander, while the transverse stretch is slightly more homogeneous.

### 9.3.3 Control Patches vs. Expanded Patches: Expansion-Induced Skin Growth

By combining the information from the control patches and the expanded patches we can quantify the amount of growth caused by the expansion process alone. Figure 9.4 indicates the mappings associated with the control patches through blue arrows and with the expanded patches through green arrows. The black arrow connecting the subdivided *ex vivo* control patch and the subdivided *ex vivo* expanded patch is the deformation that characterizes expansion-induced growth.

Table 9.7 summarizes the results. The total area growth averages 1.17 for the spherical and 1.10 for the crescent expander. Growth is anisotropic with larger longitudinal than transverse growth. On average, a unit square from patch P grows into a rectangle of dimensions  $1.11 \times 1.05$ , a unit square on patch R becomes a rectangle of  $1.08 \times 1.02$ .

Figure 9.10 shows the contour plots of the growth measures for the spherical and crescent

Table 9.7: Summary of expansion-induced growth  $\mathbf{F}^{\text{ge}}$  from combining the analysis of the excised patches P and R corresponding to the spherical and crescent expanders with the analysis of the control patch S.

deformation	sphere			crescent		
	max	min	avg	max	min	avg
$\vartheta^{\text{ge}} [-]$	2.65	0.43	1.17	2.53	0.55	1.10
$\lambda_1^{\text{ge}} [-]$	2.13	0.47	1.11	2.26	0.57	1.08
$\lambda_2^{\text{ge}} [-]$	1.79	0.45	1.05	1.68	0.59	1.02

expanders. The spherical expander triggers a growth pattern that reflects the placement of the expander. The crescent expander triggers larger growth in the regions above the expander towards the end of the expansion process; however, it also triggers growth in remote regions.

## 9.4 Discussion

This manuscript presents the kinematic characterization of a skin expansion procedure on a porcine model using multi-view stereo, isogeometric analysis, and the continuum theory of finite growth. The present work builds upon a methodology recently introduced by our group [54]. Our first experiment reported growth induced by a rectangular expander and it served as a proof of concept. Here we aimed at comparing three different expander geometries: spherical, rectangular and crescent. Unfortunately, the rectangular expander migrated out of the reference grid and we disregarded its analysis. For all other patches, we not only compared the growth itself, but also characterized the incompatibility of living systems.

The core of the theory of finite growth is the notion of an incompatible grown configuration [209]. The deformation gradient is split into elastic contributions and growth,  $\mathbf{F} = \mathbf{F}^e \cdot \mathbf{F}^g$ . The tensor field  $\mathbf{F}^g$  reflects the biological response, it captures mathematically how tissues respond to mechanical cues. This field is not the gradient of a deformation, which implies that it introduces incompatibility. To quantify incompatibility experimentally, we subdivide the excised grown skin patches into  $5 \times 5$  smaller pieces and calculate the corresponding deformation fields. While incompatibility has been characterized in tubular tissues through the global measure of the opening angle [128], this study is the first to

quantify incompatibility for an entire field quantity.

We characterize the kinematics of skin expansion through three modular analyses: The kinematics of the control patch provide information about natural growth and tissue pre-strain. The kinematics of the expanded patches provide information about the deformation induced by the device and the elastic deformation released upon excision. The combination of these two analyses defines the growth attributed to the expansion process alone.

Natural growth during the  $t = 21$  period revealed that the specimen grows at a nearly linear rate and reaches a value of  $\vartheta^{\text{gn}} = 1.38$ . This is consistent with our previous experiments in which the specimen grew a total of 1.48 times in area in  $t = 37$  days. The natural growth rate for our previous experiment was 0.04/days, here it is 0.06/days. While this reveals the importance of variation between animals, these values are still within the same order of magnitude.

Prestrain agrees well with our previous results. Once more, we find the importance of inter-animal variation. While previously we reported an isotropic area prestrain prior to subdivision of 1.44, here the corresponding average is 1.24. We consistently observed that prestretch is isotropic although the tissue itself is highly anisotropic [321,373]. In our previous experiment, the reconstruction error for the excised control patch was 10%, significantly larger than here with 2% and less. Here, after excising the entire grid, we further release residual stress by subdividing the patch into smaller pieces. The resulting deformation field becomes discontinuous across the patch boundaries. Naturally, this additional subdivision step alters the total prestrain and reveals anisotropy, which had been undetected when considering the full patch. We now define the total prestrain as the composition of excision and subdivision. With the subdivision included, the total prestrain averages 1.38, an increase of 11.3% as compared to excision alone. When the full, intact patch is considered, both longitudinal and transverse directions show stretches of 1.12. Upon subdivision, the transverse direction shows a higher total pre-stretch of 1.19 compared to 1.14 in the longitudinal direction. This suggests that the incompatibility of living systems plays an important role in the *in vivo* setting.

The *in vivo* deformation and the elastic deformation upon excision differ significantly for different expander geometries. In clinical practice, expanders come in different sizes and shapes. Simulations and experiments have shown that varying the expander geometry alters the resulting deformation field and, consequently, the regional variation of skin growth

[48, 51]. Choosing the *in vivo* state at day  $t = 0$  as reference configuration, allows us to characterize the *chronic* tissue response. As we had previously predicted computationally [51], even though both expanders were filled to the same volume of 225 cc, the spherical device induces an average area change of 1.70 at  $t = 21$  days while the crescent expander results in an area change of 1.49. In our previous experiment we determined an area change of 1.73 at  $t = 20$  days for a filling volume of 200cc for the rectangular expander. In agreement with our computational predictions, both spherical and rectangular expanders induce larger deformations than the crescent device. The comparison with the rectangular expander from the previous experiment has to be done with caution though since the inflation protocol was not exactly the same as the one followed here. The deformation induced by the devices is anisotropic and displays the same trend for both expander geometries: longitudinal stretches are always larger than transverse stretches. This finding is also consistent with our initial experiment, and suggests that anisotropic material properties of porcine skin are significant and more important than the shape of the expander [182].

In addition to the *chronic* response, we also characterize the *acute* response by choosing the patch right before the inflation as reference configuration and the patch immediately after inflation as deformed configuration. The average values for the strains are surprising. On average, the area change over the grid is close to one. In fact, the average longitudinal stretches always always tensile,  $\lambda_1^a \geq 1.0$ , and the average transverse stretches are always compressive,  $\lambda_2^a \leq 1.0$ . This seems counterintuitive, since we would expect that each inflation step imposes stretches larger than one. Looking closer at the regional stretch variation, we do find this to be the case: the contour maps for  $\lambda_1^a$  reflect the placement of the expander, with values in the range 1.00 to 1.50. The contours of  $\lambda_2^a$  seem to capture the region along the longitudinal axis in which the expander is placed, but they do not show great variation along the transverse axis. It seems reasonable to assume that the acute response is dominated by the elastic properties of the tissue and not by growth. Coherent with this assumption, the acute response is indeed very similar across all inflation steps. Furthermore, longitudinal stretches are always larger, consistent with the orientation of Langer's lines, which are representative of the collagen orientation [214, 321]. The fact that the average deformation is close to unity questions the choice of the grid size since we are unable to determine how far beyond the grid the skin is being deformed.

The total elastic deformation  $\mathbf{F}^e$  follows upon excision of the entire expanded patches. We observe a significant difference between the spherical and crescent expanders upon

excision: Patch R corresponding to the crescent expander retracts 1.27 in area with an almost isotropic distribution of strain in the two directions of interest; patch P also retracts almost isotropically, but the total area change of 1.42 is significantly larger. The variation between spherical and crescent expanders seems to correlate with the amount of *in vivo* deformation  $\mathbf{F}$ . In our initial experiment, the retraction of 1.20 was slightly smaller. One major difference between both inflation protocols is the duration of the expansion process. In the first experiment, we harvested the patches at  $t = 37$  days and the rate of inflation was lower compared to the present protocol. In both experiments, it is impossible to determine whether the tissues have reached a steady state in the adaptation process at the time of tissue harvest. This remains one critical question in our research agenda.

In addition to the elastic patch kinematics, we also quantified the incompatibility. It has been hypothesized that tissue growth increases the effect of residual deformation [249]. By subdividing the excised patches we confirm this hypothesis. The composition of mappings  $\mathbf{F}^e \cdot \mathbf{F}^{es}$  is the total elastic deformation, and not just  $\mathbf{F}^e$  as we had proposed previously. Including the subdivision step, the total elastic area change is 1.39 for the spherical and 1.32 for the crescent expander. Although the longitudinal stretches are always larger than the transverse ones, for the expansion-induced deformation  $\mathbf{F}$ , the opposite happens to the elastic deformation  $\mathbf{F}^e \cdot \mathbf{F}^{es}$ . This is thought provoking and could point to a difference in the growth rates along and perpendicular to the collagen fibers. The contour plots of the elastic deformation depict clearly the discontinuity of the deformation across the smaller patches. Once again, we highlight the importance of carefully considering the residual deformations induced by growth, which enter our theoretical framework through the intermediate, incompatible configuration. The contours of  $\vartheta^e \cdot \vartheta^{es}$  and  $\lambda_1^e \cdot \lambda_1^{es}$  closely resemble the placement of the expander. The contours of  $\lambda_2^e \cdot \lambda_2^{es}$  are more homogeneous.

The final goal of our analysis is to determine the amount of skin growth attributed to the expansion process. As expected, we confirm that both spherical and crescent expanders result in a net tissue gain [52]. It has been hypothesized that chronic hyper-stretch is the driver of new skin growth [342]. Our results support this hypothesis. All external parameters are the same for both expanders. The difference between both expansion protocols is the amount of expansion-induced deformation  $\mathbf{F}$ . The spherical expander induces larger deformations and results in an average area growth of 1.17. The area gain for the crescent expander was 1.10. The contour plots support the hypothesis of hyper-stretch driven growth and are in agreement with our previous finite element predictions [51]: Regions where the

expander was placed display a larger amount of growth; regions in the periphery display smaller growth.

The anisotropy of tissue growth deserves special attention. The end result shows that skin grows more in the longitudinal than in the transverse direction. It seems overly simplified though to attribute this difference solely to the expansion-induced deformation  $\mathbf{F}$ . A comparison of the differences in the elastic deformation  $\mathbf{F}^e \cdot \mathbf{F}^{es}$  suggests that the growth rates along and perpendicular to the fiber orientation may be different. A biological explanation of such difference is not possible with our current data and motivates further experiments.

Tissue expansion was introduced half a century ago and has since revolutionized the field of plastic and reconstructive surgery [270]. Even 50 years later, there is still no reliable, quantitative preoperative planning tool [39, 341]; treatment planning is done on a case by case basis and puts an unnecessary burden on the surgeon's experience and training [139, 239]. Even with careful planning, treatment is not free of suboptimal outcomes and complications [238]. One of the many important choices is the selection of an appropriate expander geometry [274]. This decision is difficult to rationalize without a fundamental understanding of the basic mechanisms of skin adaptation to mechanical stimuli [115]. One key element to advance predictive medicine—and tissue expansion in particular—is to synthesize clinical experience and basic sciences into a theoretical model to predict treatment outcomes within a personalized scenario [418]. Our group and others have previously proposed a theoretical and computational model for skin expansion based on the theory of finite growth and finite element analysis [51, 288, 351]. To demonstrate its clinic potential, we have now established a novel experimental protocol towards a detailed kinematic characterization of skin deformation, prestrain, and growth in a chronic porcine model that closely resembles the clinical scenario [54]. We believe that our results constitute a major step towards validating skin expansion models. We hope to continue this work and inspire similar efforts to advance predictive medicine in procedures in which mechanics play a central role.

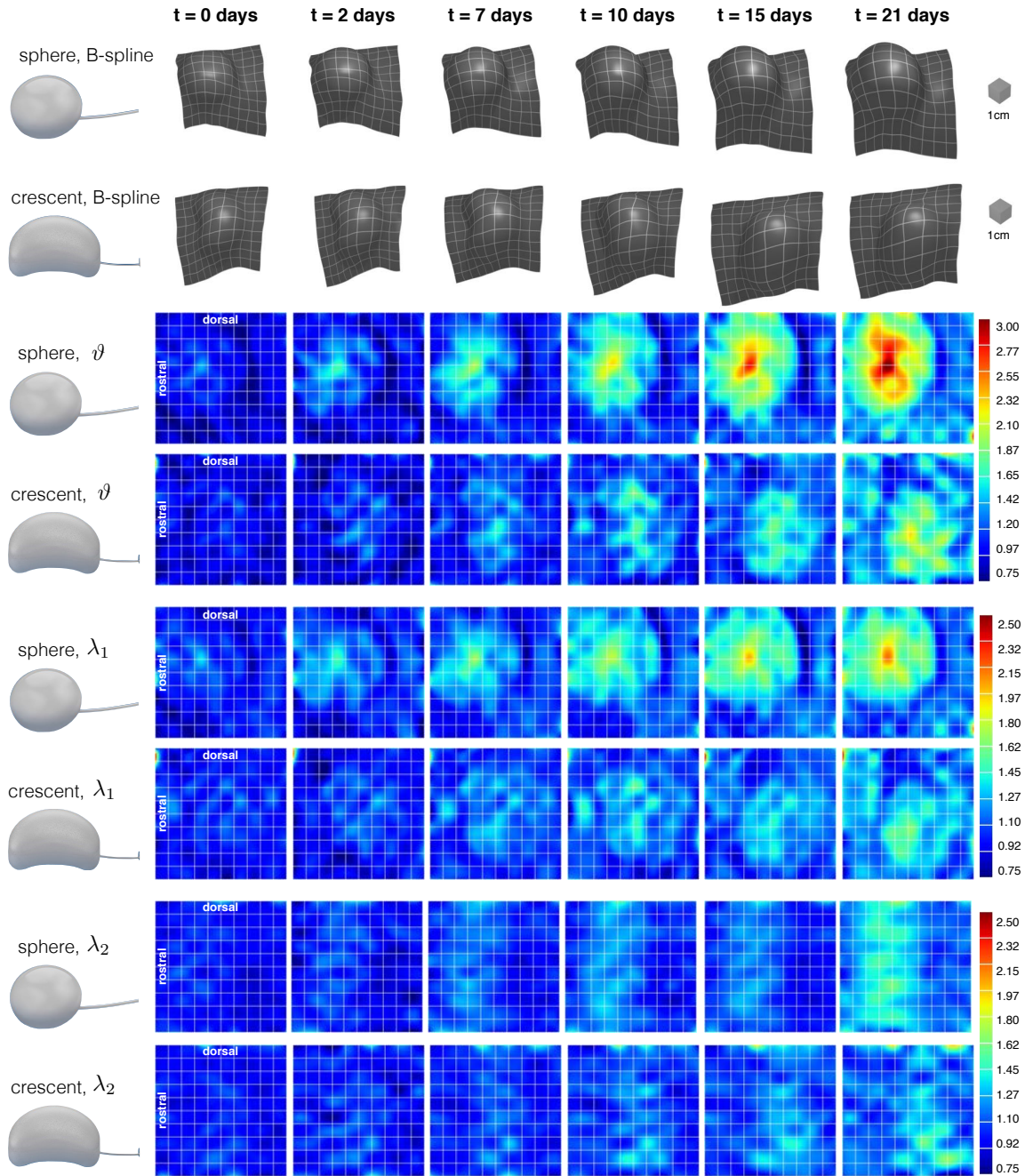


Figure 9.7: Chronic deformation induced by tissue expansion. The columns depict the chronic overstretch due to a sequence of inflations at the given time points. The first two rows show the total area change  $\vartheta$  for the spherical and crescent expanders in the patches P and R. The middle and bottom rows show the corresponding stretches  $\lambda_1$  and  $\lambda_2$  aligned with and perpendicular to the long axis of the pig. Deformations along the long axis are greater than those perpendicular to the long axis. Deformations induced by the spherical expander are larger than those by the crescent expander even though both devices were filled to the same volume.

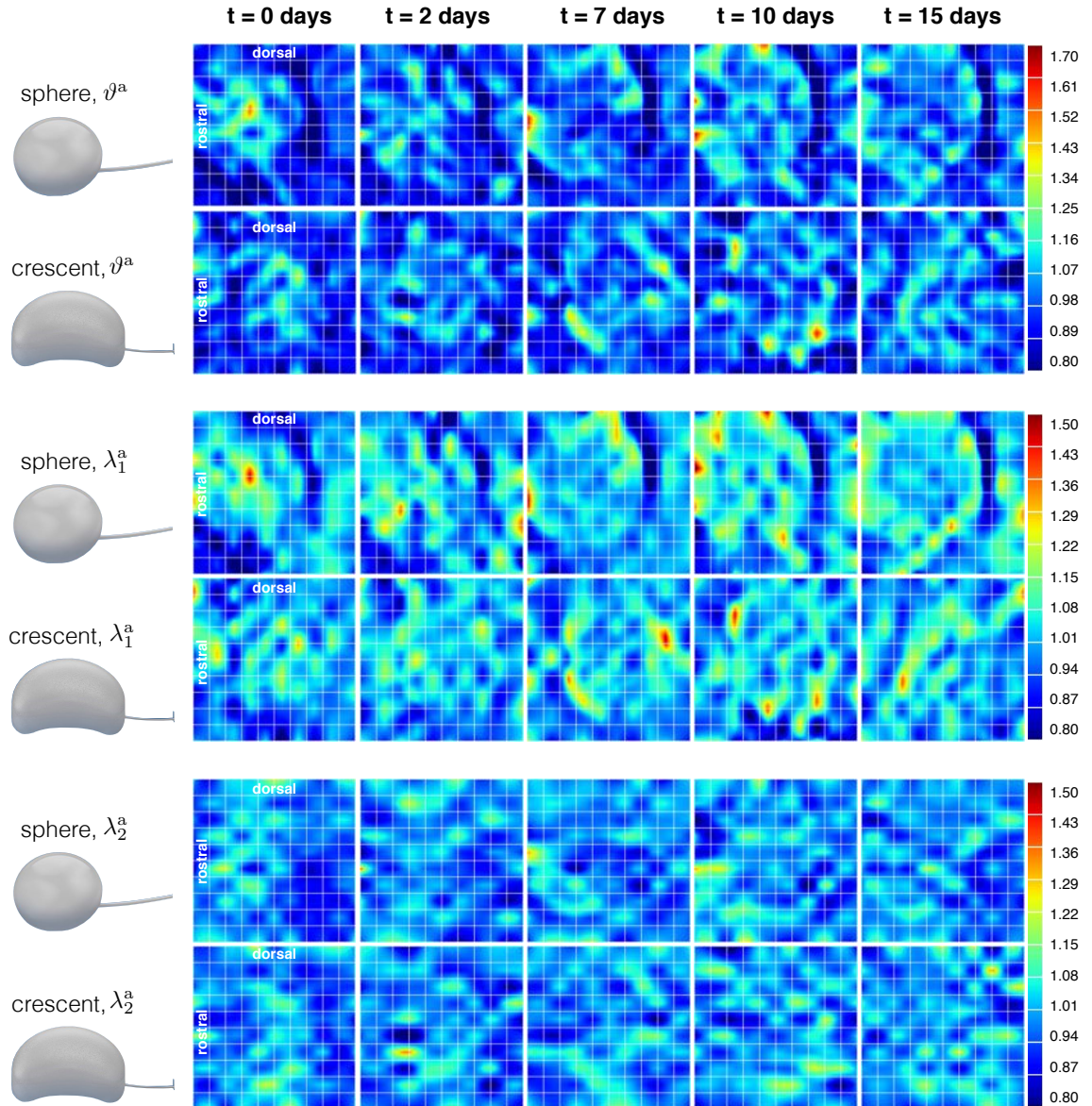


Figure 9.8: Acute deformation induced by tissue expansion. The columns depict the acute deformation imposed by a single inflation step at different time points. The first two rows show the acute area change  $\vartheta^a$  for the spherical and crescent expanders in the patches P and R. The middle and bottom rows show the corresponding acute stretches  $\lambda_1^a$  and  $\lambda_2^a$  aligned with and perpendicular to the long axis of the pig. Deformations along the long axis are greater than those perpendicular to the long axis. Deformations induced by the spherical expander are larger than those by the crescent expander even though both devices were filled to the same volume at each inflation step.

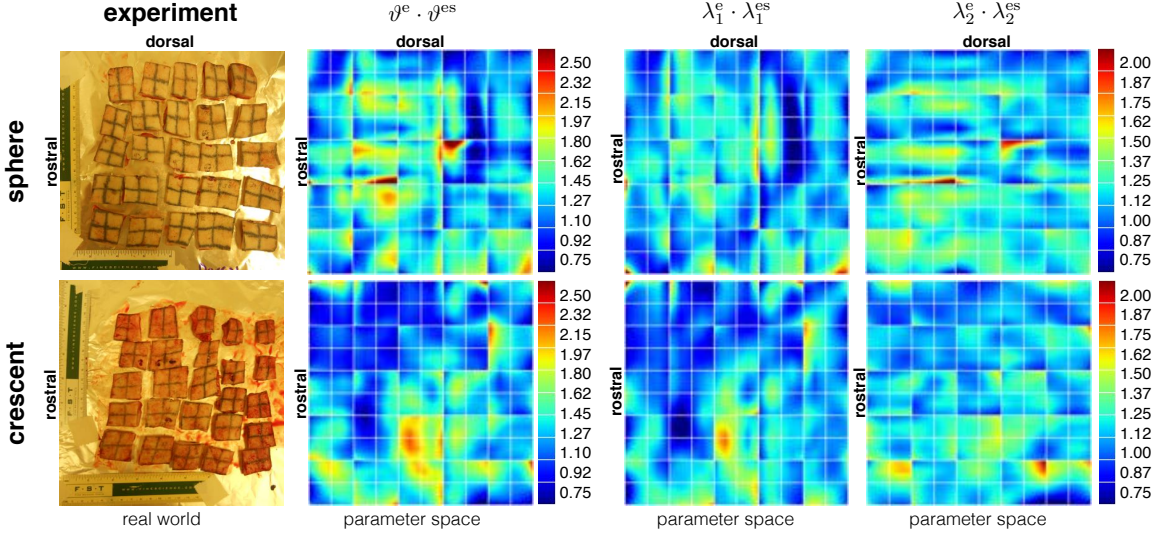


Figure 9.9: Elastic deformation released upon excision and further subdivision of the expanded patches P and R. Skin releases the elastic stress upon excision and subdivision, left. The total elastic deformation is a composition of excision and subdivision maps  $\mathbf{F}^e$  and  $\mathbf{F}^{es}$ . The resulting configurations are incompatible. The contour maps highlight the incompatibility of the total elastic area deformation and the elastic stretch in longitudinal and transverse directions.

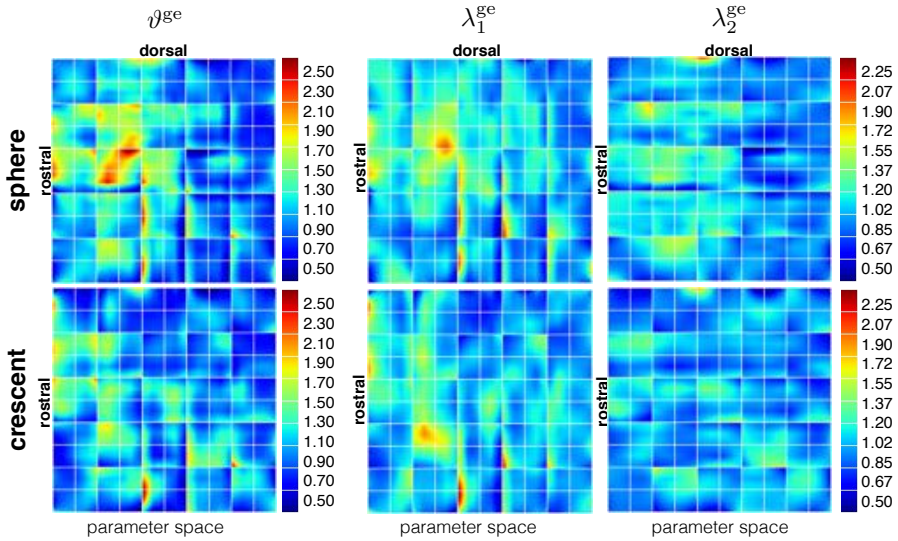


Figure 9.10: Growth induced by the expansion process. The spherical expander, top, induces a larger amount of growth compared to the crescent expander, bottom. The contour maps highlight area growth and the growth in the longitudinal and transverse directions.

## Chapter 10

# Computational Modeling of Flap Design

**Abstract.** The use of local skin flaps harvested following skin expansion has revolutionized the field of plastic and reconstructive surgery. In the surgical planning process, it is now commonly accepted that mechanical loading plays a crucial role in chronic and acute tissue response with excessive loads associated to pathological growth and remodeling. However, despite this knowledge, flap design has never been analyzed from a structural point of view before. Here we show the application of computational mechanics in the simulation of three dimensional transversely isotropic membranes undergoing large deformations. In this manuscript we show regional variations of stress for the two most common flap designs; we explore also variations coming from different fiber orientations taken into account in the constitutive equations. Based on our results, zones of maximum stress are in agreement with zones of compromised tissue integrity due to mechanical forces and seem to be a reasonable predictor for necrosis and analogous complications. This model is, therefore, a first step paramount for the ongoing progress of personalized medicine and surgery planning.

### 10.1 Motivation

Tissue expansion is a reconstructive surgery technique that has established itself as a revolutionary option for the surgeon to correct birth defects and after burns and tumor removal [141]. The procedure was first introduced fifty years ago by Neumann, who implanted a balloon and grew skin in situ that he then utilized to resurface an ear [270]. Since then,

skin expansion has been eagerly adopted by clinicians, revolutionizing the field of plastic and reconstructive surgery because of its obvious advantages of generating flaps of skin with the same mechanical, hair bearing, color and texture characteristics of the surrounding tissue, making it ideal from an aesthetic standpoint [13, 319]. In current clinical practice, a medical device resembling a balloon is implanted subcutaneously and inflated gradually over a period of 4 to 6 weeks. Skin responds to the gradual over-stretch by growing tissue in-plane in order to achieve a homeostatic state [92, 342]. When the expander is removed, newly grown skin is available for reconstructive purposes through a process called flap design [185]. Careful planning of flap design is key to successful defect repair in plastic and reconstructive surgery. However, despite significant efforts from the surgeon during pre-operative planning, flap failure still occurs [231]. Furthermore, even though flap survival is the top-most priority, sub-optimal flap design can lead to a poor healing response which ultimately culminates in undesired outcomes such as hypertrophic scars and keloids [388]. The causes of flap complications are numerous, but mechanical factors are believed to play a central role [278]. For instance, excessive tension of the tissue can create compression of the pedicle, compromising blood supply and leading to tissue necrosis [376]. Figure 10.1 illustrates this, tissue expanders were inserted to resurface a pigmented nevus, however, distal flap necrosis originating from excessive tissue tension lead to an undesired second intervention in order to debride the necrotic tissue and resume healing.

Mechanical loads have been shown to also influence healing at the suture lines, with extreme loading conditions causing a hypertrophic growth response characterized by an increased inflammatory signal and increased collagen deposition [1]. Thus, mechanical loading greatly influences the result of reconstructive procedures. Nonetheless, despite of these evidences, flap design following skin expansion has never been analyzed from a mechanistic point of view.

One of the principal causes for the recurrence of sub-optimal flap designs arises from the inherent constraints in determining stresses *in vivo*, a problem that spans all of surgical disciplines [400]. Even if mechanical cues are recognized as critical factors for the outcome of the surgery, measuring the stress distribution in the clinical setting is impossible. Computational models offer an excellent alternative in this situation [72, 232]. The past two decades are populated with remarkable advances in computational modeling as an extremely useful tool in surgery planning and optimization [396, 412]. Amongst soft tissues, skin has also received important attention [8, 111].

Skin is a remarkable tissue, one of the largest organs of our body it covers an area of approximately  $2m^2$  and weights around  $3.5kg$  in the adult. The main function of this organ is to serve as a protective barrier from the outside world, regulating temperature and water exchange, as well as insulating our internal machinery from harmful substances and solar radiation [306]. Additionally, skin is densely packed with neural receptors that make this organ our largest sensor, the one responsible for our tactile sense [90]. Despite of being a very thin membrane, 8 to 14mm thick, skin consists of three very distinct layers resembling the structure of a composite material. The outermost layer, the epidermis, consists in turn of several layers of cells stacked on top of each other. The cells near the base undergo constant mitosis to continuously regenerate the epidermis. In contrast, the cells closer to the surface are dead [344]. Immediately below the epidermis there is the dermis, which is the main load bearing layer of the skin [350]. The dermis consists of a water-based matrix that serves as a scaffold for a collagen and elastin fiber network. Finally, the bottom layer, the hypodermis, consists primarily of fat and its function is to anchor the skin to the underlying bone and muscle.

From a mechanical point of view, skin is an outstanding material. Like many other collagen-based tissues, in skin, the fiber network present in the dermis is the main responsible for its elastic properties [217]. The collagen bundles in the dermis form an interwoven network aligned with a preferred direction [218]. This was first noticed more than a century ago by Langer who created a map of the preferred collagen orientations over the human body [215]. Skin is stiffer along this direction making it highly anisotropic. The undulation of the fibers also contributes to an overall non-linear response characterized by locking stretches [52]. Taking this into account, accurately determining a suitable material model and parameters for skin has not been a trivial task.

One of the pioneer works on skin modeling was conducted by Tong and Fung who performed biaxial tests to rabbit skin patches and fitted the data to an exponential strain energy function [373]. Then, a constitutive model based on the microstructure of the tissue was introduced by Lanir [219]. The latter model established a strain energy arising from the sum of the response of the matrix and that of the fibers. Jor et al. used this model to determine the material parameters of two pig specimens [182]. More recently, an invariant formulation for the strain energy of soft tissues based as well on the material microstructure was utilized to model the arterial walls and afterwards extended as well to characterize skin [161, 273].

Several groups have tested skin in uniaxial and biaxial settings to determine the corresponding material parameters. However, the material models employed are different from one group to another and little consensus exists on which is the most suitable constitutive law. In most cases, isotropy has been assumed as a simplification considered valid for some practical circumstances [3, 93, 155]. Nonetheless, it is generally accepted that an accurate representation of skin should incorporate the anisotropic response [110, 357].

In the context of flap design, in which accurately determining the stresses distribution over the skin patches could lead to an optimal pre-operative planning, careful consideration of available constitutive models and parameters is necessary. Moreover, an accurate modeling of the acute response has the potential to improve our understanding of the chronic adaptation of tissue following the surgical procedure.

Determining the stress distribution during flap design poses several challenges. Following expansion skin is present in a three dimensional dome-like shape which is stretched to resurface nearly flat zones [139, 140]. During this process, skin undergoes large deformations that require the consideration of nonlinearity, anisotropy and locking stretches. As recognized above, a problem with this characteristics presents a niche for computational mechanists. In this manuscript we investigate the two most common flap designs used following skin expansion: direct advancement and double back-cut flap [416]. To model skin we use a hyper elastic description based on a micro-structural approach following the invariant formulation proposed by Gasser et al. [126].

The manuscript is organized as follows. In section 2 we describe the constitutive equations used for the continuum mechanics modeling of skin. Section 3 presents the finite element formulation of the problem. We show the results of our simulations in Section 4 and draw important conclusions and implications of the present work to improve surgical outcomes in the plastic and reconstructive field in Section 5.

## 10.2 Governing Equations

The mechanical response of skin is determined by its middle layer, the dermis, which exhibits a well organized micro-structure characterized by a collagen fiber network with a preferred orientation embedded in a water-based matrix [3, 417]. This composition is common amongst soft biological tissues, it is associated with highly anisotropic behavior and locking stretches,



Figure 10.1: Distal flap necrosis induced by excessive tissue tension. a) Giant congenital pigmented nevus on the right lower leg of a two-year old boy. b) Tissue expanders inserted on the lateral and medial sides of the upper thigh, filled to capacity. c) Lateral leg two days after resurfacing with rotation-advancement flap from expanded lateral thigh tissue. d) Medial leg two days after resurfacing with direct-advancement flap from expanded medial thigh tissue demonstrating distal flap necrosis. e) Necrotic tissue of distal flap debrided to promote healing by secondary intention. f) Medial leg two months after flap advancement, with healing of distal aspect of flap by secondary intention

and it has been extensively modeled in the past two decades [205, 208]. Here we follow the constitutive model proposed by Gasser et al. to capture the mechanical response of skin during flap design [126].

Let  $\mathcal{B} \subset \mathbb{R}^3$  be the reference configuration of a body that occupies  $\mathcal{S} \subset \mathbb{R}^3$  in the deformed state. Material points  $\mathbf{X} \in \mathcal{B}$  are mapped to points  $\mathbf{x} \in \mathcal{S}$  through the deformation map  $\varphi$ . We define the deformation gradient  $\mathbf{F} = \nabla \varphi$  to be the spatial gradient of the deformation map, which relates the tangent space of the reference to the tangent space of the current configuration. Moreover, the jacobian  $J = \det(\mathbf{F})$  introduces the map of volume from one configuration to the other. Due to the incompressible nature of skin we have the multiplicative decomposition of  $\mathbf{F}$  into an isochoric and a isovolumetric part as:

$$\mathbf{F} = \mathbf{F}^{\text{vol}} \cdot \bar{\mathbf{F}} \text{ with } \mathbf{F}^{\text{vol}} = J^{1/3} \mathbf{I} \text{ and } \bar{\mathbf{F}} = J^{-1/3} \mathbf{F} \quad (10.1)$$

where  $\det(\bar{\mathbf{F}}) = 1$  and, consequently,  $J = \det(\mathbf{F}) = \det(\mathbf{F}^{\text{vol}}) \geq 0$ .

Local deformation is captured with the right Cauchy-Green deformation tensor  $\mathbf{C}$  and its

isochoric part  $\bar{\mathbf{C}}$

$$\mathbf{C} = \mathbf{F}^t \cdot \mathbf{F} = J^{2/3} \bar{\mathbf{F}} \quad \text{with} \quad \bar{\mathbf{C}} = \bar{\mathbf{F}}^t \cdot \bar{\mathbf{F}} \quad (10.2)$$

Attending to skin's microstructure we incorporate Langer's lines into the model obtaining a transversely isotropic constitutive response. The direction of Langer's lines in the reference configuration, which is parallel to the preferred collagen orientation, is denoted by  $\mathbf{n}_0$ . This vector defines the structural tensor

$$\mathbf{N} = \mathbf{n}_0 \otimes \mathbf{n}_0 \quad \text{with} \quad \|\mathbf{n}_0\| = 1 \quad (10.3)$$

Three principal invariants and two pseudo-invariants characterize a generic transversely isotropic constitutive behavior. Here we select the jacobian  $J$  to capture the incompressible response, the first isochoric invariant  $\bar{I}_1$  for the isotropic response, and the fourth isochoric invariant  $\bar{I}_4$  to account for the anisotropic response,

$$\begin{aligned} J &= \det(\mathbf{F}) & \partial_C J &= \frac{1}{2} J \mathbf{C}^{-1} \\ \bar{I}_1 &= \bar{\mathbf{C}} : \mathbf{I} & \text{with} & \quad \partial_{\bar{C}} \bar{I}_1 = \mathbf{I} \\ \bar{I}_4 &= \bar{\mathbf{C}} : \mathbf{N} & \partial_{\bar{C}} I_4 &= \mathbf{N} \end{aligned} \quad (10.4)$$

We are now able to define the incompressible, transversely isotropic, hyperelastic free energy function

$$\psi = \psi^{\text{vol}}(J) + \bar{\psi}(\bar{I}_1, \bar{I}_4) \quad (10.5)$$

which consists of a volumetric part  $\psi^{\text{vol}}$  and an isochoric part  $\bar{\psi}$ , parameterized in terms of the first and fourth isochoric invariants  $\bar{I}_1$  and  $\bar{I}_4$  as

$$\bar{\psi} = c_0[\bar{I}_1 - 3] + \frac{c_1}{2c_2} [\exp(c_2 [\kappa \bar{I}_1 + [1 - 3\kappa] \bar{I}_4 - 1]^2) - 1] \quad (10.6)$$

where the first term corresponds to a Neo-Hookean material response defined by the bulk modulus  $c_0$ . The second term depicts the anisotropic fiber family contribution parametrized by  $c_1$ , and  $c_2$ . The anisotropic terms act in tension only,  $\bar{I}_4 \geq 1$ , and are inactive under compressive loading,  $\bar{I}_4 < 0$ .

In contrast to original Holzapfel model [161], this revised version accounts for a constitutive coupling of the first and fourth invariants through the additional parameter  $\kappa$  to incorporate microstructural fiber dispersion. The lower limit of  $\kappa = 0$  recovers the initial model without fiber dispersion and suppresses the constitutive coupling between the first and fourth

invariants; in the upper limit of  $\kappa = \frac{1}{3}$ , we attain a random fiber dispersion leading to a completely isotropic material with vanishing anisotropic terms.

The additive decomposition of the strain energy function translates in the decomposition of the Piola-Kirchhoff stress

$$\mathbf{S} = 2 \frac{\partial \psi}{\partial \mathbf{C}} = \mathbf{S}^{\text{vol}} + \mathbf{S}^{\text{iso}} \quad (10.7)$$

into volumetric and isochoric parts

$$\mathbf{S}^{\text{vol}} = 2 \frac{\partial \psi^{\text{vol}}}{\partial \mathbf{C}} = J p \mathbf{C}^{-1}, \quad \mathbf{S}^{\text{iso}} = 2 \frac{\partial \bar{\psi}}{\partial \bar{\mathbf{C}}} J^{-2/3} \mathbb{P} : \bar{\mathbf{S}} \quad (10.8)$$

where  $p = \partial \psi^{\text{vol}} / \partial J$  is the pressure, which we prescribe constitutively in the context of incompressibility. The second order tensor  $\bar{\mathbf{S}}$  comes from

$$\bar{\mathbf{S}} = 2 \frac{\partial \bar{\psi}}{\partial \bar{\mathbf{C}}} = 2 \bar{\psi}_1 \mathbf{I} + 2 \bar{\psi}_4 \mathbf{N} \quad (10.9)$$

in which  $\bar{\psi}_i = \partial \bar{\psi} / \partial \bar{I}_i$  are the derivatives of the isochoric free energy function  $\bar{\psi}$ :

$$\begin{aligned} \bar{\psi}_1 &= c_0 + c_1 \kappa & [\kappa \bar{I}_1 + [1 - 3\kappa] \bar{I}_4 - 1] \\ && \exp(c_2 [\kappa \bar{I}_1 + [1 - 3\kappa] \bar{I}_4 - 1]^2) \\ \bar{\psi}_4 &= c_1 [1 - 3\kappa] & [\kappa \bar{I}_1 + [1 - 3\kappa] \bar{I}_4 - 1] \\ && \exp(c_2 [\kappa \bar{I}_1 + [1 - 3\kappa] \bar{I}_4 - 1]^2) \end{aligned} \quad (10.10)$$

The fourth order tensor  $\mathbb{P} = \mathbb{I} - \frac{1}{3} \mathbf{C}^{-1} \otimes \mathbf{C}$  denotes the isochoric projection tensor, where  $\mathbb{I} = \frac{1}{2} [\mathbf{I} \bar{\otimes} \mathbf{I} + \mathbf{I} \underline{\otimes} \mathbf{I}]$  is the fourth order identity tensor with  $\{\bullet \bar{\otimes} \circ\}_{ijkl} = \{\bullet\}_{ik} \{\circ\}_{jl}$  and  $\{\bullet \underline{\otimes} \circ\}_{ijkl} = \{\bullet\}_{il} \{\circ\}_{jk}$ .

To solve for the deformation within a standard nonlinear finite element framework, we require the linearization of the Piola-Kirchhoff stress  $\mathbf{S}$  with respect to the right Cauchy-Green deformation tensor  $\mathbf{C}$  which defines the fourth order tangent moduli

$$\mathbb{C} = 4 \frac{\partial^2 \psi}{\partial \mathbf{C} \otimes \partial \mathbf{C}} = 2 \frac{\partial \mathbf{S}}{\partial \mathbf{C}} = \mathbb{C}^{\text{vol}} + \mathbb{C}^{\text{iso}} \quad (10.11)$$

consisting as well of volumetric and isochoric parts

$$\begin{aligned}\mathbb{C}^{\text{vol}} &= 2 \frac{\partial \mathbf{S}^{\text{vol}}}{\partial \mathbf{C}} = \tilde{p} \mathbf{C}^{-1} \otimes \mathbf{C}^{-1} - 2 J p \mathbb{I}_{C^{-1}} \\ \mathbb{C}^{\text{iso}} &= 2 \frac{\partial \mathbf{S}^{\text{iso}}}{\partial \mathbf{C}} = J^{-4/3} \mathbb{P} : \bar{\mathbb{C}} : \mathbb{P}^t \\ &\quad + \frac{2}{3} [J^{-2/3} \bar{\mathbf{S}} : \mathbf{C} \bar{\mathbb{P}} - [\bar{\mathbf{S}} \otimes \mathbf{C}^{-1}]^{\text{sym}}].\end{aligned}\tag{10.12}$$

The linearization introduces the derivative of the pressure with respect to the jacobian in the volumetric part  $\tilde{p} = J p + J^2 \partial p / \partial J$ .

The first term in the isochoric part comes from the derivative of  $\bar{\mathbf{S}}$  with respect to  $\bar{\mathbf{C}}$  that can be expanded as

$$\bar{\mathbb{C}} = 2 \frac{\partial \bar{\mathbf{S}}}{\partial \bar{\mathbf{C}}} = 4 [\bar{\psi}_{11} \mathbf{I} \otimes \mathbf{I} + 2 \bar{\psi}_{14} [\mathbf{I} \otimes \mathbf{N}]^{\text{sym}} + \bar{\psi}_{44} \mathbf{N} \otimes \mathbf{N}],\tag{10.13}$$

where the common abbreviation  $\bar{\psi}_{ij} = \partial^2 \bar{\psi} / \partial \bar{I}_i \partial \bar{I}_j$  for the second derivatives has been used:

$$\begin{aligned}\bar{\psi}_{11} &= c_1 \kappa^2 \frac{[1 + 2 c_2 [\kappa \bar{I}_1 + [1 - 3\kappa] \bar{I}_4 - 1]]}{\exp(c_2 [\kappa \bar{I}_1 + [1 - 3\kappa] \bar{I}_4 - 1]^2)} \\ \bar{\psi}_{14} &= c_1 \kappa [1 - 3\kappa] \frac{[1 + 2 c_2 [\kappa \bar{I}_1 + [1 - 3\kappa] \bar{I}_4 - 1]]}{\exp(c_2 [\kappa \bar{I}_1 + [1 - 3\kappa] \bar{I}_4 - 1]^2)} \\ \bar{\psi}_{44} &= c_1 [1 - 3\kappa]^2 \frac{[1 + 2 c_2 [\kappa \bar{I}_1 + [1 - 3\kappa] \bar{I}_4 - 1]]}{\exp(c_2 [\kappa \bar{I}_1 + [1 - 3\kappa] \bar{I}_4 - 1]^2)}\end{aligned}\tag{10.14}$$

The second term of the isochoric part of  $\mathbb{C}$  introduces another fourth order projection tensor  $\bar{\mathbb{P}} = \mathbb{I}_{C^{-1}} - \frac{1}{3} \mathbf{C}^{-1} \otimes \mathbf{C}^{-1}$ , where  $\mathbb{I}_{C^{-1}} = \frac{1}{2} [\mathbf{C}^{-1} \bar{\otimes} \mathbf{C}^{-1} + \mathbf{C}^{-1} \underline{\otimes} \mathbf{C}^{-1}]$ .

The derivation we outlined yields the constitutive equations in the Lagrangian setting. To obtain the cauchy stress  $\boldsymbol{\sigma}$  and the Eulerian tangent moduli  $\mathbb{c}$  used in several commercial finite element packages, we perform push forward operations to the second Piola-Kirchhoff stress and the Lagrangian tangent respectively:  $\boldsymbol{\sigma} = \frac{1}{J} \mathbf{F} \cdot \mathbf{S} \cdot \mathbf{F}^t$ ,  $\mathbb{c} = \frac{1}{J} [\mathbf{F} \bar{\otimes} \mathbf{F}] : \mathbb{C} : [\mathbf{F}^t \bar{\otimes} \mathbf{F}^t]$ .

### 10.3 Finite Element Model

We performed all simulations using a commercially available, general purpose, implicit finite element solver, Abaqus Standard Version 6.9. To obtain the dome-like three-dimensional

geometry that exists after expansion we virtually grew skin by inflating an originally flat square of tissue with a computational tool previously developed and published by our group [51]. We created two idealized geometries to be used in two different flap designs. The first geometry we modeled was a rectangular sample of tissue with dimensions  $26 \times 26 \times 0.5\text{cm}^3$  which we divided into 3328 trilinear brick elements. The second geometry had dimensions  $24 \times 22 \times 0.5\text{cm}^3$  which we discretized with 4224 trilinear brick elements. In both cases we used two layers of elements across the thickness.

We applied pressure underneath the tissue to a region of  $11 \times 11\text{cm}^2$  to induce tissue growth. Computationally, this was achieved by the multiplicative decomposition of the deformation gradients into a growth part and an elastic part. The growth part of the deformation gradient was modeled as a function of stretch, such that deforming the skin patch beyond a physiological limit translated in area growth [418].

After achieving the desired area gain we released the pressure to allow for the elastic part of the deformation to vanish. The net area gain was 40.9% corresponding to  $49.6\text{cm}^2$ . Growth induced residual stresses did not fully disappear even after expander removal, nonetheless, stresses were considered negligible compared to the physiological state of tissue pre-tension *in vivo* such that the resulting deflated geometry was assumed stress-free for the purpose of the flap design simulations. At the end of this step we no longer had an idealized patch of skin but a complex three-dimensional geometry which is what surgeons have to deal with in their daily clinical practice [341, 385].

We used the expanded skin geometries to simulate two common flap designs, the direct advancement flap and the double back-cut flap.

We used material parameters fitted for pig skin using the model proposed by Lanir [219]. For our simulations we used  $c_0 = 0.0511\text{MPa}$ ,  $c_1 = 0.015\text{MPa}$ ,  $c_2 = 0.0418$ , and a fiber dispersion  $\kappa = 0.05$ .

### 10.3.1 Direct Advancement Flap

Figure 10.2 shows the schematic design of the direct advancement flap. To obtain this flap from our grown skin geometry we cut along the base of the expander parallel to the direction in which the skin is going to be stretched. We then removed the damaged zone adjacent to the grown skin to complete the pre-processing of the finite element mesh prior to the utilization of the flap.

The direct advancement flap is the simplest of all available designs and it facilitates the

job of the surgeon to estimate the size of the defect to be excised, however, it has the disadvantage of wasting tissue on the sides and thus is not the most efficient of the common flap designs.

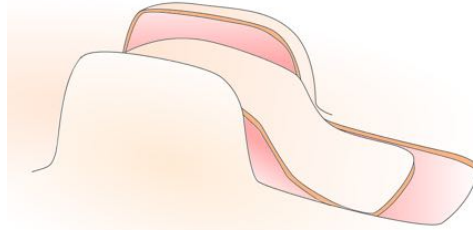


Figure 10.2: Direct advancement flap. Skin is cut along the base of the expander in the advancement direction. Damaged tissue is removed next to the frontal edge and the flap is then stretched to cover the excised area.

### 10.3.2 Double Back-Cut Flap

Figure 10.3 illustrates schematically the design of the double back-cut flap. To create the flap from our model we cut along the base of the expander, parallel to the advancement direction, from the front to the middle of the expanded skin. Then we cut towards the center of the expander. Finally, we removed the damaged region of tissue contiguous to the expanded skin to complete the pre-processing of the mesh to account for this surgical procedure prior to flap utilization.

The double back-cut flap, as opposed to the direct advancement flap, does not disregard newly grown skin and therefore it is more efficient in terms of tissue utilization. However, this type of flap induces a combination of advancement and rotation that leads to a non-intuitive mechanical deformation and rotation of Langer's lines with respect to the reference configuration.

## 10.4 Results

To simulate the clinical procedure we performed the utilization of the flap by placing wire connectors between pairs of nodes of the finite element mesh. We brought the nodes together by prescribing the displacements of the wire connectors. This resembles the surgical scenario in which opposite skin edges are joined together by means of suture at discrete

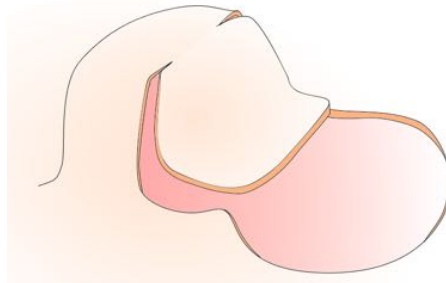


Figure 10.3: Double back-cut flap. First, cuts are made along the base parallel to the advancement direction from the front to the middle of the expanded skin. Then, perpendicular cuts towards the middle are performed. Finally, the damaged zone is removed next to the front of the expander and the flap is stretched to resurface the area.

locations.

We performed two sequences of simulations for each flap design. Since skin exhibits highly anisotropic behavior it was of interest to explore the effects of different fiber orientations in the final stress distribution. Thus, in one set of simulations, collagen fibers were considered aligned with the advancement direction and perpendicular to it in the second set of simulations.

#### 10.4.1 Direct Advancement Flap

Figure 10.4 shows the time sequence of the simulation when the fibers were originally oriented parallel to the advancement direction. In Figure 10.5 the fibers were modeled perpendicular to this direction. Comparison of the two time sequences demonstrates the importance of considering the anisotropic nature of skin when performing predictions of the mechanical stress distribution for clinical procedures.

In the parallel case, maximum stresses were twice as much in the base and the front edge as compared to the perpendicular fiber case. The maximum stress value for the parallel case reached 2.00MPa. Additionally, as illustrated by Figure 10.5, the stress distribution was more homogenous in the second set of simulations.

#### 10.4.2 Double Back-Cut Flap

Figure 10.4 shows the time sequence of the simulation when the fibers were originally oriented parallel to the advancement direction. Maximum stress values reached 1.50MPa.

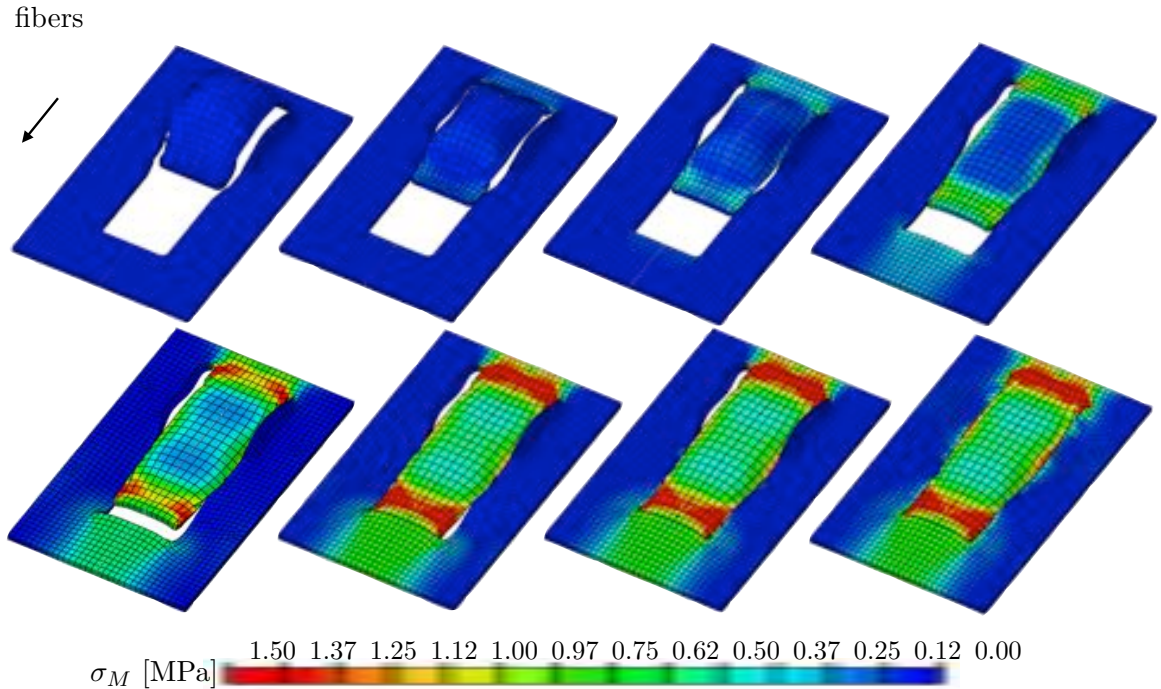


Figure 10.4: Direct advancement flap simulation when fibers are parallel to the advancement direction. Color code represented von Misses stress.

There were four regions of stress concentration: at the base, at the distal edge, and at both corners where skin was not only stretched along the advancement direction but also rotated towards the side edges.

In Figure 10.5 we depict four time frames of the simulation corresponding to the case where the collagen fibers were modeled perpendicular to the direction of advancement. Maximum stress values were similar to the parallel case, reaching 1.50MPa in zones of stress concentration. However, the stress contours were substantially different. In the perpendicular case, the maximum zones of stress were the four corners of the resurfaced area and the base and distal edges showed von Mises stress around 0.75MPa.

## 10.5 Conclusion

In this manuscript we show the application of finite elements to analyze the stresses in skin during reconstructive surgery procedures. We present the continuum mechanics framework

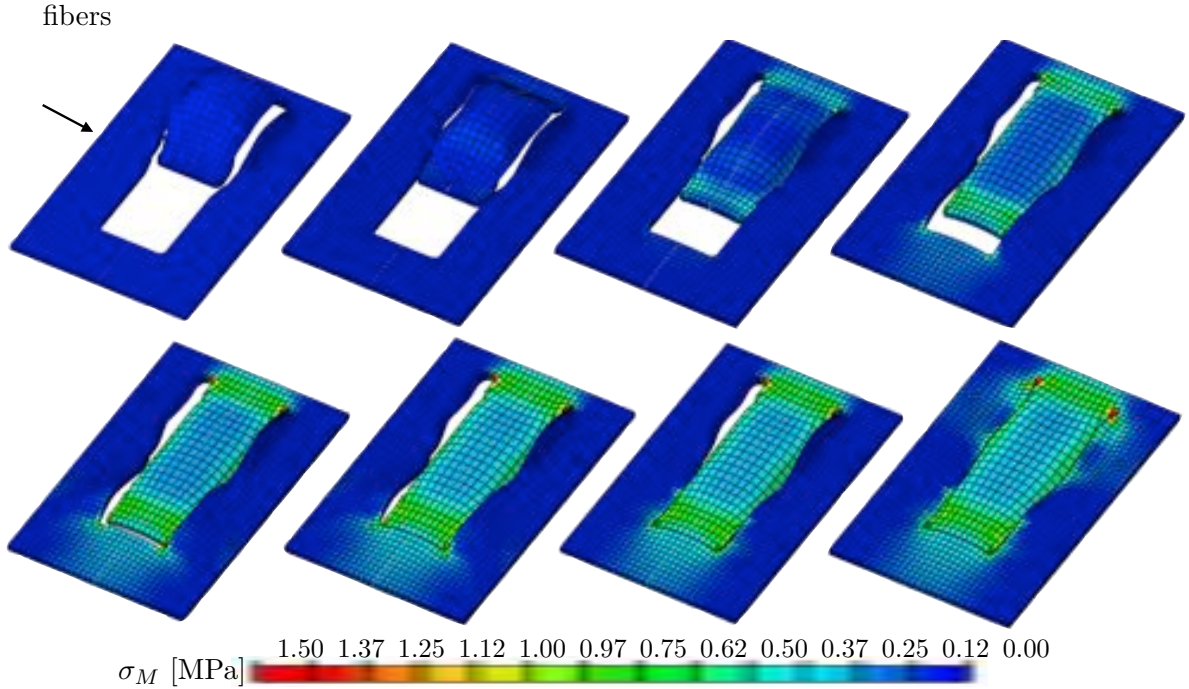


Figure 10.5: Direct advancement flap simulation when fibers are perpendicular to the advancement direction. Color code represented von Misses stress.

to model skin as a hyper elastic, transversely isotropic material characterized by a preferred orientation of a collagen fiber family. The constitutive equations we present are inspired by the tissue microstructure and follow closely the derivation proposed by Gasser et al, which has been successfully applied to other soft biological tissues [126]. We apply this model in the context of flap design after skin expansion, a clinically relevant scenario in which accurate prediction of the stress fields is peremptory yet challenging since flaps undergo large deformations. We simulate the direct advancement flap and the double back-cut flap, two widely popular flap methodologies, when the fibers are oriented parallel and perpendicular to the advancement direction.

Computational methods have proven to be an excellent alternative to determine stress profiles especially in situations in which it is impossible to gather such data experimentally [67, 151]. In particular, the outcome of reconstructive procedures is greatly affected by the mechanical loading and stress concentrations. Extreme loading conditions on the skin can dramatically affect the success of an intervention, in some cases causing tissue necrosis.

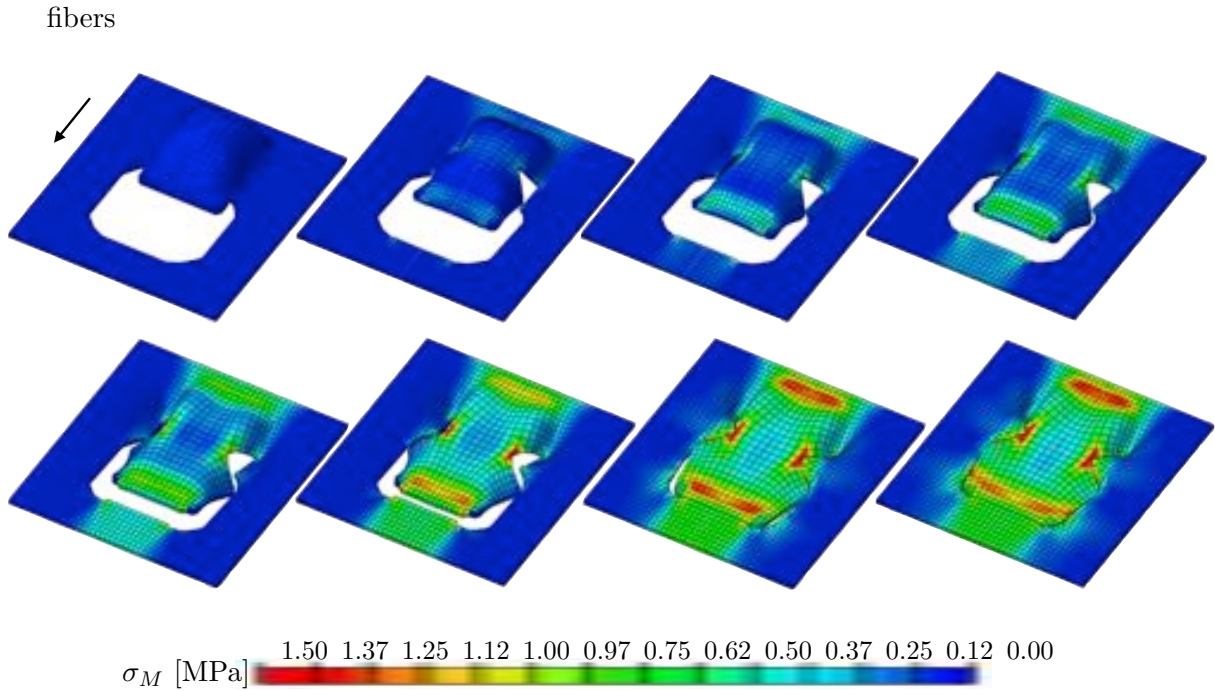


Figure 10.6: Double back-cut flap simulation when fibers are parallel to the advancement direction. Color code represented von Misses stress.

Even moderate deviations from physiological ranges of mechanical forces and stretches can trigger pathological responses. The most common of complications is hyperthrophic scarring [403].

Motivated by this needs, several groups have modeled skin and used finite elements to simulate reconstructive procedures employing idealized geometries and simplified tissue constitutive models that consider skin as an isotropic material [220]. Skin is, however, highly anisotropic and the deformations undergone by the tissue in reconstructive procedures are not usually limited to flat surfaces but rather three-dimensional membranes undergoing large deformations [212].

In this manuscript we explore, for the first time, the mechanical characterization of flap design after skin expansion, a meaningful clinical problem [239]. Tissue expansion is a well established reconstructive procedure that allows to resurface zones of damaged tissue with skin that bears the same texture, color and mechanical properties [21,25,31]. During expansion, skin is grown into dome-like shapes that are stretched and undergo large deformations

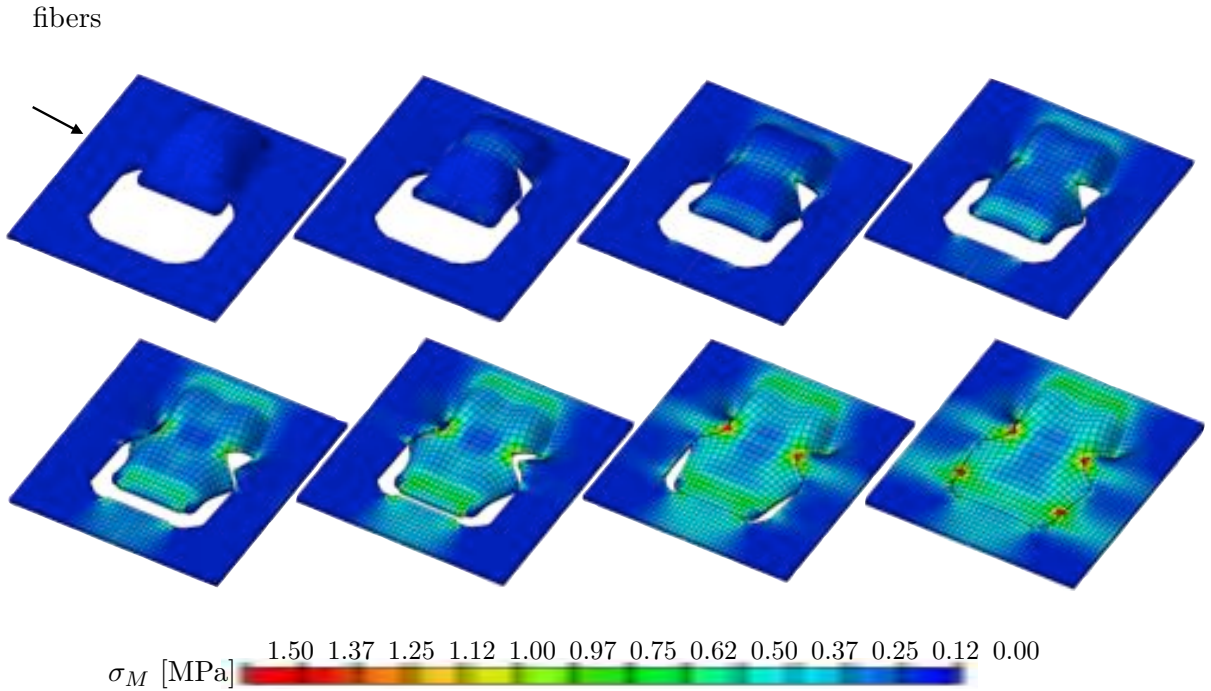


Figure 10.7: Double back-cut flap simulation when fibers are parallel to the advancement direction. Color code represented von Misses stress.)

to resurface nearly flat zones in the process called flap design .

We simulate a direct advancement flap and a double back-cut flap. The direct advancement flap shows stress concentrations at the base and at the front edge both when fibers are considering parallel and perpendicular to the advancement direction respectively. However, stress distribution is more uniform in the latter case and the maximum stresses are half in magnitude compared to the latter. The double back-cut with fibers parallel to the advancement direction exhibits zones of high stress in the base and the distal edge in the same manner as the direct advancement flap, however, it also induces zones of high stress in the corners where tissue rotates towards the sides. The double back-cut simulation with the fibers oriented perpendicular to the advancement direction shows stress concentration in the four corners of the resurfaced region.

The results of our simulations are consistent with the complications encountered in clinical practice. While all flap designs are accompanied by high regions of stress at the base, the distal end shows peak stresses when the fibers are aligned with the advancement direction.

These regions of high stress at the distal end correspond to the regions in which flap necrosis frequently occurs. Additionally, it is worth noticing that the stress values for the double back-cut flap are in the same range as those for the direct advancement flap even though the resurfaced area is greater in the double back-cut case since no tissue is wasted. On the other hand, the double back-cut flap induces additional regions of stress concentration. Finally, comparison of the two different flap designs and the different fiber orientations allows us to support the recommendation that the expander should be placed such that the flap is advanced perpendicularly to the fibers in order to attain a more homogeneous stress distribution.

Overall, the simulations we present here are a first approach towards the optimization of surgical reconstructive procedures in which an accurate representation of skin as a non-linear and highly anisotropic material is required. Nevertheless, it still remains to incorporate constitutive laws that account for the damage, growth, remodeling and healing process that accompanies these clinical scenarios [293].

We believe our results set the stage for the consideration of patient specific geometries, which would constitute a major breakthrough in computer-aided pre-operative planning and computational mechanics.

## Chapter 11

# Application of finite element modeling to optimize flap design with tissue expansion

### Abstract

**Background.** Tissue expansion is a widely used technique to create skin flaps for the correction of sizeable defects in reconstructive plastic surgery. Major complications following the inset of expanded flaps include breakdown and uncontrolled scarring secondary to excessive tissue tension. While it is recognized that mechanical forces may significantly impact the success of defect repair with tissue expansion, a mechanical analysis of tissue stresses has not previously been attempted. Such analyses have the potential to optimize flap design pre-operatively.

**Methods.** We establish computer-aided design as a tool to explore stress profiles for two commonly employed flap designs, the direct advancement flap and the double back-cut flap. We advanced both flaps parallel and perpendicular to the relaxed skin tension lines to quantify the impact of tissue anisotropy on stress distribution profiles.

**Results.** Stress profiles were highly sensitive to flap design and orientation of relaxed skin tension lines, with stress minimized when flaps were advanced perpendicular to relaxed skin tension lines. Maximum stresses in advancement flaps occurred at the distal end of the flap, followed by the base. The double back-cut design increased stress at the lateral edges of the flap.

**Conclusions.** We conclude that finite element modeling may be used to effectively predict areas of increased flap tension. Performed pre-operatively, such modeling can allow for the optimization of flap design and a potential reduction in complications such as flap dehiscence or hypertrophic scarring.

## 11.1 Motivation

Tissue expansion is a widely used technique in plastic and reconstructive surgery to create local flaps of skin for the correction of large defects and deformities [142, 239]. A major determinant of flap complications following the inset of expanded tissue is excessive mechanical loading, or tissue tension. Tension has been shown to be a key factor in the healing and scarring processes following reconstructive surgery [146]. Acutely, local stress concentrations may cause vascular insufficiency and localized flap necrosis [376]. Chronically, local stress concentrations may induce excessive wound tension resulting in dehiscence and/or hypertrophic scarring [406] (Fig. 1). Unfortunately, determining regional stress distributions *in vivo* is virtually impossible. However, computational simulations present an excellent alternative to virtually explore stress distributions during pre-operative planning. With this motivation, recent studies have simulated sutures of local flaps in idealized plane sheets of tissue using finite element analyses [66, 232]. However, realistic three-dimensional flap geometries have not been studied to date.

After tissue expansion, skin is no longer a flat sheet [231] but instead presents itself as a three-dimensional membrane that has undergone significant stretching and growth under extreme mechanical conditions [52]. Although the consequences of large tissue deformation on appropriate flap design are critical to repair durability, it remains a major challenge to accurately predict the mechanics of skin flap advancement. An important mechanical



Figure 11.1: Demonstration of complications of tissue expansion due to excessive tension. a) Tissue expanders inserted in thigh in preparation for of a giant pigmented nevus and resurfacing with advancement flap. b) Dehiscence of flap secondary to tension. c) Patient with scar hypertrophy and widening due to tension following expanded flap advancement for resurfacing of back following resection of a giant pigmented nevus; additional tissue expansion will be required to address residual pigmented nevus of lower back

effect is the rotation of the relaxed skin tension lines associated with rotation of the dermal collagen fiber bundles [182]. Another challenge is the flattening of a three-dimensionally grown membrane [51,417], which creates a complex stress profile that is difficult to estimate intuitively and impossible to measure experimentally. In an *in vivo* scenario, computational modeling has the potential to reduce flap tension and to therefore optimize healing and scarring.

The goal of the present study is to explore, via finite element modeling, local stress concentrations within expanded flaps and the degree to which this may be influenced by flap design. We focus on two commonly employed flap designs, the direct advancement and double back-cut flaps [416]. We test the hypothesis that flap stresses are highly sensitive to the location of expander placement and the direction of flap advancement with respect to lines of relaxed skin tension.

## 11.2 Materials and Methods

### 11.2.1 Flap Design

The present study evaluated the direct advancement flap and the double back-cut flap designs following tissue expansion (Fig. 2) [416]. To create a direct-advancement flap, two parallel cuts are made along the sides of the expanded skin. Extra tissue at both sides along the cuts is discarded and the resulting flap is stretched along the advancement direction to cover the defect. The direct-advancement flap is associated with a significant waste of tissue; however, the relaxed skin tension lines of the utilized skin flap remain aligned with the relaxed skin tension lines of the native skin. To create a double back-cut flap, the grown skin is first cut along the sides, from front to middle, and then perpendicular cuts are made towards the center. The flap is advanced at the front, but is rotated at the edges. The double back-cut flap allows a resourceful and more efficient tissue use; however, the relaxed skin tension lines of the flap are rotated with respect to the relaxed skin tension lines of the native skin.

### 11.2.2 Creation of Three-dimensional Model

To create the complex three-dimensional geometry of expanded skin, we virtually created new skin by implanting and inflating a rectangular expander using a computational tissue expansion tool previously developed by our group [51, 417]. Briefly, we considered an idealized skin sample and modeled skin as a flat, rectangular, thin tissue. We focused on simulating the middle layer of the skin, the dermis, since the dermal layer is the major load-carrying element due to its high collagen content [373]. For the direct-advancement flap, we divided a rectangular tissue sample with dimensions  $26 \times 16 \times 0.5\text{cm}^3$  into 3,328 brick-shaped elements. For the double back-cut flap, we simulated a  $24 \times 22 \times 0.5\text{cm}^3$  tissue sample divided into 4,224 brick-shaped elements. Both geometries consisted of two layers of elements across the thickness. In both cases, the expanders covered an initial base area of  $11 \times 11\text{cm}^2$ . We gradually filled the expanders and allowed the skin to grow. Our computational model was inspired by the natural response of skin, in which mechanotransduction of non-physiological mechanical cues triggers a net gain in skin area until the skin re-establishes a homeostatic equilibrium state [418]. Finally, we slowly decreased the pressure to deflate and remove the expanders. Our virtual tissue expansion naturally accounted for reversible, elastic deformation: upon deflation, skin retracts and the final surface is the

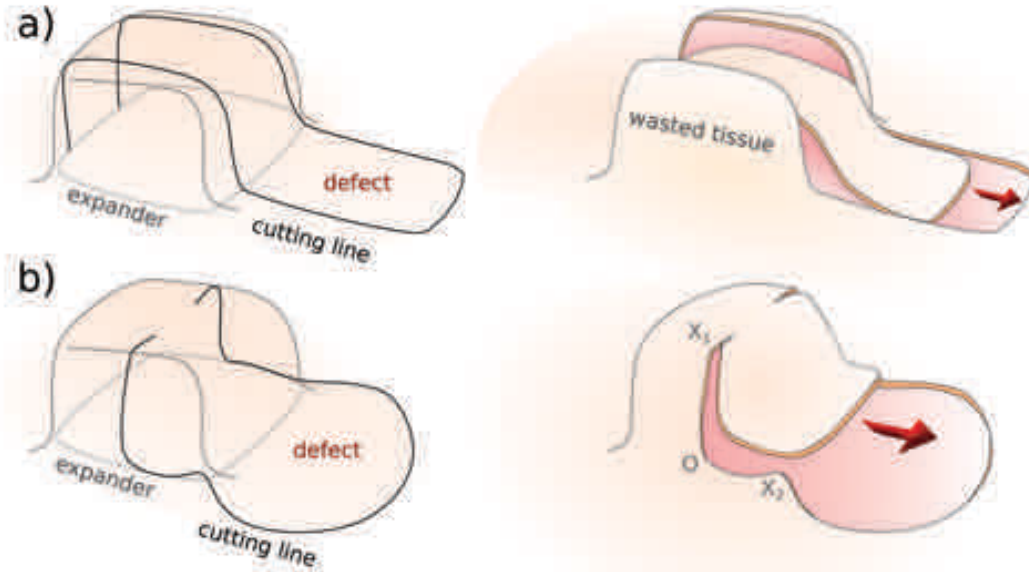


Figure 11.2: Two commonly used flap designs after tissue expansion. a) Direct-advancement flap. Two parallel cuts are made along the sides of the expanded skin. The extra tissue is discarded and the resulting flap is stretched to cover the defect. b) Double back-cut flap. The expanded skin is cut along the sides from the front to the middle and then perpendicular cuts towards the center are made. The flap is advanced at the front but there is rotation at the edges.

net tissue surface available for reconstructive purposes [51]. However, the geometry of the newly grown skin is no longer flat, but now has the shape of a three-dimensional membrane, from which we can create the desired skin flap.

### 11.2.3 Simulation of Flap Design

After our virtual tissue expansion, the net skin area gain was 40.9% of the initial base surface area, which corresponded to a total area gain of  $49.6\text{cm}^2$ . We then post-processed the grown geometry to create a direct-advancement flap and a double back-cut flap. To this end, we first cut the region where the expander was placed in order to generate the flap, and then removed the defect zone adjacent to the flap.

To create the direct advancement flap, we first performed two cuts parallel to the advancement direction and then performed another cut along the base of the expanded area as illustrated in Fig. 2a. We determined the area of the defect to be removed, dividing the area gain by the width of the direct advancement flap. We excised the defect by removing elements in the finite element mesh. This resulted in a rectangular hole of  $54\text{cm}^2$  that had to be resurfaced.

To create the double back-cut flap, we first cut along the sides from the front to the middle of the expanded region and then performed perpendicular cuts towards the center. Finally, we cut along the base of the expanded region to create the flap as illustrated in Figure 2b. The flap was advanced at the front, which induced a rotation at the edges. We considered the same advancement distance as for the direct advancement flap, but now excised a total area of  $80\text{cm}^2$ . The additional area that could be covered by the double back-cut flap resulted from the semi-circular regions excised at the sides as shown in Figure 2b. We advanced both flaps through wire connectors between nodes [346], and pulled these nodes together to closely mimic the clinical procedure, in which two opposite skin edges are joined by means of suture at discrete locations.

To monitor the mechanical forces acting on the flap throughout the advancement procedure, we calculated the von Mises stress distribution in the affected skin region. Tissue stresses are an important indicator for local tissue damage and long-term repair durability. Here, we used a transversely isotropic material model for skin, which explicitly accounts for the characteristic tissue microstructure with dermal collagen fiber bundles as the major load-bearing constituents [126]. This allowed us to explore the stress profiles upon flap advancement parallel and perpendicular to the relaxed skin tension lines, which we assumed to be aligned with the collagen fiber bundles. For the model parameters, we selected an extracellular matrix stiffness of  $0.0511\text{MPa}$ , a fiber stiffness of  $0.015\text{MPa}$ , an exponential fiber stiffness of  $0.0418$ , and a fiber dispersion of  $0.05$ . These parameters were adopted from the literature from recent *ex vivo* biaxial tests of pig skin [182].

In summary, for these simulations we started with a three dimensional geometric model of skin including an expanded region and an adjacent flat, unexpanded region. We excised a portion from the flat zone which corresponded to a defect to be reconstructed. We cut the surrounding, expanded skin to generate the flap and we extended this tissue to cover the region from where the defect was removed. We carried out the computational analysis with the commercial Finite Element Package Abaqus. In addition to the geometry, the Finite

Element technology requires a mathematical model to describe the characteristics of the tissue and its behavior under different deformations and forces. We used a well established model in the biomechanics community that accounts for the different stiffness of skin with respect to the orientation of the relaxed skin tension lines. The solution of the computational analysis outputs the stresses felt everywhere on the tissue. These stress values quantify the mechanical tension of skin at every point and are a well known engineering indicator for zones of risk due to potential tissue damage.

## 11.3 Results

### 11.3.1 Direct Advancement Flap

Figures 11.3 and 11.4 show the von Mises stress contours of the direct advancement flap at four distinct time points during the procedure with the advancement direction oriented parallel and perpendicular to the relaxed skin tension lines, respectively. The direct comparison of both figures documents the significant influence of the flap orientation, which affects the peak stresses, the stress profiles, and the geometries of the resurfaced zone. When the flap is advanced parallel to the relaxed skin tension lines (Fig. 3) maximum stresses of 2.00 MPa and more occur at the base and at the distal end of the flap. When the flap is advanced perpendicular to the relaxed skin tension lines (Fig. 4) maximum stresses of 0.75 MPa occur in the same regions; however, the overall stress distribution is a lot more homogeneous and stresses are of a much smaller magnitude.

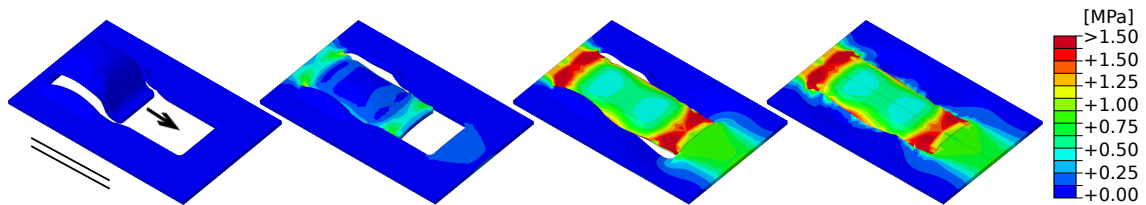


Figure 11.3: Direct-advancement flap oriented parallel to relaxed skin tension lines. Consecutive time frames show the evolution of the stress distribution in skin as the flap is pulled over the defect. Maximum stresses of 2.00MPa occur at the base and at the distal end of the flap. Arrow: Direction of flap advancement. Solid lines: Direction of relaxed skin tension lines.

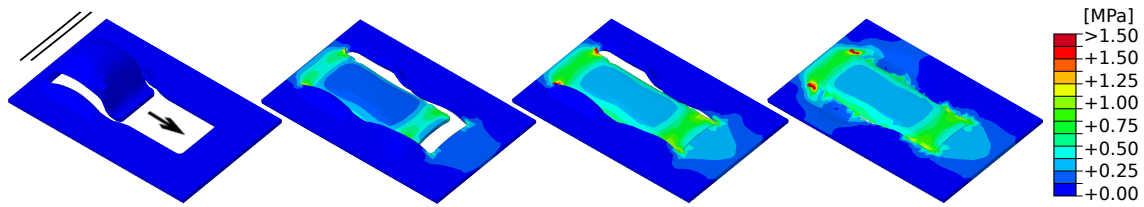


Figure 11.4: Direct-advancement flap oriented perpendicular to relaxed skin tension lines. Consecutive time frames show the stress distribution in skin as the flap is pulled over the defect. Maximum stresses of 0.75MPa occur at the base and at the distal end of the flap. Arrow: Direction of flap advancement. Solid lines: Direction of relaxed skin tension lines.

Figure 5 illustrates collagen fiber orientation when performing the direct advancement flap. For illustrative purposes, we highlight the suture regions as dashed black lines. For a flap advancement parallel to the relaxed skin tension lines in Figure 5a, collagen fibers run parallel to the suture lines in region A and perpendicular to the suture lines in region B. For a flap advancement perpendicular to the relaxed skin tension lines in Figure 5b, collagen fibers run perpendicular to the suture lines in region A, and parallel to the suture lines in region B. In both cases, the fibers maintain their initial orientations and rotate only marginally upon flap advancement.

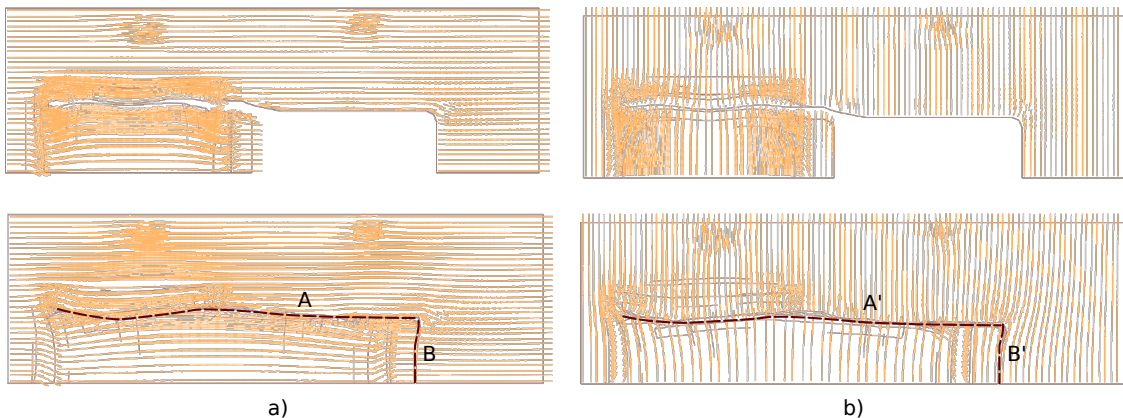


Figure 11.5: Collagen fiber orientations for direct-advancement flap oriented a) parallel and b) perpendicular to relaxed skin tension lines. Dashed lines highlight the suture regions. Collagen fibers maintained their initial orientations and rotated only marginally upon flap advancement.

### 11.3.2 Double Back-Cut Flap

Figures 6 and 7 show the von Mises stress contours of the double back-cut flap at four distinct time points during the procedure with the advancement direction oriented parallel and perpendicular to the relaxed skin tension lines, respectively. In general, maximum stress values for the double back-cut flap are slightly lower in magnitude than those for the direct advancement flap. When the flap is advanced parallel to the relaxed skin tension lines (Fig. 6) maximum stresses of 1.50 MPa occur at the base and at the distal end of the flap, located in similar regions as for the direct advancement flap. However, now, there are additional high stress regions of 1.50 MPa at both lateral sides where the tissue was rotated. When the flap is advanced perpendicular to the relaxed skin tension lines (Fig. 7) the stress contours are entirely different from the parallel orientation in Figure 6. In this case, maximum stresses of 1.50MPa are locally concentrated at all four corners of the resurfaced region while the base and the distal end experience stresses of only 0.75 MPa.

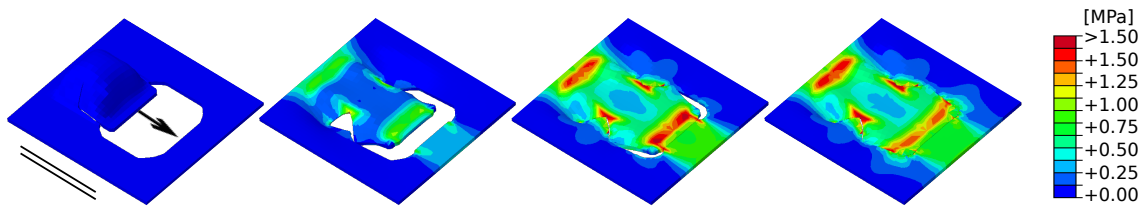


Figure 11.6: Double back-cut flap oriented parallel to relaxed skin tension lines.. Consecutive time frames of the stress distribution in skin as the direct-advancement flap is pulled over the defect. Maximum stresses of 1.50MPa occur at the base and at the distal end of the flap. Additional stress concentrations of 1.50MPa occur at the lateral sides, in regions where the tissue is rotated. Arrow: Direction of flap advancement. Solid lines: Direction of relaxed skin tension lines.

Figure 8 illustrates the collagen fiber orientation when performing the double back-cut flap. For illustrative purposes, we highlight the suture regions as dashed black lines. The collagen fiber orientation maps demonstrate that the double back-cut flap involves both advancement and rotation. As a result of the rotation, different fiber orientations meet at the suture lines. For the advancement parallel to the relaxed skin tension lines in Figure 8a, collagen fibers run parallel to the suture lines in region C, and perpendicular to the suture lines in regions A, B and D. For the advancement perpendicular to the relaxed skin tension

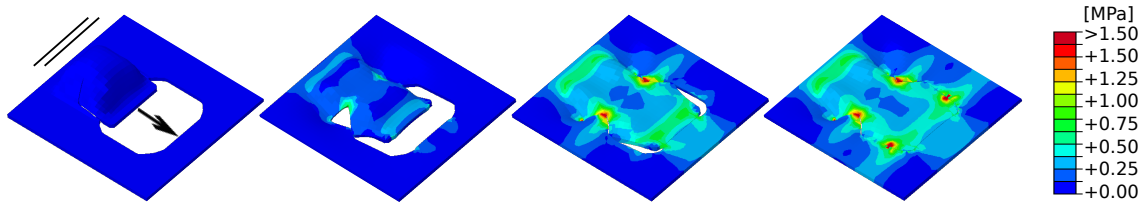


Figure 11.7: Double back-cut flap oriented perpendicular to relaxed skin tension lines. Consecutive time frames show the stress distribution in skin as the flap is pulled over the defect. Maximum stresses of 1.50MPa are locally concentrated at all four corners of the resurfaced region, while the base and the distal end experience stresses of only 0.75MPa. Arrow: Direction of flap advancement. Solid lines: Direction of relaxed skin tension lines.

lines in Figure 8b, the orientation is opposite and collagen fibers run perpendicular to the suture lines in region C, and parallel to the suture lines in regions A, B and D.

## 11.4 Discussion

Excessive skin tension is a major contributor to complications following the inset of tissue expanded flaps. In this analysis, we have studied the involved mechanical forces to address the fundamental question: Can mechanics be used to inform flap design? Our studies reveal three major findings, which have critical clinical implications.

First, we find that elevated stresses at the base of the flap are inherent to all flap designs, while stress concentrations at the distal end and at the sides of the flap are flap-specific: the direct advancement flap induces high stress concentrations at its distal end (Fig. 3). The double back-cut flap induces slightly lower stress concentrations at its distal end; however, it induces additional regions of high stresses at the lateral sides (Fig. 6).

Second, we find that stress profiles are highly sensitive to the orientation of the relaxed skin tension lines. Advancing the flap parallel to the direction of the relaxed skin tension lines creates stress maxima of 2.00 MPa and 1.50 MPa at the distal end (Figs. 3 and 6). Advancing the flap perpendicular to the direction of the relaxed skin tension lines creates stress maxima of 0.75 MPa and 0.75 MPa at the distal end (Figs. 4 and 7). As a useful byproduct of the simulation, we explored changes in orientation of the relaxed skin tension lines. For the direct advancement flap, the relaxed skin tension line orientation remains virtually unchanged (Fig. 5). For double back-cut flap, however, after flap advancement,

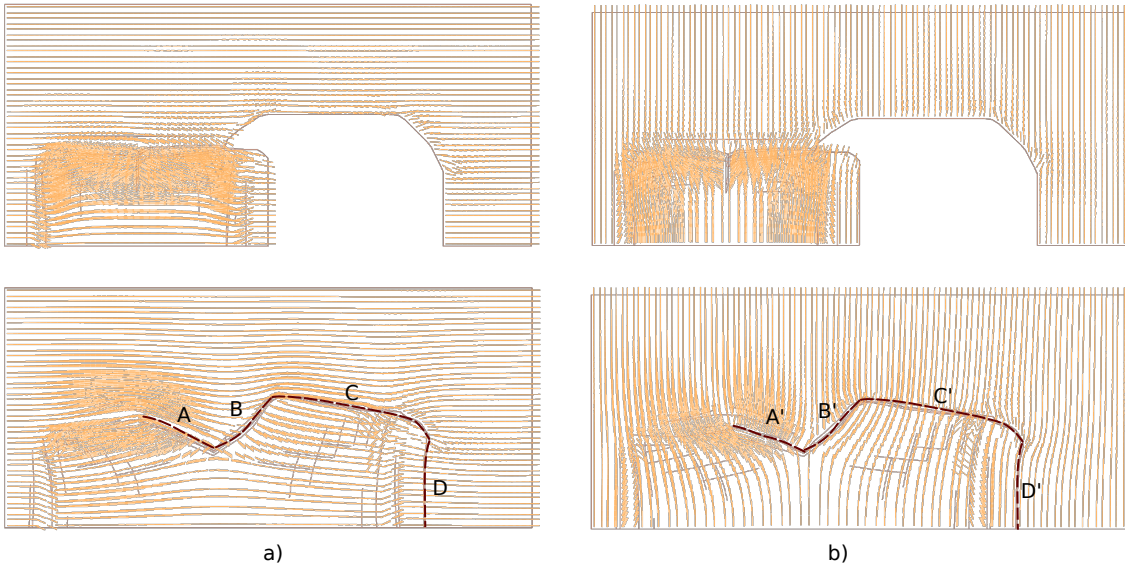


Figure 11.8: Collagen fiber orientations for double back-cut flap oriented a) parallel and b) perpendicular to relaxed skin tension lines. Dashed lines highlight the suture regions. Different fiber orientations meet at the suture lines because of collagen fibers rotation.

relaxed skin tension lines with different orientations meet at the same suture lines (Fig. 8). Flap-induced rotation of the relaxed skin tension lines might have a critical impact on improved healing and reduced scar formation. Our findings suggest that a surgeon who is not limited by anatomic zones or local geometries can minimize stresses by placing the expander such that the flap is advanced perpendicular to the relaxed skin tension lines. Overall, our simulations support our hypothesis that stresses in the flap are highly sensitive to the location of expander placement and the direction of flap advancement with respect to the relaxed skin tension lines.

Third, we have shown that stress profiles are sensitive to the chosen flap design. The direct advancement technique mainly affects the base and the distal end, while all other regions are stressed homogeneously to the same level (Figs. 3 and 6). The double back-cut technique equally affects the base and the distal end, but also adds critical zones at the lateral sides (Figs. 4 and 7). Although we used the same expander size in all four cases, the defect region covered by the double back-cut flap is significantly larger than the region covered by the direct advancement flap. Taken together, these analyses do not support a single

uniform recommendation in favor of one flap design over the other. Rather, they underline the critical need to consider each individual case on a patient-specific basis. The design of a successful flap is a complex procedure, which is highly sensitive to the balance of mechanical forces. Computational simulation, as we have shown here, offers a powerful tool to account for patient-specific geometries and local anatomies on an individual basis. A detailed knowledge of regional stress distributions might help the surgeon to identify regions of high stress that require special care or to select regions of low stress for safe suture placement.

Although this study provides mechanistic insight into the design of skin flaps in reconstructive surgery, it is not free of limitations. First, the underlying technology, the finite element method, is inherently ill conditioned and overestimates the absolute stress values at corners or sharp cuts. Thus, unrealistic large stresses result at singular points of the finite element mesh. Second, the truly quantitative comparison of tissue stresses requires a precise knowledge about the material properties of human skin. Here we have used parameters which had been fit to pig skin experiments *ex vivo*. Unfortunately, most of the published material parameters of human skin are associated with isotropic material models that do not account for relaxed skin tension lines and collagen fiber orientations. More experimental efforts are needed to determine the appropriate parameters for anisotropic models of human skin suitable for large deformations. Last, as a first proof of principle, we have only compared the performance of two specific flap designs advanced on a flat geometry. However, the inherent versatility of the finite element method conceptually allows us to analyze various different flap designs, and to expand the analysis to characteristic anatomic regions in the body such as the forehead, the scalp, the torso, or the upper and lower extremities. In particular, it remains to conduct a computational parametric study to quantify the effect of different flap sizes in the final stress distribution for each of the flap designs.

Overall, we believe that computational modeling is a powerful tool to guide individualized flap design with the common goal to minimize tissue stresses, accelerate healing, minimize scarring, and optimize tissue use. Mechanistic finite element analyses allow the surgeon to account for personalized anatomies and patient-specific geometries for individualized flap design. Today, the application of finite element analyses in plastic and reconstructive surgery is still in its infancy. Once this technology has advanced to a reliable, predictive tool, it could be tremendously helpful to integrate computer-aided pre-surgical planning in the daily surgical routine.

## Chapter 12

# Systems-Based Approaches Towards Wound Healing

**Abstract** Wound healing in the pediatric patient is of utmost clinical and social importance, since hypertrophic scarring can have aesthetic and psychological sequelae, from early childhood to late adolescence. Wound healing is a well-orchestrated reparative response affecting the damaged tissue at different scales. While tremendous progress has been made towards understanding wound healing at the individual temporal and spatial scales, the interaction between the different scales remains severely understudied and poorly understood. Here we discuss the critical need for systems-based computational modeling of wound healing across the scales. We illustrate the state of the art in systems modeling by means of three key signaling mechanisms of pathologic wound healing: oxygen tension, regulating angiogenesis and revascularization, TGF- $\beta$  kinetics, controlling collagen deposition, and mechanical stretch, stimulating cellular mitosis and extracellular matrix remodeling. The complex network of biochemical and biomechanical signaling mechanisms and the multi-scale character of the healing process make systems modeling an integral tool in exploring personalized strategies for wound repair. A better mechanistic understanding of wound healing in the pediatric patient could open new avenues in treating children with skin disorders such as birth defects, skin cancer, wounds, and burn injuries.

## 12.1 Introduction

Dermal wound healing in the pediatric patient is a symphony of events, precisely synchronized to repair the damaged tissue, restore its protective barrier function, and safely return it to its homeostatic equilibrium state [98]. Although the underlying processes, cell-matrix interaction, cell-cell cross-talk, and cellular mechanotransduction, involve a complex cascade of events, dermal wound healing is robust and rarely diverges to malignant transformation [145]. Yet, it is not always perfect. While pre-natal skin usually heals smoothly to seamlessly restore the state prior to injury [79], post-natal skin is incapable of healing wounds tracelessly, leaving scar behind. Post-natal skin can easily restore its protective barrier function; however, the resulting scar rarely has the same microstructure, collagen content, and mechanical properties as the native tissue [268]. In extreme cases, pronounced fibrotic activity might even initiate hypertrophic scarring, characterized through an excessive collagen deposition [388]. In the pediatric patient, excessive scarring has consequences throughout early childhood and adolescence, and can lead to low self-esteem or even stigmatization [50]. The prevalence of hypertrophic scarring in the pediatric population is overwhelming: Of the total cases of burn scars and keloids, 70% occur in children [29].

The underlying mechanisms of scar formation are now better understood than ever before, and we have made tremendous progress towards improving and accelerating healing mechanisms [146]. We have come to appreciate that the healing process spans various temporal and spatial scales and that is affected by both chemical and mechanical cues. However, even with the detailed insight that traditional approaches have provided on the individual scales, the behavior of the system as a whole remains elusive. Computational modeling is increasingly recognized as a powerful tool to provide insight into the dynamics of wound healing and the interaction of biochemical and biomechanical phenomena across the different scales [75].

Fortunately, dermal wound healing, like all inflammation-based processes in the human body, is based on various redundant signals and cross talk between different signaling networks [392]. While redundancy is hugely beneficial for the biological system itself, it complicates the overall understanding of the healing process: Even if individual elements of the signaling network are well understood in isolation, the coupling of these elements is hugely complex, and it is virtually impossible to gain basic insights based on sparse experimental

data. Computational systems biology is of acknowledged importance to advance our holistic understanding of pediatric wound healing: Short term, computational systems biology allows us to systematically explore controlled what-if-scenarios and virtually probe various hypothesis to better understand the healing process as a whole [193]. Long term, given the incredible variability of healing responses between different individuals, computational systems biology is an integral ingredient to shape the future of personalized medicine [393].

## 12.2 Temporal Spectrum of Wound Healing

From the moment of injury until the tissue reaches its final configuration in the form of a mature scar, months or even years may elapse. However, the protective function of skin has to resume immediately to avoid dehydration, infection, and loss of tissue integrity. Accordingly, the initial phase of healing only takes a few minutes. The process of wound healing is commonly divided into four overlapping phases: hemostasis, inflammation, proliferation, and remodeling, see Figure 1, rows 1 through 4.

### During hemostasis, the injured region fills with a platelet-rich fibrin clot

Hemostasis occurs in the order of minutes. During hemostasis, the wounded space rapidly fills with a clot to stop blood loss and to reestablish a barrier from the outside world. In the later phases of healing, this clot will serve as a temporary matrix for the cells that migrate towards the wound to reconstruct the dermal tissue (Figure 1.1c) [240]. The clot is composed mainly of fibrin fibers and platelets. The cytoplasm of the platelets carries granules from which a cocktail of growth factors and cytokines is released when the cells degranulate (Figure 1.1b) [386]. Pro-inflammatory signals from the platelets are directly reflected in molecular changes in the endothelial cells of the blood vessels near the injury site. A chemotactic response attracts leukocytes, such as neutrophils and monocytes (Figure 1.1a), which sense these molecular changes and adhere to the endothelial cells. The ongoing chemotactic pathway and the interaction between leukocytes and endothelial cells lead to the capture and transmigration of the neutrophils and monocytes in a process called diapedesis [283].

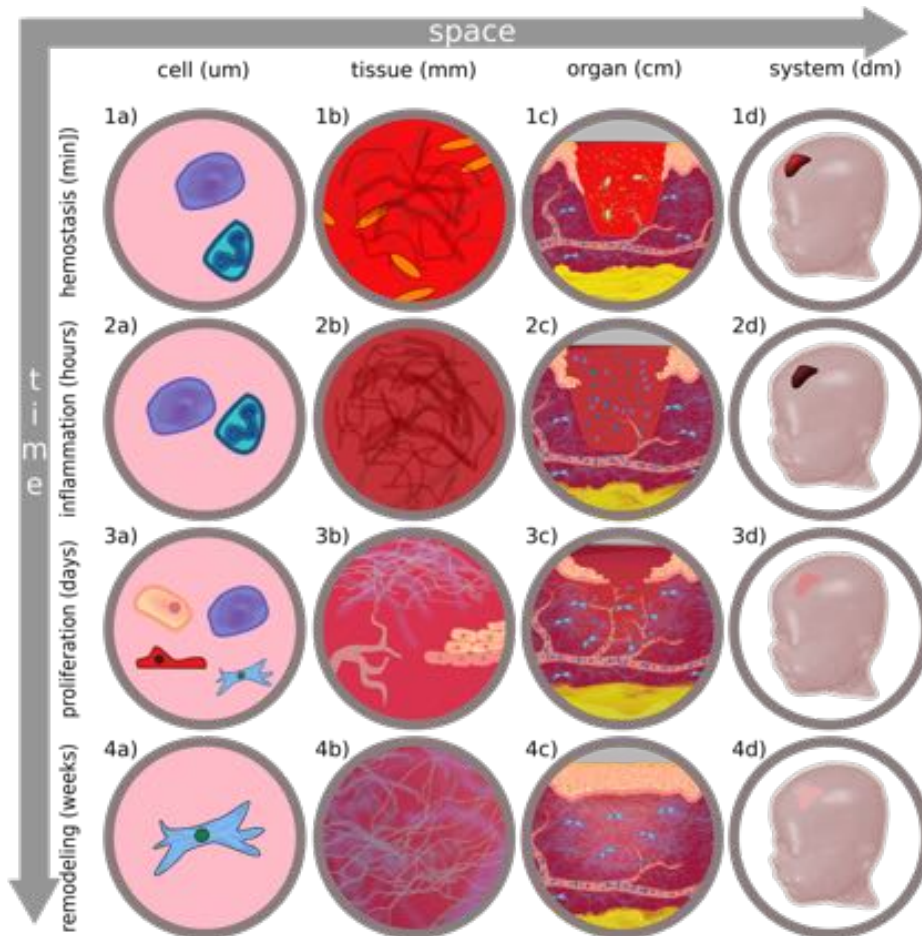


Figure 12.1: Spatio-temporal spectrum of wound healing. Wound healing is a hierarchically orchestrated process that spans interacting phenomena from minutes to months, from the cellular to the system level. Temporally, homeostasis takes place within minutes (row 1), inflammation within hours (row 2), proliferation within days (row 3), and remodeling within weeks to months (row 4). Spatially, the cellular level is associated with length scales in the order of micrometers (column a), the tissue level with millimeters (column b), the organ level with centimeters (column c), and the system level with decimeters (column d).

**During inflammation, leukocytes establish chemotactic gradients**

Neutrophil diapedesis marks the beginning of the inflammatory phase. Neutrophil transmigration occurs also very rapidly; in fact, the first neutrophils reach the wound within a few minutes, but they keep being recruited for the next two or three days. The primary function of neutrophils is to dispose pathogens entrapped in the clot at the moment of injury. Their secondary function is to amplify the pro-inflammatory indicators. Monocytes arrive at the wound within two days of the initial insult and differentiate into macrophages (Figure 1.2a). The role of monocytes is twofold, they phagocytose the remaining matrix debris, pathogens and neutrophils, and they produce soluble chemical mediators such as Transforming Growth Factor  $\beta$  (TGF- $\beta$ ) and Vascular Endothelial Growth Factor (VEGF). Both TGF- $\beta$  and VEGF are crucial to guide the recruitment of fibroblasts and endothelial cells later in the healing process (Figure 1.2c).

**During proliferation, fibroblasts deposit collagen and new vasculature forms**

During the proliferative phase, two processes occur simultaneously: re-epithelialization and replacement of the fibrin clot by granulation tissue (Figure 1.3c). These steps in the repair process continue throughout two to three weeks. In this phase, the sharp chemoattractant gradients generated through the inflammatory phase attract different cell types to manufacture new tissue (Figure 1.3a). At the epidermal level, keratinocytes in the wound edge dissolve their adhesions to the basal lamina in order to crawl and reproduce on top of the fibrin matrix, rebuilding the epidermis over the injured region (Figure 1.3b). On the dermal level, fibroblasts are in charge of depositing collagen, the main load-bearing constituent of skin (Figure 1.3b). The metabolic needs resulting from increased cellular proliferation and migration require the formation of a vast network of capillary tubes to provide nutrients and oxygen. Endothelial cells rapidly form a new vasculature in a process referred to as angiogenesis (Figure 1.3b). Towards the end of this phase, some fibroblasts transform into myofibroblasts, which actively pull on the wound edges to contract the injured tissue.

**During remodeling, fibroblasts gradually restore skin integrity and homeostasis**

Once the fibrin matrix has been replaced by granulation tissue made of fibroblasts, the remaining macrophages, and a vascular network, the remodeling phase begins. At this

point, the wound is fully closed, yet the tissue has very poor quality. It consists primarily of thick, aligned collagen bundles, instead of the interwoven collagen networks found in native skin (Figure 1.4b). Dynamic changes continue, but on a much slower time scale. Remodeling can go on for months or even years. Finally, the vascular network retracts and most of the cells undergo apoptosis or migrate out of the affected region. The remaining fibroblasts (Figure 1.4a) gradually restore skin integrity and mechanical homeostasis (Figure 1.4c). However, unlike pre-natal skin, post-natal skin usually never fully recovers its original native state.

### 12.3 Spatial Spectrum of Wound Healing

Similar to virtually all biological phenomena, in wound healing, temporally and spatially interacting events at the molecular, subcellular, cellular, tissue and organ levels ultimately converge to a well-defined system level response [172], see Figure 1, columns a through d. This macroscopic response is inherently rooted in the hierarchical structure, which is established through a precisely defined biological organization [310]. Although it is in principle possible to zoom in to the subcellular or even molecular scales, the cellular level is the preferred starting point in the context of wound healing modeling, mainly because cells are the smallest autonomous building blocks in the biological hierarchy [352]. One level above in the organization, at the tissue level, we find interacting cell aggregates embedded in the extra-cellular matrix (ECM). The next larger scale corresponds to the organ level, the level of the wound itself. In principle, we could even contemplate higher levels of organization, for example entire organ systems. Here, however, we do not consider larger spatial scales, because all relevant phenomena take place within the local wound environment.

#### At the cellular level, chemomechanical stimuli guide cellular decision making

The smallest scale we explore here is the cellular level, a scale in the order of  $10\mu\text{m}$ . At this scale, four cell-types are critical to wound healing: endothelial cells, fibroblasts, macrophages, and keratinocytes (Figures 1.1a to 1.4a). For each cell type, there are specific regulatory mechanisms, which are key to a successful repair process. The most important control mechanism is chemotaxis, the migration of cells in the direction of increasing chemical gradients [289]. Endothelial cells, fibroblasts, and leukocytes migrate into the wound site

attracted by the strong concentration of different growth factors and other chemical mediators released during the inflammatory phase [300,353,377]. Chemotaxis in eukaryotic cells is complex and, unlike for prokaryotic systems, there are no established models to predict how eukaryotic cells migrate as a function of chemical gradients. Prokaryotic cell migration resembles a biased random walk, which can be easily represented by simple mathematical models. Eukaryotic cells, however, move in continuous paths with smooth turns towards ascending signal concentrations, but display an overall stochastic behavior [174,394].

In addition to chemical cues, mechanical cues play a significant role in wound healing [277,406]. The ultimate goal of skin repair is to reestablish the mechanical load bearing capacity to restore the homeostatic equilibrium state. Key to this restoration is the translation of mechanical signals into chemical reactions, a process known as mechanotransduction, which is the landmark characteristic of fibroblasts in the repair sequence (Figure 1.4a) [403]. Fibroblasts anchor to the ECM through focal adhesions. These adhesion sites are linked to stretch-activated ion channels across the cell membrane and to the cytoskeleton inside the cell. Altering the mechanical scenario of the ECM directly creates a flow of charged ions via these ion channels and indirectly governs cellular behavior through perturbed cytoskeletal dynamics [74]. Fibroblasts respond to mechanical changes in the ECM in several ways: by depositing collagen, by decreasing apoptosis rates, by increasing inflammatory signals, and by transforming into myofibroblasts to actively pull on the wound edges [1,292,404].

For endothelial cells and keratinocytes (Figure 1.3a), cell-cell and cell-matrix adhesions are of primary importance throughout the entire repair process. Keratinocytes critically depend on cell-cell and cell-matrix crosstalk to define their position in the epidermal lattice. The polarization of keratinocytes directs lateral migration and proliferation during re-epithelialization [344]. Endothelial cells also depend on these types of interaction during angiogenesis [224]. Some cells in the tip of sprouting vessels are activated and protrude filopodial extensions, which actively interact with their immediate microenvironment to guide angiogenesis. The remaining endothelial cells support the leading tip by maintaining the connectivity with the parent vessels, and by helping in the maturation of the newly formed capillary tubes [156].

### **At the tissue level, chemomechanical fields coordinate cellular organization**

On the next level of the hierarchy, we are interested in the bulk mechanical properties of the ECM, the diffusion of growth factors, and the overall behavior of cellular aggregates

(Figures 1.1b to 1.4.b). The properties of the ECM and the diffusion of growth factors are crucial at this scale, because they contribute a key aspect of the healing process: They pass information across distances larger than the characteristic cell size, coordinating the action of multiple cells without using direct cell-cell communication. Soluble mediators diffuse chemical cues and the ECM transmits mechanical cues across the tissue (Figures 1.1b and 1.2b). To characterize chemical diffusion in an isotropic medium, only a single constant needs to be specified. To characterize mechanical signaling of the ECM, however, we can select from a huge variety of constitutive models, and two or even more constants need to be determined (Figure 1.4b) [111, 219, 373].

Two other phenomena that become important at the tissue level are pattern formation and collective cell migration. An illustrative example is re-epithelialization, associated with the formation of an advancing front that has distinct collective features entirely different from the individual cellular response. The leading edge of keratinocytes that invade the wound adopts a wave propagation profile, which can be characterized using Fisher's equation (Figure 1.3b) [237]. Another even more intriguing proof of complex organization is angiogenesis, a highly coordinated process that cannot be understood solely from the study of a single cell. During angiogenesis, a new vasculature forms from existing blood vessels that surround the injured region [70]. This process consists of combined tip chemotactic diffusion and sprouting to create a new network of capillary tubes (Figure 1.3b) [297].

### **At the organ level, the chemomechanical environment controls wound healing**

The final level of interest in wound healing is the spatial region that contains the injured skin and its immediate surrounding healthy tissue (Figures 1.1c to 1.4c). At this level, we witness the healing capacities of skin as the result of a perfectly organized interaction of all phenomena described above: from microstructural decisions of the individual cells, via mesostructural properties of the cells embedded in the ECM, to macrostructural reaction-diffusion systems of the soluble mediators and the patterning capabilities of cellular aggregates.

## 12.4 Overview of Computational Modeling for Systems Biology

Mathematical representations can foster our understanding of biological systems. An abstraction of a biological system consists of characteristic variables, such as the concentration of a chemical substance or the amount of cells in a region of tissue over time, and the interaction rules between the different components of the system. Mathematical models are representations of the real world and, as such, they can be created in many different ways depending on the features of the problem itself, on the information at hand, and on the mathematical tools preferred by the modeler. Furthermore, creating a mathematical representation is only one facet of the simulation process. The second stage consists of the computational simulation itself, in which the model is solved numerically.

### Biological systems can be modeled with well-established mathematical tools

The two conceptually different mathematical approaches used in the context of systems biology are continuum models and discrete models. In the physical world, substances can vary smoothly over a geometry. In this case we represent them like a continuous function called field. Fields are the basic representation of continuum models. Typical examples in wound healing are concentrations of chemical mediators such as TGF- $\beta$ . In some cases, some components of the system may be large enough to be considered as independent entities. In these cases, we prefer discrete model that represent each individual entity explicitly and characterize their interaction through simple mathematical equations. Typical examples in wound healing are cell populations, such as populations of fibroblasts and macrophages. The choice between continuum and discrete representations is relative to the scale of interest. Components that can be seen as discrete entities at the nanometer scale become smeared out at larger scales, where they can be approximated as fields. Therefore, the scale of the model will determine which approach is more convenient.

In the context of systems biology, several interacting components have to be represented in the mathematical model, either as fields or sets of individual entities. A multi-field model is one that consists of several interacting fields, such as models encountered in wound healing simulations that consider various chemical signaling pathways acting simultaneously, for example TGF- $\beta$  and VEGF. In some cases, it might be advantageous to represent some

variables as continuous fields while others might be represented as discrete entities. Thus there are three basic types of representations: purely continuum, purely discrete and hybrid continuum/discrete. In addition, a mathematical model can span different spatial scales, e.g., cell, tissue, organ, system, leading to a multi-scale model.

Usually, biological systems consist of three basic ingredients: chemical substances, cell populations, and mechanical factors. Chemical substances are generally treated as continuous fields. Cells, on the other hand, can either be modeled individually or as fields, depending on the scale of the model. The term biological field refers to a field that represents a cell population. Finally, the mechanical factors include forces and deformations and are almost always treated as continuous fields.

In continuum models, the evolution of the different fields in space and time is governed by partial differential equations. A partial differential equation establishes: i) the way a field interacts with other fields through coupling terms; ii) how it changes in time, and iii) how it varies in space, over the geometry of interest. One partial differential equation is needed for each field. Continuum models represented through partial differential equations are an elegant and compact way to characterize spatial variations of chemical concentrations, mechanical strains, or mechanical stresses.

In discrete models, the behavior of each entity is governed by one or more ordinary differential equations. An ordinary differential equation defines: i) how does a characteristic variable of a single entity evolve in time; and ii) how is that variable related to others again through coupling terms.

### **Discretization schemes transfer a mathematical model into a computational simulation tool**

Continuum models are solved over the entire geometry at every point in time. To solve the underlying partial differential equations, it is necessary to subdivide or discretize both space and time. Time is almost always discretized in small intervals by means of finite difference methods. Discretizing space can be done in several ways. The simplest approach is to use a mesh of regular size to represent the geometry through finite difference methods. To represent arbitrary geometries, the preferred approach is the use of finite element methods. This method approximates the geometry by cutting it in little pieces called elements. However, finite element methods are more sophisticated and require special care of implementation. Yet another alternative are finite volume methods, which discretize the geometry similar

to finite difference methods. Once time and space are discretized, we obtain a system of algebraic equations. The solution of this system provides the information of all continuous fields over the geometry as time progresses.

The solution of the governing equations over an arbitrary geometry can become a challenging task; in consequence, several simplifications are often used. In the physical world, the geometry is three-dimensional, however, we can still extract useful information of the dynamics of the system by analyzing the solution of the equations in a one or two-dimensional approximation. Another simplification comes from geometries that are symmetric about an axis, such as cylinders, which require also a one-dimensional formulation referred to as axisymmetric.

A discrete representation, however, does not need to be solved over the entire geometry, but is solved locally for each entity. The ordinary differential equations of each individual can be solved easily using finite difference methods since only the time needs to be partitioned in small intervals. The major disadvantage of discrete models comes, however, from having to solve as many systems of equations as entities are in the system. When dealing with entire cell populations, their computational cost becomes overwhelming.

## 12.5 Guidelines

From the above discussion on the basic approaches towards systems-based mathematical representations, and to establish a framework for a guided discussion of the most recent wound healing models, we propose a few useful guidelines for effective computational modeling of wound healing:

One-dimensional and axisymmetric models provide a quick first insight into the interplay of individual signaling pathways during healing. As such, they are of great value to test therapeutic hypotheses. Because of their computational simplicity, one-dimensional and axisymmetric modeling should be viewed as a validated and well-calibrated starting point for further model refinement. For analyses that focus on the spatio-temporal variation of signaling pathways in wound healing, however, we recommend using two- or three-dimensional models.

When choosing between discrete and continuum two- or three-dimensional models, we suggest considering mechanics as the limiting factor: Analyses emphasizing mechanical cues

should avoid fully discrete models. We recommend using discrete models to study the biochemistry of individual cells. Discrete models are typically based on simple relations and straightforward to implement. Since they are computationally expensive, however, they are only feasible to answer fundamental scientific questions at small scales. We recommend using continuum models to study the interaction of biochemical and biomechanical fields. Continuum models are computationally efficient, but require special care when translating the collective action of individual cells to a continuous field. When embedded in efficient finite element solvers, continuum models allow for a patient-specific analysis based on individualized, realistic three-dimensional geometries. Continuum models are ideal to answer translational clinical questions at larger scales.

Although models focusing on a single individual aspect of wound healing can provide specific insight, holistic models are currently becoming the gold standard in wound healing simulations. In contrast to single-field models, multi-field holistic models reliably represent the cross-signaling networks during wound healing. We recommend to include a representation of at least five interacting fields: 1) fibroblast population, 2) endothelial cell population and/or nutrient concentration, 3) indicator of ECM restoration such as collagen content, 4) chemoattractant concentration, and 5) inflammatory cells population. This baseline five-field model can, of course, be further refined if specific aspects of the healing process are of interest.

## 12.6 Systems-Based Mathematical Models of Wound Healing

Over the past two decades, mathematical and computational modeling have advanced as key players in the quest for understanding the complex multi-scale phenomena involved in wound healing. Ideally, once calibrated and validated, these models can serve as tools to quantify the impact of selected perturbations to the baseline system, and, ultimately, to predict the effect of different therapeutic treatment options.

In an effort to gain basic scientific insight into the process of wound healing, researchers in the early nineties started to develop mathematical models of the repair response of skin. Sherratt and Murray are often considered as the fathers of modern mathematical modeling of wound healing [338]. Since their first model was published more than two decades ago, a multitude of modifications, improvements and enhancements have been proposed.

The characteristics, the focus, and the simplifications of each model are different, based on the fundamental question it seeks to answer. This makes it challenging to define a unique benchmark for a scientist or a clinician that would like to make use of the existing models or propose a new one.

It is becoming clear, however, that the current trend in computational systems biology converges towards multi-scale, multi-field modeling. In the time domain, most analyses focus on short time scales, mainly on the inflammatory and proliferative phases, and only a few more recent models integrate larger times scales including the remodeling period [77]. In the space domain, modelers are now giving priority to multi-scale integration, from a basic mathematical representation of the cell to fully three-dimensional models of the wound site. Here, we suggest a classification of existing models based on the aspect of wound healing they seek to address and on the mathematical tools they use to derive their governing equations, see Table 1. In this classification, the three major focus areas are: i) re-epithelialization and cell migration, ii) angiogenesis, and iii) wound contraction and collagen deposition. The four degrees of modeling complexity are i) one-dimensional or axisymmetric continuum models; ii) two-dimensional continuum models; iii) two- or three-dimensional discrete models; and iv) two-dimensional hybrid discrete/ continuum approaches.

Table 12.1: Systematic classification of mathematical models for wound healing based on model complexity and focus area

Complexity vs Focus	Re-epithelialization Cell migration	Angiogenesis Angiogenesis	Wound contraction Collagen deposition
One-dimensional continuum	[237, 339]	[10, 118, 224, 297, 410], [61, 85, 235, 284, 334]	[77, 281, 282, 379] [259, 267]
Two-dimensional continuum	[154, 176]	[70]	[389]
Two/three-dimensional discrete	[62, 63]	[294, 349, 354, 358]	
Two-dimensional hybrid discrete/continuum		[262]	[86, 88, 246]

We hope this classification alongside with the guidelines discussed above will provide new computational scientists and clinicians with the necessary framework to make use of the existing models or to create improved versions attending to the specific question they

want to answer.

To better illustrate which modeling approaches have been used and how they have enhanced the understanding of wound healing from the perspective of systems biology, the following subsections present, for each major focus area defined in Table 1, the modeling and solution methods that have proved to be more effective followed by an example of how computational simulations have tested virtual hypothesis by altering the baseline model and analyzing the outcome of the computations.

### **Re-epithelialization creates propagation patterns of constant velocity waves**

The simplest mathematical models in wound healing focus on re-epithelialization and cell migration. These models typically characterize a cell population over a domain in terms of point-wise cell densities rather than considering each individual cell. Fisher's equation is the preferred representation of the population behavior. It consists of a diffusion term to capture cell migration and a logistic term to capture cell proliferation [237]. This abstraction is well-suited for the study of re-epithelialization, and is also considered useful for fibroblast and endothelial cell migration in wound healing [237, 339]. During re-epithelialization, keratinocytes remain in stretch contact with one another, maintaining tissue continuity throughout the epidermis. A continuum assumption is therefore well justified. The solution to Fisher's equation is a wave propagation pattern where the advancing front of cells moves with an almost constant velocity [339]. Although the model is conceptually two dimensional [154, 176], most numerical implementations are based on the additional assumption of axisymmetry to further simplify the modeling. A more sophisticated alternative to these continuum models are discrete models, which represent each individual cell explicitly [62]. Discrete models typically describe the motion of each cell as a reinforced random walk in the direction of a stimulus and regulate cell division through an internal clock [63].

### **Re-epithelialization can be manipulated by altering TGF- $\beta$ 1 kinetics**

During wound healing, keratinocytes, initially located at the edge of the lesion, crawl over the lesion to restore the protective barrier. While cell-cell cross-talk is key to this process, external signaling strongly influences the behavior of the leading edge. It overwrites the default program to initiate horizontal growth of skin, temporally bypassing the upward motion of keratinocytes from the basal membrane to the stratum corneum. In this early response of keratinocytes, TGF- $\beta$ 1 has been recognized as a crucial signaling pathway controlling two

major events: It increases keratinocyte migration and decreases keratinocyte proliferation. A balanced action of TGF- $\beta$ 1 is therefore critical to avoid pathological re-epithelialization. With the help of agent-based computational models, Sun et al. [358] explored the role of TGF- $\beta$ 1 in epidermal wound healing and identified spatio-temporal sequences of events in normal and pathological wound healing. In their baseline model, increased concentration of TGF- $\beta$ 1 at the edge of the wound induced a population of keratinocytes to migrate inwards and blocked their proliferation. As the leading edge moves into the lesion, the adjacent population of keratinocytes was exposed to normal levels of TGF- $\beta$ 1 but to an increased presence of other growth factors that stimulate cell proliferation. Normal re-epithelialization can thus be viewed as a non-proliferative, highly motile leading edge followed by a proliferative population of keratinocytes. In these computational experiments, disrupting the balance of TGF- $\beta$ 1 created either chronic wounds or hypertrophic scars [358].

### **Angiogenesis creates fractal patterns of vascular networks.**

The aspect of wound healing that has received the most attention in modeling is angiogenesis. The reason for the disproportional interest in new vessel formation is that it is not only crucial to wound healing but also to tumor growth. The basic assumptions of angiogenesis models are valid for both circumstances, and combined efforts between these two scientific communities have markedly pushed the frontiers in mathematical modeling of angiogenesis within the past decade [70, 295]. Researchers in wound healing and tumor growth have collectively used various approaches to study the creation of new vasculature and some of their most remarkable models are extremely elaborate. They include most features of the repair sequence: inflammatory cells, one or more chemoattractants, fibroblasts, and the ECM [297, 410]. In continuum models, new vasculature is represented as the density of endothelial cells in a point-wise fashion or as a combination of capillary tip and sprout densities [118]. A partial differential equation dictates the evolution of the endothelial cell density field, in analogy to Fisher's equation, but with additional coupling terms between the endothelial cells and the other fields in their immediate environment [10, 61]. In discrete models, fractal-like approaches or cellular automata have been proposed to account for the contact between individual endothelial cells as the capillary tubes branch out [294, 349]. Hybrid models have also successfully reproduced the angiogenesis mechanism [262]. The greatest value of angiogenesis models, continuous or discrete, is that they allow us to explore the effects of altered nutrient and oxygen supplies on the healing process.

### **Angiogenesis can be manipulated by altering hyperbaric oxygen levels**

During wound healing, elevated metabolic needs in the proliferative phase increase oxygen demand. In fact, the lack of oxygen or hypoxia is prevalent in the wound during the inflammatory phase and is an important cue for macrophages to release cytokines that recruit other cell types for the subsequent phases [195,235,284]. If hypoxia is severe, for example in chronic wounds, the tissue is incapable of creating new vasculature, and the healing process is significantly impaired [336]. Thus, oxygen therapy has been proposed to accelerate the healing process [135]. However, excess of oxygen can also be harmful, because it can lead to intoxication [371]. Hypoxia is an essential cue during the inflammatory phase and is linked indirectly to fibroblast recruitment [135]. The interplay of oxygen and cellular recruitment has successfully been studied with the aid of computational models [85].

For example, Schugart et al. proposed a model of wound healing, in which oxygen tension across the wound is considered as an additional variable [334]. Their baseline model reproduced a normal healing response throughout a period of 10 days. Then, different degrees of hypoxia and hyperoxia were simulated. Their simulations revealed that severe hypoxia cannot sustain angiogenesis, and that extreme hyperoxia reduces the proliferation of endothelial cells, see Figure 2, top. Finally, they studied different hyperbaric oxygen therapies and concluded that 90 minutes of hyperbaric oxygen per day, enhance the healing process, see Figure 2, bottom.

### **Wound contraction by myofibroblasts creates tension in the ECM**

Similar to angiogenesis, collagen deposition and wound contraction have mainly been studied holistically [281,282]. Unique features of their mathematical models are the consideration of fibroblasts and myofibroblasts [88,379]. Fully discrete models are not appealing to represent the ECM, and therefore modelers have either turned to hybrid or fully continuous frameworks. In the former, the chemical species and the ECM are modeled as continuous fields, whereas the cells are modeled discretely as individual entities [246]. The major focus of hybrid discrete/continuum models has been on collagen deposition. If we decide to also represent cell populations as continuous fields, we can select plain continuum models and more advanced mechanical theories to answer questions such as myofibroblasts-based active wound contraction [389].

### Collagen deposition can be manipulated by altering TGF- $\beta$ kinetics

While the biochemical aspects of wound healing have received significant attention, mathematical modeling of the mechanical aspects of wound healing remains largely unexplored. The role of mechanical cues is currently gaining importance though since recent experimental data suggest that releasing mechanical stresses in the wound may shorten the inflammatory phase and reduce scarring [145, 411]. Mechanical stress is transmitted across the ECM and directly affects fibroblast behavior [302, 303]. For example, the local environment of a fibroblast can induce its transformation into a myofibroblast [267]. Myofibroblasts are responsible for contracting the tissue and bringing the edges of the wound together [379]. Although there are a few models that have incorporated wound contraction by myofibroblasts, these models have not yet been used to optimize the mechanical environment and enhance therapeutic outcomes. Nonetheless, since pathologic scarring is a major concern in wound healing, researchers have focused on modeling the flow of chemical information, which regulates collagen deposition and creation of the new ECM [267].

For example, Cumming et al. studied the response of fibroblasts to transforming growth factor- $\beta$  (TGF- $\beta$ ), a cytokine released by macrophages during inflammation, throughout a period of 14 days [86]. Using a predictive mathematical model, they were able to show that altered TGF- $\beta$  kinetics in the wound have a significant impact on the healing process. They found that in their baseline model, fibroblasts tend to cluster around the zones with highest concentration of chemoattractants, where they gradually replace the fibrin clot with collagen as they reach the damaged region, see Figure 3, left. According to the simulations, reduced TGF- $\beta$  diffusion causes a clustering of fibroblasts, reduced collagen synthesis, and significantly altered healing kinetics, see Figure 3, right. Another remarkable example of the use of agent based models is the study conducted by Mi et al. [259] , which focuses on TGF- $\beta$ 1, a specific isoform of TGF- $\beta$ . Altered kinetics of this chemokine are an important factor in diabetic ulcer pathology. According to their simulations, increased tumor necrosis factor- $\alpha$  (TNF) and decreased TGF- $\beta$ 1 lead to an impaired healing response of diabetic patients. The model further showed that altering these chemoattractants increased the concentration of TGF- $\beta$ 1, increased collagen deposition, reduced concentration of TNF- $\alpha$ , and reduced necrosis.

### **Collagen deposition and mitosis can be manipulated by altering stretch levels**

Despite intense research over the past two decades, most existing models for wound healing are still one or two-dimensional and focus on the acute rather than on the chronic response, see Table 1. The majority of these models use finite difference or finite volume methods to discretize their governing equations in space, limiting the geometries to idealized settings. An elegant way to incorporate realistic three-dimensional geometries of the wound and skin anatomy is finite element modeling. Recent trends in computational biology focus on predicting chronic soft tissue adaptation using mechanistic finite element models [8, 251]. In an attempt to quantify how elevated mechanical stretch can alter collagen deposition and fibroblast mitosis, several groups have recently modeled chronic skin growth in response to changes in the mechanical environment [52, 351]. These models have immediate clinical applications in skin expansion in plastic and reconstructive surgery. Predicting stress, strain, and skin area gain, skin growth models have the potential to enhance treatment for patients with birth defects, burn injuries, or breast tumor removal [51].

For example, Zoellner et al. simulated skin expansion in pediatric forehead reconstruction of a one-year old girl throughout a period of 12 weeks [417]. Their model incorporated a thermo-mechanically consistent representation of the dermis and a phenomenological scalar field that quantified the amount of newly grown skin [51]. A conceptually simple and elegant abstraction of the mechanotransduction pathways and the corresponding cellular response defined the evolution of this scalar field in terms of mechanical stimuli such as tissue stretch [417, 418], see Figure 4. Refining this framework to incorporate the true mechanotransduction pathways during mechanical overstretch or during wound healing appears to be a next logical step towards predicting and improving of wound healing therapies in realistic three-dimensional geometries of pediatric patients.

## **12.7 Perspective**

Systems-based mathematical modeling of wound healing has achieved remarkable sophistication and is on its way to becoming an irreplaceable tool in personalized medicine. The first mathematical models of wound healing were proposed two decades ago and considered only specific aspects of the healing process. Current models include most of the key components that interact throughout the repair sequence. They have opened the floor to

advanced hypotheses testing and enhanced wound management therapies. The state of the art in computational modeling of wound healing is the temporal and spatial integration of different cell types, chemoattractants, nutrients, and the ECM, interacting jointly to restore tissue integrity. Current trends in computational modeling indicate that this knowledge gained on the cellular level should be integrated in holistic multi-scale multi-fields continuum models through a bottom-up approach. The ultimate goal would be to create high-resolution system-level models with parameters calibrated at their generative level of resolution. Rather than fitting physiologically meaningless phenomenological parameters to system-level measurements, which has been the standard for the past decades, all parameters would then have a clear physiological interpretation.

Greatest attention has been paid to the biochemical features of healing such as diffusion of chemoattractants and oxygen tension. The first models have now advanced far enough to reliably predict how systematic manipulations of baseline parameters in chemical signaling can change the healing process. The biomechanical features of healing are currently receiving increasing attention. Mechanical models focus primarily on collagen deposition and active wound contraction. Yet, to date, it still remains unclear, how exactly these mechanisms are regulated when the injured skin tries to recover its homeostatic equilibrium state.

One of the major challenges in the mathematical and computational modeling of wound healing is the consideration of complex, physiological geometries in two and three dimensions. Current models have been tested primarily in axisymmetric conditions, which limits their application to a clinical setting and reduces their translational potential. Another current roadblock is the incorporation of a detailed mechanical representation of skin with temporally, spatially, and directionally varying material properties. Fortunately, recent advances in molecular biology, mechanotransduction, soft tissue mechanics, and computational modeling of soft tissues might soon allow us to bridge these gaps. The first patient-specific computational model of pediatric wound healing is likely to appear within this decade and it will constitute a major breakthrough in the progress of systems biology towards a better care for the pediatric patient.

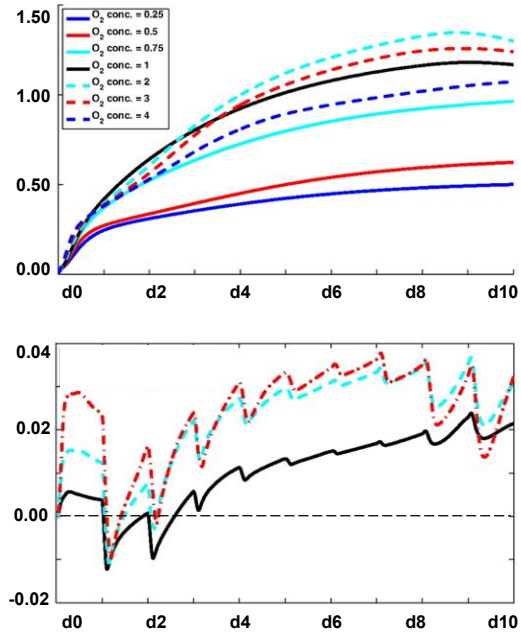


Figure 12.2: Angiogenesis can be manipulated by altering hyperbaric oxygen levels. The baseline system (panel a, solid black line) shows endothelial cell density for oxygen levels in the absence of hyperbaric oxygen therapy during a period of 10 days. Hyperoxic conditions can enhance healing, however, excess of oxygen can be harmful (panel a, dashed cyan:  $O_2 = 2.00\%$ ; dashed red:  $O_2 = 3.00\%$ ; dashed blue:  $O_2 = 4.00\%$ ). Hypoxic conditions impair the healing response (panel a, solid cyan:  $O_2 = 0.75\%$ ; solid red:  $O_2 = 0.50\%$ ; solid blue:  $O_2 = 0.25\%$ ). Hyperbaric oxygen therapy is not constant over the healing period, rather, oxygen is administered daily in short sessions (panel b). A common therapy consists of  $O_2 = 2.00\%$ , 90min/day (panel b, solid black line) leading to increased endothelial cell density over the same 10-day period. Computational simulations can predict alternative therapies (panel b, dashed cyan:  $O_2 = 3.00\%$ , 90min/day; dashed red:  $O_2 = 4.00\%$ , 90min/day). Adopted with permission from: Schugart RC, Friedman A, Zhao R, Sen CK. Wound angiogenesis as a function of tissue oxygen tension: A mathematical model. Proc Natl Acad Sci USA 2008;105:2628-33, Copyright (2008) National Academy of Sciences, U.S.A.

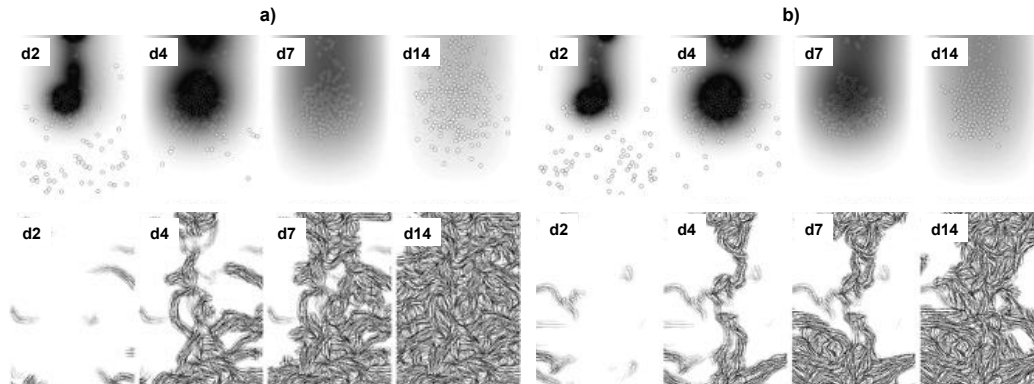


Figure 12.3: Collagen deposition can be manipulated by altering TGF- $\beta$  kinetics. Two-dimensional hybrid discrete/continuum simulation of wound healing with TGF- $\beta$  concentration color-coded in gray, top, fibroblasts displayed as discrete cells, top, and collagen fibers displayed through local fiber orientation maps, bottom. Normal TGF- $\beta$  diffusion initiates progressive collagen deposition at days 2, 4, 7, and 14 (panel a), while reduced TGF- $\beta$  diffusion generates localized fibroblast concentrations and reduced collagen deposition (panel b). Adopted with permission from Figures 7 and 9 in: Cumming BD, McElwain DLS, Upton Z. A mathematical model of wound healing and subsequent scarring. Journal of The Royal Society Interface 2009;7:19-34.

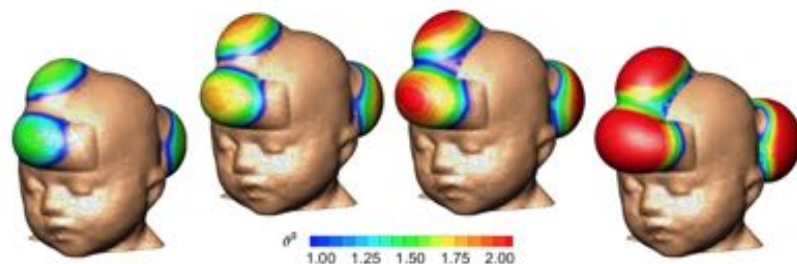


Figure 12.4: Collagen deposition and mitosis can be manipulated by altering stretch levels. Tissue expansion uses the concept of systematic overstretch to create extra skin for defect repair in reconstructive surgery. Gradually increasing the mechanical stretch over a period of 12 weeks, from left to right, triggers a graduate increase in skin area, from blue to red. In the red regions, skin has more than doubled its initial size [417]

## Chapter 13

# Computational Modeling of Chemo-Bio-Mechanical Coupling: A Systems-Biology Approach Towards Wound Healing

**Abstract.** Wound healing is a synchronized cascade of chemical, biological, and mechanical phenomena, which act in concert to restore the damaged tissue. An imbalance between these events can induce painful scarring. Despite intense efforts to decipher the mechanisms of wound healing, the role of mechanics remains poorly understood. Here we establish a computational systems biology model to identify the chemical, biological, and mechanical mechanisms of scar formation. First, we introduce the generic problem of coupled chemo-bio-mechanics. Then, we introduce the model problem of wound healing in terms of a particular chemical signal, inflammation, a particular biological cell type, fibroblasts, and a particular mechanical model, isotropic hyperelasticity. We explore the cross-talk between chemical, biological, and mechanical signals and show that all three fields have a significant impact on scar formation. Our model is the first step towards rigorous multiscale, multifield modeling in wound healing. Our formulation has the potential to improve effective wound management and optimize treatment on an individualized patient-specific basis.

## 13.1 Motivation

Effective wound management is a quotidian concern in clinical practice. Abnormal wound healing can initiate hypertrophic scars associated with serious complications from deteriorated skin characteristics to psychological trauma [29]. The health care cost related to wound treatment is jolting; wounds are common to many clinical procedures and span all patient demographics [50]. Fostering a healthy tissue response is a non-trivial task. The process of wound healing is a complex sequence of interrelated events that involve mechanical cues, coordinated cell behavior, and the interaction of numerous chemical signals [98]. In such a scenario, planning effective healing on a patient-specific basis becomes almost impossible. Computational systems biology has found a niche to enrich our understanding of this complex problem [193]. However, despite intense efforts to characterize the healing process with mathematical models, simulation of wound healing in arbitrary three-dimensional geometries remains an open problem. Disrupting the integrity of skin triggers a cascade of events that are common to all inflammation-based systems in the human body [392]. Additionally, during dermal wound healing, specialized processes take place to restitute the particular functional requirements of dermal tissue [145]. Perhaps the most distinct feature of this system is the interaction of different key players across scales, both in space and time. During the past decades, scientists have successfully identified and characterized the individual aspects of this network, but a holistic understanding of the healing process as a whole remains obscure [393].

### 13.1.1 Wound Healing Across the Spatial Scales

The spatial scales of interest for the healing system range from the order of micrometers, to millimeters, centimeters, and decimeters [53]. Figure 13.1 illustrates the multi-scale nature of the healing process with four interacting spatial scales [310]: the system level, the organ level, the tissue level, and the cell level [172].

On the cell level, the smallest spatial scale of the order of micrometers, single cells are the individual actors, which directly affect the healing process [352]. In the damaged dermal tissue and its surroundings, the following cell types are present: two types of leukocytes, neutrophils and macrophages, dispose pathogens and debris and establish gradients of growth factors; endothelial cells generate a new vasculature; keratinocytes divide and migrate across the epidermis to produce a new protective outermost layer; and fibroblasts deposit collagen

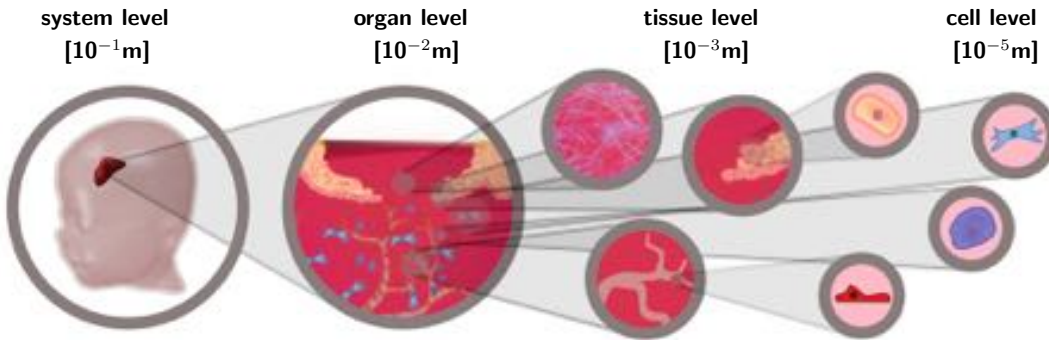


Figure 13.1: Wound healing across the spatial scales. The chemo-bio-mechanical problem of wound healing spans from the cellular level via the tissue level and organ level to the system level bridging four orders of magnitude in space.

and generate active stresses to contract the wound [283, 386].

On the tissue level, the next larger scale of the order of millimeters, the actions of the individual cells are smeared out by meso-scale patterns, which emanate from the collective cell behavior. This collective response exhibits distinctive characteristics, which cannot be extrapolated directly from single cell actions. Populations of keratinocyte generate a well-organized traveling wave inwards, and populations of endothelial cells keep strong cell-cell interactions to create fractal-like vascular networks [237, 297]. From this scale upward, both the mechanical response and the reaction-diffusion response of the chemical species can be characterized through field variables using a continuum approach [111, 219].

On the organ level, the scale of the order of centimeters, we can explore the interaction of the mechanical properties, different cell populations, and reaction-diffusion systems of chemical concentrations. The organ level provides a holistic approach to study the role of the individual key players of wound healing, and allows us to explore tissue function in health and disease.

On the system level, the scale of the order of decimeters, we can study the entire system created by the interplay of different organs. Ideally, system level models are generated on a patient-specific basis from individual clinical imaging data [417].

### 13.1.2 Wound Healing Across the Temporal Scales

The temporal scales of interest for the healing system range from the order of minutes, to hours, days, and weeks [53]. Figure 13.2 illustrates the multi-scale nature of the healing process with four overlapping temporal scales: hemostasis, inflammation, proliferation, and remodeling [240]. Immediately after the injury occurs, healing is critical to restore the barrier function of skin. Unfortunately, the initially generated temporary scaffold has only poor mechanical characteristics. Accordingly, subsequent stages of the healing process gradually reconstruct the tissue to ultimately restore the constitution of the uninjured skin [268]. The entire healing process can last for weeks or even months.

During hemostasis, within the order of minutes, the injured region fills with blood, which quickly coagulates. This results in the formation of an emergency scaffold of fibrin fibers. The only cells present in the clot are platelets, responsible for coagulation and the release of growth factors. At the end of this stage, degranulation of the platelets floods the injured site with chemicals to attract leukocytes.

During inflammation, within the order of hours, the first population of leukocytes, neutrophils, arrive at the wound site. Neutrophils remove pathogens and dispose of tissue debris from the injury. Shortly after, a second population of leukocytes, macrophages, migrate into the wound and continue the cleaning process. In addition, they establish gradients of various chemical signals to attract other cell populations [377]. After one or two days, the inflammatory phase smoothly blends into the proliferative phase.

During proliferation, within the order of days, the chemical signaling established by the macrophages attracts specialized cell populations that reconstruct skin. Endothelial cells generate a new vasculature that provides nutrients to the other cell populations [156]. Keratinocytes reconstruct the outermost protective layer, the epidermis, in a process called re-epithelialization [344]. Fibroblasts replace the temporary fibrin scaffold with a collagenous matrix that restitutes the desired mechanical properties of the healed tissue [74]. Although the proliferation phase creates a somewhat functional tissue, the mechanical properties of the newly reconstructed skin are not nearly identical to healthy, uninjured skin: The newly generated material is stiff scar tissue, which is partly provisional and will be replaced during the final remodeling phase [388].

During remodeling, within the order of weeks, fibroblasts slowly tear down and deposit collagen until the matrix approaches the structure of healthy tissue. The remodeling phase can continue for months or even years.

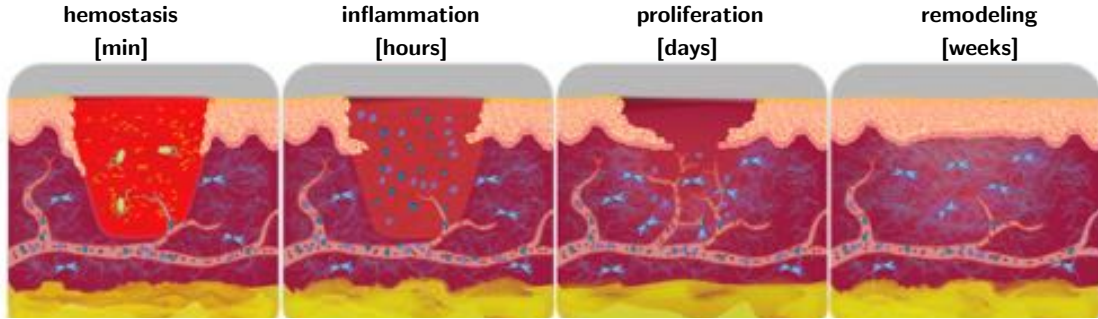


Figure 13.2: Wound healing across the temporal scales. The chemo-bio-mechanical problem of wound healing spans from the homeostatic phase via the inflammatory phase and proliferative phase to the remodeling phase bridging four orders of magnitude in time.

### 13.1.3 Modeling Wound Healing

Wound healing has been studied assiduously both experimentally and theoretically. Recent developments in computational systems biology suggest that we cannot gain a complete understanding of wound healing from studying isolated spatial or temporal scales alone [358]. Rather, trends in modeling seem to converge towards assembling the individual building blocks for a holistic model that, once calibrated, can provide new insight into the baseline system [88]. Systematic perturbations of this system allow us to probe different healing scenarios to ultimately link computational tools with personalized models [410].

The first mathematical model of wound healing was introduced in the early 1990s. Its initial goal was to simulate the traveling wave front of growing cell populations at the edge of a wound [338]. Since then, mathematical models have gained in complexity and have gradually incorporated the different components that interact in synchrony to heal the damaged tissue [410]. Recent models can be categorized according to two criteria, the aspect of healing they seek to analyze in detail and the simulation framework employed for the analysis. Three aspects of healing are particularly relevant: re-epithelialization and cell migration [33]; angiogenesis [390]; and mechanical aspects of wound healing such as collagen deposition and wound contraction [125]. Four modeling strategies are prevalent: one-dimensional and axisymmetric continuum models; two-dimensional continuum models; two- and three-dimensional discrete models; and two-dimensional hybrid discrete/continuum models. A

recent review article highlights the state of the art in systems biology approaches towards wound healing [53].

Among the different variables that influence the outcome of healing, the importance of mechanical cues has recently been identified with more clarity [4]. Fibroblasts have the capability to sense mechanical signals, to translate them into specific action such as active contraction, and to release chemical substances [403]. We now know that increased stress in the wound site alters fibroblast phenotype by reducing their apoptotic rate and inducing the release of pro-inflammatory signals [1, 292]. In turn, when the inflammation phase is prolonged, fibroblasts divide and migrate into the wound at higher rates, which results in an increased collagen deposition. The ultimate consequence is a poorly structured dermal tissue with thick collagen bundles instead of the smooth, inter-woven collageneous network found in healthy tissue. Visually, the result of such pathological reaction is very clear to the human eye, which can readily recognize hypertrophic scars [406]. However, despite this obvious evidence, only few models have incorporated a detailed mechanical description of the wound environment. While some models have addressed collagen deposition and active wound contraction, their application is limited by the underlying simplified constitutive models for the tissue structure [177, 379]. While such simplifications are adequate for base-line studies and first prototype simulations [204], in the current state, these models are unable to bridge the gap towards arbitrary geometries, large deformations, and complex stress distributions that arise in more realistic settings.

Motivated by the need for a computational framework that incorporates the state-of-the-art development in wound healing, here we present a novel finite element formulation for the chemo-bio-mechanical problem of wound healing in arbitrary geometries. The manuscript is structured as follows: In Section 13.2, we introduce the generic continuum framework of wound healing. In Section 13.3, we specify a particular type of the model parameterized in terms of a single chemical signal, a single biological cell density, and the mechanical deformation. In Section 13.4, we derive the discrete formulation of the particular model problem. In Section 13.5, we present sensitivity studies and selected examples to showcase the features of the model. Finally, in Section 13.6, we provide a discussion and a brief outlook.

## 13.2 Chemo-Bio-Mechanical Problem

We begin by introducing the generic equations that govern the dynamics of inflammation-based systems. In general, the underlying chemo-bio-mechanical problem can be characterized through three spatially and temporally interacting building blocks: chemical fields including substances such as growth factors and inflammation signals, here summarized in the vector  $\mathbf{c}(\mathbf{X}, t) = [c_1(\mathbf{X}, t), c_2(\mathbf{X}, t), \dots, c_{n_c}(\mathbf{X}, t)]^t$ ; biological fields including cell populations, here summarized in the vector  $\boldsymbol{\rho}(\mathbf{X}, t) = [\rho_1(\mathbf{X}, t), \rho_2(\mathbf{X}, t), \dots, \rho_{n_\rho}(\mathbf{X}, t)]^t$ ; and mechanical fields including the deformation  $\boldsymbol{\varphi}(\mathbf{X}, t)$ , which can be locally supplemented by microstructural internal variables such as microstructural directions  $\mathbf{n}(\mathbf{X}, t) = [\mathbf{n}_1(\mathbf{X}, t), \mathbf{n}_2(\mathbf{X}, t), \dots, \mathbf{n}_{n_n}(\mathbf{X}, t)]^t$  or microstructural concentrations  $\mathbf{w}(\mathbf{X}, t) = [w_1(\mathbf{X}, t), w_2(\mathbf{X}, t), \dots, w_{n_w}(\mathbf{X}, t)]^t$ . In the following, we characterize the evolution equations of these sets of variables in a continuum setting.

### 13.2.1 Chemical Problem: Chemical Concentrations

Chemically, the evolution of the set of chemical concentrations  $\mathbf{c}$  is balanced by the chemical flux  $\mathbf{q}^c$  and the chemical source  $\mathbf{f}^c$ ,

$$\dot{\mathbf{c}} = -\operatorname{div} \mathbf{q}^c(\nabla \mathbf{c}) + \mathbf{f}^c(\mathbf{c}, \boldsymbol{\rho}), \quad (13.1)$$

where  $\{\dot{\circ}\} = d\{\circ\}/dt$  denotes the material time derivative and  $\nabla\{\circ\}$  and  $\operatorname{div}\{\circ\}$  denote the spatial gradient and divergence. The chemical flux  $\mathbf{q}^c$  is typically modeled as a linear function of the gradient of the chemical concentration  $\nabla \mathbf{c}$  to indicate that the chemical signal can diffuse freely in the domain of interest,

$$\mathbf{q}^c = -\mathbf{D}^{cc} \cdot \nabla \mathbf{c}, \quad (13.2)$$

where  $\mathbf{D}^{cc}$  denotes the chemical diffusion tensor. The chemical source  $\mathbf{f}^c$  typically consists of a production term  $\mathbf{f}_p^c$  and a degradation term  $\mathbf{f}_d^c$ , whereby the degradation typically scales linearly with the concentration  $\mathbf{c}$  [338],

$$\mathbf{f}^c(\mathbf{c}, \boldsymbol{\rho}) = \mathbf{f}_p^c(\mathbf{c}, \boldsymbol{\rho}) - \mathbf{f}_d^c(\mathbf{c}, \boldsymbol{\rho}) \mathbf{c}. \quad (13.3)$$

In general,  $\mathbf{f}_p^c$  and degradation  $\mathbf{f}_d^c$  can be functions of all chemical concentrations  $\mathbf{c}$  and all cell populations  $\rho$ . They contain the information about how chemical substances are produced and degraded through chemical reactions with other chemical substances and by the different biological cells. In homeostasis, in the absence of chemical gradients  $\nabla \mathbf{c} = \mathbf{0}$ , the chemical production and degradation balance each other,  $\mathbf{f}_p^c = \mathbf{f}_d^c \mathbf{c}$ .

### 13.2.2 Biological Problem: Biological Cell Densities

Biologically, the evolution of the set of cell densities  $\rho$  is balanced by the biological flux  $\mathbf{q}^\rho$  and the biological source  $\mathbf{f}^\rho$ ,

$$\dot{\rho} = -\operatorname{div} \mathbf{q}^\rho(\mathbf{c}, \nabla \mathbf{c}, \rho, \nabla \rho, \nabla \varphi) + \mathbf{f}^\rho(\mathbf{c}, \rho, \nabla \varphi). \quad (13.4)$$

The biological flux  $\mathbf{q}^\rho$  typically consists of three contributions,

$$\mathbf{q}^\rho = -\mathbf{D}^{\rho\rho} \cdot \nabla \rho - \mathbf{D}^{\rho c}(\mathbf{c}, \rho, \nabla \varphi) \cdot \nabla \mathbf{c} - \mathbf{D}^{\rho\varphi} : \nabla \varphi. \quad (13.5)$$

The first contribution,  $-\mathbf{D}^{\rho\rho} \cdot \nabla \rho$ , describes the free diffusion of cells along cell density gradients  $\nabla \rho$ . It mimics the continuum representation of random walk and contact inhibition at the cellular level represented through the biological diffusion tensor  $\mathbf{D}^{\rho\rho}$ . The second contribution,  $-\mathbf{D}^{\rho c} \cdot \nabla \mathbf{c}$ , characterizes the phenomenon of chemotaxis. It is associated with the directed diffusion along chemical concentration gradients  $\nabla \mathbf{c}$  represented through the chemotactic diffusion tensor  $\mathbf{D}^{\rho c}$ , which can either be constant or depend on chemical concentrations  $\mathbf{c}$ , cell densities  $\rho$ , and deformation  $\varphi$ . The third contribution,  $-\mathbf{D}^{\rho\varphi} : \nabla \varphi$ , represents the phenomenon of mechanotaxis. It reflects the directed diffusion along mechanical cues  $\nabla \varphi$  represented through the mechanotactic diffusion tensor  $\mathbf{D}^{\rho\varphi}$ . The biological source consists of a mitotic contribution  $\mathbf{f}_m^\rho$  and an apoptotic contribution  $\mathbf{f}_a^\rho$ , which typically scales linearly with the cell density  $\rho$ ,

$$\mathbf{f}^\rho(\mathbf{c}, \rho, \nabla \varphi) = \mathbf{f}_m^\rho(\mathbf{c}, \rho, \nabla \varphi) - \mathbf{f}_a^\rho(\mathbf{c}, \rho, \nabla \varphi) \rho \quad (13.6)$$

The mitotic and apoptotic terms  $\mathbf{f}_m^\rho$  and  $\mathbf{f}_a^\rho$  can be functions of all chemical concentrations  $\mathbf{c}$ , of all cell populations  $\rho$ , and of mechanical cues  $\nabla \varphi$ . The latter dependency mimics the effects of mechanotransduction, the impact of mechanical cues on biological phenomena. In homeostasis, in the absence of biological gradients  $\nabla \rho = \mathbf{0}$ , the mitotic and apoptotic rates

balance each other,  $\mathbf{f}_m^\rho = \mathbf{f}_a^\rho \boldsymbol{\rho}$ .

### 13.2.3 Mechanical Problem: Mechanical Deformation

Mechanically, we assume that the mechanical problem is quasi-static and balances the mechanical flux  $\boldsymbol{\sigma}$  with the mechanical source  $\mathbf{f}^\varphi$ ,

$$\mathbf{0} = \operatorname{div} \boldsymbol{\sigma}(\nabla\varphi, \mathbf{n}, \mathbf{w}) + \mathbf{f}^\varphi. \quad (13.7)$$

The mechanical flux  $\boldsymbol{\sigma}$ , the Cauchy stress, can be additively decomposed into passive and active contributions,

$$\boldsymbol{\sigma} = \boldsymbol{\sigma}^{\text{pas}}(\nabla\varphi, \mathbf{n}, \mathbf{w}) + \boldsymbol{\sigma}^{\text{act}}(\nabla\varphi, \mathbf{n}, \mathbf{w}). \quad (13.8)$$

The active stress accounts for tissue contraction by cells such as fibroblasts [178]. The passive stress typically consists of two contributions,

$$\boldsymbol{\sigma}^{\text{pas}} = \boldsymbol{\sigma}^{\text{mat}}(\nabla\varphi) + \mathbf{w} \boldsymbol{\sigma}^{\text{fib}}(\nabla\varphi, \mathbf{n}). \quad (13.9)$$

The first contribution  $\boldsymbol{\sigma}^{\text{mat}}$  describes the isotropic water-based matrix as a function of the deformation gradient  $\nabla\varphi$ . The second contribution  $\boldsymbol{\sigma}^{\text{fib}}$  describes the anisotropic response of fibrous constituents such as elastin, collagen, or smooth muscle as a function of the deformation gradient  $\nabla\varphi$  and preferred microstructural directions  $\mathbf{n}$ , scaled by the fiber content  $\mathbf{w}$ . The mechanical source  $\mathbf{f}^\varphi$ , the external mechanical force such as gravity, is typically negligible in the context of inflammation-based systems,

$$\mathbf{f}^\varphi = \mathbf{0}. \quad (13.10)$$

Biological cells continuously interact with and remodel the tissue in their immediate environment to establish a well defined microstructural arrangement in healthy tissue. After an injury, this microstructure of the healthy skin disappears. Local remodeling by cells becomes the crucial connecting point between the chemical, biological, and mechanical fields [246]. We typically model this coupling through the internal variables  $\mathbf{n}$  and  $\mathbf{w}$ , which evolve in response to cell population dynamics  $\boldsymbol{\rho}$ . In the most general setting, we allow the microstructural directions  $\mathbf{n}$  to gradually reorient according to a set of local evolution equations [123], e.g., driven by chemical gradients  $\nabla\mathbf{c}$  [47], by biological gradients  $\nabla\boldsymbol{\rho}$ , by

mechanical gradients  $\nabla\varphi$ , and by the current microstructural directions  $\mathbf{n}$ ,

$$\dot{\mathbf{n}} = \mathbf{f}^n(\nabla\mathbf{c}, \nabla\rho, \nabla\varphi, \mathbf{n}) . \quad (13.11)$$

Similarly, the local fiber content  $\mathbf{w}$  can evolve in time, e.g., driven by chemical concentrations  $\mathbf{c}$ , by biological cell densities  $\rho$ , by mechanical gradients  $\nabla\varphi$ , and by the current fiber content  $\mathbf{w}$ ,

$$\dot{\mathbf{w}} = \mathbf{f}^w(\mathbf{c}, \rho, \nabla\varphi, \mathbf{w}) . \quad (13.12)$$

Even though the microstructural direction  $\mathbf{n}$  and the microstructural fiber content  $\mathbf{w}$  are parametrized in terms of inhomogeneous fields, their evolution equations are strictly local as they do not contain any gradient or divergence terms. This suggests to treat the microstructural information  $\mathbf{n}$  and  $\mathbf{w}$  as a set of internal variables [159, 250]. In summary, we represent the chemo-bio-mechanical problem through a system of three sets of partial differential equations for the chemical concentrations  $\mathbf{c}$ , the biological cell densities  $\rho$ , and the mechanical deformation  $\varphi$ , locally supplemented by two sets of ordinary differential equations for the microstructural directions  $\mathbf{n}$  and the microstructural fiber content  $\mathbf{w}$ . In the following section, we will specify these generic equations to explore a particular model problem of wound healing.

### 13.3 Model Problem of Wound Healing

In this section, we illustrate the features of the proposed generic framework in terms of a simple model problem of wound healing restricting attention to a few key players. We represent the chemical problem through the concentration of the inflammatory signal  $c(\mathbf{X}, t)$ , the biological problem through the fibroblast density  $\rho(\mathbf{X}, t)$ , and the mechanical problem through the deformation  $\varphi(\mathbf{X}, t)$  supplemented by the collagen content  $w(\mathbf{X}, t)$  as local internal variable. We assume that the collagen fiber orientation  $\mathbf{n}(\mathbf{X}, t)$  remains constant throughout the healing process.

#### 13.3.1 Chemical Problem: Inflammatory Signal

Chemically, we characterize the response through the inflammatory signal  $c$ , which represents the initial recruitment of macrophages and their contribution to generate growth factor attractors for fibroblasts. In reality, the cascade of chemical signaling of inflammation

is much more complex and includes several cytokines and other cell types such as endothelial cells and neutrophils [338, 399]. Nonetheless, previous mathematical models have shown good qualitative behavior considering only macrophages and fibroblasts [86]. We follow that approach here and synthesize the inflammatory signal into a single field variable. According to the generic chemical balance law (13.1), we balance its rate of change with the chemical flux  $\mathbf{q}^c$  and the chemical source  $f^c$ ,

$$\dot{c} = -\operatorname{div} \mathbf{q}^c + f^c. \quad (13.13)$$

For the chemical flux  $\mathbf{q}^c$  we assume a linear isotropic function of the gradient of the chemical concentration  $\nabla c$  to indicate that the chemical signal can diffuse freely and isotropically in the domain of interest [71],

$$\mathbf{q}^c = -D^{cc} \nabla c. \quad (13.14)$$

where  $D^{cc}$  is the isotropic chemical diffusion coefficient. For the chemical source, we assume that the inflammatory signal has no production component and displays a linear degradation,

$$f^c = -k c, \quad (13.15)$$

where  $k$  is the chemical degradation rate.

### 13.3.2 Biological Problem: Fibroblasts

Biologically, we characterize the response through the fibroblast density  $\rho$ . According to the generic biological balance law (13.4), we balance its rate of change with the biological flux  $\mathbf{q}^\rho$  and the biological source  $f^\rho$ ,

$$\dot{\rho} = -\operatorname{div} \mathbf{q}^\rho + f^\rho. \quad (13.16)$$

For the biological flux, we assume that fibroblasts are motile cells, which diffuse freely along their own gradients  $\nabla \rho$  perturbed by a biased diffusion towards the gradient of the inflammatory signal  $\nabla c$ ,

$$\mathbf{q}^\rho = -D^{\rho\rho} \nabla \rho - a \rho \nabla c, \quad (13.17)$$

where  $D^{\rho\rho}$  and  $D^{\rho c} = a \rho$  denote the isotropic biological and chemotactic diffusion coefficients. For the biological source, we make the following ansatz in terms of the fibroblast

density  $\rho$  and the intensity of the inflammatory signal  $c$ ,

$$f^\rho = k_1 [\rho_0 - \rho] + k_2 c \rho \quad (13.18)$$

where  $\rho_0$  is the homeostatic fibroblast concentration,  $k_1$  is the physiological mitotic and apoptotic rate, and  $k_2$  is the mitotic rate induced by the inflammatory signal  $c$ . Under healthy conditions, fibroblast mitosis and apoptosis balance one another to ensure a stable fibroblast population  $\rho_0$ . However, in the presence of inflammatory signals, the mitotic rate increases and creates an imbalance with respect to the steady state  $\rho_0$  to increase the fibroblast density.

### 13.3.3 Mechanical Problem: Deformation

Mechanically, we characterize the response through the deformation  $\varphi$ , from which we derive the deformation gradient  $\mathbf{F} = \nabla\varphi$  and the left Cauchy-Green deformation tensor  $\mathbf{b} = \mathbf{F} \cdot \mathbf{F}^t$  as key kinematic variables. According to the mechanical balance law (13.7), we balance the mechanical flux  $\boldsymbol{\sigma}$  characterizing the Cauchy stress and the mechanical source  $\mathbf{f}^\varphi$  characterizing the external mechanical forces,

$$\mathbf{0} = \operatorname{div} \boldsymbol{\sigma} + \mathbf{f}^\varphi. \quad (13.19)$$

Skin has a well organized microstructure with an isotropic water-based matrix that serves as a scaffold for the anisotropic collagen network with a preferred orientation  $\mathbf{n}_0$  [52]. For this simple model problem of wound healing we do not consider the active stress exerted by the fibroblast cell population. We characterize only its passive constitutive response through a compressible, transversely isotropic, hyperelastic free energy function,

$$\psi = \psi^{\text{mat}}(J, I_1) + w \psi^{\text{fib}}(I_1, I_4), \quad (13.20)$$

which consists of an isotropic part  $\psi^{\text{mat}}$  for the non-collagenous isotropic matrix and an anisotropic part  $\psi^{\text{fib}}$  for the collagen network weighted by the collagen content  $w$ . Here, we have introduced three kinematic invariants, the Jacobian  $J = \det \mathbf{F}$  for the volumetric response, the first invariant  $I_1 = \mathbf{b} : \mathbf{I}$  for the isotropic response, and the fourth invariant  $I_4 = [\mathbf{n} \otimes \mathbf{n}] : \mathbf{I}$  for the anisotropic response, where  $\mathbf{n} = \mathbf{F} \cdot \mathbf{n}_0$  is the preferred collagen fiber orientation in the deformed configuration. We model the matrix material as standard

isotropic, compressible Neo-Hooke-type parameterized in terms of the Lamé constants  $\lambda$  and  $\mu$  and the collagen fibers as Holzapfel-type [161], parameterized in terms of the collagen stiffness  $c_1$ , the nonlinearity  $c_2$ , and the fiber dispersion  $\kappa$ ,

$$\begin{aligned}\psi^{\text{mat}} &= \frac{1}{2} \mu [I_1 - 3] - \mu \ln J + \frac{1}{2} \lambda \ln^2 J \\ \psi^{\text{fib}} &= \frac{1}{2} c_1/c_2 [\exp(c_2 [\kappa I_1 + [1 - 3\kappa] I_4 - 1]^2) - 1].\end{aligned}\quad (13.21)$$

The additive decomposition of the strain energy function translates into the additive decomposition of the Cauchy stress according to the generic ansatz (13.9),

$$\boldsymbol{\sigma} = \mathbf{F} \cdot \frac{2}{J} \frac{\partial \psi}{\partial \mathbf{C}} \cdot \mathbf{F}^t = \boldsymbol{\sigma}^{\text{mat}} + w \cdot \boldsymbol{\sigma}^{\text{fib}}, \quad (13.22)$$

with the following matrix and fiber contributions,

$$\begin{aligned}\boldsymbol{\sigma}^{\text{mat}} &= \mathbf{F} \cdot \frac{2}{J} \frac{\partial \psi^{\text{mat}}}{\partial \mathbf{C}} \cdot \mathbf{F}^t = \mu [\mathbf{b} - \mathbf{I}] + \lambda \ln J \mathbf{I} \\ \boldsymbol{\sigma}^{\text{fib}} &= \mathbf{F} \cdot \frac{2}{J} \frac{\partial \psi^{\text{fib}}}{\partial \mathbf{C}} \cdot \mathbf{F}^t = 2\psi_1 \mathbf{b} + 2\psi_4 \mathbf{n} \otimes \mathbf{n}.\end{aligned}\quad (13.23)$$

Here,  $\psi_1$  and  $\psi_4$  denote the first derivatives of the fiber energy with respect to the first and fourth invariants,  $\psi_i = \partial \psi^{\text{fib}} / \partial I_i$ ,

$$\begin{aligned}\psi_1 &= c_0 + c_1 \kappa [\kappa I_1 + [1 - 3\kappa] I_4 - 1] \\ &\quad \exp(c_2 [\kappa I_1 + [1 - 3\kappa] I_4 - 1]^2) \\ \psi_4 &= c_1 [1 - 3\kappa] [\kappa I_1 + [1 - 3\kappa] I_4 - 1] \\ &\quad \exp(c_2 [\kappa I_1 + [1 - 3\kappa] I_4 - 1]^2).\end{aligned}\quad (13.24)$$

For the mechanical source, we assume that external forces such as gravity do not play a major role during wound healing and can therefore be neglected,

$$\mathbf{f}^\varphi = \mathbf{0}. \quad (13.25)$$

It remains to characterize the evolution of the collagen content  $w$  and its reference orientation  $\mathbf{n}$ , which we treat locally as internal variables. In the interest of simplification we assume that the fiber orientation remains constant, this implies that the new collagen is being deposited in the same direction as in the surrounding, healthy tissue. We assume that healthy skin possess a homeostatic collagen content  $w_0$ . After an injury, the collagen

content decreases dramatically in the affected region. It is the task of the fibroblasts to deposit new collagen to restore skin's mechanical properties. We therefore model the evolution of the collagen content  $\dot{w}$  to depend on the chemical signal  $c$ , the fibroblast density  $\rho$ , and the current collagen content  $w$  itself, specifically,

$$\dot{w} = f^w \quad \text{with} \quad f^w = \frac{\rho \gamma}{1 + w^2} \left[ 1 - w + \frac{\alpha c \gamma}{1 + c} \right]. \quad (13.26)$$

Here,  $\gamma$  denotes the physiological collagen deposition rate and  $\alpha$  denotes the increase in collagen synthesis in response to inflammation  $c$ .

## 13.4 Computational Modeling of Wound Healing

To characterize the spatio-temporal evolution of the inflammatory signal  $c$ , the fibroblast density  $\rho$ , the deformation  $\varphi$ , and the collagen content  $w$ , we solve the global balance equations (13.13), (13.16), and (13.19) along with the local evolution equation (13.26).

### 13.4.1 Continuous Residuals

To derive the algorithmic solution we begin by restating the global balance equations (13.13), (13.16), and (13.19) in their residual forms and introduce the chemical, biological, and mechanical residuals  $\mathbf{R}^c$ ,  $\mathbf{R}^\rho$ , and  $\mathbf{R}^\varphi$  throughout the domain of interest  $\mathcal{B}$ ,

$$\begin{aligned} \mathbf{R}^c &= \dot{c} + \operatorname{div} \mathbf{q}^c - f^c \doteq 0 \\ \mathbf{R}^\rho &= \dot{\rho} + \operatorname{div} \mathbf{q}^\rho - f^\rho \doteq 0 \\ \mathbf{R}^\varphi &= -\operatorname{div} \boldsymbol{\sigma} - \mathbf{f}^\varphi \doteq \mathbf{0}. \end{aligned} \quad (13.27)$$

To define the corresponding boundary conditions, we decompose the boundary  $\partial\mathcal{B}$  into disjoint parts  $\partial\mathcal{B}^c$  and  $\partial\mathcal{B}^{qc}$  for the chemical problem,  $\partial\mathcal{B}^\rho$  and  $\partial\mathcal{B}^{qr}$  for the biological problem, and  $\partial\mathcal{B}^\varphi$  and  $\partial\mathcal{B}^\sigma$  for the mechanical problem. We prescribe Dirichlet boundary conditions  $c = c^p$  on  $\partial\mathcal{B}^c$ ,  $\rho = \rho^p$  on  $\partial\mathcal{B}^\rho$ , and  $\varphi = \varphi^p$  on  $\partial\mathcal{B}^\varphi$ , and Neumann boundary conditions  $\mathbf{q}^c \cdot \mathbf{n} = t^c$  on  $\partial\mathcal{B}^{qc}$ ,  $\mathbf{q}^\rho \cdot \mathbf{n} = t^\rho$  on  $\partial\mathcal{B}^{qr}$ , and  $\boldsymbol{\sigma} \cdot \mathbf{n} = \mathbf{t}^\varphi$  on  $\partial\mathcal{B}^\sigma$ , where  $\mathbf{n}$  denotes the outward normal to  $\partial\mathcal{B}$ . To obtain the weak forms of the chemical, biological, and mechanical problems, we multiply the residual statements (13.27) and the corresponding Neumann boundary conditions with the scalar- and vector-valued test functions  $\delta c$ ,  $\delta\rho$  and  $\delta\varphi$  and integrate them over the domain  $\mathcal{B}$ .

### 13.4.2 Discretization in Time

To discretize the weak forms of the residual statements (13.27) in time, we partition the time interval of interest  $\mathcal{T}$  into  $n_{stp}$  subintervals  $[t_n, t]$  as  $\mathcal{T} = \bigcup_{n=0}^{n_{step}-1} [t_n, t]$ . Here and from now on we omit the subscript  $\{\circ\}_{n+1}$  to denote the current time point. We assume, that the primary unknowns  $c_n$ ,  $\rho_n$  and  $\varphi_n$  and all derivable quantities are known at the last time point  $t_n$ . To advance the unknowns  $c$ ,  $\rho$ , and  $\varphi$  to the current time point  $t$ , we apply the classical implicit backward Euler time integration scheme and evaluate the governing equations at time  $t$ . We apply a finite difference scheme to approximate the first order material time derivatives as

$$\dot{c} = [c - c_n] / \Delta t \quad \text{and} \quad \dot{\rho} = [\rho - \rho_n] / \Delta t, \quad (13.28)$$

where  $\Delta t := t - t_n > 0$  denotes the current time increment.

### 13.4.3 Discretization in Space

To discretize the weak forms of the residual statements (13.27) in space, we apply a  $\mathcal{C}^0$ -continuous interpolation for the inflammatory signal  $c$ , the fibroblast density  $\rho$ , and the deformation  $\varphi$ , and allow the collagen content  $w$  to be  $\mathcal{C}^{-1}$  continuous. Accordingly, we introduce  $c$ ,  $\rho$ , and  $\varphi$  globally on the node point level, and store  $w$  locally on the integration point level. We discretize the domain of interest  $\mathcal{B}$  into  $n_{el}$  elements  $\mathcal{B}_e$  as  $\mathcal{B} = \bigcup_{e=1}^{n_{el}} \mathcal{B}_e$ . We adopt a Bubnov-Galerkin approach and interpolate the trial functions  $c^h, \rho^h, \varphi^h$  in  $\mathcal{H}_1(\mathcal{B})$  with the same basis function  $N^c$ ,  $N^\rho$ , and  $N^\varphi$  as the test functions  $\delta c^h, \delta \rho^h, \delta \varphi^h$  in  $\mathcal{H}_1^0(\mathcal{B})$  on the element level,

$$\begin{aligned} \delta c &= \sum_i N_i^c \delta c_i & \delta \rho &= \sum_j N_j^\rho \delta \rho_j & \delta \varphi &= \sum_k N_k^\varphi \delta \varphi_k \\ c &= \sum_l N_l^c c_l & \rho &= \sum_m N_m^\rho \rho_m & \varphi &= \sum_n N_n^\varphi \varphi_n. \end{aligned} \quad (13.29)$$

We adopt the isoparametric concept and interpolate the local element geometry with the same basis functions  $N^\varphi$  as the test and trial functions  $\varphi^h$  and  $\delta \varphi^h$ .

### 13.4.4 Discrete Algorithmic Residuals

With the discretizations in time (13.28) and space (13.29), and the assumption of homogeneous Neumann boundary conditions,  $t^c = 0$ ,  $t^\rho = 0$ , and  $\mathbf{t}^\varphi = \mathbf{0}$ , the weak forms of the

continuous residuals (13.27) translate into the discrete algorithmic residuals,

$$\begin{aligned} \mathbf{R}_I^c &= \mathbf{A} \sum_{e=1}^{n_{el}} \int_{\mathcal{B}_e} N_i^c \frac{c - c_n}{\Delta t} - \nabla N_i^c \cdot \mathbf{q}^c - N_i^c f^c \, dv \doteq 0 \\ \mathbf{R}_J^\rho &= \mathbf{A} \sum_{e=1}^{n_{el}} \int_{\mathcal{B}_e} N_j^\rho \frac{\rho - \rho_n}{\Delta t} - \nabla N_j^\rho \cdot \mathbf{q}^\rho - N_j^\rho f^\rho \, dv \doteq 0 \\ \mathbf{R}_K^\varphi &= \mathbf{A} \sum_{e=1}^{n_{el}} \int_{\mathcal{B}_e} \nabla N_k^\varphi \cdot \boldsymbol{\sigma} - N_k^\varphi \mathbf{f}^\varphi \, dv \doteq \mathbf{0}. \end{aligned} \quad (13.30)$$

Here, the operator  $\mathbf{A}$  symbolizes the assembly of all element contributions at the element nodes  $i, j, k$ , to the overall residuals at the global nodes  $I, J, K$ .

### 13.4.5 Linearization

Although it is possible and sometimes advantageous to solve the discrete residual equations (13.30) sequentially in a staggered sense, here we discuss the overall solution within a monolithic incremental iterative Newton–Raphson scheme. The Newton–Raphson scheme relies on a consistent algorithmic linearization of the governing equations,

$$\begin{aligned} \mathbf{R}_I^c + \sum_{L=1}^{n_{nc}} \mathbf{K}_{IL}^{cc} \, dc_L + \sum_{M=1}^{n_{n\rho}} \mathbf{K}_{IM}^{c\rho} \, d\rho_M + \sum_{N=1}^{n_{n\varphi}} \mathbf{K}_{IN}^{c\varphi} \cdot d\varphi_N &\doteq 0 \\ \mathbf{R}_J^\rho + \sum_{L=1}^{n_{nc}} \mathbf{K}_{JL}^{\rho c} \, dc_L + \sum_{M=1}^{n_{n\rho}} \mathbf{K}_{JM}^{\rho\rho} \, d\rho_M + \sum_{N=1}^{n_{n\varphi}} \mathbf{K}_{JN}^{\rho\varphi} \cdot d\varphi_N &\doteq 0 \\ \mathbf{R}_K^\varphi + \sum_{L=1}^{n_{nc}} \mathbf{K}_{KL}^{\varphi c} \, dc_L + \sum_{M=1}^{n_{n\rho}} \mathbf{K}_{LM}^{\varphi\rho} \, d\rho_M + \sum_{N=1}^{n_{n\varphi}} \mathbf{K}_{KN}^{\varphi\varphi} \cdot d\varphi_N &\doteq \mathbf{0}. \end{aligned} \quad (13.31)$$

Here we have introduced the iteration matrices

$$\begin{aligned}
 \mathbf{K}_{IL}^{cc} &= \mathbf{A} \int_{\mathcal{B}^e} N_i^c \left[ \frac{1}{\Delta t} - k \right] N_l^c + \nabla N_i^c \cdot D^{cc} \nabla N_l^c \quad dV \\
 \mathbf{K}_{JL}^{pc} &= \mathbf{A} \int_{\mathcal{B}^e} N_j^\rho [-k_2] N_l^c + \nabla N_j^\rho \cdot a \rho \nabla N_l^c \quad dV \\
 \mathbf{K}_{JM}^{\rho\rho} &= \mathbf{A} \int_{\mathcal{B}^e} N_j^\rho \left[ \frac{1}{\Delta t} - k_1 - k_2 c \right] N_m^\rho + \nabla N_j^\rho \cdot D^{\rho\rho} \nabla N_m^\rho \quad dV \\
 \mathbf{K}_{KL}^{c\varphi} &= \mathbf{A} \int_{\mathcal{B}^e} \nabla N_k^\varphi \cdot d_c w \boldsymbol{\sigma}^{\text{fib}} N_l^c \quad dV \\
 \mathbf{K}_{KM}^{\varphi\rho} &= \mathbf{A} \int_{\mathcal{B}^e} \nabla N_k^\varphi \cdot d_\rho w \boldsymbol{\sigma}^{\text{fib}} N_m^\rho \quad dV \\
 \mathbf{K}_{KN}^{\varphi\varphi} &= \mathbf{A} \int_{\mathcal{B}^e} \nabla N_\varphi^k \cdot \mathbf{c} \cdot \nabla N_\varphi^n + \nabla N_\varphi^k \cdot \hat{\boldsymbol{\sigma}} \cdot \nabla N_\varphi^n \quad dV
 \end{aligned} \tag{13.32}$$

with the understanding that, for this special model problem,  $\mathbf{K}_{IM}^{c\rho} = \mathbf{0}$ ,  $\mathbf{K}_{IN}^{c\varphi} = \mathbf{0}$ , and  $\mathbf{K}_{JN}^{\rho\varphi} = \mathbf{0}$ . The solution of the system of equations (13.31) renders the iterative update for the increments of the chemical, biological, and mechanical global unknowns as  $\Delta c_I \leftarrow \Delta c_I + d_c I$ ,  $\Delta \rho_J \leftarrow \Delta \rho_J + d_\rho J$  and  $\Delta \varphi_K \leftarrow \Delta \varphi_K + d\varphi K$ . It remains to determine the sensitivities of the collagen content  $d_c w$  and  $d_\rho w$  and the Eulerian tangent moduli  $\mathbf{c}$  at the constitutive level.

### 13.4.6 Algorithmic Constitutive Equations

On the constitutive level, we first update all internal variables, for our model problem the collagen content  $w$ . Then, we determine the chemical, biological, and mechanical fluxes  $\mathbf{q}^c$ ,  $\mathbf{q}^\rho$ , and  $\boldsymbol{\sigma}$  and sources  $f^c$ ,  $f^\rho$ , and  $\mathbf{f}^\varphi$ , which enter the discrete algorithmic residuals (13.30). Last, we determine their consistent algorithmic linearizations, for our model problem  $d_c w$  and  $d_\rho w$  and  $\mathbf{c}$ , which enter the iterations matrices (13.32). We treat the collagen content  $w$  as internal variable and store it locally on the integration point level. To discretize its evolution in time, we apply a finite difference approximation,

$$\dot{w} = [w - w_n] / \Delta t, \tag{13.33}$$

combined with an implicit backward Euler time integration scheme. To solve its nonlinear evolution equation, we adopt a local Newton-Raphson scheme. We rephrase the evolution

equation (13.26) in its residual form,

$$\mathbf{R}^w = w - w_n - \frac{\rho\gamma}{1+w^2} \left[ 1 - w + \frac{\alpha c \gamma}{1+c} \right] \Delta t \doteq 0 \quad (13.34)$$

and linearize it consistently as  $\mathbf{K}^w = d_w \mathbf{R}^w$  with

$$\mathbf{K}^w = 1 + \frac{\rho\gamma}{1+w^2} \left[ 1 + \frac{2w}{1+w^2} \left[ 1 - w - \frac{\alpha c \gamma}{1+c} \right] \right] \Delta t \quad (13.35)$$

to incrementally update the collagen content  $w \leftarrow w - \mathbf{R}^w / \mathbf{K}^w$  on the integration point level. Upon local equilibrium, we determine the fluxes  $\mathbf{q}^c$ ,  $\mathbf{q}^\rho$ , and  $\boldsymbol{\sigma}$  and sources  $f^c$ ,  $f^\rho$ , and  $\mathbf{f}^\varphi$  for the global residuals (13.30). Next, we determine the linearizations  $d_c w = \partial_c \dot{w} \Delta t / \mathbf{K}^w$  with  $\partial_c \dot{w}$  from equation (13.26),

$$d_c w = \frac{\rho\gamma}{1+w^2} \left[ \frac{\alpha\gamma}{1+c} - \frac{\alpha c \gamma}{[1+c]^2} \right] \Delta t / \mathbf{K}^w, \quad (13.36)$$

and  $d_\rho w = \partial_\rho \dot{w} \Delta t / \mathbf{K}^w$  with  $\partial_\rho \dot{w}$  from equation (13.26),

$$d_\rho w = \frac{\gamma}{1+w^2} \left[ 1 - w + \frac{\alpha c \gamma}{1+c} \right] \Delta t / \mathbf{K}^w, \quad (13.37)$$

for the global iterations matrices (13.32). Last, we determine the Eulerian constitutive moduli  $\mathbb{C}$ ,

$$\mathbb{C} = \mathbb{C}^{\text{mat}} + w \cdot \mathbb{C}^{\text{fib}}, \quad (13.38)$$

with matrix and fiber contributions,

$$\begin{aligned} \mathbb{C}^{\text{mat}} &= [\lambda \mathbf{I} \otimes \mathbf{I} + 2[\mu - \lambda \ln J] \mathbf{i}] / J \\ \mathbb{C}^{\text{fib}} &= 4 [\psi_{11} \mathbf{b} \otimes \mathbf{b} + 2\psi_{14} [\mathbf{b} \otimes \mathbf{n} \otimes \mathbf{n}]^{\text{sym}} \\ &\quad + \psi_{44} \mathbf{n} \otimes \mathbf{n} \otimes \mathbf{n} \otimes \mathbf{n}] / J. \end{aligned} \quad (13.39)$$

where  $\mathbf{i}$  is the symmetric fourth order unit tensor. The abbreviations  $\psi_{11}$ ,  $\psi_{14}$  and  $\psi_{44}$  denote the second derivatives of the fiber energy with respect to the first and fourth invariants,

$\psi_{ij} = \partial^2\psi / \partial I_i \partial I_j$  with

$$\begin{aligned}\psi_{11} &= c_1 [1 + 2c_2 [\kappa I_1 + [1 - 3\kappa] I_4 - 1]] \\ &\quad \exp(c_2 [\kappa I_1 + [1 - 3\kappa] I_4 - 1]^2) \kappa^2 \\ \psi_{14} &= c_1 [1 + 2c_2 [\kappa I_1 + [1 - 3\kappa] I_4 - 1]] \\ &\quad \exp(c_2 [\kappa I_1 + [1 - 3\kappa] I_4 - 1]^2) \kappa [1 - 3\kappa] \\ \psi_{44} &= c_1 [1 + 2c_2 [\kappa I_1 + [1 - 3\kappa] I_4 - 1]] \\ &\quad \exp(c_2 [\kappa I_1 + [1 - 3\kappa] I_4 - 1]^2) [1 - 3\kappa]^2.\end{aligned}\tag{13.40}$$

## 13.5 Examples

In this section, we present selected examples to showcase the features of the present formulation in different wound healing scenarios. The first example is a homogeneous setting, in which we explore wound healing across the temporal scales. We monitor the temporal evolution of the chemical, biological, and mechanical variables and systematically probe the constitutive equations for the chemical, biological, and mechanical source terms. The second example is a heterogeneous setting, in which we explore wound healing across the spatio-temporal scales. We monitor the spatio-temporal evolution of the chemical, biological, and mechanical variables and systematically probe the constitutive equations for the chemical, biological, and mechanical flux terms. We run all the simulations on software developed in-house.

### 13.5.1 Wound Healing Across the Temporal Scales

First, we explore the temporal evolution of the chemical, biological, and mechanical variables, the inflammatory signal  $c$ , the fibroblast density  $\rho$ , and the collagen content  $w$  in a homogeneous setting. This allows us to systematically probe the constitutive equations for the chemical, biological, and mechanical source terms  $f^c$ ,  $f^\rho$ , and  $f^w$  defined in equations (13.15), (13.18), and (13.26) and perform sensitivity analyses with respect to the associated material parameters. The homogeneous setting is characterized through the local versions of equations (13.1), (13.4), and (13.7) resulting in the following system of ordinary differential

Table 13.1: Values for the parameters used in the computations.

parameter	physical interpretation	value/range	reference
$k$	degradation rate of inflammatory signal	0.5 [1/day]	[281]
$k_1$	physiological mitotic and apoptotic rate	0.833 [1/day]	[378]
$k_2$	mitosis induced by inflammation	0.3 [1/day]	[178]
$\rho_0$	homeostatic fibroblast concentration	0.5	(—)
$\gamma$	physiological collagen deposition rate	0.1 [1/day]	[221]
$\alpha$	increase of collagen deposition by inflammation	0.5	[86]
$w_0$	homeostatic collagen concentration	1.0	(—)
$D^{cc}$	chemical diffusion coefficient	0.05 cm/day	[281]
$D_{\rho\rho}$	cell diffusion coefficient	0.02 cm/day	[178]

equations,

$$\begin{aligned}\dot{c} &= -k c \\ \dot{\rho} &= k_1 [\rho_0 - \rho] + k_2 c \rho \\ \dot{w} &= \rho \gamma [1 - w + [\alpha c \gamma]/[1 + c]]/[1 + w^2].\end{aligned}$$

In the following, we use normalized variables for  $c$  and  $\rho$  to facilitate the interpretation of the simulations. The normalized value is arbitrary. For instance, we choose the homeostatic fibroblast concentration  $\rho_0 = 0.5$  because it allows a better visualization of the dynamical response with respect to other variables. Nonetheless, this choice does not have an impact on the overall system response. For the chemical and biological systems, we choose the values listed in Table 13.1. The proposed constitutive equations do not overlap entirely with any particular model found in the literature and thus some values have been estimated to provide a good qualitative match to the references cited. Further, it might be more appropriate to consider ranges instead of fixed values since even across different computational approaches the choice of of parameters has not been unique, for this reason we perform numerical sensitivity experiments. Initially, the wound is defined by a peak inflammatory signal,  $c|_{t=0} = 1$ , a negligible fibroblast concentration,  $\rho|_{t=0} = 0$ , and a clot without collagen,  $w|_{t=0} = 0$ .

Figure 13.3 illustrates the temporal evolution of the chemical, biological, and mechanical variables, the inflammatory signal  $c$ , the fibroblast density  $\rho$ , and the collagen content

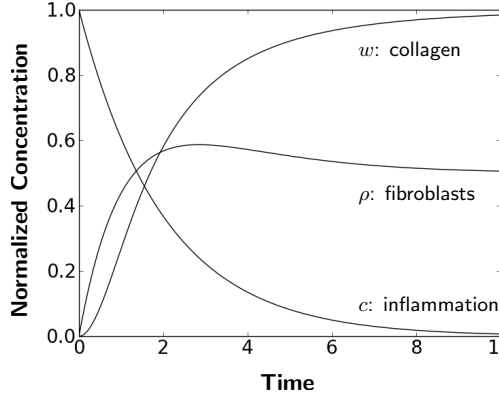


Figure 13.3: Wound healing across the temporal scales. Temporal evolution of the the inflammatory signal  $c$ , the fibroblast density  $\rho$ , and the collagen content  $w$ .

$w$ . During the initial phase of wound healing, the inflammatory signal  $c$  is significantly elevated. Inflammation induces an increase in the mitotic rate of fibroblasts, which gradually increase in density. At the same time, the chemoattractant decays exponentially towards its baseline value of  $c = 0$ . The fibroblast density  $\rho$  initially overshoots, but then gradually returns to its homeostatic equilibrium value of  $\rho = 0.5$ . From a structural point of view, the collagen content  $w$  is the primary indicator of the healing progress. It increases gradually as the wound recovers. Once the collagen content stabilizes at its physiological value of  $w_0 = 1$ , the wound is assumed to have healed. Overall, the dynamics of the chemical, biological, and mechanical variables shown in Figure 13.3 are in qualitative and quantitative agreement with the characteristic features of wound healing.

Next, we perform a systematic sensitivity analysis to explore the impact of the physiological collagen deposition rate  $\gamma$ , the inflammation-induced collagen synthesis rate  $\alpha$ , and the inflammation-induced fibroblast mitosis  $k_2$  on the healing process. In all three cases, we monitor the temporal evolution of the collagen content  $w$  as the primary mechanical indicator of the healing progress.

Figure 13.4 illustrates the sensitivity of the collagen content for varying collagen deposition rates  $\gamma$ . Mathematically, the collagen deposition rate  $\gamma$  directly scales the effects of the fibroblast density  $\rho$  on the collagen content  $w$ . Biologically, a stronger response by fibroblasts drives an overproduction of collagen, which can be associated with hypertrophic scarring. Figure 13.5 illustrates the sensitivity of the collagen content for varying inflammation-induced collagen synthesis rates  $\alpha$ . Mathematically, the collagen synthesis rate  $\alpha$  directly

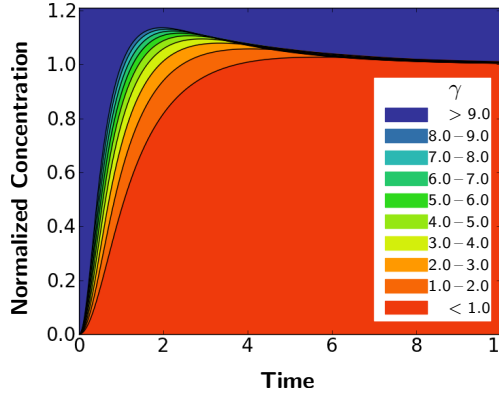


Figure 13.4: Wound healing across the temporal scales. Sensitivity of collagen content  $w$  with respect to collagen deposition rate  $\gamma$ . Increasing the collagen deposition rate induces an overproduction of collagen associated with hypertrophic scarring.

scales the effects of the inflammatory signal  $c$  on the collagen content  $w$ . Increasing the influence of the inflammatory signal through  $\alpha$  has a similar effect as increasing the collagen deposition rate  $\gamma$ . However, increasing  $\alpha$  has a much longer lasting effect, and the collagen content returns to its baseline value much slower. Biologically, a larger influence of the inflammatory signal drives an overproduction of collagen, which can be associated with hypertrophic scarring.

Figure 13.6 illustrates the sensitivity of the collagen content for varying inflammation-induced mitotic rates  $k_2$ . Mathematically, the mitotic rate  $k_2$  increases the fibroblast concentration  $\rho$ , which, in turn, increases the collagen content  $w$ . Although  $k_2$  does not directly impact the collagen content  $w$ , its variation displays some secondary effects. However, these secondary effects are less pronounced and the collagen concentration remains within normal levels.

Our model reproduces the trends of healing systems that have been previously reported in the literature. In regards to the inflammatory signal, PDGF was considered in [281] to be responsible for regulating the response of fibroblasts. They show a fast decay illustrated in Fig. 13.7-left. TGF-beta has also been considered as one of the primary regulators of collagen deposition by fibroblast [86]. The TGF-beta curve in Fig. 13.7 decays at a much slower rate than PDGF. Another pro-inflammatory cytokine is TNF considered in [259], which shows an intermediate decay speed in Fig. 13.7-left. Finally, in the experimental results provided in [324], a cell type, macrophages, is regarded as an indicator for inflammation

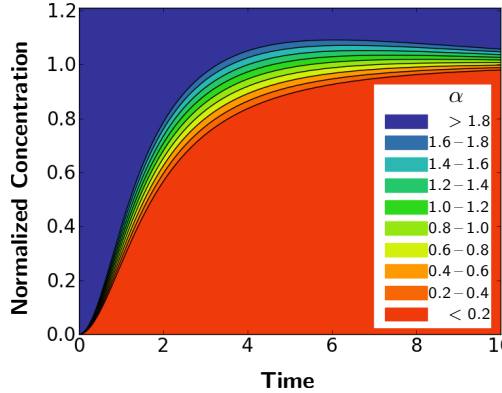


Figure 13.5: Wound healing across the temporal scales. Sensitivity of collagen content  $w$  with respect to inflammation-induced collagen synthesis rate  $\alpha$ . Increasing the collagen synthesis rate induces an overproduction of collagen associated with hypertrophic scarring.

which decreases rapidly within 7 days after injury. Fig. 13.7-left captures the variability in the inflammation signal data presented in the literature and how our simple model problem exhibits a response within the range of previous observations.

With regards to the fibroblast concentration, in [86], fibroblasts slowly populate the wound region in a monotonic fashion. A sharp contrast is observed with respect to the curve reported in [259], where an overshoot in the cell population occurs days after the peak of inflammation. Eq. (13.4) of our model lies between these two curves in Fig.13.7-middle.

The collagen content reported in [86] and [259] follow a very similar profile and we are also able to capture the same trend based on Eq. (13.7). Collagen monotonically increases during the first ten days of healing as depicted in 13.7-right. This set of homogeneous examples provides confidence that our constitutive equations are indeed able to capture a range of realistic scenarios in wound healing. Nonetheless, the calibration of the model with realistic clinical data remains the next important step.

### 13.5.2 Wound Healing Across the Spatio-Temporal Scales

Now, we explore the spatio-temporal evolution of the chemical, biological, and mechanical variables in a heterogeneous three-dimensional setting. In contrast to the first problem, this now allows us to probe the constitutive equations for the chemical, biological, and mechanical flux terms  $\mathbf{q}^c$ ,  $\mathbf{q}^\rho$  and  $\boldsymbol{\sigma}$  defined in equations (13.14), (13.17), and (13.22) and

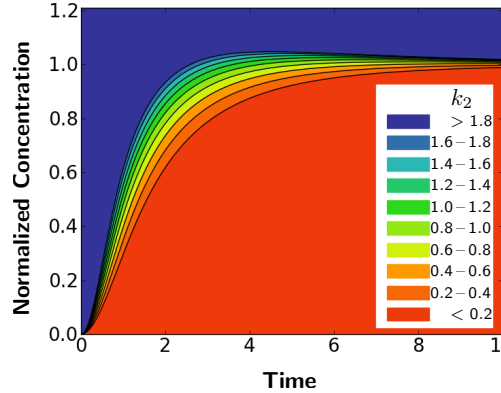


Figure 13.6: Wound healing across the temporal scales. Sensitivity of collagen content  $w$  with respect to inflammation-induced mitotic rate  $k_2$ . Increasing the mitotic rate induces an overproduction of collagen associated with hypertrophic scarring.

perform sensitivity analyses with respect to the associated material parameters. We idealize the tissue sample as a rectangular prism and model the wound as an elliptical enclosure at its center [408]. The tissue has dimensions of  $4 \times 4 \times 1\text{cm}^3$ . Since the problem has two planes of symmetry, we discretize a quarter of the system using trilinear brick elements. The boundary conditions are the same for all examples of this subsection. For the chemical and biological problems, we assume homogeneous Neumann boundary conditions. This choice of boundary conditions implies that the particular problem is local enough and the size of the domain is adequate such that cells or chemicals can be realistically assumed to not cross the boundary within the time period of interest. For the mechanics problem, we impose a constant pre-strain of 10% along the  $x$ -direction by solving a mechanical equilibrium problem with the appropriate displacement boundary condition before the onset of injury.. This boundary condition resembles the pre-stretched state of skin *in vivo*. In addition, we apply symmetric boundary conditions to reflect the two planes of symmetry.

In addition to the material parameters for the source terms described in detail for the homogeneous problem in Section 13.5.1, we now need to specify the material parameters for the flux terms. The diffusion coefficients for the chemical and biological fields are listed in Table 13.1. For the mechanical problem, the Lamé constants are  $\lambda = 0.385 \text{ MPa}$  and  $\mu = 0.254 \text{ MPa}$ , and the Holzapfel parameters are  $c_1 = 0.15 \text{ MPa}$ ,  $c_2 = 0.0418$ , and  $\kappa = 0.05$  as calibrated from experiments in pig skin [183]. The collagen fiber orientation is  $\mathbf{n} = [1, 0, 0]^t$ . The initial conditions for the chemical, biological, and mechanical fields are heterogeneous,

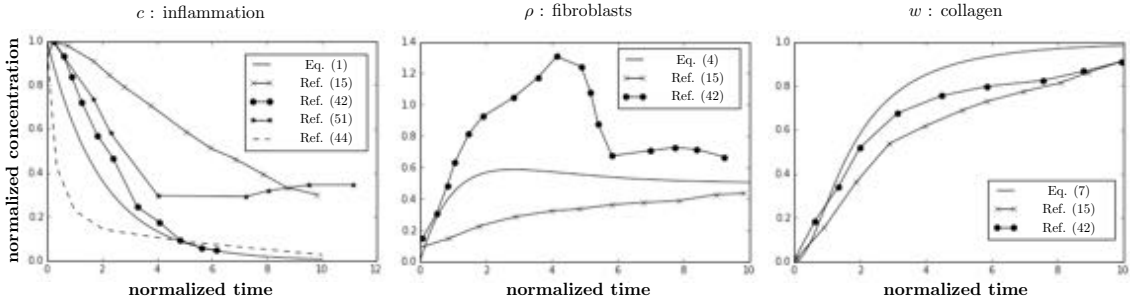


Figure 13.7: Comparison of simulations based on local versions of equations (13.1), (13.4), and (13.7), with respect to existing models and experimental data reported in the literature. There exists significant variation across models. Our simple equations are able to capture the overall trends: An exponential decay in the inflammatory signal, a rapid increase in the cell population with a possible overshoot, and a monotonic increase in the collagen concentration that approaches the normalized homeostatic concentration within a few days after the peak inflammatory signal takes place.

with similar values as in Section 13.5.1 inside an elliptical wounded region and baseline values outside. We choose the center of the wound at  $[x_c, y_c, z_c]$ , and parameterize the injured as  $[x - x_c]^2/r_x^2 + [y - y_c]^2/r_y^2 < 1$  and  $z - z_c < 0.5$ . The injured region initially has an elevated inflammatory signal,  $c = 1$ , and is completely depleted of fibroblasts,  $\rho = 0$ , and collagen,  $w = 0$ . The healthy tissue outside the wound is free of inflammation,  $c = 0$ , and has a baseline fibroblasts density,  $\rho = \rho_0 = 0.5$ , and collagen content,  $w = 1$ .

Figure 13.8 shows the spatio-temporal and tempo-spatial evolution of the inflammatory signal  $c$ , the fibroblast density  $\rho$ , the Green Lagrange strain  $E_{xx}$ , and the collagen content  $w$  for a circular wound with a radius of 1 cm. The overall behavior is similar to that of the homogeneous wound depicted in Figure 13.3: An elevated inflammatory signal  $c$  increases the fibroblast density  $\rho$ . This increases the collagen content  $w$  and the tissue stiffness, which gradually reduces the strain  $E_{xx}$ , see Figure 13.8a. The differences between the individual curves in each graph reflect the regional variation across the wound. These differences disappear over time as the injured region gradually recovers its healthy state, see Figure 13.8b. The most distinguishing feature of our model is the inclusion of common mechanical features like deformation, stress, and strain. The third row of Figure 13.8a displays the spatio-temporal evolution of the Green Lagrange strain  $E_{xx}$  in the direction of the collagen fibers. The initial pre-strain of 10%, applied at the edges of the wound, generates an initially

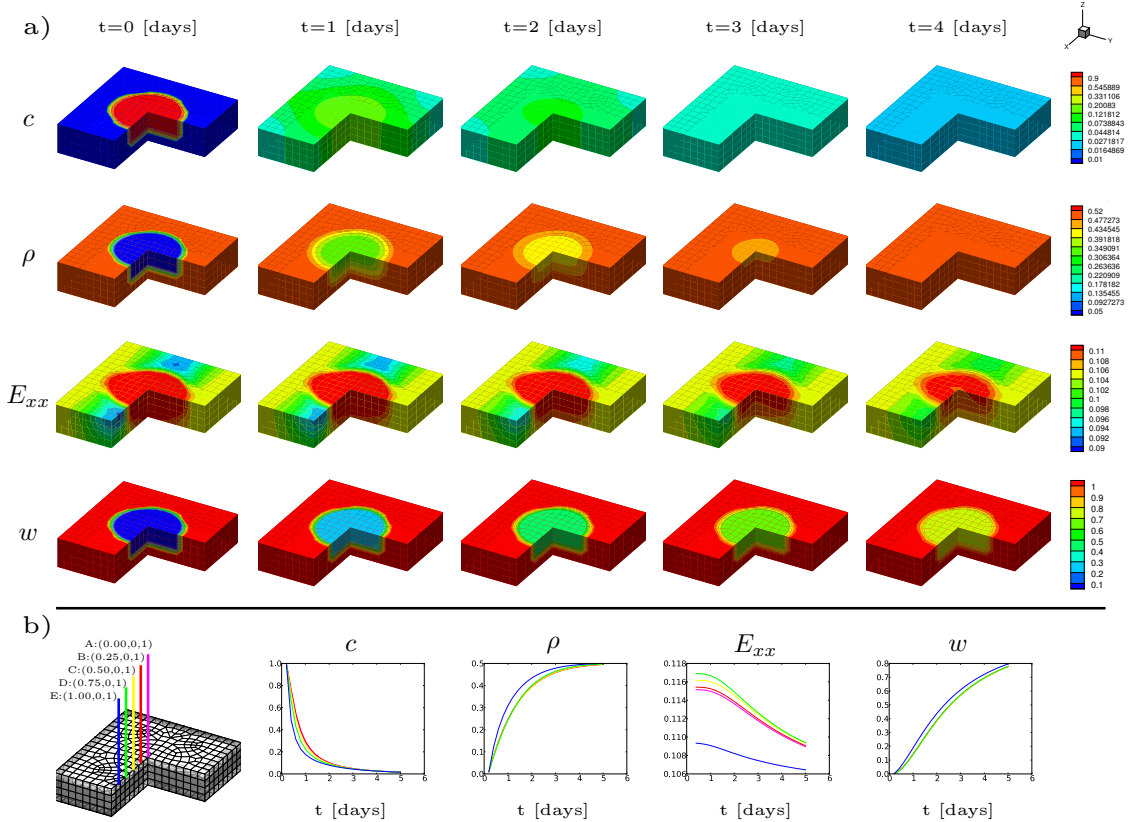


Figure 13.8: Wound healing across the spatio-temporal scales for a circular wound. a) Spatio-temporal evolution and b) Tempo-spatial evolution of inflammatory signal  $c$ , fibroblast density  $\rho$ , Green Lagrange strain  $E_{xx}$  in collagen fibers direction, and collagen content  $w$ . An elevated inflammatory signal  $c$  increases the fibroblast density  $\rho$ . This increases the collagen content  $w$  and the tissue stiffness, which gradually reduces the strain  $E_{xx}$ .

heterogeneous strain profile. The strain distribution results from the heterogeneous tissue stiffness introduced through the regionally varying collagen content, with no collagen in the wounded region,  $w = 0$ , and baseline values around the wound,  $w = 1$ . As healing progresses, the distribution of the strains becomes more and more homogenous as the collagen content in the wound gradually returns to its baseline value: The tissue gradually recovers its healthy material properties. Here we consider the pre-strain as existing before injury, relying on evidence that tissues *in vivo* have some amount of residual deformation [54], however, including the active stress of fibroblasts would create an additional heterogeneity in the strain profiles as healing progresses. Moreover, we have assumed that the collagen fibers retain their orientation throughout the process. For this particular case, we believe that such simplification is reasonable since the applied load coincides with the original fiber orientation.

Next, we perform a systematic sensitivity analysis to explore the impact of the wound size and shape on the healing process. First, we vary the size of the injured region while maintaining its circular shape. We study a larger wound with a radius of 1.5 cm and a smaller wound with a radius of 0.5 cm. Then, we vary the wound shape by changing the degree of ellipticity. We study a moderately elliptic wound with an aspect ratio of 3 : 2 and an elongated wound with an aspect ratio of 3 : 1.

Figure 13.9 displays the spatio-temporal and tempo-spatial evolution of the inflammatory signal  $c$ , the fibroblast density  $\rho$ , the Green Lagrange strain  $E_{xx}$ , and the collagen content  $w$  for a large and small circular wound with a radii of 1.5 cm and 0.5 cm. The large wound displays larger strain variations  $E_{xx}$  than the small wound indicating that it takes longer to heal, see Figure 13.9a. The elevated inflammatory signal  $c$  in the large wound takes longer to decay than in the small wound, which confirms this trend, see Figure 13.9b. For the chosen set of material parameters, the time course of healing is only marginally affected by the wound size. Mathematically, this implies that the evolution equations are dominated by local source rather than global flux terms, and diffusion plays a minor role. Biologically, this implies that, for small wounds on the order of one centimeter, the wound size does not affect the recovery time of the wound as a whole.

Figure 13.10 displays the spatio-temporal and tempo-spatial evolution of the inflammatory signal  $c$ , the fibroblast density  $\rho$ , the Green Lagrange strain  $E_{xx}$ , and the collagen content  $w$  for a moderately elliptical and elongated wound with aspect ratios of 3 : 2 and 3 : 1. The moderately elliptical wound displays larger strain variations  $E_{xx}$  than the elongated wound

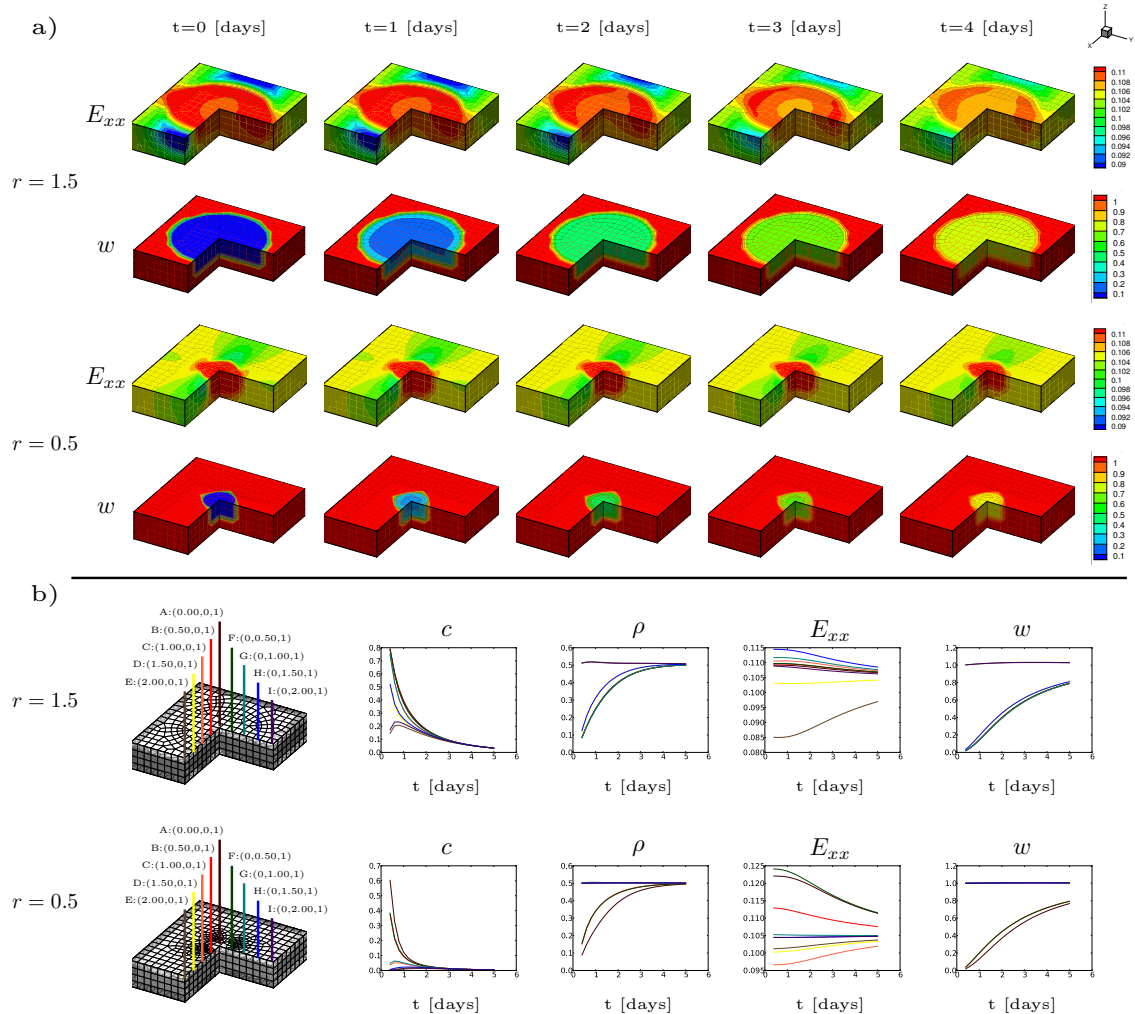


Figure 13.9: Wound healing across the spatio-temporal scales for varying wound sizes with radii of  $r = 1.5$  and  $r = 0.5$ . a) Spatio-temporal evolution and b) Tempo-spatial evolution of inflammatory signal  $c$ , fibroblast density  $\rho$ , Green Lagrange strain  $E_{xx}$  in collagen fibers direction, and collagen content  $w$ . The large wound displays larger strain variations  $E_{xx}$  than the small wound indicating that it takes longer to heal. The elevated inflammatory signal  $c$  in the large wound takes longer to decay than in the small wound, which confirms this trend.

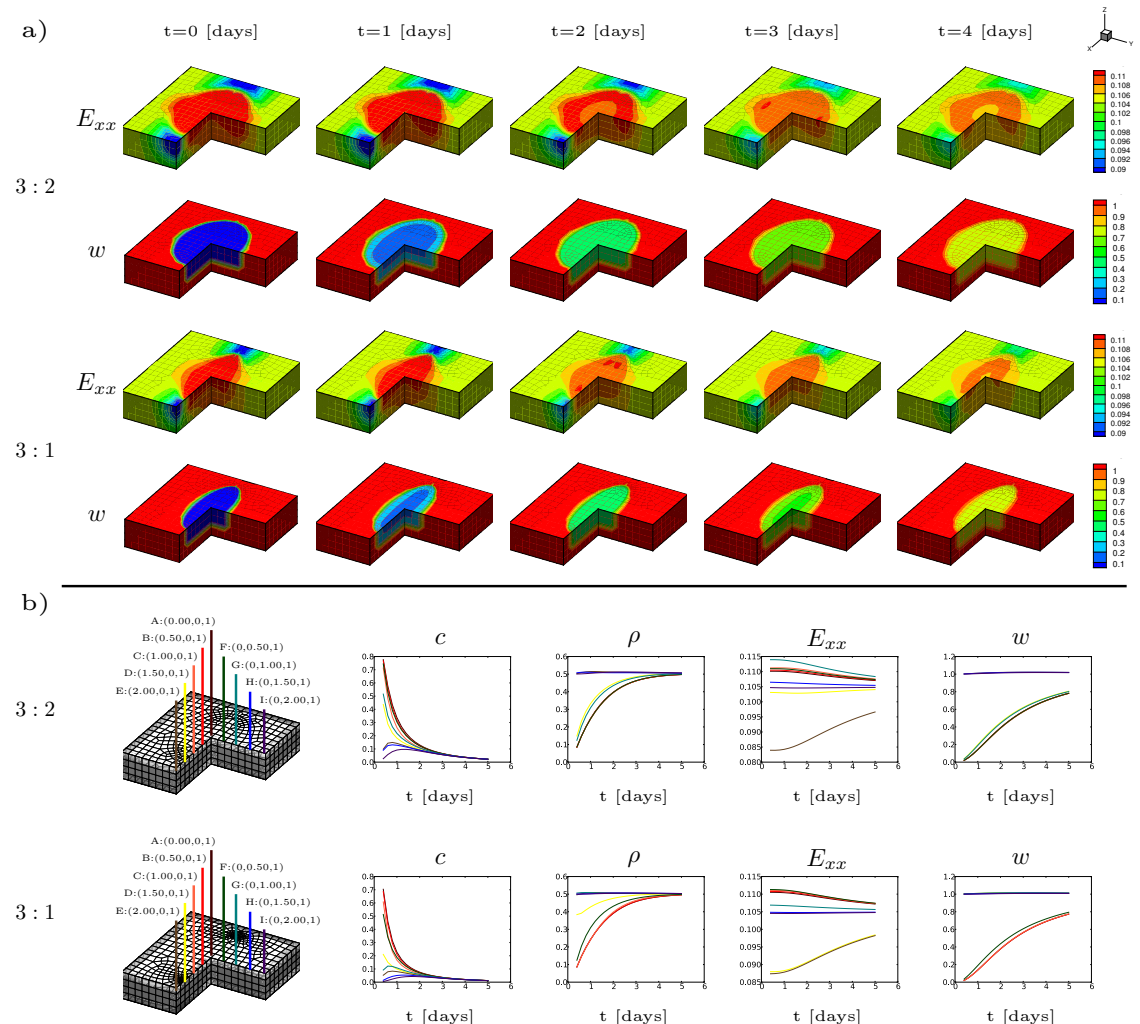


Figure 13.10: Wound healing across the spatio-temporal scales for varying wound ellipticities with aspect ratios of 3 : 2 and 3 : 1. a) Spatio-temporal evolution and b) Tempo-spatial evolution of inflammatory signal  $c$  fibroblast density  $\rho$ , Green Lagrange strain  $E_{xx}$  in collagen fibers direction, and collagen content  $w$ . The moderately elliptical wound displays larger strain variations  $E_{xx}$  than the elongated wound indicating that it takes longer to heal. The elevated inflammatory signal  $c$  in the moderately elliptical wound takes longer to decay than in the elongated wound, which confirms this trend.

indicating that it takes longer to heal, see Figure 13.10a. The elevated inflammatory signal  $c$  in the moderately elliptical wound takes longer to decay than in the elongated wound, which confirms this trend, see Figure 13.10b. For the chosen set of material parameters, the time course of the healing process is only marginally affected by the wound shape. Similar to the previous example of varying wound sizes, in which the evolution equations are dominated by local source rather than global flux terms, and diffusion plays a minor role. Unfortunately, calibration of our model in the three dimensional setting is hindered due to the lack of experimental data on spatial gradients of fibroblast and chemical signals over the wound site. Measurements of wound area over time abound [324]. However, evolution of wound area is a combination of re-epithelialization and contraction which we do not consider in our model problem. Nevertheless, in addition to area measurements, recent experiments have highlighted the direct correlation between strains beyond the physiological regime and the degree of fibrosis [146]. With the proposed framework we are able to capture large spatial variations of strains and a logical next step will be to calibrate the collagen deposition constitutive law based on these experimental observations.

## 13.6 Discussion

Hypertrophic scarring is a cutaneous condition characterized by the excessive deposition of collagen, which gives rise to red, thick, stiff, and sometimes painful scar tissue [69]. In physiological wound healing, the production of new collagen and breakdown of old collagen balance one another and the overall collagen content remains constant. In pathological wound healing, however, collagen production dominates collagen breakdown and the overall amount of collagen increases. Fortunately, hypertrophic scars do not extend beyond the initial wounded region, but they may continue to grow for weeks or even months [145]. Mechanics has long been neglected to play a crucial role in scar formation [4]. It is well-known that an increased collagen deposition increases tissue stiffness, and might result in impaired motion when the wound is located close to a joint [388]. In regenerative medicine, surgeons now manipulate the mechanical microenvironment to their advantage: They minimize scarring through negative pressure wound therapy using vacuum-assisted closure devices [4] or through controlled stress shielding using pre-strained polymeric patches [146]. A computational model could help identify optimal pressure or pre-strain ranges to accelerate wound healing and reduce scarring. Here we have established a novel computational framework for

the chemo-bio-mechanics of wound healing to understand the fundamental mechanisms of scar formation. Our novel approach towards simulating wound healing is unconditionally stable, geometrically flexible, and conceptually modular.

Unconditional stability is guaranteed by the use of an implicit backward Euler scheme to discretize the evolution equations in time, both globally and locally. Using implicit time integration schemes is algorithmically robust and allows for larger time steps than explicit schemes. For the solution of the resulting nonlinear system of equations, we suggest an incremental iterative Newton-Raphson scheme, again both globally and locally. While the generic equations of wound healing can be bi-directionally coupled, here we have focused on a unidirectionally coupled model problem. For this specific case, we could have used a sequential solution algorithm. However, we are currently in the process of introducing bi-directional coupling. To advance all fields simultaneously in time, it proves convenient to adopt a Newton-Raphson based solution strategy. The conceptual advantage of Newton-Raphson schemes is that they are not only computationally efficient, but they can easily be supplemented by ad hoc time adaptive schemes, which simply adjust the times step based on the number of required Newton iterations.

Geometrical flexibility is a crucial novelty of the proposed model. Existing models have mainly been restricted to zero-, one-, and two-dimensional approximations [334]. Our general three-dimensional setting allows us to move forward in the spatial complexity. It is a pivotal step towards the simulation of healing in patient specific geometries [46]. We achieve this flexibility by using a finite element discretization [178]. As opposed to conventional finite volume or finite difference techniques, finite elements, by design, allow for arbitrary geometries [418]. For the first time, we have simulated the healing process in an arbitrary three-dimensional domain. For the sake of illustration, we have used idealized circular and elliptical wound geometries [408]. The extension to more realistic geometries is, of course, straightforward and part of our current work.

Conceptual modularity allows us to adjust our approach to other existing models [86] or to expand on the particular model proposed here [358, 410]. We have systematically divided the problem of wound healing into three building blocks: chemical, biological, and mechanical [53]. The chemical fields obey a system of partial differential equations common to all reaction-diffusion systems. The biological fields follow a more complex system of partial differential equations that can be specialized for the individual cell populations involved in

the healing process. The mechanical fields fall into two categories, global and local, characterized through systems of partial and ordinary differential equations well-established for the continuum mechanics of soft biological tissues. We have highlighted the constitutive coupling between these three different fields for general chemo-bio-mechanical problems. Within this generic setup, we have specified particular constitutive equations to model specific aspects of wound healing [338]. For conceptual simplicity, here we have focused only on studying the impact of biology on mechanics through the collagen deposition by fibroblast. In the future, we will also include active mechanical effects such as tissue contraction. We will also include the impact of mechanics on biology. This will allow us to simulate effects of mechanotaxis through an additional flux term for mechanically guided diffusion and of mechanotransduction through an additional source term for mechanically induced mitosis and apoptosis [403,419]. Along these lines, we have considered tissues to deform quasi statically, we could also include the effect of passive convection through deformation-dependent chemical and biological flux terms [178,390]. In contrast to the several simplifications, our elemental model problem depends on only a few parameters and thus allows for systematic parametric experiments. By identifying the critical players, it is our goal to sophisticate the constitutive equations incrementally to investigate the pathways of pathological scarring. We have seen that the collagen deposition rate can have an impact well beyond the transient phase of the healing process. Concomitantly, hypertrophic scars are characterized by increased collagen concentrations that also prevail for months after injury. We believe that refining the constitutive equation for collagen deposition, transitioning from a more phenomenological equation to one that is biologically consistent by incorporating the influence of growth factors and mechanical cues is a logical next step to model hypertrophic scars. In addition, our approach thus far not only explores relevant healing scenarios for a particular model, but effectively creates a generic framework that can be easily expanded to incorporate other features such as the impact of mechanical cues on cell mitosis or apoptosis. As such, it is not only applicable to explore chemo-bio-mechanical interaction during wound healing in skin, but also in other inflammation-based systems, for example in healing infarcts in cardiac muscle [323]. Ultimately, a better understanding of the healing mechanisms in living systems can inspire the design of novel, self-healing engineering systems [252]. In addition to these algorithmic aspects, our model accounts for a state-of-the-art mechanical characterization of skin [228] within a continuum mechanics approach [183]. Recently

there has been significant development in the theory of the mechanics of living soft collagenous tissues [51, 161, 327]. Unfortunately, these advances have been almost entirely disconnected from recent trends in systems biology, which have been confined to either rigid geometries or viscoelastic fluids [410]. These simplifications impose great limitations towards understanding the role of mechanical cues during wound healing. A rigorous, accurate mechanical characterization is a fundamental knowledge gap in existing models for wound healing. Here we characterize skin using a hyperelastic strain energy function parametrized in terms of a set of microstructure variables such as collagen orientation [207] and collagen content [326]. The importance of time-varying material properties has recently been identified as a critical aspect in wound healing [33]. By allowing our microstructural variables to evolve in time, we establish clear relations between the action of the different cell populations and tissue remodeling [251]. Recent studies also provide evidence that pre-strain and tissue tension have a significant effect on the healing characteristics of circular and elliptical wounds [54, 408]. Our model allows us to impose physiological boundary conditions such as pre-strain [317] and predict the spatio-temporal evolution of tissue tension across arbitrarily shaped wounds throughout the healing process.

In conclusion, the proposed framework introduces a new generation of wound healing models that may provide fundamental insight into the role of mechanics in scar formation. A unified monolithic finite element treatment of the underlying chemical, biological, and mechanical fields is a first step towards the smooth incorporation of realistic environmental conditions and personalized individual geometries. Our model has the potential to significantly improve effective wound management and optimize treatment options on a patient-specific basis.

# Bibliography

- [1] S. Aarabi, K.A. Bhatt, Y. Shi, et al. Mechanical load initiates hypertrophic scar formation through decreased cellular apoptosis. *FASEB J.* 2007;21:325061.
- [2] Ackerman JM, Nocera CC, and Bargh JA. Incidental haptic sensations influence social judgments and decisions. *Science*. 2010; 328(5986): 1712-1715.
- [3] Agache PG, Monneur C, Leveque JL, DeRigal J. Mechanical properties and Young's modulus of human skin in vivo. *Arch Dermatol Res*. 1980;269:221-232.
- [4] R. Agha, R. Ogawa, G. Pietramaggiori, D.P. Orgill. A review of the role of mechanical forces in cutaneous wound healing. *J Surg Res*. 2011; 171: 700-708.
- [5] Alford PW, Humphrey JD, Taber LA. Growth and remodeling in a thick-walled artery model: effects of spatial variations in wall constituents. *Biomech Model Mechanobiol*. 2008;7:245-262.
- [6] Ambrosi D, Mollica F. On the mechanics of a growing tumor. *Int J Eng Sci*. 2002;40:1297-1316.
- [7] Ambrosi D, Preziosi L, Vitale G. The insight of mixtures theory for growth and remodeling. *ZAMP*. 2010;61:177-191.
- [8] Ambrosi D, Ateshian GA, Arruda EM, Cowin SC, Dumais J, Goriely A, Holzapfel GA, Humphrey JD, Kemkemer R, Kuhl E, Olberding JE, Taber LA, Garikipati K. Perspectives on biological growth and remodeling. *J Mech Phys Solids*. 2011;59:863-883.
- [9] Amini R, Eckert CE, Koomalsingh K, McGarvey J, Minakawa M, Gorman JH, Gorman RC, Sacks MS. On the in vivo deformation of the mitral valve anterior leaflet: Effects of annular geometry and referential configuration. *Ann Biomed Eng*. 2012;40:1455-1467.

- [10] Anderson A. A mathematical model for capillary network formation in the absence of endothelial cell proliferation. *Appl Math Lett.* 1998;11:109-114.
- [11] Annaidh AN, Bruyere K, Destrade M, Gilchrist MD, and Ottenio M. Characterization of the anisotropic mechanical properties of excised human skin. *J Mech Behav Biomed Mat.* 2012; 5(1), 139-148.
- [12] Annaidh AN, Bruyère K, Destrade M, Gilchrist MD, Maurini C, Otténio M and Saccomandi G. Automated estimation of collagen fibre dispersion in the dermis and its contribution to the anisotropic behaviour of skin. *Ann Biomed Eng.* 2012; 40(8): 1666-1678.
- [13] Argenta LC, Watanabe MJ, Grabb WC. The use of tissue expansion in head and neck reconstruction. *Annals Plast Surg.* 1983;11:31-37.
- [14] Armstrong NJ, Painter KJ, and Sherratt JA. A continuum approach to modelling cell-cell adhesion. *J Theor Biol.* 2006; 243(1), 98-113.
- [15] Arneja JS, Gosain AK. Giant congenital melanocytic nevi of the trunk and an algorithm for treatment. *J Craniofac Surg.* 2005;16:886-893.
- [16] Arneja JS, Gosain AK. Giant congenital melanocytic nevi. *Plast Reconstr Surg.* 2007;120:26e-40e.
- [17] Arneja JS, Gosain AK. Giant congenital melanocytic nevi. *Plast Reconstr Surg.* 2009;124:1e-13e.
- [18] Astanin S, Preziosi L. Mathematical modelling of the Warburg effect in tumour cords. *J Theor Bio.* 2009;258:578-590.
- [19] Arruda EM, Boyce MC. A three-dimensional constitutive model for the large stretch behavior of rubber elastic materials. *J Mech Phys Solids.* 1993;41:389-412.
- [20] Ateshian GA. On the theory of reactive mixtures for modeling biological growth. *Biomech Model Mechanobiol.* 2007; 6(6), 423-445.
- [21] Austad ED, Pasyk KA, McClatchey KD, Cheery GW. Histomorphologic evaluation of guinea pig skin and soft tissue after controlled tissue expansion. *Plast Reconstr Surg.* 1982;70:704-710.

- [22] Austad ED, Thomas SB, Pasyk KA. Tissue expansion: Divided or loan? *Plast Reconstr Surg.* 1982;78:63-67.
- [23] Autodesk 123D Catch. <http://www.123dapp.com/catch> 2014 Autodesk, Inc.
- [24] Badir S, Bajka M, Mazza E. A novel procedure for the mechanical characterization of the uterine cervix during pregnancy. *J Mech Beh Biomed Mat.* 2013;27:143-153.
- [25] Baker SR. Fundamentals of expanded tissue. *Head & Neck.* 1991;13:327-333.
- [26] Bao G, Bazilevs Y, Chung JH, Decuzzi P, Espinosa HD, Ferrari M, Gao H, Hossain SS, Hughes TJR, Kamm RD, Liu WK, Marsden A, Schrefler B USNCTAM perspectives on mechanics in medicine. *J R Soc Interface* 2014; 11:20140301.
- [27] Barone FE, Perry L, Keller T, Maxwell GP. The biomechanical and histopathologic effect of surface texturing with silicone and polyurethane in tissue implantation and expansion. *Plast Reconstr Surg.* 1992;90:77-86.
- [28] Bartell TH and Mustoe TA. Animal models of human tissue expansion. *Plast Reconstr Surg.* 1989;83:681-686.
- [29] A. Bayat, D.A. McGrouther, M.W. Ferguson. Skin scarring. *BMJ.* 2003; 326: 8892.
- [30] Bazilevs Y, Hsu MC, and Scott MA. Isogeometric fluid-structure interaction analysis with emphasis on non-matching discretizations, and with application to wind turbines. *Comput Methods Appl Mech Eng.* 2012; 249: 28-41.
- [31] Beauchenne JG, Chambers MM, Peterson AE, Scott PG. Biochemical, biomechanical, and physical changes in the skin in an experimental animal model of therapeutic tissue expansion. *J Surg Res.* 1989;47:507-514.
- [32] Ben Amar M, Goriely A. Growth and instability in elastic tissues. *J Mech Phys Solids.* 2005;53:2284-2319.
- [33] M. Ben Amar, M. Wu. Re-epithelialization: advancing epithelium frontier during wound healing. *Royal Soc Interface.* 2013; 11(93):20131038.
- [34] Benson DJ, Bazilevs Y, Hsu MC and Hughes TJR. Isogeometric shell analysis: The Reissner-Mindlin shell. *Comput Methods Appl Mech Eng.* 2011; 199: 276-289

- [35] Benson DJ, Bazilevs Y, Hsu MC and Hughes TJR. A large deformation, rotation-free, isogeometric shell. *Comput Methods Appl Mech Eng.* 2011; 200: 1367-1378.
- [36] Benson DJ, Hartmann S, Bazilevs Y, Hsu MC, and Hughes TJR. Blended isogeometric shells. *Comput Methods Appl Mech Eng.* 2013; 255: 133-146.
- [37] Bernardini F, Mittleman J, Rushmeiner H, Silva C, Taubin G. The ball-pivoting algorithm for surface reconstruction. *IEEE Trans Vis Comp Graph.* 1999;5:349-359.
- [38] Bertin C, Lopes DaCunha A, Nkengne A, Roure R, and Stamatias GN. Striae distensae are characterized by distinct microstructural features as measured by non-invasive methods in vivo. *Skin Res Technol.* 2014; 20(1): 81-86.
- [39] Bhandari PS Mathematical calculations in a spherical tissue expander. *Ann Plast Surg* 2009; 62(2):200-204.
- [40] Bickel B, Botsch M, Angst R, Matusik W, Otaduy M, Pfister H, and Gross M. Multi-scale capture of facial geometry and motion. *ACM Transactions on Graphics (TOG)*. 2007; 26(3), 33.
- [41] Bischoff JE, Arruda EM, Grosh K. Finite element modeling of human skin using an isotropic, nonlinear elastic constitutive model. *J Biomech.* 2000;33:645-652.
- [42] Bischoff JE, Arruda EM, Grosh K. A microstructurally based orthotropic hyperelastic constitutive law. *J Appl Mech.* 2002;69:570579.
- [43] Bischofs IB, and Schwarz US. Cell organization in soft media due to active mechanosensing. *Proc Nat Acad Sci.* 2003; 100(16), 9274-9279.
- [44] Böl M, Reese S. Micromechanical modelling of skeletal muscles based on the finite element method. *Comp Meth Biomed Eng.* 2008;11:489504.
- [45] Böl M, Ehret AE, Leichsenring K, Weichert C, Kruse R. On the anisotropy of skeletal muscle tissue under compression. *Acta Biomat.* 2014; doi:10.1016/j.actbio.2014.03.003.
- [46] M. Böl, M. Sturmat, C. Weichert, C. Kober. A new approach for the validation of skeletal muscle modeling using MRI data. *Comp Mech.* 2011; 47: 591-601.

- [47] Bowes LE, Jimenez MC, Hiester ED, Sacks MS, Brahmatewari J, Mertz PE and William H. Collagen fiber orientation as quantified by small angle light scattering in wounds treated with transforming growth factor-beta2 and its neutralizing antibody. *Wound Repair Regen.* 1999; 7: 179-186.
- [48] Brobmann GF, Huber J. Effects of different-shaped tissue expanders on transluminal pressure, oxygen tension, histopathologic changes, and skin expansion in pigs. *Plast Reconstr Surg.* 1985;76:731-736.
- [49] Brown IA. Scanning electron microscopy of human dermal fibrous tissue. *J Anatomy.* 1972; 113(Pt 2), 159.
- [50] B.C. Brown, S.P. McKenna, K. Siddhi, D.A. McGrouther, A. Bayat. The hidden cost of skin scars: quality of life after skin scarring. *J Plast Reconstr Aesthet Surg.* 2008; 61 10491058.
- [51] Buganza Tepole A, Ploch CJ, Wong J, Gosain AK, Kuhl E. Growing skin - A computational model for skin expansion in reconstructive surgery. *J Mech Phys Solids.* 2011; 59:2177-2190.
- [52] Buganza Tepole A, Gosain AK, Kuhl E. Stretching skin: The physiological limit and beyond. *Int J Nonlin Mech.* 2012;47:938-949
- [53] Buganza Tepole A, Kuhl E. Review: Systems-based approaches towards wound healing. *Pediatric Res.* 2013;73:553-563.
- [54] Buganza Tepole A, Gart M, Gosain AK, and Kuhl E. Characterization of living skin using multi view stereo and isogeometric analysis. *Acta Biomat.* 2014; 10: 4822-4831.
- [55] Buganza Tepole A, Gosain AK and Kuhl E. Computational modeling of skin: Using stress profiles as predictor for tissue necrosis in reconstructive surgery. *Comput Struct.* 2014; 143: 32-39.
- [56] Buganza Tepole A, Steinberg JP, Kuhl E, Gosain AK Application of finite element modeling to optimize flap design with tissue expansion. *Plast Reconstr Surg.* 2014; 134:785-792.

- [57] Buganza Tepole A, Kabaria H, Bletzinger KU, Kuhl E. Isogeometric Kirchhoff-Love shell formulations for biological membranes. *Comp Meth Appl Mech Eng.* 2015; doi:10.1016/j.cma.2015.05.006.
- [58] Buganza Tepole A, Kuhl E. Computational modeling of chemo-bio-mechanical coupling: A systems-biology approach towards wound healing. *Comp Meth Biomed Eng.* 2015; doi:10.1080/10255842.2014.980821
- [59] Buganza Tepole A, Gart M, Purnell CA, Gosain AK, Kuhl E. The incompatibility of living systems: Experimental characterization on expanded skin. *submitted for publication.* 2015.
- [60] Buganza Tepole A, Gart M, Purnell CA, Gosain AK, and Kuhl E. Multi-view stereo analysis reveals anisotropy of prestrain, deformation, and growth in living skin. *Biomech Mod Mechanobiol.* 2015. doi:10.1007/s10237-015-0650-8.
- [61] Byrne HM, Chaplain MAJ, Evans DL, Hopkinson I. Mathematical modelling of angiogenesis in wound healing: Comparison of theory and experiment. *J Theor Med* 2000;2:175-97.
- [62] Cai AQ, Landman KA, Hughes BD. Multi-scale modeling of a wound-healing cell migration assay. *J Theor Biol.* 2007;245(3):576-594.
- [63] Callaghan T, Khain E, Sander L. A stochastic model for wound healing. *J Stat Phys.* 2006;122:909-924.
- [64] Caspers PJ, Lucassen GW, and Puppels GJ. Combined in vivo confocal Raman spectroscopy and confocal microscopy of human skin. *Biophys L.* 2003; 85(1): 572-580.
- [65] Castilla EE, da Graca Dutra M, Orioli-Parreira IM. Epidemiology of congenital pigmented naevi: I. Incidence rates and relative frequencies. *Br J Dermatol.* 1981;104:307-315.
- [66] Cavicchi A, Gambarotta L, Massab R. Computational modeling of reconstructive surgery: The effects of the natural tension on skin wrinkling. *Finite Elements in Analysis and Design.* 2009;45:519-529.
- [67] Cerdá E. Mechanics of scars. *J Biomech.* 2005;38(8):1598-1603.

- [68] Cermelli P, and Gurtin ME. On the characterization of geometrically necessary dislocations in finite plasticity. *J Mech Phys Solids.* 2001; 49(7), 1539-1568.
- [69] J. Chambert, L. Zhao, D. Remache, E. Jacquet. Numerical analysis of keloid scar in the presternal area. *Comp Meth Biomech Biomed Eng.* 2012; 15: 23-24.
- [70] Chaplain M. Mathematical modelling of angiogenesis. *JNO.* 2000; 50:37-51.
- [71] Chary SR and Jain RK. Direct measurement of interstitial convection and diffusion of albumin in normal and neoplastic tissues by fluorescence photobleaching. *Proc. Natl. Acad. Sci. USA.* 1989; 86: 5385-5389.
- [72] Chaudhry HR. Optimal patterns for suturing wounds. *J Biomech.* 1998;31(7):653-662.
- [73] Chen L, Nguyen-Thanh N, Nguyen-Xuan H, Rabczuk T, Bordas SPA, Limbert G. Explicit finite deformation analysis of isogeometric membranes. *Comp Meth Appl Mech Eng.* 2014;277:104-130.
- [74] M. Chiquet, L. Gelman, R. Lutz, S. Maier. From mechanotransduction to extracellular matrix gene expression in fibroblasts. *Biochim Biophys Acta.* 2009; 1793: 911920.
- [75] Christley S, Lee B, Dai X, Nie Q. Integrative multicellular biological modeling: A case study of 3D epidermal development using GPU algorithms. *BMC Syst Biol* 2010;4:107.
- [76] Ciarletta P., Ben Amar M. Papillary networks in the dermal-epidermal junction of skin: a biomechanical model. *Mech Res Comm.* in press.
- [77] Cobbold C. Mathematical modelling of nitric oxide activity in wound healing can explain keloid and hypertrophic scarring. *J Theor Biol* 2000;204:257-288.
- [78] Collis N, Sharpe DT. Breast reconstruction by tissue expansion. A retrospective technical review of 197 two-stage delayed reconstructions following mastectomy for malignant breast disease in 189 patients. *Brit J Plast Surg.* 2000;53:37-41.
- [79] Colwell AS, Longaker MT. Fetal wound healing. *Front Biosci.* 2003;8:1240-1248.
- [80] Cooper L, Johnson C, Burslem F, and Martin P. Wound healing and inflammation genes revealed by array analysis of 'macrophageless' PU. 1 null mice. *Genome biology.* 2004; 6(1), R5.

- [81] Cortes DH, Lake SP, Kadlowec JA, Soslowsky LJ and Elliott DM. Characterizing the mechanical contribution of fiber angular distribution in connective tissue: comparison of two modeling approaches. *Biome Model Mechanobiol.* 2010;9:651-658.
- [82] Cottrell JA, Hughes TJ and Bazilevs Y. Isogeometric analysis: toward integration of CAD and FEA. *John Wiley & Sons.* 2009.
- [83] Cox B. A multi-scale, discrete-cell simulation of organogenesis: Application to the effects of strain stimulus on collective cell behavior during ameloblast migration. *J Theor Bio.* 2010;262:58-72.
- [84] Criscione JC, Sacks MS and Hunter WC. Experimentally tractable, pseudo-elastic constitutive law for biomembranes: II. Application. *J Biomech Eng.* 2003;125:100-105.
- [85] Croll TI, Gentz S, Mueller K, et al. Modelling oxygen diffusion and cell growth in a porous, vascularising scaffold for soft tissue engineering applications. *Chem Eng Sci.* 2005;60:4924-34.
- [86] B.D. Cumming, D.L.S. McElwain, Z. Upton. A mathematical model of wound healing and subsequent scarring. *J Royal Soc Interface.* 2009; 7: 19-34.
- [87] Cyganek B, Siebert JP. An introduction to 3D computer vision techniques and algorithms. *John Wiley & Sons Ltd, West Sussex.* 2009.
- [88] J.C. Dallon, J.A. Sherratt, P.K. Maini. Modeling the effects of transforming growth factor-beta on extracellular matrix alignment in dermal wound repair. *Wound Repair Regen.* 2001; 9: 278286.
- [89] Daly CH. Biomechanical properties of dermis. *J Invest Dermatol.* 1982; 79, 17-20.
- [90] Dandekar K., Raju B. and Srinivasan M. 3-D finite-element models of human and monkey fingertips to investigate the mechanics of tactile sense. *J Biomech Eng* 2003;125:682-691
- [91] Das D, Gosain AK. Burned facial skin. In: Hom DB, Hebda PA, Gosain AK, Friedman CD (Eds.) Essential Tissue Healing of the Face and Neck. *Hamilton: B.C. Decker, Inc.*, 2009;181-194.

- [92] De Filippo RE, Atala A. Stretch and growth: the molecular and physiologic influences of tissue expansion. *Plast Reconstr Surg.* 2002;109:2450-2462.
- [93] Delalleau et al. A nonlinear elastic behavior to identify the mechanical parameters of human skin in vivo *Skin Res Technol.* 2008;14(2):152-164.
- [94] Derderian CA, Bastidas N, Lerman OZ, Bhatt KA, Lin SE, Voss J, Holmes JW, Levine JP, and Gurtner GC. Mechanical strain alters gene expression in an in vitro model of hypertrophic scarring. *Ann Plast Surg.* 2005; 55(1): 69-75.
- [95] Dervaux J, Ciarletta P, Ben Amar M. Morphogenesis of thin hyperelastic plates: A constitutive theory of biological growth in the Föppl-von Karman limit. *J Mech Phys Solids.* 2009;57:458-471.
- [96] Dervaux J, Ben Amar M. Buckling consideration in constrained growth. *J Mech Phys Solids.* 2011;59:538-560.
- [97] Clore JN, Cohen IK, and Diegelmann RF. Quantitation of collagen types I and III during wound healing in rat skin. *Exp Biol Med.* 1979; 161(3): 337-340.
- [98] R.F. Diegelmann, M.C. Evans. Wound healing: an overview of acute, fibrotic and delayed healing. *Front Biosci.* 9 (2004) 283289.
- [99] Diridollou S, Patat F, Gens F, Vaillant L, Black D, Lagarde JM, Gall Y, and Berson M. In vivo model of the mechanical properties of the human skin under suction. *Skin Res Technol.* 2000; 6(4), 214-221.
- [100] Doillon CJ, Dunn MG, Bender E, and Silver FH. Collagen fiber formation in repair tissue: development of strength and toughness. *Collagen Relat Res.* 1985; 5(6), 481-492.
- [101] Drasdo D, Kree R, and McCaskill JS. Monte Carlo approach to tissue-cell populations. *Physical Review E* 1995; 52(6): 6635.
- [102] Dunlop JWC, Fischer FD, Gamsjäger E, Fratzl P. A theoretical model for tissue growth in confined geometries. *J Mech Phys Solids.* 2010;58:1073-1087.
- [103] Duits EHA, Molenaar J, van Rappard JHA. The modeling of skin expanders. *Plast Reconstr Surg.* 1989;83:362-367.

- [104] Ebersole GC, Anderson PM, and Powell HM. Epidermal differentiation governs engineered skin biomechanics. *J Biomech.* 2010; 43(16), 3183-3190.
- [105] Echter R, Oesterle B and Bischoff M. A hierachic family of isogeometric shell finite elements. *Comput Methods Appl Mech Eng.* 2013; 254: 170-180.
- [106] Epstein M, Maugin GA. Thermomechanics of volumetric growth in uniform bodies. *Int J Plast.* 2000;16:951-978.
- [107] Ermentrout GB, and Edelstein-Keshet L. Cellular automata approaches to biological modeling. *J Theor Biol.* 1993; 160(1): 97-133.
- [108] Famaey N and Vander Sloten J. Soft tissue modelling for applications in virtual surgery and surgical robotics. *Comput Methods Biomed Eng.* 2008; 11: 351-366.
- [109] Fang R and Sacks MS. Simulation of planar soft tissues using a structural constitutive model: Finite element implementation and validation. *J Biomech.* 2014; 47: 2043-2054.
- [110] Flynn C and McCormack B. Finite element modelling of forearm skin wrinkling *Skin Res Technol.* 2008;14(3) 261-269
- [111] Flynn C, Taberner A, Nielsen P. Mechanical characterisation of in vivo human skin using a 3D force-sensitive micro-robot and finite element analysis. *Biomech Model Mechanobiol.* 2011;10:27-38.
- [112] Flynn C, Taberner A and Nielsen P. Modeling the mechanical response of in vivo human skin under a rich set of deformations. *Ann Biomed Eng.* 2011; 39(7):1935-1946.
- [113] Flynn C, Taberner AJ, Nielsen PM, and Fels S. Simulating the three-dimensional deformation of in vivo facial skin. *J Mech Behav Biomed Mat.* 2013; 28, 484-494.
- [114] Fung, YC. What are the residual stresses doing in our blood vessels? *Ann Biomed Eng.* 1991; 19:237-249.
- [115] Fu S, Fan J, Liu L, Jiao H, Gan C, Tian J, Chen W, Yang Z, Yin Z . A uniaxial cell stretcher in vitro model simulating tissue expansion of plastic surgery. *J Craniofac Surg.* 2013; 24(4):1431-1435.

- [116] Fuchs E, and Raghavan, S. Getting under the skin of epidermal morphogenesis. *Nature Reviews Genetics.* 2002; 3(3): 199-209.
- [117] Furukawa Y, Ponce J. Accurate, dense, and robust multi view stereopsis. *IEEE T Pattern Anal.* 2010;32:1362-1376.
- [118] Gaffney EA, Pugh K, Maini PK, Arnold F. Investigating a simple model of cutaneous wound healing angiogenesis. *J Math Biol* 2002;45:337-74.
- [119] Galle J, Hoffmann M, and Aust G. From single cells to tissue architecture: a bottom-up approach to modelling the spatio-temporal organisation of complex multi-cellular systems. *J Math Biol.* 2009; 58(1-2): 261-283.
- [120] Ganghoffer JF. Mechanical modeling of growth considering domain variation. Part II: Volumetric and surface growth involving Eshelby tensors. *J Mech Phys Solids.* 2010;58:1434-1459.
- [121] Garcia-Aznar JM, Sanz-Herrera JA, and Moreo P. Cell-Material Communication: Mechanosensing Modelling for Design in Tissue Engineering. In Cellular and Biomolecular Mechanics and Mechanobiology. *Springer Berlin Heidelberg.* 2011; (pp. 451-462).
- [122] Garikipati K, Arruda EM, Grosh K, Narayanan H, Calve S. A continuum treatment of growth in biological tissue: The coupling of mass transport and mechanics. *J Mech Phys Solids.* 2004;1595-1625.
- [123] K. Garikipati, J.E. Olberding, H. Narayanan, E.M. Arruda, K. Grosh, S. Calve. Biological remodeling: Stationary energy, configurational change, internal variables and dissipation. *J Mech Phys Solids.* 2006; 54: 1493-1515.
- [124] Garikipati K. The kinematics of biological growth. *Appl Mech Rev.* 2009;62:030801.1-030801.7.
- [125] D.A. Garzon-Alvarado, R.P.C. Sandoval, R.C.V. Acosta. A mathematical model of medial collateral ligament repair: migration, fibroblast proliferation and collagen formation. *Comp Meth Biomech Biomed Eng.* 2012; 15: 571-583.
- [126] Gasser TC, Ogden RW and Holzapfel GA. Hyperelastic modelling of arterial layers with distributed collagen fibre orientations. *J R Soc interface.* 2006; 3(6): 15-35.

- [127] Geffeney SL, and Goodman MB. How we feel: ion channel partnerships that detect mechanical inputs and give rise to touch and pain perception. *Neuron*. 2012; 74(4), 609-619.
- [128] Genet M, Rausch MK, Lee LC, Choy S, Zhao X, Kassab GS, Kozerke S, Guccione JM, Kuhl E Heterogeneous growth-induced prestrain in the heart. *J Biomech* 2015; doi:10.1016/j.jbiomech.2015.03.012.
- [129] Gerhardt LC, Schmidt J, Sanz-Herrera JA, Baaijens FPT, Ansari T, Peters GWM, and Oomens CWJ. A novel method for visualising and quantifying through-plane skin layer deformations. *J Mech Behav Biomed Mat*. 2012; 14, 199-207.
- [130] Gerisch A, and Chaplain MAJ. Mathematical modelling of cancer cell invasion of tissue: local and non-local models and the effect of adhesion. *J Theor Biol*. 2008; 250(4), 684-704.
- [131] Gibson T, Kenedi RM, and Craik JE. The mobile micro-architecture of dermal collagen: A bio-engineering study. *Br J Surg*. 1965; 52(10): 764-770.
- [132] Gloeckner DG, Bihir KL, and Sacks MS. Effects of mechanical fatigue on the bending properties of the porcine bioprosthetic heart valve. *ASAIO Journal*. 1999; 45(1): 59-63.
- [133] Göktepe S, Abilez OJ, Parker KK, Kuhl E. A multiscale model for eccentric and concentric cardiac growth through sarcomerogenesis. *J Theor Bio*. 2010; 265:433-442.
- [134] Göktepe S, Abilez OJ, Kuhl E. A generic approach towards finite growth with examples of athlete's heart, cardiac dilation, and cardiac wall thickening. *J Mech Phys Solids*. 2010; 58:1661-1680.
- [135] Gordillo GM. Revisiting the essential role of oxygen in wound healing. *The Am J Surg*. 2003; 186:259-263.
- [136] Goriely A, Tabor M. Biomechanical models of hyphal growth in actinomycetes. *J Theor Bio*. 2003; 222:211218.
- [137] Goriely A, BenAmar M. Differential growth and instability in elastic shells. *Phys Rev Letters*. 2005; 94:198103.

- [138] Goriely A, BenAmar M. On the definition and modeling of incremental, cumulative, and continuous growth laws in morphoelasticity. *Biomech Mod Mechanobiol.* 2007;6:289296.
- [139] Gosain AK, Santoro TD, Larson DL, Gingrass RP. Giant congenital nevi: A 20-year experience and an algorithm for their management. *Plast Reconstr Surg.* 2001;108:622-636.
- [140] Gosain AK, Cortes W. Pediatric tissue expansion for forehead reconstruction: A 13-year review and an algorithm for its use. *Am Soc Plast Surg.* Baltimore, 2007; Abstract 13288.
- [141] Gosain AK, Zochowski CG, Cortes W. Refinements of tissue expansion for pediatric forehead reconstruction: A 13-year experience. *Plast Reconstr Surg.* 2009;124:1559-1570.
- [142] Gosain AK, Chepla KJ. Giant nevus sebaceus: Definition, surgical techniques, and rationale for treatment. *Plast Reconstr Surg.* 2012;130:296e-304e.
- [143] Gowrishankar TR, Stewart DA, Martin GT, and Weaver JC. (2004). Transport lattice models of heat transport in skin with spatially heterogeneous, temperature-dependent perfusion. *BMC.*2004; 3(1); 42.
- [144] Gruttmann F and Taylor RL. Theory and finite element formulation of rubberlike membrane shells using principal stretches. *Int J Numer Meth Eng.* 1992;35: 1111-1126.
- [145] G.C. Gurtner, S. Werner, Y. Barrandon, M.T. Longaker. Wound repair and regeneration. *Nature.*2008; 453 : 314321.
- [146] G.C. Gurtner, R.H. Dauskardt, V.W. Wong, K.A. Bhatt, K. Wu, I.N. Vial, K. Padois, J.M. Korman, M.T. Longaker. Improving cutaneous scar formation by controlling the mechanical environment. *Annals Surg.*2011; 254: 217225.
- [147] Gurtin, ME, and Struthers A. Multiphase thermomechanics with interfacial structure. *Arch Ration Mech Anal.* 1990;112: 97-160.
- [148] Guo Y, and Ruess M. Nitsche's method for a coupling of isogeometric thin shells and blended shell structures. *Comput Methods Appl Mech Eng.* 2015; 284: 881-905.

- [149] Halfter W, Liverani D, Vigny M, and Monard D. Deposition of extracellular matrix along the pathways of migrating fibroblasts. *Cell Tissue Res.* 1990; 262(3), 467-481.
- [150] Han Z, Vondriska TM, Yang L, MacLellan WR, Weiss JN, and Qu Z. Signal transduction network motifs and biological memory. *J Theor Biol.* 2007; 246(4), 755-761.
- [151] Harrigan TP. Analysis of the fixation of total hip femoral components using ADINA. *Comput Struct.* 1991;40:463-8
- [152] Haseganu EM and Steigmann DJ. Analysis of partly wrinkled membranes by the method of dynamic relaxation. *Comput Mech* 1994; 14(6): 596-614.
- [153] Hatami-Marbini H, and Mofrad MR. Cytoskeletal mechanics and cellular mechanotransduction: a molecular perspective. In Cellular and Biomolecular Mechanics and Mechanobiology Springer Berlin Heidelberg. 2011; 3-27.
- [154] Haugh JM. Deterministic model of dermal wound invasion incorporating receptor-mediated signal transduction and spatial gradient sensing. *Biophys J* 2006;90:2297-2308.
- [155] Hendriks F. et al. A numerical-experimental method to characterize the non-linear mechanical behaviour of human skin. *Skin Res Technol.* 2003;9(3):274-283.
- [156] S.P. Herbert, D.Y. Stainier. Molecular control of endothelial cell behaviour during blood vessel morphogenesis. *Nat Rev Mol Cell Biol.* 2011;12: 551564.
- [157] Hiep V, Keriven P, Labatut P and Pons JP. Towards high-resolution large-scale multi view stereo. *IEEE Conference on CVPR.* 2009.
- [158] Himpel G, Kuhl E, Menzel A, Steinmann P. Computational modeling of isotropic multiplicative growth. *Comp Mod Eng Sci.* 2005;8:119-134.
- [159] Himpel G, Menzel A, Kuhl E, Steinmann P. Time-dependent fibre reorientation of transversely isotropic continua - Finite element formulation and consistent linearization. *Int J Num Meth Eng.* 2008;73:1413-1433.
- [160] Holzapfel GA, Eberlein R, Wriggers P and Weizsäcker W. Large strain analysis of soft biological membranes: Formulation and finite element analysis. *Comput Methods Appl Mech Eng.* 1996; 132(1), 45-61.

- [161] Holzapfel GA, Gasser TC, Ogden RW. A new constitutive framework for arterial wall mechanics and a comparative study of material models. *J Elast.* 61:1-48,2000. *Comput Methods Appl Mech Eng.* 1996;132:45-61.
- [162] Holzapfel GA and Ogden RW. Constitutive modeling of arteries. *Proc R Soc A.* 2010;466:1551-1597.
- [163] Hsu MC, Kamensky D, Bazilevs Y, Sacks MS and Hughes TJR. Fluid-structure interaction analysis of bioprosthetic heart valves: significance of arterial wall deformation. *Comp Mech.* 2014;54:1055-1071.
- [164] Hughes TJR and Liu WK. Nonlinear finite element analysis of shells: Part I. Three dimensional shells. *Comput Methods Appl Mech Eng.* 1981; 26: 331-362.
- [165] Hughes, TJR and Carnoy E. Nonlinear finite element shell formulation accounting for large membrane strains. *Comput Methods Appl Mech Eng.* 1983;39:69-82.
- [166] Hughes, TJ. The finite element method: Linear static and dynamic finite element analysis. *Prentice Hall Inc. Englewood Cliffs, NJ.* 1987.
- [167] Hughes TJ, Cottrell JA and Bazilevs Y. Isogeometric analysis: CAD, finite elements, NURBS, exact geometry and mesh refinement. *Comput Methods Appl Mech Eng.* 2005;194(39), 4135-4195.
- [168] Humphrey JD, Strumpf RK and Yin FC. A constitutive theory for biomembranes: application to epicardial mechanics. *J Biomech Eng.* 1992; 114: 461-466.
- [169] Humphrey JD. Computer methods in membrane biomechanics. *Comput Methods Biomed Eng.* 1998;1(3): 171-210.
- [170] Humphrey J. Cardiovascular tissue mechanics: Cells, tissues, and organs. *Springer.* 2002.
- [171] Humphrey JD. Review Paper: Continuum biomechanics of soft biological tissues *Proc R Soc Lond A.* 2003;459:3-46.
- [172] P.J. Hunter, T.K. Borg. Integration from proteins to organs: the Physiome Project. *Nat Rev Mol Cell Biol.* 2001; 4: 237243.

- [173] Ingram PJ, Stumpf MP, and Stark J. Network motifs: structure does not determine function. *BMC Genomics.* 2006; 7(1), 108.
- [174] Insall RH. Understanding eukaryotic chemotaxis: a pseudopod-centred view. *Nat Rev Mol Cell Biol.* 2010;11:453-8.
- [175] Jaalouk DE, Lammerding J. Mechanotransduction gone awry. *Nature Rev Mol Cell Bio.* 2009;10:63-73.
- [176] Javierre E, Vermolen FJ, Vuik C, Zwaag S. A mathematical analysis of physiological and morphological aspects of wound closure. *J Math Biol.* 2008;59:605-30.
- [177] E. Javierre, F.J. Vermolen, C. Vuik, S. Zwaag. A mathematical analysis of physiological and morphological aspects of wound closure. *J Math Biol.* 2009; 59: 605-630.
- [178] E. Javierre, P. Moreno, M. Doblare, J.M. Garcia-Aznar. Numerical modeling of a mechano-chemical theory for wound contraction analysis. *Int J Solids Struct.* 2009; 46: 3597-3606.
- [179] Javili A, Steinmann P. On the thermodynamics of solids with boundary structures. *Int J Solids & Structures.* 2010;47:3245-3253.
- [180] Jepps OG, Dancik Y, Anissimov YG, and Roberts MS. Modeling the human skin barrier: Towards a better understanding of dermal absorption. *Adv Drug Deliv Rev.* 2013; 65(2): 152-168.
- [181] Johnson PE, Kernahan DA, Bauer BS Dermal and epidermal response to soft-tissue expansion in the pig. *Plast Reconst Surg.* 1988; 81:390-395.
- [182] Jor JWY, Nash MP, Nielsen PMF and Hunter PJ. Estimating material parameters of a structurally based constitutive relation for skin mechanics. *Biomech Model Mechanobiol.* 2010;10:767-778.
- [183] Jor JW, Nielsen PM, Nash MP, and Hunter PJ. Modelling collagen fibre orientation in porcine skin based upon confocal laser scanning microscopy. *Skin Res Technol.* 2011; 17(2), 149-159.
- [184] Jor JWY, Parker MD, Taberner AJ, Nash MP and Nielsen PMF. Computational and experimental characterization of skin mechanics: Identifying current challenges

- and future directions. *Wiley Interdisciplinary Reviews: Systems Biology and Medicine.* 2013; 5:539-556.
- [185] Joss GS, Zoltie N, Chapman P. Tissue expansion technique and the transposition flap. *Brit J Plast Surg* 1990;43:328-333.
- [186] Kaplan EN. The risk of malignancy in large congenital nevi. *Plast Reconstr Surg.* 1974;53:421-428.
- [187] Khalatbari B, Bakhshaeekia A. Ten-year experience in face and neck unit reconstruction using tissue expanders. *Burns.* 2013; 39(3):522-527.
- [188] Kiendl J, Bletzinger KU, Linhard J and Wüchner R. Isogeometric shell analysis with Kirchhoff-Love elements. *Comput Methods Appl Mech Eng.* 2009; 198: 3902-3914.
- [189] Kiendl J, Bazilevs Y, Hsu MC, W chner R and Bletzinger KU. The bending strip method for isogeometric analysis of Kirchhoff-Love shell structures comprised of multiple patches. *Comput Methods Appl Mech Eng.* 2010; 199(37), 2403-2416.
- [190] Kiendl J, Schmidt R, Wuchner R, and Bletzinger, KU. Isogeometric shape optimization of shells using semi-analytical sensitivity analysis and sensitivity weighting. *Comput Methods Appl Mech Eng.* 2014; 274: 148-167.
- [191] Kim H, Chandran KB, Sacks MS and Lu J. An experimentally derived stress resultant shell model for heart valve dynamic simulations. *Ann Biomed Eng.* 2007; 35(1): 30-44.
- [192] Kim DH, Lu N, Ma R, Kim YS, Kim RH, Wang S, Wu J, Won SM, Tao H, Islam A, Yu KJ, KimT, Chowdhury R, Ying M, Xu L, Li M, Chung HJ, Keum H, McCormick M, Liu P, Zhang YW, Omenetto FG, Huang Y, Coleman T, and Rogers JA. Epidermal electronics. *Science.* 2011; 333(6044): 838-843.
- [193] H. Kitano. Computational systems biology. *Nature.* 2002; 420: 206210.
- [194] Klinkel S, and Govindjee S. Using finite strain 3D-material models in beam and shell elements. *Eng Comp.* 2012; 19(8): 902-921.
- [195] Knighton D, Hunt T, Scheuenstuhl H, Halliday B, Werb Z, Banda M. Oxygen tension regulates the expression of angiogenesis factor by macrophages. *Science.* 1983;221:128-35.

- [196] Ko KS, and McCulloch CA. Intercellular mechanotransduction: cellular circuits that coordinate tissue responses to mechanical loading. *Biochem Biophys Res Commun.* 2001; 285(5), 1077-1083.
- [197] Kobbelt LP, Vorsatz J, Labsik U, Seidel HP. A shrink wrapping approach to remeshing polygonal surfaces. *Comp Graph Forum.* 1999;18:119-130.
- [198] Kohl P, and Noble D. Systems biology and the virtual physiological human. *Mol Syst Biol.* 2009; 5(1): 292.
- [199] Kroon M, Holzapfel GA. A model for saccular cerebral aneurysm growth by collagen fibre remodelling. *J Theor Bio.* 2007;247:775-787.
- [200] Kroon W, Delhaas T, Arts T, Bovendeerd P. Computational modeling of volumetric soft tissue growth: Application to the cardiac left ventricle. *Biomech Model Mechanobio.* 2009;8:310-309.
- [201] Kuhl E, Steinmann P. Mass- and volume specific views on thermodynamics for open systems. *Proc Royal Soc.* 2003;459:2547-2568.
- [202] Kuhl E, Steinmann P. On spatial and material settings of thermohyperelstodynamics for open systems. *Acta Mech.* 2003;160:179-217.
- [203] Kuhl E, Menzel A, Steinmann P. Computational modeling of growth - A critical review, a classification of concepts and two new consistent approaches. *Comp Mech.* 2003;32:71-88.
- [204] Kuhl E, Steinmann P. Computational modeling of healing - An application of the material force method. *Biomech Model Mechanobio.* 2004;2:187-203.
- [205] Kuhl E, Garikipati K, Arruda EM, Grosh K. Remodeling of biological tissue: Mechanically induced reorientation of a transversely isotropic chain network. *J Mech Phys Solids.* 2005;53:1552-1573.
- [206] Kuhl E, Menzel A, Garikipati K. On the convexity of transversely isotropic chain network models. *Phil Mag.* 2006;86:3241-3258.
- [207] Kuhl E, Maas R, Himpel G, Menzel A. Computational modeling of arterial wall growth: Attempts towards patient-specific simulations based on computer tomography. *Biomech Mod Mechanobio.* 2007;6:321-331.

- [208] Kuhl E, Holzapfel GA. A continuum model for remodeling in living structures. *J Mat Sci.* 2007;2:8811-8823.
- [209] Kuhl E Growing matter - A review of growth in living systems. *J Mech Behavior Biomed Mat.* 2014; 29:529-543.
- [210] Kusuma S, Vuthoori RK, Piliang M, and Zins JE. Skin anatomy and Physiology. In Plastic and Reconstructive Surgery (pp. 161-171). *Springer London.* 2010.
- [211] Kvisttedal YA, Nielsen PMF. Estimating material parameters of human skin in vivo. *Biomech Mod Mechanobio.* 2009;8:1-8.
- [212] Kyriacou, SK, Humphrey JD and Schwab C. Finite element analysis of nonlinear orthotropic hyperelastic membranes. *Comput Mech.* 1996;18:269-278.
- [213] Lamers E, Van Kempen, THS, Baaijens FPT, Peters GWM, and Oomens CWJ. Large amplitude oscillatory shear properties of human skin. *J Mech Behav Biomed Mat.* 2013; 28, 462-470.
- [214] Langer K. Zur Anatomie und Physiologie der Haut. I. Über die Spaltbarkeit der Cutis. Sitzungsbericht der Mathematisch-naturwissenschaftlichen Classe der Kaiserlichen Academie der Wissenschaften. 1861;44:19.
- [215] On the anatomy and physiology of the skin. I. The cleavability of the cutis. (Translated from Langer, K. (1861). Zur Anatomie und Physiologie der Haut. I. Über die Spaltbarkeit der Cutis. Sitzungsbericht der Mathematisch-naturwissenschaftlichen Classe der Kaiserlichen Academie der Wissenschaften, 44, 19.). *Br J Plast Surg.* 1978 Jan;31(1):3-8.
- [216] Langevin HM, Bouffard NA, Badger GJ, Iatridis JC, Howe AK. Dynamic fibroblast cytoskeletal response to subcutaneous tissue stretch ex vivo and in vivo. *Am J Physiol Cell Physiol.* 2005;288:C747C756.
- [217] Lanir Y, Fung YC. Two-dimensional mechanical properties of rabbit skin II Experimental results. *J Biomech.* 1974;7:171182.
- [218] A structural theory for the homogeneous biaxial stress-strain relationships in flat collagenous tissues *J Biomech.* 1979;12:423-436.

- [219] Lanir Y. Constitutive equations for fibrous connective tissues. *J Biomech* 1983; 16:1-12.
- [220] Lapeer RJ, Gasson PD and Karri V. Simulating plastic surgery: From human skin tensile tests, through hyperelastic finite element models to real-time haptics. *Prog Biophys Mol Bio.* 2010;103:208-216.
- [221] Laurent GJ. Dynamic state of collagen: pathways of collagen degradation in vivo and their possible role in regulation of collagen mass. *Am J Physiol Cell Physiol.* 1987; 252:1-9.
- [222] Lee EH. Elastic-plastic deformation at finite strains. *J Appl Mech.* 1969;36:1-6.
- [223] Levi K, Kwan A, Rhines AS, Gorcea M, Moore DJ, Dauskardt RH. Emollient molecule effects on the drying stresses in human stratum corneum. *Brit J Dermatol.* 2010;163:695-703.
- [224] Levine HA, Sleeman BD. Mathematical modeling of the onset of capillary formation initiating angiogenesis. *J Math Biol.* 2001;42:195-238.
- [225] Lhuillier M, Quan L. A quasi-dense approach to surface reconstruction from uncalibrated images. *IEEE T Pattern Anal* 2005;27:418-433.
- [226] Li B, Cao YP, Feng XQ, Gao H. Surface wrinkling of mucosa induced by volumetric growth: Theory, simulation and experiment. *J Mech Phys Solids.* 2011;59:758-774.
- [227] Lim KH, Jeyapalina S, Ho HN, Chew CM, Chen PCY, Teo CL and Lim BH Non-invasive prediction of skin flap shrinkage: A new concept based on animal experimental evidence. *J Biomech.* 2008; 41:1668-1674.
- [228] Limbert G, Simms C. Special issue on skin mechanobiology. *J Mech Beh Biomed Mat.* 2013;28:395-396.
- [229] Liu SQ, and Fung YC. Zero-stress states of arteries. *J Biomech Eng.* 1988; 110(1), 82-84.
- [230] Liu SQ, Fung YC Relationships between hypertension, hypertrophy, and opening angle of zero-stress state of arteries following aortic constriction. *J Biomech Eng.* 1989; 111:325-335.

- [231] LoGiudice J, Gosain AK. Pediatric tissue expansion: Indications and complications. *J Craniofac Surg.* 2003;14:866-872.
- [232] Lott-Crumpler D. Optimal patterns for suturing wounds of complex shapes to foster healing. *J Biomech.* 2001;34(1):51-58
- [233] Lubarda A, Hoger A. On the mechanics of solids with a growing mass. *Int J Solids & Structures.* 2002;39:4627-4664.
- [234] Lubarda VA. Constitutive theories based on the multiplicative decomposition of deformation gradient: Thermoelasticity, elastoplasticity and biomechanics. *Appl Mech Rev.* 2004;57:95108.
- [235] Maggelakis SA. A mathematical model of tissue replacement during epidermal wound healing. *Appl Math Model* 2003;27:189-196.
- [236] Mahmud J, Holt CA, Evans SL. An innovative application of a small-scale motion analysis technique to quantify human skin deformation in vivo. *J Biomech.* 2010; 43:1002-1006.
- [237] P.K. Maini, D.L. McElwain, D.I. Leavesley. Traveling wave model to interpret a wound-healing cell migration assay for human peritoneal mesothelial cells. *Tissue Eng.* 2004; 10: 475482.
- [238] Manders EK, Schenden MJ, Furrey JA, Hetzler PT, Davis TS, Graham WP. Soft-tissue expansion: concepts and complications. *Plast Reconstr Surg.* 1984; 74:493-507.
- [239] Marcus J, Horan D, Robinson J. Tissue expansion: Past, present and future. *J Am Acad Dermatol.* 1990; 23:813-825.
- [240] P. Martin. Wound healing aiming for perfect skin regeneration. *Science.* 1997; 276: 7581.
- [241] Martin C, and Sun W. Simulation of long-term fatigue damage in bioprosthetic heart valves: effects of leaflet and stent elastic properties. *Biomech Mod Mechanobiol.* 2014; 13(4): 759-770.
- [242] May-Newman K and Yin FCP. A constitutive law for mitral valve tissue. *J Biomech Eng.* 1998; 120(1): 38-47.

- [243] Mazza E, Papes O, Rubin MB, Bodner SR, Binur NS. Nonlinear elastic-viscoplastic constitutive equations for aging facial tissues. *Biomech Model Mechanobiol.* 2005;4:178-189.
- [244] Mazza E, Nava A, Bauer M, Winter R, Bajka M, Holzapfel GA. Mechanical properties of the human uterine cervix: An in vivo study. *Med Im Anal.* 2006;125-136.
- [245] Mazza E, Papes O, Rubin MB, Bodner SR, Binur NS. Simulation of the aging face. *J Biomech Eng.* 2007;129:619-623.
- [246] S. McDougall, J. Dallon, J. Sherratt, P. Maini. Fibroblast migration and collagen deposition during dermal wound healing: mathematical modelling and clinical implications. *Philos Transact A Math Phys Eng Sci.* 2006; 364: 13851405.
- [247] McGrath JA, Eady RAJ, and Pope FM. Anatomy and organization of human skin. *Rook's Textbook of Dermatology.* 2008; Seventh Edition, 45-128.
- [248] McMahon J, Goriely A. Spontaneous cavitation in growing elastic membranes. *Math Mech Solids.* 2010;15:57-77.
- [249] Menzel A. Modelling of anisotropic growth in biological tissues - A new approach and computational aspects. *Biomech Model Mechanobiol.* 2005;3:147-171.
- [250] Menzel A. A fibre reorientation model for orthotropic multiplicative growth. *Biomech Model Mechanobiol.* 2007;6:303-320.
- [251] Menzel A and Kuhl E Frontiers in growth and remodeling. *Mech Res Commu.* 2012; n 42:1-14.
- [252] J. Mergheim, P. Steinmann. Phenomenological modelling of self-healing polymers based on integrated healing agents. *Comp Mech.* 2013; 52: 681-892.
- [253] Merks RM, and Glazier JA. A cell-centered approach to developmental biology. *Physica A: Statistical Mechanics and its Applications.* 2005; 352(1): 113-130.
- [254] Merodio J, Ogden RW. Material instabilities in fiber-reinforced nonlinearly elastic solids under plane deformation. *Arch Mech.* 2002;54:525-552.

- [255] Merodio J, Ogden RW. Instabilities and loss of ellipticity in fiber-reinforced compressible non-linearly elastic solids under plane deformation *Int J Solids & Struct.* 2003;40:4707-4727.
- [256] Meyer W, Schwarz R, Neurand K. The skin of domestic mammals as a model for the human skin, with special reference to the domestic pig. *Curr Probl Dermatol.* 1978;7:39-52.
- [257] Meyer W, Neurand K, Radke B Elastic fibre arrangement in the skin of the pig. *Arch Dermatol Res.* 1981; 270:391-401.
- [258] Meyer W, Neurand K, Radke B Collagen fibre arrangement in the skin of the pig. *J Anat* 1982; 134:139-148.
- [259] Mi Q, Riviere B, Clermont G, Steed DL and Vodovotz Y. Agent-based model of inflammation and wound healing: insights into diabetic foot ulcer pathology and the role of transforming growth factor-beta1 *Wound Repair Regen.* 2007; 15: 671-682.
- [260] Miehe C. A constitutive frame of elastoplasticity at large strains based on the notion of a plastic metric. *Int J Solids & Struct.* 1998;30:3859-3897.
- [261] Miehe C, Göktepe S, Lulei F. A micro-macro approach to rubber-like materials - Part I: The non-affine micro-sphere model of rubber elasticity *J Mech Phys Solids.* 2004;52:2617-2660.
- [262] Milde F, Bergdorf M. A hybrid model for three-dimensional simulations of sprouting angiogenesis. *Biophys J.* 2008;95:3146-3160.
- [263] Montagna W, Yun JS. The skin of the domestic pig. *J Invest Dermatol.* 1964;42:11-21.
- [264] Montesano R, and Orci L. Transforming growth factor beta stimulates collagen-matrix contraction by fibroblasts: implications for wound healing. *Proc Nat Acad Sci.* 1988; 85(13), 4894-4897.
- [265] Morykwas MJ, Marks MW, Argenta LC. Surface area and tissue volume increases with differential expansion. *Ann Plast Surg.* 1992; 28:311-314.
- [266] Moulton DE, Goriely A. Circumferential buckling instability of a growing cylindrical tube. *J Mech Phys Solids.* 2011;59:525-537.

- [267] Murphy KE, McCue SW, McElwain DLS. Clinical strategies for the alleviation of contractures from a predictive mathematical model of dermal repair. *Wound Repair Regen.* 2012;20:194-202.
- [268] S.E. Mutsaers, J.E. Bishop, G. McGrouther, G.J. Laurent. Mechanisms of tissue repair: from wound healing to fibrosis. *Int J Biochem Cell Biol.* 1997; 29: 517.
- [269] Myers KM, Coudrillier B, Boyce BL, Nguyen TD. The inflation response of the posterior bovine sclera. *Acta Biomat.* 2010;6:4327-4335.
- [270] Neumann CG. The expansion of an area of skin by progressive distension of a subcutaneous balloon; use of the method for securing skin for subtotal reconstruction of the ear. *Plast Reconstr Surg.* 1959;19:124-130.
- [271] Ng PC, Murray SS, Levy, S, and Venter JC. (2009). An agenda for personalized medicine. *Nature.* 2009; 461(7265): 724-726.
- [272] Nguyen-Thanh N, Kiendl J, Nguyen-Xuan H, Wüchner R, Bletzinger KU, Bazilevs Y and Rabczuk, T. Rotation free isogeometric thin shell analysis using PHT-splines. *Comput Methods Appl Mech Eng.* 2011; 200(47): 3410-3424.
- [273] N AA et al. Automated Estimation of Collagen Fibre Dispersion in the Dermis and its Contribution to the Anisotropic Behaviour of Skin. *Ann Biomed Eng.* 2012;40:1666-1678.
- [274] Nikkhah D, Yildirimer L and Bulstrode NW Tissue expansion. Plastic and Reconstructive Surgery: Approaches and Techniques. *John Wiley & Sons.* 2015.
- [275] Noorlander ML, Melis P, Jonker A, and Van Noorden CJ. A quantitative method to determine the orientation of collagen fibers in the dermis. *J Histochem Cytochem.* 2002; 50(11): 1469-1474.
- [276] Notman R, and Anwar J. Breaching the skin barrier: Insights from molecular simulation of model membranes. *Adv Drug Deliv Rev.* 2013; 65(2), 237-250.
- [277] Ogawa R. Keloid and hypertrophic scarring may result from a mechanoreceptor or mechanosensitive nociceptor disorder. *Med Hypotheses.* 2008;71:493-500.

- [278] Ogawa R, Pkai K, Tokumura F, Mori K, Ohmori Y, Huang C, Hyakusoku H, Akaishi S. The relationship between skin stretching/contraction and pathologic scarring: The important role of mechanical forces in keloid generation. *Wound Rep Reg.* 2012;20:149-157.
- [279] Ogden RW. Large deformation isotropic elasticity - On the correlation of theory and experiment for incompressible rubberlike solids. *Proc Royal Soc London - A Math Phys Sci.* 1972;326:565-584.
- [280] Ogden RW. Recent advances in the phenomenological theory of rubber elasticity. *Rubber Chem Technol.* 1986;59:361-383.
- [281] Olsen L, Sherratt JA and Maini P. A mechanochemical model for adult dermal wound contraction: On the permanence of the contracted tissue displacement profile. *J Theor Bio.* 1995; 177:113-128
- [282] Olsen L, Sherratt JA, Maini PK. A mathematical model for fibro-proliferative wound healing disorders. *Bull Math Biol.* 1996;58:787-808.
- [283] O.O. Olutoye, X. Zhu, D.L. Cass, C.W. Smith. Neutrophil recruitment by fetal porcine endothelial cells: implications in scarless fetal wound healing. *Pediatr Res.* 2005; 58: 1290-1294.
- [284] Owen MR, Byrne HM, Lewis CE. Mathematical modelling of the use of macrophages as vehicles for drug delivery to hypoxic tumour sites. *J Theor Biol.* 2004;226:377-91.
- [285] Pailler-Mattei C, Bec S, Zahouani H. In vivo measurements of the elastic mechanical properties of human skin by indentation tests. *Med Eng Phys.* 2008;30:599-606.
- [286] Pamplona DC, Carvalho CR Characterization of human skin through skin expansion. *J Mech Mat Struct.* 2012; 7:641-655.
- [287] Pamplona DC, Mota DEJS Numerical and experimental analysis of inflating a circular hyperelastic membrane over a rigid and elastic foundation. *Int J Mech Sci.* 2012; 65:18-23.
- [288] Pamplona DC, Velloso RQ, Radwanski HN. On skin expansion. *J Mech Beh Biomed Mat.* 2014; 29:655-662.

- [289] Painter KJ. Continuous Models for cell migration in tissues and applications to cell sorting via differential chemotaxis. *Bull Math Biol.* 2009;71:1117-47.
- [290] Pang H, Shiwalkar AP, Madormo CM, Taylor RE, Andriacchi TP, Kuhl E. Computational modeling of bone density profiles in response to gait: A subject-specific approach. *Biomech Model Mechanobiol.* 2011; 11(3-4), 379-390.
- [291] Park SI, and Hodgins JK. Capturing and animating skin deformation in human motion. In ACM Transactions on Graphics (TOG) *ACM*. 2006; (Vol. 25, No. 3, pp. 881-889).
- [292] J. Paterno, I.N. Vial, V.W. Wong, K.C. Rustad, M. Sorkin, Y. Shi, K.A. Bhatt, H. Thangarajah, J.P. Glotzbach, G.C. Gurtner. Akt-mediated mechanotransduction in murine fibroblasts during hypertrophic scar formation. *Wound Repair Regen.* 2011; 19: 4958.
- [293] Pena E. Computational aspects of the numerical modelling of softening, damage and permanent set in soft biological tissues. *Comput Struct.* 2014;130:57-72.
- [294] Peirce SM. Multicellular simulation predicts microvascular patterning and in silico tissue assembly. *FASEB J.* 2004;18:731-733.
- [295] Peirce SM. Computational and mathematical modeling of angiogenesis. *Microcirculation.* 2008;15:739-51.
- [296] Peterson TA, Doughty E, and Kann MG. Towards precision medicine: advances in computational approaches for the analysis of human variants. *J Mol Biol.* 2013; 425(21): 4047-4063.
- [297] G.J. Pettet, H.M. Byrne, D.L. McElwain, J. Norbury. A model of wound-healing angiogenesis in soft tissue. *Math Biosci.* 1996; 136: 35-63.
- [298] Piegl L, Tiller W Curve and surface constructions using rational B-splines. *Comput Aided Des.* 1987; 19:485-498.
- [299] Pietramaggiori G, Liu P, Scherer SS, Kaipainen A, Prsa MJ, Mayer H, Newalder J, Alperovich M, Mentzer SJ, Konerding MA, Huang S, Ingber DE, Orgill DP Tensile forces stimulate vascular remodeling and epidermal cell proliferation in living skin. *Ann Surg.* 2007; 246:896-902.

- [300] Postlethwaite AE, Keski-Oja J, Moses HL, Kang AH. Stimulation of the chemotactic migration of human fibroblasts by transforming growth factor beta. *J Exp Med.* 1987;165:251-256.
- [301] Powell HM, McFarland KL, Butler DL, Supp DM, and Boyce ST. Uniaxial strain regulates morphogenesis, gene expression, and tissue strength in engineered skin. *Tissue Eng Part A.* 2010; 16(3), 1083-1092.
- [302] Prajapati RT, Eastwood M, Brown RA. Duration and orientation of mechanical loads determine fibroblast cyto-mechanical activation: Monitored by protease release. *Wound Repair Regen.* 2000;8:238-46.
- [303] Prajapati RT, Chavally-Mis B, Herbage D, Eastwood M, Brown RA. Mechanical loading regulates protease production by fibroblasts in three-dimensional collagen substrates. *Wound Repair Regen.* 2000;8:226-37.
- [304] Preziosi L, Tosin AR. Multiphase modelling of tumour growth and extracellular matrix interaction: Mathematical tools and applications. *J Math Bio.* 2009;58:625-656.
- [305] Prokop A, and Csukas B. Systems Biology: Integrative Biology and Simulation Tools (Vol. 1). *Springer Science & Business Media.* 2013.
- [306] Proksch E., Brandner J. and Jensen J. The skin: an indispensable barrier *Exp Dermatol.* 2008;17:1063-1072
- [307] Prot V, Skallerud B, and Holzapfel GA. Transversely isotropic membrane shells with application to mitral valve mechanics. Constitutive modelling and finite element implementation. *Int J Numer Meth Eng.* 2007;71:987-1008.
- [308] Purnell CA, Gart MS, Buganza Tepole A, Tomaszewski JP, Topczewska JM, Kuhl E, Gosain AK. Determining the differential effects of stretch and growth in tissue expanded skin. *submitted for publication.* 2015.
- [309] Quaba AA, Wallace AF. The incidence of malignant melanoma (0 to 15 years of age) arising in large congenital nevocellular nevi. *Plast Reconstr Surg.* 1986;78:174-178.
- [310] A.A. Qutub, F. Mac Gabhann, E.D. Karagiannis, P. Vempati, A.S. Popel. Multiscale models of angiogenesis. *IEEE Eng Med Biol Mag.* 28 (2009) 1431.

- [311] Radovan C. Breast reconstruction after mastectomy using the temporary expander. *Plast Reconstr Surg.* 1982;69:195-208.
- [312] Raghupathy R, and Barocas VH. A closed-form structural model of planar fibrous tissue mechanics. *J Biomech.* 2009; 42(10), 1424-1428.
- [313] Rajadhyaksha M, Grossman M, Esterowitz D, Webb RH, and Anderson RR. In vivo confocal scanning laser microscopy of human skin: melanin provides strong contrast. *J Invest Dermatol.* 1995; 104(6): 946-952.
- [314] Rausch MK, Dam A, Göktepe S, Abilez OJ, Kuhl E. Computational modeling of growth: Systemic and pulmonary hypertension in the heart. *Biomech Model Mechanobiol.* 2011; 10(6), 799-811.
- [315] Rausch MK, Bothe W, Kvitting JP, Göktepe S, Miller DC, Kuhl E. In vivo dynamic strains of the ovine anterior mitral valve leaflet. *J Biomech.* 2011;44:1149-1157.
- [316] Rausch MK, Famaey N, O'Brien Shultz T, Bothe W, Miller DC, and Kuhl E. Mechanics of the mitral valve: A critical review, an in vivo parameter identification, and the effect of prestrain. *Biomech Mod Mechanobiol.* 2013;12:1053-1071.
- [317] Rausch MK, Kuhl E. On the effect of prestrain and residual stress in thin biological membranes. *J Mech Phys Solids.* 2013;61:1955-1969.
- [318] Rausch MK, Kuhl E. On the mechanics of growing thin biological membranes. *J Mech Phys Solids.* 2014;63:128-140.
- [319] Rivera R, LoGiudice J, Gosain AK. Tissue expansion in pediatric patients. *Clin Plast Surg.* 2005;32:35-44.
- [320] Rodriguez EK, Hoger A, McCulloch AD. Stress-dependent finite growth in soft elastic tissues. *J Biomech.* 1994;27:455-467.
- [321] Rose EH, Ksander GA, Vistnes LM Skin tension lines in the domestic pig. *Plast Reconstr Surg.* 1976; 57:729-732.
- [322] Roudaut Y, Lonigro A, Coste B, Hao J, Delmas P, and Crest M. Touch sense: functional organization and molecular determinants of mechanosensitive receptors. *Channels.* 2012; 6(4): 234-245.

- [323] A.D. Rouillard, J.W. Holmes. Mechanical regulation of fibroblast migration and collagen remodeling in healing myocardial infarcts. *J Physiol.* 2012; 590: 4585-4602.
- [324] Roy S, Biswas S, Khanna S, Gordillo G, Bergdall V, Green J, Marsh CB, Gould LJ and Sen CK Characterization of a preclinical model of chronic ischemic wound. *Physiological genomics.* 2009; 37: 211-224.
- [325] Sacks MS, He Z, Baijens L, Wanant S, Shah P, Sugimoto H, and Yoganathan AP. Surface strains in the anterior leaflet of the functioning mitral valve. *Ann Biomed Eng.* 2002; 30(10): 1281-1290.
- [326] P. Saez, E. Pena, M.A. Martinez, E. Kuhl. Mathematical modeling of collagen turnover in biological tissue. *J Math Bio.* 2013; 67: 1765-1793.
- [327] P. Saez, E. Pena, M.A. Martinez, E. Kuhl. Computational modeling of hypertensive growth in the human carotid artery. *Comp Mech.* 2014; 53: 1183-1196.
- [328] Sand P, McMillan L, and Popovic J. Continuous capture of skin deformation. In ACM Transactions on Graphics (TOG) *ACM.* 2003;(Vol. 22, No. 3, pp. 578-586).
- [329] Sander EA, Barocas VH, and Tranquillo RT. Initial fiber alignment pattern alters extracellular matrix synthesis in fibroblast-populated fibrin gel cruciforms and correlates with predicted tension. *Ann Biomed Eng.* 2011; 39(2), 714-729.
- [330] Santoro MM, and Gaudino G. Cellular and molecular facets of keratinocyte reepithelialization during wound healing. *Exp Cell Res.* 2005; 304(1), 274-286.
- [331] Sauer RA, Duong TX and Corbett CJ. A computational formulation for constrained solid and liquid membranes considering isogeometric finite elements. *Comput Methods Appl Mech Eng.* 2014; 271: 48-68.
- [332] Schmid H, Pauli L, Paulus A, Kuhl E, Itskov M. Consistent formulation of the growth process at the kinematic and constitutive level for soft tissues composed of multiple constituents. *Comp Meth Biomech Biomed Eng.* 2012;15:547-561
- [333] Schreml S, Szeimies RM, Prantl L, Karrer S, Landthaler M, and Babilas P. Oxygen in acute and chronic wound healing. *Brit J Dermatol.* 2010; 163(2), 257-268.

- [334] R.C. Schugart, A. Friedman, R. Zhao, C.K. Sen. Wound angiogenesis as a function of tissue oxygen tension: A mathematical model. *Proc Nat Acad Sci.* 2008;105: 2628-2633.
- [335] Seitz SM, Curless B, Diebel J, Scharstein D, Szeliski R. A comparison and evaluation of multi-view stereo reconstruction algorithms. *IEEE Conference on Computer Vision and Pattern Recognition.* 2006;1:519-528.
- [336] Sen CK. Wound healing essentials: Let there be oxygen. *Wound Repair Regen* 2009;17:1-18.
- [337] Serup J, Jemec GBE, Grove GL. Handbook of Non-Invasive Methods and the Skin. *Informa Healthcare.* 2003.
- [338] J.A. Sherratt, J.D. Murray. Models of epidermal wound healing. *Proc Royal Soc B Bio Sci.* 1990; 241: 29-36.
- [339] Sherratt JA, Murray JD. Mathematical analysis of a basic model for epidermal wound healing. *J Math Biol.* 1991;29:389-404.
- [340] Sherratt JA. Chemotaxis and chemokinesis in eukaryotic cells: the Keller-Segel equations as an approximation to a detailed model. *Bull Math Biol.* 1994; 56(1), 129-146.
- [341] Shively RE. Skin expander volume estimator. *Plast Reconstr Surg.* 1986;77:482-483.
- [342] Silver FH, Siperko LM, Seehra GP. Mechanobiology of force transduction in dermal tissue. *Skin Res Tech.* 2003;9:3-23.
- [343] Silver FH. Mechanosensing and mechanochemical transduction in extracellular matrix: Biological, chemical, engineering, and physiological aspects. *Springer Science & Business Media.* 2006.
- [344] Simpson CL, Patel DM, Green KJ. Deconstructing the skin. Cytoarchitectural determinants of epidermal morphogenesis. *Nature Rev Mol Cell Bio.* 2011;12:565-580.
- [345] Simo JC, Miehe C. Associative coupled thermoplasticity at finite strains: Formulation, numerical analysis and implementation. *Comp Meth Appl Mech Eng.* 1992;98:41-104.
- [346] SIMULIA. Abaqus 6.9 Documentation [Internet]. Available from: <http://abaqusdoc.ucalgary.ca/v6.9/index.html>

- [347] Skalak R, Tozeren A, Zarda RP and Chien S. Strain energy function of red blood cell membranes. *Biophysical Journal* 1973; 13(3): 245-264.
- [348] Slabaugh G, Culbertson B. A survey of methods for volumetric scene reconstruction from photographs. *Int WS on Volume Graphics*. 2001.
- [349] Sleeman BD, Levine HA. Partial differential equations of chemotaxis and angiogenesis. *Math Meth Appl Sci* 2001;24:405-26.
- [350] Smalls LK, Randall WR and Visscher MO. Effect of dermal thickness, tissue composition, and body site on skin biomechanical properties. *Skin Res Technol*. 2006;12:43-49.
- [351] Socci L, Rennati G, Gervaso F, Vena P. An axisymmetric computational model of skin expansion and growth. *Biomech Model Mechanobiol*. 2007;6:177-188.
- [352] J. Southern, J. Pitt-Francis, J. Whiteley, D. Stokeley, H. Kobashi, R. Nobes, Y. Kadooka, D. Gavaghan. Multi-scale computational modelling in biology and physiology. *Prog Biophys Mol Biol*. 2008; 96: 6089.
- [353] Steenfos HH. Growth factors and wound healing. *Scand J Plast Reconstr Hand Surg*. 1994;28:95-105.
- [354] Stokes CL, Lauffenburger DA. Analysis of the roles of microvessel endothelial cell random motility and chemotaxis in angiogenesis. *J Theor Biol*. 1991;152:377-403.
- [355] Stretcha C, von Hansen W, Van Gool L, Fua P, Thoennessen U. On benchmarking camera calibration and multi view stereo for high resolution imagery. *IEEE Conference on CVPR*. 2008.
- [356] Sullivan TP, Eaglstein WH, Davis SC, Mertz P. The pig as a model for human wound healing. *Wound Repair Regen*. 2001;9:66-76.
- [357] Sun W and Sacks M. Finite element implementation of a generalized Fung-elastic constitutive model for planar soft tissues. *Biomech Model Mecanobiol*. 2005;4:190-199.
- [358] Sun T, Adra S, Smallwood R, Holcombe M, MacNeil S. Exploring hypotheses of the actions of TGF-beta1 in epidermal wound healing using a 3D computational multiscale model of the human epidermis. *PLoS ONE*. 2009;4:e8515.

- [359] Swat MH, Thomas GL, Belmonte JM, Shirinifard A, Hmeljak D, and Glazier JA. (2012). Multi-scale modeling of tissues using CompuCell3D. *Methods in cell biology* 2012; 110: 325.
- [360] Sze KY, Liu XH and Lo SH. Popular benchmark problems for geometric nonlinear analysis of shells. *Finite Elem Anal Des.* 2004;40:1551-1569.
- [361] Taber LA. Biomechanics of growth, remodeling and morphogenesis. *Appl Mech Rev.* 1995;48:487-545.
- [362] Taber LA, Eggers DW. Theoretical study of stress-modulated growth in the aorta. *J Theor Bio.* 1996;180:343-357.
- [363] Taber LA, Humphrey JD. Stress-modulated growth, residual stress, and vascular heterogeneity. *J Biomech Eng.* 2001;123:528-535.
- [364] Takei T, Mills I, Arai K, Sumpio BE. Molecular basis for tissue expansion: Clinical implications for the surgeon. *Plast Reconstr Surg.* 1998;102:247-258.
- [365] Tanaka RJ, and Ono M. Skin disease modeling from a mathematical perspective. *J Invest Dermatol.* 2013; 133(6): 1472-1478.
- [366] Taylor RL. FEAP - A Finite Element Analysis Program. *User Manual, Version 8.2,* University of California at Berkeley, 2008.
- [367] Taylor CA, and Figueroa CA. Patient-specific modeling of cardiovascular mechanics. *Annu Rev Biomed Eng.* 2009; 11: 109-134.
- [368] Taylor RE, Zheng C, Jackson PR, Doll JC, Chen JC, Holzbaur KRS, Besier T, Kuhl E. The phenomenon of twisted growth: Humeral torsion in dominant arms of high performance tennis players. *Comp Meth Biomech Biomed Eng.* 2009;12:83-93.
- [369] Taylor RL. FEAP - A Finite Element Analysis Program. *Version 8.3, User Manual,* University of California at Berkeley, 2011.
- [370] Taylor CA, Fonte TA, and Min JK. Computational fluid dynamics applied to cardiac computed tomography for noninvasive quantification of fractional flow reserve: scientific basis. *J Am Coll Cardiol.* 2013; 61(22): 2233-2241.

- [371] Tibbles PM. Hyperbaric-oxygen therapy. *New Engl J Med.* 1996;334:1642-1648.
- [372] Tomasek JJ, Gabbiani G, Hinz B, Chaponnier C, and Brown RA. Myofibroblasts and mechano-regulation of connective tissue remodelling. *Nature Rev Mol Cell Biol.* 2002; 3(5), 349-363.
- [373] Tong P, Fung YC. The stress-strain relationship for the skin. *J Biomech.* 1976;9:649-657.
- [374] Tonge TK, Atlan LS, Voo LM, Nguyen TD. Full-field bulge test for planar anisotropic tissues: Part I - Experimental methods applied to human skin tissue. *Acta Biomat.* 2013;9:5913-5925.
- [375] Tonge TK, Voo LM, Nguyen TD. Full-field bulge test for planar anisotropic tissues: Part II - A think shell method for determining material parameters and comparison of two distributed fiber modeling approaches. *Acta Biomat.* 2013;9:5926-5942.
- [376] Toutain CE, Brouchet L, Raymond-Letron I, et al. Prevention of skin flap necrosis by estradiol involves reperfusion of a protected vascular network. *Circ Res* 2009;104:245-254.
- [377] R.T. Tranquillo. Stochastic model of leukocyte chemosensory movement. *J Math Biol.* 1987; 25: 229-262.
- [378] Tranquillo R, Murray J (1992) Continuum model of fibroblast-driven wound contraction - inflammation-mediation. *J Theor Biol.* 1992; 158: 135-172.
- [379] R.T. Tranquillo, J.D. Murray. Continuum model of fibroblast-driven wound contraction: Inflammation-mediation. *Biomech Model Mechanobiol.* 2007; 158: 361-371.
- [380] Valdés JG. and Oñate E. Orthotropic rotation-free basic thin shell triangle. *Comput Mech.* 2009; 44(3): 363-375.
- [381] Valero C, Javierre E, Garcia-Aznar, JM, Menzel A, and Gomez-Benito MJ. Challenges in the modeling of wound healing mechanisms in soft biological tissues. *Ann Biomed Eng.* 2014; 1-12.
- [382] van der Kolk CA, McCann JJ, Knight KR, O'Brien BM. Some further characteristics of expanded tissue. *Clin Plast Surg.* 1987;14:447-453.

- [383] VanderKolk CA, McCann JJ, Mitchell GM, and O'Brien BM. (1988). Changes in area and thickness of expanded and unexpanded axial pattern skin flaps in pigs. *Br J Plast Surg.* 1988; 41(3): 284-293.
- [384] Vandiver R, Goriely A. Differential growth and residual stress in cylindrical elastic structures. *Phil Trans R Soc A.* 2009;367:3607-3630.
- [385] van Rappard JHA, Molenaar J, van Doorn K, Sonneveld GJ, Borghouts JMHM. Surface-area increase in tissue expansion. *Plast Reconstr Surg.* 1988;82:833-839.
- [386] T. Velnar, T. Bailey, V. Smrkolj. The wound healing process: an overview of the cellular and molecular mechanisms. *J Int Med Res.* 2009; 37: 15281542.
- [387] Verdier C, Etienne J, Duperray A, Preziosi L. Review: Rheological properties of biological materials. *Comptes Rendus Phys.* 2009;10:790-811.
- [388] Verhaegen PDH, van Zuijlen PPM, Pennings NM, van Marle J, Niessen FB, van der Horst CMAM, Middelkoop E. Differences in collagen architecture between keloid, hypertrophic scar, normotrophic scar, and normal skin: An objective histopathological analysis *Wound Rep Reg* 2009;17:649-656.
- [389] F.J. Vermolen, E. Javierre. Computer simulations from a finite-element model for wound contraction and closure. *J Tissue Viabil.* 2010; 19: 43-53.
- [390] F.J. Vermolen, E. Javierre. A finite-element model for healing of cutaneous wounds combining contraction, angiogenesis and closure. *J Math Bio.* 2012; 65: 967-996.
- [391] Vetter R, Stoop N, Jenni T, Wittel FK and Herrmann HJ. Subdivision shell elements with anisotropic growth. *Int J Numer Meth Eng.* 2013; 95(9): 791-810.
- [392] Y. Vodovotz, M. Csete, J. Bartels, S. Chang, G. An. Translational systems biology of inflammation. *PLoS Comput Biol.* 2008; 4: e1000014.
- [393] Y. Vodovotz. Translational systems biology of inflammation and healing. *Wound Repair Regen.* 2010; 18: 37.
- [394] Wadhams GH, Armitage JP. Making sense of it all: Bacterial chemotaxis. *Nat Rev Mol Cell Biol.* 2004;5:1024-37.

- [395] Wang JHC, and Thampatty BP. An introductory review of cell mechanobiology. *Biomech Model Mechanobiol.* 2006; 5(1), 1-16.
- [396] Wang JHC, Thampatty BP, Lin JS, Im HJ. Mechanoregulation of gene expression in fibroblasts. *Gene.* 2007; 391: 1-15
- [397] Weinberg EJ and Mofrad KM. A finite shell element for heart mitral valve leaflet mechanics, with large deformations and 3D constitutive material model. *J Biomech.* 2007;40:705:711.
- [398] Weintraub JL, Kahn DM. The timing of implant exchange in the development of capsular contracture after breast reconstruction. *Eplasty.* 2008;8:303-311.
- [399] Werner S and Grose R. Regulation of wound healing by growth factors and cytokines. *Physiol Rev.* 2003; 83: 835-870.
- [400] Whitcher FD. Simulation of in vivo loading conditions of nitinol vascular stent structures. *Comput Struct.* 1997;64:1005-11.
- [401] Winslow RL, Trayanova N, Geman D, and Miller MI. (2012). Computational medicine: translating models to clinical care. *Science Translational Medicine.* 2012; 4(158): 118rv11.
- [402] Wollina U, Berger U, Stolle C, Stolle H, Schubert H, Zieger M, Hippler C, Schumann D. Tissue expansion in pig skin - A histochemical approach. *Anat Histol Embryol.* 1992;21:101-11.
- [403] Wong VW, Akaishi S, Longaker MT, Gurtner GC. Pushing back: Wound mechanotransduction in repair and regeneration. *J Invest Dermatol.* 2011;131(11), 2186-2196.
- [404] Wong VW, Rustad KC, Akaishi S, Sorkin M, Glotzbach JP, Januszyk M, Nelson ER, Levi K, Paterno J, Vial IN, Kuang AA, Longaker MT, Gurtner GC. Focal adhesion kinase links mechanical force to skin fibrosis via inflammatory signaling. *Nat Med.* 2011;18:148-152.
- [405] Wong VW, Longaker MT, and Gurtner GC. Soft tissue mechanotransduction in wound healing and fibrosis. In Seminars in Cell & Developmental Biology. Academic Press. 2012; (Vol. 23, No. 9, pp. 981-986).

- [406] Wong VW, Levi K, Akaishi S, Schultz G, Dauskardt RH Scar Zones: Region-Specific Differences in Skin Tension May Determine Incisional Scar Formation. *Plast Reconstr Surg.* 2012; 129: 1272-1276.
- [407] Wu KS, van Osdol WW, Dauskardt RH. Mechanical properties of human stratum corneum: Effects of temperature, hydration, and chemical treatment. *Biomaterials.* 2006;27:785-795.
- [408] M.A. Wyczalkowski, V.D. Varner, L.A. Taber. Computational and experimental study of the mechanics of embryonic wound healing. *J Mech Beh Biomed Mat.* 2012; 28: 125-146.
- [409] Xu F, Lu TJ, and Seffen KA. Biothermomechanics of skin tissues. *J Mech Phys Solids.* 2008; 56(5): 1852-1884.
- [410] C. Xue, A. Friedman, C.K. Sen. A mathematical model of ischemic cutaneous wounds. *Proc Natl Acad Sci.* 2009; 106: 16782-16787.
- [411] Yagmur C, Akaishi S, Ogawa R, Guneren E. Mechanical receptor-related mechanisms in scar management: A review and hypothesis. *Plast Reconstr Surg.* 2010;126:426-34.
- [412] Yang C, Tang D, Haber I, Geva T, del Nido PJ. In vivo MRI-based 3D FSI RV/LV models for human right ventricle and patch design for potential computer-aided surgery optimization. *Comput Struct.* 2007;85:988-97.
- [413] Zaidi Z, and Lanigan SW. Dermatology in clinical practice. *Springer Science & Business Media.* 2010.
- [414] Zeng Y, Xu C, Yang J, Sun G, Xu X. Biomechanical comparison between conventional and rapid expansion of skin. *Brit Assoc Plast Surg.* 2003;56:660-666.
- [415] Zeng YJ, Liu YH, Xu CQ, Xu XH, Xu H, Sun GC Biomechanical properties of skin in vitro for different expansion methods. *Clinical Biomech.* 2004; 19:853-857.
- [416] Zide BM, Karp NS. Maximizing gain from rectangular tissue expanders. *J Plast Reconstr Surg* 1992;90:500-504.
- [417] Zöllner AM, Buganza Tepole A and Kuhl E. On the biomechanics and mechanobiology of growing skin. *J Theor Bio.* 2012;297:166-175.

- [418] Zöllner AM, Buganza Tepole A, Gosain AK, Kuhl E. Growing skin - Tissue expansion in pediatric forehead reconstruction. *Biomech Mod Mechanobio.* 2012;11:855-867.
- [419] Zöllner AM, Holland MA, Honda KS, Gosain AK, and Kuhl E. Growth on demand: reviewing the mechanobiology of stretched skin. *J Mech Behav Biomed.* 2013;28:495-509.